JPL Space Science and Technology Series
Joseph H. Yuen, Series Editor

Fundamentals of Electric Propulsion

Ion and Hall Thrusters

Dan M. Goebel
Ira Katz

WILEY

Fundamentals of Electric Propulsion

Fundamentals of Electric Propulsion

Ion and Hall Thrusters

Dan M. Goebel
Ira Katz
Jet Propulsion Laboratory
California Institute of Technology

A JOHN WILEY & SONS, INC., PUBLICATION

Copyright © 2008 by John Wiley & Sons, Inc. All rights reserved.

Published by John Wiley & Sons, Inc., Hoboken, New Jersey.
Published simultaneously in Canada.

No part of this publication may be reproduced, stored in a retrieval system, or transmitted in any form or by any means, electronic, mechanical, photocopying, recording, scanning, or otherwise, except as permitted under Section 107 or 108 of the 1976 United States Copyright Act, without either the prior written permission of the Publisher, or authorization through payment of the appropriate per-copy fee to the Copyright Clearance Center, Inc., 222 Rosewood Drive, Danvers, MA 01923, (978) 750-8400, fax (978) 750-4470, or on the web at www.copyright.com. Requests to the Publisher for permission should be addressed to the Permissions Department, John Wiley & Sons, Inc., 111 River Street, Hoboken, NJ 07030, (201) 748-6011, fax (201) 748-6008, or online at http://www.wiley.com/go/permission.

Limit of Liability/Disclaimer of Warranty: While the publisher and author have used their best efforts in preparing this book, they make no representations or warranties with respect to the accuracy or completeness of the contents of this book and specifically disclaim any implied warranties of merchantability or fitness for a particular purpose. No warranty may be created or extended by sales representatives or written sales materials. The advice and strategies contained herein may not be suitable for your situation. You should consult with a professional where appropriate. Neither the publisher nor author shall be liable for any loss of profit or any other commercial damages, including but not limited to special, incidental, consequential, or other damages.

For general information on our other products and services or for technical support, please contact our Customer Care Department within the United States at (800) 762-2974, outside the United States at (317) 572-3993 or fax (317) 572-4002.

Wiley also publishes its books in a variety of electronic formats. Some content that appears in print may not be available in electronic format. For information about Wiley products, visit our web site at www.wiley.com.

Library of Congress Cataloging-in-Publication Data is available.

ISBN 978-0-470-42927-3

Printed in the United States of America.

10 9 8 7 6 5 4 3 2 1

Contents

Note from the Series Editor	ix
Foreword	xi
Preface	xiii
Acknowledgments	xv
Chapter 1: Introduction	**1**
1.1 Electric Propulsion Background	2
1.2 Electric Thruster Types	3
1.3 Ion Thruster Geometry	6
1.4 Hall Thruster Geometry	6
1.5 Beam/Plume Characteristics	9
References	11
Chapter 2: Thruster Principles	**15**
2.1 The Rocket Equation	15
2.2 Force Transfer in Ion and Hall Thrusters	18
2.3 Thrust	21
2.4 Specific Impulse	25
2.5 Thruster Efficiency	27
2.6 Power Dissipation	30
2.7 Neutral Densities and Ingestion in Electric Thrusters	32
References	34
Problems	35
Chapter 3: Basic Plasma Physics	**37**
3.1 Introduction	37
3.2 Maxwell's Equations	38
3.3 Single Particle Motions	39
3.4 Particle Energies and Velocities	43
3.5 Plasma as a Fluid	46
3.5.1 Momentum Conservation	46
3.5.2 Particle Conservation	48
3.5.3 Energy Conservation	51
3.6 Diffusion in Partially Ionized Gases	54
3.6.1 Collisions	55
3.6.2 Diffusion and Mobility Without a Magnetic Field	60
3.6.3 Diffusion Across Magnetic Fields	66

3.7 Sheaths at the Boundaries of Plasmas 71
3.7.1 Debye Sheaths 73
3.7.2 Pre-Sheaths 76
3.7.3 Child–Langmuir Sheaths 79
3.7.4 Generalized Sheath Solution 81
3.7.5 Double Sheaths 84
3.7.6 Summary of Sheath Effects 86
References 88
Problems 89

Chapter 4: Ion Thruster Plasma Generators 91
4.1 Introduction 91
4.2 Idealized Ion Thruster Plasma Generator 93
4.3 DC Discharge Ion Thruster 100
4.3.1 Generalized 0-D Ring-Cusp Ion Thruster Model 102
4.3.2 Magnetic Multipole Boundaries 105
4.3.3 Electron Confinement 108
4.3.4 Ion Confinement at the Anode Wall 110
4.3.5 Ion and Excited Neutral Production 117
4.3.6 Neutral and Primary Densities in the Discharge Chamber 120
4.3.7 Power and Energy Balance in the Discharge Chamber 124
4.3.8 Discharge Loss 126
4.3.9 Discharge Stability 133
4.3.10 Recycling Behavior 137
4.3.11 Limitations of a 0-D Model 141
4.4 Kaufman Ion Thrusters 142
4.5 rf Ion Thrusters 148
4.6 Microwave Ion Thrusters 158
4.7 2-D Computer Models of the Ion Thruster Discharge Chamber 171
4.7.1 Neutral Atom Model 172
4.7.2 Primary Electron Motion and Ionization Model 176
4.7.3 Discharge Chamber Model Results 179
References 182
Problems 187

Chapter 5: Ion Thruster Accelerator Grids 189
5.1 Grid Configurations 190
5.2 Ion Accelerator Basics 196
5.3 Ion Optics 200
5.3.1 Ion Trajectories 200
5.3.2 Perveance Limits 204
5.3.3 Grid Expansion and Alignment 206
5.4 Electron Backstreaming 208
5.5 High-Voltage Considerations 216
5.5.1 Electrode Breakdown 217

5.5.2 Molybdenum Electrodes 218
5.5.3 Carbon–Carbon Composite Materials 221
5.5.4 Pyrolytic Graphite 223
5.5.5 Hold-off and Conditioning in Ion Thrusters 224
5.6 Ion Accelerator Grid Life 225
5.6.1 Grid Models 227
5.6.2 Barrel Erosion 230
5.6.3 Pits-and-Grooves Erosion 232
References 235
Problems 240

Chapter 6: Hollow Cathodes 243
6.1 Introduction 243
6.2 Cathode Configurations 248
6.3 Thermionic Electron Emitter Characteristics 251
6.4 Insert Region Plasma 256
6.5 Orifice Region Plasma 270
6.6 Hollow Cathode Thermal Models 281
6.7 Cathode Plume-Region Plasma 283
6.8 Hollow Cathode Life 292
6.8.1 Dispenser Cathodes in Insert Plasmas 293
6.8.2 Cathode Insert Temperature 296
6.8.3 Barium Depletion Model 298
6.8.4 Bulk-Material Insert Life 302
6.8.5 Cathode Poisoning 304
6.9 Keeper Wear and Life 306
6.10 Hollow Cathode Operation 309
References 315
Problems 321

Chapter 7: Hall Thrusters 325
7.1 Introduction 325
7.2 Thruster Operating Principles and Scaling 329
7.2.1 Crossed-Field Structure and the Hall Current 330
7.2.2 Ionization Length and Scaling 334
7.2.3 Potential and Current Distributions 337
7.3 Hall Thruster Performance Models 341
7.3.1 Hall Thruster Efficiency 341
7.3.2 Multiply Charged Ion Correction 345
7.3.3 Dominant Power Loss Mechanisms 347
7.3.4 Plasma Electron Temperature 357
7.3.5 Hall Thruster Efficiency (Dielectric Walls) 359
7.3.6 TAL Hall Thruster Efficiency (Metallic Walls) 363
7.3.7 Dielectric-Wall Versus Metallic-Wall Comparison 364
7.4 Channel Physics and Numerical Modeling 365

7.4.1 Hybrid Hall Thruster Models 366
7.4.2 Steady-State Modeling Results 372
7.4.3 Oscillations in Hall Thrusters 376
7.5 Hall Thruster Life 379
References 384
Problems 389

Chapter 8: Ion and Hall Thruster Plumes **393**
8.1 Introduction 393
8.2 Plume Physics 395
8.2.1 Plume Measurements 395
8.2.2 Flight Data .396
8.2.3 Laboratory Plume Measurements 398
8.3 Plume Models 400
8.3.1 Primary Beam Expansion 400
8.3.2 Neutral Gas Plumes 407
8.3.3 Secondary-Ion Generation 408
8.4 Spacecraft Interactions 410
8.4.1 Momentum of the Plume Particles 412
8.4.2 Sputtering and Contamination 413
8.4.3 Plasma Interactions with Solar Arrays 415
8.5 Interactions with Payloads 418
8.5.1 Microwave Phase Shift 418
8.5.2 Plume Plasma Optical Emission 419
References 422
Problems 424

Chapter 9: Flight Ion and Hall Thrusters **429**
9.1 Introduction 429
9.2 Ion Thrusters 429
9.3 Hall Thrusters 440
References 443

Appendices
A: Nomenclature 447
B: Gas Flow Unit Conversions and Cathode Pressure Estimates 463
C: Energy Loss by Electrons 467
D: Ionization and Excitation Cross Sections for Xenon 471
E: Ionization and Excitation Reaction Rates for Xenon in Maxwellian Plasmas 475
F: Electron Relaxation and Thermalization Times 479
G: Clausing Factor Monte Carlo Calculation 483

Index **487**

Note from the Series Editor

The Jet Propulsion Laboratory (JPL) Space Science and Technology Series broadens the range of the ongoing JPL Deep Space Communications and Navigation Series to include disciplines other than communications and navigation in which JPL has made important contributions. The books are authored by scientists and engineers with many years of experience in their respective fields, and lay a foundation for innovation by communicating state-of-the-art knowledge in key technologies. The series also captures fundamental principles and practices developed during decades of space exploration at JPL, and celebrates the successes achieved. These books will serve to guide a new generation of scientists and engineers.

We would like to thank the Office of the Chief Scientist and Chief Technologist for their encouragement and support. In particular, we would like to acknowledge the support of Thomas A. Prince, former JPL Chief Scientist; Erik K. Antonsson, former JPL Chief Technologist; Daniel J. McCleese, JPL Chief Scientist; and Paul E. Dimotakis, JPL Chief Technologist.

JOSEPH H. YUEN, Editor-in-Chief
JPL Space Science and Technology Series
Jet Propulsion Laboratory
California Institute of Technology

Foreword

I am very pleased to commend the Jet Propulsion Laboratory (JPL) Space Science and Technology Series, and to congratulate and thank the authors for contributing their time to these publications. It is always difficult for busy scientists and engineers, who face the constant pressures of launch dates and deadlines, to find the time to tell others clearly and in detail how they solved important and difficult problems, so I applaud the authors of this series for the time and care they devoted to documenting their contributions to the adventure of space exploration.

JPL has been NASA's primary center for robotic planetary and deep-space exploration since the Laboratory launched the nation's first satellite, Explorer 1, in 1958. In the 50 years since this first success, JPL has sent spacecraft to all the planets except Pluto, studied our own planet in wavelengths from radar to visible, and observed the universe from radio to cosmic ray frequencies. Current plans call for even more exciting missions over the next decades in all these planetary and astronomical studies, and these future missions must be enabled by advanced technology that will be reported in this series. The JPL Deep Space Communications and Navigation book series captured the fundamentals and accomplishments of these two related disciplines, and we hope that this new series will expand the scope of those earlier publications to include other space science, engineering, and technology fields in which JPL has made important contributions.

I look forward to seeing many important achievements captured in these books.

CHARLES ELACHI, Director
Jet Propulsion Laboratory
California Institute of Technology

Preface

Electric propulsion was first envisioned 100 years ago, and throughout most of the 20th century was considered the technology of the future for spacecraft propulsion. With literally hundreds of electric thrusters now operating in orbit on communications satellites, and ion and Hall thrusters both having been successfully used for primary propulsion in deep-space scientific missions, the future for electric propulsion has arrived.

The literature contains several books from the 1960s and numerous journal articles and conference papers published over the years discussing electric thruster concepts, benefits, physics, and technological developments. Much of this work has been based on empirical investigations and laboratory-based development programs of different thruster types. As such, the fundamental understanding of how these thrusters work has generally lagged behind the technological achievements and applications of electric thrusters in space.

The quest over the past 10 years to improve often technically mature thruster performance and significantly extend thruster life for applications in deep-space propulsion and satellite station-keeping requires a much deeper understanding of the physics of electric thrusters. The purpose of this book is to discuss and explain how modern ion and Hall thrusters work by describing the fundamental physics of these devices. This is a challenging task requiring a basic knowledge of plasma physics, ion accelerators, cathodes, electrical discharges, high voltage, gas dynamics, and many other technologies. As such, we rely heavily on physics-based models that are often greatly simplified compared to the complex two-dimensional and three-dimensional codes required to accurately predict the plasma dynamics that drive thruster performance, and ultimately determine their life. Work in this field is still progressing, and we hope this book will lead to further research and advances in our understanding of these surprisingly complex devices.

While this effort encompasses a large body of literature in the area of ion and Hall thrusters, it is based largely on the research and development performed at the Jet Propulsion Laboratory (JPL). Therefore, this book should not be considered an all-inclusive treatise on the subject of electric thrusters or a review of their development history, but rather one that delves into the basics of two of the more modern electric engines that are finding increasingly more applications, specifically ion and Hall thrusters, in an attempt to provide a better understanding of their principles.

DAN M. GOEBEL and IRA KATZ
March 2008

Acknowledgments

We are greatly indebted to our colleagues at the Jet Propulsion Laboratory who both collaborated in the research and development of these thrusters and provided valuable comments and material for this manuscript. We gratefully acknowledge the many contributions of John Anderson, John Brophy, Richard Hofer, Kristina Jameson, Ioannis Mikellides, Timothy O'Donnell, James Polk, Thomas Randolph, J. Steven Snyder, and Richard Wirz. The research and development at JPL on ion and Hall thrusters has been supported through the years by NASA and the Jet Propulsion Laboratory, California Institute of Technology. The authors would also like to thank the developers and manufacturers of the flight thrusters described here for performance data and photographs of their thrusters. Finally, we would like to thank Joseph Yuen for his support in the preparation and publication of this book, and gratefully acknowledge the extensive and skillful efforts by Patricia Ehlers, Judi Dedmon, and Katherine Goebel in the editing and preparation of this book.

Fundamentals of Electric Propulsion: Ion and Hall Thrusters
by Dan M. Goebel and Ira Katz
Copyright © 2008 John Wiley & Sons, Inc.

Chapter 1
Introduction

Electric propulsion is a technology aimed at achieving thrust with high exhaust velocities, which results in a reduction in the amount of propellant required for a given space mission or application compared to other conventional propulsion methods. Reduced propellant mass can significantly decrease the launch mass of a spacecraft or satellite, leading to lower costs from the use of smaller launch vehicles to deliver a desired mass into a given orbit or to a deep-space target.

In general, electric propulsion (EP) encompasses any propulsion technology in which electricity is used to increase the propellant exhaust velocity. There are many figures of merit for electric thrusters, but mission and application planners are primarily interested in thrust, specific impulse, and total efficiency in relating the performance of the thruster to the delivered mass and change in the spacecraft velocity during thrust periods. While thrust is self-explanatory, specific impulse (Isp) is defined as the propellant exhaust velocity divided by the gravitational acceleration constant g, which results in the unusual units of seconds. The total efficiency is the jet power produced by the thrust beam divided by the electrical power into the system. Naturally, spacecraft designers are then concerned with providing the electrical power that the thruster requires to produce a given thrust, as well as with dissipating the thermal power that the thruster generates as waste heat.

In this book, the fundamentals of the ion and Hall thrusters that have emerged as leading electric propulsion technologies in terms of performance (thrust, Isp, and efficiency) and use in space applications will be presented. These thrusters operate in the power range of hundreds of watts up to tens of kilowatts with an Isp of thousands of seconds to tens of thousands of seconds, and they produce thrust levels typically of some fraction of a newton. Ion and Hall thrusters generally use heavy inert gases such as xenon as the propellant. Other propellant materials, such as cesium and mercury, have been investigated in the

past, but xenon is generally preferable because it is not hazardous to handle and process, it does not condense on spacecraft components that are above cryogenic temperatures, its large mass compared to other inert gases generates higher thrust for a given input power, and it is easily stored at high densities and low tank mass fractions. Therefore, the main focus will be on xenon as the propellant in ion and Hall thrusters, although performance with other propellants can be examined using the basic information provided here.

1.1 Electric Propulsion Background

A detailed history of electric propulsion up to the 1950s was published by Choueiri [1], and information on developments in electric propulsion since then can be found in reference books, e.g., [2], and on various internet sites, e.g., [3]. Briefly, electric propulsion was first conceived by Robert Goddard [4] in 1906 and independently described by Tsiolkovskiy [5] in Russia in 1911. Several electric propulsion concepts for a variety of space applications were included in the literature by Hermann Oberth in Germany in 1929 and by Shepherd and Cleaver in Britain in 1949. The first systematic analysis of electric propulsion systems was made by Ernst Stuhlinger [6] in his book *Ion Propulsion for Space Flight*, published in 1964, and the physics of electric propulsion thrusters was first described comprehensively in a book by Robert Jahn [7] in 1968. The technology of early ion propulsion systems that used cesium and mercury propellants, along with the basics of low-thrust mission design and trajectory analysis, was published by George Brewer [8] in 1970. Since that time, the basics of electric propulsion and some thruster characteristics have been described in several chapters of textbooks published in the United States on spacecraft propulsion [9–12]. An extensive presentation of the principles and working processes of several electric thrusters was published in 1989 in a book by S. Grishin and L. Leskov [13 (in Russian)].

Significant electric propulsion research programs were established in the 1960s at the National Aeronautics and Space Administration (NASA) Glenn Research Center, Hughes Research Laboratories, NASA's Jet Propulsion Laboratory (JPL), and at various institutes in Russia to develop this technology for satellite station-keeping and deep-space prime propulsion applications. The first experimental ion thrusters were launched into orbit in the early 1960s by the U.S. and Russia using cesium and mercury propellants. Experimental test flights of ion thrusters and Hall thrusters continued from that time into the 1980s.

The first extensive application of electric propulsion was by Russia using Hall thrusters for station keeping on communications satellites [14]. Since 1971 when the Soviets first flew a pair of SPT-60s on the Meteor satellite, over 238 Hall thrusters have been operated on 48 spacecraft to date [15]. Japan launched

the first ion thruster system intended for north–south station keeping on the communications satellite Engineering Test Satellite (ETS) VI in 1995 [16]. Although a launch vehicle failure did not permit station keeping by this system, the ion thrusters were successfully operated in space. The commercial use of ion thrusters in the United States started in 1997 with the launch of a Hughes Xenon Ion Propulsion System (XIPS) [17], and the first NASA deep-space mission using the NASA Solar Electric Propulsion Technology Applications Readiness (NSTAR) ion thruster was launched in 1998 on Deep Space 1 [18]. Since then, Hughes/Boeing launched their second-generation 25-cm XIPS ion thruster system [19] in 2000 for station-keeping applications on the high-power 702 communications satellite [20]. The Japanese have successfully used ion thrusters to provide the prime propulsion for the Hayabusa asteroid sample return mission [21], and the European Space Agency (ESA) has used Snecma's PPS-1350-G Hall thruster on its SMART-1 mission to the moon [22]. The Russians have been steadily launching communications satellites with Hall thrusters aboard and will continue to use these devices for future station-keeping applications [15]. The first commercial use of Hall thrusters by a U.S. spacecraft manufacturer was in 2004 on Space Systems Loral's MBSAT, which used the Fakel SPT-100 [23]. Additional ion and Hall thruster launches are planned in the U.S. in the near future using thrusters produced by commercial vendors [24–26].

In the past 20 years, electric propulsion use in spacecraft has grown steadily worldwide, and advanced electric thrusters have emerged over that time in several scientific missions and as an attractive alternative to chemical thrusters for station-keeping applications in geosynchronous communication satellites. Rapid growth has occurred in the last 10 years in the use of ion thrusters and Hall thrusters in communications satellites to reduce the propellant mass for station keeping and orbit insertion. The U.S. and the Russians have now each flown well over a hundred thrusters in communications satellites, and will continue to launch more ion and Hall thrusters in the future. The use of these technologies for primary propulsion in deep-space scientific applications has also been increasing over the past 10 years. There are many planned launches of new communications satellites and scientific missions that use ion and Hall thrusters in the coming years as the acceptance of the reliability and cost benefits of these systems grows.

1.2 Electric Thruster Types

Electric thrusters are generally described in terms of the acceleration method used to produce the thrust. These methods can be easily separated into three categories: electrothermal, electrostatic and electromagnetic. Common EP thruster types are described in the following.

Resistojet

Resistojets are electrothermal devices in which the propellant is heated by passing through a resistively heated chamber or over a resistively heated element before entering a downstream nozzle. The increase in exhaust velocity is due to the thermal heating of the propellant, which limits the Isp to low levels (<500 s).

Arcjet

An arcjet is also an electrothermal thruster that heats the propellant by passing it though a high current arc in line with the nozzle feed system. While there is an electric discharge involved in the propellant path, plasma effects are insignificant in the exhaust velocity because the propellant is weakly ionized. The Isp is limited by the thermal heating to less than about 700 s for easily stored propellants.

Ion Thruster

Ion thrusters employ a variety of plasma generation techniques to ionize a large fraction of the propellant. These thrusters then utilize biased grids to electrostatically extract ions from the plasma and accelerate them to high velocity at voltages up to and exceeding 10 kV. Ion thrusters feature the highest efficiency (from 60% to >80%) and very high specific impulse (from 2000 to over 10,000 s) compared to other thruster types.

Hall Thruster

This type of electrostatic thruster utilizes a cross-field discharge described by the Hall effect to generate the plasma. An electric field established perpendicular to an applied magnetic field electrostatically accelerates ions to high exhaust velocities, while the transverse magnetic field inhibits electron motion that would tend to short out the electric field. Hall thruster efficiency and specific impulse is somewhat less than that achievable in ion thrusters, but the thrust at a given power is higher and the device is much simpler and requires fewer power supplies to operate.

Electrospray/Field Emission Electric Propulsion Thruster

These are two types of electrostatic electric propulsion devices that generate very low thrust (<1 mN). Electrospray thrusters extract ions or charged droplets from conductive liquids fed through small needles and accelerate them electrostatically with biased, aligned apertures to high energy. Field emission electric propulsion (FEEP) thrusters wick or transport liquid metals (typically indium or cesium) along needles, extracting ions from the sharp tip by field

emission processes. Due to their very low thrust, these devices will be used for precision control of spacecraft position or attitude in space.

Pulsed Plasma Thruster

A pulsed plasma thruster (PPT) is an electromagnetic thruster that utilizes a pulsed discharge to ionize a fraction of a solid propellant ablated into a plasma arc, and electromagnetic effects in the pulse to accelerate the ions to high exit velocity. The pulse repetition rate is used to determine the thrust level.

Magnetoplasmadynamic Thruster

Magnetoplasmadynamic (MPD) thrusters are electromagnetic devices that use a very high current arc to ionize a significant fraction of the propellant, and then electromagnetic forces (Lorentz $\mathbf{J} \times \mathbf{B}$ forces) in the plasma discharge to accelerate the charged propellant. Since both the current and the magnetic field are usually generated by the plasma discharge, MPD thrusters tend to operate at very high powers in order to generate sufficient force for high specific impulse operation, and thereby also generate high thrust compared to the other technologies described above.

Some of the operating parameters of thrusters with flight heritage (resistojet, arcjet, ion, Hall, and PPT) are summarized in Table 1-1. There are many other types of electric propulsion thrusters in development or merely conceived that are too numerous to be described here. This book will focus on the fundamentals of electrostatic ion and Hall thrusters.

Table 1-1. Typical operating parameters for thrusters with flight heritage [30].

Thruster	Specific Impulse (s)	Input Power (kW)	Efficiency Range (%)	Propellant
Cold gas	50–75	—	—	Various
Chemical (monopropellant)	150–225	—	—	N_2H_4 H_2O_2
Chemical (bipropellant)	300–450	—	—	Various
Resistojet	300	0.5–1	65–90	N_2H_4 monoprop
Arcjet	500–600	0.9–2.2	25–45	N_2H_4 monoprop
Ion thruster	2500–3600	0.4–4.3	40–80	Xenon
Hall thrusters	1500–2000	1.5–4.5	35–60	Xenon
PPTs	850–1200	<0.2	7–13	Teflon

1.3 Ion Thruster Geometry

An ion thruster consists of basically three components: the plasma generator, the accelerator grids, and the neutralizer cathode. Figure 1-1 shows a schematic cross section of an electron-bombardment ion thruster that uses an electron discharge to generate the plasma. The discharge cathode and anode represent the plasma generator in this thruster, and ions from this region flow to the grids and are accelerated to form the thrust beam. The plasma generator is at high positive voltage compared to the spacecraft or space plasma and, therefore, is enclosed in a "plasma screen" biased near the spacecraft potential to eliminate electron collection from the space plasma to the positively biased surfaces. The neutralizer cathode is positioned outside the thruster and provides electrons at the same rate as the ions to avoid charge imbalance with the spacecraft.

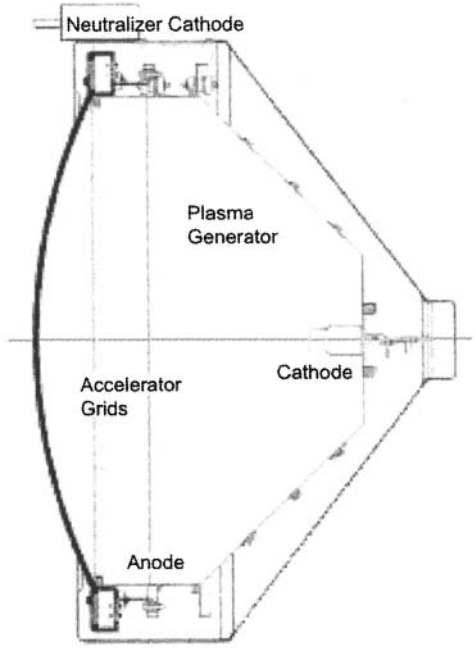

Fig. 1-1. Ion thruster schematic showing grids, plasma generator, and neutralizer cathode.

Ion thrusters that use alternative plasma generators, such as microwave or radio frequency (rf) plasma generators, have the same basic geometry with the plasma generator enclosed in a plasma screen and coupled to a gridded ion accelerator with a neutralizer cathode. The performance of the thruster depends on the plasma generator efficiency and the ion accelerator design. A photograph of a large, 57-cm-diameter ion thruster fabricated by JPL, called NEXIS [26], is shown in Fig. 1-2. This thruster is capable of operating at over 20 kW of power with an Isp exceeding 7000 s and a design lifetime of over 100,000 hours.

1.4 Hall Thruster Geometry

A Hall thruster can also be thought of as consisting of basically three components: the cathode, the discharge region, and the magnetic field

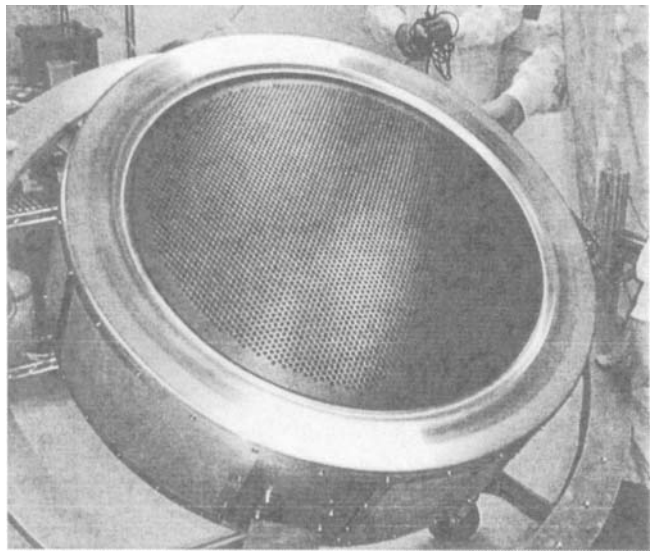

Fig. 1-2. Photograph of the NEXIS ion thruster [27] showing the 57-cm-diameter multiaperture grids and plasma screen enclosing the thruster body.

generator. Figure 1-3 shows a schematic cross section of a Hall thruster. In this example, a cylindrical insulating channel encloses the discharge region. Magnetic coils (not shown) induce a radial magnetic field between the center pole piece and the flux return path at the outside edge. The cathode of the discharge is an external hollow cathode, and the anode is a ring located at the base of the cylindrical slot shown. Gas is fed into the discharge channel through the anode and dispersed into the channel. Electrons attempting to reach the anode encounter a transverse radial magnetic field, which reduces their mobility in the axial direction and inhibits their flow to the anode. The electrons tend to spiral around the thruster axis in the $\mathbf{E} \times \mathbf{B}$ direction and represent the Hall current from which the device derives its name. Ions generated by these electrons are accelerated by the electric field from the anode to the cathode-potential plasma produced at the front of the thruster. Some fraction of the electrons emitted from the hollow cathode also leave the thruster with the ion beam to neutralize the exiting charge. The shape and material of the discharge region channel and the details of the magnetic field determine the performance of the thruster.

Figure 1-4 shows a photograph of an Aerojet BPT-4000 Hall thruster [25,26] that has completed qualification for flight. This thruster operates from 1 to 5 kW with an Isp near 2000 s and a total system efficiency of up to 52%. This

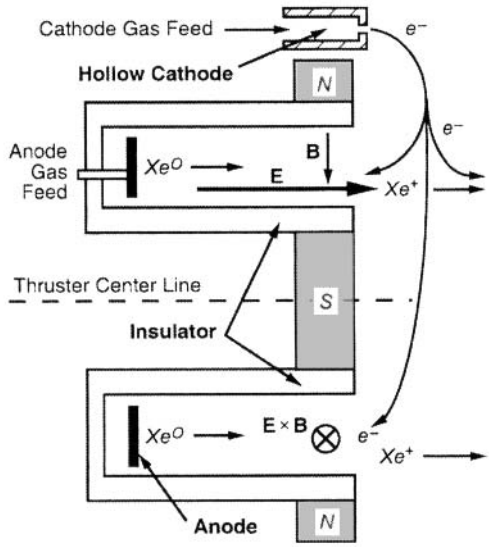

Fig. 1-3. Schematic illustration of a Hall thruster showing the radial magnetic field and the accelerating electric field.

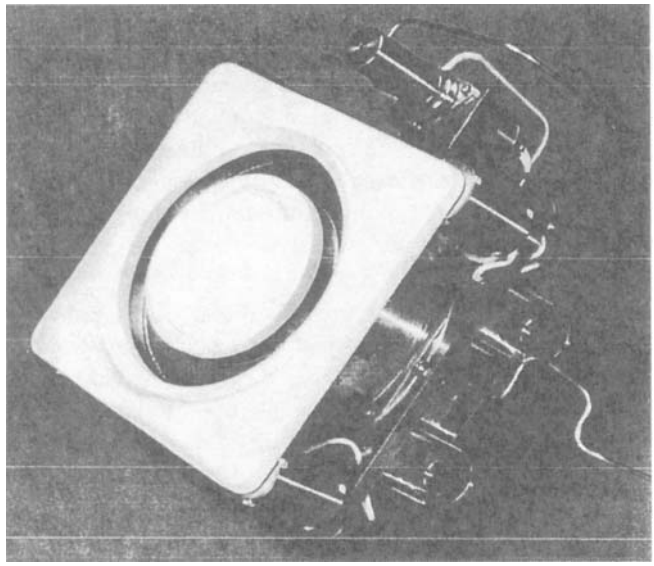

Fig. 1-4. Photograph of a BPT-4000 Hall thruster manufactured by Aerojet [25,26].

thruster is in development for satellite station-keeping and deep-space propulsion applications. The more familiar Russian SPT-100 Hall thruster, which has considerable flight heritage on Russian spacecraft [15] and is described in Chapter 9, operates nominally [28,29] at a power of 1.35 kW and an Isp of 1600 s. This thruster includes a redundant hollow cathode to increase the reliability and features a lifetime in excess of 9000 hours[12]. In addition, the SPT-100 has also been flown on U.S. commercial communications satellites [23].

1.5 Beam/Plume Characteristics

The ion beam exiting the thruster is often called the thruster plume, and the characteristics of this plume are important in how the exhaust particles interact with the spacecraft. Figure 1-5 shows the generic characteristics of a thruster plume. First, the beam has an envelope and a distribution of the ion currents in that envelope. Second, the energetic ions in the beam can charge exchange with neutral gas coming from the thruster or the neutralizer, producing fast neutrals propagating in the beam direction and slow ions. These slow ions then move in the local electric fields associated with the exit of the acceleration region and the neutralizer plasma, and can backflow into the thruster or move radially to potentially bombard any spacecraft components in the vicinity. Third, energetic ions are often generated at large angles from the thrust axis due either to edge effects (fringe fields) in the acceleration optics of ion thrusters, large gradients in the edge of the acceleration region in Hall thrusters, or scattering of the beam ions with the background gas. Finally, the thruster evolves impurities associated

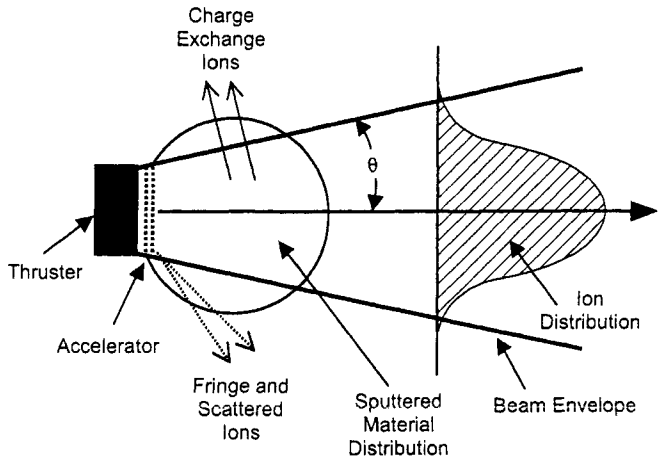

Fig. 1-5. Generic thruster-beam plume showing the ion distribution, sputtered material, and "large angle" or charge exchange ions.

with the wear of the thruster components. This can be due to the sputtering of the grids in ion thrusters, the erosion of the ceramic channel in Hall thrusters, or the evolution of cathode materials or sputtering of other electrodes in the engines. This material can deposit on spacecraft surfaces, which can change surface properties such as emissivity, transparency, etc.

The plume from a thruster typically has a complex structure. Figure 1-6 shows an exploded view of a calculated three-dimensional plume from a three-grid ion thruster. In this case, the ion beam is shown as the extended plume, and the molybdenum atom plume escaping through the third grid from sputter erosion of the center-accel grid is shown by the wider angular divergent dark plume and several beam lobes. Since the energetic ions tend to sputter surfaces that they come into contact with, and the metal atoms tend to deposit and coat surfaces they come in contact with, the net interaction of these plumes with the spacecraft is very different and must be examined with three-dimensional (3-D) codes of the spacecraft layout coupled to these types of thruster plume plots. Techniques and models for doing this are described in detail in Chapter 9,

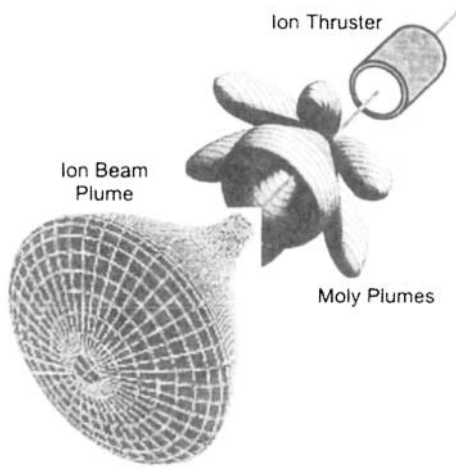

Fig. 1-6. Example of a 3-D plot of an ion thruster plume. Calculated and plotted by Dr. Thomas LaFrance, Manhattan Beach, California, 2007, and used here with permission.

References

[1] E. Y. Choueiri, "A Critical History of Electric Propulsion: The First 50 Years (1906-1956)," *Journal of Propulsion and Power*, vol. 20, pp. 193–203, 2004.

[2] R. G. Jahn and E. Y. Choueiri, "Electric Propulsion," *Encyclopedia of Physical Science and Technology*, third edition, vol. 5, New York: Academic Press, 2002.

[3] http://en.wikipedia.org/wiki/Field Emission_Electric_Propulsion

[4] R. H. Goddard, *The Green Notebooks*, vol. 1, The Dr. Robert H. Goddard Collection at the Clark University Archives, Clark University, Worchester, Massachusetts.

[5] T. M. Mel'kumov, ed., *Pioneers of Rocket Technology, Selected Works*, Academy of Sciences of the USSR, Institute for the History of Natural Science and Technology, Moscow, 1964; translated from the 1964 Russian text by NASA as NASA TT F-9285, 1965.

[6] E. Stuhlinger, *Ion Propulsion for Space Flight*, New York: McGraw-Hill, 1964.

[7] R. G. Jahn, *Physics of Electric Propulsion*, New York: McGraw-Hill, 1968.

[8] G. R. Brewer, *Ion Propulsion Technology and Applications*, New York: Gordon and Breach, 1970.

[9] H. R. Kaufman, "Technology of Electron-Bombardment Ion Thrusters," in *Advances in Electronics and Electron Physics*, vol. 36, edited by L. Marton, New York: Academic Press, 1974.

[10] P. J. Turchi, "Electric Rocket Propulsion Systems," Chapter 9 in *Space Propulsion Analysis and Design*, edited by R. W. Humble, G .N. Henry, and W. J. Larson, New York: McGraw-Hill, pp. 509–598, 1995.

[11] J. R. Wertz and W. J. Larson, eds., *Space Mission Analysis and Design*, third edition, New York: Springer Publishing Co., 1999.

[12] G. P. Sutton and O. Biblarz, *Rocket Propulsion Elements*, New York: John Wiley and Sons, pp. 660–710, 2001.

[13] S. D. Grishin and L. V. Leskov, *Electrical Rocket Engines of Space Vehicles*, Moscow, Russia: Mashinostroyeniye Publishing House, 1989 (in Russian).

[14] A. S. Boever, V. Kiim, A. S. Koroteev, L. A. Latyshev, A. I. Morozov, G. A. Popov, Y. P. Rylov, and V. V. Zhurin, "State of the Works of Electrical Thrusters in the USSR," IEPC-91-003, 22nd International Electric Propulsion Conference, Viareggio, Italy, 1991.

[15] V. Kim, "Electric Propulsion Activity in Russia," IEPC-2001-005, 27th International Electric Propulsion Conference, Pasadena, California, October 14–19, 2001.

[16] S. Shimada, K. Sato, and H. Takegahara, "20-mN Class Xenon Ion Thruster for ETS-VI," AIAA-1987-1029, 19th International Electric Propulsion Conference, Colorado Springs, Colorado, May 11–13, 1987.

[17] J. R. Beattie, "XIPS Keeps Satellites on Track," *The Industrial Physicist*, June 1998.

[18] J. R. Brophy, "NASA's Deep Space 1 Ion Engine," *Review Scientific Instruments*, vol. 73, pp. 1071–1078, 2002.

[19] J. R. Beattie, J. N. Matossian, and R. R. Robson, "Status of Xenon Ion Propulsion Technology," *Journal of Propulsion and Power*, vol. 6, no. 2, pp. 145–150, 1990.

[20] D. M. Goebel, M. Martinez-Lavin, T. A. Bond, and A. M. King, "Performance of XIPS Electric Propulsion in Station Keeping of the Boeing 702 Spacecraft," AIAA-2002-4348, 38th Joint Propulsion Conference, Indianapolis, Indiana, July 7–10, 2002.

[21] H. Kuninaka, K. Nishiyama, I. Funakai, K. Tetsuya, Y. Shimizu, and J. Kawaguchi, "Asteroid Rendezvous of Hayabusa Explorer Using Microwave Discharge Ion Engines," 29th International Electric Propulsion Conference, IEPC-2005-010, Princeton, New Jersey, October 31–November 4, 2005.

[22] C. R. Koppel and D. Estublier, "The SMART-1 Hall Effect Thruster around the Moon: In Flight Experience," 29th International Electric Propulsion Conference, IEPC-2005-119, Princeton, New Jersey, October 31–November 4, 2005.

[23] D. J. Pidgeon, R. L. Corey, B. Sauer, and M. L. Day, "Two Years On-Orbit Performance of SPT-100 Electric Propulsion," AIAA-2006-5353, 24th AIAA International Communications Satellite Systems Conference, San Diego, California, June 11–14, 2006.

[24] K. R. Chien, W. G. Tighe, and S. Hart, "L-3 Communications ETI Electric Propulsion Overview," 29th International Electric Propulsion Conference, IEPC-2005-315, Princeton, New Jersey, October 31–November 4, 2005.

[25] F. Wilson, D. King, M. Willey, R. Aadland, D. Tilley, and K. deGrys, "Development Status of the BPT Family of Hall Current Thrusters," AIAA-99-2573, 35th Joint Propulsion Conference, Los Angeles, California, June 20–24, 1999.

[26] K. H. de Grys, B. Welander, J. Dimicco, S. Wenzel, and B. Kay, "4.5 kW Hall Thruster System Qualification Status," AIAA-2005-3682, 41st Joint Propulsion Conference, Tucson, Arizona, July 10–13, 2005.

[27] J. E. Polk, D. M. Goebel, I. Katz, J. S. Snyder, A. Schneider, L. Johnson, and A. Sengupta, "Performance and Wear Test Results for a 20-kW Class Ion Engine with Carbon-Carbon Grids," AIAA-2005-4393, 41st Joint Propulsion Conference, Tucson, Arizona, July 10–13, 2005.

[28] V. Kim, "Main Physical Features and Processes Determining the Performance of Stationary Plasma Thrusters," *Journal of Propulsion and Power*, vol. 14, pp. 736–743, 1998.

[29] J. R. Brophy, J. W. Barnett, J. M. Sankovic, and D. A. Barnhart, "Performance of the Stationary Plasma Thruster: SPT-100," AIAA-92-3155, 28th Joint Propulsion Conference, Nashville, Tennessee, June 1992.

[30] J. R. Wertz and W. J. Larson, eds., *Space Mission Analysis and Design*, Torrance, California: Microcosm Press, 1999.

Fundamentals of Electric Propulsion: Ion and Hall Thrusters
by Dan M. Goebel and Ira Katz
Copyright © 2008 John Wiley & Sons, Inc.

Chapter 2
Thruster Principles

Electric thrusters propel the spacecraft using the same basic principle as chemical rockets—accelerating mass and ejecting it from the vehicle. The ejected mass from electric thrusters, however, is primarily in the form of energetic charged particles. This changes the performance of the propulsion system compared to other types of thrusters and modifies the conventional way of calculating some of the thruster parameters, such as specific impulse and efficiency. Electric thrusters provide higher exhaust velocities than is available from gas jets or chemical rockets, which either improves the available change in vehicle velocity (called Δv or delta-v) or increases the delivered spacecraft and payload mass for a given Δv. Chemical rockets generally will have exhaust velocities of 3 to 4 km/s, while the exhaust velocity of electric thrusters can approach 10^2 km/s for heavy propellant such as xenon atoms, and 10^3 km/s for light propellants such as helium.

2.1 The Rocket Equation

The mass ejected to provide thrust to the spacecraft is the propellant, which is carried onboard the vehicle and expended during thrusting. From conservation of momentum, the ejected propellant mass times its velocity is equal to the spacecraft mass times its change in velocity. The "rocket equation" describing the relationship between the spacecraft velocity and the mass of the system is derived as follows. The force on a spacecraft, and thus the thrust on the vehicle, is equal to the mass of the spacecraft, M, times its change in velocity, v:

$$\text{Force} = T = M\frac{dv}{dt}. \tag{2.1-1}$$

The thrust on the spacecraft is equal and opposite to the time rate of change of the momentum of the propellant, which is the exhaust velocity of the propellant times the time rate of change of the propellant mass:

$$T = -\frac{d}{dt}\left(m_p v_{\text{ex}}\right) = -v_{\text{ex}}\frac{dm_p}{dt}, \tag{2.1-2}$$

where m_p is the propellant mass on the spacecraft and v_{ex} is the propellant exhaust velocity in the spacecraft frame of reference.

The total mass of the spacecraft at any time is the delivered mass, m_d, plus the propellant mass:

$$M(t) = m_d + m_p. \tag{2.1-3}$$

The mass of the spacecraft changes due to consumption of the propellant, so the time rate of change of the total mass is

$$\frac{dM}{dt} = \frac{dm_p}{dt}. \tag{2.1-4}$$

Substituting Eq. (2.1-4) into Eq. (2.1-2) and equating with Eq. (2.1-1) gives

$$M\frac{dv}{dt} = -v_{\text{ex}}\frac{dM}{dt}, \tag{2.1-5}$$

which can be written as

$$dv = -v_{\text{ex}}\frac{dM}{M}. \tag{2.1-6}$$

For motion in a straight line, this equation is solved by integrating from the spacecraft initial velocity, v_i, to the final velocity, v_f, during which the mass changes from its initial value, $m_d + m_p$, to its final delivered mass, m_d:

$$\int_{v_i}^{v_f} dv = -v_{\text{ex}}\int_{m_d+m_p}^{m_d}\frac{dM}{M}. \tag{2.1-7}$$

The solution to Eq. (2.1-7) is

$$v_i - v_f = \Delta v = v_{ex} \ln\left(\frac{m_d}{m_d + m_p}\right). \tag{2.1-8}$$

The final mass of a spacecraft delivered after a given amount of propellant has been used to achieve the specified Δv is

$$m_d = (m_d + m_p)e^{-\Delta v / v_{ex}}. \tag{2.1-9}$$

The specific impulse, Isp, will be shown in Section 2.4 to be equal to the propellant exhaust velocity, v_{ex}, divided by the gravitational acceleration g. The change in velocity of the spacecraft is then

$$\Delta v = (\text{Isp}^* g)\ln\left(\frac{m_d + m_p}{m_d}\right), \tag{2.1-10}$$

where g is the acceleration by gravity, 9.8067 m/s^2.

Equation (2.1-10) shows that for a given mission with a specified Δv and final delivered mass, m_d, the initial spacecraft wet mass $(m_d + m_p)$ can be reduced by increasing the Isp of the propulsion system, which has implications for the launch vehicle size and cost. High delta-v missions are often enabled by electric propulsion because it offers much higher exhaust velocities and Isp than do conventional chemical propulsion systems.

Equation (2.1-9) can be written in terms of the required propellant mass:

$$m_p = m_d\left[e^{\Delta v/(v_{ex})} - 1\right] = m_d\left[e^{\Delta v/(\text{Isp}^* g)} - 1\right]. \tag{2.1-11}$$

The relationship between the amount of propellant required to perform a given mission and the propellant exhaust velocity (or the propulsion system Isp) shows that the propellant mass increases exponentially with the delta-v required. Thrusters that provide a large propellant exhaust velocity compared to the mission Δv will have a propellant mass that is only a small fraction of the initial spacecraft wet mass.

The exhaust velocity of chemical rockets is limited by the energy contained in the chemical bonds of the propellant used; typical values are up to 4 km/s. Electric thrusters, however, separate the propellant from the energy source (which is now a power supply) and thus are not subject to the same limitations.

Modern ion and Hall thrusters operating on xenon propellant have exhaust velocities in the range of 20–40 km/s and 10–20 km/s, respectively.

The dramatic benefits of the high exhaust velocities of electric thrusters are clearly seen from Eq. (2.1-11). For example, consider an asteroid rendezvous mission for which it is desired to deliver 500 kg of payload with a mission Δv of 5 km/s. A spacecraft propelled by a chemical engine with a 3-km/s exhaust velocity, corresponding to an Isp of 306 s, would require 2147 kg of propellant to accomplish the mission. In contrast, an ion thruster with a 30-km/s exhaust velocity, corresponding to an Isp of 3060 s, would accomplish the same mission using only 91 kg of propellant. High-Δv missions such as this are often enabled by electric propulsion, allowing either a significant reduction in the amount of required propellant that has to be launched or the ability to increase the spacecraft dry mass for a given wet mass associated with a launch vehicle or mission requirement.

2.2 Force Transfer in Ion and Hall Thrusters

The propellant ionized in ion and Hall thrusters is accelerated by the application of electric fields. However, the mechanism for transferring the thrust from the ion motion to the thruster body, and thereby the spacecraft, is different for ion thrusters and Hall thrusters.

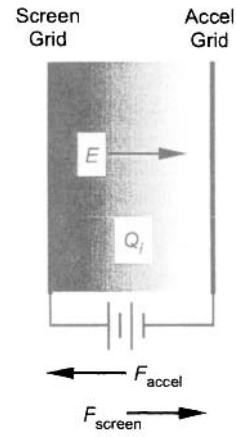

Fig. 2-1. Schematic of ion thruster acceleration region.

In ion thrusters, ions are produced by a plasma source and accelerated electrostaticly by the field applied between two (or more) grids, as illustrated in Fig. 2-1. The voltage applied between the two grids creates a vacuum electric field between the grids of the voltage divided by the gap d. The ions represent additional charge in the gap between the grids that modifies the electric field. Assuming infinitely large grids, the electric field distribution between the grids can be found from the one-dimensional Poisson's Equation:

$$\frac{dE(x)}{dx} = \frac{\rho(x)}{\varepsilon_o} = \frac{qn_i(x)}{\varepsilon_o}, \tag{2.2-1}$$

where ε_o is the permittivity of free space, ρ is the ion charge density in the gap, q is the charge on an ion, and n_i is the ion number density in the gap. Equation (2.2-1) can be integrated from the screen grid to the accel grid to give

$$E(x)=\frac{q}{\varepsilon_o}\int_0^x n_i(x')dx' + E_{\text{screen}}, \tag{2.2-2}$$

where E_{screen} is the electric field at the screen grid. Assuming that the screen grid is a perfect conductor, its surface charge density, σ, is

$$\sigma = \varepsilon_o E_{\text{screen}}. \tag{2.2-3}$$

The surface charge is an image charge and is attracted by the ion charge in the gap. Since the field drops to zero inside the conductor, the screen grid feels a force per unit area equal to the charge density times the average field (which is half the field on the outside of the conductor):

$$F_{\text{screen}} = \sigma \frac{(E_{\text{screen}} + 0)}{2} = \frac{1}{2}\varepsilon_o E_{\text{screen}}^2, \tag{2.2-4}$$

where F_{screen} is the force on the screen grid. Correspondingly, at the accelerator grid there is an electric field, E_{accel}, and a surface charge density equal to that on the screen grid but of the opposite sign. The accel grid feels a force is in the opposite direction:

$$F_{\text{accel}} = -\sigma \frac{(E_{\text{accel}} + 0)}{2} = -\frac{1}{2}\varepsilon_o E_{\text{accel}}^2. \tag{2.2-5}$$

The net thrust on the ion engine is the sum of the forces on the screen and accel grids,

$$T = F_{\text{screen}} + F_{\text{accel}} = \frac{1}{2}\varepsilon_o\left(E_{\text{screen}}^2 - E_{\text{accel}}^2\right), \tag{2.2-6}$$

where T is the force in newtons. The force per unit area on the ions in the gap between the grids can be calculated using the fact that the force on an ion equals its charge times the local electric field, and integrating that force across the gap:

$$F_{\text{ion}} = q\int_0^d n_i(x)E(x)dx. \tag{2.2-7}$$

Eliminating the ion density $n_i(x)$ using Eq. (2.2-1), the integral can be done directly:

$$F_{\text{ion}} = \varepsilon_o \int_0^d \frac{dE(x)}{dx} E(x)\,dx = \varepsilon_o \int_{E_{\text{screen}}}^{E_{\text{accel}}} E\,dE = \frac{1}{2}\varepsilon_o \left(E_{\text{accel}}^2 - E_{\text{screen}}^2 \right). \quad (2.2\text{-}8)$$

The net force on the grids, which is the thrust, is equal and opposite to the electric field forces on the ions between the grids:

$$T = -F_{\text{ion}} = -\frac{1}{2}\varepsilon_o \left(E_{\text{accel}}^2 - E_{\text{screen}}^2 \right). \quad (2.2\text{-}9)$$

Therefore, the thrust in an ion engine is transferred by the electrostatic force between the ions and the two grids.

In Hall thrusters, ions are generated in a plasma volume and accelerated by an electric field in the plasma. However, the presence of the transverse magnetic field responsible for the rotational Hall current modifies the force transfer mechanism. Assume for argument that the Hall thruster plasma is locally quasi-neutral ($qn_i \approx qn_e$) in the acceleration region, where n_e is the electron plasma density, and that in the acceleration zone the electric and magnetic fields are uniform. The geometry is shown schematically in Fig. 2-2. The ions are essentially unmagnetized and feel the force of the local electric field, so the force on the ions is

$$\mathbf{F}_{\text{ion}} = 2\pi \iint q\, n_i\, \mathbf{E}\, r dr\, dz \quad (2.2\text{-}10)$$

The electrons in the plasma feel an $\mathbf{E} \times \mathbf{B}$ force and circulate in the system transverse to the electric and magnetic fields with the velocity

$$\mathbf{v}_e = \frac{\mathbf{E} \times \mathbf{B}}{B^2}. \quad (2.2\text{-}11)$$

The electrostatic force on the ions is the negative of the electrostatic force on the electrons due to their sign differences. The electrons are constrained not to move axially by the transverse magnetic field, so the force per unit area on the electrons (to the left) is balanced by the Lorentz force:

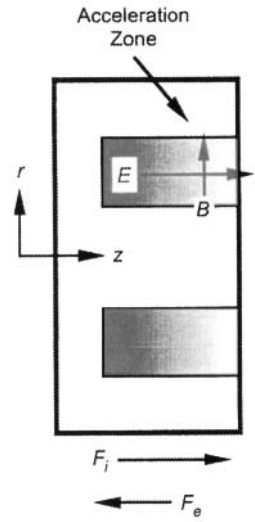

Fig. 2-2. Cross section of a Hall thruster showing electric and magnetic fields.

$$\mathbf{F}_e = -2\pi \iint q\, n_e\, \mathbf{E}\, r dr\, dz - 2\pi \iint e n_e \mathbf{v}_e \times \mathbf{B}\, r dr\, dz = 0 \quad (2.2\text{-}12)$$

Using quasi-neutrality and the definition of the Hall current density, $\mathbf{J}_{\text{Hall}} = -en_e\mathbf{v}_e$, the force on the ions is shown to be equal to Lorentz forces on the electrons:

$$\mathbf{F}_i = -2\pi\iint q\, n_i\, \mathbf{E}\; r dr\, dz \; + 2\pi\iint \mathbf{J}_{\text{Hall}} \times \mathbf{B}\; r dr\, dz = 0\,. \tag{2.2-13}$$

Solving Eq. (2.2-13), the force on the ions is then

$$\mathbf{F}_i = \mathbf{J}_{\text{Hall}} \times \mathbf{B} \tag{2.2-14}$$

By Newton's second law, the Hall current force on the magnets is equal and opposite to the Hall current force on the electrons and, therefore, is also equal and opposite to the force on the ions:

$$\mathbf{T} = \mathbf{J}_{\text{Hall}} \times \mathbf{B} = -\mathbf{F}_i\,. \tag{2.2-15}$$

In Hall thrusters the thrust is transferred from the ions to the thruster body through the electromagnetic Lorentz force. These thrusters are sometimes called *electromagnetic thrusters* because the force is transferred through the magnetic field. However, since the ion acceleration mechanism is by the electrostatic field, we will choose to call them *electrostatic thrusters*.

2.3 Thrust

Thrust is the force supplied by the engine to the spacecraft. Since the spacecraft mass changes with time due to the propellant consumption, the thrust is given by the time rate of change of the momentum, which can be written as

$$T = \frac{d}{dt}\left(m_p v_{\text{ex}}\right) = \frac{dm_p}{dt}\; v_{\text{ex}} = \dot{m}_p v_{\text{ex}} \tag{2.3-1}$$

where $\dot{m}_p$ is the propellant mass flow rate in kg/s. The propellant mass flow rate is

$$\dot{m}_p = QM\,, \tag{2.3-2}$$

where Q is the propellant particle flow rate (in particles/s) and M is the particle mass.

The kinetic thrust power of the beam, called the jet power, is defined as

$$P_{\text{jet}} = \frac{1}{2}\dot{m}_p v_{\text{ex}}^2\,. \tag{2.3-3}$$

Using Eq. (2.3-1), the jet power is then

$$P_{\text{jet}} = \frac{T^2}{2\dot{m}_p}. \tag{2.3-4}$$

This expression shows that techniques that increase the thrust without increasing the propellant flow rate will result in an increase in the jet power.

For ion and Hall thrusters, ions are accelerated to high exhaust velocity using an electrical power source. The velocity of the ions greatly exceeds that of any unionized propellant that may escape from the thruster, so the thrust can be described as

$$T = \frac{dm_p}{dt} v_{\text{ex}} \approx \dot{m}_i v_i, \tag{2.3-5}$$

where $\dot{m}_i$ is the ion mass flow rate and v_i is the ion velocity. By conservation of energy, the ion exhaust velocity is given by

$$v_i = \sqrt{\frac{2qV_b}{M}}, \tag{2.3-6}$$

where V_b is the net voltage through which the ion was accelerated, q is the charge, and M is the ion mass. The mass flow rate of ions is related to the ion beam current, I_b, by

$$\dot{m}_i = \frac{I_b M}{q}. \tag{2.3-7}$$

Substituting Eqs. (2.3-6) and (2.3-7) into Eq. (2.3-5), the thrust for a singly charged propellant ($q = e$) is

$$T = \sqrt{\frac{2M}{e}} I_b \sqrt{V_b} \text{ [newtons]}. \tag{2.3-8}$$

The thrust is proportional to the beam current times the square root of the acceleration voltage. In the case of Hall thrusters, there is a spread in beam energies produced in the thruster, and V_b represents the effective or average beam voltage. If the propellant is xenon, $\sqrt{2M/e} = 1.65 \times 10^{-3}$, the thrust is given by

$$T = 1.65\, I_b \sqrt{V_b} \ \text{[mN]}, \tag{2.3-9}$$

where I_b is in amperes and V_b is in volts.

Equation (2.3-9) is the basic thrust equation that applies for a unidirectional, singly ionized, monoenergetic beam of ions. The equation must be modified to account for the divergence of the ion beam and the presence of multiply charged ions commonly observed in electric thrusters. The assumption of a monoenergetic ion beam in Eq. (2.3-6) is generally valid for ion thrusters, but is only an approximation for the beam characteristics in Hall thrusters, which will be discussed in Chapter 7.

The correction to the thrust equation for beam divergence is straightforward for a beam that diverges uniformly upon exiting from the thruster. For a thruster with a constant ion current density profile accelerated by uniform electric fields, the correction to the force due to the effective thrust-vector angle is simply

$$F_t = \cos\theta\,, \tag{2.3-10}$$

where θ is the average half-angle divergence of the beam. If the thrust half angle is 10 deg, then cos $\theta = 0.985$, which represents a 1.5% loss in thrust. If the plasma source is not uniform and/or the accelerator system has curvature, then the thrust correction must be integrated over the beam and grid profiles. For cylindrical thrusters, the correction factor is then

$$F_t = \frac{\int_0^r 2\pi r\, J(r)\, \cos\theta(r)\, dr}{I_b}, \tag{2.3-11}$$

where $J(r)$ is the ion current density which is a function of the radius. The ion current density is usually determined from direct measurement of the current distribution in the plume by plasma probes. For a constant value of $J(r)$, Eq. (2.3-11) reduces to Eq. (2.3-10).

The second correction applied to the thrust equation for electric thrusters accounts for the presence of multiply charged ion species. If the beam contains both singly charged and doubly charged ions such that the total beam current is

$$I_b = I^+ + I^{++}, \tag{2.3-12}$$

where I^+ is the singly charged ion current and I^{++} is the doubly charged ion current, the total thrust for the multiple species, T_m, is the sum of the thrust from each species:

$$T_m = I^+ \sqrt{\frac{2MV_b}{e}} + I^{++} \sqrt{\frac{MV_b}{e}} = I^+ \sqrt{\frac{2MV_b}{e}} \left(1 + \frac{1}{\sqrt{2}} \frac{I^{++}}{I^+} \right). \tag{2.3-13}$$

The thrust correction factor, α, for thrust in the presence of doubly ionized atoms is defined by the ratio of Eqs. (2.3-13) and (2.3-8), where the beam current in Eq. (2.3-8) is given by Eq. (2.3-12):

$$\alpha = \frac{I^+ + \frac{1}{\sqrt{2}} I^{++}}{I^+ + I^{++}} = \frac{1 + 0.707 \frac{I^{++}}{I^+}}{1 + \frac{I^{++}}{I^+}}, \tag{2.3-14}$$

where I^{++}/I^+ is the fraction of double ion current in the beam. A similar correction factor can be easily derived for higher charged ions (see Problem 4), although the number of these species is typically found to be relatively small in most ion and Hall thrusters.

The total thrust correction is the product of the divergence and multiply charged species terms:

$$\gamma = \alpha F_t . \tag{2.3-15}$$

The total corrected thrust is then given by

$$T = \gamma \dot{m}_i v_i = \gamma \sqrt{\frac{2M}{e}} I_b \sqrt{V_b} . \tag{2.3-16}$$

The total thrust for xenon can be simply written as

$$T = 1.65 \gamma I_b \sqrt{V_b} \ \text{[mN]}. \tag{2.3-17}$$

For example, assuming an ion thruster with a 10-deg half-angle beam divergence and a 10% doubles-to-singles ratio results in $\gamma = 0.958$. For a thruster producing 2 A of xenon ions at 1500 V, the thrust produced is 122.4 mN.

2.4 Specific Impulse

Specific impulse, termed Isp, is a measure of thrust efficiency and is defined as the ratio of the thrust to the rate of propellant consumption. Specific impulse for constant thrust and propellant flow rate is

$$\text{Isp} = \frac{T}{\dot{m}_p g}, \tag{2.4-1}$$

where g is the acceleration of gravity, 9.807 m/s^2. For a xenon thruster, the Isp can be expressed as

$$\text{Isp} = 1.037 \times 10^6 \frac{T[\text{N}]}{Q[\text{sccm}]} = 1.02 \times 10^5 \frac{T[\text{N}]}{Q[\text{mg/s}]}, \tag{2.4-2}$$

where Eq. (2.3-2) and the flow conversions in Appendix B have been used.

Using Eq. (2.3-1) for the thrust in Eq. (2.4-1), the Isp for any thruster is

$$\text{Isp} = \frac{v_{\text{ex}}}{g}, \tag{2.4-3}$$

where v_{ex} is the effective exhaust velocity.

Defining the Isp in terms of the exhaust velocity relative to g is what gives rise to the unusual units of seconds for Isp. In electric thrusters, the thrust is due primarily to the ions. Using Eq. (2.3-5), the Isp is given by

$$\text{Isp} = \frac{v_i}{g} \frac{\dot{m}_i}{\dot{m}_p}. \tag{2.4-4}$$

where v_i is the exhaust velocity for unidirectional, monoenergetic ion exhaust.

The thruster mass utilization efficiency, which accounts for the ionized versus unionized propellant, is defined for singly charged ions as

$$\eta_m = \frac{\dot{m}_i}{\dot{m}_p} = \frac{I_b}{e} \frac{M}{\dot{m}_p}. \tag{2.4-5}$$

In the event that the thruster produces a significant number of multiply charged ions, the expression for the propellant utilization efficiency must be redefined.

For thrusters with both singly and doubly charged ions, the corrected mass utilization efficiency for multiple species is

$$\eta_{m^*} = \alpha_m \frac{I_b}{e} \frac{M}{\dot{m}_p}, \tag{2.4-6}$$

where α_m is a term that accounts for the fact that a doubly charged ion in the beam current carries two charges but only one unit of mass. In a manner similar to the derivation of the thrust correction due to double ions, the mass utilization correction α_m is given by

$$\alpha_m = \frac{1 + \frac{1}{2}\frac{I^{++}}{I^{+}}}{1 + \frac{I^{++}}{I^{+}}}. \tag{2.4-7}$$

For small ratios of double-to-single ion content, α_m is essentially equal to one.

Substituting Eq. (2.3-16) for the thrust and Eq. (2.4-5) for the propellant utilization efficiency into Eq. (2.4-3) yields an expression for the Isp:

$$\text{Isp} = \frac{\gamma \eta_m}{g} \sqrt{\frac{2eV_b}{M}}, \tag{2.4-8}$$

where the propellant utilization efficiency for singly charged ions must be used because Eq. (2.3-16) defines the beam current that way, and again the effective beam voltage must be used for Hall thrusters. Using the values for g and e, the Isp for an arbitrary propellant is

$$\text{Isp} = 1.417 \times 10^3 \gamma \eta_m \frac{\sqrt{V_b}}{\sqrt{M_a}}, \tag{2.4-9}$$

where V_b is the beam voltage in volts and M_a is the ion mass in atomic mass units [1 AMU = 1.6605×10^{-27} kg]. For xenon, the atomic mass $M_a = 131.29$, and the Isp is given by

$$\text{Isp} = 123.6\, \gamma \eta_m \sqrt{V_b}. \tag{2.4-10}$$

Using our previous example of a 10-deg half-angle beam divergence and a 10% doubles-to-singles ratio with a 90% propellant utilization of xenon [in Eq. (2.4-5)] at 1500 V, the Isp is $123.6*0.958*0.9*\sqrt{1500} = 4127$ s.

Specific impulse is functionally equivalent to gas mileage in a car. Cars with high gas mileage typically don't provide much acceleration, just as thrusters with high Isp don't provide as much thrust for a given input electrical power. Of critical importance is the ratio of the thrust achieved to total power used, which depends on the electrical efficiency of the thruster (to be described in the next section).

2.5 Thruster Efficiency

The mass utilization efficiency, defined in Eq. (2.4-6), describes the fraction of the input propellant mass that is converted into ions and accelerated in the electric thruster. The electrical efficiency of the thruster is defined as the beam power, P_b, out of the thruster divided by the total input power, P_T:

$$\eta_e = \frac{P_b}{P_T} = \frac{I_b V_b}{I_b V_b + P_o}, \tag{2.5-1}$$

where P_o represents the other power input to the thruster required to create the thrust beam. Other power will include the electrical cost of producing the ions, cathode heater or keeper power, grid currents in ion thrusters, etc.

The cost of producing ions is described by an ion production efficiency term, sometimes called the discharge loss:

$$\eta_d = \frac{\text{Power to produce the ions}}{\text{Current of ions produced}} = \frac{P_d}{I_b}, \tag{2.5-2}$$

where η_d has units of watts per ampere (W/A) or equivalently electron-volts per ion (eV/ion). Contrary to most efficiency terms, it is desirable to have η_d as small as possible since this represents a power loss. For example, if an ion thruster requires a 20-A, 25-V discharge to produce 2 A of ions in the beam, the discharge loss is then 20*25/2 = 250 eV/ion.

The performance of a plasma generator is usually characterized by plotting the discharge loss versus the propellant utilization efficiency. An example of this is shown in Fig. 2-3. At low propellant efficiencies, the neutral pressure in the thruster is high and the performance curves are relatively flat. As the propellant efficiency is increased, the neutral pressure in the thruster decreases, the

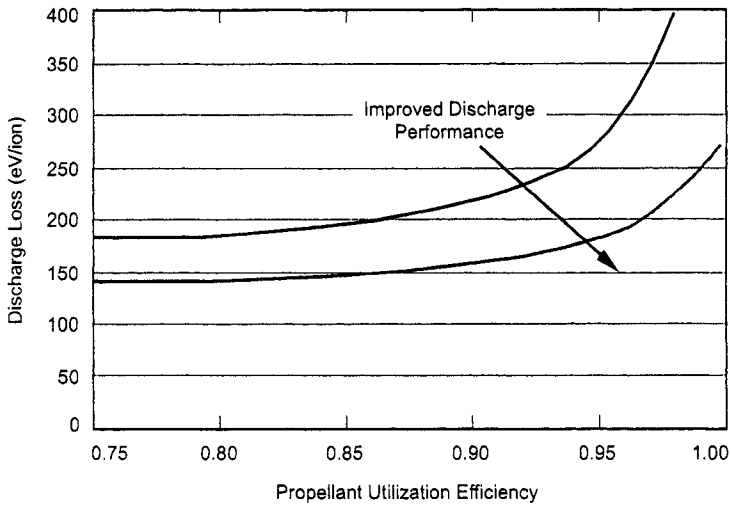

Fig. 2-3. Ion thruster performance curves consisting of discharge loss versus propellant utilization efficiency.

electron temperature increases, and the loss mechanisms in the thruster become larger. Thrusters are normally operated near the knee of this curve such that high mass utilization efficiency is achieved without excessive discharge loss. Optimized thruster designs result in lower discharge losses and low loss at high propellant efficiency.

The total efficiency of an electrically powered thruster is defined as the jet power divided by the total electrical power into the thruster:

$$\eta_T = \frac{P_{\text{jet}}}{P_{\text{in}}}. \tag{2.5-3}$$

Using Eq. (2.3-4) for the jet power, the efficiency of any electric propulsion thruster is

$$\eta_T = \frac{T^2}{2\dot{m}_p P_{\text{in}}}. \tag{2.5-4}$$

Measurements made of the thruster's input electrical power, input mass flow rate, and thrust output (measured in the vacuum system by a thrust stand) during testing can be used to calculate the total efficiency of the thruster using Eq. (2.5-4). This is the preferred technique for determining the efficiency of Hall thrusters because the beam parameters (current and velocity) are not

known outright from measurements of electrical or gas flow parameters external to the vacuum system.

In ion thrusters, the beam is nearly monoenergetic, the exhaust velocity can be found from the net acceleration voltage applied to the thruster [using Eq. (2.3-6)], and the beam current is measured by the high voltage power supply. This allows the total efficiency to be accurately calculated from the electrical and gas flow inputs to the thruster. Using Eq. (2.3-16) for the thrust, Eq. (2.3-6) for the exhaust velocity, and Eq. (2.4-5) for the propellant flow rate, the total efficiency in Eq. (2.5-4) can be written as

$$\eta_T = \frac{\gamma \eta_m T v_i}{2 \dot{m}_i P_{\text{in}}} = \gamma^2 \eta_m \frac{I_b V_b}{P_{\text{in}}} . \tag{2.5-5}$$

The input power into the thruster, from Eq. (2.5-1), is

$$P_{\text{in}} = \frac{P_b}{\eta_e} = \frac{I_b V_b}{\eta_e} , \tag{2.5-6}$$

Substituting Eq. (2.5-6) into Eq. (2.5-5) gives

$$\eta_T = \gamma^2 \eta_e \eta_m . \tag{2.5-7}$$

Measurements of the input propellant flow rate and electrical parameters (currents and voltages), and knowledge of the thrust correction factors from thruster plume measurements or code predictions, permit the total efficiency of ion thrusters to be calculated with high accuracy using Eq. (2.5-7).

Using our previous example of an ion thruster with 10-deg half-angle divergence, 10% double ion current, 90% mass utilization efficiency, and 250 eV/ion to produce a 2-A beam at 1500 V, the electrical efficiency is

$$\eta_e = \frac{2 * 1500}{2 * 1500 + 250 * 2} = 0.857 ,$$

and the total efficiency is

$$\eta_T = (0.958)^2 \ (0.857) \ (0.9) = 0.708 ,$$

which says that the thruster converts 70.8% of the supplied electrical energy into useful kinetic energy imparted to the spacecraft.

Thrusters with high exhaust velocities, and thus high Isp's, are desirable to maximize a mission payload mass. It was shown in Eq. (2.4-9) that to achieve high Isp, it is necessary to operate at a high ion acceleration voltage and high mass utilization efficiency. Reductions in ion mass also increase the Isp, but at the cost of thrust at the same power level. This is seen by examining the thrust-to-total input power ratio. The total power is just the beam power divided by the electrical efficiency, so the thrust-to-power ratio using Eq. (2.5.1) is

$$\frac{T}{P_T} = \frac{T\eta_e}{P_b}. \tag{2.5-8}$$

The beam power is the beam current times the beam voltage. Using Eq. (2.3-16) for the thrust and Eq. (2.4-8) to put this in terms of Isp, the thrust per unit input power is

$$\frac{T}{P_T} = \frac{2\gamma^2\eta_m\eta_e}{g\ \mathrm{Isp}} = \frac{2}{g}\frac{\eta_T}{\mathrm{Isp}}. \tag{2.5-9}$$

Equation (2.5-9) shows that for a given input power and total thruster efficiency, increasing the Isp reduces the thrust available from the electric engine. This trade of thrust for Isp at a constant input power can only be improved if higher efficiency ion thrusters are employed.

2.6 Power Dissipation

The power into a thruster that does not result in thrust must be dissipated primarily by radiating the unused power into space. If the thruster electrical efficiency is accurately known, the dissipated power is

$$P_{\mathrm{dissipated}} = P_{\mathrm{in}}\left(1-\eta_e\right). \tag{2.6-1}$$

If the electrical efficiency is not well known, alternative techniques can be used to determine the dissipated power. For example, in an ion thruster, the power in the beam is well known, and a simple difference between the total input power and the beam power represents the dissipated power. The various input powers can be measured externally to the thruster on the power supplies. For example, assuming the heaters have been turned off and the hollow cathodes are self-heating, the power into the ion thruster is given by

$$\begin{aligned} P_{\mathrm{in}} = {} & I_b V_b + I_d V_d + I_{\mathrm{ck}} V_{\mathrm{ck}} + I_{\mathrm{nk}} V_{\mathrm{nk}} \\ & + I_{A1}\left(V_b + V_a\right) + I_{A2} V_a + I_{\mathrm{DE1}} V_b + I_{\mathrm{DE2}} V_G, \end{aligned} \tag{2.6-2}$$

where the subscript "b" represents the beam current and voltage, "d" is the discharge current and voltage, "ck" is the cathode keeper current and voltage, "nk" is the neutralizer keeper current and voltage, "$A1$" represents beam ions incident on the accel grid, "$A2$" represents charge exchange ions at the accel grid potential V_a, "I_{DE1}" represents the decel grid (if present) current from beam ions, and "I_{DE2}" represents the decel grid current from backstreaming ions from the beam plume. In reality, the accel and decel grid power are very small compared to the other power levels in the thruster.

The power that must be dissipated by the thruster is Eq. (2.6.2) minus the beam power:

$$P_{\mathrm{in}} = I_d V_d + I_{\mathrm{ck}} V_{\mathrm{ck}} + I_{\mathrm{nk}} V_{\mathrm{nk}} + I_{A1}\left(V_b + V_a\right) + I_{A2} V_a + I_{\mathrm{DE1}} V_b + I_{\mathrm{DE2}} V_G . \tag{2.6-3}$$

Using the same ion thruster example used previously in this chapter, producing a 2-A beam at 1500 V as an example, Table 2-1 shows some example electrical parameters for a generic ion thruster. Assuming 10% of the grid currents are due to direct interception, using the table parameters in Eq. (2.5-12) gives a dissipated power of 528.3 W. Since the discharge power in this example is

Table 2-1. Example of ion thruster parameters used for power dissipation calculation.

Parameter	Term	Nominal
Discharge voltage	V_d	25
Discharge current (A)	I_d	20
Beam voltage	V_B	1500
Beam current (A)	I_B	2
Discharge keeper voltage	V_{ck}	10
Discharge keeper current (A)	I_{ck}	1
Neutralizer keeper voltage	V_{nk}	10
Neutralizer keeper current (A)	I_{nk}	1
Accel current (mA)	I_A	20
Accel voltage	V_A	250
Decel current (mA)	I_{DE}	2
Coupling voltage	V_G	20

500 W, the other power levels are relatively insignificant. However, the thruster will have to be of sufficient size to radiate all this power to space at a reasonable temperature that the materials and construction are designed to handle.

Unlike ion thrusters, power dissipation in Hall thrusters is not easily obtained from the external power supply readings. However, two techniques can be used to estimate the dissipated power. First, the dissipated power can be inferred from measurements of the thruster efficiency and the beam power (ion current and energy), which involves calculating the difference between the total beam power and the input electrical power. Another technique is to assume that the dissipated power is primarily the loss due to the electron current flowing from the exterior cathode through the thruster to the high voltage anode. If the fraction of the discharge current that becomes beam ions can be determined from the external diagnostics, then the difference between the discharge current and beam current times the discharge voltage is approximately the dissipated power. This technique neglects the ionization power and energy carried by the electrons in the beam, and so produces only a rough estimate. Hall thruster efficiency and performance useful in determining the power dissipation are described in detail in Chapter 7.

2.7 Neutral Densities and Ingestion in Electric Thrusters

In electric propulsion thrusters, the propellant is injected as a neutral gas into a chamber or region where ionization takes place. Accurately knowing the flow rate of the propellant gas is important in determining the performance and efficiency of the thruster and allows the operator to find the impact of finite pumping speed of test chambers on the thruster operation. The gas flow into the thruster, which is sometimes called the throughput, is often quoted in a number of different units. The most common units are standard cubic centimeters per minute (sccm) for ion thrusters and mg/s for Hall thrusters. Additional flow rate units include atoms per second, equivalent amperes, and torr-liter per second (torr-l/s). Conversion factors between these systems of flow units are derived in Appendix B.

The neutral pressure in the thruster discharge chamber or in the vacuum system follows standard gas law [1,2]:

$$PV = N\,\mathrm{k}\,T\,, \tag{2.7-1}$$

where P is the pressure in pascals, V is the volume, N is the number of particles, k is Boltzman's constant (1.38×10^{-23} W/s/K), and T is the temperature in kelvins. Since there are 133.32 pascals per torr, the number density of the neutral gas is

$$n = \frac{P_T \text{ [torr]} * 133.32 \text{ [pascal/torr]}}{1.38 \times 10^{-23} \text{ [J/K]} * T\text{[K]}} = 9.66 \times 10^{24} * \frac{P_T}{T} \left[\frac{\text{particles}}{m^3}\right], \tag{2.7-2}$$

where P_T is the pressure in the vacuum system in torrs and T is the gas temperature in kelvins. It should be noted that the pressure must be corrected for the gas type in whatever measurement system is used to obtain the actual pressure data. As an example, for a pressure of 10^{-6} torr and a temperature of 290 K, the density of gas atoms is 3.3×10^{16} per cubic meter.

The pressure in a vacuum system [3] in which a thruster is being tested is determined by the gas flow rate and the pumping speed

$$P = \frac{Q}{S}, \tag{2.7-3}$$

where Q is the total propellant throughput and S is the pumping speed. The most common units for pumping speed are liters per second, so utilizing a throughput in torr-l/s directly provides the pressure in the vacuum system in torr. The conversions of different flow units to torr-l/s can be obtained from Appendix B.

The finite pressure in the test vacuum system causes a backflow of neutral gas into the thruster that may artificially improve the performance. This ingestion of facility gas by the thruster can be calculated if the pressure in the chamber is known by evaluating the flux of neutral gas from the chamber into the thruster ionization region. The equivalent flow into the thruster is then the injected flow Q plus the equivalent ingested flow. The ingested flow (in particles per second) is given by

$$Q_{\text{ingested}} = \frac{n\bar{c}}{4} A^* \eta_c, \tag{2.7-4}$$

where n is the neutral density in the chamber, $\bar{c}$ is the gas thermal velocity, A is the total open area fraction of the thruster to the vacuum system, and η_c is a correction factor related to the conductance into the thruster from the vacuum system. The neutral gas density is given by Eq. (2.7-2), and the gas thermal velocity is given by

$$\bar{c} = \sqrt{\frac{8kT}{\pi M}}, \tag{2.7-5}$$

where M is the atom mass in kg. The conductance correction factor is sometimes called the Clausing factor [4] and describes the conductance reduction due to the finite axial length of the effective entrance aperture(s) to the thruster. This factor is generally negligible for Hall thrusters but appreciable for the apertured grids of ion thrusters. Due to the large diameter-to-length ratio of the accelerator grid apertures in ion thrusters, the Clausing factor is usually calculated by Monte-Carlo gas flow codes. An example of a simple spreadsheet Monte-Carlo code for calculating the Clausing factor for ion thruster grids is given in Appendix G.

The ingested flow of gas from the finite pressure in the vacuum system is then

$$Q_{\text{ingested}} = \frac{133.2\,P}{4\,\text{k}\,T}\sqrt{\frac{8\,\text{k}T}{\pi M}}\,\frac{A*\eta_c}{4.479\times10^{17}}\ [\text{sccm}]. \tag{2.7-6}$$

This expression for the ingested flow can be rewritten as

$$Q_{\text{ingested}} = 7.82\times10^{8}\,\frac{P*A*\eta_c}{\sqrt{T\,M_a}}\ [\text{sccm}], \tag{2.7-7}$$

where P is the vacuum chamber pressure in torr, T is the backflowing neutral gas temperature in K, M_a is the gas mass in AMU, and A is the open area in m^2. The total flow rate into the thruster is then

$$Q_{\text{total}} = Q_{\text{injected}} + Q_{\text{ingested}}\,. \tag{2.7-8}$$

References

[1] J. M. Lafferty, *Foundations of Vacuum Science and Technology*, New York: John Wiley and Sons, 1998.

[2] A. Ross, *Vacuum Technology*, Amsterdam, Holland: Elsevier, 1990.

[3] G. Lewin, *Fundamentals of Vacuum Science and Technology*, New York: McGraw-Hill, 1965.

[4] P. Clausing, "The Flow of Highly Rarefied Gases Through Tubes of Arbitrary Length," *Journal of Vacuum Science and Technology*, vol. 8, pp. 636–646, 1971.

Problems

1. Assume that the ion charge density in a one-dimensional (1-D) accelerator gap between two grids varies as $\rho = \rho_o x / d$, and that a voltage V_o is applied to the electrodes bounding the gap.
   a. Find the potential and electric field as a function of position in the gap.
   b. Find the force on each of the grids.
   c. Find the total electrostatic force between the ions and the grids.
2. A mission under study desires to deliver a 800-kg payload through 8 km/s of Δv. The spacecraft has 3 kW of electric power available for propulsion. The mission planners want to understand the trade-offs for different thrusters and operating conditions, and they want you to make plots of propellant mass and trip time required versus specific impulse for the following cases. Assume xenon is the propellant.
   a. Ion thruster case: The ion thruster can run at full power from 1 kV to 2 kV. For all throttle conditions, assume the following parameters are constant: total efficiency of 55%, propellant utilization of 85%, beam divergence angle of 12 deg, and double-to-single ion current ratio of 10%.
   b. Hall thruster case: The Hall thruster can run at full power from 300 V to 400 V. For all throttle conditions, assume the following parameters are constant: total efficiency of 45%, propellant utilization of 85%, beam divergence angle of 25 deg, and double-to-single ion current ratio of 15%.
3. Derive Eq. (2.4-7) for the mass utilization efficiency correction due to double ions.
4. Derive the thrust correction factor and the resulting thrust equation accounting for the presence of triply ionized atoms. Assuming 10% doubles, what is the error in the calculated thrust if 5% actually present triples have been neglected?
5. Mission planners have two candidate ion and Hall thrusters to place on a spacecraft and want to understand how they compare for thrust-to-power ratio and performance. The xenon ion thruster has a total power of 5 kW, a 1200-V, 3.75-A beam with 10% double ions, a total efficiency of 65%, and a mass utilization efficiency of 86%. The Hall thruster has a total power of 5 kW, a 300-V discharge voltage and a 12.5-A beam with 10% double ions, a total efficiency of 50%, and an input xenon gas flow of 19 mg/s.

a. What is the thrust-to-power ratio (usually expressed in mN/kW) for each thruster?

b. What is the Isp for each engine?

c. For a 1000-kg spacecraft, what is the fuel mass required to achieve a 5-km/s delta-v?

d. What is the trip time to expend all of the fuel for each thruster type if the thrusters are on 90% of the time?

6. The thrust correction factor for multiply ionized species is based on the current of charges in the beam (see Eq. (2.3-12) for singles and doubles).

a. Derive an expression for the number of atoms of each ionized species in the beam for a given value of I^{++}/I^{+} and I^{+++}/I^{+}.

b. If $I^{++}/I^{+} = 10\%$ and $I^{+++}/I^{+} = 5\%$, what are the actual percentages of the number of atoms of each species in the beam compared to the total beam current?

7. An ion thruster is being tested in a vacuum chamber with a measured xenon pressure of 1×10^{-5} torr at room temperature (300°C). The thruster grids have a 25-cm grid diameter and a Clausing factor of 0.5.

a. If the thruster is producing a 3-A beam with 15% double ions with a total of 50 sccm of xenon gas flow into the thruster, what is the mass utilization efficiency neglecting gas ingestion?

b. What is the mass utilization efficiency including the effects of ingestion?

Fundamentals of Electric Propulsion: Ion and Hall Thrusters
by Dan M. Goebel and Ira Katz
Copyright © 2008 John Wiley & Sons, Inc.

Chapter 3
Basic Plasma Physics

3.1 Introduction

Electric propulsion achieves high specific impulse by the acceleration of charged particles to high velocity. The charged particles are produced by ionization of a propellant gas, which creates both ions and electrons and forms what is called a plasma. Plasma is then a collection of the various charged particles that are free to move in response to fields they generate or fields that are applied to the collection and, on the average, is almost electrically neutral. This means that the ion and electron densities are nearly equal, $n_i \approx n_e$, a condition commonly termed "quasi-neutrality." This condition exists throughout the volume of the ionized gas except close to the boundaries, and the assumption of quasi-neutrality is valid whenever the spatial scale length of the plasma is much larger than the characteristic length over which charges or boundaries are electrostatically shielded, called the Debye length. The ions and electrons have distributions in energy usually characterized by a temperature T_i for ions and T_e for electrons, which are not necessarily or usually the same. In addition, different ion and electron species can exist in the plasma with different temperatures or different distributions in energy.

Plasmas in electric propulsion devices, even in individual parts of a thruster, can span orders of magnitude in plasma density, temperature, and ionization fraction. Therefore, models used to describe the plasma behavior and characteristics in the thrusters must be formed with assumptions that are valid in the regime being studied. Many of the plasma conditions and responses in thrusters can be modeled by fluid equations, and kinetic effects are only important in specific instances.

There are several textbooks that provide very comprehensive introductions to plasma physics [1–3] and the generation of ion beams [4]. This chapter is

intended to provide the basic plasma physics necessary to understand the operation of ion and Hall thrusters. The units used throughout the book are based on the International System (SI). However, by convention we will occasionally revert to other metric units (such as A/cm^2, mg/s, etc.) commonly used in the literature describing these devices.

3.2 Maxwell's Equations

The electric and magnetic fields that exist in electric propulsion plasmas obey Maxwell's equations formulated in a vacuum that contains charges and currents. Maxwell's equations for these conditions are

$$\nabla \cdot \mathbf{E} = \frac{\rho}{\varepsilon_o} \tag{3.2-1}$$

$$\nabla \times \mathbf{E} = -\frac{\partial \mathbf{B}}{\partial t} \tag{3.2-2}$$

$$\nabla \cdot \mathbf{B} = 0 \tag{3.2-3}$$

$$\nabla \times \mathbf{B} = \mu_o \left(\mathbf{J} + \varepsilon_o \frac{\partial \mathbf{E}}{\partial t} \right), \tag{3.2-4}$$

where ρ is the charge density in the plasma, $\mathbf{J}$ is the current density in the plasma, and ε_o and μ_o are the permittivity and permeability of free space, respectively. Note that ρ and $\mathbf{J}$ comprise all the charges and currents for all the particle species that are present in the plasma, including multiply charged ions. The charge density is then

$$\rho = \sum_s q_s n_s = e\left(Zn_i - n_e\right), \tag{3.2-5}$$

where q_s is the charge state of species s, Z is the charge state, n_i is the ion number density, and n_e is the electron number density. Likewise, the current density is

$$J = \sum_s q_s n_s v_s = e\left(Zn_i v_i - n_e v_e\right), \tag{3.2-6}$$

where v_s is the velocity of the charge species, v_i is the ion velocity, and v_e is the electron velocity. For static magnetic fields $\left(\partial \mathbf{B}/\partial t = 0\right)$, the electric field can be expressed as the gradient of the electric potential,

$$\mathbf{E} = -\nabla\phi, \tag{3.2-7}$$

where the negative sign comes from the convention that the electric field always points in the direction of ion motion.

3.3 Single Particle Motions

The equation of motion for a charged particle with a velocity **v** in a magnetic field **B** is given by the Lorentz force equation:

$$\mathbf{F} = m\frac{d\mathbf{v}}{dt} = q(\mathbf{E} + \mathbf{v}\times\mathbf{B}). \tag{3.3-1}$$

Particle motion in a magnetic field in the $\hat{z}$ direction for the case of negligible electric field is found by evaluating Eq. (3.3-1):

$$\begin{aligned} m\frac{\partial v_x}{\partial t} &= qBv_y \\ m\frac{\partial v_y}{\partial t} &= -qBv_x \\ m\frac{\partial v_z}{\partial t} &= 0. \end{aligned} \tag{3.3-2}$$

Taking the time derivative of Eq. (3.3-2) and solving for the velocity in each direction gives

$$\begin{aligned} \frac{\partial^2 v_x}{\partial t^2} &= \frac{qB}{m}\frac{\partial v_y}{\partial t} = -\left(\frac{qB}{m}\right)^2 v_x \\ \frac{\partial^2 v_y}{\partial t^2} &= -\frac{qB}{m}\frac{\partial v_x}{\partial t} = -\left(\frac{qB}{m}\right)^2 v_y. \end{aligned} \tag{3.3-3}$$

These equations describe a simple harmonic oscillator at the cyclotron frequency:

$$\omega_c = \frac{|q|B}{m}. \tag{3.3-4}$$

For electrons, this is called the electron cyclotron frequency.

The size of the particle orbit for finite particle energies can be found from the solution to the particle motion equations in the axial magnetic field. In this case, the solution to Eq. (3.3-3) is

$$v_{x,y} = v_{\perp} e^{i\omega_c t} . \tag{3.3-5}$$

The equation of motion in the y-direction in Eq. (3.3-2) can be rewritten as

$$v_y = \frac{m}{qB}\frac{\partial v_x}{\partial t} = \frac{1}{\omega_c}\frac{\partial v_x}{\partial t} . \tag{3.3-6}$$

Utilizing Eq. (3.3-5), Eq. (3.3-6) becomes

$$v_y = \frac{1}{\omega_c}\frac{\partial v_x}{\partial t} = iv_{\perp} e^{i\omega_c t} = \frac{\partial y}{\partial t} . \tag{3.3-7}$$

Integrating this equation gives

$$y - y_o = \frac{v_{\perp}}{\omega_c} e^{i\omega_c t} . \tag{3.3-8}$$

Taking the real part of Eq. (3.3-8) gives

$$y - y_o = \frac{v_{\perp}}{\omega_c} \cos\ \omega_c t = r_L\ \cos\ \omega_c t , \tag{3.3-9}$$

where $r_L = v_{\perp} / \omega_c$ is defined as the Larmor radius. A similar analysis of the displacement in the $\hat{x}$ direction gives the same Larmor radius 90 degrees out of phase with the $\hat{y}$-direction displacement, which then with Eq. (3.3-9) describes the particle motion as a circular orbit around the field line at x_o and y_o with a radius given by r_L.

The Larmor radius arises from very simple physics. Consider a charged particle of mass, m, in a uniform magnetic field with a velocity in one direction, as illustrated in Fig. 3-1. The charge will feel a Lorentz force

$$\mathbf{F} = q\mathbf{v}_{\perp} \times \mathbf{B} . \tag{3.3-10}$$

Since the charged particle will move under this force in circular orbits in the $\mathbf{v}_{\perp} \times \mathbf{B}$ direction, it feels a corresponding centripetal force such that

$$\mathbf{F_c} = q\mathbf{v}_\perp \times \mathbf{B} = \frac{mv_\perp^2}{r}, \qquad (3.3\text{-}11)$$

where r is the radius of the cycloidal motion in the magnetic field. Solving for the radius of the circle gives

$$r = r_L = \frac{mv_\perp}{qB}, \qquad (3.3\text{-}12)$$

which is the Larmor radius.

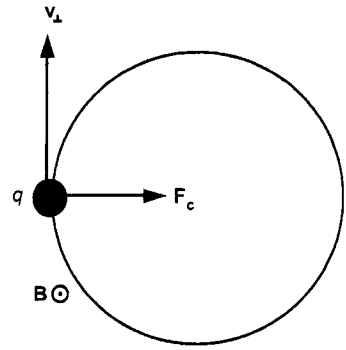

Fig. 3-1. Positively charged particle moving in a uniform vertical magnetic field.

The Larmor radius can be written in a form simple to remember:

$$r_L = \frac{v_\perp}{\omega_c} = \frac{1}{B}\sqrt{\frac{2mV_\perp}{e}}, \qquad (3.3\text{-}13)$$

using $1/2\,mv_\perp^2 = eV_\perp$ for the singly charged particle energy in the direction perpendicular to the magnetic field. The direction of particle gyration is always such that the induced magnetic field is opposite in direction to the applied field, which tends to reduce the applied field, an effect called diamagnetism. Any particle motion along the magnetic field is not affected by the field, but causes the particle motion to form a helix along the magnetic field direction with a radius given by the Larmor radius and a pitch given by the ratio of the perpendicular to parallel velocities.

Next consider the situation in Fig. 3-1, but with the addition of a finite electric field perpendicular to **B**. In this case, **E** is in some direction in the plane of the page. The equation of motion for the charged particle is given by Eq. (3.3-1). Considering the drift to be steady-state, the time derivative is equal to zero, and Eq. (3.3-1) becomes

$$\mathbf{E} = -\mathbf{v} \times \mathbf{B}. \qquad (3.3\text{-}14)$$

Taking the cross product of both sides with **B** gives

$$\mathbf{E} \times \mathbf{B} = (-\mathbf{v} \times \mathbf{B}) \times \mathbf{B} = \mathbf{v}B^2 - \mathbf{B}(\mathbf{B} \cdot \mathbf{v}). \qquad (3.3\text{-}15)$$

The dot product is in the direction perpendicular to B, so the last term in Eq. (3.3-15) is equal to zero. Solving for the transverse velocity of the particle gives

$$\mathbf{v} = \frac{\mathbf{E} \times \mathbf{B}}{B^2} \equiv \mathbf{v}_E , \tag{3.3-16}$$

which is the "E cross B" drift velocity. In this case, the drift is in the direction perpendicular to both E and B, and arises from the cycloidal electron motion in the magnetic field being accelerated in the direction of $-\mathbf{E}$ and decelerated in the direction of $\mathbf{E}$. This elongates the orbit on one-half cycle and shrinks the orbit on the opposite half cycle, which causes the net motion of the particle in the $\mathbf{E} \times \mathbf{B}$ direction. The units of the $\mathbf{E} \times \mathbf{B}$ velocity are

$$v_E = \frac{E\ [\mathrm{V/m}]}{B\ [\mathrm{tesla}]}\ (\mathrm{m/s}) . \tag{3.3-17}$$

Finally, consider the situation of a particle gyrating in a magnetic field that is changing in magnitude along the magnetic field direction $\hat{z}$. This is commonly found in electric propulsion thrusters relatively close to permanent magnets or electromagnetic poles-pieces that produce fields used to confine the electrons. Since the divergence of B is zero, Eq. (3.2-3), the magnetic field in cylindrical coordinates is described by

$$\frac{1}{r}\frac{\partial}{\partial r}(rB_r) + \frac{\partial B_z}{\partial z} = 0 . \tag{3.3-18}$$

Assuming that the axial component of the field does not vary significantly with r and integrating yields the radial component of the magnetic field with respect to r,

$$B_r \approx -\frac{r}{2}\frac{\partial B_z}{\partial z} . \tag{3.3-19}$$

The Lorentz force on a charged particle has a component along $\hat{z}$ given by

$$F_z \approx -q v_\phi B_r , \tag{3.3-20}$$

where the azimuthal particle velocity averaged over a Larmor-radius ($r = r_L$) gyration is $v_\phi = -v_\perp$. The average force on the particle is then

$$\overline{F_z} \approx -\frac{1}{2}\frac{m v_\perp^2}{B}\frac{\partial B_z}{\partial z} . \tag{3.3-21}$$

The magnetic moment of the gyrating particle is defined as

$$\mu = \frac{1}{2}\frac{mv_{\perp}^2}{B}. \tag{3.3-22}$$

As the particle moves along the magnetic field lines into a stronger magnitude field, the parallel energy of the particle is converted into rotational energy and its Larmor radius increases. However, its magnetic moment remains invariant because the magnetic field does no work and the total kinetic energy of the particle is conserved. For a sufficiently large increase in the field, a situation can arise where the parallel velocity of the particle goes to zero and the Lorentz force reflects the particle from a "magnetic mirror." By conservation of energy, particles will be reflected from the magnetic mirror if their parallel velocity is less than

$$v_{\parallel} < v_{\perp}\sqrt{R_m - 1}, \tag{3.3-23}$$

where $v_{\parallel}$ is the parallel velocity and R_m is the mirror ratio given by $B_{\max} / B_{\min}$. This effect is used to provide confinement of energetic electrons in ion-thruster discharge chambers.

There are a number of other particle drifts and motions possible that depend on gradients in the magnetic and electric fields, and also on time-dependent or oscillating electric or magnetic fields. These are described in detail in plasma physics texts such as Chen [1], and while they certainly might occur in the electric propulsion devices considered here, they are typically not of critical importance to the thruster performance or behavior.

3.4 Particle Energies and Velocities

In ion and Hall thrusters, the charge particles may undergo a large number of collisions with each other, and in some cases with the other species (ions, electrons, and/or neutrals) in the plasma. It is therefore impractical to analyze the motion of each particle to obtain a macroscopic picture of the plasma processes that is useful to for assessing the performance and life of these devices. Fortunately, in most cases it is not necessary to track individual particles to understand the plasma dynamics. The effect of collisions is to develop a distribution of the velocities for each species. On the average, and in the absence of other forces, each particle will then move with a speed that is solely a function of the macroscopic temperature and mass of that species. The charged particles in the thruster, therefore, can usually be described by different velocity distribution functions, and the random motions can be calculated by taking the moments of those distributions.

Most of the charged particles in electric thrusters have a Maxwellian velocity distribution, which is the most probable distribution of velocities for a group of particles in thermal equilibrium. In one dimension, the Maxwellian velocity distribution function is

$$f(v)=\left(\frac{m}{2\pi kT}\right)^{1/2}\exp\left(-\frac{mv^2}{2kT}\right), \tag{3.4-1}$$

where m is the mass of the particle, k is Boltzmann's constant, and the width of the distribution is characterized by the temperature T. The average kinetic energy of a particle in the Maxwellian distribution in one dimension is

$$E_{\text{ave}}=\frac{\int_{-\infty}^{\infty}\frac{1}{2}mv^2 f(v)\,dv}{\int_{-\infty}^{\infty}f(v)\,dv}. \tag{3.4-2}$$

By inserting in Eq. (3.4-1) and integrating by parts, the average energy per particle in each dimension is

$$E_{\text{ave}}=\frac{1}{2}kT. \tag{3.4-3}$$

If the distribution function is generalized into three dimensions, Eq. (3.2-8) becomes

$$f(u,v,w)=\left(\frac{m}{2\pi kT}\right)^{3/2}\exp\left[-\frac{m}{2kT}\left(u^2+v^2+w^2\right)\right], \tag{3.4-4}$$

where u, v, and w represent the velocity components in the three coordinate axes. The average energy in three dimensions is found by inserting Eq. (3.4-2) in Eq. (3.4-4) and performing the triple integration to give

$$E_{\text{ave}}=\frac{3}{2}kT. \tag{3.4-5}$$

The density of the particles is found from

$$\begin{aligned} n &= \iiint_{-\infty}^{+\infty} nf(\mathbf{v})\,d\mathbf{v} \\ &= \iiint_{-\infty}^{+\infty} n\left(\frac{m}{2\pi kT}\right)^{3/2}\exp\left(-\frac{m\left(u^2+v^2+w^2\right)}{2kT}\right)dudvdw. \end{aligned} \tag{3.4-6}$$

The average speed of a particle in the Maxwellian distribution is

$$\bar{v} = \int_0^\infty v \left(\frac{m}{2\pi kT} \right)^{3/2} \exp\left(-\frac{v^2}{v_{th}^2} \right) 4\pi v^2 dv , \tag{3.4-7}$$

where v in Eq. (3.4-7) denotes the particle speed and v_{th} is defined as $(2kT/m)^{1/2}$. Integrating Eq. (3.4-7), the average speed per particle is

$$\bar{v} = \left(\frac{8kT}{\pi m} \right)^{1/2} . \tag{3.4-8}$$

The flux of particles in one dimension (say in the $\hat{z}$ direction) for a Maxwellian distribution of particle velocities is given by $n < v_z >$. In this case, the average over the particle velocities is taken in the positive v_z direction because the flux is considered in only one direction. The particle flux (in one direction) is then

$$\Gamma_z = \int n v_z f(\mathbf{v}) d^3\mathbf{v}, \tag{3.4-9}$$

which can be evaluated by integrating the velocities in spherical coordinates with the velocity volume element given by

$$d^3v = v^2 dv d\Omega = v^2 dv \sin\theta d\theta d\phi , \tag{3.4-10}$$

where the $d\Omega$ represents the element of the solid angle. If the incident velocity has a cosine distribution ($v_z = v\cos\theta$), the one-sided flux is

$$\Gamma_z = n \left(\frac{m}{2\pi kT} \right)^{3/2} \int_0^{2\pi} d\phi \int_0^{\pi/2} \sin\theta \, d\theta \int_0^\infty v\cos\theta \, \exp\left(-\frac{v^2}{v_{th}} \right) v^2 dv , \tag{3.4-11}$$

which gives

$$\Gamma_z = \frac{1}{4} n\bar{v} = \frac{1}{4} n \left(\frac{8kT}{\pi m} \right)^{1/2} . \tag{3.4-12}$$

Since the plasma electrons are very mobile and tend to make a large number of coulomb collisions with each other, they can usually be characterized by a Maxwellian temperature T_e and have average energies and speeds well described by the equations derived in this section. The random electron flux inside the plasma is also well described by Eq. (3.4-12) if the electron

temperature and density are known. The electrons tend to be relatively hot (compared to the ions and atoms) in ion and Hall thrusters because they typically are injected into the plasma or heated by external mechanisms to provide sufficient energy to produce ionization. In the presence of electric and magnetic fields in the plasma and at the boundaries, the electron motion will no longer be purely random, and the flux described by Eq. (3.4-12) must be modified as described in the remainder of this chapter.

The ions in thrusters, on the other hand, are usually relatively cold in temperature (they may have high directed velocities after being accelerated, but they usually have low random velocities and temperatures). This occurs because the ions are not well confined in the plasma generators because they must be extracted to form the thrust beam, and so they leave the plasma after perhaps only a single pass. The ions are also not heated efficiently by the various mechanisms used to ionize the gas. Therefore, the plasmas in ion and Hall thrusters are usually characterized as having cold ions and Maxwellian electrons with a high electron-to-ion temperature ratio ($T_e / T_i \approx 10$). As a result, the velocity of the ions in the plasma and the fluxes to the boundaries tend to be determined by the electric fields generated inside the plasma to conserve charge, and to be different from the expressions derived here for the electron velocity and fluxes. This effect will be described in more detail in Section 3.6.

3.5 Plasma as a Fluid

The behavior of most of the plasma effects in ion and Hall thrusters can be described by simplified models in which the plasma is treated as a fluid of neutral particles and electrical charges with Maxwellian distribution functions, and the interactions and motion of only the fluid elements must be considered. Kinetic effects that consider the actual velocity distribution of each species are important in some instances, but will not be addressed here.

3.5.1 Momentum Conservation

In constructing a fluid approach to plasmas, there are three dominant forces on the charged particles in the plasma that transfer momentum that are considered here. First, charged particles react to electric and magnetic field by means of the Lorentz force, which was given by Eq. (3.3-1):

$$\mathbf{F}_L = m\frac{d\mathbf{v}}{dt} = q\left(\mathbf{E} + \mathbf{v} \times \mathbf{B}\right). \tag{3.5-1}$$

Next, there is a pressure gradient force,

$$\mathbf{F}_p = -\frac{\nabla \cdot \mathbf{p}}{n} = -\frac{\nabla(\mathbf{nkT})}{n}, \tag{3.5-2}$$

where the pressure is given by $P = nkT$ and should be written more rigorously as a stress tensor since it can, in general, be anisotropic. For plasmas with temperatures that are generally spatially constant, the force due to the pressure gradient is usually written simply as

$$\mathbf{F}_p = -kT\frac{\nabla \mathbf{n}}{n}. \tag{3.5-3}$$

Finally, collisions transfer momentum between the different charged particles, and also between the charged particles and the neutral gas. The force due to collisions is

$$\mathbf{F}_c = -m\sum_{a,b} \nu_{ab}\left(\mathbf{v}_a - \mathbf{v}_b\right), \tag{3.5-4}$$

where ν_{ab} is the collision frequency between species a and b.

Using these three force terms, the fluid momentum equation for each species is

$$mn\frac{d\mathbf{v}}{dt} = mn\left[\frac{\partial \mathbf{v}}{\partial t} + (\mathbf{v}\cdot\nabla)\mathbf{v}\right] = qn(\mathbf{E}+\mathbf{v}\times\mathbf{B}) - \nabla\cdot\mathbf{p} - mn\nu(\mathbf{v}-\mathbf{v}_o), \tag{3.5-5}$$

where the convective derivative has been written explicitly and the collision term must be summed over all collisions.

Utilizing conservation of momentum, it is possible to evaluate how the electron fluid behaves in the plasma. For example, in one dimension and in the absence of magnetic fields and collisions with other species, the fluid equation of motion for electrons can be written as

$$mn_e\left[\frac{\partial v_z}{\partial t} + (v\cdot\nabla)v_z\right] = qn_eE_z - \frac{\partial p}{\partial z}, \tag{3.5-6}$$

where v_z is the electron velocity in the z-direction and p represents the electron pressure term. Neglecting the convective derivative, assuming that the velocity is spatially uniform, and using Eq. (3.5-3) gives

$$m\frac{\partial v_z}{\partial t} = -eE_z - \frac{kT_e}{n_e}\frac{\partial n_e}{\partial z}. \tag{3.5-7}$$

Assuming that the electrons have essentially no inertia (their mass is small and so they react infinitely fast to changes in potential), the left-hand side of Eq. (3.5-7) goes to zero, and the net current in the system is also zero. Considering only electrons at a temperature T_e, and using Eq. (3.2-7) for the electric field, gives

$$qE_z = e\frac{\partial \phi}{\partial z} = \frac{kT_e}{n_e}\frac{\partial n_e}{\partial z}. \tag{3.5-8}$$

Integrating this equation and solving for the electron density produces the Boltzmann relationship for electrons:

$$n_e = n_e(0)\, e^{\left(e\phi/kT_e\right)}, \tag{3.5-9}$$

where ϕ is the potential relative to the potential at the location of $n_e(0)$. Equation (3.5-9) is also sometimes known as the barometric law. This relationship simply states that the electrons will respond to electrostatic fields (potential changes) by varying their density to preserve the pressure in the system. This relationship is generally valid for motion along a magnetic field and tends to hold for motion across magnetic fields if the field is weak and the electron collisions are frequent.

3.5.2 Particle Conservation

Conservation of particles and/or charges in the plasma is described by the continuity equation:

$$\frac{\partial n}{\partial t} + \nabla \cdot n\mathbf{v} = \dot{n}_s, \tag{3.5-10}$$

where $\dot{n}_s$ represents the time-dependent source or sink term for the species being considered. Continuity equations are sometimes called mass-conservation equations because they account for the sources and sinks of particles into and out of the plasma.

Utilizing continuity equations coupled with momentum conservation and with Maxwell's equations, it is possible to calculate the response rate and wave-like behavior of plasmas. For example, the rate at which a plasma responds to changes in potential is related to the *plasma frequency* of the electrons. Assume that there is no magnetic field in the plasma or that the electron motion is along the magnetic field in the z-direction. To simplify this derivation, also assume that the ions are fixed uniformly in space on the time scales of interest here due to their large mass, and that there is no thermal motion of the particles ($T = 0$).

Since the ions are fixed in this case, only the electron equation of motion is of interest:

$$mn_e\left[\frac{\partial v_z}{\partial t}+(v\cdot\nabla)v_z\right]=-en_eE_z, \tag{3.5-11}$$

and the electron equation of continuity is

$$\frac{\partial n_e}{\partial t}+\nabla\cdot(n_e\mathbf{v})=0. \tag{3.5-12}$$

The relationship between the electric field and the charge densities is given by Eq. (3.2-1), which for singly ionized particles can be written using Eq. (3.2-5) as

$$\nabla\cdot\mathbf{E}=\frac{\rho}{\varepsilon_o}=\frac{e}{\varepsilon_o}(n_i-n_e). \tag{3.5-13}$$

The wave-like behavior of this system is analyzed by linearization using

$$\mathbf{E}=\mathbf{E}_o+\mathbf{E}_1 \tag{3.5-14}$$

$$\mathbf{v}=\mathbf{v}_o+\mathbf{v}_1 \tag{3.5-15}$$

$$n=n_o+n_1, \tag{3.5-16}$$

where $\mathbf{E}_o$, $\mathbf{v}_o$, and n_o are the equilibrium values of the electric field, electron velocity, and electron density, and $\mathbf{E}_1$, $\mathbf{B}_1$, and $\mathbf{j}_1$ are the perturbed values of these quantities. Since quasi-neutral plasma has been assumed, $\mathbf{E}_o=0$, and the assumption of a uniform plasma with no temperature means that $\Delta n_o=\mathbf{v}_o=0$. Likewise, the time derivatives of these equilibrium quantities are zero.

Linearizing Eq. (3.5-13) gives

$$\nabla\cdot\mathbf{E}_1=-\frac{e}{\varepsilon_o}n_1. \tag{3.5-17}$$

Using Eqs. (3.5-14), (3.5-15), and (3.5-16) in Eq. (3.5-11) results in

$$\frac{dv_1}{dt}=-\frac{e}{m}E_1\,\hat{z}, \tag{3.5-18}$$

where the linearized convective derivative has been neglected. Linearizing the continuity Eq. (3.5-12) gives

$$\frac{dn_1}{dt} = -n_o \nabla \cdot \mathbf{v}_1 \, \hat{z}, \tag{3.5-19}$$

where the quadratic terms, such as $n_1 v_1$, etc., have been neglected as small. In the linear regime, the oscillating quantities will behave sinusoidally:

$$\mathbf{E}_1 = E_1 \, e^{i(kz-\omega t)} \, \hat{z} \tag{3.5-20}$$

$$\mathbf{v}_1 = v_1 \, e^{i(kz-\omega t)} \, \hat{z} \tag{3.5-21}$$

$$n_1 = n_1 \, e^{i(kz-\omega t)}. \tag{3.5-22}$$

This means that the time derivates in momentum and continuity equations can be replaced by $-i\omega t$, and the gradient in Eq. (3.5-17) can be replaced by ik in the $\hat{z}$ direction. Combining Eqs. (3.5-17), (3.5-18), and (3.5-19), using the time and spatial derivatives of the oscillating quantities, and solving for the frequency of the oscillation gives

$$\omega_p = \left(\frac{n_e e^2}{\varepsilon_o m} \right)^{1/2}, \tag{3.5-23}$$

where ω_p is the electron plasma frequency. A useful numerical formula for the electron plasma frequency is

$$f_p = \frac{\omega_p}{2\pi} \approx 9\sqrt{n_e}, \tag{3.5-24}$$

where the plasma density is in m^{-3}. This frequency is one of the fundamental parameters of a plasma, and the inverse of this value is approximately the minimum time required for the plasma to react to changes in its boundaries or in the applied potentials. For example, if the plasma density is 10^{18} m^{-3}, the electron plasma frequency is 9 GHz, and the electron plasma will respond to perturbations in less than a nanosecond.

In a similar manner, if the ion temperature is assumed to be negligible and the gross response of the plasma is dominated by ion motions, the ion plasma frequency can be found to be

$$\Omega_p = \left(\frac{n_e e^2}{\varepsilon_o M} \right)^{1/2} . \tag{3.5-25}$$

This equation provides the approximate time scale in which ions move in the plasma. For our previous example for a 10^{18} m^{-3} plasma density composed of xenon ions, the ion plasma frequency is about 18 MHz, and the ions will respond to first order in a fraction of a microsecond. However, the ions have inertia and respond at the ion acoustic velocity given by

$$v_a = \sqrt{\frac{\gamma_i k T_i + k T_e}{M}} , \tag{3.5-26}$$

where γ_i is the ratio of the ion specific heats and is equal to one for isothermal ions. In the normal case for ion and Hall thrusters, where $T_e >> T_i$, the ion acoustic velocity is simply

$$v_a = \sqrt{\frac{k T_e}{M}} . \tag{3.5-27}$$

It should be noted that if finite-temperature electrons and ions had been included in the derivations above, the electron-plasma and ion-plasma oscillations would have produced waves that propagate with finite wavelengths in the plasma. Electron-plasma waves and ion-plasma waves (sometimes called ion acoustic waves) occur in most electric thruster plasmas with varying amplitudes and effects on the plasma behavior. The dispersion relationships for these waves, which describe the relationship between the frequency and the wavelength of the wave, are derived in detail in plasma textbooks such as Chen [1] and will not be re-derived here.

3.5.3 Energy Conservation

The general form of the energy equation for charged species "*s*," moving with velocity $\mathbf{v}_s$ in the presence of species "*n*" is given by

$$\begin{aligned} \frac{\partial}{\partial t}\left(n_s m_s \frac{v_s^2}{2} + \frac{3}{2} p_s \right) + \nabla \cdot \left(n_s m_s \frac{v_s^2}{2} + \frac{5}{2} p_s \right) \mathbf{v}_s + \nabla \cdot \boldsymbol{\theta}_s \\ = q_s n_s \left(\mathbf{E} + \frac{\mathbf{R}_s}{q_s n_s} \right) \cdot \mathbf{v}_s + Q_s - \Psi_s . \end{aligned} \tag{3.5-28}$$

For simplicity, Eq. (3.5-28) neglects viscous heating of the species. The divergence terms on the left-hand side represent the total energy flux, which

includes the work done by the pressure, the macroscopic energy flux, and the transport of heat by conduction $\boldsymbol{\theta}_s = \boldsymbol{\kappa}_s \Delta T_s$. The thermal conductivity of the species is denoted by $\boldsymbol{\kappa}_s$, which is given in SI units [5] by

$$\boldsymbol{\kappa}_s = 3.2 \frac{\tau_e n e^2 T_{eV}}{m}, \tag{3.5-29}$$

where T_{eV} in this equation is in electron volts (eV). The right-hand side of Eq. (3.5-28) accounts for the work done by other forces as well for the generation/loss of heat as a result of collisions with other particles. The term $\mathbf{R}_s$ represents the mean change in the momentum of particles "s" as a result of collisions with all other particles:

$$\mathbf{R}_s \equiv \sum_n \mathbf{R}_{sn} = -\sum_n n_s m_s \nu_{sn} (\mathbf{v}_s - \mathbf{v}_n). \tag{3.5-30}$$

The heat-exchange terms are Q_s, which is the heat generated/lost in the particles of species "s" as a result of elastic collisions with all other species, and Ψ_s, the energy loss by species "s" as a result of inelastic collision processes such as ionization and excitation.

It is often useful to eliminate the kinetic energy from Eq. (3.5-28) to obtain a more applicable form of the energy conservation law. The left-hand side of Eq. (3.5-28) is expanded as

$$\begin{aligned} n_s m_s \mathbf{v}_s \cdot \frac{D\mathbf{v}_s}{Dt} + \frac{m_s v_s^2}{2} \frac{Dn_s}{Dt} + n_s m_s \frac{v_s^2}{2} \nabla \cdot \mathbf{v}_s + \frac{3}{2} \frac{\partial p_s}{\partial t} + \nabla \cdot \left(\frac{5}{2} p_s \mathbf{v}_s + \boldsymbol{\theta}_s \right) \\ = q_s n_s \mathbf{E} \cdot \mathbf{v}_s + \mathbf{R}_s \cdot \mathbf{v}_s + Q_s - \Psi_s. \end{aligned} \tag{3.5-31}$$

The continuity equation for the charged species is in the form

$$\frac{Dn_s}{Dt} = \frac{\partial n_s}{\partial t} + \mathbf{v}_s \cdot \nabla n_s = \dot{n} - n_s \nabla \cdot \mathbf{v}_s. \tag{3.5-32}$$

Combining these two equations with the momentum equation dotted with $\mathbf{v}_s$ gives

$$n_s m_s \mathbf{v}_s \cdot \frac{D\mathbf{v}_s}{Dt} = n_s q_s \mathbf{v}_s \cdot \mathbf{E} - \mathbf{v}_s \cdot \nabla p_s + \mathbf{v}_s \cdot \mathbf{R}_s - \dot{n} m_s v_s^2. \tag{3.5-33}$$

The energy equation can now be written as

$$\frac{3}{2}\frac{\partial p_s}{\partial t}+\nabla\cdot\left(\frac{5}{2}p_s\mathbf{v}_s+\boldsymbol{\theta}_s\right)-\mathbf{v}_s\cdot\nabla p_s=Q_s-\Psi_s-\dot{n}\frac{m_s v_s^{\,2}}{2}. \qquad (3.5\text{-}34)$$

The heat-exchange terms for each species Q_s consists of "frictional" (denoted by superscript R) and "thermal" (denoted by superscript T) contributions:

$$\begin{aligned} Q_s &= Q_s^R + Q_s^T, \\ Q_s^R &\equiv -\sum_n \mathbf{R}_{sn}\cdot\mathbf{v}_s, \\ Q_s^T &\equiv -\sum_n n_s\frac{2m_s}{m_a}\nu_{sn}\frac{3}{2}\left(\frac{kT_s}{e}-\frac{kT_n}{e}\right). \end{aligned} \qquad (3.5\text{-}35)$$

In a partially ionized gas consisting of electrons, singly charged ions, and neutrals of the same species, the frictional and thermal terms for the electrons take the form

$$\begin{aligned} Q_e^R &= -\left(\mathbf{R}_{ei}+\mathbf{R}_{en}\right)\cdot\mathbf{v}_e=\left(\frac{\mathbf{R}_{ei}+\mathbf{R}_{en}}{en_e}\right)\cdot\mathbf{J}_e \\ Q_e^T &= -3n_e\frac{m}{M}\left[\nu_{ei}\frac{k}{e}\left(T_e-T_i\right)+\nu_{en}\frac{k}{e}\left(T_e-T_n\right)\right], \end{aligned} \qquad (3.5\text{-}36)$$

where as usual M denotes the mass of the heavy species, and the temperature of the ions and neutrals is denoted by T_i and T_n, respectively. Using the steady-state electron momentum equation, in the absence of electron inertia, it is possible to write

$$Q_e^R=\left(\frac{\mathbf{R}_{ei}+\mathbf{R}_{en}}{en_e}\right)\cdot\mathbf{J}_e=\left(\mathbf{E}+\frac{\nabla p_e}{en_e}\right)\cdot\mathbf{J}_e. \qquad (3.5\text{-}37)$$

Thus Eq. (3.5-34) for the electrons becomes

$$\begin{aligned} \frac{3}{2}\frac{\partial p_e}{\partial t}+\nabla\cdot\left(\frac{5}{2}p_e\mathbf{v}_e+\boldsymbol{\theta}_e\right) &= Q_e-\mathbf{J}_e\cdot\frac{\nabla p_e}{en}-\dot{n}eU_i \\ &= \mathbf{E}\cdot\mathbf{J}_e-\dot{n}eU_i, \end{aligned} \qquad (3.5\text{-}38)$$

where the inelastic term is expressed as $\Psi_e=e\dot{n}U_i$ to represent the electron energy loss duc to ionization, with U_i (in volts) representing the first ionization potential of the atom. In Eq. (3.5-38), the $m_e v_e^2/2$ correction term has been neglected because usually in ion and Hall thrusters $eU_i >> m_e v_e^2/2$. If multiple

ionization and/or excitation losses are significant, the inelastic terms in Eq. (3.5-38) must be augmented accordingly.

In ion and Hall thrusters, it is common to assume a single temperature or distribution of temperatures for the heavy species without directly solving the energy equation(s). In some cases, however, such as in the plume of a hollow cathode for example, the ratio of T_e / T_i is important for determining the extent of Landau damping on possible electrostatic instabilities. The heavy species temperature is also important for determining the total pressure inside the cathode. Thus, separate energy equations must be solved directly. Assuming that the heavy species are slow moving and the inelastic loss terms are negligible, Eq. (3.5-34) for ions takes the form

$$\frac{3}{2}\frac{\partial p_{\text{in}}}{\partial t} + \nabla \cdot \left(\frac{5}{2} p_{\text{in}} \mathbf{v}_{\text{in}} + \boldsymbol{\theta}_{\text{in}} \right) - \mathbf{v}_{\text{in}} \cdot \nabla p_{\text{in}} = Q_{\text{in}}, \tag{3.5-39}$$

where the subscript "in" represents ion-neutral collisions.

Finally, the total heat generated in partially ionized plasmas as a result of the (elastic) friction between the various species is given by

$$\begin{aligned} \sum_s Q_s^R &= Q_e^R + Q_i^R + Q_n^R \\ &= -\left(\mathbf{R}_{ei} + \mathbf{R}_{en}\right) \cdot \mathbf{v}_e - \left(\mathbf{R}_{ie} + \mathbf{R}_{\text{in}}\right) \cdot \mathbf{v}_i - \left(\mathbf{R}_{ne} + \mathbf{R}_{ni}\right) \cdot \mathbf{v}_n . \end{aligned} \tag{3.5-40}$$

Since $\mathbf{R}_{\text{sa}} = -\mathbf{R}_{\text{as}}$, it is possible to write this as

$$\sum_s Q_s^R = -\mathbf{R}_{ei} \cdot \left(\mathbf{v}_e - \mathbf{v}_i\right) - \mathbf{R}_{en} \cdot \left(\mathbf{v}_e - \mathbf{v}_n\right) - \mathbf{R}_{\text{in}} \cdot \left(\mathbf{v}_i - \mathbf{v}_n\right) \cdot \tag{3.5-41}$$

The energy conservation equation(s) can be used with the momentum and continuity equations to provide a closed set of equations for analysis of plasma dynamics within the fluid approximations.

3.6 Diffusion in Partially Ionized Gases

Diffusion is often very important in the particle transport in ion and Hall thruster plasmas. The presence of pressure gradients and collisions between different species of charged particles and between the charged particles and the neutrals produces diffusion of the plasma from high density regions to low density regions, both along and across magnetic field lines.

To evaluate diffusion-driven particle motion in ion and Hall thruster plasmas, the equation of motion for any species can be written as

$$mn\frac{d\mathbf{v}}{dt} = qn(\mathbf{E}+\mathbf{v}\times\mathbf{B}) - \nabla\cdot\mathbf{p} - mn\nu\ (\mathbf{v}-\mathbf{v}_o), \tag{3.6-1}$$

where the terms in this equation have been previously defined and ν is the collision frequency between two species in the plasma. In order to apply and solve this equation, it is first necessary to understand the collisional processes between the different species in the plasma that determine the applicable collision frequency.

3.6.1 Collisions

Charged particles in a plasma interact with each other primarily by coulomb collisions and also can collide with neutral atoms present in the plasma. These collisions are very important when describing diffusion, mobility, and resistivity in the plasma.

When a charged particle collides with a neutral atom, it can undergo an elastic or an inelastic collision. The probability that such a collision will occur can be expressed in terms of an effective cross-sectional area. Consider a thin slice of neutral gas with an area A and a thickness dx containing essentially stationary neutral gas atoms with a density n_a. Assume that the atoms are simple spheres of cross-sectional area σ. The number of atoms in the slice is given by $n_a A dx$. The fraction of the slice area that is occupied by the spheres is

$$\frac{n_a A\sigma dx}{A} = n_a\sigma dx. \tag{3.6-2}$$

If the incident flux of particles is Γ_o, then the flux that emerges without making a collision after passing through the slice is

$$\Gamma(x) = \Gamma_o(1 - n_a\sigma dx). \tag{3.6-3}$$

The change in the flux as the particles pass through the slice is

$$\frac{d\Gamma}{dx} = -\Gamma n_a\sigma. \tag{3.6-4}$$

The solution to Eq. (3.6-4) is

$$\Gamma = \Gamma_o \exp(-n_a \sigma\, x) = \Gamma_o \exp\left(-\frac{x}{\lambda}\right), \tag{3.6-5}$$

where λ is defined as the mean free path for collisions and describes the distance in which the particle flux would decrease to $1/e$ of its initial value. The mean free path is given by

$$\lambda = \frac{1}{n_a \sigma}, \tag{3.6-6}$$

which represents the mean distance that a relatively fast-moving particle, such as an electron or ion, will travel in a stationary density of neutral particles.

The mean time between collisions for this case is given by the mean free path divided by the charged particle velocity:

$$\tau = \frac{1}{n_a \sigma v}. \tag{3.6-7}$$

Averaging over all of the Maxwellian velocities of the charged particles, the collision frequency is then

$$\nu = \frac{1}{\tau} = n_a \sigma \bar{v}. \tag{3.6-8}$$

In the event that a relatively slowly moving particle, such as a neutral atom, is incident on a density of fast-moving electrons, the mean free path for the neutral particle to experience a collision is given by

$$\lambda = \frac{v_n}{n_e \langle \sigma v_e \rangle}, \tag{3.6-9}$$

where v_n is the neutral particle velocity and the reaction rate coefficient in the denominator is averaged over all the relevant collision cross sections. Equation (3.6-9) can be used to describe the distance that a neutral gas atom travels in a plasma before ionization occurs, which is sometimes called the *penetration distance*.

Other collisions are also very important in ion and Hall thrusters. The presence of inelastic collisions between electrons and neutrals can result in either ionization or excitation of the neutral particle. The ion production rate per unit volume is given by

$$\frac{dn_i}{dt} = n_a n_e \langle \sigma_i v_e \rangle , \tag{3.6-10}$$

where σ_i is the ionization cross section, v_e is the electron velocity, and the term in the brackets is the reaction rate coefficient, which is the ionization cross section averaged over the electron velocity distribution function.

Likewise, the production rate per unit volume of excited neutrals, n^*, is

$$\frac{dn^*}{dt} = \sum_j n_a n_e \langle \sigma_* v_e \rangle_j , \tag{3.6-11}$$

where σ_* is the excitation cross section and the reaction rate coefficient is averaged over the electron distribution function and summed over all possible excited states j. A complete listing of the ionization and excitation cross sections for xenon is given in Appendix D, and the reaction rate coefficients for ionization and excitation averaged over a Maxwellian electron distribution are given in Appendix E.

Charge exchange [2,6] in ion and Hall thrusters usually describes the resonant charge transfer between like atoms and ions in which essentially no kinetic energy is exchanged during the collision. Because this is a resonant process, it can occur at large distances, and the charge exchange (CEX) cross section is very large [2]. For example, the charge exchange cross section for xenon is about 10^{-18} m^2 [7], which is significantly larger than the ionization and excitation cross sections for this atom. Since the ions in the thruster are often energetic due to acceleration by the electric fields in the plasma or acceleration in ion thruster grid structures, charge exchange results in the production of energetic neutrals and relatively cold ions. Charge exchange collisions are often a dominant factor in the heating of cathode structures, the mobility and diffusion of ions in the thruster plasma, and the erosion of grid structures and surfaces.

While the details of classical collision physics are interesting, they are well described in several other textbooks [1,2,5] and are not critically important to understanding ion and Hall thrusters. However, the various collision frequencies and cross sections are of interest for use in modeling the thruster discharge and performance.

The frequency of collisions between electrons and neutrals is sometimes written [8] as

$$\nu_{en} = \sigma_{en}(T_e) n_a \sqrt{\frac{8kT_e}{\pi m}}, \tag{3.6-12}$$

where the effective electron–neutral scattering cross section $\sigma(T_e)$ for xenon can be found from a numerical fit to the electron–neutral scattering cross section averaged over a Maxwellian electron distribution [8]:

$$\sigma_{en}(T_e) = 6.6 \times 10^{-19} \left[\frac{\frac{T_{eV}}{4} - 0.1}{1 + \left(\frac{T_{eV}}{4} \right)^{1.6}} \right] \quad [\mathrm{m}^2], \tag{3.6-13}$$

where T_{eV} is in electron volts. The electron–ion collision frequency for coulomb collisions [5] is given in SI units by

$$\nu_{ei} = 2.9 \times 10^{-12} \frac{n_e \ln \Lambda}{T_{eV}^{3/2}}, \tag{3.6-14}$$

where $\ln\Lambda$ is the coulomb logarithm given in a familiar form [5] by

$$\ln \Lambda = 23 - \frac{1}{2} \ln \left(\frac{10^{-6} n_e}{T_{eV}^3} \right). \tag{3.6-15}$$

The electron–electron collision frequency [5] is given by

$$\nu_{ee} = 5 \times 10^{-12} \frac{n_e \ln \Lambda}{T_{eV}^{3/2}}, \tag{3.6-16}$$

While the values of the electron–ion and the electron–electron collision frequencies in Eqs. (3.6-14) and (3.6-16) are clearly comparable, the electron–electron thermalization time is much shorter than the electron–ion thermalization time due to the large mass difference between the electrons and ions reducing the energy transferred in each collision. This is a major reason that electrons thermalize rapidly into a population with Maxwellian distribution, but do not thermalize rapidly with the ions.

In addition, the ion–ion collision frequency [5] is given by

$$\nu_{ii} = Z^4 \left(\frac{m}{M} \right)^{1/2} \left(\frac{T_e}{T_i} \right)^{3/2} \nu_{ee}, \tag{3.6-17}$$

where Z is the ion charge number.

Collisions between like particles and between separate species tend to equilibrate the energy and distribution functions of the particles. This effect was analyzed in detail by Spitzer [9] in his classic book. In thrusters, there are several equilibration time constants of interest. First, the characteristic collision times between the different charged particles is just one over the average collision frequencies given above. Second, equilibration times between the species and between different populations of the same species were calculated by Spitzer. The time for a monoenergetic electron (sometimes called a *primary electron*) to equilibrate with the Maxwellian population of the plasma electrons is called the slowing time, τ_s. Finally, the time for one Maxwellian population to equilibrate with another Maxwellian population is called the equilibration time, τ_{eq}. Expressions for these equilibration times, and a comparison of the rates of equilibration by these two effects, are found in Appendix F.

Collisions of electrons with other species in the plasma lead to resistivity and provide a mechanism for heating. This mechanism is often called ohmic heating or joule heating. In steady state and neglecting electron inertia, the electron momentum equation, taking into account electron–ion collisions and electron-neutral collisions, is

$$0 = -en\left(\mathbf{E} + \mathbf{v_e} \times \mathbf{B}\right) - \nabla \cdot \mathbf{p_e} - mn\left[\nu_{ei}\left(\mathbf{v_e} - \mathbf{v_i}\right) + \nu_{en}\left(\mathbf{v_e} - \mathbf{v_n}\right)\right]. \quad (3.6\text{-}18)$$

The electron velocity is very large with respect to the neutral velocity, and Eq. (3.6-18) can be written as

$$0 = -en\left(\mathbf{E} + \frac{\nabla \mathbf{p_e}}{en}\right) - en\mathbf{v_e} \times \mathbf{B} - mn\left(\nu_{ei} + \nu_{en}\right)\mathbf{v_e} + mn\nu_{ei}\mathbf{v_i}. \quad (3.6\text{-}19)$$

Since charged particle current density is given by $\mathbf{J} = qn\mathbf{v}$, Eq. (3.6-19) can be written as

$$\eta \mathbf{J_e} = \mathbf{E} + \frac{\nabla \mathbf{p} - \mathbf{J}_e \times \mathbf{B}}{en} - \eta_{ei}\mathbf{J_i}, \quad (3.6\text{-}20)$$

where $\mathbf{J}_e$ is the electron current density, $\mathbf{J_i}$ is the ion current density, and η_{ei} is the plasma resistivity. Equation (3.6-20) is commonly known as Ohm's law for partially ionized plasmas and is a variant of the well-known generalized Ohm's law, which usually is expressed in terms of the total current density, $\mathbf{J} = en(\mathbf{v_i} - \mathbf{v_e})$, and the ion fluid velocity, $\mathbf{v_i}$. If there are no collisions or net

current in the plasma, this equation reduces to Eq. (3.5-7), which was used to derive the Boltzmann relationship for plasma electrons.

In Eq. (3.6-20), the total resistivity of a partially ionized plasma is given by

$$\eta = \frac{m(\nu_{ei} + \nu_{en})}{e^2 n} = \frac{1}{\varepsilon_o \tau_e \omega_p^2}, \tag{3.6-21}$$

where the total collision time for electrons, accounting for both electron–ion and electron–neutral collisions, is given by

$$\tau_e = \frac{1}{\nu_{ei} + \nu_{en}}. \tag{3.6-22}$$

By neglecting the electron–neutral collision terms in Eq. (3.6-19), the well-known expression for the resistivity of a fully ionized plasma [1,9] is recovered:

$$\eta_{ei} = \frac{m\nu_{ei}}{e^2 n} = \frac{1}{\varepsilon_o \tau_{ei} \omega_p^2}. \tag{3.6-23}$$

In ion and Hall thrusters, the ion current in the plasma is typically much smaller than the electron current due to the large mass ratio, so the ion current term in Ohm's law, Eq. (3.6-20), is sometimes neglected.

3.6.2 Diffusion and Mobility Without a Magnetic Field

The simplest case of diffusion in a plasma is found by neglecting the magnetic field and writing the equation of motion for any species as

$$mn\frac{d\mathbf{v}}{dt} = qn\mathbf{E} - \nabla \cdot \mathbf{p} - mn\nu\left(\mathbf{v} - \mathbf{v}_o\right), \tag{3.6-24}$$

where m is the species mass and the collision frequency is taken to be a constant. Assume that the velocity of the particle species of interest is large compared to the slow species ($\mathbf{v} >> \mathbf{v}_o$), the plasma is isothermal ($\nabla p = kT\nabla n$), and the diffusion is steady state and occurring with a sufficiently high velocity that the convective derivative can be neglected. Equation (3.6-24) can then be solved for the particle velocity:

$$\mathbf{v} = \frac{q}{m\nu}\mathbf{E} - \frac{kT}{m\nu}\frac{\nabla n}{n}. \tag{3.6-25}$$

The coefficients of the electric field and the density gradient terms in Eq. (3.6-25) are called the mobility,

$$\mu = \frac{|q|}{m\nu}\ [\mathrm{m^2/V\text{-}s}], \tag{3.6-26}$$

and the diffusion coefficient,

$$D = \frac{kT}{m\nu}\ [\mathrm{m^2/s}]. \tag{3.6-27}$$

These terms are related by what is called the *Einstein relation*:

$$\mu = \frac{|q|\,D}{kT}. \tag{3.6-28}$$

3.6.2.1 Fick's Law and the Diffusion Equation. The flux of diffusing particles in the simple case of Eq. (3.6-25) is

$$\Gamma = n\,\mathbf{v} = \mu n\,\mathbf{E} - D\,\nabla n. \tag{3.6-29}$$

A special case of this is called *Fick's law*, in which the flux of particles for either the electric field or the mobility term being zero is given by

$$\Gamma = -D\,\nabla n. \tag{3.6-30}$$

The continuity equation, Eq. (3.5-10), without sink or source terms can be written as

$$\frac{\partial n}{\partial t} + \nabla\cdot\Gamma = 0, \tag{3.6-31}$$

where Γ represents the flux of any species of interest. If the diffusion coefficient D is constant throughout the plasma, substituting Eq. (3.6-30) into Eq. (3.6-31) gives the well-known diffusion equation for a single species:

$$\frac{\partial n}{\partial t} - D\nabla^2 n = 0. \tag{3.6-32}$$

The solution to this equation can be obtained by separation of variables. The simplest example of this is for a slab geometry of finite width, where the

plasma density can be expressed as having separable spatial and temporal dependencies:

$$n(x,t) = X(x)\bar{T}(t). \tag{3.6-33}$$

Substituting into Eq. (3.6-32) gives

$$X\frac{d\bar{T}}{dt} = D\bar{T}\frac{d^2X}{dx^2}. \tag{3.6-34}$$

Separating the terms gives

$$\frac{1}{\bar{T}}\frac{d\bar{T}}{dt} = D\frac{1}{X}\frac{d^2X}{dx^2} = \alpha, \tag{3.6-35}$$

where each side is independent of the other and therefore can be set equal to a constant α. The time dependent function is then

$$\frac{d\bar{T}}{dt} = -\frac{\bar{T}}{\tau}, \tag{3.6-36}$$

where the constant α will be written as $-1/\tau$. The solution to Eq. (3.6-36) is

$$\bar{T} = \bar{T}_o e^{-t/\tau}. \tag{3.6-37}$$

Since there is no ionization source term in Eq. (3.6-32), the plasma density decays exponentially with time from the initial state.

The right-hand side of Eq. (3.6-35) has the spatial dependence of the diffusion and can be written as

$$\frac{d^2X}{dx^2} = -\frac{X}{D\tau}, \tag{3.6-38}$$

where again the constant α will be written as $-1/\tau$. This equation has a solution of the form

$$X = A\cos\frac{X}{L} + B\sin\frac{X}{L}, \tag{3.6-39}$$

where A and B are constants and L is the diffusion length given by $(D\tau)^{1/2}$. If it is assumed that X is zero at the boundaries at $\pm d/2$, then the lowest-order

solution is symmetric ($B = 0$) with the diffusion length equal to π. The solution to Eq. (3.6-38) is then

$$X = \cos\frac{\pi x}{d}. \tag{3.6-40}$$

The lowest-order complete solution to the diffusion equation for the plasma density is then the product of Eq. (3.6-37) and Eq. (3.6-40):

$$n = n_o e^{-t/\tau} \cos\frac{\pi x}{d}. \tag{3.6-41}$$

Of course, higher-order odd solutions are possible for given initial conditions, but the higher-order modes decay faster and the lowest-order mode typically dominates after a sufficient time. The plasma density decays with time from the initial value n_o, but the boundary condition (zero plasma density at the wall) maintains the plasma shape described by the cosine function in Eq. (3.6-41).

While a slab geometry was chosen for this illustrative example due to its simplicity, situations in which slab geometries are useful in modeling ion and Hall thrusters are rare. However, solutions to the diffusion equation in other coordinates more typically found in these thrusters are obtained in a similar manner. For example, in cylindrical geometries found in many hollow cathodes and in ion thruster discharge chambers, the solution to the cylindrical differential equation follows Bessel functions radially and still decays exponentially in time if source terms are not considered.

Solutions to the diffusion equation with source or sink terms on the right-hand side are more complicated to solve. This can be seen in writing the diffusion equation as

$$\frac{\partial n}{\partial t} - D\nabla^2 n = \dot{n}, \tag{3.6-42}$$

where the source term is described by an ionization rate equation given by

$$\dot{n} = n_a n\langle\sigma_i v_e\rangle \approx n_a n\sigma_i(T_e)\bar{v}, \tag{3.6-43}$$

and where $\bar{v}$ is the average particle speed found in Eq. (3.4-8) and $\sigma_i(T_e)$ is the impact ionization cross section averaged over a Maxwellian distribution of electrons at a temperature T_e. Equations for the xenon ionization reaction rate coefficients averaged over a Maxwellian distribution are found in Appendix E.

A separation of variables solution can still be obtained for this case, but the time-dependent behavior is no longer purely exponential as was found in Eq. (3.6-37). In this situation, the plasma density will decay or increase to an equilibrium value depending on the magnitude of the source and sink terms.

To find the steady-state solution to the cylindrical diffusion equation, the time derivative in Eq. (3.6-42) is set equal to zero. Writing the diffusion equation in cylindrical coordinates and assuming uniform radial electron temperatures and neutral densities, Eq. (3.6-42) becomes

$$\frac{\partial^2 n}{\partial r^2}+\frac{1}{r}\frac{\partial n}{\partial r}+\frac{\partial^2 n}{\partial z^2}+C^2 n=0, \tag{3.6-44}$$

where the constant is given by

$$C^2=\frac{n_a\sigma_i(T_e)\bar{v}}{D}. \tag{3.6-45}$$

This equation can be solved analytically by separation of variables of the form

$$n=n(0,0)f(r)g(z). \tag{3.6-46}$$

Using Eq. (3.6-46), the diffusion equation becomes

$$\frac{1}{f}\frac{\partial^2 f}{\partial r^2}+\frac{1}{rf}\frac{\partial f}{\partial r}+C^2+\alpha^2=-\frac{1}{g}\frac{\partial^2 g}{\partial z^2}+\alpha^2=0. \tag{3.6-47}$$

The solution to the radial component of Eq. (3.6-47) is the sum of the zero-order Bessel functions of the first and second kind, which is written in a general form as

$$f(r)=A_1 J_o(\alpha r)+A_2 Y_o(\alpha r). \tag{3.6-48}$$

The Bessel function of the second kind, Y_o, becomes infinite as (αr) goes to zero, and because the density must always be finite, the constant A_2 must equal zero. Therefore, the solution for Eq. (3.6-47) is the product of the zero-order Bessel function of the first kind times an exponential term in the axial direction:

$$n(r,z)=n(0,0)J_o\left(\sqrt{C^2+\alpha^2}\,r\right)e^{-\alpha z}. \tag{3.6-49}$$

Assuming that the ion density goes to zero at the wall,

$$\sqrt{C^2+\alpha^2}=\frac{\lambda_{01}}{R}, \tag{3.6-50}$$

where λ_{01} is the first zero of the zero-order Bessel function and R is the internal radius of the cylinder being considered. Setting $\alpha=0$, this eigenvalue results in an equation that gives a direct relationship between the electron temperature, the radius of the plasma cylinder, and the diffusion rate:

$$\left(\frac{R}{\lambda_{01}}\right)^2 n_a \sigma_i(T_e)\sqrt{\frac{8kT_e}{\pi m}}-D=0. \tag{3.6-51}$$

The physical meaning of Eq. (3.6-51) is that particle balance in bounded plasma discharges dominated by radial diffusion determines the plasma electron temperature. This occurs because the generation rate of ions, which is determined by the electron temperature from Eq. (3.6-43), must equal the loss rate, which is determined by the diffusion rate to the walls, in order to satisfy the boundary conditions. Therefore, the solution to the steady-state cylindrical diffusion equation specifies both the radial plasma profile and the maximum electron temperature once the dependence of the diffusion coefficient is specified. This result is very useful in modeling the plasma discharges in hollow cathodes and in various types of electric thrusters.

3.6.2.2 Ambipolar Diffusion Without a Magnetic Field. In many circumstances in thrusters, the flux of ions and electrons from a given region or the plasma as a whole are equal. For example, in the case of microwave ion thrusters, the ions and electrons are created in pairs during ionization by the plasma electrons heated by the microwaves, so simple charge conservation states that the net flux of both ions and electrons out of the plasma must be the same. The plasma will then establish the required electric fields in the system to slow the more mobile electrons such that the electron escape rate is the same as the slower ion loss rate. This finite electric field affects the diffusion rate for both species.

Since the expression for the flux in Eq. (3.6-29) was derived for any species of particles, a diffusion coefficient for ions and electrons can be designated (because D contains the mass) and the fluxes equated to obtain

$$\mu_i n\mathbf{E}-D_i\,\nabla n=-\mu_e n\mathbf{E}-D_e\,\nabla n, \tag{3.6-52}$$

where quasi-neutrality ($n_i\approx n_e$) in the plasma has been assumed. Solving for the electric field gives

$$\mathbf{E} = \frac{D_i - D_e}{\mu_i + \mu_e} \frac{\nabla n}{n}. \tag{3.6-53}$$

Substituting **E** into Eq. (3.6-29) for the ion flux,

$$\Gamma = -\frac{\mu_i D_e + \mu_e D_i}{\mu_i + \mu_e} \nabla n = -D_a \nabla n, \tag{3.6-54}$$

where D_a is the ambipolar diffusion coefficient given by

$$D_a = \frac{\mu_i D_e + \mu_e D_i}{\mu_i + \mu_e}. \tag{3.6-55}$$

Equation (3.6-54) was expressed in the form of Fick's law, but with a new diffusion coefficient reflecting the impact of ambipolar flow on the particle mobilities. Substituting Eq. (3.6-54) into the continuity equation without sources or sinks gives the diffusion equation for ambipolar flow:

$$\frac{\partial n}{\partial t} - D_a \nabla^2 n = 0. \tag{3.6-56}$$

Since the electron and ion mobilities depend on the mass

$$\mu_e = \frac{e}{mv} >> \mu_i = \frac{e}{Mv}, \tag{3.6-57}$$

it is usually possible to neglect the ion mobility. In this case, Eq. (3.6-55) combined with Eq. (3.6-28) gives

$$D_a \approx D_i + \frac{\mu_i}{\mu_e} D_e = D_i \left(1 + \frac{T_e}{T_i} \right). \tag{3.6-58}$$

Since the electron temperature in thrusters is usually significantly higher than the ion temperature ($T_e >> T_i$), ambipolar diffusion greatly enhances the ion diffusion coefficient. Likewise, the smaller ion mobility significantly decreases the ambipolar electron flux leaving the plasma.

3.6.3 Diffusion Across Magnetic Fields

Charged particle transport across magnetic fields is described by what is called *classical diffusion* theory and non-classical or *anomalous diffusion*. Classical diffusion, which will be presented below, includes both the case of particles of one species moving across the field due to collisions with another species of

particles, and the case of ambipolar diffusion across the field where the fluxes are constrained by particle balance in the plasma. Anomalous diffusion can be caused by a number of different effects. In ion and Hall thrusters, the anomalous diffusion is usually described by Bohm diffusion [10].

3.6.3.1 Classical Diffusion of Particles Across B Fields. The fluid equation of motion for isothermal electrons moving in the perpendicular direction across a magnetic field is

$$mn\frac{d\mathbf{v}_\perp}{dt} = qn\left(\mathbf{E} + \mathbf{v}_\perp x\mathbf{B}\right) - kT_e\nabla n - mn\nu\,\mathbf{v}_\perp . \tag{3.6-59}$$

The same form of this equation can be written for ions with a mass M and temperature T_i. Consider steady-state diffusion and set the time and convective derivatives equal to zero. Separating Eq. (3.6-59) into x and y coordinates gives

$$mn\nu\, v_x = qnE_x + qnv_yB_o - kT_e\frac{\partial n}{\partial x} \tag{3.6-60}$$

and

$$mn\nu\, v_y = qnE_y + qnv_xB_o - kT_e\frac{\partial n}{\partial y}, \tag{3.6-61}$$

where $\mathbf{B} = B_o(z)$. The x and y velocity components are then

$$v_x = \pm\mu E_x + \frac{\omega_c}{\nu}v_y - \frac{D}{n}\frac{\partial n}{\partial x} \tag{3.6-62}$$

and

$$v_y = \pm\mu E_y + \frac{\omega_c}{\nu}v_x - \frac{D}{n}\frac{\partial n}{\partial y}. \tag{3.6-63}$$

Solving Eqs. (3.6-62) and (3.6-63), the velocities in the two directions are

$$\left[1+\omega_c^2\tau^2\right]v_x = \pm\mu E_x - \frac{D}{n}\frac{\partial n}{\partial x} + \omega_c^2\tau^2\frac{E_y}{B_o} - \omega_c^2\tau^2\frac{kT_e}{qB_o}\frac{1}{n}\frac{\partial n}{\partial y} \tag{3.6-64}$$

and

$$\left[1+\omega_c^2\tau^2\right]v_y = \pm\mu E_y - \frac{D}{n}\frac{\partial n}{\partial y} + \omega_c^2\tau^2\frac{E_x}{B_o} - \omega_c^2\tau^2\frac{kT_e}{qB_o}\frac{1}{n}\frac{\partial n}{\partial x}, \qquad (3.6\text{-}65)$$

where $\tau = 1/\nu$ is the average collision time.

The perpendicular electron mobility is defined as

$$\mu_\perp = \frac{\mu}{1+\omega_c^2\tau^2} = \frac{\mu}{1+\Omega_e^2}, \qquad (3.6\text{-}66)$$

where the perpendicular mobility is written in terms of the electron Hall parameter defined as $\Omega_e = eB/m\nu$. The perpendicular diffusion coefficient is defined as

$$D_\perp = \frac{D}{1+\omega_c^2\tau^2} = \frac{D}{1+\Omega_e^2}. \qquad (3.6\text{-}67)$$

The perpendicular velocity can then be written in vector form again as

$$\mathbf{v}_\perp = \pm\mu_\perp E - D_\perp\frac{\nabla n}{n} + \frac{\mathbf{v}_E + \mathbf{v}_D}{1+\left(\nu^2/\omega_c^2\right)}. \qquad (3.6\text{-}68)$$

This is a form of Fick's law with two additional terms, the azimuthal $\mathbf{E}\times\mathbf{B}$ drift,

$$\mathbf{v}_E = \frac{\mathbf{E}\times\mathbf{B}}{B_o^2}, \qquad (3.6\text{-}69)$$

and the diamagnetic drift,

$$\mathbf{v}_D = -\frac{kT}{qB_o^2}\frac{\nabla n\times\mathbf{B}}{n}, \qquad (3.6\text{-}70)$$

both reduced by the fluid drag term $(1+\nu^2/\omega_c^2)$. In the case of a thruster, the perpendicular cross-field electron flux flowing toward the wall or toward the anode is then

$$\mathbf{\Gamma}_e = n\mathbf{v}_\perp = \pm\mu_\perp n\mathbf{E} - D_\perp\nabla n, \qquad (3.6\text{-}71)$$

which has the form of Fick's law but with the mobility and diffusion coefficients modified by the magnetic field.

The "classical" cross-field diffusion coefficient $D_\perp$, derived above and found in the literature [1,2], is proportional to $1/B^2$. However, in measurements in many plasma devices, including in Kaufman ion thrusters and in Hall thrusters, the perpendicular diffusion coefficient in some regions is found to be close to the Bohm diffusion coefficient:

$$D_B = \frac{1}{16}\frac{kT_e}{eB}, \tag{3.6-72}$$

which scales as $1/B$. Therefore, Bohm diffusion often progresses at orders of magnitude higher rates than classical diffusion. It has been proposed that Bohm diffusion results from collective instabilities in the plasma. Assume that the perpendicular electron flux is proportional to the $\mathbf{E}\times\mathbf{B}$ drift velocity,

$$\Gamma_e = nv_\perp \propto n\frac{E}{B}. \tag{3.6-73}$$

Also assume that the maximum electric field that occurs in the plasma due to Debye shielding is proportional to the electron temperature divided by the radius of the plasma:

$$E_{\max} = \frac{\phi_{\max}}{r} = \frac{kT_e}{qr}. \tag{3.6-74}$$

The electron flux to the wall is then

$$\Gamma_e \approx C\frac{n}{r}\frac{kT_e}{qB} \approx -C\frac{kT_e}{qB}\nabla n = -D_B\nabla n. \tag{3.6-75}$$

where C is a constant less than 1. The Bohm diffusion coefficient has an empirically determined value of C =1/16, as shown in Eq. (3.6-72), which fits most experiments with some uncertainty. As pointed out in Chen [1], this is why it is no surprise that Bohm diffusion scales as kT_e/eB.

3.6.3.2 Ambipolar Diffusion Across B Fields. Ambipolar diffusion across magnetic fields is much more complicated than the diffusion cases just covered because the mobility and diffusion coefficients are anisotropic in the presence of a magnetic field. Since both quasi-neutrality and charge balance must be satisfied, ambipolar diffusion dictates that the sum of the cross field and parallel to the field loss rates for both the ions and electrons must be the same. This means that the divergence of the ion and electron fluxes must be equal. While it is a simple matter to write equations for the divergence of these

two species and equate them, the resulting equation cannot be easily solved because it depends on the behavior both in the plasma and at the boundaries conditions.

A special case in which only the ambipolar diffusion toward a wall in the presence of a transverse magnetic field is now considered. In this situation, charge balance is conserved separately along and across the magnetic field lines. The transverse electron equation of motion for isothermal electrons, including electron–neutral and electron–ion collisions, can be written as

$$mn\left(\frac{\partial \mathbf{v}_e}{\partial t}+(\mathbf{v_e}\cdot\nabla)\mathbf{v_e}\right)=-en(\mathbf{E}+\mathbf{v}_e\times\mathbf{B})-kT_e\nabla n - mn\nu_{en}(\mathbf{v}_e-\mathbf{v}_o)-mn\nu_{ei}(\mathbf{v}_e-\mathbf{v}_i), \tag{3.6-76}$$

where $\mathbf{v}_o$ is the neutral particle velocity. Taking the magnetic field to be in the z-direction, and assuming the convective derivative to be negligibly small, then in steady-state this equation can be separated into the two transverse electron velocity components:

$$v_x+\mu_eE_x+\frac{e}{m\nu_e}v_yB+\frac{kT_e}{mn\nu_e}\frac{\partial n}{\partial x}-\frac{\nu_{ei}}{\nu_e}v_i=0 \tag{3.6-77}$$

$$v_y+\mu_eE_y-\frac{e}{m\nu_e}v_xB+\frac{kT_e}{mn\nu_e}\frac{\partial n}{\partial y}-\frac{\nu_{ei}}{\nu_e}v_i=0\,, \tag{3.6-78}$$

where $\nu_e=\nu_{en}+\nu_{ei}$ is the total collision frequency, $\mu_e=e/m\nu_e$ is the electron mobility including both ion and neutral collisional effects, and v_o is neglected as being small compared to the electron velocity v_e. Solving for v_y and eliminating the $\mathbf{E}\times\mathbf{B}$ and diagmagnetic drift terms in the x-direction, the transverse electron velocity is given by

$$v_e\left(1+\mu_e^2B^2\right)=\mu_e\left(E+\frac{kT_e}{e}\frac{\nabla n}{n}\right)+\frac{\nu_{ei}}{\nu_e}v_i\,, \tag{3.6-79}$$

Since ambipolar flow and quasi-neutrality are assumed everywhere in the plasma, the transverse electron and ion transverse velocities must be equal, which gives

$$v_i\left(1+\mu_e^2B^2-\frac{\nu_{ei}}{\nu_e}\right)=\mu_e\left(E+\frac{kT_e}{e}\frac{\nabla n}{n}\right). \tag{3.6-80}$$

The transverse velocity of each species is then

$$v_i = v_e = \frac{\mu_e}{\left(1+\mu_e^2 B^2 - \frac{\nu_{ei}}{\nu_e}\right)}\left(E + \frac{kT_e}{e}\frac{\nabla n}{n}\right). \tag{3.6-81}$$

In this case, the electron mobility is reduced by the magnetic field (the first term on the right-hand side of this equation), and so an electric field E is generated in the plasma to actually slow down the ion transverse velocity in order to balance the pressure term and maintain ambipolarity. This is exactly the opposite of the normal ambipolar diffusion without magnetic fields or along the magnetic field lines covered in Section 3.6.2, where the electric field slowed the electrons and accelerated the ions to maintain ambipolarity. Equation (3.6-81) can be written in terms of the transverse flux as

$$\Gamma_\perp = \frac{\mu_e}{\left(1+\mu_e^2 B^2 - \nu_{ei}/\nu_e\right)}\left(enE + kT_e \nabla n\right). \tag{3.6-82}$$

3.7 Sheaths at the Boundaries of Plasmas

While the motion of the various particles in the plasma is important in understanding the behavior and performance of ion and Hall thrusters, the boundaries of the plasma represent the physical interface through which energy and particles enter and leave the plasma and the thruster. Depending on the conditions, the plasma will establish potential and density variations at the boundaries in order to satisfy particle balance or the imposed electrical conditions at the thruster walls. This region of potential and density change is called the sheath, and understanding sheath formation and behavior is also very important in understanding and modeling ion and Hall thruster plasmas.

Consider the generic plasma in Fig. 3-2, consisting of quasi-neutral ion and electron densities with temperatures given by T_i and T_e, respectively. The ion current density to the boundary "wall" for singly charged ions, to first order, is given by $n_i e v_i$, where v_i is the ion velocity. Likewise, the electron flux to the boundary wall, to first order, is given by $n_e e v_e$, where v_e is the electron velocity. The ratio of the electron flux to the ion current density going to the boundary, assuming quasi-neutrality, is

$$\frac{J_e}{J_i} = \frac{n_e e v_e}{n_i e v_i} = \frac{v_e}{v_i}. \tag{3.7-1}$$

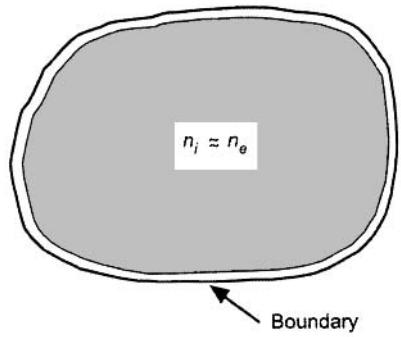

Fig. 3-2. Generic quasi-neutral plasma enclosed in a boundary.

In the absence of an electric field in the plasma volume, conservation of energy for the electrons and ions is given by

$$\frac{1}{2}mv_e^2 = \frac{kT_e}{e},$$
$$\frac{1}{2}Mv_i^2 = \frac{kT_i}{e}.$$

If it is assumed that the electrons and ions have the same temperature, the ratio of current densities to the boundary is

$$\frac{J_e}{J_i} = \frac{v_e}{v_i} = \sqrt{\frac{M}{m}}. \tag{3.7-2}$$

Table 3-1 shows the mass ratio *M/m* for several gas species. It is clear that the electron current out of the plasma to the boundary under these conditions is orders of magnitude higher than the ion current due to the much higher electron mobility. This would make it impossible to maintain the assumption of quasi-neutrality in the plasma used in Eq. (3.7-1) because the electrons would leave the volume much faster than the ions.

If different temperatures between the ions and electrons are allowed, the ratio of the current densities to the boundary is

$$\frac{J_e}{J_i} = \frac{v_e}{v_i} = \sqrt{\frac{M}{m}\frac{T_e}{T_i}}. \tag{3.7-3}$$

To balance the fluxes to the wall to satisfy charge continuity (an ionization event makes one ion and one electron), the ion temperature would have to again

Table 3-1. Ion-to-electron mass ratios for several gas species.

Gas	Mass ratio *M/m*	Square root of the mass ratio *M/m*
Protons (H^+)	1836	42.8
Argon	73440	270.9
Xenon	241066.8	490.9

be orders of magnitude higher than the electron temperatures. In ion and Hall thrusters, the opposite is true and the electron temperature is normally about an order of magnitude higher than the ion temperature, which compounds the problem of maintaining quasi-neutrality in a plasma.

In reality, if the electrons left the plasma volume faster than the ions, a charge imbalance would result due to the large net ion charge left behind. This would produce a positive potential in the plasma, which creates a retarding electric field for the electrons. The electrons would then be slowed down and retained in the plasma. Potential gradients in the plasma and at the plasma boundary are a natural consequence of the different temperatures and mobilities of the ions and electrons. Potential gradients will develop at the wall or next to electrodes inserted into the plasma to maintain quasi-neutrality between the charged species. These regions with potential gradients are called sheaths.

3.7.1 Debye Sheaths

To start an analysis of sheaths, assume that the positive and negative charges in the plasma are fixed in space, but have any arbitrary distribution. It is then possible to solve for the potential distribution everywhere using Maxwell's equations. The integral form of Eq. (3.2-1) is Gauss's law:

$$\oint_s \mathbf{E} \cdot d\mathbf{s} = \frac{1}{\varepsilon_o} \int_V \rho \, dV = \frac{Q}{\varepsilon_o}, \tag{3.7-4}$$

where Q is the total enclosed charge in the volume V and s is the surface enclosing that charge. If an arbitrary sphere of radius r is drawn around the enclosed charge, the electric field found from integrating over the sphere is

$$\mathbf{E} = \frac{Q}{4\pi\varepsilon_o r^2} \hat{r}. \tag{3.7-5}$$

Since the electric field is minus the gradient of the potential, the integral form of Eq. (3.2-5) can be written

$$\phi_2 - \phi_1 = -\int_{p1}^{p2} \mathbf{E} \cdot d\mathbf{l}, \tag{3.7-6}$$

where the integration proceeds along the path $d\mathbf{l}$ from point p1 to point p2. Substituting Eq. (3.7-5) into Eq. (3.7-6) and integrating gives

$$\phi = \frac{Q}{4\pi\varepsilon_o r}. \tag{3.7-7}$$

The potential decreases as $1/r$ moving away from the charge.

However, if the plasma is allowed to react to a test charge placed in the plasma, the potential has a different behavior than predicted by Eq. (3.7-7). Utilizing Eq. (3.2-7) for the electric field in Eq. (3.2-1) gives Poisson's equation:

$$\nabla^2\phi = -\frac{\rho}{\varepsilon_o} = -\frac{e}{\varepsilon_o}\left(Zn_i - n_e\right), \tag{3.7-8}$$

where the charge density in Eq. (3.2-5) has been used. Assume that the ions are singly charged and that the potential change around the test charge is small ($e\phi << kT_e$), such that the ion density is fixed and $n_i \approx n_o$. Writing Poisson's equation in spherical coordinates and using Eq. (3.5-9) to describe the Boltzmann electron density behavior gives

$$\frac{1}{r^2}\frac{\partial}{\partial r}\left(r^2\frac{\partial\phi}{\partial r}\right) = -\frac{e}{\varepsilon_o}\left[n_o - n_o \exp\left(\frac{e\phi}{kT_e}\right)\right] = \frac{en_o}{\varepsilon_o}\left[\exp\left(\frac{e\phi}{kT_e}\right) - 1\right]. \tag{3.7-9}$$

Since $e\phi << kT_e$ was assumed, the exponent can be expanded in a Taylor series:

$$\frac{1}{r^2}\frac{\partial}{\partial r}\left(r^2\frac{\partial\phi}{\partial r}\right) = \frac{en_o}{\varepsilon_o}\left[\frac{e\phi}{kT_e} + \frac{1}{2}\left(\frac{e\phi}{kT_e}\right)^2 + \ldots\right]. \tag{3.7-10}$$

Neglecting all the higher-order terms, the solution of Eq. (3.7-10) can be written

$$\phi = \frac{e}{4\pi\varepsilon_o r}\exp\left(-r\Big/\sqrt{\frac{\varepsilon_o kT_e}{n_o e^2}}\right). \tag{3.7-11}$$

By defining

$$\lambda_D = \sqrt{\frac{\varepsilon_o k T_e}{n_o e^2}} \tag{3.7-12}$$

as the characteristic Debye length, Eq. (3.7-12) can be written

$$\phi = \frac{e}{4\pi\varepsilon_o r}\exp\left(-\frac{r}{\lambda_D}\right). \tag{3.7-13}$$

This equation shows that the potential would normally fall off away from the test charge inserted in the plasma as $1/r$, as previously found, except that the electrons in the plasma have reacted to shield the test charge and cause the potential to decrease exponentially away from it. This behavior of the potential in the plasma is, of course, true for any structure such as a grid or probe that is placed in the plasma and that has a net charge on it.

The Debye length is the characteristic distance over which the potential changes for potentials that are small compared to kT_e. It is common to assume that the sheath around an object will have a thickness of the order of a few Debye lengths in order for the potential to fall to a negligible value away from the object. As an example, consider a plasma with a density of 10^{17} m^{-3} and an electron temperature of 1 eV. Boltzmann's constant k is 1.3807×10^{-23} J/K and the charge is 1.6022×10^{-19} coulombs, so the temperature corresponding to 1 electron volt is

$$T = 1\left(\frac{e}{k}\right) = \frac{1.6022 \times 10^{-19}}{1.3807 \times 10^{-23}} = 11604.3 \text{ K}.$$

The Debye length, using the permittivity or free space as 8.85×10^{-12} F/m is then

$$\lambda_D = \left[\frac{\left(8.85 \times 10^{-12}\right)\left(1.38 \times 10^{-23}\right)11604}{10^{17}\left(1.6 \times 10^{-19}\right)^2}\right]^{1/2}$$

$$= 2.35 \times 10^{-5} \text{ m} = 23.5\,\mu\text{m}.$$

A simplifying step to note in this calculation is that kT_e / e in Eq. (3.7-12) has units of electron volts. A handy formula for the Debye length is $\lambda_D(\text{cm}) \approx 740\sqrt{T_{ev} / n_o}$, where T_{ev} is in electron volts and n_o is in cm^{-3}.

3.7.2 Pre-Sheaths

In the previous section, the sheath characteristics for the case of the potential difference between the plasma and an electrode or boundary being small compared to the electron temperature ($e\phi << kT_e$) was analyzed and resulted in Debye shielding sheaths. What happens for the case of potential differences on the order of the electron temperature? Consider a plasma in contact with a boundary wall, as illustrated in Fig. 3-3. Assume that the plasma is at a reference potential Φ at the center (which can be arbitrarily set), and that cold ions fall through an arbitrary potential of ϕ_o as they move toward the boundary. Conservation of energy states that the ions arrived at the sheath edge with an energy given by

$$\frac{1}{2}Mv_o^2 = e\phi_o . \tag{3.7-14}$$

This potential drop between the center of the plasma and the sheath edge, ϕ_o, is called the pre-sheath potential. Once past the sheath edge, the ions then gain an additional energy given by

$$\frac{1}{2}Mv^2 = \frac{1}{2}Mv_o^2 - e\phi(x) , \tag{3.7-15}$$

where v is the ion velocity in the sheath and ϕ is the potential in the sheath (becoming more negative relative to the center of the plasma). Using Eq. (3.7-14) in Eq. (3.7-15) and solving for the ion velocity in the sheath gives

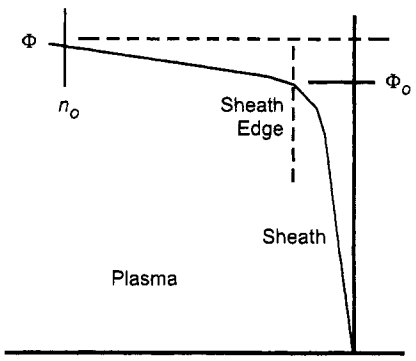

Fig. 3-3. Plasma in contact with a boundary.

$$v = \sqrt{\frac{2e}{M}}\left[\phi_o - \phi\right]^{1/2}. \tag{3.7-16}$$

However, from Eq. (3.7-14), $v_o = \sqrt{2e\phi_o/M}$, so Eq. (3.7-16) can be rearranged to give

$$\frac{v_o}{v} = \sqrt{\frac{\phi_o}{\phi_o - \phi}}, \tag{3.7-17}$$

which represents an acceleration of the ions toward the wall. The ion flux during this acceleration is conserved:

$$\begin{aligned} n_i v &= n_o v_o \\ n_i &= n_o \frac{v_o}{v}. \end{aligned} \tag{3.7-18}$$

Using Eq. (3.7-17) in Eq. (3.7-18), the ion density in the sheath is

$$n_i = n_o \sqrt{\frac{\phi_o}{\phi_o - \phi}}. \tag{3.7-19}$$

Examining the potential structure close to the sheath edge such that ϕ is small compared to the pre-sheath potential ϕ_o, Eq. (3.7-19) can be expanded in a Taylor series to give

$$n_i = n_o\left(1 - \frac{1}{2}\frac{\phi}{\phi_o} + \ldots\right), \tag{3.7-20}$$

where the higher-order terms in the series will be neglected.

The electron density through the sheath is given by the Boltzmann relationship in Eq. (3.5-9). If it is also assumed that the change in potential right at the sheath edge is small compared to the electron temperature, then the exponent in Eq. (3.5-9) can be expanded in a Taylor series to give

$$n_e = n_o \exp\left(\frac{e\phi}{kT_e}\right) = n_o\left[1 - \frac{e\phi}{kT_e} + \ldots\right]. \tag{3.7-21}$$

Using Eqs. (3.7-20) and (3.7-21) in Poisson's equation, Eq. (3.7-8), for singly charged ions in one dimension gives

$$\frac{d^2\phi}{dx^2} = -\frac{e}{\varepsilon_o}(n_i - n_e) = -\frac{en_o}{\varepsilon_o}\left[1 - \frac{1}{2}\frac{\phi}{\phi_o} - 1 + \frac{e\phi}{kT_e}\right] = \frac{en_o\phi}{\varepsilon_o}\left[\frac{1}{2\phi_o} - \frac{e}{kT_e}\right]. \tag{3.7-22}$$

In order to avoid a positive-going inflection in the potential at the sheath edge, which would then slow or even reflect the ions going into the sheath, the right-hand side of Eq. (3.7-22) must always be positive, which implies

$$\frac{1}{2\phi_o} > \frac{e}{kT_e}. \tag{3.7-23}$$

This expression can be rewritten as

$$\phi_o > \frac{kT_e}{2e}, \tag{3.7-24}$$

which is the Bohm sheath criterion [10] that states that the ions must fall through a potential in the plasma of at least $T_e/2$ before entering the sheath to produce a monotonically decreasing sheath potential. Since $v_o = \sqrt{2e\phi_o/M}$, Eq. (3.7-24) can be expressed in familiar form as

$$v_o \geq \sqrt{\frac{kT_e}{M}}. \tag{3.7-25}$$

This is usually called the Bohm velocity for ions entering a sheath. Equation (3.2-25) states that the ions must enter the sheath with a velocity of at least $\sqrt{kT_e/M}$ (known as the acoustic velocity for cold ions) in order to have a stable (monotonic) sheath potential behavior. The plasma produces a potential drop of at least $T_e/2$ prior to the sheath (in the pre-sheath region) in order to produce this ion velocity. While not derived here, if the ions have a temperature T_i, it is easy to show that the Bohm velocity will still take the form of the ion acoustic velocity given by

$$v_o = \sqrt{\frac{\gamma_i kT_i + kT_e}{M}}. \tag{3.7-26}$$

It is important to realize that the plasma density decreases in the pre-sheath due to ion acceleration toward the wall. This is easily observed from the Boltzmann behavior of the plasma density. In this case, the potential at the sheath edge has

fallen to a value of $-kT_e/2e$ relative to the plasma potential where the density is n_o (far from the edge of the plasma). The electron density at the sheath edge is then

$$n_e = n_o \exp\left(\frac{e\phi_o}{kT_e}\right) = n_o \exp\left[\left(\frac{e}{kT_e}\right)\left(\frac{-kT_e}{2e}\right)\right] \qquad (3.7\text{-}27)$$
$$= 0.606\, n_o.$$

Therefore, the plasma density at the sheath edge is about 60% of the plasma density in the center of the plasma.

The current density of ions entering the sheath at the edge of the plasma can be found from the density at the sheath edge in Eq. (3.7-27) and the ion velocity at the sheath edge in Eq. (3.7-25):

$$J_i = 0.6\, n_o e v_i \approx \frac{1}{2} ne\sqrt{\frac{kT_e}{M}}, \qquad (3.7\text{-}28)$$

where n is the plasma density at the start of the pre-sheath, which is normally considered to be the center of a collisionless plasma or one collision-mean-free path from the sheath edge for collisional plasmas. It is common to write Eq. (3.7-28) as

$$I_i = \frac{1}{2} ne\sqrt{\frac{kT_e}{M}} A, \qquad (3.7\text{-}29)$$

where A is the ion collection area at the sheath boundary. This current is called the Bohm current. For example, consider a xenon ion thruster with a 10^{18}m^{-3} plasma density and an electron temperature of 3 eV. The current density of ions to the boundary of the ion acceleration structure is found to be $118\ A/\text{m}^2$, and the Bohm current to an area of 10^{-2} m^2 is 1.18 A.

3.7.3 Child–Langmuir Sheaths

The simplest case of a sheath in a plasma is obtained when the potential across the sheath is sufficiently large that the electrons are repelled over the majority of the sheath thickness. This will occur if the potential is very large compared to the electron temperature ($\phi >> kT_e/e$). This means that the electron density goes to essentially zero relatively close to the sheath edge, and the electron space charge does not significantly affect the sheath thickness. The ion velocity through the sheath is given by Eq. (3.7-16). The ion current density is then

$$J_i = n_i e v = n_i e \sqrt{\frac{2e}{M}} \left[\phi_o - \phi\right]^{1/2} . \tag{3.7-30}$$

Solving Eq. (3.7-30) for the ion density, Poisson's equation in one dimension and with the electron density contribution neglected is

$$\frac{d^2\phi}{dx^2} = -\frac{en_i}{\varepsilon_o} = -\frac{J_i}{\varepsilon_o}\left(\frac{M}{2e(\phi_o - \phi)}\right)^{1/2} . \tag{3.7-31}$$

The first integral can be performed by multiplying both sides of this equation by $d\phi / dx$ and integrating to obtain

$$\frac{1}{2}\left[\left(\frac{d\phi}{dx}\right)^2 - \left(\frac{d\phi}{dx}\right)_{x=o}^2\right] = \frac{2J_i}{\varepsilon_o}\left[\frac{M(\phi_o - \phi)}{2e}\right]^{1/2} . \tag{3.7-32}$$

Assuming that the electric field ($d\phi / dx$) is negligible at $x = 0$, Eq. (3.7-32) becomes

$$\frac{d\phi}{dx} = 2\left(\frac{J_i}{\varepsilon_o}\right)^{1/2}\left[\frac{M(\phi_o - \phi)}{2e}\right]^{1/4} . \tag{3.7-33}$$

Integrating this equation and writing the potential across the sheath of thickness d as the voltage V gives the familiar form of the Child–Langmuir law:

$$J_i = \frac{4\varepsilon_o}{9}\left(\frac{2e}{M}\right)^{1/2}\frac{V^{3/2}}{d^2} . \tag{3.7-34}$$

This equation was originally derived by Child [11] in 1911 and independently derived by Langmuir [12] in 1913. Equation (3.7-34) states that the current per unit area that can pass through a planar sheath is limited by space-charge effects and is proportional to the voltage to the 3/2 power divided by the sheath thickness squared. In ion thrusters, the accelerator structure can be designed to first order using the Child–Langmuir equation where d is the gap between the accelerator electrodes. The Child–Langmuir equation can be conveniently written as

$$
\begin{aligned}
J_e &= 2.33\times10^{-6}\,\frac{V^{3/2}}{d^2} && \text{electrons} \\
J_i &= \frac{5.45\times10^{-8}}{\sqrt{M_a}}\,\frac{V^{3/2}}{d^2} && \text{singly charged ions} \\
&= 4.75\times10^{-9}\,\frac{V^{3/2}}{d^2} && \text{xenon ions,}
\end{aligned}
\tag{3.7-35}
$$

where M_a is the ion mass in atomic mass units. For example, the space-charge-limited xenon ion current density across a planar 1-mm grid gap with 1000 V applied is 15 mA/cm^2.

3.7.4 Generalized Sheath Solution

To find the characteristics of any sheath without the simplifying assumptions used in the above sections, the complete solution to Poisson's equation at a boundary must be obtained. The ion density through a planar sheath, from Eq. (3.7-19), can be written as

$$
n_i = n_o\left(1-\frac{\phi}{\phi_o}\right)^{-1/2}, \tag{3.7-36}
$$

and the electron density is given by Eq. (3.5-9),

$$
n_e = n_o\,\exp\left(\frac{e\phi}{kT_e}\right). \tag{3.7-37}
$$

Poisson's equation (3.7-8) for singly charged ions then becomes

$$
\frac{d^2\phi}{dx^2} = -\frac{e}{\varepsilon_o}\left(n_i - n_e\right) = -\frac{en_o}{\varepsilon_o}\left[\left(1-\frac{\phi}{\phi_o}\right)^{-1/2} - \exp\left(\frac{e\phi}{kT_e}\right)\right]. \tag{3.7-38}
$$

Defining the following dimensionless variables,

$$\chi = -\frac{e\phi}{kT_e},$$

$$\chi_o = \frac{e\phi_o}{kT_e},$$

$$\xi = \frac{x}{\lambda_D},$$

Poisson's equation becomes

$$\frac{d^2\chi}{d\xi^2} = \left(1+\frac{\chi}{\chi_o}\right)^{-1/2} - e^{-\chi}. \tag{3.7-39}$$

This equation can be integrated once by multiplying both sides by the first derivative of χ and integrating from $\xi_1 = 0$ to $\xi_1 = \xi$:

$$\int_0^{\xi} \frac{\partial\chi}{\partial\xi}\,\frac{\partial^2\chi}{\partial\xi^2}\,d\xi_1 = \int_0^{\xi}\left(1+\frac{\chi}{\chi_o}\right)^{-1/2} \partial\chi - \int_0^{\xi} e^{-\chi}\,d\chi. \tag{3.7-40}$$

where ξ_1 is a dummy variable. The solution to Eq. (3.7-40) is

$$\frac{1}{2}\left[\left(\frac{\partial\chi}{\partial\xi}\right)^2 - \left(\frac{\partial\chi}{\partial\xi}\right)^2_{\xi=0}\right] = 2\chi_o\left[\left(1+\frac{\chi}{\chi_o}\right)^{1/2} - 1\right] + e^{-\chi} - 1. \tag{3.7-41}$$

Since the electric field ($d\phi/dx$) is zero away from the sheath where $\xi = 0$, rearrangement of Eq. (3.7-41) yields

$$\frac{\partial\chi}{\partial\xi} = \left[4\chi_o\left(1+\frac{\chi}{\chi_o}\right)^{1/2} + 2e^{-\chi} - 2(2\chi_o - 1)\right]^{1/2}. \tag{3.7-42}$$

To obtain a solution for $\chi(\xi)$, Eq. (3.7-42) must be solved numerically. However, as was shown earlier for Eq. (3.7-22), the right-hand side must always be positive or the potential will have an inflection at or near the sheath edge. Expanding the right-hand side in a Taylor series and neglecting the higher-order terms, this equation will also produce the Bohm sheath criterion and specify that the ion velocity at the sheath edge must equal or exceed the ion acoustic (or Bohm) velocity. An examination of Eq. (3.7.42) shows that the Bohm sheath criterion forces the ion density to always be larger than the

electron density through the pre-sheath and sheath, which results in the physically realistic monotonically decreasing potential behavior through the sheath.

Figure 3-4 shows a plot of the sheath thickness d normalized to the Debye length versus the potential drop in the sheath normalized to the electron temperature. The criterion for a Debye sheath derived in Section 3.7.1 was that the potential drop be much less than the electron temperature ($e\phi << kT_e$), which is on the far left-hand side of the graph. The criterion for a Child–Langmuir sheath derived in Section 3.7.3 is that the sheath potential be large compared to the electron temperature ($e\phi >> kT_e$), which occurs on the right-hand side of the graph. This graph illustrates the rule-of-thumb that the sheath thickness is several Debye lengths until the full Child–Langmuir conditions are established. Beyond this point, the sheath thickness varies as the potential to the 3/2 power for a given plasma density.

The reason for examining this general case is because sheaths with potential drops on the order of the electron temperature or higher are typically found at both the anode and insulating surfaces in ion and Hall thrusters. For example, it will be shown later that an insulating surface exposed to a xenon plasma will self-bias to a potential of about $6T_e$, which is called the *floating potential.* For a plasma with an electron temperature of 4 eV and a density of 10^{18}m^{-3}, the Debye length from Eq. (3.7-12) is 1.5×10^{-5}m. Since the potential is actually

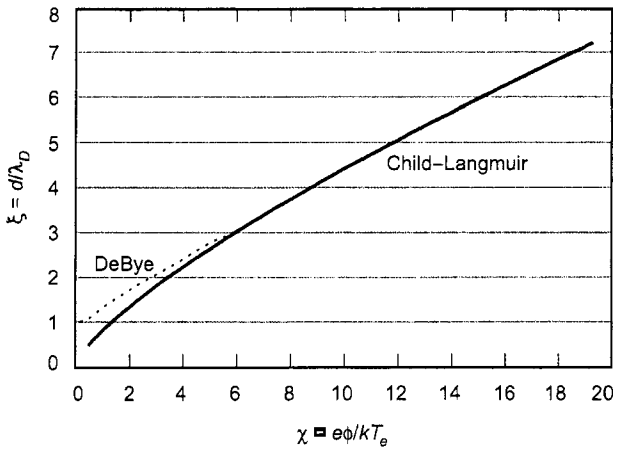

Fig. 3-4. Normalized sheath thickness as a function of the normalized sheath potential showing the transition to a Child–Langmuir sheath as the potential becomes large compared to the electron temperature.

significantly greater than the electron temperature, the sheath thickness is several times this value and the sheath transitions to a Child–Langmuir sheath.

3.7.5 Double Sheaths

So far, only plasma boundaries where particles from the plasma are flowing toward a wall have been considered. At other locations in ion and Hall thrusters, such as in some cathode and accelerator structures, a situation may exist where two plasmas are in contact but at different potentials, and ion and electron currents flow between the plasmas in opposite directions. This situation is called a double sheath, or double layer, and is illustrated in Fig. 3-5. In this case, electrons flow from the zero-potential boundary on the left, and ions flow from the boundary at a potential ϕ_s on the right. Since the particle velocities are relatively slow near the plasma boundaries before the sheath acceleration takes place, the local space-charge effects are significant and the local electric field is reduced at both boundaries. The gradient of the potential inside the double layer is therefore much higher than in the vacuum case where the potential varies linearly in between the boundaries.

Referring to Fig. 3-5, assume that the boundary on the left is at zero potential and that the particles arrive at the sheath edge on both sides of the double layer with zero initial velocity. The potential difference between the surfaces accelerates the particles in the opposite direction across the double layer. The electron conservation of energy gives

$$\frac{1}{2}mv_e^2 = e\phi$$
$$v_e = \left(\frac{2e\phi}{m}\right)^{1/2}, \tag{3.7-43}$$

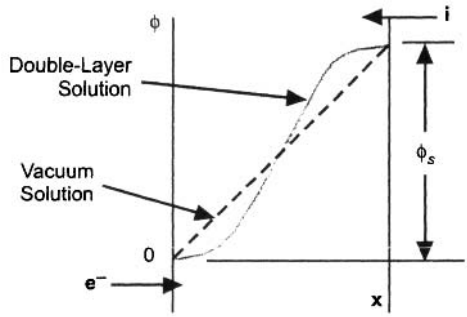

Fig. 3-5. Schematic of the double-layer potential distribution.

and the ion energy conservation gives

$$\frac{1}{2}Mv_i^2 = e(\phi_s - \phi)$$
$$v_i = \left[\frac{2e}{M}(\phi_s - \phi)\right]^{1/2}. \tag{3.7-44}$$

The charge density in Eq. (3.2-5) can be written

$$\rho = \rho_i + \rho_e$$
$$= \frac{J_i}{v_i} - \frac{J_e}{v_e} = \frac{J_i}{\sqrt{\phi_s - \phi}}\sqrt{\frac{M}{2e}} - \frac{J_e}{\sqrt{\phi}}\sqrt{\frac{m}{2e}}. \tag{3.7-45}$$

Poisson's equation can then be written in one dimension as

$$\frac{dE}{dx} = \frac{\rho}{\varepsilon_o} = \frac{J_i}{\varepsilon_o\sqrt{\phi_s - \phi}}\sqrt{\frac{M}{2e}} - \frac{J_e}{\varepsilon_o\sqrt{\phi}}\sqrt{\frac{m}{2e}}. \tag{3.7-46}$$

Integrating once gives

$$\frac{\varepsilon_o}{2}E^2 = 2J_i\sqrt{\frac{M}{2e}}\left[\phi_s - (\phi_s - \phi)^{1/2}\right] - 2J_e\sqrt{\frac{m}{2e}}\phi^{1/2}. \tag{3.7-47}$$

For space-charge-limited current flow, the electric field at the right-hand boundary (the edge of the plasma) is zero and the potential is $\phi = \phi_s$. Putting that into Eq. (3.7-47) and solving for the current density gives

$$J_e = \sqrt{\frac{M}{m}}\,J_i. \tag{3.7-48}$$

If the area of the two plasmas in contact with each other is the same, the electron current crossing the double layer is the square root of the mass ratio times the ion current crossing the layer. This situation is called the Langmuir condition (1929) and describes the space-charge-limited flow of ions and electrons between two plasmas or between a plasma and an electron emitter.

For finite initial velocities, Eq. (3.7-48) was corrected by Andrews and Allen [13] to give

$$J_e = \kappa\sqrt{\frac{M}{m}}\,J_i, \tag{3.7-49}$$

where κ is a constant that varies from 0.8 to 0.2 for T_e / T_i changing from 2 to about 20. For typical thruster plasmas where $T_e / T_i \approx 10$, k is about 0.5.

While the presence of free-standing double layers in the plasma volume in thrusters is often debated, the sheath at a thermionic cathode surface certainly satisfies the criteria of counter-streaming ion and electron currents and can be viewed as a double layer. In this case, Eq. (3.7-49) describes the space-charge-limited current density that a plasma can accept from an electron-emitting cathode surface. This is useful in that the maximum current density that can be drawn from a cathode can be evaluated if the plasma parameters at the sheath edge in contact with the cathode are known (such that J_i can be evaluated from the Bohm current), without requiring that the actual sheath thickness be known.

Finally, there are several conditions for the formation of the classic double layer described here. In order to achieve a potential difference between the plasmas that is large compared to the local electron temperature, charge separation must occur in the layer. This, of course, violates quasi-neutrality locally. The current flow across the layer is space-charge limited, which means that the electric field is essentially zero at both boundaries. Finally, the flow through the layer discussed here is collisionless. Collisions cause resistive voltage drops where current is flowing, which can easily be confused with the potential difference across a double layer.

3.7.6 Summary of Sheath Effects

It is worthwhile to summarize here some of the important equations in this section related to sheaths because these will be very useful later in describing thruster performance. These equations were derived in the sections above, and alternative derivations can be found in [1–3].

The current density of ions entering the sheath at the edge of the plasma is given by

$$J_i = 0.6\, nev_i \approx \frac{1}{2} ne\sqrt{\frac{kT_e}{M}}, \tag{3.7-50}$$

where n is the plasma density at the start of the pre-sheath far from the boundary, which was considered to be the center of the plasma by Langmuir for his collisionless plasmas. The convention of approximating the coefficient 0.6 as 1/2 was made by Bohm in defining what is now called the "Bohm current."

If there is no net current to the boundary, the ion and electron currents must be equal. The Bohm current of ions through the sheath is given by the current density in Eq. (3.7-50) times the wall area A:

$$I_i = \frac{1}{2} n_i \, e \sqrt{\frac{kT_e}{M}} A. \tag{3.7-51}$$

The electron current through the sheath is the random electron flux times the Boltzmann factor:

$$I_e = \frac{1}{4} \sqrt{\frac{8kT_e}{\pi m}} \, n_e \, eA \, \exp\left(-\frac{e\phi}{kT_e} \right), \tag{3.7-52}$$

where the potential is by convention a positive number in this formulation. Equating the total ion and electron currents ($I_i = I_e$), assuming quasi-neutrality in the plasma ($n_i = n_e$), and solving for the potential gives

$$\phi = \frac{kT_e}{e} \ln\left[\sqrt{\frac{2M}{\pi m}} \right]. \tag{3.7-53}$$

This is the potential at which the plasma will self-bias in order to have zero net current to the walls and thereby conserve charge and is often called the *floating potential*. Note that the floating potential is negative relative to the plasma potential.

For sheath potentials less than the electron temperature, the sheath thickness is given by the Debye length:

$$\lambda_D = \sqrt{\frac{\varepsilon_o kT_e}{n_o e^2}}. \tag{3.7-54}$$

For sheath potentials greater than the electron temperature ($e\phi > kT_e$), a pre-sheath forms to accelerate the ions into the sheath to avoid any inflection in the potential at the sheath edge. The collisionless pre-sheath has a potential difference from the center of the plasma to the sheath edge of $T_e / 2$ and a density decrease from the center of the plasma to the sheath edge of $0.61 \, n_o$. The $T_e / 2$ potential difference accelerates the ions to the Bohm velocity:

$$v_{\text{Bohm}} = v_B = \sqrt{\frac{kT_e}{M}}. \tag{3.7-55}$$

The sheath thickness at the wall depends on the plasma parameters and the potential difference between the plasma and the wall, and is found from the solution of Eq. (3.7-42).

For the case of sheath potentials that are large compared to the electron temperature ($e\phi >> kT_e$), the current density through the sheath is described by the Child–Langmuir equation:

$$J_i = \frac{4e_o}{9}\left(\frac{2e}{M}\right)^{1/2}\frac{\phi^{3/2}}{d^2}. \tag{3.7-56}$$

Finally, for the case of double sheaths where ion and electrons are counterstreaming across the boundary between two plasmas, the relationship between the two currents is

$$J_e = \kappa\sqrt{\frac{M}{m}}\,J_i. \tag{3.7-57}$$

If one boundary of the double layer is the sheath edge at a thermionic cathode, Eq. (3.7-51) can be used for the Bohm current to the opposite boundary to give the maximum emission current density as

$$J_e = \frac{\kappa}{2} n_i\, e\sqrt{\frac{kT_e}{m}} \approx \frac{1}{4} n_e\, e\sqrt{\frac{kT_e}{m}}. \tag{3.7-58}$$

This is the maximum electron current density that can be accepted by a plasma due to space-charge effects at the cathode double sheath. For example, the maximum space-charge-limited cathode emission current into a xenon plasma with a density of 10^{18} m^{-3} and an electron temperature of 5 eV is about 3.8 A/cm^2.

These summary equations are commonly seen in the literature on the design and analysis of ion sources, plasma processing sources, and, of course, many electric propulsion thrusters.

References

[1] F. F. Chen, *Introduction to Plasma Physics and Controlled Fusion*, vol. 1, New York: Plenum Press, 1984.

[2] M. Lieberman and A. Lichtenberg, *Principles of Plasma Discharges and Materials Processing*, New York: John Wiley and Sons, 1994.

[3] R. J. Goldston and P. H. Rutherford, *Introduction to Plasma Physics*, London: Institute of Physics Publishing, 1995.

[4] A. T. Forrester, *Large Ion Beams*, New York: John Wiley and Sons, 1988.

[5] D. L. Book, *NRL Plasma Formulary*, Washington, D.C.: Naval Research Laboratory, 1987.

[6] E. A. Mason and E. W. McDaniel, *Transport Properties of Ions in Gases*, New York: John Wiley and Sons, 1988.

[7] J. S. Miller, S. H. Pullins, D. J. Levandier, Y. Chiu, and R. A. Dressler, "Xenon Charge Exchange Cross Sections for Electrostatic Thruster Models," *Journal of Applied Physics*, vol. 91, no. 3, pp. 984–991, 2002.

[8] I. Katz, J. Anderson, J. Polk and J. Brophy, "One Dimensional Hollow Cathode Model," *Journal of Propulsion and Power*, vol. 19, no. 4, pp. 595–600, 2003.

[9] L. Spitzer, Jr., *Physics of Fully Ionized Gases*, New York: Interscience, pp. 127–135, 1962.

[10] D. Bohm, Chapter 1, *The Characteristics of Electric Discharges in Magnetic Fields*, edited by A. Guthrie and R. Wakerling, New York: McGraw-Hill, pp. 1–76, 1949.

[11] C. D. Child, "Discharge from Hot CaO," *Physical Review*, vol. 32, p. 492, 1911.

[12] I. Langmuir, "The Effect of Space Charge and Residual Gases on Thermionic Currents in High Vacuum," *Physical Review*, vol. 2, p. 450, 1913.

[13] J. G. Andrews and J. E. Allen, "Theory of a Double Sheath Between Two Plasmas," *Proceedings of the Royal Society of London*, series A, vol. 320, pp. 459–472, 1971.

Problems

1. Show that Eq. (3.2-7) becomes $\mathbf{E} = -\nabla\phi - \partial\mathbf{A}/\partial t$ when $\mathbf{B}$ is varying with time, where $\mathbf{A}$ is the "vector potential." How are $\mathbf{A}$ and $\mathbf{B}$ related?
2. Derive Eq. (3.3-21) for the force on a particle in a magnetic mirror.
3. Show that the magnetic moment is invariant and derive Eq. (3.3-23).
4. Derive the expression for ion acoustic velocity in Eq. (3.5-26).

5. Answer the following question that might be brought up by a student working in the lab: "In a plasma discharge set up in my vacuum chamber the other day, I measured an increase in the plasma potential with an electrostatic probe. How do I know if it's a double layer or just a potential gradient within which the ionized gas is quasi-neutral?"
6. Derive Eq. (3.6-9) for the penetration distance of neutral particles in a plasma.
7. Derive the expression for Ohm's law for partially ionized plasmas, Eq. (3.6-20).
8. Derive Eq. (3.6-81) for the transverse ambipolar ion velocity across magnetic field lines.
9. Derive the Bohm sheath criteria including the presence of double ions.
10. Derive an expression equivalent to the Child–Langmuir law for the condition where the initial ion velocity entering the sheath is not neglected (ions have an initial velocity v_o at the sheath edge at $z = 0$).
11. A 2-mm by 2-mm square probe is immersed in a 3 eV xenon plasma.
    a. If the probe collects 1 mA of ion current, what is the plasma density? (Hint: the probe has two sides and is considered infinitely thin.)
    b. What is the floating potential?
    c. What is the probe current collected at the plasma potential?
12. A 2-mm-diameter cylindrical probe 5 mm long in a xenon plasma with $T_e = 3$ eV collects 1 mA of ion saturation current.
    a. What is the average plasma density?
    b. How much electron current is collected if the probe is biased to the plasma potential?
    c. Why is this electron current the same as the solution to Problem 11.c when the plasma densities are so different?
13. An electron emitter capable of emitting up to 10 A/cm^2 is in contact with an Xe^+ plasma with an electron temperature of 2 eV. Plot the emission current density versus plasma density over the range from 10^{10} to 10^{13} cm^{-3}. At what density does the emission become thermally limited (the maximum current density that the electron emitter can emit)?

Fundamentals of Electric Propulsion: Ion and Hall Thrusters
by Dan M. Goebel and Ira Katz
Copyright © 2008 John Wiley & Sons, Inc.

Chapter 4
Ion Thruster Plasma Generators

Ion thrusters are characterized by the electrostatic acceleration of ions extracted from a plasma generator. Ion thruster geometries are best described in terms of three basic components: the ion accelerator, the plasma generator, and the electron neutralizer. The ion accelerator, described in Chapter 5, typically uses electrically biased multi-aperture grids to produce the ion beam. The neutralizer cathode, which is discussed in Chapter 6, is positioned outside the thruster body to provide electrons to neutralize the ion beam and maintain the potential of the thruster and spacecraft relative to the space plasma potential. In this chapter, three types of the third component of modern flight ion thrusters, namely the plasma generator, are discussed. These plasma generators utilize direct current (DC) electron discharges, radio frequency (rf) discharges and microwave discharges to produce the plasma. Physics-based models will be developed and used throughout the chapter to describe the performance and characteristics of these different plasma-generation techniques.

4.1 Introduction

The basic geometry of an ion thruster plasma generator is illustrated well by the classic DC electron discharge plasma generator. This version of the thruster plasma generator utilizes an anode potential discharge chamber with a hollow cathode electron source to generate the plasma from which ions are extracted to form the thrust beam. A simplified schematic of a DC electron bombardment ion thruster with these components coupled to a multi-grid accelerator is shown in Fig. 4-1. Neutral propellant gas is injected into the discharge chamber, and a small amount is also injected through the hollow cathode. Electrons extracted from the hollow cathode enter the discharge chamber and ionize the propellant gas. To improve the efficiency of the discharge in producing ions, some form of magnetic confinement typically is employed at the anode wall. The magnetic fields provide confinement primarily of the energetic electrons, which increases the electron path length prior to loss to the anode wall and improves the

ionization probability of the injected electrons. Proper design of the magnetic field is critical to providing sufficient confinement for high efficiency while maintaining adequate electron loss to the anode to produce stable discharges over the operation range of the thruster.

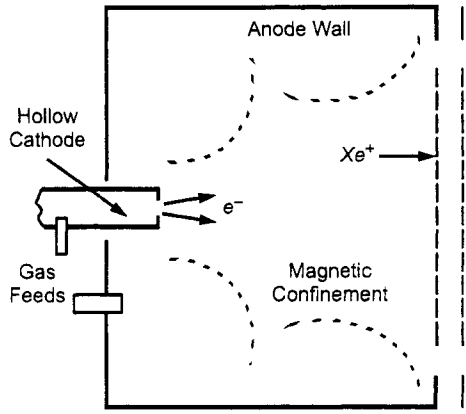

Fig. 4-1. Illustration of a DC-discharge electron bombardment ion thruster.

Several power supplies are required to operate the cathode and plasma discharge. A simplified electrical schematic typically used for DC-discharge plasma generators is shown in Fig. 4-2. The cathode heater supply raises the thermionic emitter to a sufficient temperature to emit electrons, and is turned off once the plasma discharge is ignited. The keeper electrode positioned around the hollow cathode tube is used to facilitate striking the hollow cathode discharge, and also protects the cathode from ion bombardment from the discharge chamber region. The cathode and keeper are discussed in Chapter 6. The discharge supply is connected between the hollow cathode and the anode, and normally is run in the current-regulated mode in order to provide a stable discharge at different power levels.

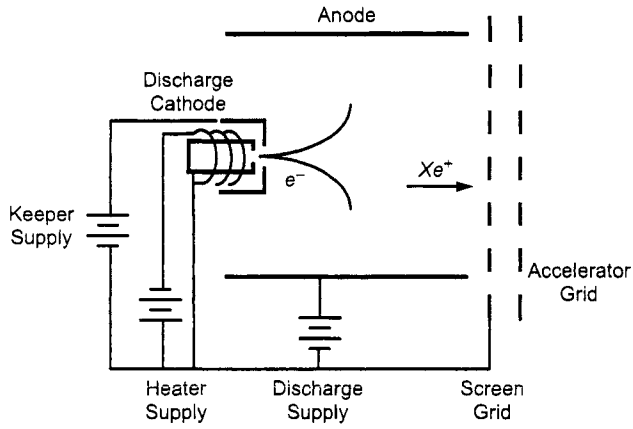

Fig. 4-2. Electrical schematic of a DC-discharge ion thruster with the cathode heater, keeper and discharge power supplies.

RF and microwave ion thrusters utilize ion accelerator and electron-neutralizer implementations nearly identical to that of the DC-discharge ion thruster. However, these thrusters do not employ a discharge hollow cathode or anode power supply. These components are replaced by rf or microwave antenna structures, sources of microwave radiation and compatible discharge chambers to ionize the propellant gas and deliver the ions to the accelerator structure. These thrusters also utilize either applied or self-generated magnetic fields to improve the ionization efficiency of the system.

The three thruster plasma generators to be discussed here, DC electron discharge, rf, and microwave discharge, have been successfully developed and flown in space. The principles of these different classes of plasma generators are described in the following sections after a discussion of the plasma generator efficiency that can be expected in an idealized case.

4.2 Idealized Ion Thruster Plasma Generator

It is worthwhile to examine an ion thruster in the simplest terms to provide an understanding of the dominant processes in the particle flows and energy transport required to produce the plasma. The idealized thruster model has power injected by arbitrary means into a volume filled with neutral gas to produce ionization and neutral gas excitation, with all the ions going to the accelerator grids and an equal number of plasma electrons going to the wall to conserve charge. This is illustrated schematically in Fig. 4-3. For this model, the thruster discharge chamber has a volume V that fully encloses the plasma that is produced by ionization of neutral gas by the plasma electrons. The ions from the plasma flow only to the accelerator grid structure (perfect confinement elsewhere in the discharge chamber) with a current given by the Bohm current:

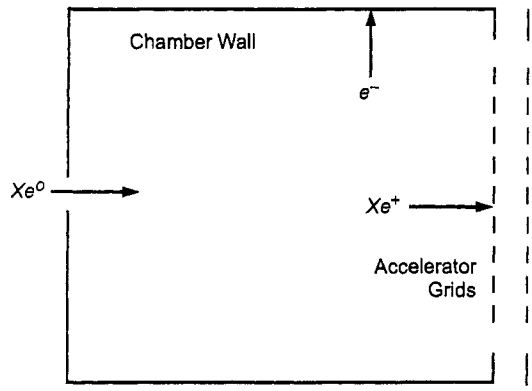

Fig. 4-3. Idealized ion thruster with the ions assumed going to the grids and electrons going to the chamber wall.

$$I_i = \frac{1}{2} n_i e v_a A , \tag{4.2-1}$$

where n_i is the ion density in the center of the volume; v_a is the ion acoustic velocity; A is the total ion loss area, which is assumed to be only the grid area; and the ions are assumed to be cold relative to the electrons. The ion beam current is then the total ion current to the grids multiplied by the effective grid transparency, T_g:

$$I_b = \frac{1}{2} n_i e v_a A T_g , \tag{4.2-2}$$

where the current lost to the accel and decel grids has been neglected as small. Ions are assumed to be produced by ionization of neutral particles by the plasma electrons in the discharge chamber, with a rate given by

$$I_p = n_o n_e e \langle \sigma_i v_e \rangle V , \tag{4.2-3}$$

where n_o is the neutral gas density, n_e is the plasma electron density, σ_i is the ionization cross section, v_e is the electron velocity, and the term in the brackets is the reaction rate coefficient which is the ionization cross section averaged over the Maxwellian electron velocity distribution function. The formulation of the reaction rate coefficient was described in Chapter 3, and the values for xenon as a function of electron temperature are given in Appendix E.

Power is conserved in the system, so the power put into the plasma is equal to the power that comes out in the form of charged particles and radiation. To first order, the power injected into the plasma goes into ionization and excitation of the neutral gas, heating of the electrons, and power that is carried to the walls and the grids by the ions and electrons. The power that is put into the system is then

$$P_{\text{in}} = I_p U^+ + I^* U^* + I_i \varepsilon_i + \frac{n_e V}{\tau} \varepsilon_e , \tag{4.2-4}$$

where U^+ is the ionization potential of the propellant gas, U^* is the excitation potential of the gas, τ is the average electron confinement time, ε_i is the ion energy carried to the walls, and ε_e is the electron energy carried to the walls by the electrons leaving the plasma. The term I^* is the excited neutral production rate, given by

$$I^* = \sum_j n_o n_e e \left\langle \sigma_* v_e \right\rangle_j V, \tag{4.2-5}$$

where σ_* is the excitation cross section and the reaction rate coefficient is averaged over the electron distribution function and summed over all possible excited states j. Using Eqs. (4.2-3) and (4.2-5) in Eq. (4.2-4), the power input can then be written as

$$P_{\text{in}} = n_o n_e \langle \sigma_i v_e \rangle V \left[U^+ + \frac{\left\langle \sigma_* v_e \right\rangle_j}{\langle \sigma_i v_e \rangle} U^* \right] + I_i \varepsilon_i + \frac{n_e V}{\tau} \varepsilon_e. \tag{4.2-6}$$

Assuming quasi-neutrality ($n_i \approx n_e$) and that the ions and electrons leave the volume by ambipolar flow at the same rate, which is a function of the mean confinement time τ, the ion current out is given by

$$I_i = \frac{1}{2} n_i e v_a A = \frac{n_i e V}{\tau}. \tag{4.2-7}$$

The mean confinement time for ions and electrons is then

$$\tau = \frac{2V}{v_a A}. \tag{4.2-8}$$

The energy that an electron removes from the plasma as it goes to the wall is given by

$$\varepsilon_e = 2\frac{kT_e}{e} + \phi, \tag{4.2-9}$$

where ϕ is the plasma potential relative to the wall. Equation (4.2-9) is derived in Appendix C. The ions fall first through the pre-sheath potential, approximated by $T_{eV}/2$ to produce the Bohm velocity, and then through the sheath potential. Each ion then removes from the plasma a total energy per ion of

$$\varepsilon_i = \frac{1}{2}\frac{kT_e}{e} + \phi. \tag{4.2-10}$$

The plasma potential in these two equations is found from the electron current leaving the plasma, which is given by Eq. (3.7-52):

$$I_a = \frac{1}{4}\left(\frac{8kT_e}{\pi\, m}\right)^{1/2} e\, n_e\, A_a \exp^{-e\phi/kT_e}, \tag{4.2-11}$$

where A_a is the electron loss area and m is the electron mass. Since ambipolar ion and electron flow to the wall was assumed, equate Eqs. (4.2-1) and (4.2-11) and use $\sqrt{T_e/M}$ for the ion acoustic velocity to give the plasma potential relative to the wall:

$$\phi = \frac{kT_e}{e}\ln\left[\frac{A_a}{A}\sqrt{\frac{2M}{\pi m}}\right]. \tag{4.2-12}$$

Equation (4.2-12) is normally called the *floating potential* and applies in this case because there are no applied potentials in our ideal thruster to draw a net current.

The electron temperature can be found by equating the ion production and loss rates, Eqs. (4.2-1) and (4.2-3), which gives

$$\frac{\sqrt{kT_e/M}}{\langle\sigma_i v_e\rangle} = \frac{2n_o V}{A}. \tag{4.2-13}$$

The reaction rate coefficient in the denominator depends on the electron temperature, and so this equation can be solved for T_e if the discharge chamber volume, neutral pressure, and ion loss area are known.

The discharge loss is defined as the power into the plasma divided by the beam current out of the thruster, which is a figure of merit for the efficiency of the plasma-generation mechanism. The discharge loss for this idealized thruster, using Eq. (4.2-2) for the beam current, is then given by

$$\eta_d = \frac{P_{in}}{I_b} = \frac{2n_o\langle\sigma_i v_e\rangle V}{v_a\, A\, T_g}\left[U^+ + \frac{\langle\sigma_* v_e\rangle_j}{\langle\sigma_i v_e\rangle}U^*\right] + \frac{1}{T_g e}\left[2.5kT_e + 2kT_e \ln\left(\frac{A_a}{A}\sqrt{\frac{2M}{\pi m}}\right)\right]. \tag{4.2-14}$$

As evident in Eq. (4.2-14), the grid transparency (T_g) directly affects the discharge loss, and the input power is distributed between the first term related

to producing ions and excited neutrals, and the second term related to heating the electrons that are lost to the walls.

To evaluate Eq. (4.2-14), the ratio of the excitation to ionization reaction rates as a function of the Maxwellian electron temperature must be known. This is shown in Fig. 4-4 for xenon gas from data in Appendix E. For electron temperatures below about 8 V, the excitation rate exceeds the ionization rate in xenon for Maxwellian electrons. Since the lowest excitation potential is near the ionization potential in xenon, this higher excitation rate results in more of the input power being radiated to the walls than producing ions. This effect explains at least part of the inefficiency inherent in xenon plasma generators. Excitation rates equal to or higher than the ionization rate at low electron temperatures are also generally found for other inert gas propellants.

The discharge loss from Eq. (4.2-14) for this ideal thruster example is plotted as a function of the mass utilization efficiency for a generic 20-cm-diameter thruster in Fig. 4-5, where the ionization potential of xenon is 12.13 V, the average excitation potential is 10 V, and 80% of the ions incident on the grids become beam ions ($T_g = 0.8$). It was also assumed for simplicity that the plasma electrons were lost to the floating screen grid and the chamber wall. The mass utilization efficiency is inversely proportional to the neutral density in the thruster, which will be derived in Section 4.3.6. In the figure, the discharge loss is shown in (eV/ion), which is equivalent to watts of discharge power per ampere of beam ions (W/A). In an ideal plasma-generator case with 80% of the ions that are generated assumed to become beam current, the amount of power

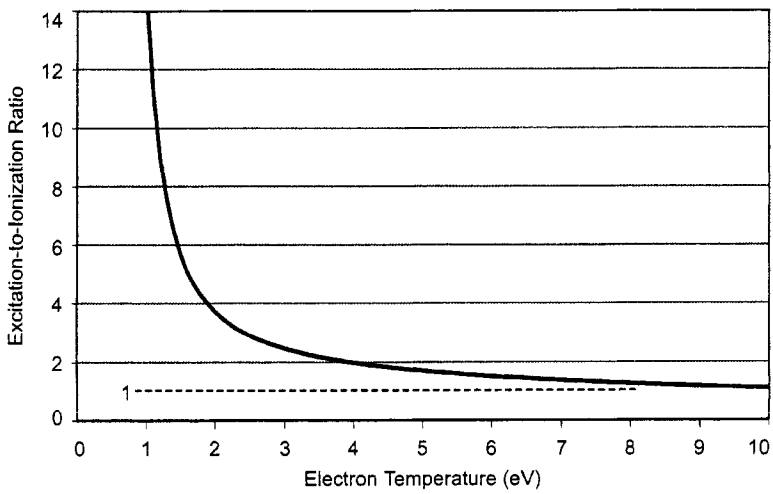

Fig. 4-4. Ratio of the excitation to ionization rate coefficients for xenon as a function of the electron temperature.

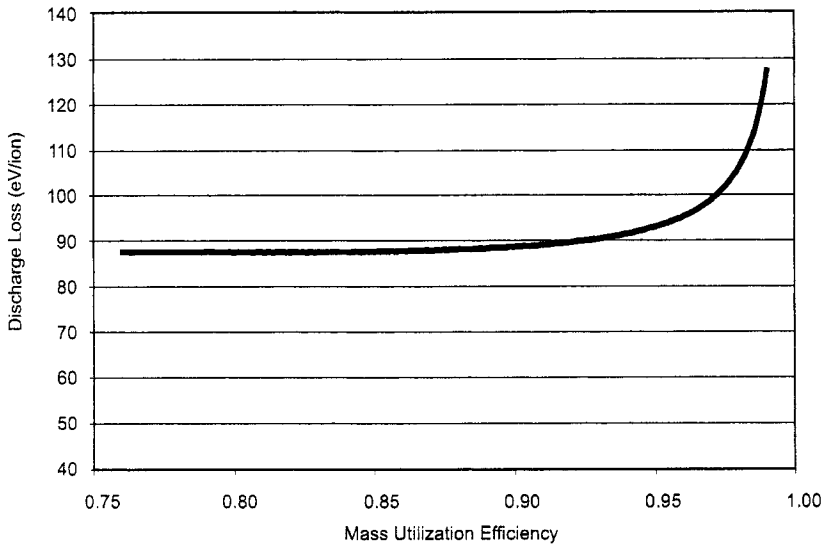

Fig. 4-5. Discharge loss for the ideal thruster example as a function of mass utilization efficiencies for a 30-cm plasma generator length.

required to produce one ampere of beam current is about 90 watts. While it only takes 12.13 eV to ionize a xenon atom, even in an idealized thruster it takes 7.5 times this energy to produce and deliver an ion into the beam due to other losses.

It is informative to see where the extra input power goes in the thruster. Figure 4-6 shows the power lost in each of the four energy loss mechanisms described above for an ideal thruster 30-cm long producing 1 A of beam current. The ionization power is constant in this case because this example was constrained to produce 1 A, and the power required per beam ampere is then (1/0.8)*12.13 = 15.1 W. The major power loss is excitation at low mass utilization where the electron temperature is low, as suggested by Fig. 4-4. The ion and electron convection losses to the wall also increase at higher mass utilization efficiencies because the neutral density is decreasing, which increases the electron temperature, raises the plasma potential, and thereby increases the energy lost per electron and ion.

Many thruster design concepts use electron confinement to improve the efficiency. The impact of this can be examined in this ideal thruster model by reducing the anode area A_a. Figure 4-7 shows the four energy-loss mechanisms for the same idealized thruster example just used, but with the effective anode area collecting electrons decreased to 1 cm^2. By conservation of charge,

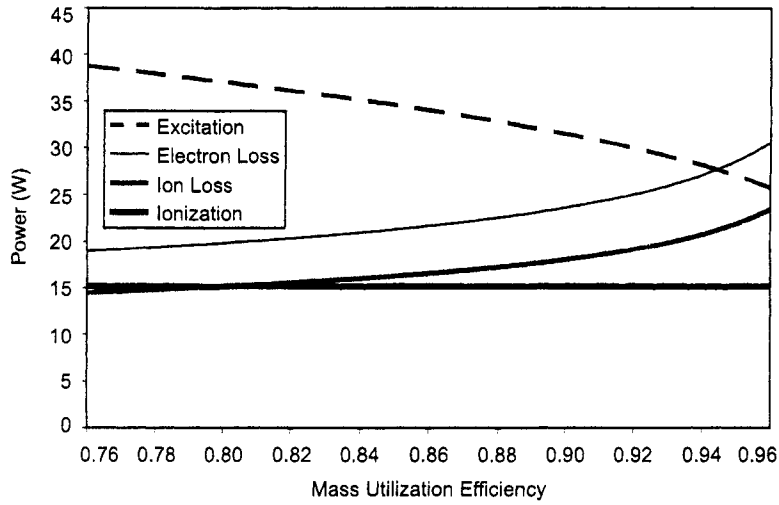

Fig. 4-6. Discharge loss for each of the energy loss mechanisms for the ideal thruster example.

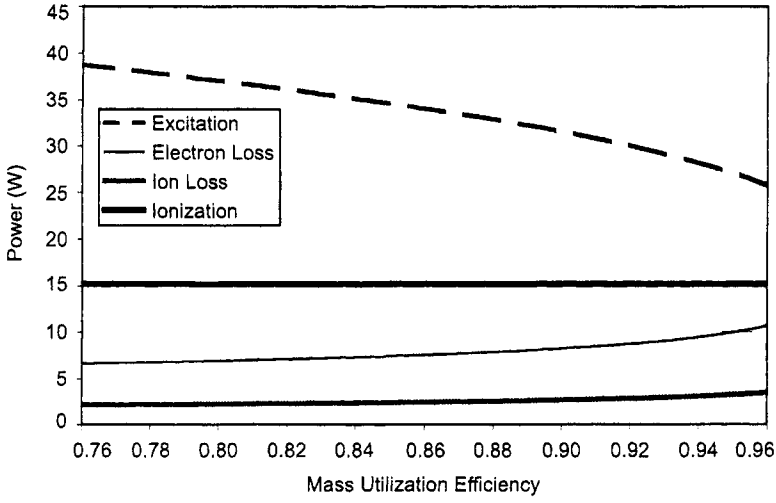

Fig. 4-7. Discharge loss for each of the energy loss mechanisms for the ideal thruster with reduced anode area.

electrons in this discharge are lost at the same rate as ions, so electron confinement does not change the number or rate of electrons lost. The reduced anode area only changes the plasma potential relative to the loss area potential in order to maintain charge balance, as seen from examining Eq. (4.2-11). This effect is clearly seen by comparing Figs. 4-6 and 4-7, where the energy loss rates for ionization and excitation have not changed with the better electron

confinement, but the energy convected out of the plasma in the form of ion and electron power to the boundaries has decreased. This is because the plasma potential described by the last term in Eq. (4.2-14) is reduced due to the smaller anode area, which reduces the ion and electron energy loss channels. This is the fundamental mechanism for making efficiency improvements (reducing the discharge loss) in plasma generators.

The idealized thruster description illustrates that the power that must be provided to produce the plasma in a thruster is large compared to that required for ionization. In terms of the total thruster efficiency, this is the majority of the "other" power in P_o in Eq. (2.5-1). In reality, the discharge loss is significantly higher than that found in this idealized example due to imperfect confinement of the ions and electrons in the thruster, and due to other loss mechanisms to be described below.

Finally, in most ion thrusters, such as electron bombardment thrusters and microwave-heated electron cyclotron resonance (ECR) thrusters, the electron distribution function is non-Maxwellian. The higher energy electrons observed in electron bombardment thrusters are often called *primaries*, and they have been found to be either monoenergetic or have some distribution in energies depending on the plasma-generator design. Primary electrons have a larger ion to excited-neutral production rate than do the plasma electrons due to their higher energy, and so even small percentages of primaries in the plasma can dominate the ionization rate. The inclusion of ionization by primary electrons in particle and energy balance models such as the one just described tends to reduce the discharge loss significantly.

4.3 DC Discharge Ion Thruster

Ion thrusters that use a DC electron-discharge plasma generator employ a hollow cathode electron source and an anode potential discharge chamber with magnetic multipole boundaries to generate the plasma and improve the ionization efficiency. Electrons extracted from the hollow cathode are injected into the discharge chamber and ionize the propellant gas introduced in the chamber. Magnetic fields applied in the discharge chamber provide confinement primarily of the energetic electrons, which increases the electron path length prior to their being lost to the anode and improves the ionization efficiency. The ions from this plasma that flow to the grids are extracted and accelerated to form the beam.

Empirical studies over the past 50 years have investigated the optimal design of the magnetic field to confine electrons and ions in thrusters. Figure 4-8 shows the evolution of the discharge chamber geometry and magnetic field shape

employed in efforts primarily aimed at improving the confinement of energetic electrons injected into the chamber from thermionic cathodes in order to more efficiently produce the plasma. Early thrusters pioneered by Kaufman utilized a solenoidal [1] or mildly divergent magnetic field [2], shown in Fig.4-8(a), which requires that electrons from the on-axis thermionic filament cathode undergo collisions in order to diffuse to the anode and complete the discharge circuit. A strongly divergent magnetic field thruster [3], shown in Fig. 4-8(b), improved the primary electron uniformity in the plasma volume and resulted in a lower discharge loss and a more uniform beam profile. This thruster introduced a baffle in front of the hollow cathode electron source to further inhibit on-axis electrons. The radial magnetic field thruster [4], shown in Fig. 4-8(c), produced very uniform plasmas and good efficiencies, as did a cusp version of the "divergent magnetic field" thruster shown in Fig. 4-8(d). The use of permanent magnet, multipole boundaries, first reported by Moore [5],

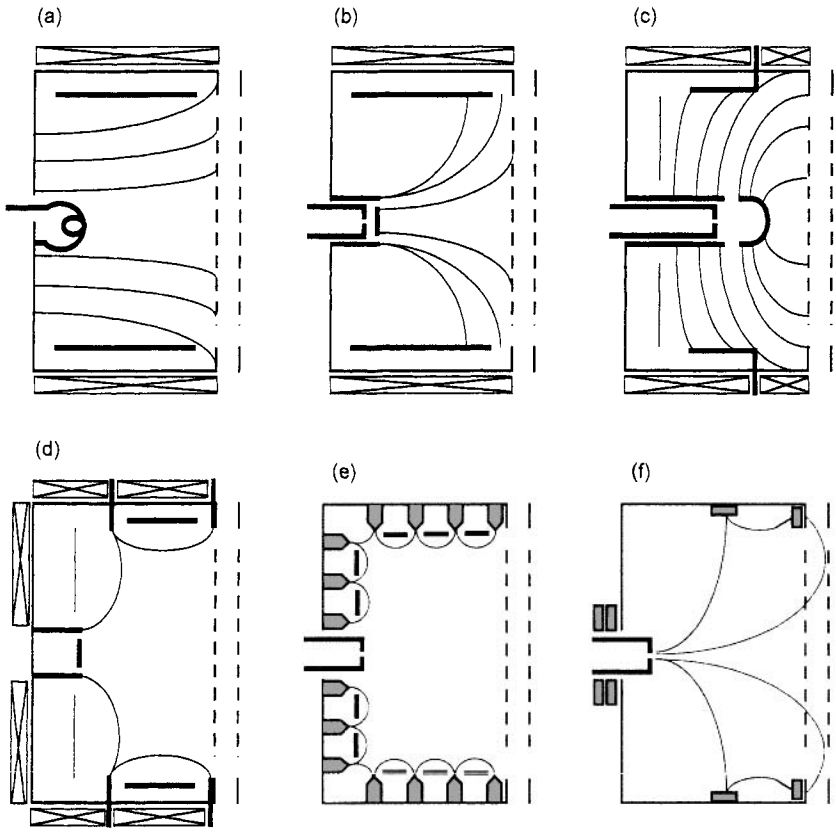

Fig. 4-8. Magnetic field types of ion thrusters: (a) mildly divergent B-field, (b) strongly divergent B-field, (c) radial field, (d) cusp field, (e) magnetic multipole field, and (f) ring-cusp fields.

created essentially a field-free region in the center of the thruster that produced uniform plasmas. The magnets in various versions of this concept were oriented in rings or in axial lines to provide plasma confinement. Moore biased the wall and magnets at cathode potential and placed the anodes inside the cusp fields, as shown in Fig. 4-8(e), to require that electrons diffuse across the field lines by collisions or turbulent transport before being lost. The permanent magnet ring-cusp thruster of Sovey [6] is shown in Fig. 4-8(f), which has become the most widely used thruster design to date.

The divergent field Kaufman ion thruster matured in the 1970s with the development of 30-cm mercury thrusters [7,8]. Kaufman thrusters are described in more detail in Section 4.4. Concerns with using mercury as the propellant resulted in the development of xenon ion thrusters [9,10], which emerged at the same time that the benefits of ring-cusp confinement geometries became apparent [6,11,12]. The design and development of the NASA Solar Electric Propulsion Technology Applications Readiness (NSTAR) [13] and Xenon Ion Propulsion System (XIPS®) [14] flight thrusters in the 1990s was based on this early work. At this time, only two of these magnetic field geometries are still used in DC ion thrusters: the multipole magnetic field ring-cusp thrusters and the divergent solenoidal magnetic fields in Kaufman-type thrusters. Ring-cusp thrusters use alternating polarity permanent magnet rings placed around the anode-potential thruster body. Energetic electrons are injected along a weak diverging magnetic field at the cathode and demagnetize sufficiently to bounce from the surface magnetic fields until they either lose their energy by collisions or find a magnetic cusp to be lost to the anode. Kaufman thrusters inject energetic electrons along a strong diverging solenoidal magnetic field with the pole-pieces typically at cathode potential and rely on cross-field diffusion of the electrons to an anode electrode placed near the cylindrical wall to produce ionization and create a stable discharge.

4.3.1 Generalized 0-D Ring-Cusp Ion Thruster Model

The idealized plasma-generator model developed in Section 4.2 is useful in describing how the discharge produces the plasma, but neglects many of the particle flows and energy transport mechanisms found in actual thrusters. The complete particle flows in a thruster discharge chamber are shown in Fig. 4-9. The primary electron current emitted by the hollow cathode, I_e, generates ions and plasma electrons. The ions flow to the accelerator structure (I_s), to the anode wall (I_{ia}), and back to the cathode (I_k). Some fraction of the primary electrons is lost directly to the anode at the magnetic cusp (I_L). The plasma electrons are also predominately lost to the anode at the cusp (I_a), with only a

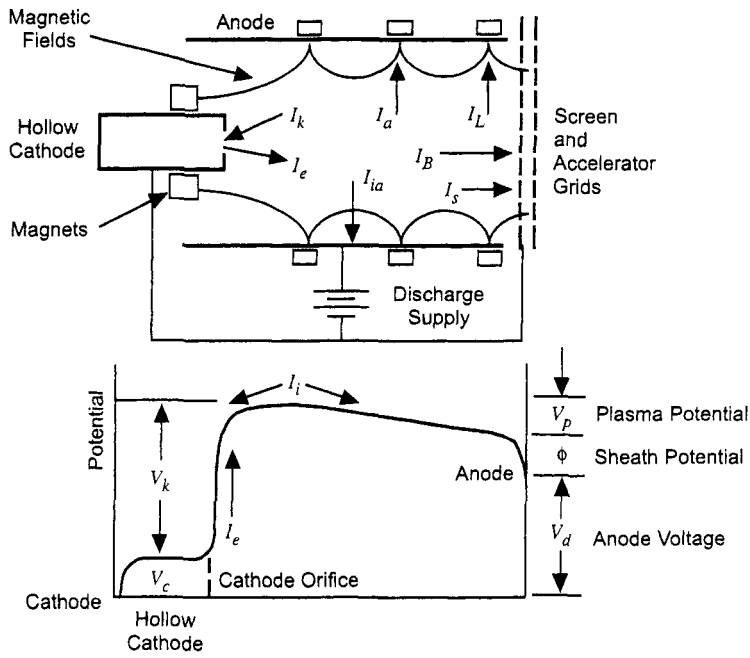

Fig. 4-9. Schematic of the thruster showing particle flows and potential distribution in the discharge chamber.

very small fraction lost across the transverse magnetic field between the cusps corresponding to the ambipolar current flows in this region.

The particle energies are determined by the potential distribution in the thruster. Figure 4-9 also schematically shows the potential in the plasma chamber. Electrons from the plasma inside the hollow cathode at a potential V_c are extracted through the orifice and into the discharge chamber where they gain energy by passing through the potential $V_k = V_d - V_c + V_p + \phi$, where V_p is the potential drop in the plasma and ϕ is the anode sheath potential. Some of these electrons cause ionization near the hollow cathode exit, which produces a higher plasma density locally near the cathode exit that must be dispersed before reaching the grid region in order to produce the desired uniform plasma profile across the grids. The potential drop V_p in the plasma, which is assumed to be uniform and quasineutral, can be reasonably approximated as $kT_e/2e$ from the pre-sheath potential in the nearly collisionless plasma. Ions leaving the plasma then gain the energy $\varepsilon_1 = kT_e/2e + \phi$, which was given in Eq. (4.2-10). Electrons in the tail of the Maxwellian distribution overcome the anode sheath

and are collected by the anode at the cusps, where they remove an energy per particle of $\varepsilon_e = (2kT_e / e + \phi)$, which is given in Eq. (4.2-9) and derived in Appendix C.

Analytic models of the discharge chamber performance in ion thrusters have been described in the literature for many years [15–17]. The first comprehensive model of the discharge chamber performance using particle and energy balance equations in ring-cusp thrusters was developed by Brophy and Wilbur [18,19] in 1984. In Brophy's model, volume-averaged particle and energy balance equations including primary electrons were used to derive expressions for the discharge loss as a function of the mass utilization efficiency in the thruster. Brophy's model was extended by Goebel [20,21] to include electrostatic ion confinement, primary confinement and thermalization, the anode sheath [22], and hollow cathode effects. This model utilizes magnetic field parameters obtained from a magnetic field solver that accurately models the magnetic boundary. Since the model assumes a uniform plasma in the volume inside the magnetic confinement in the discharge chamber, it is sometimes called a 0-dimensional (0-D) model.

The 0-D discharge chamber model to be described here [21] self-consistently calculates the neutral gas density, electron temperature, primary electron density, plasma density, plasma potential, discharge current, and ion fluxes to the boundaries of the discharge chamber. While the assumption of uniform plasma is not particularly accurate near the cathode plume, the majority of the plasma in the discharge chamber is relatively uniform, and the model predictions agree well with experimental results. The 0-D model solves for discharge loss as a function of the mass utilization efficiency, which is useful in plotting performance curves that best characterize the discharge chamber performance.

The particle flows and potential distribution in the thruster used in the 0-D model are shown schematically in Fig. 4-9. Mono-energetic primary electrons with a current I_e are assumed to be emitted from the hollow cathode orifice into the discharge chamber, where they ionize the background gas to produce a uniform plasma. Electrons produced in the ionization process and primary electrons that have thermalized with the plasma electrons create a Maxwellian plasma electron population that also contributes to the ionization. Due to the relatively high magnetic field produced by the magnets near the wall, the electron Larmor radius is much smaller than the dimensions of the discharge chamber, and both primary and plasma electrons are considered to be reflected from the boundary region between the magnetic cusps. The primary and plasma electrons can be lost at the magnetic cusps because the magnetic field lines are

essentially perpendicular to the surface. The number of electrons lost at the cusp depends on the local sheath potential and the effective loss area at the cusp. Ions produced in the discharge chamber can flow back to the hollow cathode, to the anode wall, or to the plane of the accelerator. At the accelerator, these ions are either intercepted and collected by the screen electrode with an effective transparency, T_g, or are extracted from the plasma through the grids to become beam ions. The screen grid transparency depends on the optical transparency of the grid and the penetration of the high voltage fields from the accelerator region into the screen apertures. While this transparency is an input to the discharge model, it is calculated by the ion optics codes described in Chapter 5.

In this model, the high-voltage power supply that accelerates the ions, called the screen supply, is connected to the anode. This means that the ions fall from the average plasma potential in the discharge chamber to form the beam. It is also possible to connect the screen supply to the screen and cathode, which means that the ion current in the beam must pass through the discharge supply. This changes the algebra slightly in calculating the discharge performance, but it does not change the results. The components of the particle and energy balance model are described in the following sections.

4.3.2 Magnetic Multipole Boundaries

Ring-cusp ion thrusters use alternating polarity permanent magnet rings oriented perpendicularly to the thruster axis, with the number of rings selected and optimized for different size thrusters [20]. This configuration provides magnetic confinement of the electrons with finite loss at the magnetic cusps, and electrostatic confinement of the ions from the anode wall due to the quasi-ambipolar potentials at the boundary from the transverse magnetic fields. Line-cusp thrusters also use high field magnets, but the magnets are configured in alternating polarity axial lines that run along the chamber wall. Asymmetries at the ends of the line cusps cause plasma losses and difficulties in producing a uniform symmetric field at the cathode exit, which adversely affects the electron confinement and thruster efficiency. Ring-cusp thrusters are the most commonly used discharge chamber design at this time due to their ability to produce high efficiency and uniform plasmas at the ion accelerator surface if properly designed.

A schematic representation of a section of a ring cusp magnetic multipole boundary is shown in Fig. 4-10. In this view, a cut along the axis through a six-ring boundary at the wall is made, leaving the ends of the alternating magnets visible. The magnetic field lines terminate at the magnet face, resulting in a cusp magnetic field with field lines perpendicular to the wall at the magnet.

Electrons that are incident in this area will be either reflected by the magnetic mirror, electrostatically repelled by the sheath potential, or lost directly to the anode. Electrons that are incident between the cusps encounter a transverse magnetic field and are reflected from the boundary. The contours of constant magnetic field shown on the right in Fig. 4-10 illustrate that the total field is essentially constant across the boundary at a distance sufficiently above the magnets, although the component of the field is changing from purely perpendicular at the cusp to purely parallel between the cusps.

An analysis of the magnetic field strength for various multipole boundaries was published by Forrester [23] and discussed by Lieberman [24]. Since the divergence of the magnetic field is zero, the field satisfies Laplace's equation, and the solution for the lowest-order mode at a distance from the magnets greater than the magnet separation can be expressed by a Fourier series. This gives a magnetic field strength above the magnet array described by

$$B_y(x,y) = \frac{\pi w B_o}{2d} \cos\left(\frac{\pi x}{d}\right) e^{-\pi y/d}, \qquad (4.3\text{-}1)$$

where B_o is the magnetic field at the surface of the magnet, d is the distance between the magnet centers, w is the magnet width, and the y-direction is perpendicular to the wall in Fig. 4-10. Due to localized magnet positions, the field has the periodic cosine behavior along the surface of the wall illustrated in the figure. In addition, the magnetic field decreases exponentially away from the wall all along the boundary.

At the cusp, the field actually decreases as $1/d^2$ due to the dipole nature of the permanent magnet. This rapid decrease in the field moving away from the magnet illustrates the importance of placing the magnets as close to the plasma

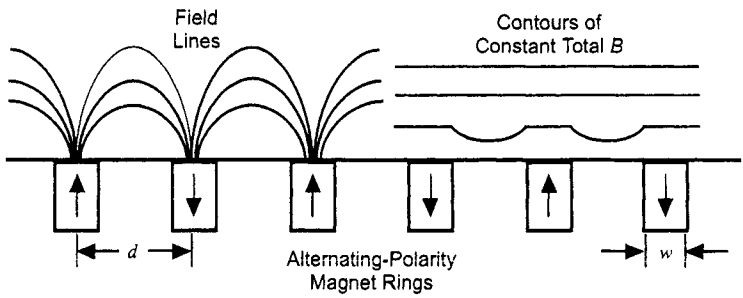

Fig. 4-10. Cross section (side) view of a six-ring-cusp magnetic multipole boundary showing the magnetic field lines and examples of contours of constant magnetic field.

as possible to maximize the field strength inside the discharge chamber for a given magnet size in order to provide sufficient field strength for primary and secondary electron confinement at the wall. Between the cusps, the dipole characteristics of the local field forces the field lines to wrap back around the magnets, which causes the magnetic field strength to have a maximum at a distance $y = 0.29*d$ from the wall, which will be derived in Section 4.3.4. The transverse maximum field strength produced between the cusps is important to provide electron and ion confinement, which improves the thruster efficiency.

While analytic solutions to the magnetic field provide insight into the field structure, the availability of commercial computer codes to calculate the fields accurately makes it much simpler to model the entire ring-cusp field. For example, Fig. 4-11 shows the contours of constant magnetic field measured and calculated using Maxwell three-dimensional (3-D) magnetic field solver [25] for the Nuclear Electric Xenon Ion Thruster System (NEXIS) [20] with six ring cusps. The measured and calculated values are within the measurement error. This type of plot shows clearly the localized surface-field characteristic of magnetic multipole boundaries, which leaves the majority of the inner volume essentially magnetic-field free. A large field-free region design significantly enhances the plasma uniformity and ion current density profile [20,26]. In this case, the 60-gauss magnetic field contour is closed throughout the inside surface of the thruster, which will be shown in the next section to provide good plasma confinement at the wall.

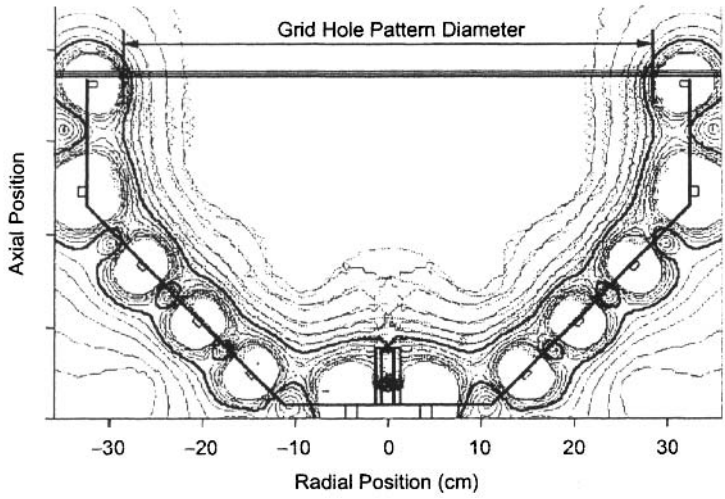

Fig. 4-11. Comparison of measured (dashed) and calculated (solid) magnetic field contours in the six-ring NEXIS thruster [20].

4.3.3 Electron Confinement

The primary electrons are injected into the discharge chamber from the hollow cathode. The discharge chamber can be viewed as a volume with reflecting boundaries and discrete loss areas for the electrons at the cusps where the magnetic fields lines are nearly perpendicular to the surface. The primary electrons then effectively bounce around in the chamber until they are either lost directly to the anode wall by encountering the finite loss area at the cusps, make an ionization or excitation collision, or are thermalized by coulomb interactions with the plasma electrons. The primary current lost directly to the anode cusps is given by

$$I_L = n_p e v_p A_p , \tag{4.3-2}$$

where n_p is the primary electron density, v_p is the primary electron velocity, and A_p is the loss area for the primaries.

The loss area for primary electrons at the cusp [27] is given by

$$A_p = 2\, r_p\, L_c = \frac{2}{B}\sqrt{\frac{2mv_p}{e}}\, L_c , \tag{4.3-3}$$

where r_p is the primary electron Larmor radius, B is the magnetic field strength at the cusp at the anode wall, v_p is the primary electron velocity, e is the electron charge, and L_c is the total length of the magnetic cusps (sum of the length of the cusps).

Using a simple probabilistic analysis, the mean primary electron confinement time can be estimated by

$$\tau_p = \frac{V}{v_p\, A_p} , \tag{4.3-4}$$

where V is the volume of the discharge chamber. The mean primary electron path length prior to finding a cusp and being lost to the wall is $L = v_p * \tau_p$. Likewise, the ionization mean free path is $\lambda = 1/n_o\sigma$, where σ represents the total inelastic collision cross section for the primary electrons. The probability that a primary electron will make a collision and not be directly lost to the anode is then

$$P = \left[1 - \exp^{-n_o \sigma L}\right] = \left[1 - \exp^{\left(-n_o \sigma V / A_p\right)}\right]. \qquad (4.3\text{-}5)$$

By providing strong magnetic field strengths at the cusp to minimize the primary loss area, the probability of a primary electron being lost directly to the anode can be made very small. Similarly, ion thrusters with large volumes and/or operated at higher internal gas densities will cause the primary electrons to undergo collisions and thermalization prior to being lost directly to the anode. Minimizing the energy loss associated with primaries being lost before making a collision in this way serves to maximize the efficiency of the thruster.

An example of the probability of a primary electron making a collision before finding a cusp is shown in Fig. 4-12 for the case of the NEXIS thruster designed with either 4 or 6 cusps [20]. For the design with 6 cusps, it is necessary to have cusp-field strengths approaching 2000 G at the surface of the anode in order to minimize primary loss. Designs with a smaller number of ring cusps, corresponding to a smaller primary anode collection area from Eq. (4.3-3), require less magnetic field strength to achieve the same benefit. However, it will be shown later that the number of cusps affects efficiency and uniformity, and that maximizing the probability of a primary making a collision before being lost is only one of the trade-offs in designing an ion thruster.

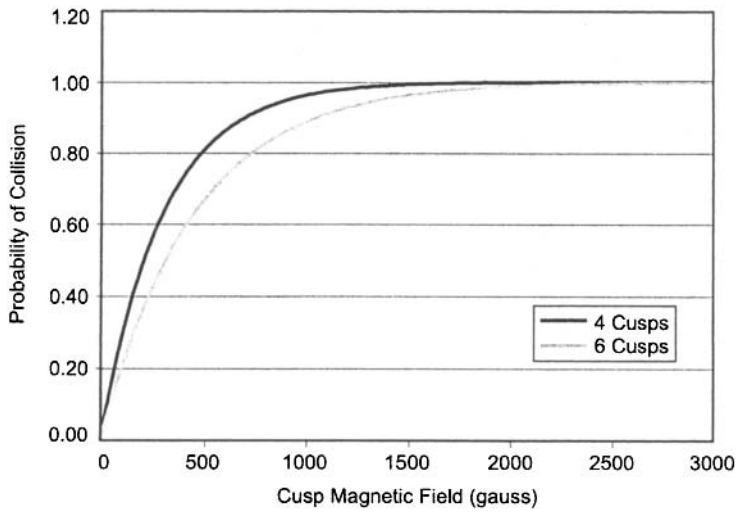

Fig. 4-12. Probability of primary electrons making a collision before being lost to the anode as a function of the cusp magnetic field strength for the NEXIS thruster design [20].

Since the primary electron current lost directly to the anode is generally minimized for best efficiency, the discharge current is carried to the anode mainly by the plasma electrons. The plasma electrons are almost exclusively lost at the magnetic cusps, but their motion is affected by the presence of ions that also penetrate the cusp. Therefore, ions and electrons are lost to a hybrid anode area [27] at the cusp given by

$$A_a = 4\, r_h\, L_c = 4\, \sqrt{r_e r_i}\, L_c, \tag{4.3-6}$$

where r_h is the hybrid Larmor radius, r_e is the electron Larmor radius, and r_i is the ion Larmor radius. The flux of plasma electrons, I_a, that overcomes the sheath at the anode is

$$I_a = \frac{1}{4}\left(\frac{8kT_e}{\pi\, m}\right)^{1/2} e\, n_e\, A_a\, \exp^{-e\phi/kT_e}, \tag{4.3-7}$$

where ϕ is the local plasma potential relative to the anode (essentially the anode sheath potential).

The plasma in the discharge chamber obeys particle conservation in that the current injected and produced in the discharge must equal the total current that leaves the discharge:

$$\sum\left(I_{\text{injected}} + I_{\text{produced}}\right) = \sum I_{\text{out}}. \tag{4.3-8}$$

The current injected into the discharge volume is the primary electron current, and the current produced is the ion and electron pairs from each ionization collision. The current lost to the anode is the sum of the direct primary loss, the plasma electron loss, and a fraction of the ion loss. There is also ion current lost to cathode potential surfaces and the accelerator structure from the balance of the ions produced in the discharge. The plasma potential will adjust itself such that the total electron current to the anode is equal to the total ion current out of the discharge. It will be shown in the following sections that changing the anode area via the magnet strength or number of magnet rings will change the plasma potential relative to the anode (essentially the anode sheath voltage), which affects both the energy loss though the sheath and the stability of the discharge.

4.3.4 Ion Confinement at the Anode Wall

Ions are typically unmagnetized in ion thruster discharge chambers because the magnetic field is relatively low throughout the bulk of the discharge chamber,

which results in a large ion Larmor radius compared to the thruster dimensions. For an unmagnetized plasma, the ion current flowing out the plasma volume in any direction is given by the Bohm current:

$$I_i = \frac{1}{2} n_i e \sqrt{\frac{kT_e}{M}} A, \tag{4.3-9}$$

where n_i is the ion density in the center of the discharge and A is the total ion loss area. The Bohm current also describes ion flow along magnetic field lines, which will be useful later in discussing other plasma generator types.

The electrons may or may not be magnetized in the main discharge chamber volume, but they are strongly affected by the magnet fields near the boundary in ring-cusp thrusters. The magnetized electrons then influence the ion motion near the boundaries by electrostatic effects. This causes the ion loss to the cusps to be the Bohm current to the hybrid area, given by Eq. (4.3-6), and a reduction in the Bohm current to the wall area between the cusps due to the ambipolar potentials that develop there. Since the cusp area is small compared to the rest of the anode surface area facing the plasma, the ion current to the hybrid cusp area often can be neglected. However, between the cusps the loss area is significant, and it is possible to analyze the electron and ion transport across the magnetic field to calculate the reduction in the ion velocity caused by the reduced transverse electron drift speed. This is then used to calculate the rate of ion loss to the anode compared to the unmagnetized Bohm current to the walls.

Ring cusp thrusters are designed with various numbers of rings, distances betweens the rings, and magnet sizes that determine the magnetic field strength in the discharge chamber transverse to the wall. The quasi-neutral plasma flow across this magnetic field to the wall is described by the diffusion equation with an ambipolar diffusion coefficient. Ambipolar diffusion across a magnetic field was analyzed in Section 3.6.3.2. The transverse ion velocity was found to be

$$v_i = \frac{\mu_e}{\left(1 + \mu_e^2 B^2 - \frac{\nu_{ei}}{\nu_e}\right)} \left(E + \frac{kT_e}{e} \frac{\nabla n}{n}\right). \tag{4.3-10}$$

Setting the transverse electric field E in the plasma to zero in Eq. (4.3-10) gives the case where the ambipolar electric field exactly cancels the pre-sheath electric field that normally accelerates the ions to the Bohm velocity. In this case, the ion velocity is just the ion thermal velocity $\left(\approx \sqrt{kT_i/M}\right)$, and the value of B in Eq. (4.3-10) is the minimum transverse magnetic field required to

reduce the electron mobility sufficiently to produce this effect. Due to the smaller ion velocity, the flux of ions passing through the transverse magnetic field is greatly reduced compared to the Bohm current. The ion flux that does reach the wall is finally accelerated to the Bohm velocity close to the anode wall to satisfy the sheath criterion. Ions are conserved in this model because ions that are inhibited from flowing to the anode wall due to the transverse fields instead flow axially toward the grids where there is no confinement.

However, it is not necessary to limit this analysis to the case of $E = 0$. If the magnetic field is smaller than the critical B that causes $E = 0$, then the transverse electron mobility increases and a finite electric field exists in the magnetic diffusion length l. The ions fall through whatever potential difference is set up by this electric field, which means that the ions are accelerated to an energy given by

$$\frac{1}{2} M v_i^2 = e\, E \cdot l. \tag{4.3-11}$$

The ambipolar flow in the transverse magnetic field changes the electric field magnitude in the pre-sheath region and reduces the acceleration of the ions toward the wall. In the limit of no magnetic field, the electric field must accelerate the ions to the Bohm velocity, which results in a net electric field in the plasma-edge region limited to

$$E = -\frac{M v_i^2}{e\, l}. \tag{4.3-12}$$

Note that the electric field sign must be negative for the ion flow in this region. Using Eq. (4.3-12) in Eq. (4.3-10), the minimum magnetic field to produce an ion velocity of v_i is

$$B = \frac{\nu_e m}{e} \sqrt{\frac{\left(kT_e - M v_i^2\right)}{v_i m \nu_e \ell} - \left(\frac{\nu}{1+\nu}\right)}, \tag{4.3-13}$$

where $\nu = \nu_{en} / \nu_{ei}$, and $kT_e \nabla n / en$ is approximately kT_e / el for l representing the length the ions travel radially in the transverse magnetic field between the cusps. The value of l can be estimated from calculations of the transverse magnetic field versus the distance from the wall between the cusps, and is usually on the order of 2 to 3 cm.

Alternatively, the modified electric field given in Eq. (4.3-12) can be inserted into Eq. (4.3-10) to produce an expression for the transverse ion velocity:

$$v_i^2 + \frac{el}{\mu_e M}\left(1+\mu_e{}^2 B^2 - \frac{\nu_{ei}}{\nu_e}\right)v_i - \frac{kT_e}{M} = 0. \tag{4.3-14}$$

This quadratic equation can be easily solved to give

$$v_i = \frac{1}{2}\sqrt{\left[\frac{e\ell}{M\mu_e}\left(1+\mu_e^2 B^2 - \frac{\nu_{ei}}{\nu_e}\right)\right]^2 + \frac{4kT_e}{M}} - \left[\frac{e\ell}{2M\mu_e}\left(1+\mu_e^2 B^2 - \frac{\nu_{ei}}{\nu_e}\right)\right]. \tag{4.3-15}$$

The collision frequencies ($\nu_e = \nu_{en} + \nu_{ei}$ and $\nu = \nu_{en} / \nu_{ei}$) in these equations for xenon plasmas were given in Chapter 3, where the electron-neutral collision frequency is given in Eq. (3.6-12) and the electron-ion collision frequency is given in Eq. (3.6-14). It is possible to show that in the limit that B goes to zero and the flow is essentially collisionless, Eq. (4.3-15) reverts to the Bohm velocity.

Defining an ion confinement factor

$$f_c \equiv \frac{v_i}{v_{\text{Bohm}}}, \tag{4.3-16}$$

and since the Bohm velocity is $v_{\text{Bohm}} = \sqrt{kT_e / M}$, it is a simple matter to calculate the reduction in the expected flux of ions going to the anode due to the reduction in the Bohm velocity at a given magnetic field strength B. The ion current transverse to the magnetic field between the cusps to the anode is then given by

$$I_{ia} = \frac{1}{2} n_i \, e \sqrt{\frac{kT_e}{M}} \, A_{as} f_c, \tag{4.3-17}$$

where A_{as} is the total surface area of the anode exposed to the plasma.

There are two issues with using Eq. (4.3-17) to evaluate ion loss rate reduction between the cusps. First, the magnetic field in the ring-cusp geometry is not transverse to the wall everywhere. Near the cusp, the field transitions from

parallel to perpendicular to the wall, where the analysis above does not apply. However, the magnetic field strength in this region increases rapidly near the magnets and some fraction of the plasma electrons is reflected from the magnetic mirror. This serves to retard the ion flux electrostatically in a manner similar to the ambipolar diffusion case between the cusps described above. Ultimately, the ions are lost at the cusp with the Bohm current to the hybrid area, and it is usually found that the transition to this unimpeded ion flow to the wall occurs over an area that is small compared to the total area between the cusps.

The second issue with using Eq. (4.3-17) is that the diffusion thickness l is not known. However, this can be estimated for ring-cusp thrusters using a dipole model for the magnets. Consider the case of two rows of opposite polarity magnets, which is illustrated in part of Fig. 4-10. Each magnet has a dipole strength M per unit length, and the magnets are separated in the x-direction by a distance d. The magnetic field along the line perpendicular to the midline between the magnets is

$$\left|\mathbf{B}^+(y)\right| = \frac{q}{r} = \frac{q}{\sqrt{\frac{d^2}{4} + (y-\delta)^2}}, \tag{4.3-18}$$

where r is the length of the line from the point on the midline to the magnet, q is the number of magnetic dipoles, and δ is the half height of the magnet. The magnetic field on the centerline between the magnets has only an x-component. The x-component of the field from one magnet (positive polarity) is given by

$$B_x^+(y) = \left|\mathbf{B}^+(y)\right| \cos\theta = \frac{q\frac{d}{2}}{r^2} = \frac{q\frac{d}{2}}{\frac{d^2}{4} + (y-\delta)^2}. \tag{4.3-19}$$

The field in the x-direction from both magnets is then

$$B_x(y) = \frac{q\,d}{\frac{d^2}{4} + (y-\delta)^2} - \frac{q\,d}{\frac{d^2}{4} + (y+\delta)^2}, \tag{4.3-20}$$

and so the total field on the center line is

$$B(y) = \frac{2(2q\delta)yd}{\left(\frac{d^2}{4} + y^2\right)^2} = \frac{2M\,yd}{\left(\frac{d^2}{4} + y^2\right)^2}, \tag{4.3-21}$$

where the magnetization M is the number of magnetic dipoles times the length of the magnet.

The maximum magnetic field strength between the magnets, found from Eq. (4.3-21), then occurs at

$$y = \frac{d}{2\sqrt{3}} = 0.29d \approx l. \tag{4.3-22}$$

It is assumed that the diffusion length l is roughly this distance. This is not an unreasonable approximation, as illustrated in Fig. 4-13. The magnetic field decreases on each side of the maximum, but is nearly the full value over the length of about 0.3 of the distance between the magnets.

The maximum transverse field strength along the centerline between the magnets, often called the "saddle-point" field, can also be calculated from this simple derivation. Using Eq. (4.3-22) in Eq. (4.3-21), the maximum magnetic field is

$$B(y_{\max}) = 5.2\frac{M}{d^2}. \tag{4.3-23}$$

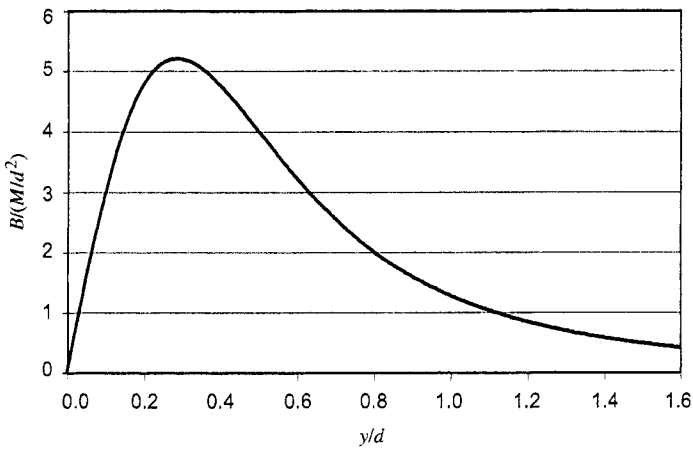

Fig. 4-13. Magnetic field strength as a function of distance above the magnets.

The dipole strength per unit length is

$$M = \frac{B_r V_m}{4\pi w}, \tag{4.3-24}$$

where B_r is the residual magnetic field of the magnet, V_m is the volume of the magnet, and w is the width of the magnet. For example, for two rows of magnets that have a residual magnetic field of 10,000 gauss, a volume per width of 0.6 cm^2, and a separation of 10 cm, the maximum transverse magnetic field is 24.8 gauss and occurs at a distance of 2.9 cm above the boundary.

As an example of the ion loss rate to the anode, the fraction of the Bohm current to the anode (I_{ia} / I_{Bohm}) is plotted in Fig. 4-14 as a function of the magnetic field at the saddle point for the NSTAR ion thruster [13]. At zero transverse magnetic field, the ion flux to the anode is the Bohm current. As the transverse field increases and reduces the electron mobility, the ions are slowed and the current loss decreases. In the NSTAR design, the last closed magnetic contour is about 20 gauss, and so roughly half of the ions initially headed radially toward the anode are lost. For closed magnetic field contours of at least about 50 gauss, the ion loss to the anode is reduced by nearly a factor of 10 compared to the unmagnetized Bohm current. This can make a significant difference in the efficiency of the plasma generator and the amount of discharge power required to produce the beam ions. Even though the ions are unmagnetized in these thrusters, it is clear that ambipolar effects make the ring-cusp magnetic fields effective in reducing the ion loss to the walls.

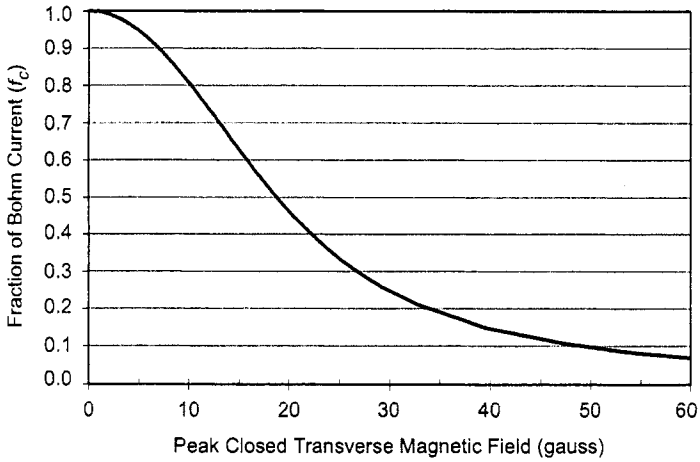

Fig. 4-14. Fraction of the Bohm current density to the anode wall as a function of the transverse magnetic field strength for the NSTAR ion thruster [13].

4.3.5 Ion and Excited Neutral Production

Ions in the discharge chamber are produced by both the primary electrons and by the tail of the Maxwellian distribution of the plasma electrons. The total number of ions produced in the discharge in particles per second is given by

$$I_p = n_o n_e \langle \sigma_i v_e \rangle V + n_o n_p \langle \sigma_i v_p \rangle V, \qquad (4.3\text{-}25)$$

where n_o is the neutral atom density, n_e is the plasma electron density, σ_1 is the ionization cross section, v_e is the plasma electron velocity, V is the plasma volume inside the discharge chamber, n_p is the primary electron density, and v_p is the primary electron velocity. The terms in the brackets are the ionization cross section averaged over the distribution of electron energies, which is usually called the reaction rate coefficient.

An example of ionization and excitation cross sections [28,29] used for electron impact on xenon is shown in Fig. 4-15. If it is assumed that the primary electrons are monoenergetic, then the reaction rate coefficient in Eq. (4.3-25) for primary ionization is just the cross section in Fig. 4-15 times the corresponding primary electron velocity. These data are listed for xenon in Appendix D. If the primaries have a distribution in energy, then the cross section must be averaged over that distribution. For Maxwellian electrons, this is calculated for xenon and listed in Appendix E.

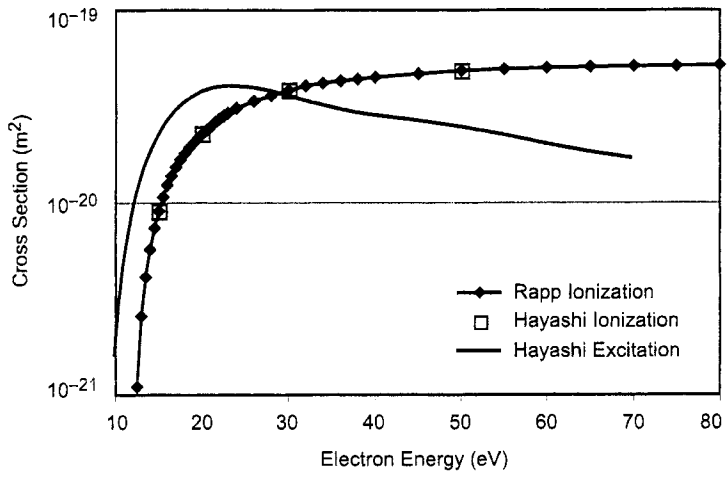

Fig. 4-15. Ionization and excitation cross sections for xenon [28,29].

Excited neutrals are also produced by both the primary electrons and the tail of the Maxwellian distribution of the plasma electrons. The total number of exited neutrals produced in the discharge in particles per second is given by

$$I^* = n_o n_e \langle \sigma_* v_e \rangle V + n_o n_p \langle \sigma_* v_p \rangle V , \qquad (4.3\text{-}26)$$

where σ_* is the excitation cross section. Again, the excitation cross section is averaged over the distribution in electron energies to produce the reaction rate coefficients in the brackets. The reaction rate coefficients calculated by averaging the ionization and excitation cross sections over the Maxwellian energy distribution are shown in Fig. 4-16 and listed in Appendix E. The rate of excitation is seen to exceed that of ionization for low electron temperatures (below about 9 eV). The ratio of excitation to ionization reaction rates for xenon is shown in Fig. 4-4. As previously described, at low electron temperatures, a significant amount of the energy in the discharge goes into excitation of the neutrals at the expense of ionization. This is one of the many reasons that the cost of producing an ion in ion thrusters is usually over ten times the ionization potential.

For inert gas propellants commonly used in ion thrusters, the second ionization potential is on the order of twice the first ionization potential. For example, the first ionization potential of xenon is 12.13 eV, and the second ionization potential is 21.2 eV. DC electron discharges that have electron energies in excess of 21.2 V can produce a significant number of double ions. In addition,

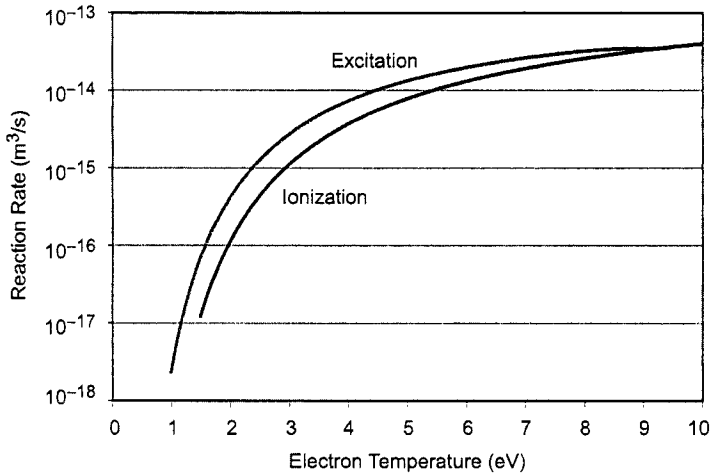

Fig. 4-16. Ionization and excitation reaction rates averaged over a Maxwellian electron distribution in a xenon plasma.

the tail of the Maxwellian electron distribution will also contain electrons with an energy that exceeds the second ionization potential, and significant numbers of double ions will be produced if the electron temperature in the discharge chamber is high.

The generation rate of double ions is determined in the same manner as single ions, discussed above, with different ionization cross sections [30]. The density of the double ions is determined by the continuity equation for that species,

$$\frac{dn^{++}}{dt} + \nabla \cdot \left(n^{++} v^{+} \sqrt{2} \right) = \dot{n}^{++}, \tag{4.3-27}$$

where it is assumed that due to the double ions' charge, the velocity will be increased over the singly ionized species by a square root of two. Defining the rate of double-ion production compared to single-ion production as

$$R^{++} = \frac{n^{++}}{n^{+}}, \tag{4.3-28}$$

the beam current density of single ions from the discharge plasma boundary through the ion optics (again with a transparency T_g) is

$$J_i^{+} = n^{+} e v_B^{+} T = n_i e v_B^{+} T_g \left(1 - R^{++} \right), \tag{4.3-29}$$

where n_i is the total ion density. The double-ion current density is likewise

$$J_i^{++} = n^{++} (2e) \left(\sqrt{2} v_B^{+} \right) T_g = \sqrt{8} n_i e v_B^{+} T_g R^{++}. \tag{4.3-30}$$

The total ion beam current is then the sum of the singly and doubly ionized particle currents.

As discussed in Chapter 2, the discharge propellant efficiency is the ratio of the propellant that becomes beam ions (of any charge) to the rate of propellant flow into the discharge chamber. Considering the effect of double ions, the propellant efficiency of the discharge chamber is then

$$\eta_{md} = \left(J_B^{+} + \frac{J_B^{++}}{2} \right) \frac{A_g}{e \dot{m}_d}, \tag{4.3-31}$$

where $\dot{m}_d$ is the mass flow into the discharge chamber and A_g is the area of the grids. In the event that there is a significant double-ion content in the discharge plasma, the beam current and the discharge chamber mass utilization efficiency must be corrected using these equations.

4.3.6 Neutral and Primary Densities in the Discharge Chamber

The ion and excited neutral production rates described by Eqs. (4.3-25) and (4.3-26) require knowledge of the neutral gas density in the discharge chamber. The neutral gas flow that escapes the chamber (the unionized propellant) is simply the gas injected into the discharge chamber minus the gas particles that are ionized and extracted to form the ion beam:

$$Q_{\text{out}} = Q_{\text{in}} - \frac{I_b}{e}. \tag{4.3-32}$$

The neutral gas that leaks through the grid is the neutral flux on the grids (in particles per second) times the grid optical transparency T_a and a conductance reduction term η_c known as the Clausing factor [31]:

$$Q_{\text{out}} = \frac{1}{4} n_o v_o A_g T_a \eta_c, \tag{4.3-33}$$

where v_o is the neutral gas velocity, A_g is the grid area, and η_c is the Clausing factor. The Clausing factor represents the reduced conductance of the grids for finite grid thicknesses and results from Clausing's original work on gas flow restriction in short tubes. For typical grid apertures with small thickness-to-length ratios, the Clausing factor must be calculated using Monte Carlo techniques, an example of which is given in Appendix G. In general, ion thruster grids will have Clausing factors on the order of 0.5.

The mass utilization efficiency of the thruster discharge chamber is defined as

$$\eta_{md} = \frac{I_b}{Q_{\text{in}} e}. \tag{4.3-34}$$

Equating Eqs. (4.3-32) and (4.3-33), using Eq. (4.3-34), and solving for the neutral gas density in the discharge chamber gives

$$n_o = \frac{4Q_{\text{in}}(1-\eta_{md})}{v_o A_g T_a \eta_c} = \frac{4\, I_B}{v_o e A_g T_a \eta_c} \frac{(1-\eta_{md})}{\eta_{md}}. \tag{4.3-35}$$

Flow is usually given in standard cubic centimeters per minute (sccm) or mg/s, and conversions from these units to number of particles per second, useful in Eq. (4.3-35), are given in Appendix B. The neutral pressure in the discharge chamber during operation of the thruster can also be found using this expression and the conversion from density to pressure given in Eq. (2.7-2), if the neutral gas temperature is known. In general, the neutral gas atoms collide with the anode wall and grids several times before being lost, and so the neutral gas can be assumed to have the average temperature of the thruster body in contact with the plasma. This temperature typically ranges from 200 to 300 deg C for operating thrusters.

The electron temperature in the discharge chamber can be found using particle balance of the ions. The total ion production rate, given by Eq. (4.3-25), must equal the total ion loss rate. The ion loss rate is given by the Bohm current in Eq. (4.3-9) with the area A representing the sum of all the surfaces that collect ions (cathode, anode, and grids), with the appropriate confinement factor f_c found in Eq. (4.3-16) multiplied by the anode surface area. Equating Eqs. (4.3-25) and (4.3-9) and using Eq. (4.3-35) for the neutral density gives

$$\frac{\sqrt{\frac{kT_e}{M}}}{\langle \sigma_i v_e \rangle V + \frac{n_p}{n_e}\langle \sigma_i v_p \rangle V} = \frac{2n_o V}{A_i} = \frac{8V\ Q_{\text{in}}(1-\eta_{md})}{v_o A_g A_i T_a \eta_c}. \qquad (4.3\text{-}36)$$

If the total flow into the discharge chamber and the mass utilization efficiency are specified, and the primary electron density is calculated as described below, then Eq. (4.3-36) can be solved for the electron temperature. This is because the ionization and excitation reaction rate coefficients are functions of the electron temperature. Alternatively, if the beam current is specified, then the right-hand side of Eq. (4.3-35) can be used in Eq. (4.3-36) to find the electron temperature. Typically, curve fits to the ionization and excitation cross section and reaction rate data shown in Figs. 4-15 and 4-16 are used to evaluate the reaction-rate coefficients in a program that iteratively solves Eq. (4.3-36) for the electron temperature.

The primary electron density in Eq. (4.3-36) can be evaluated from the total primary electron confinement time in the discharge chamber. The emitted current I_e from the hollow cathode is

$$I_e = \frac{n_p\ e\ V}{\tau_t}, \qquad (4.3\text{-}37)$$

where τ_t is the total primary confinement time that addresses all of the primary electron thermalization and loss mechanisms. The ballistic confinement time for direct primary loss to the anode, τ_p, was given in Eq. (4.3-4). It is assumed that the primary electrons have undergone an inelastic collision with the neutral gas and have lost sufficient energy such that they are then rapidly thermalized with the plasma electrons. The mean time for a collision between the primary and a neutral gas atom to occur is given by

$$\tau_c = \frac{1}{n_o \sigma v_p}, \tag{4.3-38}$$

where σ is the total inelastic collision cross section. Using Eq. (4.3-35) for the neutral density, the mean collision time for primary electrons is

$$\tau_c = \frac{v_o e A_g T_a \eta_c \eta_m}{4\ \sigma v_p I_B (1-\eta_{md})} = \frac{v_o A_g T_a \eta_c}{4 \sigma v_p Q_{\text{in}} (1-\eta_{md})}. \tag{4.3-39}$$

Finally, primary electrons can also be thermalized by equilibrating with the plasma electrons. The time for primary electrons to slow into a Maxwellian electron population was derived by Spitzer [32] and is given by

$$\tau_s = \frac{\omega}{2 A_D l_f^2 G(l_f \omega)}, \tag{4.3-40}$$

where $\omega = \sqrt{2V_{pe}/m}$, eV_{pe} is the primary energy, $l_f = \sqrt{m/2kT_e}$ is the inverse mean velocity of the Maxwellian electrons, A_D is a diffusion constant given by

$$A_D = \frac{8\pi e^4 n_e \ln\Lambda}{m^2}, \tag{4.3-41}$$

and $\ln\Lambda$ is the collisionality parameter [33] given in Eq. (3.6-15). The function $G(l_f\omega)$ is defined in Appendix F, and a curve fit to Spitzer's tabulated values (in CGS units) for this function is provided.

The total primary electron confinement time can be found from

$$\frac{1}{\tau_t} = \frac{1}{\tau_p} + \frac{1}{\tau_c} + \frac{1}{\tau_s}. \tag{4.3-42}$$

Some care needs to be used in including the Spitzer slowing time because some ion thruster designs have a very non-monoenergetic primary energy distribution, which is not described well by Eq. (4.3-40).

The current emitted from the hollow cathode is

$$I_e = I_d - I_s - I_k, \tag{4.3-43}$$

where I_s is the screen current and I_k is the ion current back to the cathode. Using Eqs. (4.3-4) and (4.3-38) in Eq. (4.3-37), the primary electron density is given by

$$\begin{aligned} n_p &= \frac{I_e\,\tau_t}{eV} = \frac{I_e}{eV}\left[\frac{1}{\tau_p}+\frac{1}{\tau_c}+\frac{1}{\tau_s}\right]^{-1} \\ &= \frac{I_e}{eV}\left[\frac{v_p A_p}{V}+\frac{4\sigma v_p Q_{\text{in}}(1-\eta_{md})}{v_o A_s T_a \eta_c}+\frac{1}{\tau_s}\right]^{-1}. \end{aligned} \tag{4.3-44}$$

Assuming that the primary electron loss directly to the anode is negligible, the electron equilibration time is long, and the ion current flowing back to the cathode is small, then Eq. (4.3-44) can be written as

$$n_p = \frac{I_e v_o A_s T_a \eta_c}{4V\sigma v_p I_b}\frac{\eta_{md}}{(1-\eta_{md})} = \frac{(I_d - I_s) v_o A_s T_a \eta_c}{4V\sigma v_p I_b}\frac{\eta_{md}}{(1-\eta_{md})}. \tag{4.3-45}$$

This equation demonstrates the characteristic behavior of the primary electron density being proportional to the mass utilization efficiency divided by one minus the mass utilization efficiency originally described by Brophy [18,19]. This dependence is valid unless there are paths for the primary electrons to be lost other than just collisionally with the neutral gas, such as ballistically to the anode or by thermalization with the plasma electrons. The behavior of the primary electron density with changes in the mass utilization efficiency is shown in Fig. 4-17, where the primary electron density is normalized to the value at $\eta_{md} = 0$. As the neutral density decreases in the discharge chamber at higher mass utilization efficiencies, the primary electron density increases rapidly. At 90% mass utilization efficiency, the primary electron density in the discharge chamber is nine times higher than at 50% mass utilization efficiency. This strongly affects the ionization rate and the discharge loss behavior with neutral gas pressure, which will be shown later.

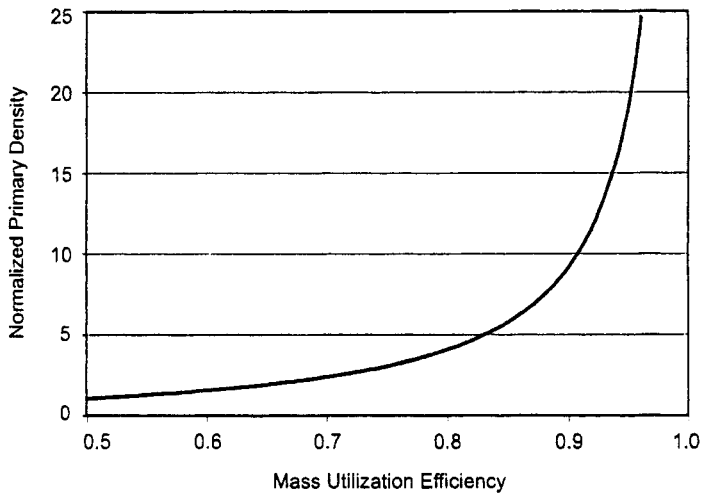

Fig. 4-17. Normalized primary electron density as a function of mass utilization efficiency.

4.3.7 Power and Energy Balance in the Discharge Chamber

The currents and potential distributions in the ring-cusp thruster discharge were shown in Fig. 4-9. The power into the discharge chamber is the emitted current from the hollow cathode multiplied by the voltage the electrons gain in the discharge chamber (V_k in Fig. 4-9):

$$P_{\text{in}} = I_e V_k = I_e\left(V_d - V_c + V_p + \phi\right), \tag{4.3-46}$$

where V_d is the discharge voltage, V_c is the cathode voltage drop, V_p is the potential drop in the plasma, and ϕ is the sheath potential relative to the anode wall. This power into the discharge is transferred from the primary electrons from the cathode into producing ions, excited neutrals, and Maxwellian electrons. The power leaving the discharge to the electrodes is from ions flowing to the anode, cathode, and screen plane, and from primary and plasma electrons flowing to the anode. The power out of the discharge is then the sum of these terms, given by:

$$\begin{aligned} P_{\text{out}} = {} & I_p U^+ + I^* U^* + \left(I_s + I_k\right)\left(V_d + V_p + \phi\right) \\ & + \left(I_b + I_{ia}\right)\left(V_p + \phi\right) + I_a \varepsilon_e + I_L\left(V_d - V_c + V_p + \phi\right), \end{aligned} \tag{4.3-47}$$

where I_p is the total number of ions produced in the discharge, U^+ is the ionization potential of the propellant gas, I^* is the number of excited ions produced in the discharge chamber, U^* is the excitation energy, I_s is the number of ions to the screen plane, I_k is the number of ions flowing back to the cathode, I_B is the beam current, I_a is the plasma electron current to the anode, T_e is the electron temperature, I_{ia} is the ion current to the anode, and I_L is the primary electron fraction lost to the anode. The plasma electron energy lost to the anode wall, ε_e, is $2kT_e/e+\phi$, which is derived in Appendix C. The ions fall through the pre-sheath potential from the center of the plasma to the sheath edge, such that V_p can be approximated as $kT_e/2e$. The ion energy to the anode, ε_i, is then $kT_e/2e+\phi$, which was given in Eq. (4.2-10).

With the screen grid connected to the cathode potential, the current emitted from the hollow cathode was given in Eq. (4.3-43) in terms of the other currents in the circuit. Likewise, conservation of particles flowing to the anode gives

$$I_a = I_d + I_{ia} - I_L, \tag{4.3-48}$$

where I_d is the discharge current measured in the discharge power supply. Equating the power into the discharge to the power out, using the particle balance equations in Eqs. (4.3-43) and (4.3-48), and solving for the beam current from the thruster gives:

$$\begin{aligned} I_b = & \frac{I_d\left(V_d - V_c + V_p - 2T_{eV}\right) - I_p U^+ - I^* U^*}{V_p + \phi} \\ & - \frac{\left(I_s + I_k\right)\left(2V_d - V_c + 2V_p + 2\phi\right)}{V_p + \phi} \\ & - \frac{I_{ia}\left(V_p + 2T_{eV} + 2\phi\right) + I_L\left(V_d - V_c + V_p - 2T_{eV}\right)}{V_p + \phi}, \end{aligned} \tag{4.3-49}$$

where T_{eV} is in electron volts.

The issue in evaluating Eq. (4.3-49) for the beam current produced by a given thruster design is that several of the current terms in the numerator contain the plasma density, which is not known. In addition, the beam current I_B is given

by the Bohm current averaged over the screen-grid plane times the effective transparency T_s of the screen grid:

$$I_b = \frac{1}{2} n_i e v_a A_s T_s \approx \frac{1}{2} n_e e \sqrt{\frac{kT_e}{M}} A_s T_s , \tag{4.3-50}$$

where n_i is the peak ion density at the screen grid, v_a is the ion acoustic velocity, A_s is the screen grid area, and T_s is the effective screen transparency with high voltage applied to the accelerator grids. In this equation, quasi-neutrality ($n_i \approx n_e$) is assumed. Equation (4.3-50) can be solved for the plasma density using Eq. (4.3-49) for the beam current, Eq. (4.3-2) for the primary electron loss current, and Eq. (4.3-17) for the ion loss to the anode wall:

$$n_e = \frac{(I_d - I_L)(V_d - V_c + V_p - 2T_{eV})}{\frac{I_p}{n_e} U^+ + \frac{I^*}{n_e} U^* + \frac{(1-T_s) v_a A_s}{2} V' + \frac{v_a A_{as} f_c}{2} (V_p + 2T_{eV} + 2\phi)}, \tag{4.3-51}$$

where $V' = 2V_d - V_c + 2V_p + 2\phi$ and the screen grid current, I_s, is given by

$$I_s = \frac{(1-T_s)}{2} n_i e v_a A_s . \tag{4.3-52}$$

The plasma density is proportional to the discharge current decreased by the amount of direct primary loss to the anode ($I_d - I_L$), as expected. This relationship shows why implementing sufficient cusp magnetic field strength is critically important to the thruster performance.

Unfortunately, the ionization and excitation terms still contain n_p / n_e, so Eq. (4.3-52) must be solved iteratively for the plasma density. Once the plasma density is known, the beam current can be calculated from Eq. (4.3-50). If the flatness parameter, which is defined as the average current density divided by the peak, is known, then the peak plasma density and peak beam current density can be obtained. The flatness parameter is found by experimental measurements of the plasma and beam profiles, or by two-dimensional (2-D) models of the discharge that are discussed in Section 4.7.

4.3.8 Discharge Loss

The discharge loss in an ion thruster is defined as the power into the thruster divided by the beam current. This parameter then describes the power required to produce the beam current, which is a good figure of merit for the discharge

chamber performance. In DC-discharge thrusters, the discharge loss for the plasma generator is given by

$$\eta_d = \frac{I_d V_d + I_{ck} V_{ck}}{I_b} \approx \frac{I_d V_d}{I_b}, \tag{4.3-53}$$

where I_B is the beam current, I_{ck} is the current to the cathode keeper electrode (if any), and V_{ck} is the keeper bias voltage. The keeper power is typically negligible in these thrusters, but it is a simple matter to include this small correction. Combining Eqs. (4.3-53) and (4.3-49), the discharge loss is

$$\begin{aligned}\eta_d = &\frac{V_d\left[\frac{I_p}{I_b}U^+ + \frac{I^*}{I_b}U^* + \frac{(I_s+I_k)}{I_B}\left(2V_d - V_c + 2V_p + 2\phi\right)\right]}{V_d - V_c + V_p - 2T_{eV}} \\ &+ \frac{V_d\left[\left(V_p+\phi\right) + \frac{I_{ia}}{I_b}\left(V_p + 2T_{eV} + 2\phi\right)\right]}{V_d - V_c + V_p - 2T_{eV}} \\ &+ \frac{V_d\left[\frac{I_L}{I_b}\left(V_d - V_c + V_p - 2T_{eV}\right)\right]}{V_d - V_c + V_p - 2T_{eV}}.\end{aligned} \tag{4.3-54}$$

To evaluate the first current fraction in this equation, the ions are produced by both primary electrons and the energetic tail of the Maxwellian distribution of the plasma electrons. The total number of ions produced in the discharge, I_p, is given in Eq. (4.3-25), and the total number of excited neutrals produced in the discharge, I^*, is given in Eq. (4.3-26).

Using Eqs. (4.3-25) and (4.3-26) for the particle production and excitation, Eq. (4.3-50) for the beam current, and assuming $n_i \approx n_e$, the first current fraction in Eq. (4.3-54) is

$$\frac{I_p}{I_b} = \frac{2n_o n_e e\langle\sigma_i v_e\rangle V}{n_i e\sqrt{\frac{kT_e}{M}}A_s T_s} + \frac{2n_o n_p e\langle\sigma_i v_p\rangle V}{n_i e\sqrt{\frac{kT_e}{M}}A_s T_s}$$
$$= \frac{2n_o V}{\sqrt{\frac{kT_e}{M}}A_s T_s}\left(\langle\sigma_i v_e\rangle + \frac{n_p}{n_e}\langle\sigma_i v_p\rangle\right). \tag{4.3-55}$$

The second current fraction is likewise:

$$\frac{I^*}{I_b} = \frac{2n_o V}{\sqrt{\frac{kT_e}{M}}A_s T_s}\left(\langle\sigma_* v_e\rangle + \frac{n_p}{n_e}\langle\sigma_* v_p\rangle\right). \tag{4.3-56}$$

Neglecting the small amount of ion current backflowing to the hollow cathode, the third current fraction is

$$\frac{I_s}{I_b} = \frac{1-T_s}{T_s}. \tag{4.3-57}$$

The ion current that goes to the anode wall is, again, the Bohm current reduced by the confinement factor f_c, given in Eq. (4.3-17). In this model, the value of the confinement factor must be evaluated for the particular ion thruster discharge chamber being analyzed. However, for most ion thruster designs, if the 50 gauss contour is closed, it is possible to assume to first order that $f_c \approx 0.1$ and the ion loss to the anode surface area is essentially one-tenth of the local Bohm current. For a given confinement factor f_c, the fourth current fraction in Eq. (4.3-54) is

$$\frac{I_{ia}}{I_b} = \frac{\frac{1}{2}n_i e\sqrt{\frac{kT_e}{M}}A_{as} f_c}{\frac{1}{2}n_i e\sqrt{\frac{kT_e}{M}}A_s T_s} = \frac{A_{as} f_c}{A_s T_s}, \tag{4.3-58}$$

where A_{as} is the surface area of the anode facing the plasma in the discharge chamber.

The primary electron current lost to the anode, I_L, is given by Eq. (4.3-2). The last current fraction in Eq. (4.3-54) is then

$$\frac{I_L}{I_b} = \frac{n_p e v_p A_p}{\frac{1}{2} n_i e v_a A_s T_s} = \frac{2 n_p v_p A_p}{n_e v_a A_s T_s}. \tag{4.3-59}$$

The discharge loss can then be written

$$\eta_d = \frac{V_d\left[\frac{I_p}{I_b}U^+ + \frac{I^*}{I_b}U^* + \frac{1-T_s}{T_s}\left(2V_d - V_c + 2V_p + 2\phi\right)\right]}{V_d - V_c - 2T_{eV}} + \frac{V_d\left[\left(V_p + \phi\right) + \frac{A_{as} f_c}{A_s T_s}\left(V_p + 2T_{eV} + 2\phi\right)\right]}{V_d - V_c - 2T_{eV}} + \frac{V_d\left[\frac{2 n_p v_p A_p}{n_e v_a A_s T_s}\left(V_d - V_c + V_p - 2T_{eV}\right)\right]}{V_d - V_c + V_p - 2T_{eV}}. \tag{4.3-60}$$

Equation (4.3-60) illuminates some of the design features that improve the discharge efficiency. Since the discharge voltage V_d appears in both the numerator and denominator of Eq. (4.3-60), there is no strong dependence of the discharge loss on voltage shown in this equation. However, increases in the discharge voltage raise the primary energy strongly, which increases the ionization rate and beam current. Therefore, higher discharge voltages always result in lower discharge losses. Higher screen grid transparency T_s, smaller ion confinement factor f_c (better ion confinement), smaller primary loss area A_p, and smaller wall surface area A_{as} all reduce the discharge loss. Lowering the plasma potential also reduces the discharge loss by reducing the energy lost to the anode by the plasma electrons, which is accomplished by reducing the anode loss area at the cusps.

The input data required to solve Eq. (4.3-60) are:

- Discharge voltage
- Discharge chamber surface area and volume
- Magnetic field design (magnetic field at the cusp and the closed contour field between the cusps)
- Grid area
- Grid transparency
- Gas temperature
- Cathode voltage drop

It is necessary to specify either the discharge current or the beam current in order to calculate the plasma density in the discharge chamber. The grid transparency is obtained from the grid codes (called "optics codes"). Several of these codes, such as the Jet Propulsion Laboratory (JPL) CEX ion optics codes [34,35] that we use, are described in Chapter 5. The cathode voltage drop is either measured inside the hollow cathode [36] or calculated using a separate 2-D hollow cathode plasma model [37] that will be described in Chapter 6.

Discharge chamber behavior is characterized by "performance curves," which were described in Chapter 2 and are graphs of discharge loss versus mass utilization efficiency. These curves plot the electrical cost of producing beam ions as a function of the propellant utilization efficiency, and they give useful information on how well the plasma generator works. Performance curves are normally taken at constant beam current and discharge voltage so that the efficiency of producing and delivering ions to the beam is not masked by changes in the discharge voltage or average plasma density at the grids.

Calculating performance curves using Eq. (4.3-60) requires iteration of the solutions for the electron temperature, discharge current, and/or beam current in the above equations. To measure the discharge loss versus mass utilization in thrusters, the discharge current, total gas flow, and gas flow split between the cathode and main discharge chamber are normally varied to produce a constant beam current and discharge voltage as the mass utilization efficiency changes. This means that a beam current and mass utilization operating point can be specified, which determines the neutral gas density in the discharge chamber from Eq. (4.3-35) and the average plasma density in the discharge chamber from the Bohm current in Eq. (4.3-9). If an initial discharge current is then specified, the primary electron density can be calculated from Eq. (4.3-45) and the electron temperature obtained by finding a solution to Eq. (4.3-36). These parameters are used to solve for the discharge loss, which is evaluated from the given beam current, discharge voltage, and discharge loss. A program is iterated until a discharge current is found that produces the correct discharge loss at the specified beam current.

An example of performance curves calculated using this model and compared to measured curves for the NEXIS ion thruster [38] are shown in Fig. 4-18. The discharge loss was measured for three different discharge voltages during operation at 4 A of beam current. The 180-eV/ion discharge loss at the 26.5-V discharge voltage required that the cathode produce a discharge current of 27.8 A to generate the 4 A of ion beam current.

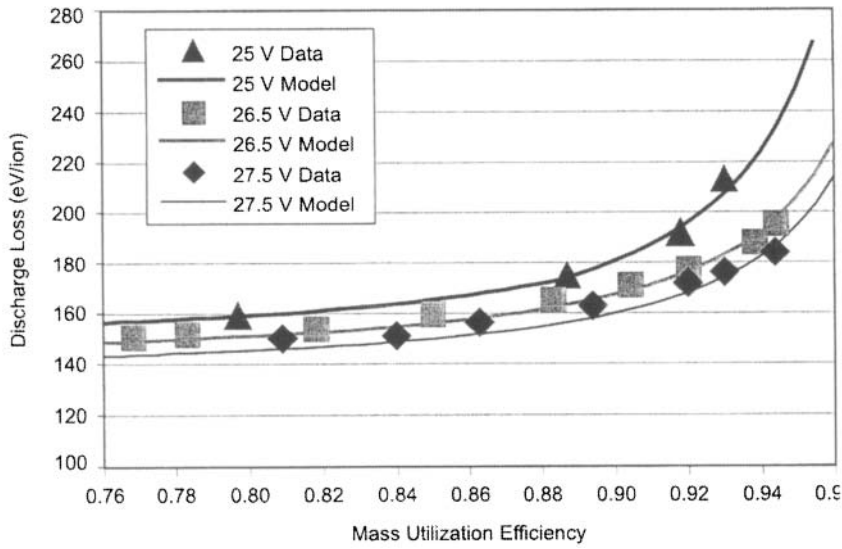

Fig. 4-18. Example of the discharge loss versus mass utilization efficiency for three discharge voltages in the NEXIS thruster [38].

The discharge model also matches the discharge loss data obtained from other thrusters. Figure 4-19 shows the discharge loss measured at JPL in a laboratory copy of the NSTAR thruster [39] operating at the full power (2.3 kW) TH15 throttle level. The model predictions agree with the thruster data if the measured 6.5-V cathode voltage drop in the NSTAR hollow cathode [40] is used for V_c. The ability of a 0-D model to match the NSTAR data is significant only in that the NSTAR plasma is not very uniform (flatness parameter ≈ 0.5) and contains over 20% double ions peaked on the axis. The 0-D model likely works in this case because the ionization is still dominated by the average volume effects, and the losses are still determined by the magnetic field structure at the wall, which 0-D models can capture sufficiently to give reasonably accurate results.

The shape of the performance curves is also important. As the mass utilization is increased, the neutral density in the discharge chamber decreases [see Eq. (4.3-35)] and more of the primary energy goes into heating the plasma electrons and energy loss directly to the anode, as was illustrated by the simplified model for the idealized thruster case in Section 4.2. Optimal thruster designs have flatter discharge performance curves that exhibit lower discharge losses as the mass utilization efficiency is increased. The model suggests that this is generally achieved in thrusters by designing for good primary and

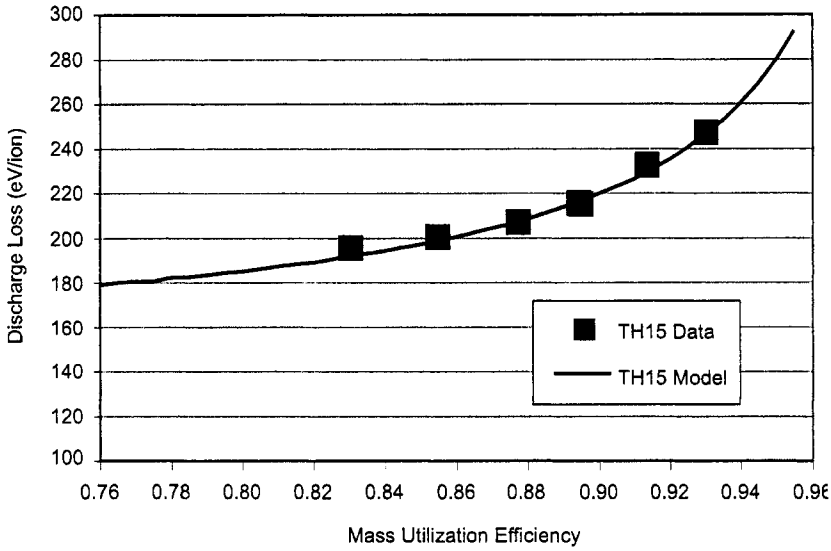

Fig. 4-19. Discharge loss versus mass utilization efficiency for the NSTAR thruster at the high power TH15 throttle point.

plasma electron confinement such that the convective losses are minimized at low neutral density and higher electron temperatures.

A significant challenge for most discharge models is handling the primary electrons correctly. For the case of monoenergetic primaries assumed in this model, the primary density is determined by collisional and ballistic (direct-to-anode) losses that change as a function of the neutral pressure, which is inversely proportional to the mass utilization efficiency. The primary electron density then varies strongly as the mass utilization efficiency is changed. However, if primary electrons are neglected altogether (i.e., assumed thermalized immediately in the cathode plume) so that the plasma in the discharge chamber is produced only by ionization by the high-energy tail of the Maxwellian electron population, the discharge loss is extremely high. This is shown in Fig. 4-20, where the discharge loss in the NEXIS thruster increases to over 240 eV/ion if the primary electron ionization effects are neglected. Likewise, if the primary electron density is independent of the neutral pressure, then the discharge loss curve in Fig. 4-20 has a steep slope resulting from an excessive number of primary electrons at low mass utilization (high pressure), which produces more ionization than actually occurs. Clearly, including the presence of primary electrons in the analysis is required for the model results to agree with the data, which, in turn, suggests that primary or energetic electrons and non-Maxwellian electron populations must exist in this type of thruster.

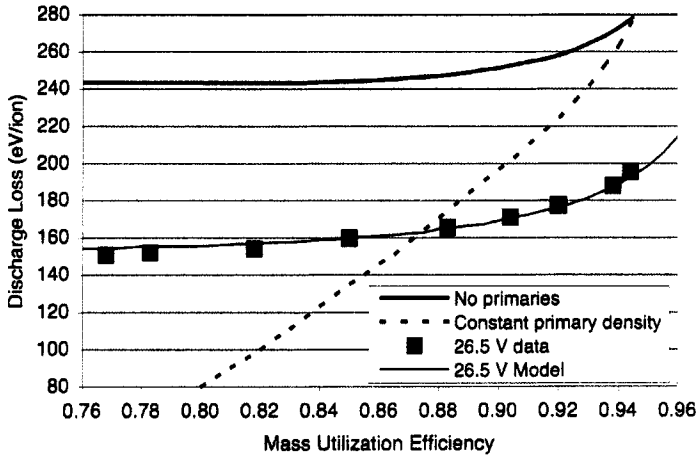

Fig. 4-20. Discharge loss predictions for the cases of no primary electron density and a constant primary electron density showing the poor agreement with the measurements.

Having a representative model of the discharge permits environmental changes to the thruster to also be understood. For example, the neutral gas temperature depends on the operating time of the thruster until equilibrium is reached, which can take hours in some cases, during which the discharge loss will vary [41]. The 0-D model predictions are shown in Fig. 4-21 for three different neutral gas temperatures. The discharge loss data points shown were measured for the NEXIS thruster operating at 26.5 V and 92% mass utilization efficiency at first turn on, after 1 hour, and after 10 hours. In this case, the thruster starts at essentially room temperature, and the model predicts that the discharge heats the thruster and neutral gas to about 470 K after about 10 hours of operation. While thruster thermal time constants are usually on the order of 1 hour, this long heating time was found to be related to the facility thermal time constant. This behavior of the discharge loss with time and temperature illustrates how characterization of the thruster must always be measured in thermal equilibrium, because the performance of the discharge chamber is strongly affected by the neutral gas density, which changes with the thruster temperature for a constant input flow rate.

4.3.9 Discharge Stability

There is a strong relationship between the discharge loss and the stability of the discharge. By inspection of Eq. (4.3-60), it is clear that the efficiency increases (discharge loss decreases) if the anode area for primary electrons A_p is minimized. While it is logical to assume that this is also true if the anode area

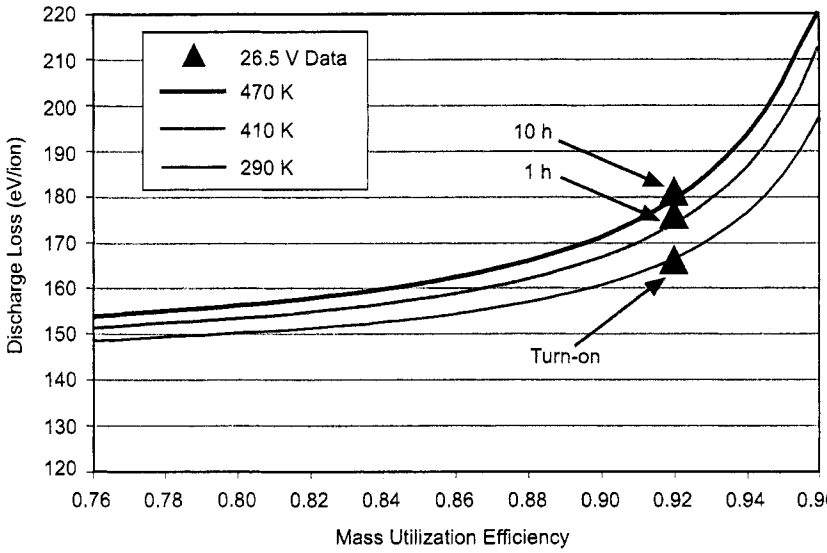

Fig. 4-21. Discharge loss versus mass utilization efficiency from the model for the NEXIS thruster [20] for three neutral gas temperatures,

for plasma electrons is minimized to reduce the energy loss from the Maxwellian-electron population, a dependence on A_a does not appear in Eq. (4.3-60). However, since the discharge current is carried to the anode primarily by the plasma electrons, the sheath potential at the anode wall in Eq. (4.3-7) is found to decrease as the anode area decreases for a given plasma electron current to the anode. A dependence on the sheath potential is seen in the discharge loss equation, which suggests that minimizing the sheath potential maximizes the efficiency. However, the anode area for plasma electrons cannot go to zero because the discharge current could not be collected by the anode, and the discharge would either interrupt or become unstable [22]. So there is some minimum anode area and plasma potential that can be tolerated for discharge stability.

The value of the plasma potential relative to the anode (the anode sheath voltage drop) can be calculated using the expression for the random electron flux to the anode given in Eq. (4.3-7). From current conservation in the discharge, an expression for the discharge current can also be found from the current to the anode [Eq. (4.3-48)]:

$$I_d = I_a + I_L - I_{ia}. \tag{4.3-61}$$

Using Eqs. (4.3-7), (4.3-2), and (4.3-17) for each of the three currents, and dividing by the beam current in Eq. (4.3-50), Eq. (4.3-61) becomes

$$\frac{I_d}{I_b} = \frac{\frac{1}{4}\left(\frac{8kT_e}{\pi\, m}\right)^{1/2} n_e A_a}{\frac{1}{2} n_e v_a A_s T_s} \exp^{-e\phi/kT_e} + \frac{n_p v_p A_p}{\frac{1}{2} n_e v_a A_s T_s} - \frac{\frac{1}{2} n_e v_a A_{as} f_c}{\frac{1}{2} n_e v_a A_s T_s}. \quad (4.3\text{-}62)$$

Solving for the plasma potential gives

$$\phi = \frac{kT_e}{e} \ln \left[\frac{\left(\frac{2M}{\pi m}\right)^{1/2} \frac{A_a}{A_s T_s}}{\frac{I_d}{I_b} + \frac{A_{as} f_c}{A_s T_s} - \frac{2 n_p v_p A_p}{n_e v_a A_s T_s}} \right]. \quad (4.3\text{-}63)$$

By inspection of Eq. (4.3-63), it is clear that as the anode area A_a decreases, the plasma potential also decreases. If the anode area is made too small, then the plasma potential will go negative relative to the anode potential. This is called a positive-going (or "electron accelerating") anode sheath, and is illustrated in Fig. 4-22. In this case, the anode area at the cusps is insufficient to collect the total discharge current by collection of the entire incident random electron flux over the cusp area. The plasma then biases itself to pull in electrons in the Maxwellian distribution that are not initially headed toward the anode, which delivers more current to satisfy the discharge current and charge balance requirements. The plasma electron current collected by the anode then becomes

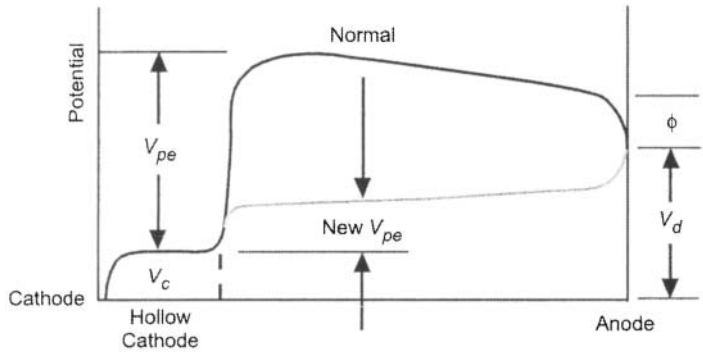

Fig. 4-22. Transition of the plasma potential to negative relative to the anode due to an anode area decrease, which results in a lower primary electron energy.

$$I_a = \frac{1}{4}\left(\frac{8kT_e}{\pi m}\right)^{1/2} en_e A_a \, e^{e\phi/kT_e}\left[1 - erf\left(\frac{-e\phi}{kT_e}\right)^{1/2}\right]^{-1}, \qquad (4.3\text{-}64)$$

where the potential ϕ is now a negative number. If the potential goes sufficiently negative relative to the anode, the current density can reach a factor of two higher than the one-sided random electron flux normally collected in order to satisfy the discharge current requirement.

However, once the potential goes sufficiently negative relative to the anode to repel the ions (about T_i), then the anode area for the plasma electron is not the hybrid area, but is just twice the plasma electron Larmor radius times the cusp length, similar to Eq. (4.3-3) for the primary loss area. This results in a significant decrease in the cusp anode area A_a in Eq. (4.3-63) for negative plasma potentials, which further lowers the plasma potential relative to the anode. Examining the potential distribution in the plasma in Fig. 4-22, the transition from the normal negative-going sheath to a negative plasma potential (positive-going anode sheath) will subtract from the primary electron energy V_{pe} at a given discharge voltage. The ionization rate then decreases, and the discharge collapses into a high impedance mode or oscillates between this mode and a positive potential typically on power supply time constants as the supply tries to reestablish the discharge by increasing the anode voltage.

The stability of the plasma discharge at a given operating point (discharge current, beam current, neutral density in the discharge chamber, etc.) is therefore determined by the magnetic field design. For example, in Fig. 4-23, plasma potential is plotted as a function of the strength of the cusp magnetic field for an arbitrary thruster design with two different numbers of ring cusps. The cusp field strength enters into the anode area A_a in Eq. (4.3-6), into the primary electron loss area A_p in Eq. (4.3-3), and into the plasma potential in Eq. (4.3-63). The model predicts that a four-ring design would be unstable (when the potential goes negative relative to the anode) for cusp magnetic fields greater than 2000 G. Since strong magnetic fields are desirable from a primary electron and ion confinement point of view, additional rings are required to maintain a positive plasma potential. A six-ring design increased the anode area sufficiently to raise the plasma potential at the 2000-G magnet design point. An analysis of the discharge loss from Eq. (4.3-60) indicates that the improved stability associated with the larger anode area of the six-ring design comes with a loss in efficiency. The trade-off between efficiency and stability is an important aspect of ion thruster design.

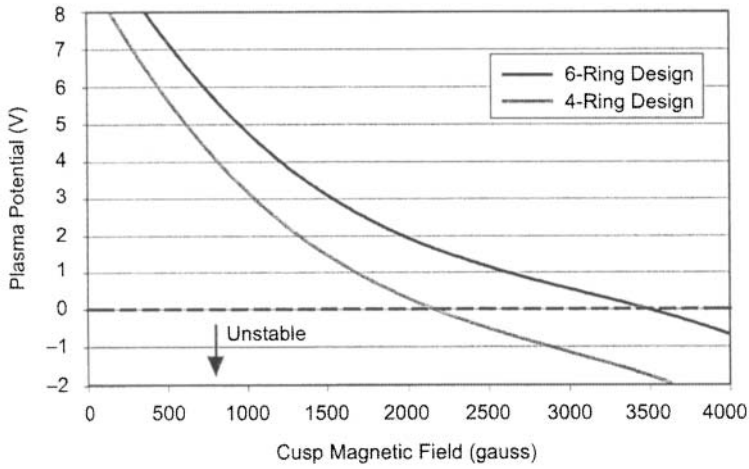

Fig. 4-23. Plasma potential versus cusp magnetic field strength for a thruster design with 4 and 6 rings.

4.3.10 Recycling Behavior

Ion thrusters clear momentary faults or breakdowns in the high voltage accelerator grids by momentarily turning off the high voltage, an event called recycling. In order to restart the thruster, the accelerator grid ("accel grid") voltage must be turned back on to avoid electron backstreaming into the thruster as the screen voltage is reapplied. If the plasma discharge is left on during this sequence, the negatively biased accel grid collects nearly the entire ion beam current at the applied accel voltage until the screen voltage is re-established. This can lead to excessive power loading and even erosion of the accel grid if a significant number of recycles are encountered. Therefore, it is standard procedure to also either turn off the discharge during recycling or cut it back to a low level such that the accel grid current surge is acceptably low during reestablishing of the beam voltages. The discharge current is then raised to the desired level with the screen voltage ramp-up.

The main issue with this process is that the thruster discharge often goes into oscillation during the cutback condition or upon restarting in the recycle sequence. When the high voltage is turned off in a recycle, ions that would have left the discharge chamber as beam ions now strike and neutralize on the accel grid, and some fraction flows back into the discharge chamber as neutral gas. This raises the neutral gas pressure in the discharge chamber, which has two effects. First, a higher neutral pressure collisionally thermalizes the primary electrons more rapidly, which can lead to a reduction in the plasma potential [22]. Second, lowering the discharge current while raising the neutral pressure

leads to a lower impedance discharge and a lower discharge voltage. These two effects will be shown next to cause a reduction in the plasma potential, and thrusters designed for low discharge loss with a minimum plasma potential at the nominal operating point can encounter negative plasma potentials and discharge instability during recycling.

The time-dependent behavior of the pressure in the discharge chamber from the high-voltage-off event can be calculated using molecular dynamics, and the subsequent time-dependent plasma potential for stability can be evaluated using the 0-D model. The time-dependent pressure [42] in the thruster is given by

$$V\frac{dP}{dt} = Q_{\text{in}} - C\Delta P\,, \tag{4.3-65}$$

where V is the discharge chamber volume, P is the pressure in the thruster discharge chamber, C is the conductance of the grids, and ΔP is the pressure drop across the grids. The initial pressure just before the start of the recycle, when the thruster is operating normally, is found from Eq. (4.3-35) and the conversion of neutral density to pressure in Eq. (2.7-2):

$$P_o = 4.1\times 10^{-25}\,\frac{T_o Q_{\text{in}}(1-\eta_m)}{v_o e A_g T_a \eta_c}\,. \tag{4.3-66}$$

With the high voltage off, the ions and neutrals flow to the grid region, where a small fraction exits through the accel aperture to escape, and the majority strike the upstream side of the grids or the grid aperture barrel wall and flow back into the thruster. Since the grid conductance is defined as the flow divided by the pressure drop [42], the final pressure after steady state has been achieved is

$$P_f = (1-T_a)\frac{Q_{\text{in}}}{C}\,, \tag{4.3-67}$$

where C is the conductance of the grids and the downstream pressure from the grids has been neglected as small. The conductance of the grids can be estimated from the molecular conductance of a thin aperture [42] times the Clausing factor for the finite thickness grids. The conductance is then

$$C = 3.64\left(\frac{T}{M_a}\right)^{1/2} T_a A_g \eta_c \text{ [liters/s]}, \tag{4.3-68}$$

where M_a is the ion mass in atomic mass units (AMU), and the effective open area of the grids is the optical transparency of the accel grid, T_a, times the grid

area, A_g. Integrating Eq. (4.3-67) from the initial pressure to the final pressure gives

$$P(t) = P_f - (P_f - P_o)e^{-t/\tau_g}, \tag{4.3-69}$$

where $\tau_g = V/C$ is the gas flow time constant for filling the thruster chamber. To use Eq. (4.3-69) to find the final pressure, the gas flow rate has to be converted from particles per second to torr-l/s by multiplying the neutral gas flow in Eq. (4.3-67) by 2.81×10^{-20}.

Figure 4-24 shows an example of the pressure increase with time calculated in the NEXIS thruster discharge chamber from the start of a recycle. The pressure in the discharge chamber during normal operation is in the mid-10^{-5} torr range due to the large grid area and high mass utilization efficiency. During a recycle, the pressure in the discharge chamber reaches equilibrium in about 60 ms, with the pressure increasing almost an order of magnitude once the high voltage is turned off. This magnitude of pressure increase in the thruster once the high voltage is turned off is consistent with the ≈90% mass utilization efficiency of many thruster designs.

The plasma potential response to pressure changes in the discharge chamber calculated using the 0-D model for two different discharge voltages is shown in Fig. 4-25(a) for a given magnetic field design. During the recycle, the discharge current is reduced (called "cutback"), which reduces the discharge voltage and

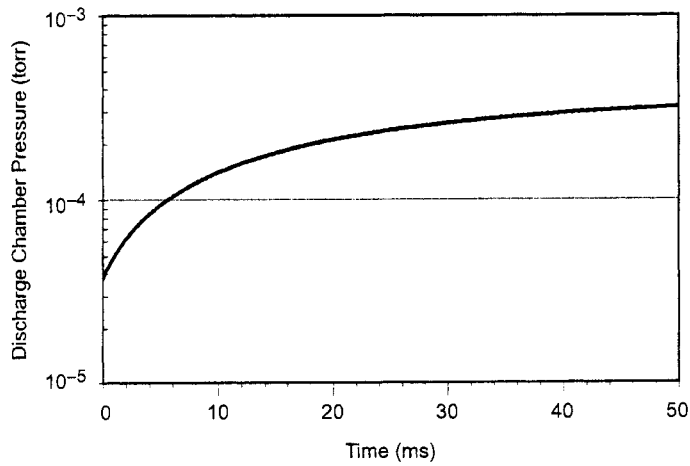

Fig. 4-24. Example of the pressure rise in the NEXIS thruster [20] calculated during a recycle.

thereby the plasma potential. The model indicates that the plasma potential reduction and subsequent unstable operation is the result of the lower discharge voltage, and does not occur directly due to the discharge current being lower. This analysis shows that a given thruster design that produces a stable discharge under normal conditions can go unstable due to negative plasma potentials as the pressure rises and the discharge voltage decreases.

The plasma potential calculated using Eq. (4.3-63) for two magnet designs is shown in Fig. 4-25(b) for the 23-V NEXIS case, which illustrates the effect of the smaller anode area reducing the plasma potential at a given pressure. In this case, increasing the anode area permitted the discharge current to be cutback

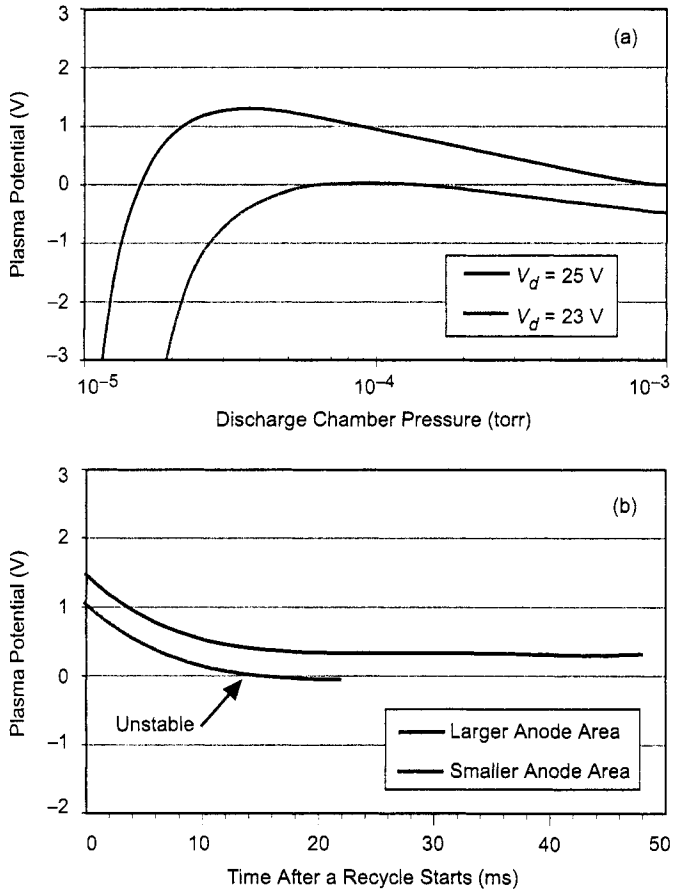

Fig. 4-25. Plasma potential as a function of pressure for two different discharge voltages (a), and plasma potential versus time (b) showing instability of the smaller anode area design at a given pressure.

during the recycle to the desired level without oscillating, which facilitates re-starting the high voltage. Of course, the larger anode area increased the loss in the discharge chamber and raised the discharge loss. This trade-off is often required to provide good performance and stable discharge operation.

4.3.11 Limitations of a 0-D Model

While the 0-D models described in this chapter provide useful information on the design parameters of ion thrusters and give good insight into the plasma production and loss mechanisms, there are several limitations to their use. First, 0-D models assume that the electron and neutral densities are uniform and averages the ion production throughout the volume of the discharge chamber. For ion thrusters with significantly non-uniform plasmas, this leads to inaccuracies in the average plasma density and beam current calculated by the 0-D model that can be handled only by multi-dimensional discharge chamber models. Second, the source of the gas in actual discharge chambers is from the localized hollow cathode aperture and the gas manifold inside the discharge chamber. The neutral density, therefore, is never completely uniform, and variations in the neutral density can affect the transport, diffusion, and ionization rates in the discharge chamber.

Third, ion thrusters with localized electron sources like hollow cathodes have strongly varying primary electron densities within the discharge chamber. As shown earlier, the primary electron density strongly affects the ionization rate, and so localized sources of primaries produce non-uniform plasmas that the 0-D models cannot address. In addition, these models utilize a monoenergetic primary energy. A distribution in the primary electron energy has been measured in some ion thrusters [43,44], which changes the ionization and primary electron thermalization rates compared to the monoenergetic calculations presented here. While primary electron energy distributions can be incorporated in 0-D models, this has not been attempted to date.

Finally, the 0-D model assumed that the monoenergetic primary electrons have an energy of $e(V_d - V_c + \phi)$. For typical discharge voltages of 25 V and cathode voltage drops of 5 to 10 V, this means that potentially none of the primaries has sufficient energy to doubly ionize xenon, which has an ionization potential of 21.2 V. Double ions can then only be produced by the tail of the plasma electron distribution. For electron temperatures of 3 to 5 eV, less than 1% of the electrons have sufficient energy to produce double ions. Since the double-ion content in NSTAR thrusters has been reported to exceed 20%, a monoenergetic primary electron energy results in a model that cannot accurately address double-ion production. While including primary electrons is necessary to obtain agreement between the 0-D models and experimental results, knowledge of the

correct energy distribution and even spatial variation in the primaries is required, and is better handled by 2-D models discussed in Section 4.7.

4.4 Kaufman Ion Thrusters

The formulation of particle and energy balance models just described applies to any ion thruster geometry where the electron loss can be defined by a finite anode electrode area collecting electrons at a fraction of the random electron flux depending on the sheath voltage. One class of thrusters still in use, the Kaufman ion thruster shown schematically in Fig. 4-26, features a strongly diverging axial magnetic field that shields a cylindrical anode electrode located near the wall of the discharge chamber. In this case, electron transport to the anode is determined by cross-field diffusion.

In Section 3.6, the flux of electrons due to cross-field diffusion is given by

$$\Gamma_e = nv_\perp = \mu_\perp n\mathbf{E} - D_\perp \nabla n. \tag{4.4-1}$$

For the case of Kaufman thrusters, the perpendicular diffusion coefficient is likely to be close to the Bohm diffusion coefficient [45]:

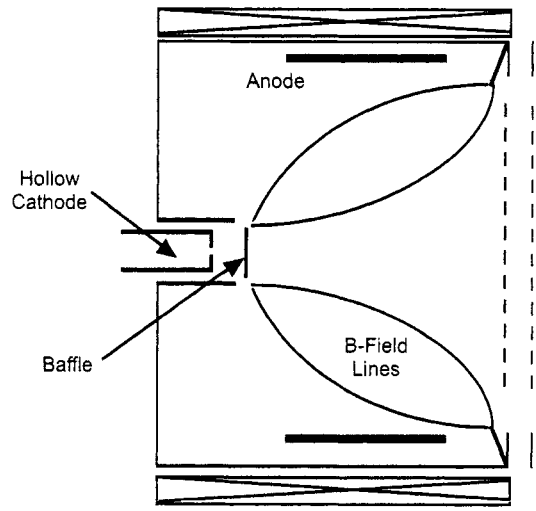

Fig. 4-26. Schematic of a Kaufman ion thruster showing the hollow cathode with a baffle, and the anode protected by magnetic fields produced by an external solenoid coil.

$$D_B = \frac{1}{16}\frac{kT_e}{eB}. \tag{4.4-2}$$

The electron current collected by the anode is the flux that diffuses through the magnetic field times the Boltzman factor at the sheath:

$$I_a = \left(\mu_\perp n\mathbf{E} - D_\perp \nabla n\right) eA_{as} e^{-e\phi/kT_e}, \tag{4.4-3}$$

where A_{as} is again the anode surface area exposed to the plasma discharge. The actual current distributions and potential distribution in a Kaufman thruster are the same as for the DC discharge thruster shown in Fig. 4-9. However, there are several terms that were analyzed for ring-cusp thrusters that can be neglected in Kaufman thrusters.

First, if the axial magnetic field in the discharge chamber is on the order of 100 G, then the Larmor radius for, say, 20-eV primaries is 1.5 mm. Since the magnetic field lines do not intersect the anode and primaries are too energetic to participate in the collective instabilities that drive Bohm diffusion, the primary electrons must make collisions in order to cross the magnetic field to be lost. That means that the fraction of the primary electron current loss directly to the anode in ring-cusp thrusters, I_L, can be neglected, which is an advantageous feature of Kaufman thrusters.

Second, the plasma flow across the magnetic field is still governed by ambipolar effects. As was shown in Section 4.3.4, if the transverse magnetic field strength is in excess of about 50 G in typical ion thruster discharge chambers, then the radial electric field in the plasma (in the magnetic field region) is near zero and the ion loss rate is on the order of one-tenth the Bohm current toward the wall. This means that the ion current to the anode term, I_{ia}, can also be neglected to first order. Since the discharge current collected through the anode leg of the discharge power supply connection was given in Eq. (4.3-61) as the plasma electron current minus the ion current and plus the primary current, the discharge current is now just

$$I_d = I_a = -D_\perp \nabla n\, eA_{as} e^{-e\phi/kT_e}. \tag{4.4-4}$$

Third, the ion current flowing back towards the hollow cathode was neglected in our treatment of ring-cusp thrusters because the hollow cathode exit area in contact with the plasma was so small. In Kaufman thrusters, a baffle is placed on axis in front of the cathode to force the primary electrons off axis to flatten the density profile. Since the magnetic field is strongly divergent, the axial plasma density gradient is significant and the plasma density in contact with the

baffle can be high. For these reasons, the ion current to the cathode, I_k, can no longer be neglected.

The power into the plasma is given by Eq. (4.3-46), and the power out of the discharge is given by

$$P_{\text{out}} = I_p U^+ + I^* U^* + I_s\left(V_d + \varepsilon_i\right) + I_k\left(V_d + \varepsilon_i\right) + I_b\varepsilon_i + I_{ia}\varepsilon_i + I_a\varepsilon_e, \quad (4.4\text{-}5)$$

where ε_i is the ion energy leaving the plasma, which is written here from Eq. (4.3-10) as $T_{eV}/2+\phi$, and ε_e is the electron energy removed from the plasma, which is written from Eq. (4.3-9) as $2T_{eV}+\phi$. Equating the power in to the power out again and solving for the discharge loss gives

$$\eta_d = \frac{V_d\left[\frac{I_p}{I_b}U^+ + \frac{I^*}{I_b}U^* + \phi + \frac{T_{eV}}{2} + \frac{\left(I_s + I_k\right)}{I_b}\left(2V_d - V_c + 2\phi + \frac{T_{eV}}{2}\right)\right]}{V_d - V_c - 2T_{eV}}. \quad (4.4\text{-}6)$$

The first current ratio, I_p / I_b, is given by Eq. (4.3-55), and the second current ratio, I^* / I_b, is given by Eq. (4.3-56). The current ratio, I_s / I_b, is given by Eq. (4.3-57), and the last current ratio is

$$\frac{I_k}{I_b} = \frac{\frac{1}{2}n_k e\sqrt{\frac{kT_e}{M}}A_k}{\frac{1}{2}n_i e\sqrt{\frac{kT_e}{M}}A_s T_s} = \frac{n_k A_{sa}}{n_e A_s T_s}, \quad (4.4\text{-}7)$$

where n_k is the plasma density at the cathode baffle. The discharge loss for Kaufman thrusters is then

$$\eta_d = \frac{V_d\left[\frac{I_p}{I_b}U^+ + \frac{I^*}{I_b}U^* + \phi + \frac{T_{eV}}{2} + \left(\frac{1-T_s}{T_s} + \frac{n_k A_{sa}}{n_e A_s T_s}\right)\left(2V_d - V_c + 2\phi + \frac{T_{eV}}{2}\right)\right]}{V_d - V_c - 2T_{eV}}. \quad (4.4\text{-}8)$$

The plasma potential in Eq. (4.4-8) is found from solving Eq. (4.4-4):

$$\phi = \frac{kT_e}{e}\ln\left[\frac{-D_\perp \nabla n e A_{as}}{I_d}\right], \quad (4.4\text{-}9)$$

and the electron temperature is found from the solution to ion particle balance in Eq. (4.3-36) in a similar manner as for ring-cusp thrusters. The negative sign in Eq. (4.4-9) appears problematic in the natural log function, but the density gradient ∇n is negative going outward from the plasma. The primary electron density is calculated from Eq. (4.3-45), with the ballistic loss term neglected as described above since primaries are not lost directly to the anode. Finally, the plasma volume term in the ion and excited neutral production rates can be assumed to be the volume of a cone from the baffle to the grids because the plasma is well confined by the strongly diverging magnetic field. Since the 0-D model assumes relatively uniform plasma, estimates for the radial gradient of the plasma density in the magnetic field region near the anode and the additional cathode voltage drop due to the baffle must be made for Eq. (4.4-8) to be accurate.

As an example, take a conceptual Kaufman thruster with a 20-cm-diameter screen grid with 80% transparency and a 25-cm-diameter anode with 25 cm between the grids and the baffle. Assuming that the average magnetic field strength in the thruster is about 50 G, the discharge loss from Eq. (4.4-8) is plotted in Fig. 4-27 for two values of the cathode voltage drop. In this case, the cathode voltage drop is higher than in a ring-cusp thruster because it includes the potential drop in the baffle region. The discharge loss is strongly dependent on this value because it directly affects the primary electron energy. Discharge losses in this range at mass utilization efficiencies of about 90% have been reported in the literature for Kaufman thrusters through the years [46–48],

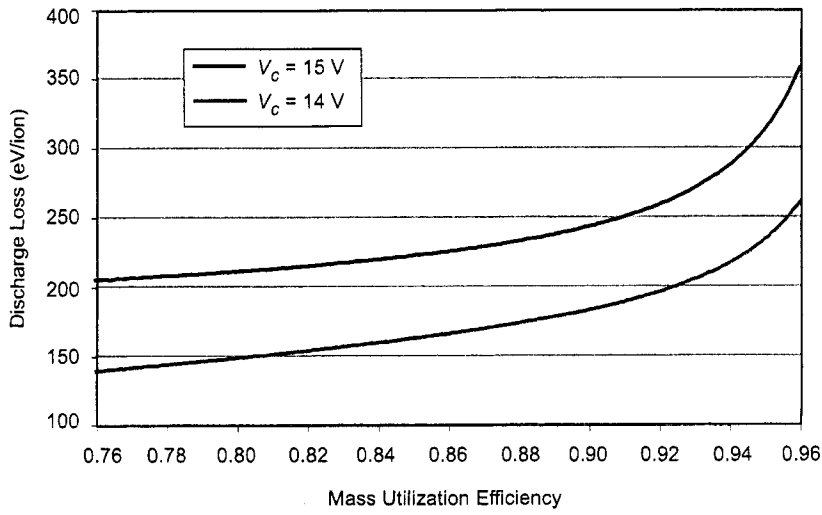

Fig. 4-27. Discharge loss calculated for Kaufman thruster example.

suggesting that the 0-D model can produce reasonable predictions of the discharge loss if the cross-field diffusion is handled properly.

The need for higher discharge voltages in Kaufman thrusters, compared to ring-cusp thrusters, is illustrated in Fig. 4-28, where the discharge loss is plotted for the Kaufman thruster example above with two cases of the discharge voltage at a constant (total) cathode voltage drop of 16 V. Low discharge loss is achieved for the 35-V discharge voltage case, but decreasing the discharge voltage to 30 V causes the discharge loss to increase dramatically. This is because the primary electron energy in the discharge chamber is near the threshold energy for ionization at this discharge voltage, and the discharge efficiency decreases as more ionization is required from the plasma electrons. In addition, the lower discharge voltage causes the plasma potential to go significantly negative relative to the anode potential ($\approx T_e$), which will cause the discharge to become unstable.

While Kaufman-type thrusters are considered to be the first ion thruster to achieve good discharge production performance, they now compete with ring-cusp thrusters for application in modern electric propulsion systems. This is because of several constraints in Kaufman thruster design. First, the strong axial magnetic field restricts electron motion to the anode to cross-field diffusion, which requires either high neutral pressures in the discharge chamber for electron-neutral collisional diffusion and, thereby, low mass utilization efficiency, or relies on collective instabilities to increase the diffusion rate to

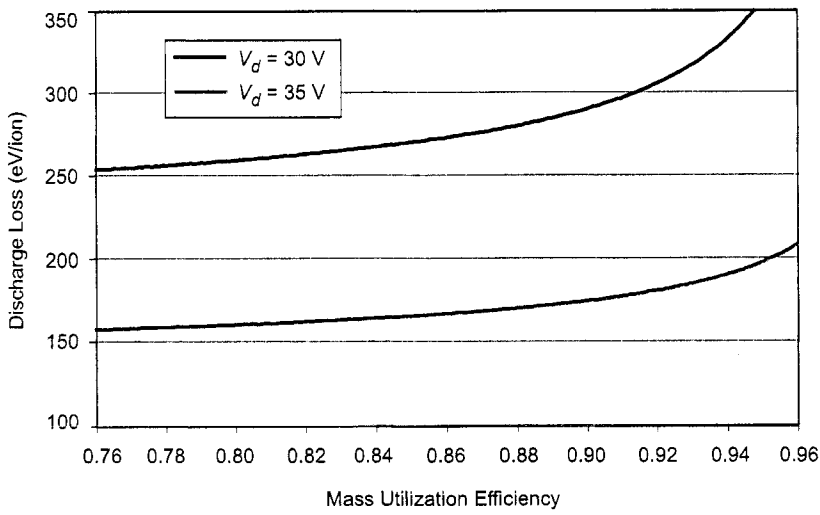

Fig. 4-28. Discharge loss calculated for Kaufman thruster example at two discharge voltages.

obtain sufficient electron loss to support the discharge. The instabilities are usually related to $\mathbf{E} \times \mathbf{B}$ driven instabilities and Bohm diffusion [24], which create significant noise in the discharge that can appear in the beam current. Second, the baffle required to force the primary electrons off axis to produce a more uniform plasma profile is susceptible to ion bombardment sputtering and plasma losses in the dense plasma region near the cathode. This has historically limited the life of these types of thrusters, although alternative materials can mitigate this problem. In addition, the primary electrons are injected purely off axis, which means that the plasma profile, and hence the beam profile, can be hollow or peaked depending on the cross-field diffusion and mobility throughout the discharge chamber.

Finally, the thruster size, shape, and magnetic field strength is limited to regimes where the magnetic field is sufficient to confine ions by electrostatic ambipolar effects to obtain good efficiency, and yet the magnetic field is not so high that the cross-field diffusion cannot provide adequate electron current for the discharge to be stable. If the field is too strong or the anode area in contact with the plasma is too small, the plasma potential goes negative relative to the anode to pull the electrons out of the discharge. Inspection of Fig. 4-22 shows that if the plasma potential is negative relative to the anode, then the primary energy is decreased at a given discharge voltage, which strongly affects the discharge efficiency [22]. Since the discharge voltage cannot be arbitrarily increased due to ion sputtering of the baffle and screen electrodes, in addition to excessive double-ion production, this will significantly reduce the discharge efficiency. In the case of negative plasma potentials, the electron loss to the anode has the form [22]

$$I_a = -D_\perp \nabla n e A_{as} e^{e\phi/kT_e} \left[1 - erf\left(\frac{-e\phi}{kT_e} \right)^{1/2} \right]^{-1}, \qquad (4.4\text{-}10)$$

where ϕ is a negative number in this case. The negative plasma potential increases the current to the anode area A_{as} by pulling some of the electrons from the plasma population that were headed away from the anode. While up to a factor of two more electron current theoretically can be drawn compared to the case for the case of positive plasma potentials, in practice drawing even the random electron flux can strongly deplete or perturb the Maxwellian population and affect the plasma discharge. The geometry of Kaufman thrusters for good efficiency is limited to configurations where the plasma potential in the discharge chamber is not allowed to go negative relative to the anode, which constrains the design space for the electrodes and fields.

4.5 rf Ion Thrusters

The ion thrusters described in the previous sections utilize a thermionic hollow cathode and DC discharge power supply to inject hot electrons into the discharge chamber to ionize the propellant gas. To eliminate any potential life or power supply issues with the hollow cathode and DC-electron discharge, an alternative thruster design utilizes electromagnetic fields to heat the plasma electrons that, in turn, ionize the injected gas. One method to achieve this goal is to use an inductive plasma generator, which is normally called a radio-frequency, or rf, ion thruster. In this case, low frequency rf voltage is applied to an antenna structure around or in the plasma, and the rf energy is coupled to the electrons.

The simplest configuration for an rf ion thruster is shown schematically in Fig. 4-29. An rf coil is wrapped around an insulating chamber with a gas feed. The chamber can be cylindrical, hemispherical, or conical in shape and is connected to an ion accelerator structure that is the same as those used for electron-bombardment ion thrusters with either two or three grids. The plasma floats relative to the first grid, and the high voltage is applied between the two grids to accelerate ions that flow through the first grid and form the beam. The rf coil is connected to an rf power supply that provides the power to generate the plasma. There is usually no applied magnetic field in rf ion thrusters, although one can be applied in principle to improve the discharge performance. As in other ion thruster designs, the entire discharge chamber is enclosed in a metallic screen or structure to eliminate electron collection from the space plasma, and a neutralizer cathode is connected to provide net charge neutralization of the beam.

The coil wrapped around the insulating thruster body can be modeled as a solenoid with N turns, and the rf voltage applied to it drives an rf current in the

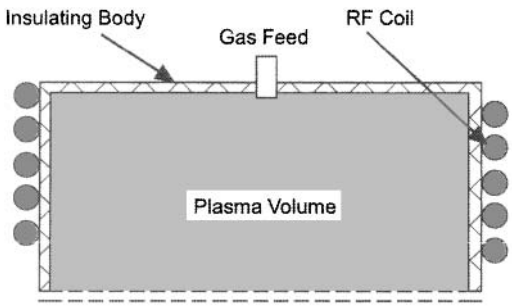

Fig. 4-29. Schematic of an rf ion thruster showing induction coil, insulating body, gas feed and two-grid accelerator structure.

coil. Typical frequencies used in rf ion thrusters are in the range of 1 MHz. At these frequencies, the penetration of the fields from the coil at the boundary is limited by the skin depth in the plasma [24], which is on the order of or slightly less than the radius of most rf ion thrusters at the plasma densities required to produce xenon ion current densities in excess of 1 mA/cm^2. This produces an attenuation of the electric and magnetic fields toward the axis, and the majority of plasma interaction with the fields occurs off axis closer to the boundary.

The axial magnetic field inside the coil induced by the rf current, neglecting end effects, is

$$B_z = \frac{NI}{\mu_o} e^{i\omega t}, \tag{4.5-1}$$

where I is the rf current in the coil, μ_o is the permeability of the vacuum, ω is the cyclic frequency ($2\pi f$) of the rf, and t is the time. From Maxwell's equation, the time-varying magnetic field creates a time-varying electric field:

$$\nabla \times \mathbf{E} = -\frac{\partial \mathbf{B}}{\partial t}. \tag{4.5-2}$$

The induced rf electric field in the rf thruster geometry is then in the azimuthal direction:

$$E_\theta = -\frac{i\omega r}{2} B_{zo} e^{i\omega t}, \tag{4.5-3}$$

where r is the distance from the axis and B_{zo} is the peak axial rf magnetic field from Eq. (4.5-1). A finite electric field is generated spatially off axis inside the thruster.

The induced electric field exists in one direction ($\pm\theta$ direction) for roughly half a period, which for a 1-MHz frequency is 0.5 microseconds. The electrons, however, don't see the oscillating component of the electric field because they transit the interaction region close to the antenna in a time much less than this value. For example, a 5-eV electron will travel a distance of about 1 meter in 1 microsecond, and so can traverse the electric field region many times within a half cycle. Therefore, electrons traversing the induced electric field region "see" a DC electric field and are accelerated. If they make a collision prior to leaving the region, they can then retain some or all of the velocity imparted by the electric field and are heated.

The criteria for the rf plasma generator to provide net heating of the electrons is that a sufficient number of electrons make a collision within the electric field interaction region. If the interaction region is, say, a few centimeters across, the mean free path should be on this order. The probability of an electron making a collision is given by

$$P = 1 - \exp^{-x/\lambda} = 1 - \exp^{-n_o \sigma x}. \tag{4.5-4}$$

Using Eq. (2.7-2) to convert from neutral density to pressure, the minimum pressure at a temperature T in the plasma chamber of an rf thruster for breakdown to occur is

$$P_{\min}[\text{torr}] = \frac{-1.04 \times 10^{-25}\ T}{\sigma\ x} \ln(1 - P). \tag{4.5-5}$$

For example, the minimum pressure for starting the rf-generated plasma is plotted in Fig. 4-30, where room temperature (290 K) xenon gas with a xenon atomic radius of 1.24 Å in a 5-cm-long interaction region is assumed. If 10% of the electrons must make an electron-neutral collision within a 5-cm interaction region to provide sufficient heating for sustaining ionization and breakdown to proceed, then the minimum pressure in the thruster is about 1×10^{-3} torr. Minimum pressures in the range of 10^{-3} to 10^{-2} torr are commonly reported in the literature for rf plasma sources to ignite the plasma. Once the plasma source is ignited, the required electron collisions to provide the heating in the rf

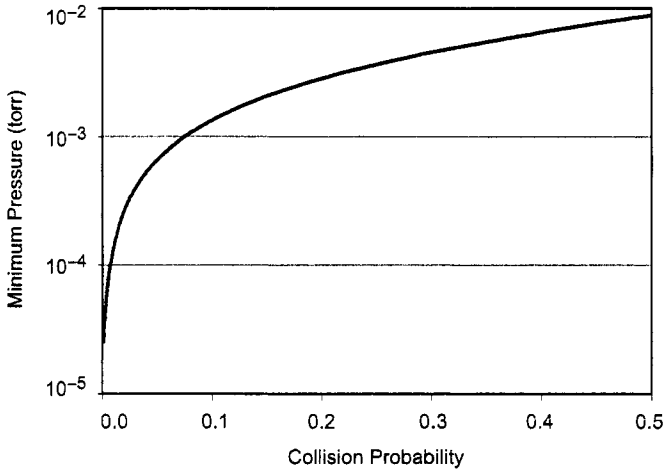

Fig. 4-30. Minimum pressure for starting a xenon rf thruster with a 5-cm interaction zone as a function of the probability of an electron having a collision.

electric fields can be supplemented by coulomb collisions between the plasma electrons, which reduce the operating pressure requirement and permit high mass utilization efficiency to be achieved.

Starting an inductive plasma discharge can also be problematic because initially there are few free electrons present to interact with the rf fields and ionize the fill gas. Prior to the plasma ignition, there is no load on the rf circuit driving the coil and the reactive power stored in the inductive components in the rf matching network grows, which increases the voltage across the coil and induces higher electric fields inside. If the minimum gas pressure is provided, the discharge will ignite when the field is either large enough to excite the few electrons naturally present in the chamber or causes field emission to occur. Another method for ignition is to inject electrons from a spark generator, small cathode, or the neutralizer cathode (with the accel voltage turned off momentarily) into the discharge chamber to provide the seed electrons for interaction with the rf electric fields.

If the antenna in rf thrusters is directly exposed to the plasma, ions in the discharge can be accelerated by the rf voltage on the surfaces and sputter-erode the antenna. This can ultimately limit the life of rf thrusters. This problem is minimized by either encasing the antenna in an insulator [49] or by making the thruster body an insulating material and mounting the antenna exterior to the plasma volume [50]. In this case, the rf voltage across the coil is shielded from the plasma, and the ions are not accelerated to high energy before striking the insulator. Mounting rf antennas outside insulating-material walls such as quartz or alumina is common practice in inductive plasma generators used in the semiconductor processing industry. An example of this arrangement applied to a radio-frequency ion thruster (RIT)-XT thruster [50] is shown in Fig. 4-31. In this case, the body of the thruster is constructed of a conical (or hemispherical) alumina insulator, and a high-conductivity-material (typically copper) antenna is coiled around the insulator. As long as the alumina body is not significantly coated by conductive layers and remains an insulator, the rf fields will couple through the wall and generate plasma.

This type of ion thruster is readily analyzed by particle and energy balance models because they do not have localized electron sources (hollow cathodes); the rf fields simply heat the Maxwellian electron distribution that provides the ionization, and the plasma in the discharge chamber is very uniform. In the energy balance equation, it is assumed that the power absorbed by the plasma is simply given by P_{abs}. Ions generated in the plasma volume drift to the interior surfaces in the thruster, and only electrons in the tail of the Maxwellian distribution have sufficient energy to overcome the potential difference

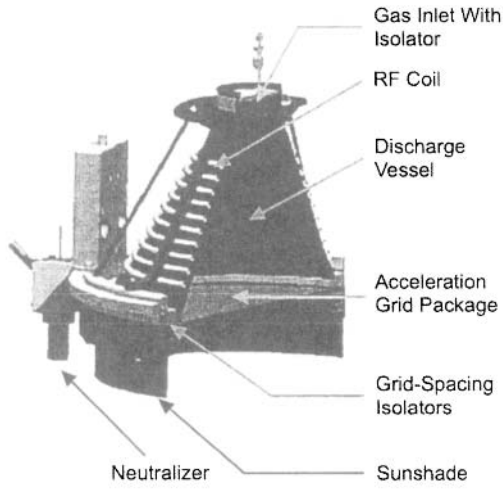

Fig. 4-31. rf ion thruster design showing the alumina body, exterior rf coil, accelerator grid assembly and neutralizer cathode. The antenna system is enclosed in a metal "plasma shield" to eliminate electron collection from the space plasma (from [50]).

between the plasma and the wall. The power out of the plasma equals the power absorbed, which is given by

$$P_{\text{abs}} = I_p U^+ + I^* U^* + \left(I_s + I_w + I_b\right)\left(\frac{T_{eV}}{2} + \phi\right) + I_a\left(2T_{eV} + \phi\right), \qquad (4.5\text{-}6)$$

where the electron and ion energy loss terms are shown explicitly. Equating the input power to the output power, the discharge loss is then

$$\begin{aligned}\eta_d &= \frac{P_{\text{abs}}}{I_b} \\ &= \frac{I_p}{I_b}U^+ + \frac{I^*}{I_b}U^* + \left(\frac{I_s}{I_b} + \frac{I_w}{I_b} + 1\right)\left(\frac{T_{eV}}{2} + \phi\right) + \frac{I_a}{I_b}\left(2T_{eV} + \phi\right).\end{aligned} \qquad (4.5\text{-}7)$$

The ionization and excitation is now only due to the plasma electrons, so the first current fraction in Eq. (4.5-7), using Eq. (4.3-50) and assuming quasi-neutrality ($n_i \approx n_e$), is

$$\frac{I_p}{I_b} = \frac{2n_o\langle\sigma_i v_e\rangle V}{\sqrt{\frac{kT_e}{M}}A_s T_s}, \qquad (4.5\text{-}8)$$

and the second current fraction is likewise:

$$\frac{I^*}{I_b} = \frac{2n_o \langle \sigma_* v_e \rangle V}{\sqrt{\frac{kT_e}{M}} A_s T_s}. \tag{4.5-9}$$

The screen current-to-beam current ratio is given in Eq. (4.3-57) as $(1-T_s)/T_s$.

The ion current that goes to the wall is the Bohm current to the wall area A_w reduced by radial confinement provided by any applied or induced magnetic fields. The fourth current ratio is then

$$\frac{I_w}{I_b} = \frac{\frac{1}{2} n_i v_a A_w f_c}{\frac{1}{2} n_i v_a A_s T_s} = \frac{A_w f_c}{A_s T_s}, \tag{4.5-10}$$

where f_c is again a confinement factor for the reduction in the Bohm velocity due to ambipolar effects in the ion and electron flows to the wall. Since there are no applied DC potentials in the discharge chamber and all the walls float, the electron current out is the same as the ion current out:

$$I_a = I_s + I_w + I_b. \tag{4.5-11}$$

Plasma potential in the expression for the discharge loss [Eq. (4.5-7)] can be evaluated by equating the total ion and electron currents exiting the plasma:

$$\frac{n_i}{2}\sqrt{\frac{kT_e}{M}}(A_w f_c + A_s) = \frac{n_e}{4}\sqrt{\frac{8kT_e}{\pi m}}\left[A_w + (1-T_s)A_s\right]\exp^{-e\phi/kT_e}. \tag{4.5-12}$$

Solving for the plasma potential gives

$$\phi = \frac{kT_e}{e}\ln\left[\frac{A_w + (1-T_s)A_s}{A_w f_c + A_s}\sqrt{\frac{2M}{\pi m}}\right]. \tag{4.5-13}$$

If the wall area is large compared to the screen area, or the grid transparency is small compared to 1, this turns into the normal equation for floating potential:

$$\phi = \frac{kT_e}{e}\ln\left[\sqrt{\frac{2M}{\pi m}}\right], \tag{4.5-14}$$

which for xenon is $5.97 * T_e$.

Using Eqs. (4.5-8) through (4.5-11), the discharge loss for rf ion thrusters can then be written

$$\eta_d = \frac{2n_o \langle \sigma_i v_e \rangle V}{\sqrt{\frac{kT_e}{M}} A_s T_s} \left(U^+ + U^* \frac{\langle \sigma_* v_e \rangle}{\langle \sigma_i v_e \rangle} \right) + \left[\frac{1 - T_s}{T_s} + \frac{A_w f_c}{A_s T_s} + 1 \right] (2.5 T_{eV} + 2\phi), \tag{4.5-15}$$

where the plasma potential ϕ is given by Eq. (4.5-13) in eV.

The electron temperature is found, again, by equating the ion production and loss terms

$$n_o n_e e \langle \sigma_i v_e \rangle V = \frac{1}{2} n_i e \sqrt{\frac{kT_e}{M}} (A_w f_c + A_s). \tag{4.5-16}$$

The electron temperature is then found from the solution to

$$\frac{\sqrt{\frac{kT_e}{M}}}{\langle \sigma_i v_e \rangle} = \frac{2n_o V}{A_w f_c + A_s}. \tag{4.5-17}$$

As an example, assume that the rf ion thruster has a 20-cm grid diameter, an 18-cm-deep conical ceramic discharge chamber, a grid transparency of 80%, and that it produces 2 A of beam current in xenon. Figure 4-32 shows the calculated discharge loss as a function of the mass utilization efficiency from Eq. (4.5-15), assuming no applied or induced magnetic fields and, therefore, no plasma confinement. A discharge loss of about 450 eV/ion is predicted at 90% mass utilization efficiency. This is a very high discharge loss, and it can be seen in Fig. 4-32 that the majority of the energy loss is carried out by the ions and electrons flowing to the floating-potential walls. This is because the Maxwellian electron temperature required to produce the ions that flow to the entire interior surface area of the discharge chamber at 90% mass utilization efficiency [from the solution of Eq. (4.5-17)] is 5 eV, and the plasma potential to achieve net ambipolar flow is, therefore, nearly 30 V. The high sheath potential required to self-confine the electrons for particle balance and the large

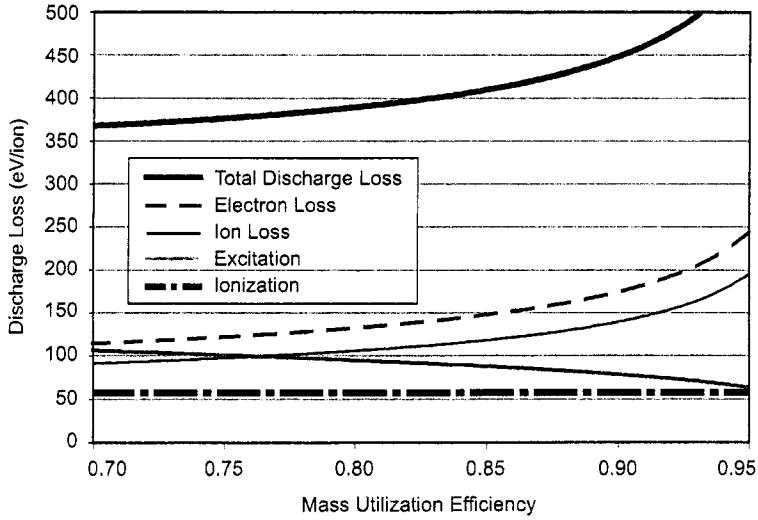

Fig. 4-32. Discharge loss calculated for the example rf ion thruster and the contribution from the four energy loss mechanisms.

plasma loss area ($A_w + A_s$) carry significant energy to the discharge chamber wall, causing a relatively high discharge loss.

The discharge loss performance of rf ion thrusters typically reported in the literature [50] is much lower than that found in our example. This is because even though these thrusters do not usually have an applied DC magnetic field, the rf coil forms a solenoid around the dielectric discharge chamber and the rf current flowing in the antenna coil induces an alternating current (AC) magnetic field in the interior of the discharge chamber with a frequency at the rf oscillator frequency. In most typical rf thrusters, this frequency is on the order of 1 MHz. The ion acoustic speed $\sqrt{kT_e/M}$ at $T_e = 5$ eV is 1.9 km/s, and so in a 1-μs cycle, the ions can only move less than 2 mm, which implies that the ions can be considered stationary on the magnetic-field cycle time. The electrons are certainly not stationary in the period, but the ion space charge will hold the electrons in place during a cycle. Therefore, the AC magnetic field from the rf coil can provide some confinement for the plasma [51] and reduce the flux to the discharge chamber walls. The magnetic field induced by the rf coil depends on the coil size and amount of power. For example, assume that the coil occupies 1 turn per centimeter (100 turns/m), and the coil impedance is 50 ohms. For an input power of 500 W, this would result in 10 A of rf current flowing in the coil. For simplicity, assume the rf coil forms a solenoid and the magnetic field inside a solenoid (neglecting end effects) is

$$B[\text{gauss}] = 10^4 \mu_o \, N \, I, \tag{4.5-18}$$

where μ_0 is the permeability of free space, equal to $4\pi \times 10^{-7}$ henries/m; N is the number of turns per meter; and I is the coil current in amperes. For this rf thruster example, a magnetic field of 12.6 G is produced. While this sounds like a low field, it is an axial field induced in the majority of the interior of the thruster depending on the plasma skin depth, which is large in these low density plasmas.

The reduction in the ion velocity flowing radially to the wall for the situation of a transverse magnetic field and ambipolar flows was analyzed in Section 4.3.5. Figure 4-33 shows the reduction in the radial Bohm current (f_c) from evaluating Eq. (4.3-15) for the condition when the diffusion length is now essentially the thruster radius. Fields on the order of 10 G throughout the thruster volume can reduce the ion and electron loss to the discharge chamber wall by over a factor of two. While the rf magnetic field strength decreases with radius due to the finite length of the antenna coil (solenoid end effects), the field strength near the axis is still sufficient to reduce the ion loss rate [51].

The discharge loss calculated by the 0-D model for our 20-cm rf thruster example is shown in Fig. 4-34 as a function of rf magnetic field induced in the plasma. The discharge loss is reduced from the case of no magnetic confinement ($B = 0$) of 450 eV/ion at 90% mass utilization to a value of

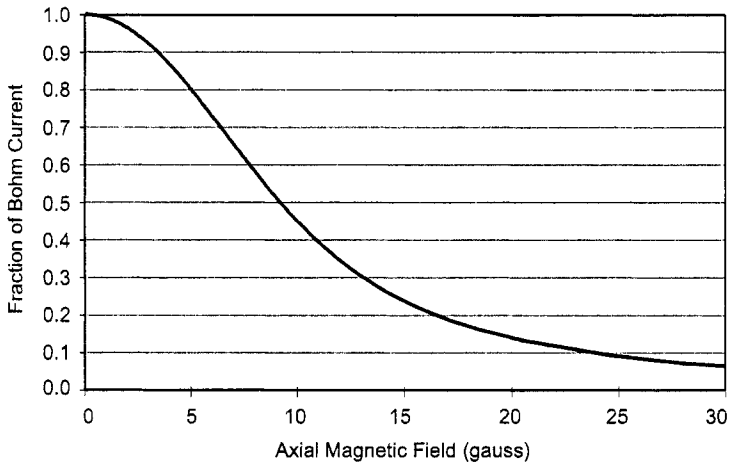

Fig. 4-33. Ion confinement factor (the fraction of the Bohm current to the wall) as a function of the induced magnetic field in the discharge chamber volume.

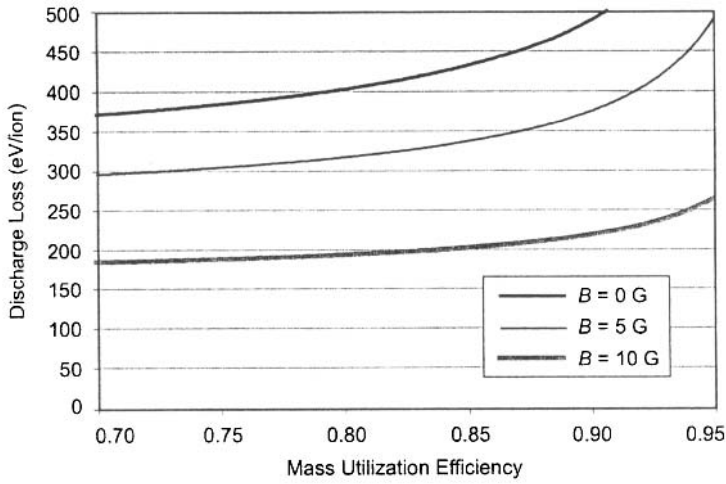

Fig. 4-34. rf ion thruster discharge loss versus mass utilization efficiency for three values of the induced magnetic field in the discharge chamber.

230 eV/ion if 10 G is induced in the chamber. This is a significant reduction in the calculated loss and is the key to rf ion thruster discharge performance.

To produce the 2-A beam in our 20-cm thruster example at 230 eV/ion, a total input power to the antenna of 460 W is required to be absorbed by the plasma. Since the rf power supplies are typically 90% efficient in this frequency range, the input power to the thruster PPU would be about 511 W. This predicted performance is in good agreement with the data about this size of rf thruster found in the literature [50], suggesting that a 0-D particle and energy balance model can provide reasonably accurate performance predictions.

One advantage of rf ion thrusters is that they have only Maxwellian electrons and ambipolar ion and electron loss rates, which simplifies the discharge loss expressions and makes it easy to analyze the few geometric parameters to optimize the discharge loss. An example of the process is as follows: First, specifying the required beam current and current density determines the grid diameter in any ion thruster. Ion optics codes then determine the grid transparency. Once the grid design is set, a Monte-Carlo gas code is used to evaluate the Clausing factor introduced in Eq. (4.3-33). Assuming a conical or cylindrical discharge chamber shape of a given length immediately specifies the loss areas and plasma volume. Then, specifying the mass utilization efficiency gives the neutral density, and the electron temperature can be found from Eq. (4.5-17) with an initial confinement factor assumption. These values are the input parameters to the discharge loss given by Eq. (4.5-15), which provides the

required input rf power to the antenna assuming that the antenna efficiency and coupling (reflected power) are known. The approximate induced AC magnetic field can then be calculated from Eq. (4.5-18) and the ion confinement factor f_c, found as in Section 4.3.4. A simple iteration then gives the final discharge loss and rf power.

It should be noted that as the discharge chamber length decreases, the antenna axial extent also decreases, which reduces the electric field interaction region and decreases the AC axial magnetic field strength due to end effects in the solenoid coil. The ability to breakdown the neutral gas initially and then couple the rf energy to the electrons efficiently may be compromised as the length decreases, which would also affect the discharge loss scaling.

A disadvantage of rf ion thrusters is that the antenna must be insulated from the plasma, and the insulator is then subject to ion bombardment and material deposition. Dielectric discharge chambers are susceptible to mechanical problems in fabrication, environmental testing and launch, and life issues from coating of the insulator surface with conducting layers. The structural issue has been addressed on some flight units by the use of a ceramic discharge chamber with an exterior mounted antenna structure to provide the rigidity required for launch survival. While the discharge loss in rf ion thrusters is typically higher than that found for well-designed electron-bombardment ion thrusters such that the total efficiency is lower, the simplified design of rf thrusters makes it easier to analyze them and predict the performance than most other ion thruster configurations. The rf thruster design concept eliminates any potential discharge cathode life issues and utilizes fewer power supplies to operate the discharge. These factors make rf ion thrusters very competitive for future spaceflight applications.

4.6 Microwave Ion Thrusters

An alternative to producing the plasma in the thruster with electron discharges or rf induction heating of the electron population is to generate the plasma using electromagnetic fields at microwave frequencies. This eliminates life issues associated with the discharge hollow cathode, and the lack of applied DC voltages in the discharge chamber can potentially reduce the sputter erosion of electrodes exposed to the plasma as compared with that of DC electron discharges. However, electromagnetic waves can propagate and be absorbed in plasmas only under certain conditions. For example, if the microwave frequency is too high or the plasma density too low, the microwave radiation is reflected completely from the plasma. If the conditions are such that the microwaves do propagate in the plasma, the microwave energy is coupled to the plasma by resonant heating of the electrons in a magnetic field in the

presence of collisions. The required magnetic field to achieve this resonance is significant, and the pressure required to achieve sufficient collisions to start the discharge can be relatively high. These effects impact the plasma generator design and performance.

The propagation of microwaves in a plasma can be understood by examining the dispersion relationship. The behavior of microwaves in the thruster plasma is described by Maxwell's Equations:

$$\nabla \times \mathbf{E} = -\frac{\partial \mathbf{B}}{\partial t} \tag{4.6-1}$$

$$\nabla \times \mathbf{B} = \mu_o \left(\mathbf{J} + \varepsilon_o \frac{\partial \mathbf{E}}{\partial t} \right). \tag{4.6-2}$$

The electromagnetic behavior is analyzed by linearizing these two equations using

$$\mathbf{E} = \mathbf{E}_0 + \mathbf{E}_1 \tag{4.6-3}$$

$$\mathbf{B} = \mathbf{B}_0 + \mathbf{B}_1 \tag{4.6-4}$$

$$\mathbf{J} = \mathbf{j}_0 + \mathbf{j}_1, \tag{4.6-5}$$

where $\mathbf{E}_0$, $\mathbf{B}_0$, and $\mathbf{j}_0$ are the equilibrium values of the electric and magnetic fields and currents, and $\mathbf{E}_1$, $\mathbf{B}_1$ and $\mathbf{j}_1$ are the perturbed values in the electromagnetic fields and current. Linearizing Eqs. (4.6-1) and (4.6.2), and realizing that the equilibrium values have no curl or time dependence and that $\varepsilon_o \mu_o = 1/c^2$ in a vacuum, gives

$$\nabla \times \mathbf{E}_1 = -\frac{\partial \mathbf{B}_1}{\partial t} \tag{4.6-6}$$

$$c^2 \nabla \times \mathbf{B}_1 = \frac{\mathbf{j}_1}{\varepsilon_o} + \frac{\partial \mathbf{E}_1}{\partial t}. \tag{4.6-7}$$

Taking the curl of Eq. (4.6-6) gives

$$\nabla \times \nabla \times \mathbf{E}_1 = \nabla(\nabla \cdot \mathbf{E}_1) - \nabla^2 \mathbf{E}_1 = -\nabla \times \frac{\partial \mathbf{B}_1}{\partial t}, \tag{4.6-8}$$

and the time derivative of Eq. (4.6-7) gives

$$c^2 \nabla \times \frac{\partial \mathbf{B}_1}{\partial t} = \frac{1}{\varepsilon_o} \frac{\partial \mathbf{j}_1}{\partial t} + \frac{\partial^2 \mathbf{E}_1}{\partial t^2}. \tag{4.6-9}$$

Combining Eq. (4.6-9) with Eq. (4.6-8) results in

$$\nabla(\nabla \cdot \mathbf{E}_1) - \nabla^2 \mathbf{E}_1 = -\frac{1}{\varepsilon_o c^2} \frac{\partial \mathbf{j}_1}{\partial t} - \frac{1}{c^2} \frac{\partial^2 \mathbf{E}_1}{\partial t^2}. \tag{4.6-10}$$

Assuming that the microwaves are plane waves that vary as

$$\mathbf{E} = E\, e^{i(kx - \omega t)} \tag{4.6-11}$$

$$\mathbf{j} = j\, e^{i(kx - \omega t)}, \tag{4.6-12}$$

where $k = 2\pi / \lambda$ and ω is the cyclic frequency $2\pi f$, then Eq. (4.6-10) becomes

$$-k(k \cdot \mathbf{E}_1) + k^2 \mathbf{E}_1 = \frac{i\omega}{\varepsilon_o c^2} \mathbf{j}_1 + \frac{\omega^2}{c^2} \mathbf{E}_1. \tag{4.6-13}$$

The electromagnetic waves are transverse waves, so $k \cdot \mathbf{E}_1 = 0$ and Eq. (4.6-13) becomes

$$\left(\omega^2 - c^2 k^2\right) \mathbf{E}_1 = \frac{-i\omega}{\varepsilon_o} \mathbf{j}_1. \tag{4.6-14}$$

Since these waves are in the microwave frequency range, the ions are too massive to move on these fast time scales and the perturbed current $\mathbf{j}_1$ can come only from electron motion. The perturbed electron current density in a plasma is

$$\mathbf{j}_1 = -n_e e \mathbf{v}_{e1}, \tag{4.6-15}$$

where n_e is the plasma density and $\mathbf{v}_{e1}$ is the perturbed electron velocity. If the applied magnetic field is zero or the perturbed electric field is parallel to the applied magnetic field (so called "O-waves"), the equation of motion for the perturbed electron motion is

$$m \frac{\partial \mathbf{v}_{e1}}{\partial t} = -e \mathbf{E}_1. \tag{4.6-16}$$

Solving for the perturbed electron velocity, assuming plane waves, and inserting this into Eq. (4.6-15), the perturbed current is

$$\mathbf{j}_1 = -n_e e \frac{\varepsilon_o \mathbf{E}_1}{i\omega m}. \tag{4.6-17}$$

Inserting Eq. (4.6-17) into Eq. (4.6-14) and solving for the frequency gives the dispersion relation for electromagnetic waves in a plasma:

$$\omega^2 = \frac{n_e e^2}{\varepsilon_o m} + c^2 k^2 = \omega_p^2 + c^2 k^2, \tag{4.6-18}$$

where the definition of the electron plasma frequency $\omega_p^2 = n_e e^2 / \varepsilon_o m$ has been used.

This expression can be solved for the wavelength of the microwaves in the plasma

$$\lambda = \frac{2\pi c}{\sqrt{\omega_p^2 - \omega^2}} = \frac{c}{\sqrt{f_p^2 - f^2}}, \tag{4.6-19}$$

where f_p is the real plasma frequency and f is the microwave frequency. If the microwave frequency exceeds the plasma electron frequency, the wavelength becomes infinitely long and the wave becomes evanescent (it will not propagate into the plasma) and is reflected. This condition, called cutoff, determines the maximum plasma density into which a microwave source can inject power to produce the plasma. Table 4-1 shows the cutoff frequency for a range of plasma densities and the ion current density from a xenon plasma at an electron temperature of 3 eV. As an example, if the ion thruster design requires an ion

Table 4-1. Cutoff frequencies for several plasma densities, and the corresponding ion current density from a xenon plasma at T_e = 3 eV.

Plasma Density (cm^{-3})	Cutoff Frequency (GHz)	J (mA/cm^2)
10^9	0.285	0.0118
10^{10}	0.900	0.118
10^{11}	2.846	1.184
10^{12}	9.000	11.84
10^{13}	28.460	118.4

current density to the grids of, say, 1.2 mA/cm^2, then a frequency in excess of 2.85 GHz must be used to produce the plasma or else some or all of the microwave power will be reflected.

The microwave energy is coupled to the plasma by electron cyclotron resonance heating, where the microwave frequency corresponds to the cyclic frequency of the electrons in a magnetic field. The resonant frequency is the electron cyclotron frequency, which was derived in Chapter 3:

$$\omega_c = \frac{|q|B}{m}. \tag{4.6-20}$$

The cyclic cyclotron frequency is easily calculated using a convenient formula of $\omega_c = 2.8$ GHz/kG. In the plasma, the actual microwave frequency is $f_c = eB/2\pi m$, which is given in Table 4-2 for several magnetic field values. If it is assumed that the microwave energy is deposited into the volume of a plasma immersed in the magnet field, the maximum plasma density (and corresponding ion current density to the grids) to avoid cutoff is shown for each of the magnetic field values. To produce current densities in excess of 1 mA/cm^2 of xenon to the accelerator grids from a 3-eV electron temperature plasma requires magnetic fields in excess of 1000 gauss, and values closer to 2000 G are required to avoid cutoff for slightly higher ion current densities to the grids. This is a significant magnetic field to produce in the discharge chamber volume.

The use of microwave radiation enables direct heating of the plasma electrons, but for the wave to add energy to the electrons, collisions must occur.

Table 4-2. Electron cyclotron frequencies for several magnetic field levels, the corresponding maximum plasma density before cutoff, and the maximum ion current density to the grids from a 3 eV electron temperature xenon plasma.

Magnetic Field (G)	Cyclotron Frequency f_c (GHz)	Maximum Plasma Density (cm^{-3})	Maximum Ion Current Density (mA/cm^2)
100	0.28	9.68×10^8	0.012
500	1.40	2.42×10^{10}	0.286
1000	2.80	9.68×10^{10}	1.146
2000	5.60	3.87×10^{11}	4.58
3000	8.40	8.71×10^{11}	10.31
4000	11.20	1.55×10^{12}	18.34

Otherwise, the energy received by an electron during acceleration on each half-cycle of its cyclotron motion is taken back by deceleration of the electron in the field on the next half-cycle. Therefore, there is a minimum pressure at which sufficient collisions occur to ignite the plasma and sustain the discharge. The probability of a collision occurring is

$$P = \left[1 - \exp^{-n_o \sigma x}\right] = \left[1 - \exp^{(-x/\lambda_{en})}\right], \tag{4.6-21}$$

where x is the path length of the electron in the neutral gas with a density of n_o, and λ_{en} is the electron-neutral collision mean-free-path. An electron entering the interaction region gyrates around the magnetic field lines due to its perpendicular velocity and travels along the magnetic field line due to its parallel velocity.

While the electron cyclotron heating tends to spin-up the electron motion around the field lines, collisions tend to scatter the motion along the direction of the field lines and thermalize the electrons into a Maxwellian distribution, sometimes with a high-energy bump or tail driven by the resonance. The collisionality requirements to achieve heating can be found from examining the path length of an electron at a temperature T_e spiraling along a field line. The distance that the electron travels when gyrating around the field lines is given by the Larmor radius, which was derived in Chapter 3:

$$r_L = \frac{v_\perp}{\omega_c} = \frac{m v_\perp}{|q|\, B} = \frac{1}{B}\sqrt{\frac{2 m v_\perp}{e}}. \tag{4.6-22}$$

The time for an electron to leave the microwave interaction region of length L is

$$t = \frac{L}{v_{//}}, \tag{4.6-23}$$

where $v_{//}$ is the parallel electron velocity along the field line. The number N of gyrations that an electron makes in the interaction region is the microwave frequency f multiplied by the time in the resonant region. The path length of the perpendicular gyration of the electron is then

$$L_g = 2\pi\, r_L N = 2\pi\, r_L\, f \frac{L}{v_{||}}. \tag{4.6-24}$$

The total path length of the helical motion of the electron is

$$L_T = \sqrt{L_g^2 + L^2} = \sqrt{\left(\frac{2\pi\, r_L\, f L}{v_{||}}\right)^2 + L^2}\,. \qquad (4.6\text{-}25)$$

Using this value for the path length x of the electron in Eq. (4.6-21) gives the probability of a collision with the neutral gas. Figure 4-35 shows this probability calculated for xenon gas at room temperature for electrons with a temperature of 2 eV in two different interaction lengths. To achieve the order of 10% of the electrons colliding with neutral gas atoms in a 5- to 10-cm-long resonance region requires an internal pressure of at least 10^{-3} torr. In reality the electrons must make multiple collisions within the interaction region because the energy gain in a single gyration is small. However, this pressure is similar to that found for rf thrusters to achieve sufficient collisions to start or sustain a discharge, for essentially the same reasons. Again, once the plasma is started, coulomb collisions will aid in transferring the electron motion in the microwave fields into heating, which reduces the pressure required to operate the plasma generator and permits higher mass utilization efficiencies to be achieved.

As was shown in Tables 4-1 and 4-2, a high magnetic field (>1 kG) and a high microwave frequency (>2.8 GHz) are required to produce sufficient plasma density to deliver reasonable current densities (>1 mA/cm^2 in xenon) to the grids in microwave thrusters. Due to the difficulty in producing these high magnetic fields throughout the discharge chamber volume, the resonance region is often localized to a small zone inside the thruster volume, and the plasma is allowed

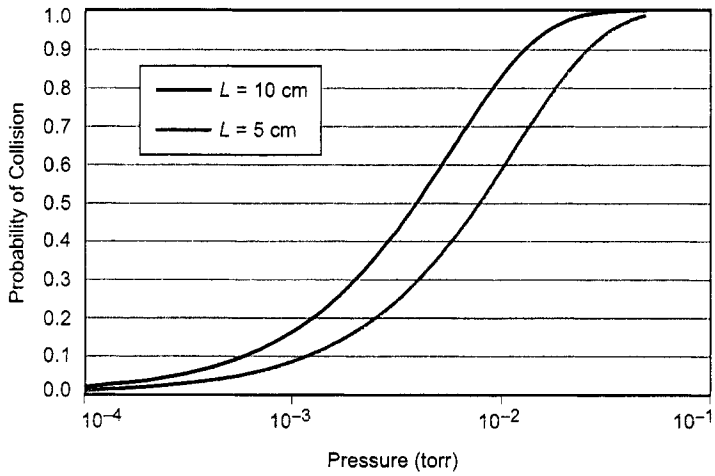

Fig. 4-35. Probability of an electron-neutral collision before leaving the resonance zone length indicated as a function of neutral pressure for 2-eV electrons.

to expand to the grids along divergent magnetic field lines. Figure 4-36 shows an ECR plasma source where a stronger magnetic field region resonant with 2.4-GHz radiation (produced by commercial magnetron microwave sources) is restricted to the rear of the discharge chamber. Of course, expanding the plasma from the resonance region to the grids decreases the plasma density and current density, so even higher magnetic fields and frequencies than just mentioned are normally required in the interaction region to produce over 1 mA/cm^2 to the grids.

The microwave radiation in this ECR plasma source is coupled into the rear of the discharge chamber through a waveguide window, and a quartz liner is used in the resonant region to ensure that the hot electrons are not lost directly to the metal walls of the chamber. The magnetic field in this geometry is produced by electromagnets, with a strong divergence in the field to spread the plasma over the grid region at the exit of the discharge chamber. This is a common geometry for industrial ion sources and plasma sources used in plasma processing, and the performance of the plasma generator is well known.

The performance of this style of microwave ion thruster can be examined with a 0-D model. Assume that the magnetic field is sufficiently strong that radial losses can be neglected. This assumption implies that the plasma is frozen on the field lines such that the density decreases linearly with the area increase as the field expands. This simplifies the model to the case of a straight cylindrical source with no radial losses. The plasma is lost axially to both the screen area A_s and the rear wall area A_w. Since there is no DC applied field, the plasma floats relative to the internal surfaces, the electrons are lost to the axial rear wall area and the collection area of the screen grid given by $(1-T_s)A_s$. Neglecting

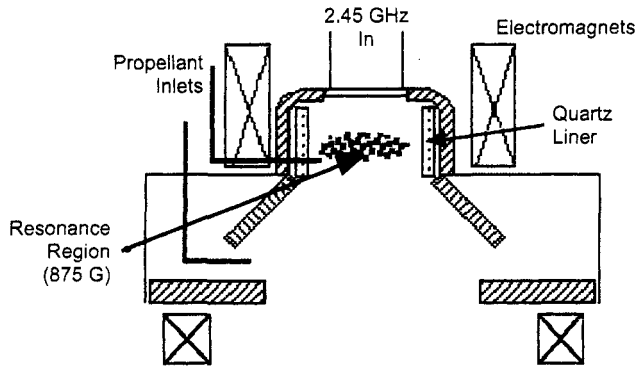

Fig. 4-36. Schematic of microwave ion source with a volume-resonance zone of strong magnetic field produced by electromagnets.

the cost of producing the microwave radiation, the power absorbed by the plasma is equal to the power lost:

$$P_{\text{abs}} = I_p U^+ + I^* U^* + \left(I_s + I_w + I_b\right)\left(\frac{T_{eV}}{2} + \phi\right) + I_a\left(2T_{eV} + \phi\right), \quad (4.6\text{-}26)$$

where I_s is the ion current collected by the screen grid, I_w is the ion current collected by the entire wall, and the ion energy loss is, again, $T_e/2 + \phi$. The amount of energy lost by electrons to the wall assumes that the electrons have a Maxwellian distribution, which may underestimate the energy lost due to the high energy tail in the electron distribution generated by the resonant ECR heating. The discharge loss is the power in (or out) divided by the beam current:

$$\begin{aligned}\eta_d &= \frac{P_{\text{abs}}}{I_b} \\ &= \frac{I_p}{I_b} U^+ + \frac{I^*}{I_b} U^* + \left(\frac{I_s}{I_b} + \frac{I_w}{I_b} + 1\right)\left(\frac{T_{eV}}{2} + \phi\right) + \frac{I_a}{I_b}\left(2T_{eV} + \phi\right).\end{aligned} \quad (4.6\text{-}27)$$

The first three current fractions in this equation are given by Eqs. (4.3-55), (4.3-56), and (4.3-57), respectively. The fourth current fraction is given by

$$\frac{I_w}{I_b} = \frac{\frac{1}{2} n_i e v_a A_w}{\frac{1}{2} n_i e v_a A_s T_s} = \frac{A_w}{A_s T_s}, \quad (4.6\text{-}28)$$

where the wall area A_w is the rear wall area only. The plasma potential is found again from charge conservation by equating the total ion and electron current:

$$\frac{n_i e}{2}\sqrt{\frac{kT_e}{M}}\left(A_w + A_s\right) = \frac{n_e e}{4}\sqrt{\frac{8kT_e}{\pi m}}\left[A_w + (1 - T_s)A_s\right]\exp^{-e\phi/kT_e}. \quad (4.6\text{-}29)$$

Solving for the plasma potential gives

$$\phi = \frac{kT_e}{e}\ln\left[\frac{A_w + (1 - T_s)A_s}{A_w + A_s}\sqrt{\frac{2M}{\pi m}}\right], \quad (4.6\text{-}30)$$

which is different from that found for rf ion thrusters because there is no ion confinement factor due to the induced magnetic fields from the antenna (the

ions are assumed perfectly confined radially due to the strong magnetic field). The electrons are lost to the rear wall and the screen grid, so the final current fraction in Eq. (4.6-27) is

$$\frac{I_a}{I_b} = \frac{\frac{1}{4}\sqrt{\frac{8kT_e}{\pi m}} n_e e\left[A_w + (1-T_s)A_s\right]}{\frac{1}{2} n_i e \sqrt{\frac{kT_e}{M}} A_s T_s} \exp^{-e\phi/kT_e}. \tag{4.6-31}$$

Using Eq. (4.6-30) for the plasma potential, this becomes

$$\frac{I_a}{I_b} = \frac{A_w + A_s}{A_s T_s}. \tag{4.6-32}$$

The discharge loss is then

$$\eta_d = \frac{2n_o \langle \sigma_i v_p \rangle V}{\sqrt{\frac{kT_e}{M}} A_s T_s} \left(U^+ + U^* \frac{\langle \sigma_* v_e \rangle}{\langle \sigma_i v_e \rangle} \right) + \left[\frac{1-T_s}{T_s} + \frac{A_w}{A_s T_s} + 1 \right] \left(\frac{T_{eV}}{2} + \phi \right) + \frac{A_w + A_s}{A_s T_s} \left(2T_{eV} + \phi \right), \tag{4.6-33}$$

with the plasma potential given by Eq. (4.6-30). The electron temperature and neutral density are solved in the same manner as previously for the other types of thrusters. The discharge loss for a generic microwave ion thruster producing 1 A of xenon ions from a 20-cm-diameter grid with 80% transparency is shown in Fig. 4-37 for several thruster lengths. Discharge losses on the order of 200 eV/ion are predicted. This discharge loss is twice that of our idealized ion thruster in Section 4.2 because both the ideal and the microwave source cases assumed ionization by Maxwellian electrons and perfect radial confinement, but the microwave source case includes plasma loss to the rear wall. While the assumption of negligible radial loss is reasonable due to the strong magnetic fields, some additional loss is expected in this direction that will degrade the actual discharge loss somewhat. The large loss area for plasma to the beam area and rear wall tend to drive up the plasma potential to maintain net ambipolar flows and charge balance, which increases the discharge loss compared to well-designed DC discharge thrusters.

Microwave ion source designers mitigate the back wall losses by imposing a stronger magnetic field upstream of the resonance zone. This creates a magnetic mirror, which was described in Chapter 3, that confines the plasma electrons

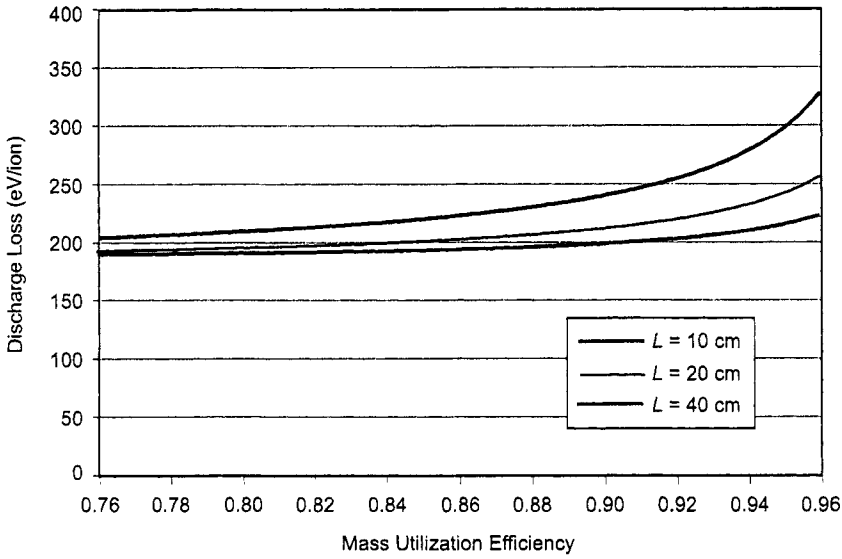

Fig. 4-37. Discharge loss versus mass utilization efficiency for our microwave thruster example with perfect radial confinement.

and reduces the axial losses. Because the magnetic moment (defined as $mv^2/2B$) is invariant along the field lines, electrons with sufficient initial perpendicular velocity are reflected from the increasing magnetic field as their parallel energy is converted into rotational energy. The electrons that are lost have a parallel velocity of

$$v_{||} > v_{\perp}\sqrt{R_m - 1}, \tag{4.6-34}$$

where R_m is the mirror ratio given by $B_{\max}/B_m$. For example, if the mirror ratio is 5, only electrons with a parallel velocity twice that of their perpendicular velocity will be lost. If the electrons have a Maxwellian distribution with a temperature T_e, then the number of particles with $v_{||} > 2v_{\perp}$ is $e^{-2} = 13.5\%$, so a large majority of the population is reflected. Since the cyclotron heating adds perpendicular energy to the electrons, mirror ratios of 4 to 6 are very efficient in confining the heated electrons that produce ionization.

The ion source shown in Fig. 4-36 utilizes electromagnets to produce the high field over a significant volume and also to create the confining mirror ratio. However, the power required to operate the electromagnets in this design increases the effective discharge loss and limits the electrical efficiency of the device in thruster applications. In addition, it is difficult to create large area

plasmas with good uniformity using microwave excitation due to the strong magnetic fields that confine the plasma and influence the profile. This leads to other magnetic configurations to produce the plasma using microwave ECR techniques.

In a volume-ionization ECR source, like that shown in Fig. 4-36, a significant fraction of the discharge chamber must be filled with a strong magnetic field to satisfy the resonance condition. If this field is produced by a solenoid, the electrical power required to achieve a sufficient field strength can represent a significant energy cost to the thruster. Likewise, if the field is produced by permanent magnets, the weight of the magnetic material required to produce this field can represent a significant weight penalty for the thruster. This problem can be mitigated by using magnetic multipole boundaries that produce strong magnetic fields at the discharge chamber wall using ring or line-cusp magnet configurations. Figure 4-38 shows the field lines between two magnet rings and the regions of strong magnetic field close to the magnet where the resonant condition is satisfied. Injection of the microwave radiation between the cusps, either by cutoff waveguides inserted between the rows [52], by slotted waveguides run along the rows [53], or by antenna structures placed between the rows, will couple the microwaves to the high magnetic field interaction region.

While this geometry eliminates the solenoidal magnet coils and minimizes the size of the permanent magnets required to produce the resonant field strength, there are several issues remaining. First, the magnetic field strength in the cusp region decreases as one over the distance from the surface squared. This means that very strong magnets are required to produce the resonant field at any significant distance from the wall. Second, electrons that gain energy from the

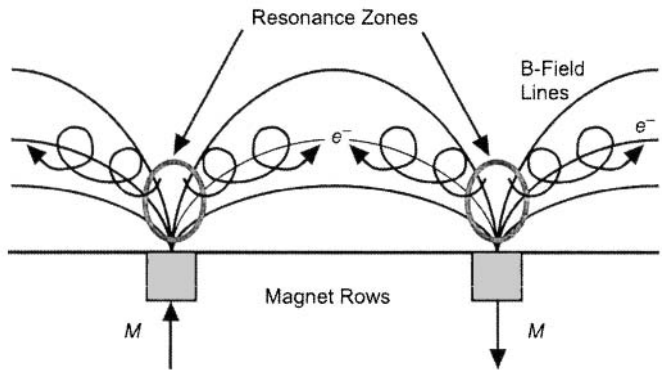

Fig. 4-38. Magnetic field lines and electron cyclotron resonant zone in a ring-cusp wall geometry.

microwaves can be easily lost along the field lines to the wall due to their finite parallel velocity. This means that optimal ECR designs using permanent multipole magnets will have the resonance region as far from the wall as possible and will produce a large mirror ratio approaching the wall to reflect the electrons to avoid excessive direct loss.

Nevertheless, wall losses are a concern in this configuration because the plasma production is a surface effect that is confined to the boundary region, as is the loss. Electrons that are heated in the resonance zone sufficiently to ionize the propellant gas generate plasma on the near-surface magnetic field lines. Coupling the plasma from the resonance region or the surface magnetic layer into the volume of the thruster is problematic due to the reduced cross-field transport. In the other thruster designs discussed in this chapter, the ion production was a volume effect and convective loss a surface effect, so thruster efficiency scaled as the volume-to-surface ratio. This means that larger DC and rf discharge thrusters can be made more efficient than smaller ones. Microwave thrusters, on the other hand, don't scale in the same manner with size because large amounts of plasma must be produced and transported from the surface region to fill the volume of larger thrusters, which can impact the discharge loss. In addition, the plasma density is limited by both cutoff and the magnitude of the resonant field, and so high current density ion production requires very high magnetic fields and high microwave frequencies. Therefore, microwave thrusters have been limited to date to lower current densities and smaller sizes than the other thrusters discussed here. However, work continues on scaling microwave thrusters to larger sizes and higher efficiencies.

The most successful design of a microwave thruster to date is the MUSES-C 10-cm ECR thruster [53–55], which is shown schematically in Fig. 4-39 from [54]. In this case, extremely strong samarium cobalt (SmCo) magnets are used to close the resonance field at the operating frequency between the magnets. This produces heating away from the wall and traps the electrons on the field lines due to an achievable mirror ratio of 2 to 3 in this geometry. The thruster volume is also minimized, with the plasma production region close to the grids. This configuration produces over 1 mA/cm^2 of xenon ions over the active grid region using a 4.2-GHz microwave source with a discharge loss of about 300 eV per ion at over 85% mass utilization efficiency [53].

Finally, there are several other components intrinsic to these thrusters that contribute to the difficulty of achieving high efficiency and compact size in a microwave thruster subsystem. Sources of microwave frequencies in the gigahertz range, such as traveling-wave tubes (TWT) and magnetrons, have efficiencies in the 50% to 70% range, and the power supply to run them is usually about 90% efficient. This represents nearly a factor of two in-line loss

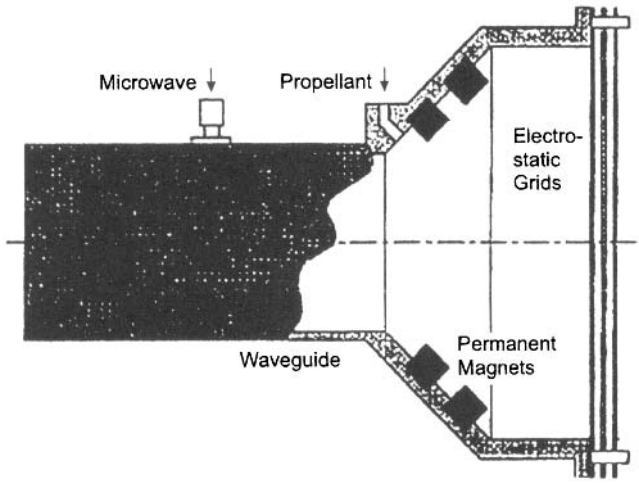

Fig. 4-39. Schematic of the MUSES-C 10-cm microwave source showing the strong magnets and small volume characteristic of these thrusters (from [54]).

of the electrical power delivered to the thruster that must be accounted for in the total discharge cost of the subsystem. The plasma is typically a difficult load to match well, and reflection of 10% to 30% of the microwave energy back into the recirculator (which absorbs the reflected power from the source in the case of mismatch or faults) is typical. The microwave source and recirculator usually represent a significant mass and volume addition to the ion thruster system. An examination of Table 4-1 shows that, in order to avoid cutoff and produce ion current densities to the grids of 1 to 2 mA/cm^2, microwave sources in the 4- to 6-GHz range are required. At this time, space TWTs in this frequency range are limited in power capability to the order of a few hundred watts. For a given discharge loss, this limits the total ion current that can be produced by a microwave thruster. While microwave thrusters hold the promise of eliminating the need for thermionic cathodes used in DC-discharge thrusters and of doing away with the requirement for dielectric discharge chambers in rf thrusters, producing high-efficiency, high-thrust ion propulsion systems based on this technology can be challenging. This is certainly an area for future research.

4.7 2-D Computer Models of the Ion Thruster Discharge Chamber

The analytical models described above can generally explain the behavior and predict the overall discharge chamber performance of well-defined configurations, but multi-dimensional computer models are required to predict

thruster performance parameters such as plasma profile and double-ion content, and to examine the details of different designs. Multi-dimensional modeling of the discharge chamber requires detailed models of discharge chamber walls and magnetic fields as well as of neutral propellant gas, ions, and primary and secondary plasma electrons [56–58]. Because the important physical mechanisms are different, each species (neutral gas, ions, and primary and secondary electrons) is modeled differently. For example, most neutral gas atoms travel in straight lines until they hit a wall or are ionized, so the neutral models can take advantage of simple straight-line trajectories to develop neutral density profiles. On the other hand, primary electron trajectories are dominated by rotation around magnetic field lines, and typically particle-tracking techniques are used to determine the density and spatial distributions. Ion and secondary electron behaviors are obtained using fluid equations due to the relatively collisional behavior of the species. Therefore, ion thruster discharge models that require computer codes that use both fluid and particle-tracking models are known as "hybrid" codes.

Figure 4-40 shows a generic flow diagram for an ion thruster hybrid model [58]. From the thruster inputs (geometry), a mesh is generated inside the discharge chamber. A magnetic field solver determines the field everywhere in the chamber. Depending on the type of mesh used, the mesh generator may be iterated with the magnetic field solver to align the mesh points with the magnetic field lines. Aligning the magnetic field line simplifies the plasma diffusion calculations since the equations can be separated into parallel and perpendicular components, which can result in improved code accuracy for a sufficiently fine mesh. A neutral gas model, such as the "view-factor" model described below, determines the neutral density throughout the volume. The "ionization model" uses the magnetic field and electric field to compute the trajectories of primary electrons and their collisions with other plasma components (i.e., neutrals, ions, secondary electrons), which create ions and serve to dissipate the primary electron energy. The ionization model also determines the collisions due to secondary electrons. The ion optics model determines the transparency of the ion optics to neutrals and ions, as described in detail in Chapter 5. The ion diffusion model uses the magnetic field information and plasma properties to determine the motion of the plasma. The electron thermal model determines the energy balance for the electrons to find the distribution of temperatures of the secondary electron population. These processes are iterated until a convergent solution is found.

4.7.1 Neutral Atom Model

Accurate knowledge of the neutral gas is required in multi-dimensional plasma codes to predict the beam profiles, details of discharge plasma behavior, and

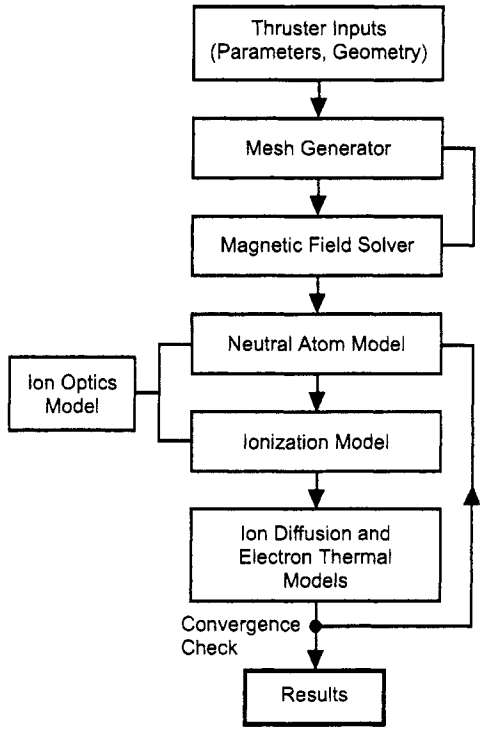

Fig. 4-40. Hybrid 2-D ion thruster discharge model flow diagram and components overview.

thruster performance. For example, many thrusters utilize localized sources and sinks of the neutral gas that produce non-uniform neutral density profiles that must be considered to understand performance.

Ion thrusters operate at internal pressures on the order of 1×10^{-4} torr or lower in order to achieve good mass utilization efficiency. In this pressure range, the neutral gas can be considered to be collisionless, and simple Knudesen-flow models are normally used to determine the average neutral gas density inside the thruster. Assuming surface adsorption, propellant atoms collide with the chamber walls and are re-emitted with a cosine distribution at the wall temperature. Collisions with the wall act to thermalize the gas to the wall temperature. Inside the discharge volume, the neutral atoms collide with electrons and ions. Some neutral atoms are "heated" by charge exchange that transfers the local ion energy to the neutral, but this process has little effect on the average gas temperature. The spatial distribution of the neutral density is dependent on the gas injection regions (sources), gas reflux from the walls, loss

of gas out the ion optic apertures, and the internal "loss" of neutral particles by ionization.

Wirz and Katz [58] developed a technique that accurately predicts the neutral gas density profiles in ion thrusters. Their model utilizes a three-dimensional generalization of the view factor formulation used in thermal models [59]. The view factor approach assumes that neutral particles travel in straight lines between surfaces, and that, after hitting a surface, they are emitted isotropically. In this technique [60], a 3-D boundary mesh and a 2-D internal mesh in the thruster discharge chamber are created for an axisymmetric discharge. The steady-state neutral fluxes are determined by balancing the injection sources, re-emission from the walls, loss through the ion optics, and loss due to ionization. The local neutral density at each of the internal mesh points is calculated by integrating its view factor from the source points (all the other mesh points in the thruster), which includes the "loss" of neutrals between the source and the mesh point due to ionization by the plasma. The ionization losses affect the neutral gas analogous to absorption diminishing the intensity of a light ray. The neutral gas code and the rest of the model components, discussed below, are iterated until a stable solution for the neutral density at each mesh point is found. One advantage of this model is that the neutral gas temperature can be tracked after the gas interacts with the wall temperatures specified at the boundary mesh points. Also, this technique is much faster than a Monte Carlo code since it requires a single matrix solution, allowing the coupling of the neutral and plasma codes to quickly determine both neutral and plasma density profiles.

An example of the axisymmetric boundary ("wall") and internal meshes for the NSTAR ion thruster from Wirz and Katz [58] is shown in Fig. 4-41. Gas enters from the hollow cathode at the center rear and the propellant injection manifold at the front corner of the discharge chamber. The neutral gas density calculated from this code for the NSTAR thruster in its high-power TH15 mode is shown in Fig. 4-42. The neutral density is highest near the injection sources at the hollow cathode and the propellant injection manifold. The neutral gas is the lowest on axis near the grids due to the NSTAR feed arrangement; however, as discussed below, the high primary electron density found in this region of the thruster produces significant ionization and "burns-out" the neutral gas. This result is critically important because the production of doubly ionized atoms increases dramatically in regions where the neutral gas is burned out and most of the electron energy goes into secondary ionization of the ions in the discharge chamber [58].

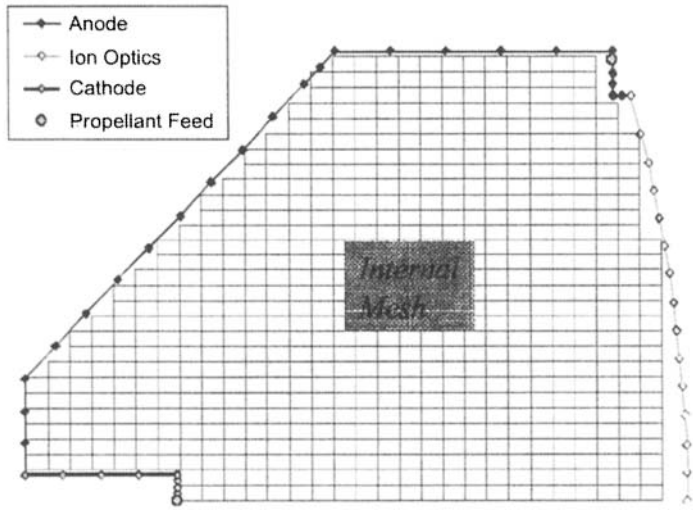

Fig. 4-41. Rectangular internal mesh in an ion thruster (from [58]).

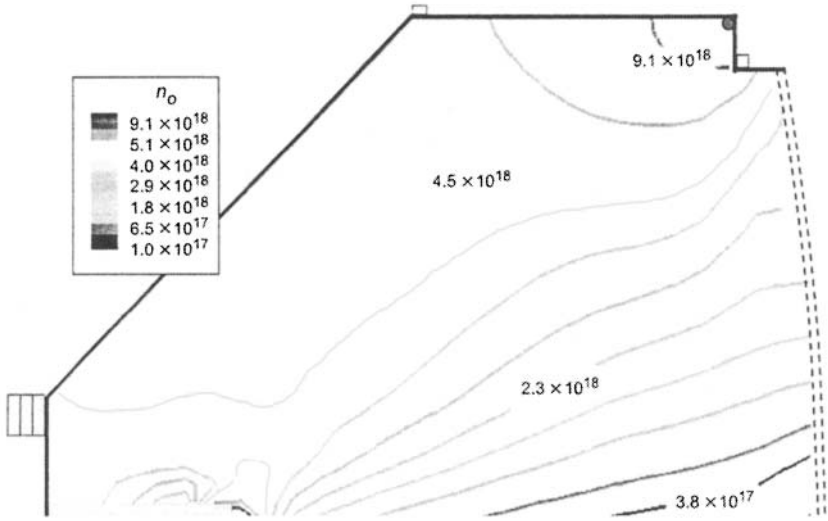

Fig. 4-42. 2-D neutral gas density profiles predicted in the NSTAR thruster for TH15 by Wirz-Katz model using the view-factor code technique [58].

4.7.2 Primary Electron Motion and Ionization Model

Particle simulation methods have been applied to the modeling of primary electron motion in ion thruster discharge chambers [58,61,62]. In particle simulations, the primary electrons are represented by particles, or macro-particles that represent a large number of primary electrons, that move in discrete time steps based on their initial conditions, applied boundary conditions, and internal electric and magnetic fields. Monte Carlo techniques are used to introduce the particles from the cathode exit into the computational domain at randomized velocities indicative of the cathode emission characteristics. During each time step, the local fields are recalculated based on the new particle position and velocity, and the particles move based on the local forces. Monte Carlo techniques typically are used to handle collisions between the particles. This procedure is repeated through many time steps until the particle is lost, after which the next particle is introduced at a unique initial velocity condition.

The primary electron motion between collisions is treated as the motion of a charged particle in the presence of an electromagnetic field, which is described by the Lorentz equation

$$m\frac{\partial \mathbf{v}}{\partial t} = q(\mathbf{E} + \mathbf{v} \times \mathbf{B}). \tag{4.7-1}$$

Wirz and Katz [58] developed an improved Boris-type particle-pushing algorithm [63] in which the motion of the particles can be described with an implicit particle-pushing algorithm, where the Lorentz forces on the particle are decomposed into electric and magnetic forces. The primary's kinetic energy is assumed to be unchanged in an elastic collision, and the particle-scattering angle is estimated by a 3-D probabilistic hard sphere scattering model [58]. In an inelastic collision, some fraction of the primary energy goes into excitation or ionization of the neutrals. Additional energy loss paths exist, as previously discussed, such as coulomb collision thermalization and anomalous processes associated with instabilities. A typical primary trajectory in the NSTAR thruster from the Wirz code [58] is shown in Fig. 4-43, where the primaries are well confined by the strong axial magnetic field component in this thruster, and collisional effects eventually scatter the primary into the cusp loss cone. Arakawa and Yamada's model for primary electron motion is derived from the Euler–Lagrange equations for the Lagrangian of a charge particle in a magnetic field [61]. However, this technique is computationally more intensive and does not improve the results in comparison with the improved Boris algorithm.

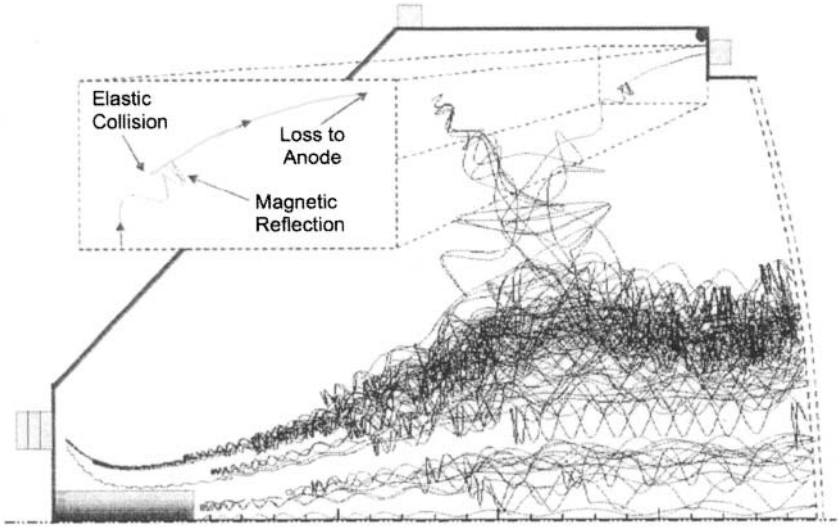

Fig. 4-43. Example primary electron trajectory calculated inside the NSTAR discharge chamber (from [60]).

The primary electron density calculated by Wirz [60] for the TH15 operating condition is shown in Fig. 4-44 and reveals that the magnetic field configuration of NSTAR tends to trap the primary electrons from the cathode on the thruster axis. This trapping of primary electrons, combined with the low neutral density on axis, causes a relatively high rate of production of double ions along the thruster axis.

The ion and secondary electron transport may be treated by an ambipolar ion diffusion equation derived from the single-ion and electron continuity and momentum equations. The steady-state continuity equation for ions is

$$\frac{\partial n}{\partial t} + \nabla \cdot (n\mathbf{v}) = \dot{n}_s, \tag{4.7-2}$$

where $\dot{n}_s$ is the ion source term. The momentum equation for ions and electrons is

$$m\left[\frac{\partial (n\mathbf{v})}{\partial t} + \nabla \cdot (n\mathbf{v}\mathbf{v})\right] = nq(\mathbf{E} + \mathbf{v} \times \mathbf{B}) - \nabla \cdot \mathbf{p} - nm\sum_n \langle n_n \rangle (\mathbf{v} - \mathbf{v}_n), \tag{4.7-3}$$

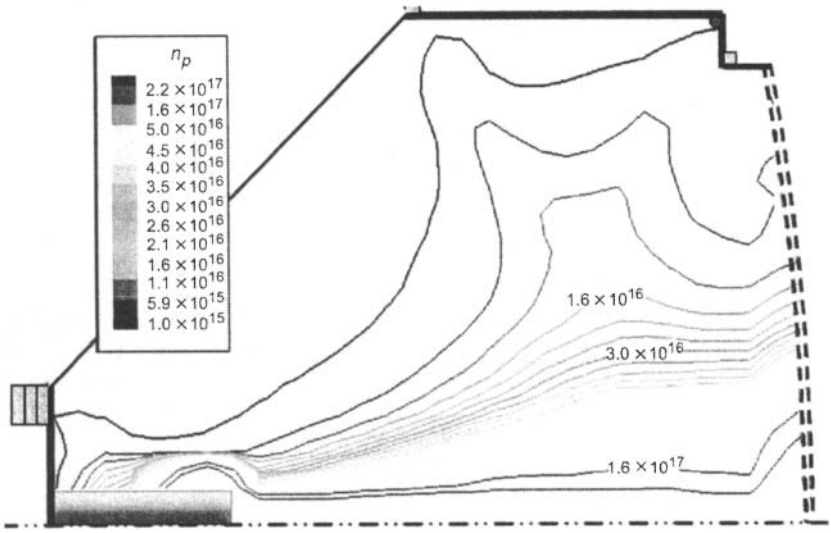

Fig. 4-44. Primary electron density (m^{-3}) for NSTAR throttle level TH15 [60].

where the subscript 'n' represents the other species in the plasma. Equations (4.7-2) and (4.7-3) can be combined to create a plasma diffusion equation

$$-\mathbf{D}_a \nabla^2 n = \dot{n}_s , \tag{4.7-4}$$

where $\mathbf{D}_a$ is the ambipolar diffusion coefficient. The diffusion coefficient is separated into parallel and perpendicular components, such that

$$\begin{aligned} \mathbf{D}_a &= \begin{bmatrix} D_{\|a} & 0 \\ 0 & D_{\perp a} \end{bmatrix} \\ D_{\|a} &= \frac{\mu_e D_i + \mu_i D_e}{\mu_i + \mu_e} \\ D_{\perp a} &= \frac{\mu_e D_{\perp i} + \mu_i D_{\perp e}}{\mu_i + \mu_e}, \end{aligned} \tag{4.7-5}$$

where the species mobilities and diffusion coefficients are determined by separately equating the parallel and cross-field fluxes of ions and electrons [64]. This simplified plasma diffusion equation assumes uniform ion and secondary electron production rates and temperatures; a derivation that does include these simplifying assumptions is given by Wirz [60].

The thermal electron energy conservation equation is derived by multiplying the Boltzmann equation by $mv^2/2$ and integrating over velocity to give

$$\frac{\partial}{\partial t}\left(\frac{nm}{2}\mathbf{v}^2+\frac{3}{2}nkT\right)+\nabla\cdot\left[\left(\frac{nm}{2}\mathbf{v}^2+\frac{5}{2}nkT\right)\mathbf{v}+\mathbf{q}\right]=en\mathbf{E}\cdot\mathbf{v}+\mathbf{R}\cdot\mathbf{v}+Q_e+Q_c, \tag{4.7-6}$$

where viscous effects are ignored and **R** is the mean change of momentum of electrons due to collisions with other species. This equation is combined with the electron fluxes to the boundaries and thermal conductivity to determine the total energy loss to the boundaries. Temperatures calculated from the electron energy equation are shown in Fig. 4-45 for the NSTAR thruster. The strong on-axis confinement of the primaries in NSTAR tends to locally heat the plasma electron population, generating a high on-axis plasma temperature.

4.7.3 Discharge Chamber Model Results

The 2-D discharge chamber model developed by Wirz and Katz [58] has been verified against beam profile and performance data for the 30-cm NSTAR thruster. The model results for the NSTAR thruster at throttle condition TH15 are plotted in Fig. 4-46, where the beam current density profile calculated by the model agrees well with experimental data obtained during the 8200-hour-

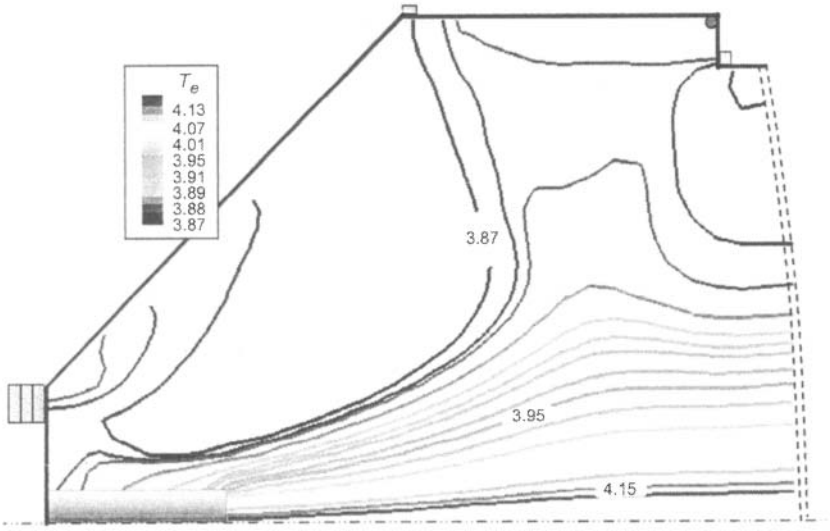

Fig. 4-45. Secondary electron temperatures (eV) for NSTAR thruster at TH15 [60].

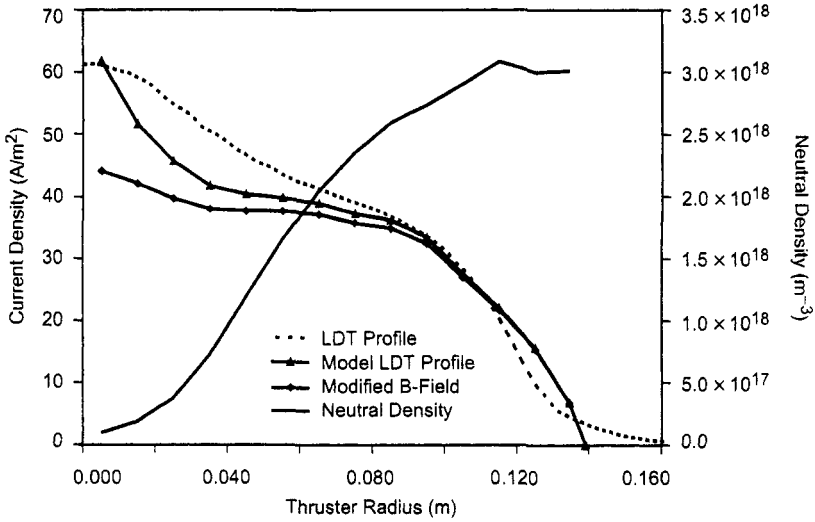

Fig. 4-46. Beam and neutral density profiles at the NSTAR grid [60].

long duration test [65]. The peaked plasma profile is due to the strong confinement of the electrons from the cathode by the NSTAR magnetic configuration, which depletes the neutral gas on axis and produces a significant number of double ions. The modified B-field profile in Fig. 4-46 is an example of the model prediction for the case of a modified magnetic field geometry that makes it easier for primary electrons to move away from the thruster axis. The ion density calculated by the Wirz–Katz model for the NSTAR magnetic is shown in Fig. 4-47. As suggested by the primary density and plasma electron temperatures in Figs. 4-44 and 4-45, the plasma density is strongly peaked on axis. Finally, the double-to-total ion ratio distribution throughout the discharge chamber is shown in Fig. 4-48. These results agree with experimental data that suggest the on-axis peak in the NSTAR beam profile is due to high centerline double-ion content.

Analysis by the Wirz–Katz model results shows that the original NSTAR magnetic field configuration tends to trap primary electrons on axis, which increases local electron temperature, ionization rate, and the generation of double ions in this region. This trapping of primary electrons also manifests in a neutral atom depletion on axis, as was shown in Fig. 4-46. The "modified" configuration in this figure shows the power of a good computer model to improve ion thruster design. By allowing the primary electrons to move away from the thruster axis, the ionization is spread more uniformly throughout the discharge chamber. The flatter profile results from a decrease in primary

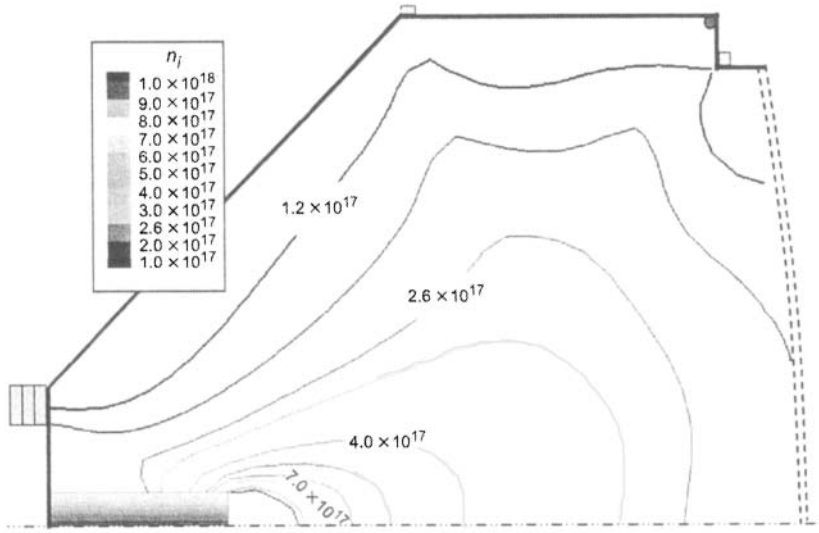

Fig. 4-47. Ion plasma density (m^{-3}) for the NSTAR at throttle level TH15 [60].

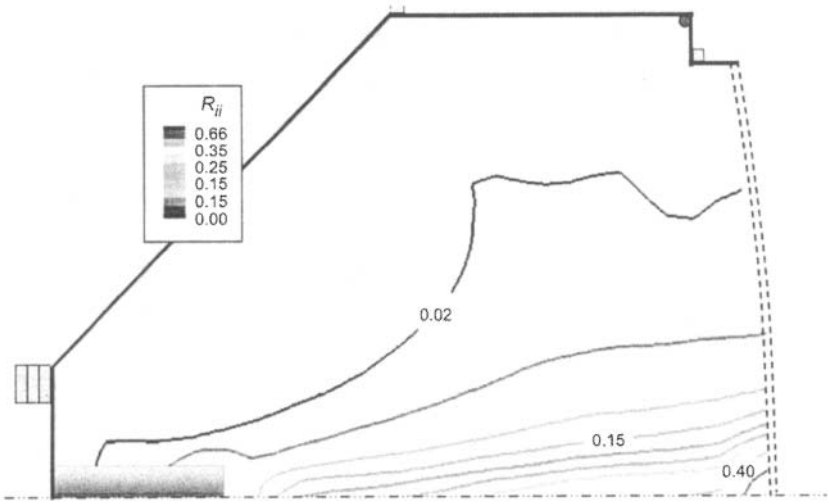

Fig. 4-48. Double ion density ratio (n^{++}/n^{+}) for NSTAR operating at a power level of TH15 [60].

electron density, and hence double-ion content, on the thruster centerline. Wirz and Goebel [66] developed "modified" NSTAR designs that guide primary electrons away from the thruster centerline to improve the profile. These designs were validated by experiments [67], and also resulted in lower double-ion content and higher neutral density along the thruster axis as predicted by the model.

References

[1] H. R. Kaufman, "An Ion Rocket with an Electron-Bombardment Ion Source," *NASA Technical Note,* D-585, January 1961.

[2] P. D. Reader, *NASA Technical Note*, TN D-1162, 1962.

[3] R. T. Bechtel, "Discharge Chamber Optimization of the Sert-II Thruster," *Journal of Spacecrafts and Rockets*, vol. 5, p. 795–800, 1968.

[4] W. Knauer, R. L. Poeschel, and J. W. Ward, "The Radial Field Kaufman Thruster," AIAA-1969-259, 7th Electric Propulsion Conference, Williamsburg, Virginia, March 3–5, 1969.

[5] R. D. Moore, "Magneto-Electrostatic Contained Plasma Ion Thruster," AIAA-1969-260, 1969.

[6] J. S. Sovey, "Improved Ion Containment Using a Ring-Cusp Ion Thruster," *Journal of Spacecraft*, vol. 21, pp. 488–495, 1984.

[7] J. S. Sovey and H. J. King, "Status of 30-cm Mercury Ion Thruster Development," NASA TMX-71603, October 1974.

[8] T. D. Masek, R. L. Poeschel, C. R. Collett, and D. E. Snelker, "Evolution and Status of the 30-cm Engineering Model Ion Thruster," AIAA-1976-1006, International Electric Propulsion Conference, Key Biscayne, Florida, November 14–17, 1976.

[9] V. K. Rawlin, "Operation of the J-Series Thruster Using Inert Gases," AIAA-1982-1929, International Electric Propulsion Conference, New Orleans, Louisiana, November 17–19, 1982.

[10] J. R. Beattie and J. N. Matossian, "Inert-Gas Ion Thruster Technology," NASA CR191093, March 1993.

[11] J. R. Beattie and R. L. Poeschel, "Ring-Cusp Ion Thrusters," Paper 84-71, *International Electric Propulsion Conference*, May 1984.

[12] J. N. Matossian and J. R. Beattie, "Characteristics of Ring-Cusp Discharge Chambers," *Journal of Propulsion and Power*, vol. 7, pp. 968–974, 1991.

[13] M. J. Patterson, T. W. Haag, V. K. Rawlin, and M. T. Kussmaul, "NASA 30-cm Ion Thruster Development Status," AIAA-1994-2849, 30th Joint Propulsion Conference, Indianapolis, Indiana, June 1994.

[14] J. R. Beattie, J. N. Matossian, and R. R. Robson, "Status of Xenon Ion Propulsion Technology," *Journal of Propulsion and Power*, vol. 7, pp. 145–150, 1990.

[15] T. D. Maske, "Plasma Properties and Performance of Mercury Ion Thrusters," *AIAA Journal*, vol. 9, pp. 205–212, 1971.

[16] J. Ward and T. Masek, "A Discharge Computer Model for an Electron Bombardment Thruster," AIAA-1976-1009, AIAA International Electric Propulsion Conference, Key Biscayne, Florida, November 14–17, 1976.

[17] J. N. Matossian and J. R. Beattie, "Model for Computing Volume Averaged Plasma Properties in Electron-Bombardment Ion Thrusters," *Journal of Propulsion and Power*, vol. 5, pp.188–196, 1989.

[18] J. R. Brophy, *Ion Thruster Performance Model*, NASA CR-174810, Ph.D. Thesis, Colorado State University, Fort Collins, Colorado, December 1984.

[19] J. R. Brophy and P. J. Wilbur, "Simple Performance Model for Ring and Line Cusp Ion Thrusters," *AIAA Journal*, vol. 23, no. 11, pp. 1731–1736, 1985.

[20] D. M. Goebel, J. E. Polk, and A. Sengupta, "Discharge Chamber Performance of the NEXIS Ion Thruster," AIAA-2004-3813, 40th AIAA Joint Propulsion Conference, Fort Lauderdale, Florida, July 11–14, 2004.

[21] D. M. Goebel, R. E. Wirz, and I. Katz, "Analytical Ion Thruster Discharge Performance Model," AIAA-2006-4486, 42nd Joint Propulsion Conference, Sacramento, California, July 10–13, 2006.

[22] D. M. Goebel, "Ion Source Discharge Performance and Stability," *Physics of Fluids*, vol. 25, no. 6, pp. 1093–1102, 1982.

[23] A. T. Forrester, *Large Ion Beams*, New York: John Wiley and Sons, 1988.

[24] M. Lieberman and A. Lichtenberg, *Principles of Plasma Discharges and Materials Processing*, New York: John Wiley and Sons, 1994.

[25] Maxwell 3-D is a product of Ansoft Corp., http://www.ansoft.com/products/em/max3d/overview.cfm.

[26] R. E. Wirz and D. M. Goebel, "Ion Thruster Discharge Performance per Magnetic Field Geometry," AIAA-2006-4487, 42nd Joint Propulsion Conference, Sacramento, California, July 10–13, 2006.

[27] K. Leung, N. Hershkowitz, and K. MacKenzie, "Plasma Confinement by Localized Cusps," *Physics of Fluids*, vol. 19, no. 7, pp. 1045–1053, 1976.

[28] D. Rapp and P. Englander-Golden, "Total Cross Sections for Ionization and Attachment in Gases by Electron Impact. I. Positive Ionization," *The Journal of Chemical Physics*, vol. 43, no. 5, pp. 1464–1479, 1965.

[29] M. Hayashi, "Determination of Electron-Xenon Total Excitation Cross-Sections, from Threshold to 100-eV, from Experimental Values of Townsend's a," *Journal of Physics D: Applied Physics*, vol. 16, pp. 581–589, 1983.

[30] R. R. Peters, P. J. Wilbur, and R. P. Vahrenkamp, "A Doubly Charged Ion Model for Ion Thrusters," *Journal of Spacecraft and Rockets*, vol. 14, no. 8, pp. 461–468, 1977.

[31] P. Clausing, "The Flow of Highly Rarefied Gases Through Tubes of Arbitrary Length," *Journal of Vacuum Science and Technology*, vol. 8, pp. 636–646, 1971.

[32] L. Spitzer, *Physics of Fully Ionized Gases*, New York: Interscience Publishers, p. 80, 1956.

[33] D. L. Book, *NRL Plasma Formulary*, Naval Research Laboratory, Washington D.C., pp. 33–34, 38, 1987.

[34] J. R. Brophy, I. Katz, J. E. Polk, and J. R. Anderson, "Numerical Simulations of Ion Thruster Accelerator Grid Erosion," AIAA Paper 2002-4261, 38th Joint Propulsion Conference, July 7–10, 2002.

[35] J. J. Anderson, I. Katz, and D. Goebel, "Numerical Simulation of Two-Grid Ion Optics Using a 3D Code," AIAA-2004-3782, 40th Joint Propulsion Conference, Ft. Lauderdale, Florida, July 2004.

[36] D. M. Goebel, K. Jameson, I. Katz, and I. Mikellades, "Hollow Cathode Theory and Modeling: I. Plasma Characterization with Miniature Fast-Scanning Probes," *Journal of Applied Physics*, vol. 98, no. 10, 113302, 2005.

[37] I. Mikellades, I. Katz, D. M. Goebel, and J. E. Polk, "Hollow Cathode Theory and Modeling: II. A Two-Dimensional Model of the Emitter Region," *Journal of Applied Physics*, vol. 98, no. 10, 113303, 2005.

[38] J. E. Polk, D. M. Goebel, I. Katz, J. Snyder, A. Schneider, L. Johnson, and A. Sengupta, "Performance and Wear Test Results for a 20-kW Class Ion Engine with Carbon-Carbon Grids," AIAA-2005-4393, 41st Joint Propulsion Conference, Tucson, Arizona, July 10–13, 2005.

[39] J. R. Brophy, "NASA's Deep Space 1 Ion Engine," *Review of Scientific Instruments*, vol. 73, pp. 1071–1078, 2002.

[40] K. K. Jameson, D. M. Goebel, and R. M. Watkins, "Hollow Cathode and Keeper-Region Plasma Measurements," AIAA-2005-3667, 41st AIAA Joint Propulsion Conference, Tucson, Arizona, July 10–13, 2005.

[41] P. J. Wilbur and J. R. Brophy, "The Effect of Discharge Chamber Wall Temperature on Ion Thruster Performance," *AIAA Journal*, vol. 24, no. 2, pp. 278–283, 1986.

[42] J. M. Lafferty, *Foundations of Vacuum Science and Technology*, New York: John Wiley and Sons, 1998.

[43] Y. Hayakawa, K. Miyazaki, and S. Kitamura, "Measurements of Electron Energy Distributions in a 14-cm Diameter Ring Cusp Ion Thruster," *Journal of Propulsion and Power*, vol. 8, pp. 118–126, 1992.

[44] D. Herman, "Discharge Cathode Electron Energy Distribution Functions in a 40-cm NEXT-type Ion Engine," AIAA-2005-4252, 41st AIAA Joint Propulsion Conference, Tucson, Arizona, July 10–13, 2005.

[45] D. Bohm, Chapter 1, *The Characteristics of Electric Discharges in Magnetic Fields*, edited by A. Guthrie and R. Wakerling, New York: McGraw-Hill, pp. 1–76, 1949.

[46] N. L. Milder, "A Survey and Evaluation of Research on the Discharge Chamber Plasma of a Kaufman Thruster," AIAA-69-494, 5th Propulsion Joint Specialist Conference, U.S. Air Force Academy, Colorado Springs, Colorado, June 9–13, 1969.

[47] H. R. Kaufman, "Performance of Large Inert-Gas Thrusters," AIAA-81-0720, 15th International Electric Propulsion Conference, Las Vegas, Nevada, April 21–23, 1981.

[48] T. Ozaki, E. Nishida, Y. Gotoh, A. Tsujihata, and K. Kajiwara, "Development Status of a 20 mN Xenon Ion Thruster," AIAA-2000-3277, 36th Joint Propulsion Conference, Huntsville, Alabama, July 16–19, 2000.

[49] W. F. Divergilio, H. Goede, and V. V. Fosnight, "High Frequency Plasma Generators for Ion Thrusters," NASA #CR-167957, November 1981.

[50] H. J. Leiter, R. Killinger, H. Bassner, J. Miller, R. Kulies, and T. Fröhlich, "Evaluation of the Performance of the Advanced 200 mN Radio Frequency Ion Thruster RIT_XT," AIAA-2002-3836, 38th Joint Propulsion Conference, Indianapolis, Indiana, July 7–10, 2002.

[51] M. Tuszewski, "Inductive Electron Heating Revisited," *Physics of Plasmas*, vol. 4, pp. 1922–1928, 1997.

[52] H. Goede, "30-cm Electron Cyclotron Plasma Generator," *Journal of Spacecraft*, vol. 24, no. 5, p. 437, 1987.

[53] H. Kuninaka and S. Satori, "Development and Demonstration of a Cathode-less Electron Cyclotron Resonance Ion Thruster," *Journal of Propulsion and Power*, vol. 14, pp. 1022–1026, 1998.

[54] H. Kuninaka, I. Funaki, and K. Toki, "Life Test of Microwave Discharge Ion Thrusters for MUSES-C in Engineering Model Phase," AIAA-99-2439, 35th Joint Propulsion Conference, Los Angeles, California, June 20–24, 1999.

[55] H. Kuninaka, I. Funaki, K. Nishiyama, Y. Shimizu, and K. Toki, "Results of 18,000 Hour Endurance Test of Microwave Discharge Ion Thruster Engineering Model," AIAA-2000-3276, 36th Joint Propulsion Conference, Huntsville, Alabama, July 16–19, 2000.

[56] Y. Arakawa and K. Ishihara, "A Numerical Code for Cusped Ion Thrusters," IEPC-91-118, 22nd International Electric Propulsion Conference, Viareggio, Italy, October 14–17, 1991.

[57] Y. Arakawa and P. J. Wilbur, "Finite Element Analysis of Plasma Flows in Cusped Discharge Chambers," *Journal of Propulsion and Power*, vol. 7, no. 1, pp. 125–128, 1991.

[58] R. Wirz and I. Katz, "Plasma Processes in DC Ion Thruster Discharge Chambers," AIAA-2005-3690, 41st AIAA Joint Propulsion Conference, Tucson, Arizona, July 10–13, 2005.

[59] R. Siegel and J. R. Howell, *Thermal Radiation Heat Transfer*, 4th Edition, New York: Taylor & Francis, pp. 226–227, 2002.

[60] R. Wirz, "Discharge Plasma Processes of Ring-Cusp Ion Thrusters," Ph.D. Dissertation, Aeronautics, California Institute of Technology, Pasadena, California, 2005.

[61] Y. Arakawa and T. Yamada, "Monte Carlo Simulation of Primary Electron Motions in Cusped Discharge Chambers," AIAA-1990-2654, 21st International Electric Propulsion Conference, Orlando, Florida, July 18–20, 1990.

[62] S. Mahalingam and J. A. Menart, "Primary Electron Modeling in the Discharge Chamber of an Ion Engine," AIAA-2002-4262, 38th Joint Propulsion Conference, Indianapolis, Indiana, July 7–10, 2002.

[63] J. P. Boris, "Relativistic Plasma Simulations-Optimization of a Hybrid Code," Proc. 4th Conf. on Numerical Simulation of Plasmas, NRL Washington, Washington DC, 1970.

[64] S. I. Braginskii, "Transport Processes in Plasmas," *Reviews of Plasma Physics*, vol. 1, pp. 205–311, 1965.

[65] J. Polk, J. R. Anderson, J. R. Brophy, V. K. Rawlin, M. J. Patterson, J. Sovey, and J. Hamley "An Overview of the Results from an 8200 Hour Wear Test of the NSTAR Ion Thruster," AIAA Paper 99-2446, 35th Joint Propulsion Conference, Los Angeles, California, 1999.

[66] R. E. Wirz and D. M. Goebel, "Ion Thruster Discharge Performance per Magnetic Field Geometry," AIAA-2006-4487, 42nd Joint Propulsion Conference, Sacramento, California, July 10–13, 2006.

[67] A. Sengupta, "Experimental Investigation of Discharge Plasma Magnetic Confinement in an NSTAR Ion Thruster," AIAA-2005-4069, 41st Joint Propulsion Conference, Tucson, Arizona, July 10–13, 2005.

Problems

1. Show the conditions under which the ambipolar velocity of the ions flowing to the wall in a transverse magnetic field reverts to the Bohm velocity.

2. An ion thruster discharge chamber has an internal pressure of 10^{-4} torr, a plasma density of 2×10^{17} m^{-3}, gas and ion temperatures of 500 K, electron temperature of 4 eV, and a transverse magnetic field of 40 G near the wall with a diffusion length of 2 cm. What is the average transverse ion velocity and the ion confinement factor (ratio of v_i / v_{Bohm})?

3. In Fig. 4-16 it is shown that the reaction rate for ionization exceeds the reaction rate for excitation if the electron temperature exceeds about 9 eV. Why not run discharges with $T_e \geq 9$ eV where ionization is greater than excitation? Give a quantitative answer for an idealized thruster producing 1 A with 10-cm-diameter grids on a discharge chamber 10 cm in diameter and 15 cm long with the anode being the full cylindrical and back wall area. Assume an 80% grid transparency and a neutral density of 10^{18} cm^{-3}, and plot the discharge loss as a function of electron temperature from 3 to 10eV. Explain why. (Hint: examine the various loss terms.)

4. What is the electron temperature in a xenon ion thruster that has an ion loss area of 200 cm^2, a plasma volume of 10^4 cm^3, neutral gas density of 10^{13} cm^{-3}, and a 5% primary electron density at 15 eV?

5. A thruster plasma has a volume of 10^4 cm^3, has a neutral density of 10^{12} cm^{-3}, is 10% ionized with 15-V primary electrons, has a 5-eV electron temperature, and has a primary loss area of 10 cm^2. What are the primary electron confinement time, the primary electron collision time (assume a collision cross section of 2×10^{-16} cm^2), and the primary electron slowing down time? What is the total effective confinement time for a primary electron, and which of the three contributors to the total confinement time is the most important?

6. For a xenon ion thruster with a grid area of 500 cm^2 with a screen grid transparency of 70%, what is the discharge current required to produce a 2.5-A ion beam? Assume a discharge voltage of 25 V, a hollow cathode voltage drop of 10 V, a plasma potential of 5 V, a primary electron density of 5%, and an excitation energy of 10 eV. You can neglect the ion and primary electron loss to the anode, the ion current back to the cathode, and any losses to the back wall of the cylindrical discharge chamber with the same diameter as the grids.

7. A xenon ion thruster discharge chamber produces a 5×10^{17} m^{-3} plasma 20 cm in diameter with an electron temperature of 5.5 eV. What is the beam current and average current density if the screen grid transparency is 80%, and what flatness parameter is required to maintain the peak current density under 10 mA/cm^2?

8. A xenon ion thruster has a grid diameter of 20 cm with a transparency of 75%, an electron temperature of 3 eV in a 30-cm-diameter, 30-cm-long cylindrical discharge chamber with an ion confinement factor of 0.1. What does the cusp anode area have to be to maintain the plasma potential at the sheath edge at 6 V? You can assume that the discharge current is 10 times the beam current and neglect the back wall loss area and primary electron effects. Assuming the ion temperature is 0.1 eV and that there are 3 magnetic rings around the cylindrical chamber, what is the magnetic field at the wall required to produce this cusp anode area?

9. An rf xenon ion thruster has a grid diameter of 10 cm, a grid transparency of 70%, and a cylindrical discharge chamber with a diameter and length of 10 cm. Assuming an electron temperature of 4 eV, an ion confinement factor of 0.5, and a neutral density of 6×10^{18} m^{-3}, what is the plasma potential and discharge loss? If the cylindrical discharge chamber is made into a cone 10 cm long from the grid diameter, how do the plasma potential and discharge loss change?

10. A microwave ion thruster produces 2 A from an 80% transparent grid using a 4-GHz microwave source. If the thruster is running at 90% of cutoff with a flatness parameter of 0.6, what must the diameter of the grid be to produce this beam current?

Fundamentals of Electric Propulsion: Ion and Hall Thrusters
by Dan M. Goebel and Ira Katz
Copyright © 2008 John Wiley & Sons, Inc.

Chapter 5
Ion Thruster Accelerator Grids

Ion thrusters are characterized by the electrostatic acceleration of ions extracted from the plasma generator [1]. An illustration of a direct current (DC) electron bombardment ion thruster showing the ion accelerator, the plasma generator, and the neutralizer cathode was shown in Fig. 1-1. The ion accelerator consists of electrically biased multi-aperture grids, and this assembly is often called the *ion optics*. The design of the grids is critical to the ion thruster operation and is a trade between performance, life, and size. Since ion thrusters need to operate for years in most applications, life is often a major design driver. However, performance and size are always important in order to satisfy the mission requirements for thrust and specific impulse (Isp) and to provide a thruster size and shape that fits onto the spacecraft.

There are many factors that determine the grid design in ion thrusters. The grids must extract the ions from the discharge plasma and focus them through the downstream accelerator grid (accel grid) and decelerator grid (decel grid) (if used). This focusing has to be accomplished over the range of ion densities produced by the discharge chamber plasma profile that is in contact with the screen grid, and also over the throttle range of different power levels that the thruster must provide for the mission. Since the screen grid transparency was shown in Chapter 4 to directly impact the discharge loss, the grids must minimize ion impingement on the screen grid and extract the maximum number of the ions that are delivered by the plasma discharge to the screen grid surface. In addition, the grids must minimize neutral atom loss out of the discharge chamber to maximize the mass utilization efficiency of the thruster. High ion transparency and low neutral transparency drives the grid design toward larger screen grid holes and smaller accel grid holes, which impacts the optical focusing of the ions and the beam divergence. The beam divergence also should be minimized to reduce thrust loss and plume impact on the spacecraft or solar arrays, although some amount of beam divergence can usually be

accommodated. Finally, grid life is of critical importance and often drives thruster designers to compromises in performance or alternative grid materials. In this chapter, the factors that determine grid design and the principles of the ion accelerators used in ion thrusters will be described.

5.1 Grid Configurations

To accelerate ions, a potential difference must be established between the plasma produced inside the thruster plasma generator and the ambient space plasma. As shown in Chapter 3, simply biasing the anode of a DC plasma generator or the electrodes of a radio frequency (rf) plasma generator relative to a spacecraft or plasma in contact with the space potential does not result in ion beam generation because the voltage will just appear in the sheath at the plasma boundary with the walls. If the potential is small compared to the electron temperature T_e, then a Debye sheath is established, and if the potential is very large compared to T_e, then a Child–Langmuir sheath exists. Therefore, to accelerate ions to high energy, it is necessary to reduce the dimension of an aperture at the plasma boundary to the order of the Child–Langmuir distance to establish a sheath that will accelerate the ions with reasonable directionality (good focusing) and reflect the electrons from the plasma. Figure 5-1 shows the Child–Langmuir length calculated from Eq. (3.7-34) for two singly charged ion current densities at an acceleration voltage of 1500 V. For xenon, the characteristic aperture dimension at this voltage is on the order of 2 to 5 mm and will decrease if the applied voltage is reduced or the current in the aperture is increased.

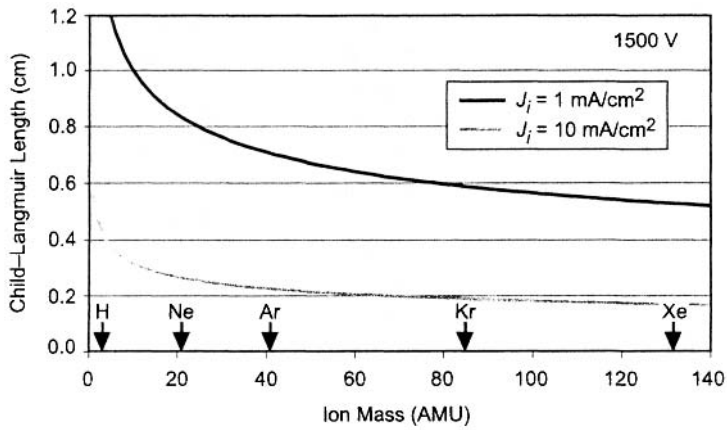

Fig. 5-1. Child–Langmuir sheath length versus ion mass for two ion current densities at 1500-V acceleration voltage.

The ion current obtainable from each grid aperture is then limited by space charge. For a 0.25-cm-diameter aperture extracting the space-charge-limited xenon current density of about 5 mA/cm^2 at 1500 V [from Eq. (3.7-56)], the total ion current per aperture is only 0.25 mA. Assuming this produces a well-focused beamlet, the thrust produced by this current and voltage according to Eq. (2.3-9) is only about 16 μnewtons. Therefore, multiple apertures must be used to obtain higher beam currents from the ion engine to increase the thrust. For example, to extract a total of 1 A of xenon ion current for this case would require over 4000 apertures, which would produce over 60 mN of thrust. In reality, for reliable high-voltage operation, and due to non-uniformities in the plasma generator producing varying ion current densities to the boundary, the current density is usually chosen to be less than the Child–Langmuir space charge maximum, and an even larger number of apertures are required. This ultimately determines the size of the ion thruster.

Figure 5-2 shows a simplified one-dimensional (1-D) view of one of these biased apertures facing the thruster plasma. The Child–Langmuir sheath is established by the bias potential between the thruster plasma and the accelerator grid and is affected by the current density of the xenon ions arriving at the sheath edge from the Bohm current. Ions that arrive on axis with the aperture are accelerated through to form the beam. However, ions that miss the aperture are accelerated into the accel grid and can erode it rapidly. For this reason, a "screen" grid with apertures aligned with the accel grid is placed upstream of the accel grid to block these ions. This is the classic two-grid accelerator system [1,2]. The screen grid is normally either allowed to float electrically or is biased to the cathode potential of the plasma generator to provide some confinement of the electrons in the plasma and so that ions that strike it have a relatively low energy and cause little sputtering. In practice, the grids are made of refractory metals or carbon-based materials, and the apertures are close-packed in a

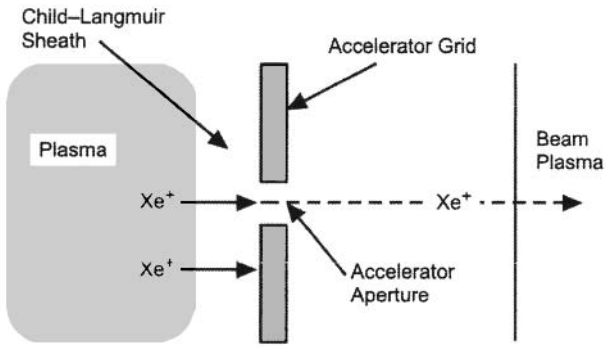

Fig. 5-2. Simplified 1-D view of an accelerator aperture in contact with a plasma.

hexagonal structure to produce a high transparency to the ions from the plasma generator. These grids are also normally dished to provide structural rigidity to survive launch loads and to ensure that they expand uniformly together during thermal loading [1,3].

The electrical configuration of an ion thruster accelerator is shown schematically in Fig. 5-3. The high-voltage bias supply (called the screen supply) is normally connected between the anode and the common of the system, which is usually connected to the neutralizer cathode (called "neutralizer common") that provides electrons to neutralize the beam. Positive ions born in the discharge chamber at high positive voltage are then accelerated out of the thruster. The accel grid is biased negative relative to the neutralizer common to prevent the very mobile electrons in the beam plasma from back-streaming into the thruster, which produces localized heating in the discharge chamber by energetic electron bombardment, and ultimately overloads the

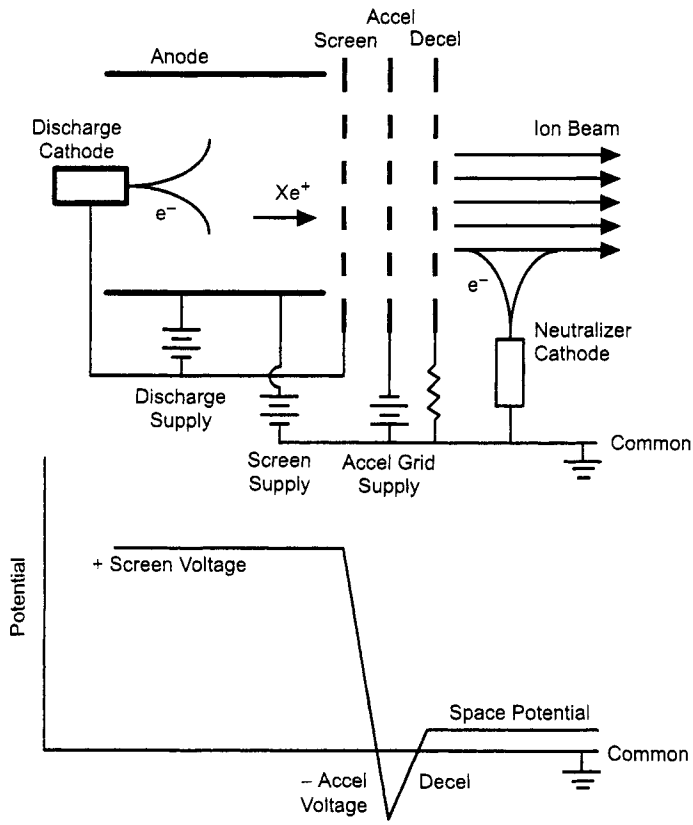

Fig. 5-3. Electrical schematic of a DC discharge ion thruster without the cathode heater and keeper supplies.

screen supply if the backstreaming current becomes large. The ion beam is current neutralized and quasi-neutral (nearly equal ion and electron densities) by the electrons extracted from the neutralizer cathode. Fortunately, the thruster self-biases the neutralizer common potential sufficiently negative relative to the beam potential to produce the required number of electrons to current neutralize the beam.

Figure 5-3 showed a generic thruster that includes a three-grid accelerator system, where a final grid called the "decel grid" is placed downstream of the accel grid. This grid shields the accel grid from ion bombardment by charge-exchanged ions produced in the beam backflowing toward the thruster, and eliminates the downstream "pits-and-grooves erosion" that will be discussed in Section 5.6. Three-grid systems then potentially have longer accel grid life than two grid systems and generate less sputtered material into the plume that can deposit on the spacecraft. These benefits are offset by the increased complexity of including the third grid.

In actual design, the diameter of each accel grid aperture is minimized to retain unionized neutral gas in the plasma generator, and the screen grid transparency is maximized so that that the grids extract the maximum possible number of ions from the plasma. The electrode diameters and spacing are then optimized to eliminate direct interception of the beam ions on the accel grid, which would cause rapid erosion due to the high ion energy. A schematic example of a three-grid system showing the ion trajectories calculated by a two-dimensional (2-D) ion optics code [4] is shown in Fig. 5-4. The ions are focused sufficiently by this electrode design to pass through the accel grid without direct interception. On the downstream side of the accel grid, the negative accel-grid bias applied to avoid electron backstreaming results in a relatively small deceleration of the ions before they enter the quasi-neutral beam potential region. This high transparency, strong "accel–decel" geometry typical of ion thrusters results in some beamlet divergence, as suggested by the figure. However, this small beamlet angular divergence of typically a few degrees causes negligible thrust lost because the loss scales as $\cos\theta$, and because most of the beam divergence discussed in Chapter 2 related to the thrust correction factor is due to the dishing of the grids.

The amount of current that an ion accelerator can extract and focus into a beam for a given applied voltage is related to the space-charge effects characterized by the Child–Langmuir equation and is called the perveance:

$$P \equiv \frac{I_b}{V^{3/2}}. \tag{5.1-1}$$

The maximum perveance that can be achieved by an accelerator is given by the coefficient in the Child–Langmuir equation:

$$P_{\max} \equiv \frac{4\varepsilon_o}{9}\sqrt{\frac{2q}{M}}\left[\mathrm{A/V^{3/2}}\right]. \tag{5.1-2}$$

For an electron accelerator, this coefficient is the familiar value of 2.33×10^{-6} $\mathrm{A/V^{3/2}}$, and for singly charged xenon ions it is 4.8×10^{-9} $\mathrm{A/V^{3/2}}$. For round apertures, the Child–Langmuir equation can be written

$$J = \frac{I_b}{\left(\pi D^2/4\right)} = \frac{4\varepsilon_o}{9}\sqrt{\frac{2q}{M}}\frac{V^{3/2}}{d^2}\left[\mathrm{A/m^2}\right], \tag{5.1-3}$$

where d is the effective grid gap and D is the beamlet diameter. Inserting Eq. (5.1-3) into Eq. (5.1-1), the maximum perveance for round apertures is

$$P_{\max} \equiv \frac{\pi\varepsilon_o}{9}\sqrt{\frac{2q}{M}}\left(\frac{D^2}{d^2}\right)\left[\mathrm{A/V^{3/2}}\right]. \tag{5.1-4}$$

Therefore, to maximize the perveance of the accelerator, it is desirable to make the grid gap smaller than the aperture diameters, as illustrated in the example configuration shown in Fig. 5-4.

The ion trajectories plotted in Fig. 5-4 that do not intercept either of the grids, and the minimal beamlet divergence, result from operating at or near the optimal ion current density and voltage for the grid geometry shown. Operating at significantly less than the optimal perveance, called "under-perveance" and

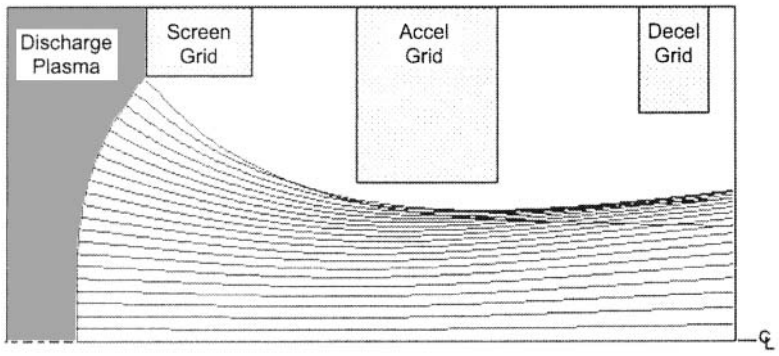

Fig. 5-4. Ion trajectories from a plasma sheath (on the left) in a half-beamlet inside an example three-grid accelerator.

corresponding to higher voltages or lower beamlet currents than the optimal combination, increases the Child–Langmuir (CL) length and pushes the sheath to the left farther into the plasma. In the extreme case, this situation can launch ions at a very large angle from the edge region near the screen aperture and cause "cross-over" trajectories, which can then produce excessive erosion of the accel grid by direct ion impingement. Likewise, operating at higher than the optimal perveance, corresponding to higher beamlet currents or lower voltages than optimal, reduces the Child–Langmuir sheath thickness, and the plasma boundary pushes toward the screen aperture. This "over-perveance" condition flattens the sheath edge and accelerates ions directly into the accel grid, again causing excessive erosion. The optical performance and life of any grid design, therefore, is acceptable only over a limited range in voltage and current density, which will be discussed in Section 5.3. For this reason, the uniformity of the plasma over the grid area is important to avoid either cross-over or direct interception in different regions of the ion optics that strongly degrade the life of the grids.

In the two- or three-grid configurations, the geometry of the grid apertures and gaps is intended to eliminate or at least minimize direct impingement by beam ions on the most negative potential electrode in the system, namely, the accel grid. This is required to minimize sputtering of the grid by the high-energy beam ions. The screen grid does receive ion bombardment from the discharge plasma due to its finite transparency, but the ions arrive with only an energy of the order of the discharge voltage in DC discharge thrusters or the floating potential in rf or microwave thrusters. Sputter erosion of the screen grid then becomes an issue only at high discharge voltages or due to the production of high-energy ions in the hollow cathode region [5,6] that can bombard the screen grid. Likewise, the decel grid is biased near the beam plasma potential and backflowing ions produced in the beam by charge exchange impact with very low energy, which causes little or no sputtering. For two grid systems, the backflowing ions bombard the accel grid with essentially the grid bias voltage. This can cause significant sputtering of the downstream face of the accel grid and may determine the grid life.

The decelerating field produced downstream of the accelerator grid by the accel grid bias acts as a weak defocusing lens for the ions, but keeps electrons emitted by the neutralizer from entering the high field region and backstreaming at high energy into the discharge chamber. This decelerating field is set up either by applying a potential between the accelerator grid and the decel grid or by applying the bias between the accelerator grid and the hollow cathode neutralizer and allowing the low energy plasma downstream of the accelerator grid to act as a virtual anode. Unfortunately, ions generated between the grids by either charge exchange with unionized neutral gas escaping the

plasma generator or by ionization from the most energetic backstreaming electrons do strike the accel grid and erode it. Charge exchange ion erosion of the accel grid ultimately limits the grid life, which will be discussed in Section 5.6.

5.2 Ion Accelerator Basics

The thruster ion optics assembly serves three main purposes:

1) Extract ions from the discharge chamber
2) Accelerate ions to generate thrust
3) Prevent electron backstreaming

The ideal grid assembly would extract and accelerate all the ions that approach the grids from the plasma while blocking the neutral gas outflow, accelerate beams with long life and with high current densities, and produce ion trajectories that are parallel to the thruster axis with no divergence under various thermal conditions associated with changing power levels in the thruster. In reality, grids are non-ideal in each of these areas. Grids have finite transparency; thus, some of the discharge chamber ions hit the upstream "screen grid" and are not available to become part of the beam. The screen grid transparency, T_s, is the ratio of the beam current, I_b, to the total ion current, I_i, from the discharge chamber that approaches the screen grid:

$$T_s = \frac{I_b}{I_i}. \tag{5.2-1}$$

This ratio is determined by comparing the ion beam current with the screen grid current. The transparency depends on the plasma parameters in the discharge chamber because the hemispherical sheath edge is normally pushed slightly into the plasma by the applied voltage if the screen grid is relatively thin. The pre-sheath fields in the plasma edge then tend to steer some ions that would have gone to the screen grid into the beam. For this reason, the effective transparency of the screen grid typically exceeds the optical transparency for relatively large apertures and thin grid thicknesses. In addition, the screen grid current must be measured with the screen grid biased negative relative to cathode potential to reflect energetic electrons in the tail of the Maxwellian distribution in the plasma. The goal for screen grid design is to maximize the grid transparency to ions by minimizing the screen thickness and the webbing between screen grid holes to that required for structural rigidity.

The maximum beam current density is limited by the ion space charge in the gap between the screen and accelerator grids [2], which was discussed above

with respect to the perveance that was specified by the Child–Langmuir equation in which the sheath was considered essentially planar. The problem is that the sheath shape in the screen aperture is not planar, as seen in Fig. 5-4, and the exact shape and subsequent ion trajectories have to be solved by 2-D axi-symmetric codes. However, a modified sheath thickness can be used in the Child–Langmuir equation to approximately account for this effect, which is written as

$$J_{\max} = \frac{4\varepsilon_o}{9}\sqrt{\frac{2e}{M}}\frac{V_T^{3/2}}{\ell_e^2}, \tag{5.2-2}$$

where V_T is the total voltage across the sheath between the two grids and the sheath thickness, , ℓ_e is given by

$$\ell_e = \sqrt{\left(\ell_g + t_s\right)^2 + \frac{d_s^2}{4}}. \tag{5.2-3}$$

The grid dimensions in Eq. (5.2-3) are defined in Fig. 5-5. As illustrated in the figure, the sheath is allowed to expand essentially spherically through the screen grid aperture. The sheath thickness ℓ_e accounts for this non-planar condition and has been found to be useful in predicting the space-charge-limited current in ion thruster grid configurations [1,7]. Note that the value of ℓ_g is the "hot grid gap" that occurs once the grids have expanded into their final shape during operation at a given beam current and voltage. For xenon ions,

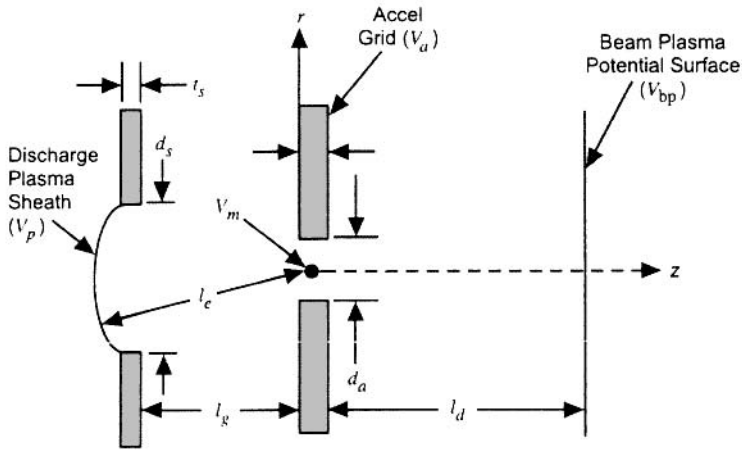

Fig. 5-5. Non-planar sheath model approximation for a two-grid system.

$$J_{\max} = 4.75 \times 10^{-9} \frac{V_T^{3/2}}{\ell_e^2}. \tag{5.2-4}$$

The units of the current density in the Child–Langmuir equations are amperes divided by the dimension used for the sheath thickness, ℓ_e, squared.

The maximum thrust per unit area possible from an ion thruster can also be found. Thrust was defined in Chapter 2 for electric thrusters as

$$T = \frac{d(mv)}{dt} = \gamma \dot{m}_i v_i. \tag{5.2-5}$$

Assuming the ions start at rest, the ion velocity leaving the accelerator is

$$v_i = \sqrt{\frac{2eV_b}{M}}, \tag{5.2-6}$$

where eV_b is the net beam energy. Using Eq. (2.2-3) for the time rate of change of the mass, the thrust per unit area of the grids becomes

$$\frac{T}{A_g} = \frac{J_{\max}\, \gamma\, T_s M v_i}{e}, \tag{5.2-7}$$

where A_g is the active grid area (with extraction apertures) and T_s is the grid transparency defined in Eq. (5.2-1). The effective electric field in the acceleration gap is

$$E = \frac{V_T}{\ell_e}, \tag{5.2-8}$$

where V_T is the total voltage across the accelerator gap (the sum of the screen and accel voltages):

$$V_T = V_s + |V_a| = \frac{V_b}{R}, \tag{5.2-9}$$

and R is the ratio of the net beam voltage to the total voltage. Using Eq. (5.2-2) for the space-charge-limited current density and the electric field from Eq. (5.2-8), the maximum achievable thrust density is

$$\frac{T_{\max}}{A_g} = \frac{4}{9}\frac{\varepsilon_o \gamma T_s}{e}\sqrt{\frac{2e}{M}}\frac{V_T{}^{3/2}}{\ell_e^2}M\sqrt{\frac{2eV_b}{M}} = \frac{8}{9}\varepsilon_o \gamma T_s \sqrt{R}E^2 . \qquad (5.2\text{-}10)$$

The maximum thrust density from an ion thruster increases with the screen grid transparency and the square of the electric field [8]. Ion thrusters with thin, high transparency grids operating near the perveance limit and at the maximum possible electric field in the acceleration gap will produce the most thrust for a given grid area. A key feature of ion thrusters illustrated by Eq. (5.2-10) is that the thrust density is independent of propellant mass.

The net-to-total voltage ratio from Eq. (5.2-9) is given by

$$R = \frac{V_b}{V_T} = \frac{V_b}{V_s + |V_a|} . \qquad (5.2\text{-}11)$$

This equation describes the relative magnitude of the accel grid bias relative to the screen potential. Operating with small values of R increases the total voltage between the screen and accel grids, which, from Eq. (5.2-2), results in a higher current density of ions accelerated from the thruster. While it appears desirable to operate with very small values of R (large accel grid negative bias) to increase the current capability of a grid set, this results in higher energy ion bombardment of the accel grid and shortens grid life. Operating with small values of R will also change the beam divergence, but this is a relatively small effect in ion thrusters for most grid designs. For applications where thruster life is important, the magnitude of accel grid bias voltage is usually minimized to the value required to just avoid electron backstreaming, and the value of R typically ranges from 0.8 to 0.9. Finally, Eq. (5.2-10) suggests that the thrust density depends on the square root of R and would increase slowly with higher beam-to-total voltage ratios. This is misleading because the total voltage also appears in the electric field term $(E = V_T / \ell_e)$, and so higher thrust densities actually occur with more negative accel grid bias because of the higher voltage applied across the screen-to-accel gap for a given net (beam) voltage.

Aside from mechanical tolerances, the minimum "hot-gap" grid separation, ℓ_g, is limited by the vacuum breakdown field of the grid material:

$$E = \frac{V}{\ell_g} < E_{\text{breakdown}} . \qquad (5.2\text{-}12)$$

In practice, grid breakdowns initiated by arcing or small micro-discharges between the grids cause "recycles" in which the voltages are temporarily

removed to extinguish the arc and then reapplied. It is common to also decrease the discharge plasma density during a recycle so that the reapplication of the acceleration voltages corresponds with ramping up the discharge current such that the accelerator approximately tracks the right perveance during start up. This minimizes ion bombardment of the accel grid during a recycle. To obtain reliable operation and avoid frequent recycles, the maximum field strength in the ion thruster typically is set to less than half the vacuum breakdown field. For example, if the grid spacing were a millimeter and the acceleration potential between the grids a thousand volts, the theoretical maximum xenon ion beam current density would be 15 mA/cm^2. A 25-cm-diameter, uniform-profile beam with a 75% transparent grid system would then produce about 5.5 A of beam current. In practice, because of high voltage breakdown considerations, the maximum beam current obtainable from grid sets is typically about half the theoretical maximum.

The ion thruster size is determined by the perveance limit on the beam current density and practical considerations on the grids, such as maximum grid transparency and electric field [1]. For this reason, ion thruster beam current densities are typically on the order of a tenth that found in Hall thrusters, resulting in a larger thruster footprint on the spacecraft. Alternatively, the maximum Isp that is achievable is limited by the voltage that can be applied to the grids to extract a given current density before electrical breakdown or electron backstreaming occurs [9]. Very high Isp thrusters (>10,000 s), with a size that depends on the thrust requirement, have been built and successfully tested.

5.3 Ion Optics

While the simple formulas above provide estimates of the ion accelerator optics performance, a number of computer simulation codes have been developed [4,10–17] to more accurately evaluate the ion trajectories produced by thruster grids. Ion optics codes solve in two or three dimensions the combined ion charge density and Poisson's equations for the given grid geometry and beamlet parameters [18]. These codes have been used for the design and analysis of two- and three-grid systems, and were extended to four-grid systems [19] to examine "two-stage" ion optics performance [20] for very high voltage, high Isp applications.

5.3.1 Ion Trajectories

There are a number of codes that calculate ion trajectories and grid performance in ion thrusters, and an extensive analysis of ion optics behavior in thrusters was recently completed by Farnell [21]. An example of a multi-dimensional code CEX-2D, which is an ion optics code developed at JPL that calculates ion

trajectories and charge exchange reactions between beam ions and un-ionized propellant gas in two [4] and three [17] dimensions. The CEX-2D code solves Poisson's equation, given in Eq. (3.7-8) in Chapter 3, on a regular mesh in cylindrical geometry. The code models a single set of screen and accel grid holes and assumes cylindrical symmetry. The computational space is divided into a grid of rectangular cells with up to 400 increments radially and 600 axially. The radial grid spacing is uniform; the axial spacing is allowed to increase in the downstream direction. The computational region is typically a few millimeters radially and up to 5 centimeters along the axis downstream of the final grid. With a few exceptions, the code uses a combination of algorithms used in earlier optics codes for ion thrusters [11–15].

Upstream of the accelerator grid, the electron density is obtained analytically from the barometric law assuming a Maxwellian distribution:

$$n_e(V) = n_e(0)\,\exp\left(\frac{\phi - \phi_o}{T_e}\right). \tag{5.3-1}$$

The upstream reference electron density, $n_e(0)$, is set equal to the input discharge chamber ion density. Downstream of the accelerator grid, the electron population is also assumed to be a Maxwellian distribution with a different reference potential:

$$n_e(V) = n_e(\infty)\,\exp\left(\frac{\phi - \phi_\infty}{T_e}\right), \tag{5.3-2}$$

where the downstream reference electron density, $n_e(\infty)$, is set equal to the calculated average downstream ion beam density. As a result, downstream potentials are determined self consistently; there is no need to assume a neutralization plane. These codes include focusing effects and the fact that the aperture dimensions are usually significantly larger than the gap size such that the electric fields are reduced from the ideal maximum.

The potential distributions are calculated using an optimized pre-conditioned least-square conjugate gradient sparse matrix solver. Results for a given upstream plasma number density, n, are found by starting from zero density and iterating. At each iteration, i, a fraction, α, of the desired discharge chamber ion density is blended into the code:

$$\begin{aligned} n^0 &= 0 \\ n^{i+1} &= (1-\alpha)n^i + \alpha n. \end{aligned} \tag{5.3-3}$$

The density that the code uses asymptotically approaches the final density:

$$n - n^i = n(1-\alpha)^i. \tag{5.3-4}$$

If α is sufficiently small, approximate results for all upstream densities less then n can be obtained in a single run:

$$n^i = \left[1-(1-\alpha)^i\right]n. \tag{5.3-5}$$

By saving the intermediate results, only a single run is needed to estimate the performance of an optics design over a wide range of discharge chamber densities. However, since the calculation is fully converged only at the final density, separate runs with different final densities may be necessary to obtain accurate results over the full range of discharge chamber ion densities. A typical CEX-2D calculation takes a few minutes on a personal computer. Ion optic assemblies designed using the CEX-2D code have met the predicted performance very closely [4], illustrating that grid design techniques are very mature.

The ion density in the beamlet is obtained in the codes by tracking representative ion trajectories and accounting for charge exchange collisions that alter the ion energy. Ions enter the computational region from the upstream boundary at the Bohm velocity, and their charge density is found by following their trajectories in a stationary electric field. This is in contrast to the time-dependent particle in cell (PIC) technique generally used in plasma physics simulations.

An example of ion trajectories calculated by CEX-2D is shown in Fig. 5-6, which shows the computational space with the dimensions given in meters used for three values of beam perveance for half a beamlet in a three-grid configuration. In this figure, ions from the discharge chamber enter from the left and are accelerated by the electric field between the screen and accel grids. The horizontal boundaries represent lines of symmetry such that an ion crossing at these boundaries has another ion coming in from outside the domain. Figure 5-6(a) shows an *over-perveance* condition representing a beamlet current too high for the applied voltage, or too low a voltage for the plasma density and ion current provided. In this case, ions directly impinge on the upstream face of the accel grid. This situation is considered to be the *perveance limit*, where

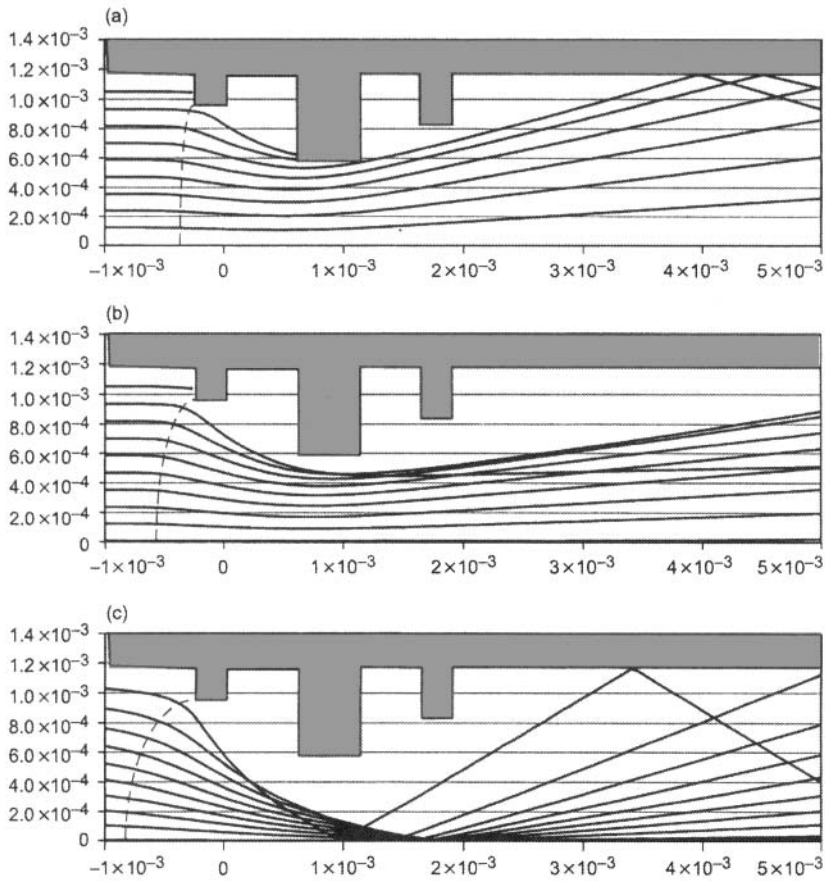

Fig. 5-6. Representative ion trajectories from a CEX2D calculation for three perveance conditions: (a) over-perveance with direct accel grid interception, (b) optimal perveance, and (c) under-perveance that can produce cross-over interception.

excessive ion current strikes the accel grid. Figure 5-6(b) shows a near-optimum perveance condition where the ions are well focused through the accel and decel grid apertures and do not directly intercept any downstream grid. Finally, Figure 5-6(c) shows an *under-perveance* condition where the ions are over focused and cross over in the accel gap. In this case, ions can directly intercept the accel grid and, eventually, the decel grid as the apertures wear open. Note that the length of the computational region shown must be long compared to its radius and is usually chosen so that neighboring beamlets will overlap.

A fraction of the ions from the plasma at the largest radii run directly into the screen grid, as seen in Fig. 5-6, and do not enter into the thrust beam. These ions represent the effect of the finite screen grid transparency that was so important in the discharge loss calculations in Chapter 4. For the near-optimal and under-perveance conditions, the screen grid transparency is greater than its geometric open area fraction, as mentioned above, because the self-consistent electric fields actually extract some of the ions at large radii that would have hit the screen grid instead of going into the screen aperture.

5.3.2 Perveance Limits

Figure 5-6 demonstrated that electrostatic accelerators produce focused ion trajectories when operated near a given design perveance and avoid grid interception or large beam divergence angles over a limited range of voltages and currents that are related by space charge considerations in the grid gap. In ion thrusters, operating sufficiently away from the perveance design of the grids results in beam interception on the downstream accel and (eventually) decel grids. Figure 5-7 shows an illustration of the accel grid current as a function of the current in a beamlet (a single aperture) for three different beam voltages. In this case, the optics were designed to run at about 2 kV and 0.8 mA of beamlet current, and the design demonstrates low grid interception over about ±50% of this current. As the beamlet current is increased, by raising the plasma density in the discharge chamber, the sheath thickness in the acceleration gap decreases, which flattens the sheath and causes the accel grid interception to increase. Eventually, the system becomes under-focused at the perveance limit where a large fraction of the beamlet is intercepted, as shown in Fig. 5-6(a). The accel grid current then increases rapidly with beamlet current due to the

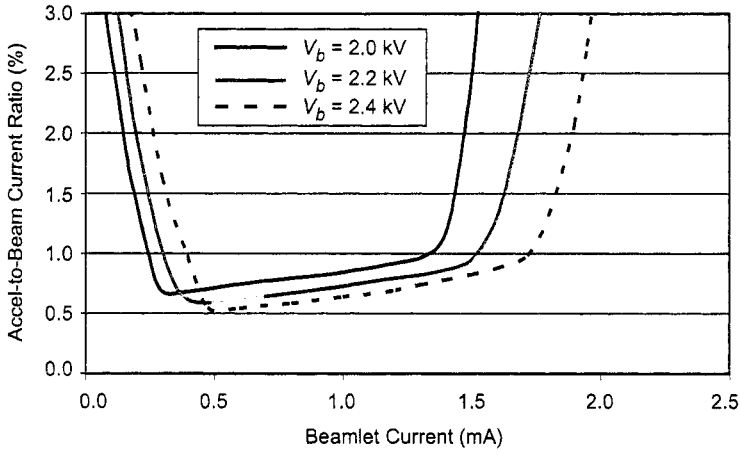

Fig. 5-7. Accel grid current-to-beam current ratio as a function of the beamlet current for three values of the beam voltage.

system running at too high a perveance. At low discharge chamber plasma densities, which produce low beamlet currents, the beam is over-focused and interception of the ions on the accel grid due to cross-over trajectories increases the accel grid current. The ion trajectories for this case are shown in Fig. 5-6(c).

At the nominal beam voltage of 2 kV, this system can be run from about 0.4 to 1.2 mA of beamlet current between the cross-over and perveance limits without producing excessive accel grid current. If the ion thruster has a current profile greater than about 3:1 peak to edge over the grid diameter (due to a poor plasma density uniformity), then grid interception will occur either in the center or at the edge of the beam. Since the grids are normally designed to deal with the high perveance condition at the peak current density near the axis, poor plasma profiles usually result in significant erosion of the edge holes due to cross-over interception. This will impact the life of the thruster and must be compensated by either changing the grid gap or screen aperture sizes as a function of the radius or modifying the plasma generator to produce more uniform profiles.

Increasing the beam voltage shifts the curves in Fig. 5-7 to higher beamlet currents. This is clear from the dependence in the Child–Langmuir equation (Eq. 5.3-2) where the current scales as $V^{3/2}$ if the sheath thickness and grid dimensions are held constant. In Fig. 5-7, the perveance-limited beamlet current, where direct grid interception occurs, increases as $V^{3/2}$ as the beam voltage is raised. Figure 5-7 also illustrates that, in situations where the thruster power must decrease, which is typical of deep space solar electric propulsion missions where the power available decreases as the spacecraft moves away from the Sun, the beam voltage and Isp of the thruster must eventually decrease as the current is reduced to avoid grid interception.

The voltage range available from a given accelerator design at a fixed (or nearly constant) beam current has limitations similar to the current dependence just discussed. However, the minimum voltage at a given current is of special interest in an ion thruster because this is related to the minimum Isp of the engine for a given thrust. The *perveance limit* of a thruster is usually defined relative to the rate at which the accel current increases as the beam voltage is decreased:

$$\text{Perveance limit} \equiv -0.02 \frac{I_A}{V_{\text{screen}}} \left[\text{mA/V}\right]. \tag{5.3-6}$$

This is related to the optics situation illustrated in Fig. 5-6(a), where the current at a given voltage is too high for the designed gap and aperture size and the under-focused beamlet starts to directly intercept accel grid. Figure 5-8 shows the behavior of the accel grid current for the NASA Solar Electric Propulsion

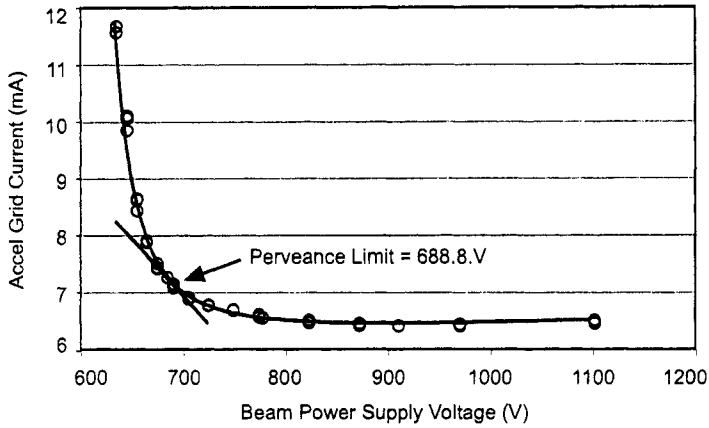

Fig. 5-8. Accel grid current versus the screen supply voltage for the NSTAR thruster at TH15 parameters, showing the perveance limit.

Technology Applications Readiness (NSTAR) engine operating at the full power parameters of TH15 but with the screen voltage decreasing. In this case, the perveance limit is found to be at 688.8 V, compared to the nominal 1100 V of the screen voltage at this throttle level. The perveance limit can also be defined by a given percentage increase in the accel current. However, the screen grid transparency usually decreases as the screen power supply voltage is decreased, which reduces the beam current and accel current during this measurement. The magnitude of the percentage increase in the accel current due to direct ion impingement then needs to be defined for the ion optics assembly.

5.3.3 Grid Expansion and Alignment

A significant issue in ion thrusters that utilize refractory metal grids is thermal expansion of the grids during thruster operation changing the acceleration gap dimension between the screen and accel grids. This will directly affect the ion trajectories and the perveance of the ion optics. Since the screen grid is heated by direct contact with the discharge plasma and is usually dished outwards and designed with a minimum thickness to increase the effective transparency, the screen grid expansion is usually larger than the accel grid and the gap tends to decrease as the thruster heats up. This shift from the *cold gap* to the *hot gap* causes the perveance of the optics to increase for convex grid curvature (grids domed outward from the thruster body) and changes the beamlet trajectories at the given operating point. In addition, for grids designed to hold the applied voltage across the cold gap, the hot gap may be so small that field emission and high voltage breakdown become problems. For ion thrusters with refractory metal grids designed with concave grid curvature (grids domed into the thruster

body), the screen grid expands away from the accel grid and the perveance decreases as the gap gets larger. In addition, concave grids have a smaller discharge chamber volume for a given thruster size, which adversely affects the discharge loss.

Ideally, the ion optics design would have sufficient margin to operate at full power over the range that the grid gap changes. This is possible for smaller thrusters and/or lower power levels where the grid deflection is a small fraction of cold gap. For thrusters with grid diameters greater than 15 to 20 cm operating at power levels in excess of 1 kW, it is often necessary to design the optics for the highest power case with the small hot gap, and to start the thruster in the diode mode (discharge only) or at lower beam powers to pre-heat the grids to avoid breakdown during thermal motion. This establishes the grid gap dimension within the range the optics can tolerate for high-power operation with minimal grid interception. It should be noted that grids fabricated from the various forms of carbon (graphite, carbon–carbon composite, or pyrolytic) have smaller or negligible thermal expansion than refractory metal grids and will have smaller grid gap changes. Ion optics sets that utilize grids made of two different materials have to deal with this issue of different thermal expansion coefficients and potentially larger grid gap changes.

Another significant grid issue is alignment of the grid apertures. The ion trajectories shown in Fig. 5-6 assumed perfect alignment of the screen and accel grid apertures, and the resultant trajectories are then axi-symmetric along the aperture centerline. Displacement of the accel grid aperture relative to the screen grid centerline causes an off-axis deflection of the ion trajectories, commonly called *beam steering*. The affect of aperture displacement on the beamlet steering has been investigated for many years in both ion sources and ion thrusters [22–25]. The beamlet is steered in the direction opposite to that of the aperture displacement due to the higher focusing electric field induced at the accel grid aperture edge. Studies of this effect in ion thruster grid geometries [24] show that small aperture displacements ($\approx$10% of the screen aperture diameter) cause a deflection in the beamlet angle of up to about 5 degrees. This phenomenon can be used to compensate for the curvature of the grids to reduce the overall beam divergence, which is called *compensation*. However, the perveance of the aperture is reduced in this case, and interception of edge ions on the accel grid due to the non-uniform electric fields can be an issue. Mechanical misalignment of the grids due to manufacturing tolerances or thermal deformation can also produce aperture displacement and unintended beamlet steering. This problem has been identified as the cause of thrust vector variations observed as thrusters heat up [24]. For this reason, precise alignment of the grid apertures and grid support mechanisms that minimize non-uniform

thermal deformation are generally required to provide stable ion optics performance with minimal beam divergence.

5.4 Electron Backstreaming

Downstream of the accelerator grid, the ion beam is charge and current neutralized by electrons from the neutralizer hollow cathode. Since electrons are much more mobile than ions, a potential barrier is needed to stop neutralizer electrons from flowing back into the discharge chamber. In the absence of a potential barrier, the electron current would be several hundred times the ion current, wasting essentially all of the electrical power. The potential barrier is produced by the negatively biased accel grid. The minimum potential established by the accel grid prevents all but the highest energy electrons from traveling backwards from the beam plasma into the discharge chamber. The so-called "backstreaming" electron current is not only a parasitic power loss since these electrons do not add thrust, but it can damage the thruster by overheating the internal components of the discharge chamber such as the cathode.

The accel grid bias voltage required to limit the electron backstreaming current to a small value (typically <1% of the beam current) can be determined by evaluating Poisson's equation in the grid aperture in the presence of the beamlet ion current with 2-D computer codes. An example of such a calculation is shown in Fig. 5-9, where the potential between the electrodes and on the axis of the half-beamlet is shown. Note that the potential minimum in the center of the beamlet is only a small fraction of the applied accel grid voltage in this

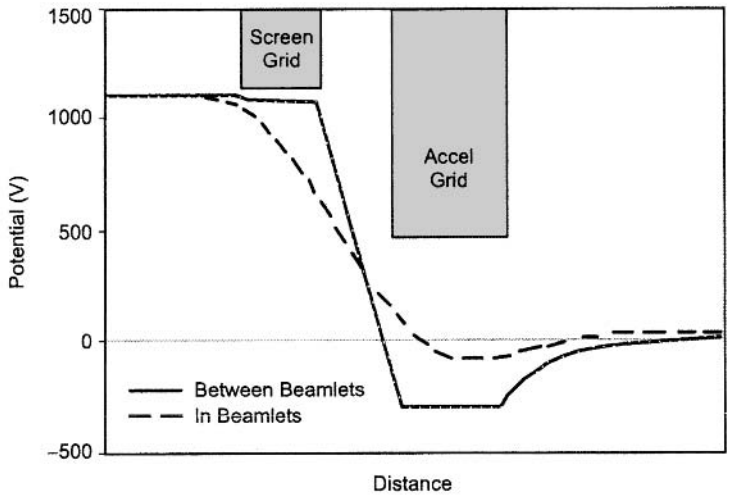

Fig. 5-9. Potentials on-axis in an individual beamlet and between the beamlets intersecting the grids.

example, which is due to the beam's space charge. The actual value of this minimum potential determines the margin to backstreaming, which should be set well above the value at which excessive backstreaming occurs.

Examining electron backstreaming in more detail shows that the minimum potential in the accel grid is determined by three factors: the electrostatic potential from the bias voltages applied to the different grids, the beamlet space charge in the accel grid aperture, and the required potential difference between the beam plasma and minimum voltage to reduce the backstreaming electron current to insignificant levels. Each of these factors can be evaluated analytically using simplifying approximations to help in understanding backstreaming physics.

As stated above, the backstreaming electron current results from the tail of the beam Maxwellian electron distribution overcoming the potential barrier established in the accel grid aperture. The current of electrons backstreaming into the thruster plasma is just the beam plasma random electron flux times the Boltzman factor for the potential difference between the beam plasma and the minimum potential in the accel grid region [26]:

$$I_{eb} = \frac{1}{4} ne \left(\frac{8kT_e}{\pi m} \right)^{1/2} e^{\frac{-(V_{bp} - V_m)}{T_e}} A_a , \tag{5.4-1}$$

where I_{eb} is the electron backstreaming current, V_{bp} is the beam plasma potential, V_m is the minimum potential in the grid aperture, and A_a is the beamlet area in the grid aperture. The current of ions in the beamlet flowing through the grid aperture is

$$I_i = n_i e v_i A_a , \tag{5.4-2}$$

and the ion velocity through the system is

$$v_i = \sqrt{\frac{2e\left(V_p - V_{bp}\right)}{M}} , \tag{5.4-3}$$

where V_p is the plasma generator plasma potential at the sheath edge. Combining Eqs. (5.4-1) through (5.4-3), the minimum potential is

$$V_m = V_{bp} + T_e \ln \left[\frac{2I_{eb}}{I_i} \sqrt{\pi \frac{m}{M} \left(\frac{V_p - V_{bp}}{T_e} \right)} \right] . \tag{5.4-4}$$

This equation describes the required potential difference between the beam potential and the minimum potential in the beamlet to produce a specified amount of electron backstreaming current relative to the beam current. Note that this equation is independent of the grid geometry because it deals solely with the potential difference between a given value of V_m (independent of how it is produced) and the beam-plasma potential. The required potential difference $(V_{bp} - V_m)$ between the beam plasma and the minimum voltage in the grids to produce a given ratio of backstreaming current to beam current is plotted from Eq. (5.4-4) in Fig. 5-10 for several values of the beam-plasma electron temperature in a thruster plume with a net accelerating voltage of $V_p - V_{bp} = 1500\,\text{V}$. For an electron temperature of 2 eV in the beam, which is consistent with values found in NSTAR thrusters plumes [27], a potential difference between the minimum potential in the beamlet and the beam plasma of only 12.5 V is required to reduce the backstreaming current to 1% of the beam current.

The actual minimum potential in the beamlet is determined by the grid geometry, the applied grid potentials, and the beam's space charge. The minimum potential in the two-grid arrangement shown in Fig. 5-5 was first found without considering space charge effects by an analytic solution to LaPlaces' equation by Spangenberg [28] for thin grids in vacuum tubes. Spangenberg's expression was simplified by Williams [26] and Kaufman [1] for most ion thruster grid configurations to

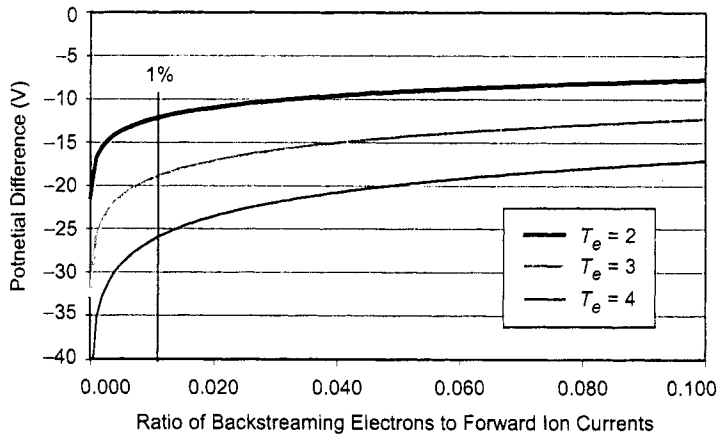

Fig. 5-10. Potential difference between the beam plasma and the beamlet potential minimum required to achieve a given electron backstreaming current-to-forward ion current ratio for several beam electron temperatures.

$$V_m^* = V_a + \frac{d_a(V_p - V_a)}{2\pi \ell_e}\left[1 - \frac{2t_a}{d_a}\tan^{-1}\left(\frac{d_a}{2t_a}\right)\right]e^{-t_a/d_a}, \qquad (5.4\text{-}5)$$

where V_m^* indicates the minimum potential with the ion space charge neglected, V_a is the applied accel grid potential, the grid dimensional terms are defined in Fig. 5-5, and ℓ_e is given by Eq. (5.2-3). Equation (5.4-5) provides the dependence on the geometry of the grids, but is only useful if the beam space charge is negligible (very low current density beamlets).

The reduction in the magnitude of the minimum beam potential due to the presence of the ion space charge in the beamlet can be estimated [26] using the integral form of Gauss's law:

$$\oint_S \mathbf{E} \cdot d\mathbf{A} = \frac{1}{\varepsilon_o}\int_V \rho \, dV, \qquad (5.4\text{-}6)$$

where $\mathbf{E}$ is the electric field, $d\mathbf{A}$ is the differential surface area element, ε_o is the permittivity of free space, and ρ is the ion charge density within the Gaussian surface which has a surface area S and encloses volume V. This equation is solved first in the beamlet and then in the charge-free space between the beamlet and the accel aperture inside diameter. Then, adding the two potentials together gives the total potential between the grid and the beamlet centerline.

Assume that the beamlet has a radius $d_b/2$ inside the accel grid aperture with a radius of $d_a/2$. Integration of the left-hand side of Eq. (5.4-6) over a cylindrical "Gaussian pillbox" aligned with the beamlet axis yields

$$\oint_S \mathbf{E} \cdot d\mathbf{A} = \int_0^{2\pi}\int_0^{r_a} E_r \, r d\theta \, dz = E_r \, 2\,\pi\, r\, z, \qquad (5.4\text{-}7)$$

where it has been assumed that E_r is constant in the axial direction over a distance z. If it is also assumed that the ion charge density is uniform in the volume of the pillbox, the right-hand side of Eq. (5.4-6) can also be integrated to obtain

$$\frac{1}{\varepsilon_o}\int_V \rho \, dV = \frac{1}{\varepsilon_o}\int_V \rho r \, dr \, d\theta \, dz = \frac{\rho}{\varepsilon_o}\pi \, r^2 \, z. \qquad (5.4\text{-}8)$$

Equating Eqs. (5.4-7) and (5.4-8), an expression for the radial electric field in the beamlet (E_{r1}) from the accel hole centerline to the outer edge of the beamlet is obtained:

$$E_{r1} = \frac{\rho\, r}{2\,\varepsilon_o}, \qquad \left(0 < r < \frac{d_b}{2}\right). \tag{5.4-9}$$

From the edge of the beam to the wall, Gauss's law is again used, but in this case the entire beam charge is enclosed in the Gaussian surface. The radial electric field in this "vacuum region" outside the beamlet (E_{r2}) is then found in a similar manner to be

$$E_{r2} = \frac{\rho d_a^2}{8\varepsilon_o r}, \qquad \left(\frac{d_b}{2} < r < \frac{d_a}{2}\right). \tag{5.4-10}$$

The voltage difference ΔV from the centerline to the accel grid barrel due to the ion space charge is obtained by integrating the electric field between these limits. Hence,

$$\Delta V = -\int_0^{d_b/2} E_{r1} dr - \int_{d_b/2}^{d_a/2} E_{r2} dr = -\int_0^{d_b/2} \frac{\rho r}{2\varepsilon_o} dr - \int_{d_b/2}^{d_a/2} \frac{\rho\, d_b^2}{8\ \varepsilon_o\ r} dr. \tag{5.4-11}$$

The total potential from the accel wall to the center of the beamlet due to ion space charge is then

$$\Delta V = \frac{\rho d_b^2}{8\varepsilon_o}\left[\ell n\left(\frac{d_a}{d_b}\right) + \frac{1}{2}\right]. \tag{5.4-12}$$

The beam current density in the accel aperture is the charge density times the beam velocity, so the ion charge density ρ is

$$\rho = \frac{4\, I_i}{\pi\, d_b^2\, v_i}, \tag{5.4-13}$$

where v_i is the ion velocity evaluated at the minimum potential point:

$$v_i = \sqrt{\frac{2e\left(V_p - V_m\right)}{M}}. \tag{5.4-14}$$

Substituting Eqs. (5.4-13) and (5.4-14) into Eq. (5.4-12) gives

$$\Delta V = \frac{I_i}{2\pi\varepsilon_o v_i}\left[\ell n\left(\frac{d_a}{d_b}\right)+\frac{1}{2}\right]. \tag{5.4-15}$$

Since scalar potentials can be added, the sum of Eqs. (5.4-15) and (5.4-5) gives the total of the potential minimum in the accel grid aperture.

$$V_m = V_a + \Delta V + \frac{d_a(V_{bp}-V_a)}{2\pi\ell_e}\left[1-\frac{2t_a}{d_a}\tan^{-1}\left(\frac{d_a}{2t_a}\right)\right]e^{-t_a/d_a}. \tag{5.4-16}$$

To calculate the backstreaming current as a function of grid voltage, Eq. (5.4-16) must be equated to Eq. (5.4-4) and solved for the current:

$$\frac{I_{be}}{I_i} = \frac{e^{(V_a+\Delta V+(V_{bp}-V_a)C-V_{bp})/T_e}}{2\sqrt{\pi\dfrac{m}{M}\dfrac{(V_p-V_{bp})}{T_e}}}, \tag{5.4-17}$$

where the geometric term C is given by

$$C = \frac{d_a}{2\pi\ell_e}\left[1-\frac{2t_a}{d_a}\tan^{-1}\left(\frac{d_a}{2t_a}\right)\right]e^{-t_a/d_a}. \tag{5.4-18}$$

In practice, the onset of backstreaming is determined by two techniques. One method is to monitor the increase in the screen power supply current as the magnitude of the accel grid voltage is decreased. Increases in the measured current are due to backstreaming electrons, and a 1% increase is defined as the minimum accel grid voltage to avoid backstreaming: the so-called *backstreaming limit*. For example, the power supply current from Eq. (5.4-17), normalized to the initial beam current, is plotted in Fig. 5-11 as a function of the accel grid voltage for the NSTAR ion optics [29] for the maximum power throttle point TH15 at the beginning of life (BOL). In this figure, the beam potential and electron temperature were assumed to be 12 V and 2 eV, respectively, consistent with measurements made on this thruster. The onset of backstreaming occurs at about −150 V on the accel grid, which is consistent with the data from tests of this engine [30,31].

A second method for determining the backstreaming limit is to monitor the ion production cost, which is the discharge power required to produce the ion beam current divided by the beam current. This is an effective method for use in

thrusters operating in the beam-current-regulated mode where the discharge power supply is controlled to fix the beam current. Backstreaming then appears as a decrease in the ion production cost. This method is shown in Fig. 5-12 for the experimental data taken from the NSTAR thruster at TH15. As the magnitude of the accel voltage is decreased, a 1% decrease in the ion production cost represents the defined onset of backstreaming. In this case, the backstreaming limit was determined to be about −148 V, consistent with the above analytical model.

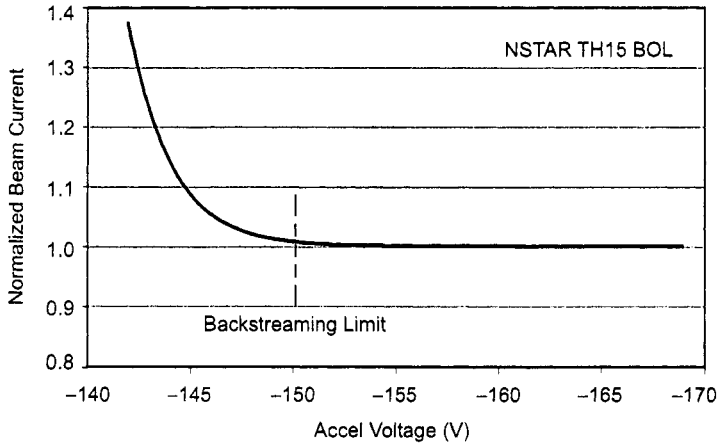

Fig. 5-11. Normalized beam current versus applied accel grid voltage, showing the onset of electron backstreaming as the voltage is decreased.

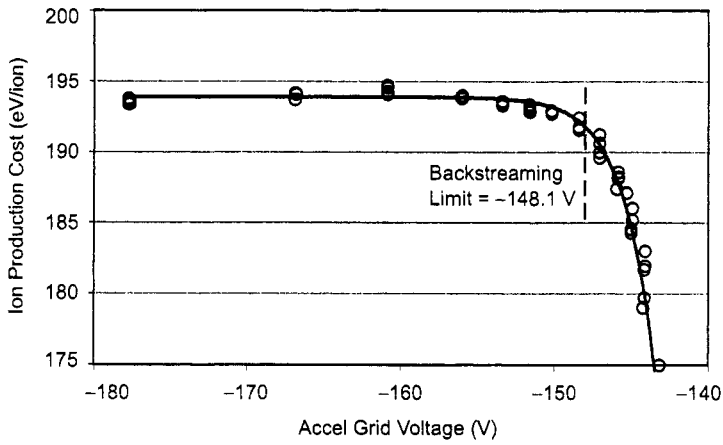

Fig. 5-12. Ion production cost for NSTAR TH15 versus applied accel grid voltage, showing the onset of electron backstreaming as the voltage is decreased.

Equations (5.4-17) and (5.4-18) show that the electron backstreaming is a function of the accel grid hole diameter. Increases in the accel hole diameter will reduce the penetration of the applied grid bias voltage to the center of the aperture and reduce the minimum potential on axis. This increases either the backstreaming current at a given voltage or the backstreaming limit at a given current. The effect of accel grid hole enlargement due to grid wear is illustrated in Fig. 5-13, where the grid voltage at which backstreaming started is plotted versus accel grid hole diameter for the NSTAR TH15 case measured during the extended life test (ELT) [31]. Larger grid-hole diameters required more negative biasing of the accel grid to avoid the onset of backstreaming.

Figure 5-13 also shows an interesting effect in that the shape of the grid hole is important. Early in life, the grid aperture diameter eroded due to sputtering, and the barrel diameter was adequately described by the minimum hole diameter observed optically during running of the test. However, as the test progressed, the erosion of the upstream aperture edge essentially stopped and the aperture was observed to be chamfered on the downstream portion. An effective grid diameter had to be calculated to take into account the non-uniform hole erosion in determining the backstreaming onset, shown on the right-hand side of Fig. 5-13. While the above analytical model accounts for grid diameter and thickness, additional terms would have to be added to account for this conical erosion shape. This situation is best handled by 2-D models that both determine the time-dependent shape of the grid hole and calculate the potential on axis appropriately.

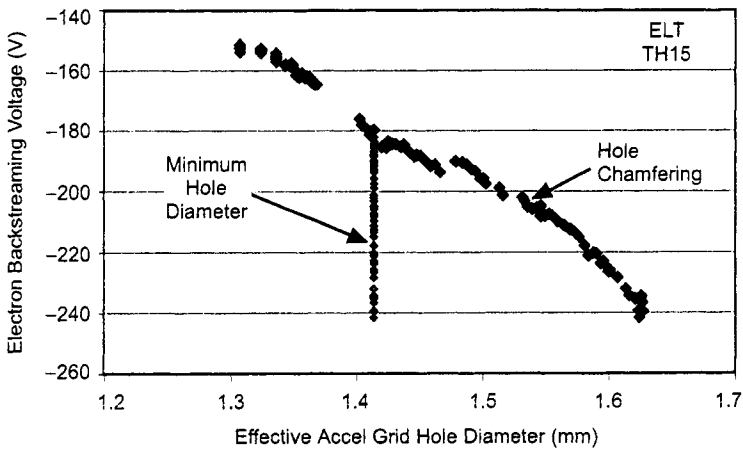

Fig. 5-13. Accel grid voltage at which electron backstreaming occurs in the NSTAR thruster at TH15 power level versus the effective accel grid aperture diameter.

It should be noted that while the analytical model described above illustrates the mechanisms involved in electron backstreaming and provides reasonable agreement with the experimental data shown, the results are very sensitive to the dimensions and beam parameters assumed in the calculation. This is largely because the potential minimum is the difference between two large numbers representing the contributions of the electrostatic fields and the space charge fields. Therefore, this backstreaming model actually provides only an estimate of the backstreaming voltage and current levels, which can easily be off 10% to 20%. The 2-D grid codes described above that solve Poisson's equation exactly provide more accurate calculations of the backstreaming limit.

Finally, electron backstreaming occurs first in the region of the highest beamlet current where the ion space charge is the highest in the ion optics assembly. Thrusters with non-uniform beam profiles, such as NSTAR with a flatness parameter (defined as average-to-peak current density) of about 0.5 and therefore a 2:1 peak-to-average current density profile [30], will tend to backstream primarily from the center beamlets. This localized backstreaming accelerates electrons on axis and can overheat components such as the cathode at the center-back of the thruster. Thrusters designed to have flat profiles, such as the Nuclear Electric Xenon Ion Thruster System (NEXIS), with a better than 0.9 flatness parameter [33], will tend not to backstream easily because of a lower peak ion current density for a given total beam current, and also, if backstreaming starts, it will be over a larger area that minimizes the localized heating issue in the discharge chamber.

5.5 High-Voltage Considerations

As shown in Section 5.3, the maximum thrust that can be produced by an ion thruster is a function of the electric field that can be sustained between the screen and accelerator grids:

$$T_{\max} = \frac{8}{9}\varepsilon_o \gamma T_s A_g \sqrt{R} E^2. \qquad (5.5\text{-}1)$$

From Eq. (5.5-1), the maximum space-charge-limited (sometimes called *perveance-limited*) thrust of the accelerator system is directly proportional to the intra-grid electric field squared. To produce compact ion thrusters with the highest possible thrust, it is necessary to maximize the electric field between the grids. The maximum thrust in ion engines is then limited primarily by the voltage hold-off capability of the grids.

The ability of the accelerator grids to hold off high voltage reliably and to withstand occasional breakdowns without significant damage or loss of voltage standoff capability is therefore of critical importance for ion thrusters. The high-voltage behavior of vacuum-compatible materials has been summarized in recent books on high-voltage engineering [34,35]. In plasma devices [36], electric fields of up to 40 kV/cm were found useful for refractory metal electrodes and of the order of 25 kV/cm for carbon materials. Degradation of the voltage hold-off due to surface damage incurred during breakdowns has been investigated for molybdenum and carbon electrodes [36] commonly used in ion thruster applications. The surfaces of these materials can be carefully prepared to withstand high electric fields required to produce the highest thrust density. However, sputter erosion over time and electrical breakdowns between grids cause some fraction of the stored energy in the power supply to be deposited on the grid surface. The formation of an arc at the cathode electrode (the accel grid) and the deposition of a significant amount of electron power from discharge into the anode electrode (the screen grid) can cause both the screen and accel grid surfaces to be modified and/or damaged. The breakdown events usually impact the subsequent voltage hold-off capability of the grid surfaces, which affects the long-term performance of the thruster.

5.5.1 Electrode Breakdown

The grids in ion thrusters have high voltages applied across small grid gaps, which can lead to high-voltage breakdown and unreliable thruster operation. High-voltage breakdown is usually described in terms of the electric field applied to the surface that causes an arc or discharge to start. Arc initiation is well correlated to the onset of field emission [37,38]. If sufficient field emission occurs due to excessive voltage or a modification to the surface that enhances field emission, the gap breaks down. Physical damage to arced surfaces during the breakdown is attributed to localized energy deposition on the electrode that causes melting or evaporation of the material. On the cathode surface (the accel grid), the energy is deposited primarily by ion bombardment from the arc plasma. On the anode surface (the screen grid), the energy is deposited from the plasma or electron stream that crosses the gap and results in localized surface heating and vaporization. The energy provided to the arc from the power supply is distributed between any series resistance in the electrical circuit, the voltage drop at the cathode surface, and the voltage drop in the plasma discharge and anode sheath. These voltage drops can be modeled using discrete series resistances in the energy balance of the system. Engineers often rate the possibility of a power supply damaging the electrodes by the amount of stored energy in the power supply. However, the amount of material removed from the surfaces and the lifetime of high-voltage electrodes is usually characterized [36] by the amount of current that passes through the arc. This "coulomb-transfer

rating" is related to the energy deposition in the electrodes in a simple manner. The power running in the arc is $P = IV_{arc}$, where I is the discharge current and V_{arc} is the voltage drop in the arc. Assuming that most of the voltage drop is in the cathode sheath, the energy E deposited by the arc on the cathode surface is

$$E = \int P\, dt = \int IV_{arc}\, dt\,. \tag{5.5-2}$$

The voltage drop of refractory metal and graphite arcs is nearly independent of the amount of current running in the arc up to several hundred amperes [39,40]. Therefore the arc voltage can be considered to be essentially a constant, and the energy deposited by the arc on the cathode is

$$E = V_{arc} \int I\, dt = V_{arc}\, Q\,, \tag{5.5-3}$$

where Q is the total charge transferred in the arc. The arc energy deposited on the cathode surface for a given electrode material is characterized by the total charge transferred by the thruster power supplies during the arc time and not just the stored energy in the power supply. Assuming that the arc remains lit during the entire time required to discharge the filter capacitor in the power supply, the total charge transferred through the arc is $Q = CV$, where C is the capacitance and V is the capacitor charging voltage. If the arc current falls below the minimum value to sustain the arc, called the "chopping current," and is prematurely extinguished, then the total charge transferred is reduced.

It should be emphasized that the amount of energy delivered to the cathode surface by the arc and the amount of damage to the surface incurred by material removal are independent of any series resistance in the circuit as long as the current is stable for the duration of the event (i.e., the current is above the chopping current). This means that simply adding a series resistor to one leg of the high-voltage power supply circuit or the accel grid circuit will not reduce the surface damage due to an arc unless the arc current drops to less than the chopping current. The only mechanism that reduces surface damage if the current is large compared to the chopping current is to limit the total charge transfer. This requires either reducing the power supply capacitance at a given voltage (which reduces the total stored energy) or actively shunting or opening the circuit to reduce the arc duration.

5.5.2 Molybdenum Electrodes

Molybdenum is a standard electrode material used in ion thrusters due to its low sputter erosion rate, ability to be chemically etched to form the aperture array, and good thermal and structural properties. The surface of the

molybdenum grid is often slightly texturized to retain sputtered material to avoid flaking of the sputter-deposited material [41]. The threshold voltage for the onset of field emission versus the gap spacing measured for molybdenum electrodes using a standard "plate-and-ball" test arrangement in a high vacuum facility [42] is shown in Fig. 5-14. The data show a classic power-law dependence of the threshold voltage with gap spacing for small gaps, which is sometimes called the "total voltage effect" [43]. While there are numerous possible mechanisms for the total-voltage effect, the increased gap reduces the surface electric field and the field emission current but increases the probability of an atom or particulate being ionized while traversing the gap. The ionized atom or particle is then accelerated into the cathode potential electrode and produces secondary electrons. If sufficient ionizations and secondary electrons are produced, the process cascades and the gap breaks down. Therefore, the voltage that can be held across a gap does not increase linearly with the gap dimension. This is equivalent to the Paschen breakdown [35] mechanism in gas-filled devices and is caused by the release of gases or particulates from the surfaces in vacuum gaps. After 10 arcs of 1 mC in charge transfer, the threshold voltage was measured again, and the threshold voltage was observed to increase for every gap tested, indicating that the surface was being conditioned. Improving voltage standoff of electrodes with a series of low coulomb-transfer arcs is common practice in the high-voltage industry and historically is often called "spot-knocking." This process removes small field emitters and tends to clean oxides and impurities off the surface without damaging the surface, which reduces the onset of field emission. Higher coulomb transfer arcs on molybdenum (10 and 20 mC) improve the voltage hold-off by cleaning larger areas of the surface and removing field emission sites. This effect will continue

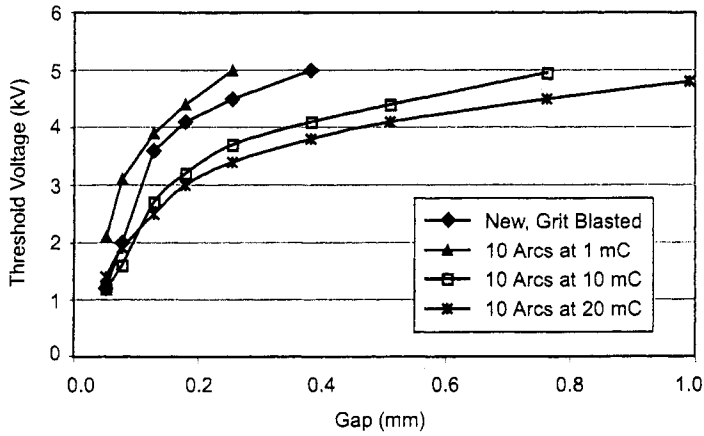

Fig. 5-14. Threshold voltage versus gap for molybdenum after 10 arcs of varying charge transfer (from [36]).

until the surface is well conditioned or the arc anchors in one spot and causes damage to the surface.

As the gap between the electrodes increases, the threshold voltage curves become more linear and the surface asymptotes to a constant threshold electric field. Figure 5-15 shows the threshold electric field for large gaps for a flat molybdenum surface texturized by grit blasting and actual texturized grid material with apertures chemically etched into the material. In this case, high coulomb transfer arcs tend to damage and degrade the voltage standoff of the grids. Scanning electron microscope photographs show localized damage to the edge of the beam apertures, resulting in more field emission sites. The molybdenum surfaces are initially capable of holding electric fields of well over 200 kV/cm, but the surface roughening to retain flakes and the aperture

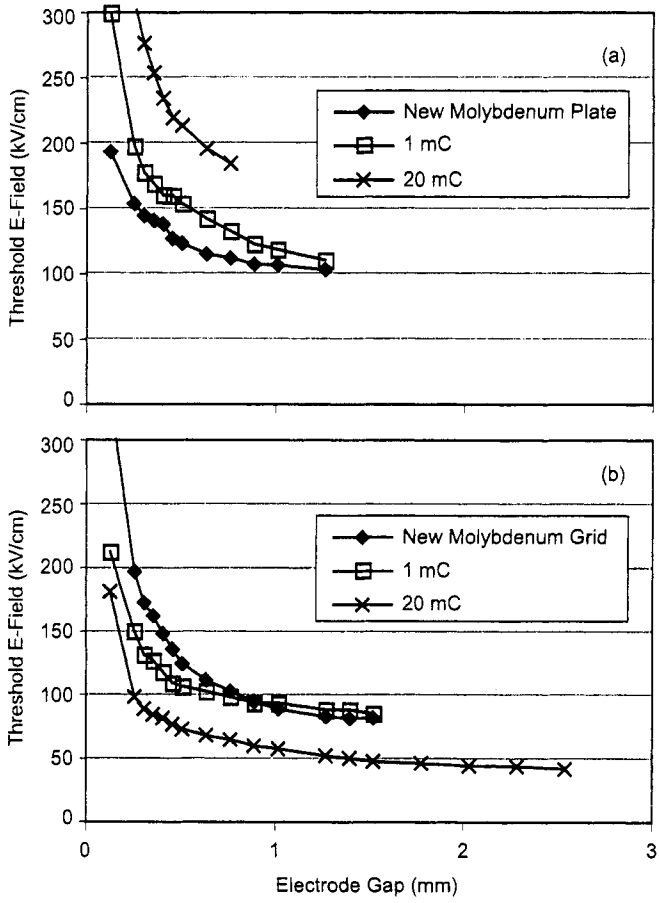

Fig. 5-15. Threshold electric field versus gap for (a) textured molybdenum plate and (b) textured grid material (from [36]).

edges associated with real grids cause the voltage hold-off to decrease. For molybdenum material with apertures, the resulting surface is susceptible to breakdown at electric fields of 40 to 50 kV/cm, which should be considered the maximum electric field for designing molybdenum grids.

5.5.3 Carbon–Carbon Composite Materials

Carbon is a desirable material for ion thruster grid electrodes because of its low sputtering yield under xenon ion bombardment [44] as compared with most refractory grid materials. However, the structural properties of graphite are usually insufficient for thin graphite grids of any reasonable size (greater than a 5- to 10-cm diameter) to survive launch vibrations. This problem can be solved by using carbon material with better structural properties, such as carbon–carbon composites and pyrolytic graphite. Grids made of these materials have demonstrated low erosion in life tests and flown successfully [45]. However, the more complex structures of these materials leads to lower thresholds for field emission and less voltage standoff for grids made of these materials.

Carbon–carbon composite material used for grid electrodes [46] is based on carbon fibers woven into a matrix with the fibers oriented in one or two dimensions. This material has enhanced strength and flexural modulus compared to pure graphite due to the carbon-fiber properties. The carbon-fiber weave is impregnated with a resin and built up to the desired shape by progressive laminate layers on a mold. The resulting material is usually densified and graphitized at high temperature, and may be further impregnated or over-coated with a thin chemical-vapor-deposition (CVD) carbon layer after this process to fill any voids or smooth the final surface. High-voltage breakdown tests were conducted with and without this final surface graphite coating.

The threshold voltage of the carbon–carbon composite samples is shown in Fig. 5-16, where the threshold for field emission is plotted as a function of the electrode gap for various levels of coulomb-transfer arcing. New material (without arcing) with a fresh CVD layer has a high threshold for field emission, and therefore holds voltage well. High coulomb-transfer arcs (>1 mC) tend to damage that surface and return it to the state of the material without the CVD over-layer. Higher coulomb-transfer arcs also tend to damage the surface. In fact, in this example, the 10-mC arcs resulted in damage to the opposite anode electrode, which evaporated and redeposited material back on the cathode-potential surface, improving its voltage hold-off capability. For this reason, the coulomb-transfer limit for carbon–carbon (CC) grids should be set to about 1 mC such that conditioning and no damage to either the screen or accel grid occurs during any breakdowns.

The threshold electric field for CC material with grid apertures is shown in Fig. 5-17 for new material and after a series of arcs. After the initial characterization with 10 arcs of 1 mC each, 10 arcs of 10 mC were delivered to the surface, which degraded the voltage standoff. However, the application of 4 sets of 10 arcs of only 1 mC re-conditioned the surface. The threshold electric field was found to asymptote to just below the same 40-kV/cm field at larger gap sizes observed for low coulomb-transfer arcs of flat material, suggesting that the aperture edges function in a similar manner as does material roughness.

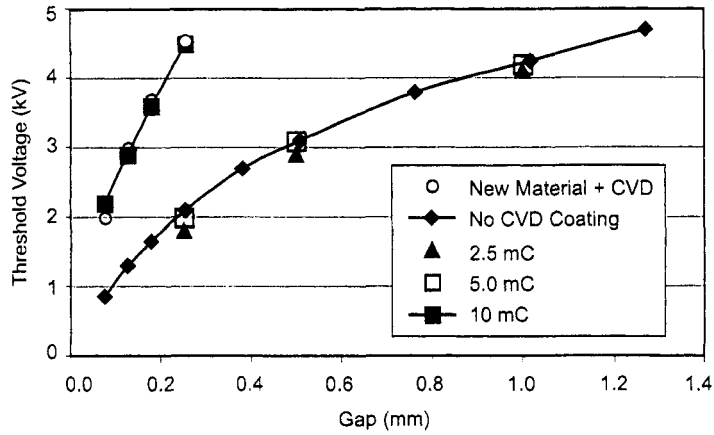

Fig. 5-16. Threshold voltage for carbon–carbon composite material after 10 arcs at various coulomb transfers (from [36]).

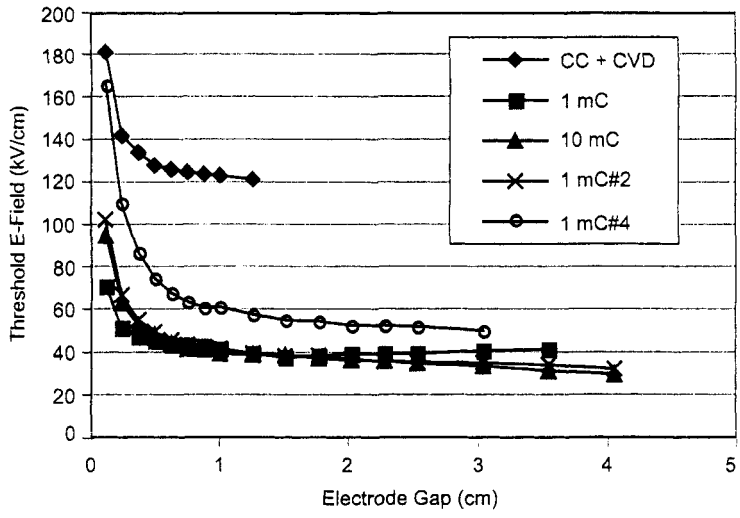

Fig. 5-17. Threshold electric field versus electrode gap for CC grid material with apertures (from [36]).

These results suggest that carbon–carbon composite grids can be designed for reliable high-voltage standoff utilizing a field emission threshold of about 35 kV/cm, even for large gaps and voltages in excess of 10 kV, provided that the coulomb transfer is limited by the power supply to less than about 1 mC. This 35-kV/cm field limit is the highest voltage stress that should be allowed, and conservative design practices suggest that a 50% margin (to ≈23 kV/cm) should be considered in designing these types of grids.

5.5.4 Pyrolytic Graphite

Pyrolytic graphite (PG) is also a candidate for accelerator grid electrodes in ion thrusters [47]. This material is configured with the carbon crystal planes parallel to the surface. Pyrolytic graphite is grown a layer at a time to near the desired shape on a mandrel and then finish machined to the final configuration. Flat test coupons were fabricated in this manner, but they featured small surface bumps and depressions that were residual from the growth process. Figure 5-18 shows the behavior of a PG grid sample that had apertures laser-machined into it and then the surface lightly grit blasted. The as-new PG material demonstrated threshold electric fields of 20 to 30 kV/cm for gaps of 1 mm or larger, which is lower than that found for the CC grid material. However, a series of ten 1-mC arcs tends to smooth and condition the surface and raise the threshold electric field to the order of 30 kV/cm. Higher coulomb arcs (up to about 10 mC) also improve the voltage standoff to about 40 kV/cm. The pyrolytic graphite is more susceptible to field emission and breakdown than the carbon–carbon material, but appears to tolerate higher coulomb-transfer arcs.

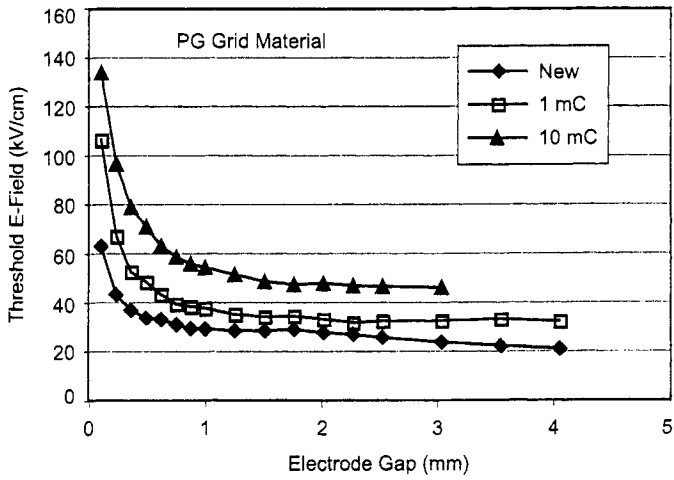

Fig. 5-18. Threshold electric field for pyrolytic graphite with grid apertures (from [36]).

5.5.5 Hold-off and Conditioning in Ion Thrusters

Tests have shown that the arc initiation voltage is directly related to the threshold voltage and electric field for field emission in Figs. 5-14 through 5-18 [36]. Arc initiation voltages tend to be less than 10% higher than the threshold values for field emission shown here. This is consistent with experimental observations that low levels of field emission and/or corona can be tolerated before full arc breakdown occurs, but arcing and recycling tend to increase once significant field emission starts. Molybdenum has been found to have a good tolerance for high coulomb-transfer arcs, and grids can be designed to reliably hold electric fields well in excess of 40 kV/cm. Carbon-based materials have more structure than the refractory metals and tend to form field emitters if excessive charge transfers are allowed. Nevertheless, grids utilizing carbon-based materials can be designed with electric fields in excess of 20 kV/cm if the coulomb transfer during breakdowns is limited to about 1 mC or less. Detailed investigations of the voltage hold-off and conditioning of carbon–carbon thruster grids were performed by Martinez [8], who documented the effect for larger area grid sets. Figure 5-19 shows their reduction in field emission from carbon–carbon grids plotted on a Fowler–Nordheim plot [43] for increasing numbers of 1-mC arcs. This work shows that even if the surface of carbon–carbon grids evolve field emitters over time due to erosion from ion bombardment, proper design of the power supply to limit the coulomb-transfer rate will result in reconditioning of the grid surfaces with every recycle event.

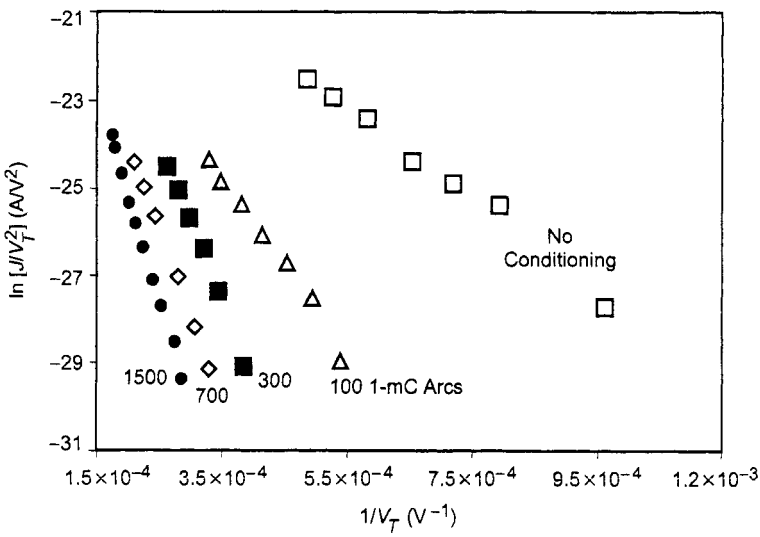

Fig. 5-19. Fowler–Nordheim plots of field emission, showing conditioning of carbon–carbon grids by increasing numbers of 1-mC arcs (from [8]).

5.6 Ion Accelerator Grid Life

The most important wear mechanism in modern ion thrusters is accelerator grid erosion. Even though properly designed optics attempt to make all of the ions extracted from the discharge chamber focus through the accelerator grid apertures, a current of secondary ions generated downstream of the discharge chamber impacts the accelerator grid. These secondary ions are generated by resonant charge exchange (CEX) between beam ions and neutral propellant gas escaping from the discharge chamber. The cross section for resonant charge exchange—that is, the transfer of an electron from a propellant atom to a beamlet ion—is very large: on the order of a hundred square angstroms [48]. This process results in a fast neutral atom in the beam and a slow thermal ion. These slow ions are attracted to the negatively charged accelerator grid, and most hit with sufficient energy to sputter material from the grid. Eventually the accelerator grid apertures become too large to prevent electron backstreaming or enough material is sputtered away that the grids fail structurally.

The erosion geometry is naturally divided into two regions. The first region, barrel erosion, is caused by ions generated between the screen grid aperture sheath and the downstream surface of the accelerator grid, as shown in Fig. 5-20. Charge exchange ions generated in this region impact the inside surface of the accelerator grid aperture, which results in enlargement of the aperture barrel. As the barrel diameter increases, the grid must be biased more and more negatively in order to establish the minimum potential required in the aperture to prevent neutralizer electrons from backstreaming into the discharge chamber. Thruster failure occurs when, at its maximum voltage, the accelerator grid power supply is unable to stop electron backstreaming.

The second region of grid erosion is caused by charge exchange ions generated downstream of the accelerator. Since the beamlets are long and thin, inside each beamlet the radial electric forces dominate and expel the slow, charge-exchange ions into the gaps between the beamlets. Charge exchange ions generated in the region before the beamlets merge to form a continuous ion density are then attracted back to the accelerator grid by its large negative potential. This is illustrated in Fig. 5-21. On impact, these ions sputter away material from the downstream surface of the accelerator grid. Sputter erosion by these backstreaming ions results in a hexagonal "pits-and-grooves" erosion pattern on the downstream grid surface, which can lead to structural failure of the grids if the erosion penetrates all the way through the grid. Erosion of the accel grid aperture edge by backstreaming ions can also effectively enlarge the accel grid aperture diameter, leading to the onset of electron backstreaming.

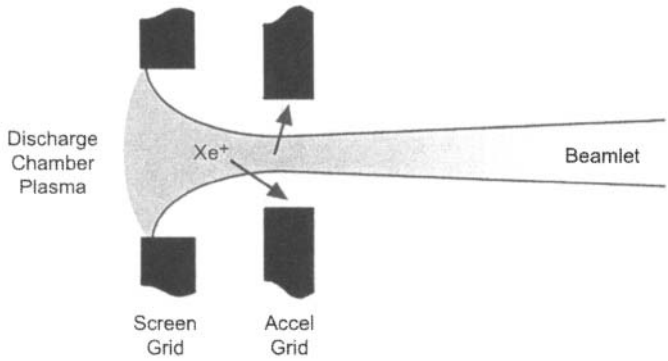

Fig. 5-20. Ions that cause barrel erosion are generated by charge exchange upstream and within the accelerator grid aperture.

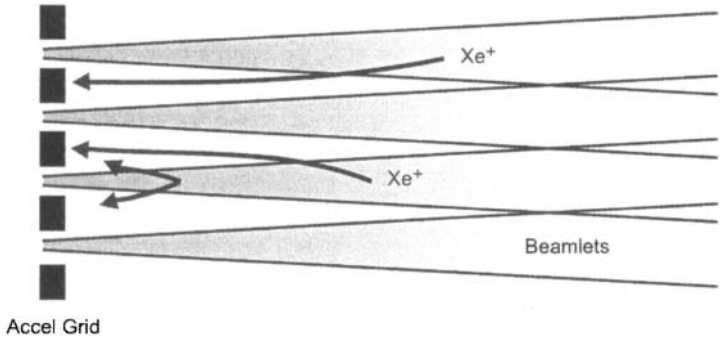

Fig. 5-21. Ions that cause pits and grooves erosion are generated between the downstream surface of the accel grid and where the beamlets overlap.

Erosion of the accelerator grid by charge exchange ion sputtering was the major life-limiting mechanism observed during the ELT of the NSTAR flight spare thruster [49] for operation at the highest power TH15 level. Photographs of center holes in the grid at the beginning and the end of the 30,000-hour test are shown in Fig. 5-22 where barrel-erosion enlargement of the aperture diameters is evident. Note that the triangle patterns where the webbing intersects in the end-of-test picture are locations where the erosion has completely penetrated the grid. The scanning electron microscope (SEM) photograph shown in Fig. 5-23 illustrates the deep erosion of the pits-and-grooves pattern and shows that full penetration of the grid had occurred when the test was stopped. Continued operation would have eventually resulted in structural failure of the grid, but this was not considered imminent at the end of the test.

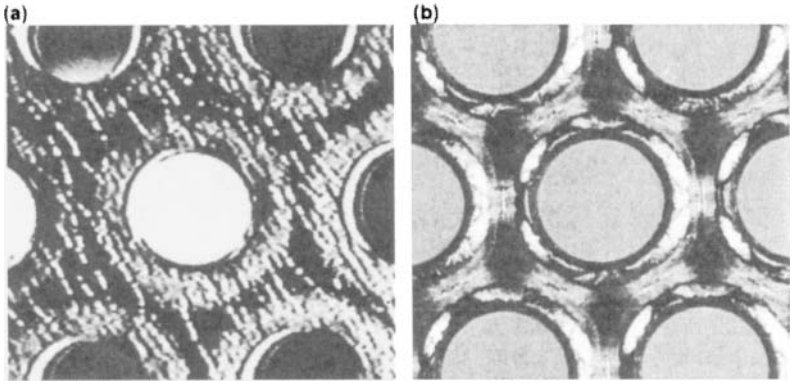

Fig. 5-22. NSTAR thruster accelerator grid at (a) 125 hours and (b) 30,352 hours.

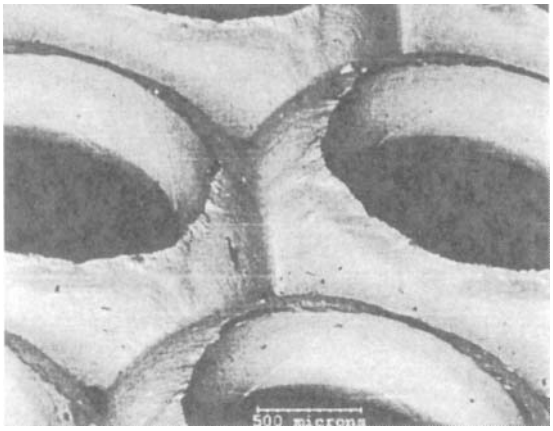

Fig. 5-23. SEM photograph shows that sputtering in the webbing between the holes had almost destroyed the structural integrity of the NSTAR grids.

5.6.1 Grid Models

As discussed above, the primary erosion mechanism of the accelerator grid is caused by sputtering from charge exchange ions. At the simplest level, all that is needed to predict erosion rates is to calculate the number of ions generated in the beamlets, find where they hit the grids, and then to determine the amount of material that they sputter. The total calculated charge exchange ion current accounts for nearly all of the measured accelerator grid current in a properly designed ion thruster (i.e., no direct interception of the beam current). The measured accelerator grid current in NASA's NSTAR thruster [30] ranged from

0.2% to 0.3% of the total beam current, which is shown in Fig. 5-24. Accel grid currents on the order of 1% or less of the beam current are standard in most ion thrusters.

Calculating the ion generation rate in the grid region due to charge exchange is relatively straightforward. The charge exchange currents generated by a single aperture's beamlet are given by

$$I_{CEX} = I_{Beamlet}\, n_o\, \sigma_{CEX}\, \ell_d, \tag{5.6-1}$$

where ℓ_d is the effective collection length downstream of the accel grid from which ions flow back to the grid and n_o is the average neutral density along this length. The charge exchange cross section, σ_{CEX}, is well known and varies slowly with beam energy [48]. The average neutral density along the path length ℓ_d is estimated from the thruster propellant flow rate utilization fraction, which is the difference between the neutral atom flow rate and the beam ion current over the open area fraction of the accel grid. The neutral density is usually assumed to remain constant in the accel grid hole and decreases as the gas expands downstream of the grid surface. The neutral gas density is normally highest in holes near the edge of the grid and lower at the center where nearly all the gas has been "burned up" through ionization in the discharge chamber. The effective path length, ℓ_d, is a basic result of the ion optics calculations, and is essentially the distance downstream at which the beamlets have completely merged to form a beam plasma with a uniform potential across the beam diameter. An estimate of the effective path length is needed when setting up a grid erosion calculation to make certain that the

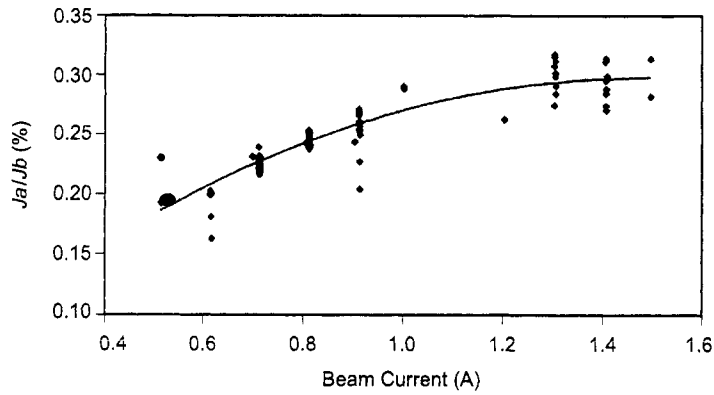

Fig. 5-24. Ratio of the accel grid current to the beam current as a function of the beam current in NSTAR, showing that the accel current is typically less than 1% of the beam current (from [30]).

computational region is long enough to include all the charge exchange ions that can return to the grid.

Using Eq. (5.6-1) and the current ratio from Fig. 5-24, an estimate can be made of the effective path length (ℓ_d) for the NSTAR thruster. If the measured accel grid current is all due to charge exchange (i.e., no direct interception), then Eq. (5.6-1) can be rewritten as

$$\ell_d = \frac{I_{\text{accel}}}{I_{\text{Beam}} \sigma_{\text{CEX}} n_o} . \tag{5.6-2}$$

Assuming the effective charge exchange path length is much longer than the gap between the screen and accelerator grids, the average neutral gas density can be estimated from the grid diameter, the flow of neutral gas out of the thruster, and the thruster beam current. The neutral gas density downstream of the grids close to the thruster is then

$$n_o = \frac{\Gamma_o}{v_o \pi r_{\text{grid}}^2} , \tag{5.6-3}$$

where v_o is the neutral velocity, and Γ_o is the flux of unutilized propellant escaping from the discharge chamber. Using the parameters for the NSTAR at TH15 from [29], the total neutral flow into the thruster is 28 sccm. The thruster discharge chamber has a mass utilization efficiency of about 88%, so the neutral gas flow escaping the thruster is about 3.4 sccm, which corresponds to 1.5×10^{18} particles per second. Assuming the gas exits the thruster at about an operating temperature of 250°C, the neutral velocity $\bar{c}/2$ is about 110 m/s. The average neutral density from Eq. (5.6-3) is then about 2.3×10^{17} m^{-3}, and neutral density varies over the grid by more than a factor of two. Using the data in Fig. 5-24 extrapolated to the beam current of 1.76 A in TH15, and a charge exchange cross section of 5×10^{-19} m^2, the average effective path length from Eq. (5.6-2) becomes

$$\ell_d = \frac{(0.003)}{(5 \times 10^{-19})(2.3 \times 10^{17})} = 0.03\,[\text{m}] . \tag{5.6-4}$$

The path length is more than an order of magnitude larger than the grid gap, consistent with our assumption. The very long path length compared with grid hole spacing means that the computational space in ion optics codes is very long (several centimeters), and so the computer codes must allow for the axial zone sizes to increase downstream of the grids.

5.6.2 Barrel Erosion

As was illustrated in Fig. 5-20, charge exchange ions generated between the screen grid and the upstream surface of the accel grid can impact the interior surface of the accel grid holes. These ions sputter away grid material, increasing the barrel radius. While computer codes, such as CEX-2D [4], are normally used to calculate the erosion rate, it is instructive to derive an analytical estimate. The following calculation is based upon published performance and erosion data for NASA's NSTAR thruster operating at its highest power TH15 level [29,50].

Assume that any ions generated downstream of the discharge chamber are not focused through the hole in the accelerator grid. For barrel erosion, the path length is taken as the sum of the grid gap and the accelerator grid thickness, which for NSTAR is about a millimeter. The upstream gas density is estimated by dividing the downstream density by the grid open area fraction, f_a, and the Clausing [51] factor, η_c, which reduces the gas transmission due to the finite thickness of the accel grid. The Clausing factor depends only on the aperture length-to-radius ratio. The neutral gas density is then

$$n_o = \frac{\Gamma_o}{v_o \pi r_{\text{grid}}^2} \frac{1}{f_a \eta_c}. \tag{5.6-5}$$

The neutral gas density in the accelerator grid apertures is higher than the gas density downstream of the accelerator grid, which was calculated using Eq. (5.6-2), due to the effects of the open area fraction and the Clausing factor. For an open area fraction of 0.24 and a Clausing factor of 0.6, the neutral density in the grid gap is about 9×10^{18} m^{-3}.

The number of grid apertures is approximately the grid open area divided by the area per aperture:

$$N_{\text{aperture}} \approx \frac{f_a \pi r_{\text{grid}}^2}{\pi r_{\text{aperture}}^2}. \tag{5.6-6}$$

The average aperture current is the total beam current divided by the number of apertures,

$$\bar{I}_{\text{aperture}} = \frac{I_b}{N_{\text{aperture}}}. \tag{5.6-7}$$

The maximum aperture current is obtained using the definition of beam flatness, which is given as

$$f_b \equiv \frac{\text{Average current density}}{\text{Peak current density}} = \frac{\bar{I}_{\text{aperture}}}{I_{\text{aperture}}^{\max}}. \tag{5.6-8}$$

The published value of NSTAR beam flatness from Polk [30] is 0.47. Using Eqs. (5.6-6), (5.6-7), and (5.6-8), the maximum current per aperture is 2.5×10^{-4} A. Charge exchange ions that can hit the accel grid are generated in between the screen grid exit and the accel grid exit. The distance d between the screen grid exit and the accel grid exit is about 1.12 mm [4]. The charge exchange ion current to the central aperture barrel is then

$$I_{\text{CEX}} = I_{\text{aperture}}^{\max} n_o \sigma_{\text{CEX}} d = 1.4 \times 10^{-6} \text{ [A]}. \tag{5.6-9}$$

The CEX-2D computer code simulations [4] show that charge exchange ions hit the accelerator grid with about three-tenths of the beam potential. For NSTAR, the beam potential is 1100 V; thus, the average charge exchange ion energy is about 330 V. Using the curve fit in reference [4] for sputtering yield Y, the aperture atom sputter rate is obtained:

$$\dot{n}_{\text{sputter}} = \frac{I_{\text{CEX}}}{e} Y \approx 3.5 \times 10^{12} \text{ [particles/s]}. \tag{5.6-10}$$

This atom sputtering rate can be used to find an initial wall erosion rate by first calculating the volumetric erosion rate:

$$\dot{V}_{\text{aperture}} = \frac{\dot{n}_{\text{sputter}}}{\left(\frac{\rho_{Mo}}{M_{Mo}}\right)}, \tag{5.6-11}$$

where the density of molybdenum is $\rho_{Mo} = 1.03 \times 10^4$ and the mass of molybdenum is $M_{Mo} = 95.94$ AMU = 1.6×10^{-25} kg. The volumetric erosion rate from Eq. (5.6-11) is then

$$\dot{V}_{\text{aperture}} = \frac{\dot{n}_{\text{sputter}}}{\left(\frac{\rho_{Mo}}{m_{Mo}}\right)} = \frac{3.5 \times 10^{12}}{\left(\frac{1.03 \times 10^4}{1.6 \times 10^{-25}}\right)} \approx 5.5 \times 10^{-17} \text{ [m}^3\text{/s]}. \tag{5.6-12}$$

Assuming the erosion rate is uniform throughout the barrel, the rate of increase of the aperture radius is just the volumetric erosion rate divided by the barrel area,

$$\dot{r}_{\text{aperture}} = \frac{\dot{V}_{\text{aperture}}}{2\pi r_a w_{\text{accel}}} \approx 3\times 10^{-11}\,[\text{m/s}], \qquad (5.6\text{-}13)$$

where the accel grid aperture radius r_a is 0.582 mm and the accel grid thickness w_{accel} is a half-millimeter. For the 8200-hour NSTAR wear test results described by Polk [30], this corresponds to an increase in diameter of about 0.2 mm, roughly what was observed.

More accurate predictions of the accel grid barrel erosion rate are found using the 2D and 3D computer simulations [4]. However, the codes use the same basic technique as that shown here to determine the amount of material removed by the charge exchange sputtering. The better predictions result from more accurate calculations of the neutral density and ion current densities across the grid surfaces and through the grid apertures.

5.6.3 Pits-and-Grooves Erosion

Using three-dimensional ion optics codes, it is possible to reproduce the details of the pits-and-grooves geometry of accelerator grid downstream surface erosion. The JPL CEX-3D code was developed [17] to solve for potentials and ion trajectories in a two-grid ion optics system, and was later modified to include a third grid [52]. The computational domain, illustrated in Fig. 5-25, is a triangular wedge extending from the axis of a hole pair to the midpoint between two aperture pairs. The wedge angle of 30 degrees is chosen to give

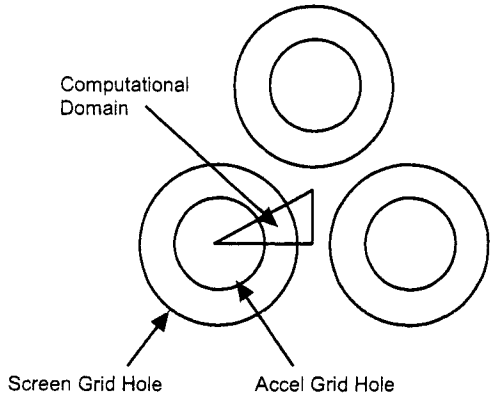

Fig. 5-25. Computational domain of the CEX-3D code (from [17]).

the smallest area that can be used to model the ion optics in order to minimize computational time. Similar triangles will cover each aperture pair by a combination of reflections and rotations. The computational domain extends from a few millimeters into the discharge chamber through the grids to a few centimeters downstream of the final grid.

In addition to tracking the beam-ion trajectories, the code calculates charge exchange ion production rates and charge exchange trajectories in three dimensions. Erosion of the accel grid barrel and downstream face is caused by these charge exchange ions. The location, kinetic energy, incidence angle, and current of each particle are recorded and used to compute the rate at which the grid material is removed. As shown above, charge exchange ions that strike the downstream surface of the accelerator grid can come from several centimeters downstream of the grid. Therefore, the computations domain is usually extended to 5-cm downstream of the final grid.

An example of the accel-grid downstream face erosion pattern predicted by CEX-3D is shown in Fig. 5-26. The triangular patches (the "pits"), where the grid webbing intersects, are shown in the photograph of the NSTAR ELT grid at the end of the test [49] and are predicted by the code in Fig. 5-26(a). In addition, the depth of the ring of erosion around the aperture ("the grooves") is also seen in Fig. 5-26(b) from the code predictions.

Accelerator grid pits-and-grooves erosion can be almost eliminated by the use of a third decelerator grid [44]. The Xenon Ion Propulsion System (XIPS®) thruster [53] is an example of an ion thruster that uses a three-grid ion optics system. As shown in Fig. 5-27, the third grid reduces from centimeters to

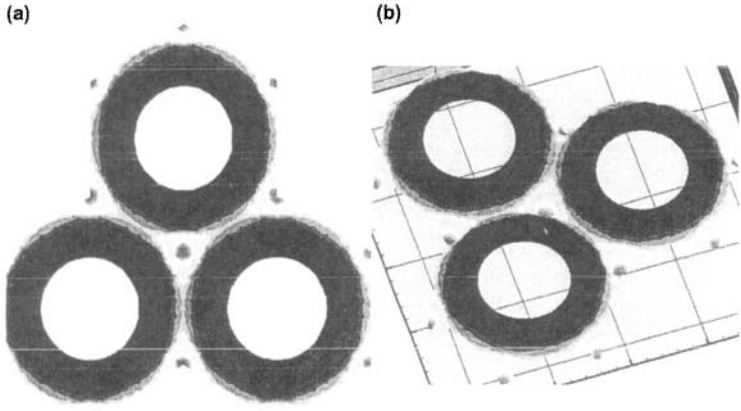

Fig. 5-26. CEX-3D calculation of the pits-and-grooves erosion wear patterns that match the experimental patterns shown in (a) Fig. 5-22(a) and (b) 5-22(b).

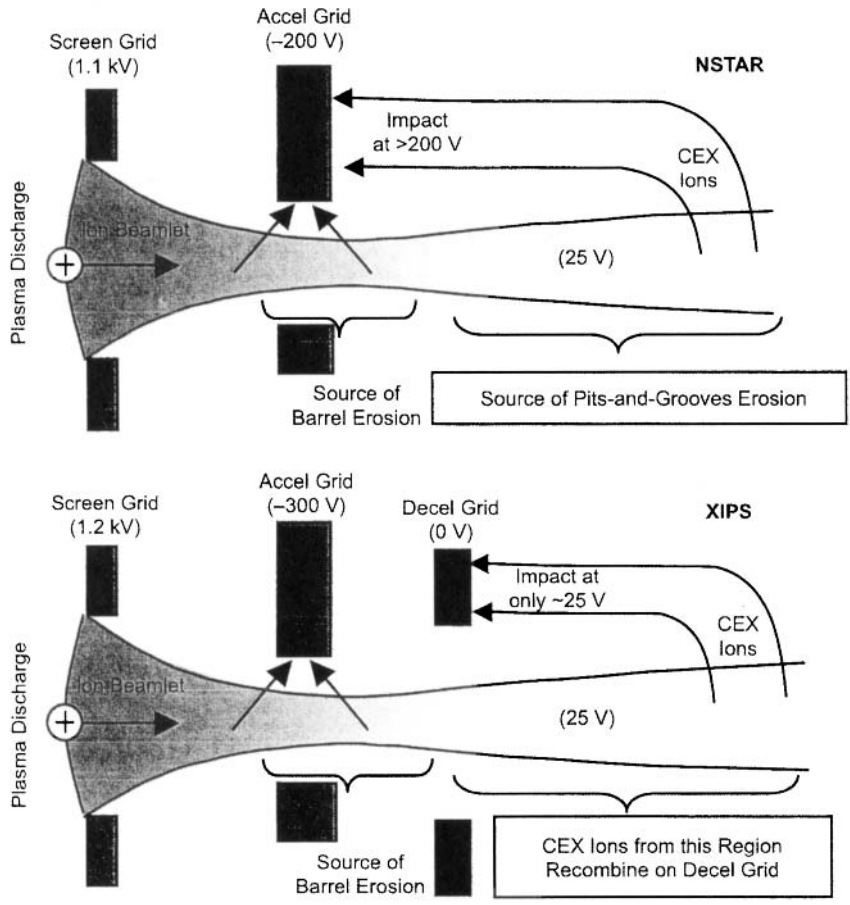

Fig. 5-27. Grid cross section comparing charge exchange generation in NSTAR, a two-grid system, with XIPS, a three-grid system.

millimeters the length of the region where charge exchange ions that can hit the accelerator grid are generated. This causes a dramatic reduction in the pits-and-grooves erosion between the two thrusters, shown in Fig. 5-28 as calculated using CEX-3D.

Although the three-dimensional code CEX-3D is used to predict erosion of the accelerator grid downstream surface, the simpler, two-dimensional CEX-2D code is typically used for accelerator grid aperture barrel erosion calculations because the apertures are cylindrical and the CEX-2D code can produce these

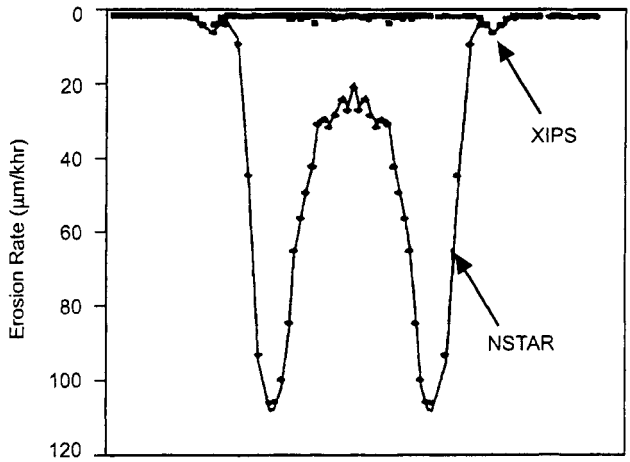

Fig. 5-28. CEX-3D results showing the XIPS third grid almost eliminates pits and grooves erosion evident in the NSTAR thruster (from [52]).

results more quickly. CEX-2D and CEX-3D use the same algorithms for the discharge chamber plasma and for beam ion trajectories. The codes have been benchmarked with each other, and for round beamlets that can be handled by CEX-2D, their results are within a few percent.

References

[1] H. R. Kaufman, "Technology of Electron-Bombardment Ion Thrusters," in *Advances in Electronics and Electron Physics*, vol. 36, edited by L. Marton, New York: Academic Press, 1974.

[2] A. T. Forrester, *Large Ion Beams*, New York: John Wiley and Sons, 1988.

[3] G. R. Brewer, *Ion Propulsion Technology and Applications*, New York: Gordon and Breach, 1970.

[4] J. R. Brophy, I. Katz, J. E. Polk, and J. R. Anderson, "Numerical Simulations of Ion Thruster Accelerator Grid Erosion," AIAA-2002-4261, 38th Joint Propulsion Conference, July 7–10, 2002.

[5] V. J. Friedly and P. J. Wilbur, "High Current Hollow Cathode Phenomena," *Journal of Propulsion and Power*, vol. 8, no. 3, pp. 635–643, 1992.

[6] I. Kameyama and P. J. Wilbur, "Measurement of Ions from High Current Hollow Cathodes Using Electrostatic Energy Analyzer," *Journal of Propulsion and Power*, vol. 16, no. 3, pp. 529–535, 2000.

[7] P. J. Wilbur, J. R. Beattie, and J. Hyman, Jr., "An Approach to the Parametric Design of Ion Thrusters," *Journal of Propulsion and Power*, vol. 6, no. 5, pp. 575–583, 1990.

[8] R. A. Martinez, J. D. Williams, and D. M. Goebel, "Electric Field Breakdown Properties of Materials Used in Ion Optics Systems," AIAA-2006-5004, 42nd Joint Propulsion Conference, Sacramento, California, July 10–13, 2006.

[9] P. Wilbur, "Limits on High Specific Impulse Ion Thruster Operation," AIAA-2004-4106, 40th Joint Propulsion Conference, Fort Lauderdale, Florida, July 11–14, 2004.

[10] J. H. Whealton, R. W. McGaffey, and P. S. Meszaros, "A Finite Difference 3-D Poisson-Vlasov Algorithm for Ions Extracted from a Plasma," *Journal of Computational Physics*, vol. 63, pp. 20–32, 1986.

[11] Y. Arakawa and M. Nakano, "An Efficient Three Dimensional Optics Code for Ion Thruster Research," AIAA-96-3198, 32nd Joint Propulsion Conference, Lake Buena Vista, Florida, July 1–3, 1996.

[12] M. Nakano and Y. Arakawa, "Ion Thruster Lifetime Estimation and Modeling Using Computer Simulation," IEPC-99-145, 27th International Electric Propulsion Conference, Pasadena, California, October 15–19, 2001.

[13] Y. Nakayama and P. Wilbur, "Numerical Simulation of High Specific Impulse Ion Thruster Optics," IEPC-01-099, 27th International Electric Propulsion Conference, Pasadena, California, October 15–19, 2001.

[14] I. Boyd and M. Crofton, "Grid Erosion Analysis of the T5 Ion Thruster," AIAA-2001-3781, 37th Joint Propulsion Conference, Salt Lake City, Utah, July 8–11, 2001.

[15] Y. Okawa, H. Takegahara, and T. Tachibana "Numerical Analysis of Ion Beam Extraction Phenomena in an Ion Thruster," IEPC-01-097, 27th International Electric Propulsion Conference, Pasadena, California, October 15–19, 2001.

[16] J. Wang, J. E. Polk, J. R. Brophy, and I. Katz, "Three-Dimensional Particle Simulations of NSTAR Ion Optics," IEPC-01-085, 27th International Electric Propulsion Conference, Pasadena, California, October 15–19, 2001.

[17] J. J. Anderson, I. Katz, and D. Goebel, "Numerical Simulation of Two-Grid Ion Optics Using a 3D Code," AIAA-2004-3782, 40th Joint Propulsion Conference, Ft. Lauderdale, Florida, July 11–14, 2004.

[18] Ian Brown, *The Physics and Technology of Ion Sources*, New York: John Wiley and Sons, 1989.

[19] Y. Nakayama and P. J. Wilbur, "Numerical Simulations of Ion Beam Optics for Many-grid Systems," *Journal of Propulsion and Power*, vol. 19, no. 4, pp. 607–613, 2003.

[20] J. Kim, J. H. Wealton, and G. Shilling, "A Study of Two-stage Ion Beam Optics," *Journal of Applied Physics*, vol. 49, no. 2, pp. 517–524, 1978.

[21] C. Farnell, "Performance and Life Simulation of Ion Thruster Optics," Ph.D. Dissertation, Colorado State University, Fort Collins, Colorado, 2007.

[22] L. D. Stewart, J. Kim, and S. Matsuda, "Beam Focusing by Aperture Displacement in Multiampere Ion Sources," *Review of Scientific Instruments*, vol. 46, pp. 1193–1196, 1975.

[23] J. H. Whealton, "Linear Optics Theory of Ion Beamlet Steering," *Review of Scientific Instruments*, vol. 48, pp. 1428–1429, 1977.

[24] M. Tarz, E. Hartmann, R. Deltschew, and H. Neumann, "Effects of Aperture Displacement in Broad-Beam Ion Extraction Systems," *Review of Scientific Instruments*, vol. 73, no. 2, pp. 928–930, 2002.

[25] Y. Okawa, Y. Hayakawa, and S. Kitamura, "Experiments on Ion Beam Deflection Using Ion Optics with Slit Apertures," *Japanese Journal of Applied Physics*, vol. 43, no. 3, pp. 1136–1143, 2004.

[26] J. D. Williams, D. M. Goebel, and P. J. Wilbur, "Analytical Model of Electron Backstreaming for Ion Thrusters," AIAA-2003-4560, 39th Joint Propulsion Conference, Huntsville, Alabama, July 20–23, 2003.

[27] V. A. Davis, I. Katz, M. J. Mandell, D. E. Brinza, M. D. Henry, and D. T. Young, "Ion Engine Generated Charge Exchange Environment: Comparison between NSTAR Flight data and Numerical Simulations," AIAA-2001-0970, 39th Aerospace Sciences Meeting, Reno, Nevada, January 8–11, 2001.

[28] K. R. Spangenberg, *Vacuum Tubes*, New York: McGraw-Hill, p. 348, 1948.

[29] J. R. Brophy "NASA's Deep Space 1 Ion Engine," *Review of Scientific Instruments*, vol. 73 pp. 1071–1078, 2002.

[30] J. Polk, J. R. Anderson, J. R. Brophy, V. K. Rawlin, M. J. Patterson, J. Sovey, and J. Hamley "An Overview of the Results from an 8200 Hour Wear Test of the NSTAR Ion Thruster," AIAA Paper 99-2446, 35th Joint Propulsion Conference, Los Angeles, California, June 20–24, 1999.

[31] A. Sengupta, J. R. Brophy, and K. D. Goodfellow, "Status of the Extended Life Test of the Deep Space 1 Flight Spare Ion Engine After 30,352 Hours of Operation," AIAA-2003-4558, 39th Joint Propulsion Conference, Huntsville, Alabama, July 20–23, 2003.

[32] A. Sengupta, "Experimental Investigation of Discharge Plasma Magnetic Confinement in an NSTAR Ion Thruster," AIAA-2005-4069, 41st Joint Propulsion Conference, Tucson, Arizona, July 10–13, 2005.

[33] J. E. Polk, D. M. Goebel, I. Katz, J. S. Snyder, A. C. Schneider, L. Johnson, and A. Sengupta, "Performance and Wear Test Results for a 20-kW Class Ion Engine with Carbon-Carbon Grids," AIAA-2005-4393, 41st Joint Propulsion Conference, Tucson, Arizona, July 10–13, 2005.

[34] E. Kuffel and W. S. Zaengl, *High Voltage Engineering Fundamentals*, Oxford, England: Pergamon Press, 1984.

[35] W. H. Kohl, *Handbook of Materials and Techniques for Vacuum Devices*, New York: Reinhold Publishing Corporation, 1967.

[36] D. M. Goebel and A. C. Schneider, "High Voltage Breakdown and Conditioning of Carbon and Molybdenum Electrodes," *IEEE Transactions on Plasma Science*, vol. 33, issue 4, pp. 1136–1148, 2005.

[37] P. A. Chatterton, "Theoretical Study of the Vacuum Breakdown Initiated by Field Emission," *Proceedings of the Physics Society*, vol. 88, pp. 231–243, 1966.

[38] F. R. Schwirzke, "Vacuum Breakdown on Metal Surfaces," *IEEE Transactions on Plasma Science*, vol. 19, pp. 690–696, 1991.

[39] W. D. Davis and H. C. Miller, "Analysis of the Electrode Products Emitted by dc Arcs in a Vacuum Ambient," *Journal of Applied Physics*, vol. 40, pp. 2212–2221, 1969.

[40] A. Anders, B. Yotsombat, and R. Binder, "Correlation Between Cathode Properties, Burning Voltage, and Plasma Parameters of Vacuum Arcs," *Journal of Applied Physics*, vol. 89, pp. 7764–7771, 2001.

[41] J. S. Sovey, J. A. Dever, and J. L. Power, "Retention of Sputtered Molybdenum on Ion Engine Discharge Chamber Surfaces," IEPC-01-86, 27th International Electric Propulsion Conference, Pasadena, California, October 15–19, 2001.

[42] D. M. Goebel, "High Voltage Breakdown Limits of Molybdenum and Carbon-based Grids for Ion Thrusters," AIAA-2005-4257, 41st Joint Propulsion Conference, Tucson, Arizona, July 10–13, 2005.

[43] M. J. Druyvesteyn and F. M. Penning, "The Mechanism of Electrical Discharge in Gases," *Reviews of Modern Physics*, vol. 12, pp. 87–174, 1940.

[44] R. Doerner, D. White, and D. M. Goebel, "Sputtering Yield Measurements during Low Energy Xenon Plasma Bombardment," *Journal of Applied Physics*, vol. 93, no. 9, pp. 5816–5823, 2003.

[45] H. Kuninaka, I. Funaki, K. Nishiyama, Y. Shimizu, and K. Toki, "Results of 18,000 hour Endurance Test of Microwave Discharge Ion Thruster Engineering Model," AIAA-2000-3276, 36th Joint Propulsion Conference, Huntsville, Alabama, July 16–19, 2000.

[46] J. S. Snyder and J. R. Brophy, "Performance Characterization and Vibration Testing of 30-cm Carbon-Carbon Ion Optics," AIAA-2004-3959, 40th Joint Propulsion Conference, Ft. Lauderdale, Florida, July 11–14, 2004.

[47] M. De Pano, S. Hart, A. Hanna, and A. Schneider, "Fabrication and Vibration Results of 30-cm Pyrolytic Graphite Ion Optics," AIAA-2004-3615, 40th Joint Propulsion Conference and Exhibit, Fort Lauderdale, Florida, July 11–14, 2004.

[48] J. S. Miller, S. H. Pullins, D. J. Levandier, Y. Chiu, and R. A. Dressler, "Xenon Charge Exchange Cross Sections for Electrostatic Thruster Models," *Journal of Applied Physics*, vol. 91, no. 3, pp. 984–991, 2002.

[49] A. Sengupta, J. R. Brophy, J. R. Anderson, C. Garner, K. deGroh, T. Karniotis, and B. Banks, "An Overview of the Results from the 30,000 Hour Life Test of the Deep Space 1 Flight Spare Ion Engine," AIAA-2004-3608, 40th Joint Propulsion Conference, Fort Lauderdale, Florida, July 11–14, 2004.

[50] J. E. Polk, R. Y. Kakuda, J. R. Anderson, J. R. Brophy, V. K. Rawlin, M. J. Patterson, J. Sovey, and J. Hamley, "Performance of the NSTAR Ion Propulsion System on the Deep Space One Mission," AIAA-2001-965, 39th Aerospace Sciences Meeting and Exhibit, Reno, Nevada, January 8–11, 2001.

[51] P. Clausing, "The Flow of Highly Rarefied Gases Through Tubes of Arbitrary Length," *Journal of Vacuum Science and Technology*, vol. 8, pp. 636–646, 1971.

[52] R. Wirz and I. Katz, "XIPS Ion Thruster Grid Erosion Predictions for Deep Space Missions," 30th International Electric Propulsion Conference, Florence, Italy, September 17–20, 2007.

[53] J. R. Beattie, J. N. Matossian, and R. R. Robson, "Status of Xenon Ion Propulsion Technology," *Journal of Propulsion and Power*, vol. 6, no. 2, pp. 145–150, 1990.

Problems

1. For an ion accelerator that is described by the Child–Langmuir law, derive the dependence of the minimum Isp on the beam voltage for a given thrust level.
2. A 1-kV ion accelerator has a grid spacing of 1 mm and a screen aperture diameter of 1 mm.
   a. What is the space-charge-limited beamlet current density for Xe^+ assuming a very thin screen grid and a planar sheath?
   b. If the screen grid is 0.25 mm thick, what is the maximum beamlet current density for a non-planar sheath? How does this compare to the classic planar Child–Langmuir result?
3. An ion thruster with a grid diameter of 20 cm has a beam current density that varies with the radius as kr^2, where k is a constant.
   a. If the peak current density on axis is J_p and the current density at the edge of the grid is $J_p/10$, find the expression for $J(r)$.
   b. If the peak current density is 5 mA/cm^2, what is the total beam current?
   c. What is the flatness parameter?
   d. What is the percent reduction in the beam current compared to the case of a uniform beam current density of the peak value (the flatness is 1)?
4. An ion thruster has a beam plasma potential of 20 V and an electron temperature in the beam of 5 eV.
   a. For a plasma potential at the screen grid sheath edge of 1000 V, what potential must be established in the accel grid aperture to keep the electron backstreaming current to 1% of the beam current?
   b. Neglecting space charge in the beamlet, what voltage must be applied to the accel grid to achieve the minimum potential in (a) for the case of a 3-mm screen grid diameter, 0.25-mm screen grid thickness, 2-mm accel grid diameter, and 0.5-mm accel grid thickness with a 1-mm grid gap?
   c. If the beamlet current is 0.2 mA and the beamlet has a diameter in the accel grid aperture of 1 mm, what must the accel grid voltage be to maintain the 1% backstreaming current specification?

5. One of the first ion thrusters to fly in space was a cesium surface ionization thruster where cesium ions were pulled from a hot surface by the electric field that also produced the beam. Model the thruster as a diode, with cesium ions at 7.5 mA/cm^2 coming from one surface and with the other electrode an accel grid with 80% transparency and a grid gap "d" from the ion source.
   a. Assuming 100% mass utilization efficiency, neglecting the angular divergence of the beam, and using a 200-V negative bias on the accel grid, what is the voltage, current, thruster diameter, and gap size required to produce 5 mN of thrust at an Isp of 3000 s?
   b. If the thruster has 95% mass utilization efficiency and a total angular divergence of the beam of 10 deg, how does that change the results of part (a)?
   c. If it takes 100 W of power to heating the cesium ion-emitting surface to the required surface temperature of about 1350 K, what is the total efficiency of the thruster, using the parameters from part (b)?

Fundamentals of Electric Propulsion: Ion and Hall Thrusters
by Dan M. Goebel and Ira Katz
Copyright © 2008 John Wiley & Sons, Inc.

Chapter 6
Hollow Cathodes

Ion and Hall thrusters that utilize an electron discharge to ionize the propellant gas and create the plasma in the thruster require a cathode to emit the electrons. In addition, thrusters must neutralize the ion beam leaving the thruster by providing electrons emitted from a cathode into the beam. The properties of the cathode material, the physical configuration hollow cathode, and structure of the cathode plasma determine, to a large extent, the performance and life of both ion and Hall thrusters.

6.1 Introduction

Early electron-bombardment ion thrusters developed in the 1960s utilized directly heated tungsten filaments as the cathode that produced electrons for the plasma discharge. Smaller tungsten filaments were also inserted into the ion beam to provide neutralizing electrons. Due to the high work function of tungsten, these filaments had to be operated at temperatures of over 2600 K in order to emit electron current densities in excess of 1 A/cm^2. Operation at these temperatures requires high heater power, often on the order of the discharge power, which significantly reduces the efficiency of the thruster. In addition, the life of filament cathodes is limited by rapid evaporation of the filament material at the elevated temperatures and by sputtering of the tungsten surface exposed to the discharge plasma or the beam by ion bombardment. Filament cathode life was typically limited to the order of only hundreds of hours or less. While the use of filament cathodes permitted development of ion thruster accelerator grids and discharge chambers, they were inadequate for long-life space applications.

These problems were solved by the development of hollow cathodes. A generic hollow cathode is shown in Fig. 6-1, where the cathode consists of a hollow refractory tube with an orifice plate on the downstream end. The tube has an insert in the shape of a cylinder that is placed inside the tube and pushed against

the orifice plate. This insert is the active electron emitter, and it can be made of several different materials that provide a low work function surface on the inside diameter in contact with the cathode plasma. The cathode tube is wrapped with a heater (a co-axial sheathed heater is shown in the figure) that raises the insert temperature to emissive temperatures to start the discharge. The electrons emitted from the insert ionize gas injected through the cathode tube and form a cathode plasma from which the discharge-current electrons are extracted through the orifice into the thruster plasma.

A hollow cathode can be separated into three distinct plasma regions illustrated in Fig. 6-2: a dense plasma in the insert region interior to the cathode, a high current density plasma in the orifice, and a diffuse plume plasma outside of the cathode that connects to the thruster discharge plasma. The plasma ions generated throughout the device neutralize the electron space charge; as a result, hollow cathodes produce high currents at low voltages as compared with vacuum cathode devices.

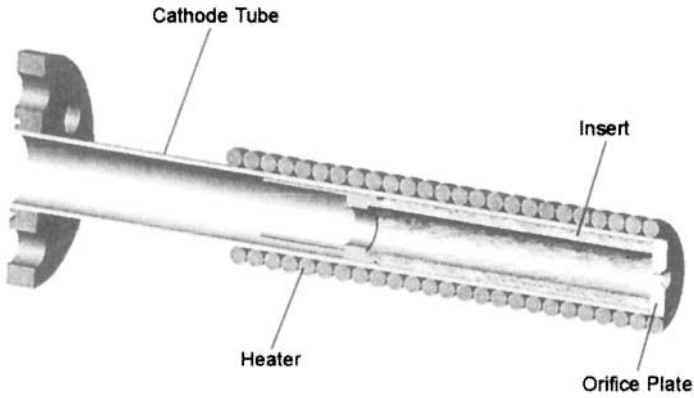

Fig. 6-1. Typical hollow cathode geometry of a refractory metal tube with an emissive insert inside and a heater wrapped on the outside.

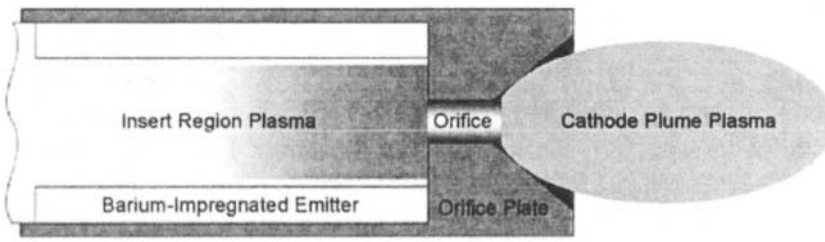

Fig. 6-2. The three plasma regions in a hollow cathode.

The structure of the hollow cathode serves three main functions. First, some fraction of the thruster propellant is injected through the hollow cathode, and the discharge inside the resulting high neutral pressure region generates a cold, high-density plasma. The plasma and neutral densities are the highest of anywhere in the thruster, and the electron temperature is correspondingly the lowest. This causes the plasma potential inside the hollow cathode to be very low, reducing the energy of the ions that arrive at the insert surface. This characteristic behavior is demonstrated in Fig. 6-3, which shows the measured potential and density profiles in the Nuclear Electric Xenon Ion Thruster System (NEXIS) hollow cathode [1] discharge. Plasma densities in excess of 10^{14} cm^{-3} are routinely generated inside hollow cathodes, and the electron temperature is found [2] to be only 1 to 2 eV. The low plasma potential in the insert region and high neutral scattering rates decrease the ion bombardment energy striking the insert surface to typically less than 20 eV, which essentially eliminates ion sputtering of the surface and greatly increases the life of the cathode. Second, the high-density plasma in the insert region eliminates space charge effects at the cathode surface that can limit the electron emission current density. Emission current densities of 1 to 10 A/cm^2 are typically employed in thruster hollow cathodes for compact size and good life, although higher

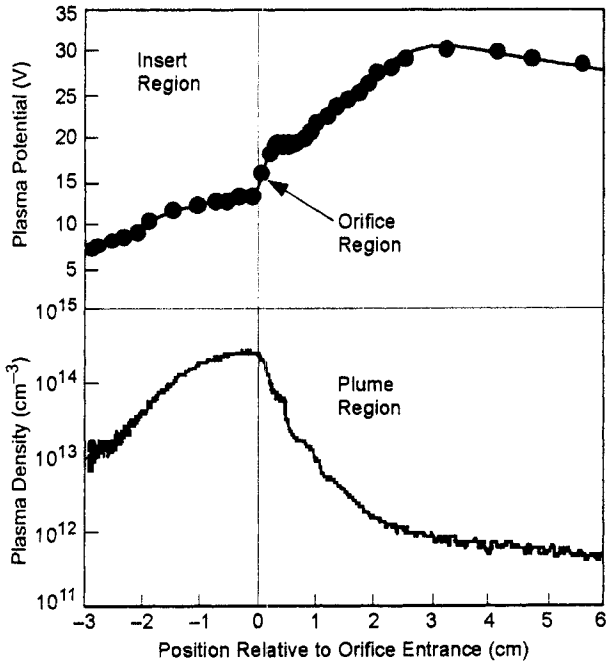

Fig. 6-3. Plasma potential (top) and density (bottom) measured on axis in the NEXIS hollow cathode at 25 A of discharge current.

current densities are achievable and sometimes used. Third, the cathode insert can be heat shielded well in this geometry, which greatly reduces the radiation losses of the cathode at operating temperatures. This decreases the amount of power that must be deposited in the cathode to maintain the required temperature for electron emission. This reduces the cathode heating losses to a small fraction of the discharge power, significantly reducing the discharge loss of the plasma generator.

Since nearly the entire discharge current runs through the orifice, the current density there is highest in the system, and a sufficient plasma density must be generated locally to carry the current. For the 25-A discharge case shown in Fig. 6-3, the plasma density in the orifice is on the order of 10^{14} cm^{-3}. The discharge current flowing through the 2.5-mm-diameter orifice is described by

$$I = n_e e v A, \tag{6.1-1}$$

where n_e is the plasma density, e is the electron charge, v is the electron drift velocity, and A is the cross-sectional area of the orifice. Solving for the drift velocity gives

$$v = \frac{I}{n_e e A} = 7.7 \times 10^4 \text{ m/s} << v_{th}, \tag{6.1-2}$$

where the thermal drift velocity $v_{th} = \sqrt{kT_e/m}$ is 6×10^5 m/s for the 2-eV plasma electron temperatures measured in this location. The current is conducted through the orifice region at relatively low drift velocities, even though the electron current density exceeds 100 A/cm^2 in this case. This is typically true even at current densities exceeding 1000 A/cm^2.

In the plume region, the expanding orifice plasma and ionization of the expanding neutral gas provide an ion background that neutralizes the space charge of the current carrying electrons. Hollow cathodes are normally enclosed in another electrode called a keeper, shown in Fig. 6-4. The major functions of the keeper electrode are to facilitate turning on the cathode discharge, to maintain the cathode temperature and operation in the event that the discharge or beam current is interrupted temporarily, and to protect the cathode orifice plate and external heater from high-energy ion bombardment that might limit the cathode life. The keeper is normally biased positive relative to the cathode, which either initiates the discharge during start-up or reduces the ion bombardment energy during normal operation. The life of the keeper electrode is very important to the life of the cathode and thruster.

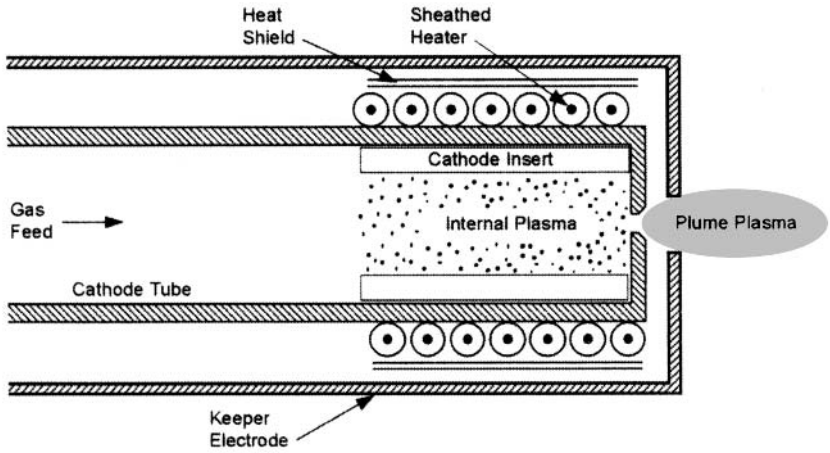

Fig. 6-4. Hollow cathode schematic showing the cathode tube, insert, and heater enclosed in a keeper electrode.

Hollow cathodes operate in a "self-heating" mode, in which the external heater is turned off during operation and the cathode insert is heated by plasma bombardment. There are three self-heating mechanisms possible in hollow cathodes: (1) orifice heating, (2) ion heating, and (3) electron heating. In orifice heating, the cathode is designed with a small, restrictive orifice, which produces a high internal pressure in both the insert and orifice regions. The plasma discharge passing through the orifice is then very resistive, causing a significant amount of power to be deposited in the orifice plasma and transferred to the orifice walls by convection. This power deposition then heats the insert by conduction and radiation. Orifice heating is used primarily in neutralizer cathodes where the discharge currents are very low. The classic mechanism for cathode heating is ion heating, where ions in the cathode insert region plasma fall through the sheath potential at the insert surface and heat the surface by ion bombardment. Electron heating occurs in a regime where both the cathode internal pressure and the discharge current are relatively high, resulting in the very high plasma densities ($>10^{15}$ cm^{-3}) generated in the insert region. The low electron temperatures and low sheath voltages produced in this situation result in the energetic tail of the Maxwellian electron distribution having sufficient energy to exceed the sheath potential and reach the insert surface. These electrons then deposit their energy on the insert and heat it to emission temperatures. The heating mechanism that dominates in any hollow cathode design depends on the geometry of the cathode, the internal neutral gas pressure in the insert and orifice regions, and the discharge current.

This chapter will start with a simple classification of different hollow cathode geometries to aid in the discussion of the important effects in the system, and

then discuss the basics of the cathode insert that provides thermionic electron emission. The characteristics of the plasmas in the insert region, the orifice, and the cathode plume in the vicinity of the keeper required to extract and transmit the electrons into the thruster will then be examined. Since the neutral gas density changes all along the discharge path in hollow cathode discharges, the plasmas generated in each location (inside the insert, in the orifice, and in the cathode plume) have different properties in terms of collisionality, temperature, potential, and density. These differences determine the applicable plasma physics in each region.

6.2 Cathode Configurations

The geometry and size of the hollow cathodes depend on the amount of current that they are required to emit. Discharge currents in ion thrusters are typically 5 to 10 times the beam current depending on the efficiency of the plasma generator, and discharge currents can range from a few amperes to over 100 amperes [3]. The hollow cathode used in a Hall thruster provides electrons for both ionization of the propellant gas and neutralization of the beam [4]. Hall thrusters also tend to run at lower specific impulse (Isp) than ion thrusters. Therefore, Hall thrusters require higher discharge currents from the cathode to achieve the same total power as compared to ion thrusters, and currents of the order of 10 amperes to hundreds of amperes are needed. Neutralizer cathodes in ion thrusters emit electrons at a current equal to the beam current. Therefore, they can be made smaller than discharge cathodes and must be designed to be self-heated and to run reliably at lower currents.

Higher discharge currents require larger insert sizes because the thermionic emission current densities from cathode surfaces are finite. Ultimately, this determines the diameter of the insert, which will be described in the next section. The cathode orifice size depends on many parameters. Ion thruster neutralizer cathodes have been designed with very small diameter orifices ($\leq 3 \times 10^{-2}$ cm), and ion thruster discharge cathodes and small Hall thruster cathodes have been designed with orifices of less than 0.1-cm diameter to over 0.3 cm in diameter. High-current hollow cathodes for large ion thrusters and Hall thrusters will have even larger orifices. These cathodes are sometimes designed even without an orifice, where the insert inside diameter forms a tube exposed to the discharge plasma.

Hollow cathodes generally fall into three categories, which will be useful later in describing the plasma characteristics in the three regions described above. The first type of hollow cathode is characterized by a small orifice with a large length-to-diameter ratio, shown schematically in Fig. 6-5 as Type A. These cathodes typically operate at low current and relatively high internal gas

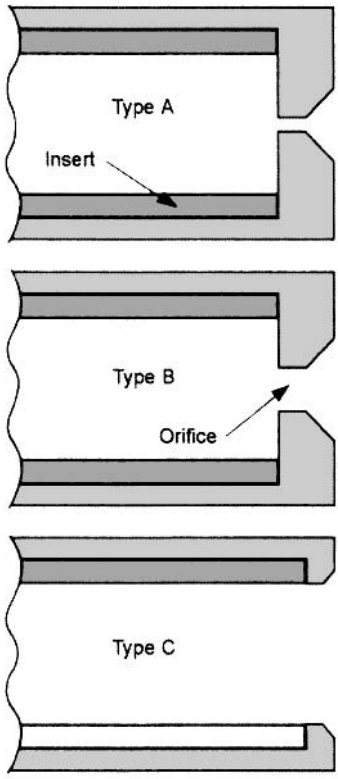

Fig. 6-5. Schematics of the three characteristic types of hollow cathodes (A, B, and C) depending on the orifice geometry.

pressures, and are heated primarily by orifice heating. The second type of cathode features has an orifice diameter typically larger than the length, shown in Fig. 6-5 as Type B, and operates at lower internal gas pressures. The heating mechanism in these cathodes can be due to electron or ion bombardment of the insert, or a combination of the two depending on the orifice size and operating conditions. The third type of cathode, typically used in high-current cathodes and shown in Fig. 6-5 as Type C, has essentially no orifice at all. These cathodes have a large neutral density gradient in the insert region, but they typically have a reduced internal pressure overall as compared to orificed cathodes. The heating mechanism for Type C cathodes is normally ion bombardment of the insert.

The value of the neutral gas pressure inside the hollow cathode affects both the plasma density and plasma profile due to collisional effects [5]. Figure 6-6 shows examples of axial plasma density profiles measured with fast scanning probes [6] inside a 0.38-cm inside-diameter (I.D.) cathode insert operating at 13 A of discharge current and a xenon flow of 3.7 standard cubic centimeters per minute (sccm) for two different orifice diameters and the case of no orifice plate at all. Small orifices, characteristic of Type A cathodes, have high internal pressures that produce high plasma densities but constrain the axial extent of the plasma to the order of a few millimeters. For a given emission current density, this can restrict the discharge current that is available. As the orifice is enlarged, the pressure decreases and the plasma extends farther into the insert, resulting in utilization of more of the insert surface area for electron emission.

The electron current density in the orifice is higher than anywhere else in the system and, depending on the orifice size, can easily exceed 1 kA/cm^2. If the orifice is long compared with its radius, as is the case in most Type A neutralizer hollow cathodes, the physics are the same as for a classical positive

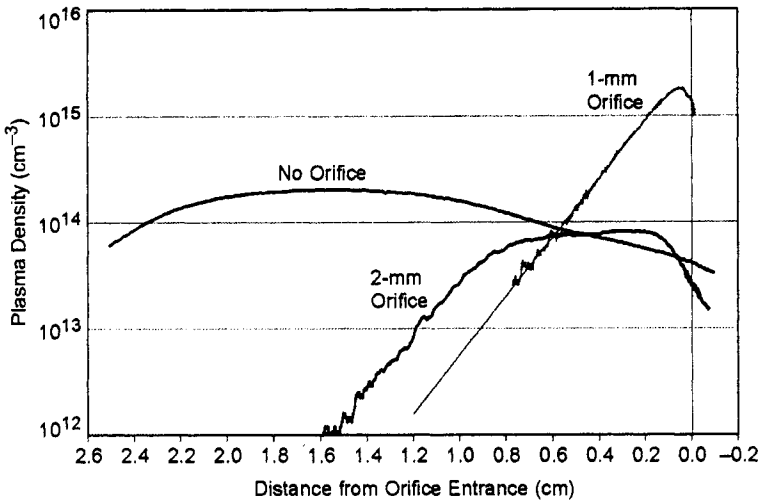

Fig. 6-6. Cathode plasma density profile examples as the orifice diameter is increased for a constant discharge current and flow rate.

column plasma where an axial electric field in the collisional plasma conducts the current and plasma resistive heating is very important. A large fraction of this ohmic power deposited in the orifice plasma goes into heating of the orifice plate by ion bombardment, which contributes to the insert heating by conduction and radiation. In Type B cathodes, the orifice is shaped nearly as an aperture, and there is little local resistive heating. The plasma in the insert region is generated by ionization of the neutral gas by the discharge current flowing through the insert region into the orifice. At high cathode neutral-gas flows (and subsequent high plasma density) in this type of cathode, the insert heating is primarily by plasma electrons. At low flow rates or with large orifices, the insert is heated predominately by the ions bombarding the emitter surface. In Type C cathodes, there is little or no orifice, and the plasma couples from a collisionally dominated region upstream inside the insert directly into the nearly collisionless cathode plume region. This creates long axial density and potential gradients and may expose some of the downstream region of the insert to higher potentials and ion bombardment. Heating in this case is predominately by ion bombardment through the higher cathode sheath potential.

Naturally, there is a continuous range of cathode operation that may demonstrate properties of all three cathode types. Indeed, a given cathode geometry can transition from low resistive heating in the orifice at low currents and low gas flow rates to substantial resistive heating and plasma generation at high currents and high gas flow rates. These three types of hollow cathodes will

be discussed in detail after the actual thermionic electron emitter properties are described.

6.3 Thermionic Electron Emitter Characteristics

Electrons are introduced into the system by thermionic emission from the insert surface. Thermionic emission by cathodes is described by the Richardson–Dushman equation [7]:

$$J = A\,T^2\,e^{-e\phi/kT}, \tag{6.3-1}$$

where A is, ideally, a constant with a value of 120 A/cm^{2}K^2, T is the temperature in kelvins, e is the charge, k is Boltzmann's constant, and ϕ is the work function. Experimental investigations of the thermionic emission of different materials reported values of A that vary considerably from the theoretical value. The cause of the deviation of A from a constant has been attributed to several different effects, such as variations in the crystal structure of the surface, variations in the surface coverage (for dispenser cathodes), changes in the density of states at the surface due to thermal expansion, etc. This issue has been handled [8] for many of the thermionic electron emitters used in hollow cathodes by introducing a temperature correction for the work function of the form

$$\phi = \phi_o + \alpha T, \tag{6.3-2}$$

where ϕ_o is the classically reported work function and α is an experimentally measured constant. This dependence can be inserted into Eq. (6.3-1) to give

$$J = Ae^{-e\alpha/k}T^2\,e^{-e\phi_o/kT} = D\,T^2\,e^{-e\phi_o/kT}, \tag{6.3-3}$$

where D is a material-specific modification to the Richardson–Dushman equation.

In the presence of strong electric fields at the surface of the cathode, the potential barrier that must be overcome by the electrons in the material's conduction band is reduced, which results effectively in a reduced work function. This effect was first analyzed by Schottky [9], and the so-called Schottky effect is included in the emission equation by the addition of a term [10] to describe the effect of the surface electric field on the emission current density:

$$J = D\,T^2\,\exp\left(\frac{-e\phi_o}{kT}\right)\exp\left[\left(\frac{e}{kT}\right)\sqrt{\frac{eE}{4\pi\varepsilon_o}}\right], \tag{6.3-4}$$

where E is the electric field at the cathode surface. The Schottky effect often becomes significant inside hollow cathodes where the plasma density is very high and the electric field in the sheath becomes significant.

The properties of the material selected for the thermionic emitter or insert determine the required operating temperature of the cathode for a given emission current. The work functions and values of D found in the literature for several common cathode materials are summarized in Table 6-1. Figure 6-7 shows the emission current density calculated using Eq. (6.3-3) for several different emitter materials. The refractory metals are seen to have work functions in excess of 4 eV, and so they must operate at very high temperatures to achieve significant emission current density.

The so-called "oxide" cathodes have work functions under about 2 eV and so are capable of producing high emission current densities at temperatures under 1000°C. Oxide layers, such as barium oxide, were first deposited on tungsten or nickel filaments to lower the work function and reduce the heater power required. However, these surface layers evaporate and are easily sputtered by ion bombardment, limiting the life in vacuum applications to thousands of hours and in plasma discharges to tens of hours. This problem was mitigated by the development of dispenser cathodes where a reservoir of the oxide material is fabricated into the tungsten substrate, which continuously re-supplies the low work function surface layer. The most commonly used dispenser cathode in thrusters, the "Phillips Type S," uses a porous tungsten matrix that is impregnated with an emissive mix of barium and calcium oxides and alumina [16]. Different molar concentrations of the three constituents of the emissive

Table 6-1. Work function and Richardson coefficients for several cathode materials.

	A	D	ϕ
BaO-Scandate [11]	120	—	$8 \times 10^{-7} T^2 - 1.3 \times 10^{3} T + 1.96$
BaO-W 411 [12]	120	—	$1.67 + 2.82 - 10^{-4}\, T$
BaO-W 411 [10]	—	1.5	1.56
LaB_6 [13]	—	29	2.66
LaB_6 [14]	—	110	2.87
LaB_6 [15]	120	—	2.91
LaB_6 [8]	120	—	$2.66 + 1.23 \times 10^{-4}\, T$
Molybdenum [8]	—	55	4.2
Tantalum [8]	—	37	4.1
Tungsten [8]	—	70	4.55

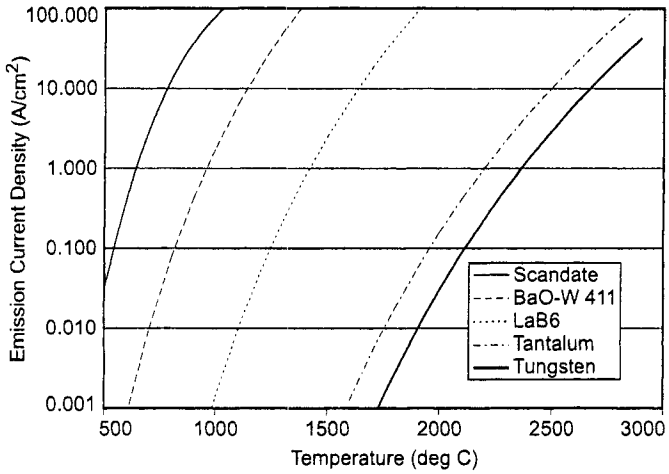

Fig. 6-7. Emission current density versus temperature for various cathode materials.

mix are used depending on the required emission current density and life. In ion thrusters, a 4:1:1 emissive mix typically is used, although other mixtures are available [1]. The matrix material containing the impregnate can be directly heated by passing a current through the material, or configured as an insert placed inside hollow cathodes.

In dispenser cathodes, chemical reactions in the pores of the matrix or at the surface at high temperatures reduce the emissive material and evolve a barium-oxide dipole attached to an active site on the tungsten substrate. The 4:1:1 Type S cathode has a work function of about 2.06 eV at temperatures in excess of about 800°C. Barium-oxide dispenser cathodes with porous matrix material made of tungsten can provide emission current densities of 10 A/cm^2 at surface temperatures of about 1000°C, as shown in Fig. 6-7. The work function can be further reduced by the introduction of small amounts of other refractory materials, such as iridium or osmium, in the tungsten matrix. These "mixed metal matrix" cathodes can have work functions below 1.9 eV, and they typically slow some of the chemical reactions that take place in the cathode. It was also found that the addition of scandium to the surface of the barium-oxide dispenser cathode reduces the work function significantly. This is reflected in Fig. 6-7, where the reported work function [11] at 1100°C is about 1.7 eV, which is significantly less than the 2.06 eV for the BaO dispenser cathode and results in much lower temperatures for a given emission current density. The mechanism for this improvement is not clear to date, and the ability to fabricate stable scandate electron emitters that maintain the low work function over time

has been problematic. However, scandate–BaO–W dispenser cathodes have been successful in several different cathode structures.

Because chemistry is involved in the formation of the low work function surface, dispenser cathodes are subject to poisoning that can significantly increase the work function [17]. Some care must be taken in handling the inserts and in the vacuum conditions used during operation of these cathodes to avoid poisoning by impurities in the gas that produce unreliable emission and shorten the lifetime. In addition, impurities in the feed gas that react with the tungsten insert can cause migration and deposition of tungsten or tungstates (compounds of tungsten, barium, and oxygen) on the surface, which change the surface structure and porosity and can reduce the surface coverage of the low work function BaO layer. One of the major drawbacks of using BaO dispenser cathodes in electric propulsion applications is the extremely high feed gas purity specified to avoid these poisoning and tungsten-material transport issues, which has resulted in a special "propulsion-grade" xenon with 99.9995% purity to be specified by some users of these cathodes for flight.

Another electron emitter material, lanthanum hexaboride [13], is a crystalline material made by press sintering LaB_6 powder into rods or plates and then machining the material to the desired shape. Polycrystalline LaB_6 cathodes have a work function of about 2.67 eV, depending on the surface stoichiometry, and will emit over 10 A/cm^2 at a temperature of 1650°C, as shown in Fig. 6-7. Since the bulk material is emitting, there is no chemistry directly involved in establishing the low work function surface, and LaB_6 cathodes are insensitive to impurities and air exposures that can destroy a BaO dispenser cathode [18]. An LaB_6 cathode can withstand gas-feed impurity levels two orders of magnitude higher than dispenser cathodes at the same emission current density. In addition, the cathode life is determined primarily by the low evaporation rate of the LaB_6 material at typical operating temperatures. The higher operating temperature of bulk LaB_6 and the need to support and make electrical contact with LaB_6 with materials that inhibit boron diffusion at the operating temperatures require some careful engineering of the cathode structure. However, LaB_6 cathodes are commonly used in Russian Hall thrusters in communications satellite applications [19].

Lanthanum hexaboride was first developed as an electron emitter by Lafferty [13] in the 1950s. The thermionic emission of lanthanum–boron compounds for various surface stoichiometries was extensively studied by several authors [14,15,19]. The first flight of Russian SPT Hall thrusters [20] in 1971, and all subsequent flights, utilized lanthanum hexaboride cathodes. The first reported use of LaB_6 in the US in a hollow cathode was by Goebel, et al. [21] in 1978, and the development of a high-current LaB_6 cathode for plasma sources that

dealt with supporting and making electrical contact with the material was described by Goebel, et al. [22] in 1985. The lanthanum–boron system can consist of combinations of stable LaB_4, LaB_6, and LaB_9 compounds, with the surface color determined [23] by the dominate compound. The evolution of LaB_4 to LaB_9 compounds is caused either by preferential sputtering of the boron or lanthanum atoms at the surface by energetic ion bombardment [14] or by preferential chemical reactions with the surface atoms [23]. However, a lanthanum–boride compound, when heated in excess of 1000°C in a reasonable vacuum, will evaporate its component atoms at rates that produce a stable $LaB_{6.0}$ surface.

Dispenser cathodes and LaB_6 cathodes offer long lifetimes in thruster applications because the evaporation rate is significantly lower than for refractory metals. Figure 6-8 shows the evaporation rate as a function of the emission current density for a Type S 4:1:1 dispenser cathode [17], LaB_6 [24], and tungsten [8] (for comparison). The dispenser cathode and LaB_6 cathode evaporation rates are more than one order of magnitude lower when compared with tungsten at the same emission current density. Excessive evaporation of barium and reduced surface coverage usually limit the current density of dispenser cathodes to less than about 20 A/cm^2 in continuous operation. In spite of operating at a significantly higher temperature than the barium cathode, the LaB_6 has a lower evaporation rate until the emission current exceeds about 15 A/cm^2 and can provide longer life. The life of these cathodes is discussed in more detail in Section 6.8.

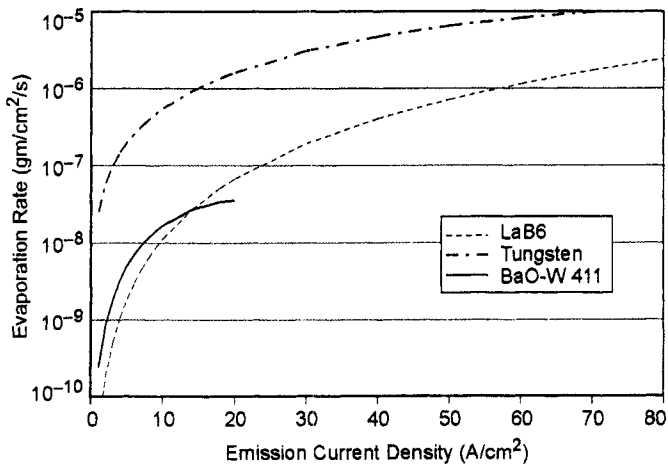

Fig. 6-8. Evaporation rate of Type-S 4:1:1-dispenser cathodes, LaB_6 and tungsten.

6.4 Insert Region Plasma

The insert region of the hollow cathode, as was illustrated in Fig. 6-4, usually has a cylindrical geometry with electron emission from the interior surface of a thermionic insert material. A plasma discharge is established inside the insert region, and electrons emitted from the insert surface are accelerated through the cathode sheath that forms between the insert surface and the plasma. The insert plasma must be capable of accepting the emitted electron current from the sheath and must provide heating of the insert for the cathode to operate properly. The maximum electron current density into the insert plasma is then determined by either space-charge limitations in the plasma at the sheath edge or by characteristics of the surface (work function and temperature) that limit the thermionic emission. As shown by the double sheath analysis in Chapter 3, ions flowing back from the plasma through the sheath to the cathode surface neutralize the electron space charge and increase the extracted electron current density from the insert surface. The electrons accelerated through the sheath quickly give up their energy to the dense collisional plasma inside the insert. Electrons in the tail of the Maxwellian distribution in this plasma have sufficient energy to ionize some portion of the thruster propellant injected through the cathode, which is only a small fraction of the total propellant injected into the thruster. Plasma electrons incident on the downstream end of the cathode tube flow through the orifice and into the main discharge chamber.

The barium evaporated from dispenser cathode inserts is easily ionized in plasmas with this electron temperature because its ionization potential is only 5.2 eV. A calculation of the ionization mean free path in NASA Solar Electric Propulsion Technology Applications Readiness (NSTAR)-sized hollow cathodes [25] predicts about 4×10^{-5} m, which is much smaller than the interior dimensions of the cathode. The ionized barium then migrates upstream because the potential gradient in the hollow cathode that pulls electrons out of the cathode plasma also accelerates barium ions in the opposite direction (upstream). This means that the barium in the insert does not leave the cathode during discharge operation, but tends to travel upstream in the plasma and is deposited in the cooler sections of the hollow cathode.

The pressure inside the hollow cathode is set primarily by the gas flow rate through the cathode and the orifice size and must be sufficiently high to produce a collisional plasma. This condition is required to slow ions backstreaming from the orifice region and from the peak plasma potential on axis (primarily by charge exchange) to avoid sputtering of the insert surface by high-energy ion bombardment. While this condition may not necessarily be satisfied everywhere inside a Type C cathode (with no orifice), at least some fraction of the insert is protected by the collisional processes for proper cathode

operation and life. The collisional plasma will also tend to have a low electron temperature, which reduces the sheath voltages and further protects the low work function insert surface from damage or modification by the plasma.

It is possible to describe [26] the insert plasma using simple particle and energy balance models and plasma diffusion models because the plasma transport inside the hollow cathode is dominated by collisions. In Chapter 3, the solution to the radial diffusion equation for ions in collisionally dominated plasmas in cylindrical geometry resulted in an eigenvalue equation with a unique dependence on the electron temperature:

$$\left(\frac{R}{\lambda_{01}}\right)^2 n_o \sigma_i(T_e)\sqrt{\frac{8kT_e}{\pi m}} - D = 0\,, \tag{6.4-1}$$

where R is the internal radius of the insert, λ_{01} is the first zero of the zero-order Bessel function, n_o is the neutral density, σ_i is the ionization cross section averaged over a Maxwellian electron temperature, and D is the diffusion coefficient. This means that the electron temperature is constrained to produce sufficient ions to offset the diffusion losses to the wall.

The diffusion in the radial direction in the insert region is ambipolar, and the ion mobility is limited by resonant charge exchange (CEX) with the xenon neutral atoms. The average collisions frequency for the ions is then

$$\nu_i = \sigma_{\mathrm{CEX}}\, n_o\, v_{\mathrm{scat}}\,, \tag{6.4-2}$$

where the effective velocity for scattering of the ions in the insert region is approximated by the ion thermal speed:

$$v_{\mathrm{scat}} = \sqrt{\frac{kT_i}{M}}\,. \tag{6.4-3}$$

Since the electron mobility is much higher than the ion mobility, the ambipolar diffusion coefficient D_a from Eq. (3.6-58) for this case is then

$$D_a = D_i\left(1+\frac{T_e}{T_i}\right) = \frac{e}{M}\frac{(T_{iV}+T_{eV})}{\sigma_{\mathrm{CEX}}\, n_o\, v_{\mathrm{scat}}}\,, \tag{6.4-4}$$

where the ion and electron temperatures are shown in eV. As an example, take two hollow cathodes operating in xenon with different inside diameters of the insert. The neutral density inside the hollow cathode is described by Eq. (2.7-2) for a given pressure, determined by the gas flow and the orifice size. A simple analytical technique to estimate the neutral pressure in the insert region is given

in Appendix B. Typical pressures inside discharge hollow cathodes usually range from 1 to 15 torr, although higher pressures are often used in neutralizer cathodes. Figure 6-9 shows the electron temperature versus internal pressure found from Eq. (6.4-1) for two insert diameters, assuming a charge exchange cross section of 10^{-18} m^2 [27] for low temperature xenon ions and neutrals inside the hollow cathode and a neutral gas temperature of 2500 K. The smaller NSTAR insert diameter requires a higher electron temperature to offset the higher diffusion losses to the closer wall at a given pressure. During operation at the high power TH15 throttle point at 13.1 A and 3.7 sccm, the internal pressure is measured to be about 7.5 torr, and the predicted electron temperature is then about 1.36 eV. This agrees well with probe data taken in the insert region [28] in this mode. The NEXIS cathode nominal discharge conditions of 25 A and 5.5 sccm produce an internal pressure of 1.8 torr, which results in a predicted electron temperature of about 1.4 eV that is also in good agreement with the measurements [28].

The radially averaged ion density in the hollow cathode is related to the ion density on the cathode centerline by

$$\bar{n} = \frac{\int_0^R n(0) J_o\left(\frac{\lambda_{01}}{R} r\right) 2\pi r \, dr}{\pi R^2} = n(0)\left[\frac{2J_1(\lambda_{01})}{\lambda_{01}}\right]. \qquad (6.4\text{-}5)$$

The ion flux going radially to the wall is

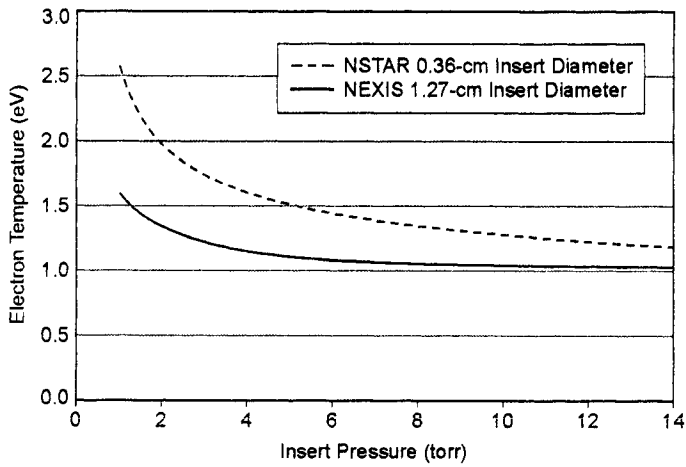

Fig. 6-9. Electron temperature in the insert region as a function of internal pressure for two cathode insert inner diameters.

$$J_i = \bar{n}v_r = -D_a \frac{\partial n}{\partial r} = n(0) D_a \frac{\lambda_{01}}{R} J_1(\lambda_{01}) = \bar{n} D_a \frac{(\lambda_{01})^2}{2R}. \qquad (6.4\text{-}6)$$

Using the ambipolar diffusion coefficient from Eq. (6.4-4), the effective radial drift velocity at the wall is then

$$v_r = \frac{(2.4)^2}{2R\sigma_{\mathrm{CEX}}\, n_o\, v_{\mathrm{scat}}} \frac{e}{M}(T_{iV} + T_{eV}). \qquad (6.4\text{-}7)$$

In the example above, the larger-diameter insert produces an electron temperature of about 1.4 eV at 1.8-torr internal xenon pressure. The effective ion velocity found near the wall outside the sheath is only 3.1 m/s due to the ion-neutral CEX collisions, which slows the ion velocity to significantly less than the 500-m/s ion thermal velocity and 1200-m/s xenon ion acoustic velocity. Since the pre-sheath potential that accelerates the ions to the Bohm velocity prior to entering the sheath extends only the order of the collision mean free path into the plasma, ions diffusing to the plasma edge are accelerated very close to the sheath to the Bohm velocity due to the high collisionality in the insert plasma.

The density of the insert plasma can be estimated by a simple 0-dimensional (0-D) particle and energy balance model. These types of models assume a fairly uniform plasma in the insert region and so provide density estimates within factors of the order of two. In the insert plasma, heating of the plasma is balanced by the energy loss:

$$I_t \phi_s + R I_e^2 = I_i U^+ + \frac{5}{2} T_{eV} I_e + (2T_{eV} + \phi_s) I_r e^{-\phi_s / T_{eV}}, \qquad (6.4\text{-}8)$$

where I_t is the thermionic electron current, ϕ_s is the cathode sheath voltage, R is the plasma resistance, I_e is the hollow cathode discharge current, I_i is the total ion current generated in the insert region, U^+ is the ionization potential, T_{eV} is the electron temperature (in volts), and I_r is the random electron flux at the sheath edge. In this case, excitation and radiation losses seen in the discharge chamber energy balance equations are ignored because the high density plasma inside the hollow cathode is optically "thick" and the radiated energy is reabsorbed by the plasma. The resistance, R, is the resistivity times the average conduction length, ℓ, divided by the cross-sectional area of the plasma:

$$R = \eta \frac{\ell}{\pi r^2}. \qquad (6.4\text{-}9)$$

The resistivity of the plasma is given from Eq. (3.6-21) by

$$\eta = \frac{1}{\varepsilon_o \tau_e \omega_p^2}, \tag{6.4-10}$$

where the collision time, τ_e, for electrons, accounting for both electron-ion and electron-neutral collisions, is given by

$$\tau_e = \frac{1}{\upsilon_{ei} + \upsilon_{en}}, \tag{6.4-11}$$

where υ_{ei} is the electron-ion collision frequency given in Eq. (3.6-14) and υ_{en} is the electron-neutral collision frequency given in Eq. (3.6-12) from [29].

At the insert, power balance gives

$$H(T) + I_t \phi_{wf} = I_i \left(U^+ + \phi_s + \frac{T_{eV}}{2} - \phi_{wf} \right) + \left(2T_{eV} + \phi_{wf} \right) I_r e^{-\phi_s / T_{eV}}, \tag{6.4-12}$$

where $H(T)$ is the total heat lost by the insert due to radiation and conduction and ϕ_{wf} is the cathode work function. Particle conservation in the discharge dictates that

$$I_e = I_t + I_i - I_r e^{-\phi_s / T_{eV}}. \tag{6.4-13}$$

The random electron flux within a collision length of the sheath edge is given by

$$I_r = \frac{1}{4} \left(\frac{8kT_e}{\pi m} \right)^{1/2} n_e \, e \, A, \tag{6.4-14}$$

where the plasma density, n_e, is evaluated at the sheath edge. The ion current is given by the Bohm current in Eq. (3.7-29), where the ion density is again evaluated within one collision length of the sheath edge.

Equations (6.4-8), (6.4-12), (6.4-13), and (6.4-14) can be combined to eliminate the ion current term, which gives

$$\frac{RI_e^2 + I_e \left(\phi_s + \frac{5}{2} T_{eV} \right)}{H(T) + I_e \phi_{wf}} = \frac{U^+ + \phi_s + 2T_{eV} \left(\frac{2M}{\pi m} \right)^{1/2} e^{-\phi_s / T_{eV}}}{U^+ + \phi_s + \frac{T_{eV}}{2} + 2T_{eV} \left(\frac{2M}{\pi m} \right)^{1/2} e^{-\phi_s / T_{eV}}}. \tag{6.4-15}$$

Since the electron temperature is given by the solution to Eq. (6.4-1) in the insert region (as shown above), Eq. (6.4-15) can be solved for the cathode sheath voltage as a function of the discharge current if the radiation and conduction heat losses are known. The insert heat losses are found from thermal models of the cathode, which will be discussed in Section 6.6. Equation (6.4-15) can be greatly simplified by realizing that in most cases $T_{eV}/2 << (U^+ + \phi_s)$, and the right-hand side is essentially equal to one. Equation (6.4-15) then reduces to a simple power balance equation, and the cathode sheath voltage is

$$\phi_s = \frac{H(T)}{I_e} + \frac{5}{2}T_{eV} + \phi_{wf} - I_e R. \tag{6.4-16}$$

Figure 6-10 shows the calculated sheath voltage from Eq. (6.4-16) for the NSTAR cathode at a fixed 3.7-sccm xenon flow rate as a function of the discharge current for four values of the combined radiated and conducted power loss. From Fig. 6-9, the electron temperature is taken to be 1.36 eV for the 7.8 torr measured at 13 A of discharge current and this flow. A thermal model of this cathode [30] indicates that the insert heat loss is about 13 W at 13 A of discharge current, resulting in a sheath voltage from the figure of only about 3.6 V. In this case, a significant fraction of the 1.36 eV electron-temperature plasma electrons can overcome the sheath voltage and be collected on the insert to provide heating. The balance of the power required to heat the insert in the NSTAR cathode comes from orifice plate heating [30], which will be discussed in the next section.

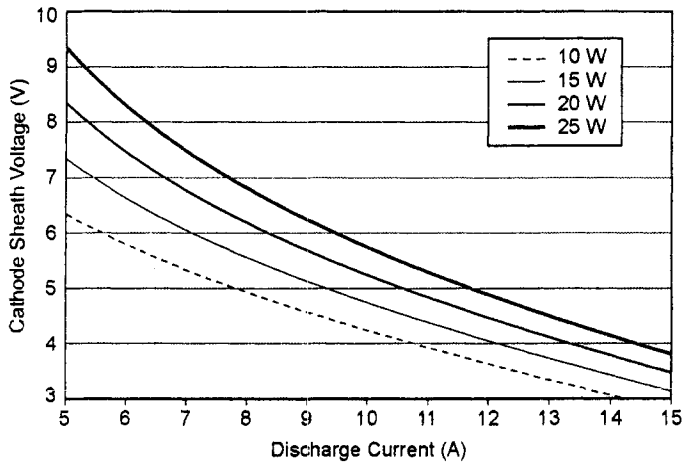

Fig. 6-10. Insert sheath voltage versus discharge current for the NSTAR cathode for four values of the radiated and conducted heat loss.

In low-pressure Type B and C cathodes, the sheath potentials are much greater than the 3.6 V calculated for the NSTAR discharge cathode. For example, in Fig. 6-9, the NSTAR solution for the electron temperature at the far right of the graph is in excess of 7 torr, while NEXIS and other large orifice cathodes are closer to the left side of the graph, between 1 and 2 torr. The sheath potential found by solving Eq. (6.4-16) for the NEXIS electron temperature is over 7 V, and so relatively few plasma electrons return to the emitter and do little heating. Most of the insert heating in lower pressure (on the order of 1 to 2 torr), lower internal plasma density cathodes is from ion bombardment of the insert surface due to the higher sheath voltage.

The insert plasma density can now be found from Eq. (6.4-8). The ion current term is given by

$$I_i = n_o \bar{n}_e e \langle \sigma_i v_e \rangle V , \tag{6.4-17}$$

where n_o is the neutral density, $< \sigma_i v_e >$ is the ionization reaction rate coefficient, V is the volume, and $\bar{n}_e$ is the average plasma density over the insert volume. Remembering that the plasma density in the random electron flux equation is evaluated at the plasma edge, Eq. (6.4-8) can be solved using the above equations to produce an expression for the average plasma density:

$$\bar{n}_e = \frac{RI_e^2 - \left(\frac{5}{2} T_{eV} - \phi_s \right) I_e}{\left[f_n \, T_e \left(\frac{kT_e}{2\pi m} \right)^{1/2} eAe^{-\phi_s / T_{eV}} + n_o e \langle \sigma v_e \rangle V \left(U^+ + \phi_s \right) \right]} , \tag{6.4-18}$$

where f_n is the edge-to-average plasma density ratio. Since the electrons in the insert plasma are Maxwellian, the value of f_n can be estimated from the potential difference between the center and the edge:

$$f_n = \frac{n_e}{\bar{n}_e} \approx e^{-(\phi_{\text{axis}} - \phi_s)/T_{eV}} , \tag{6.4-19}$$

where the potential on axis ϕ_{axis} must come from measurements or two-dimensional (2-D) codes. The plasma density calculated from Eq. (6.4-18) for the NSTAR discharge cathode at a constant xenon gas flow of 3.7 sccm, using the electron temperature from the radial diffusion model (Fig. 6-9), the sheath potential from the power balance model (Fig. 6-10), and a measured on-axis plasma potential of about 8.5 V [6], is shown in Fig. 6-11. Good agreement with the plasma density measurements made by a miniature scanning probe in this cathode [28] is obtained, and a nearly linear dependence on discharge

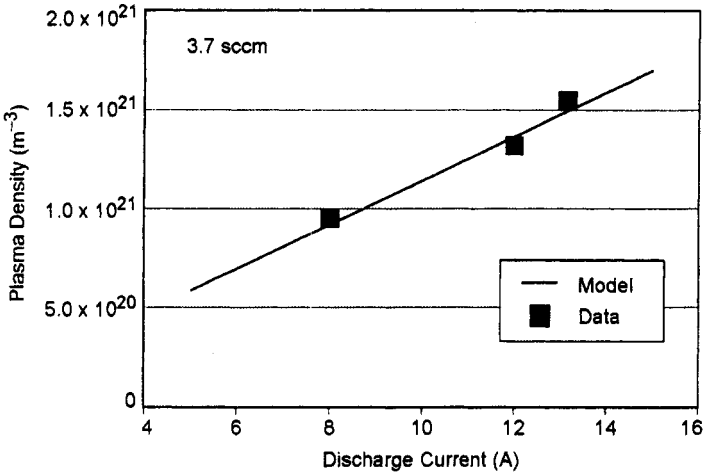

Fig. 6-11. Peak plasma density calculation for the NSTAR cathode operating at a constant gas flow of 3.7 sccm.

current is predicted by the model and shown experimentally. While the simple 0-D cathode model requires insert heat loss from a cathode thermal model and on-axis potentials from probe measurements or 2-D code runs, it provides reasonable agreement with the data and illustrates the dependence of the insert plasma density and temperature on the geometry and the plasma conditions inside the cathode.

The 0-D model also illuminates the heating mechanism in the hollow cathode. The ion heating to the insert is found in Eq. (6.4-12):

$$\text{Power}_{\text{ions}} = I_i\left(U^+ + \phi_s + \frac{T_{eV}}{2} - \phi_{wf}\right), \tag{6.4-20}$$

where the ion current is given by the Bohm current at the sheath edge. Using the above parameters for the Type B NSTAR discharge cathode shown in Fig. 6-5 at the full-power TH15 operating point of 13 A and 3.7 sccm ($U^+ = 12.1$ eV, $\phi_s = 3.6$ eV, $T_e = 1.36$ eV, $\phi_{wf} = 2.06$ V, $\phi_{\text{axis}} = 8.5$ V, and $n_i \approx 1.5 \times 10^{21}$ m^{-3}), the ion heating power from Eq. (6.4-20) is only 4.7 W. The electron heating of the insert is also found in Eq. (6.4-12):

$$\text{Power}_{\text{electrons}} = \left(2T_{eV} + \phi_{wf}\right) I_r e^{-\phi_s/T_{eV}}, \tag{6.4-21}$$

where the random electron flux is again evaluated at the sheath edge. For the same parameters for the Type B NSTAR cathode given in the paragraph above, the electron heating of the insert is found to be about 45 W. This Type B

cathode is, therefore, heated predominately by electron heating of the insert, with a comparable amount coming from orifice heating (shown in the next section). Similar analysis of Type B cathodes with larger orifices or lower flow rates, and also most Type C cathodes, indicates that ion heating will become the dominant heating mechanism due to the higher electron temperature and larger sheath potential drop at the insert.

It is important to recognize that, as the pressure in the hollow cathode is increased, much of plasma heating comes from resistive heating of the current flowing through the partially ionized plasma. The higher the neutral gas background pressure, the greater the contribution of resistive heating. In cathodes with larger orifices that produce lower internal pressures, most of the heating of the insert plasma comes from the emitted electrons being accelerated across the cathode sheath potential. In lower pressure cathodes, the sheath potential is higher and the plasma resistivity is lower, resulting in less joule heating of the plasma but more ion bombardment heating of the insert surface. This is illustrated in Fig. 6-12, which shows the sheath potential and the ion and electron currents impacting the cathode as a function of the resistive joule heating of the plasma.

The behavior shown in Fig. 6-12 can be understood by rearranging the equations in the power balance model above. Using Eqs. (6.4-13) and (6.4-14) in the power balance equation [Eq. (6.4-8)] and solving for the sheath potential gives

$$\phi_s = \frac{-RI_e^2 + I_i U^+ + \frac{5}{2} T_{eV} I_e + (2T_{eV} + \phi_s) I_i \sqrt{\frac{2m_i}{\pi m_e}} \exp(-\phi_s / T_{eV})}{\left(I_e - I_i \left(1 - \sqrt{\frac{2m_i}{\pi m_e}} \exp(-\phi_s / T_{eV}) \right) \right)} . \quad (6.4\text{-}22)$$

The decrease in the sheath potential observed in Fig 6-12 as the joule heating (RI_e^2) becomes more significant follows directly from Eq. (6.4-22), because the joule heating term enters with a negative sign. Equation (6.4-13) also shows that a decrease in the sheath potential allows for more of the electron flux to return to the emitter. Finally, if the heat loss, $H(T)$, is fixed, Eq. (6.4-12) shows that the increased electron return flux (second term on the right-hand side) must be balanced by a reduced ion flux (first term on the right-hand side). This illustrates how the design and operating conditions of the hollow cathode (sizes, flow, and discharge current) determine which terms dominate in the cathode self-heating.

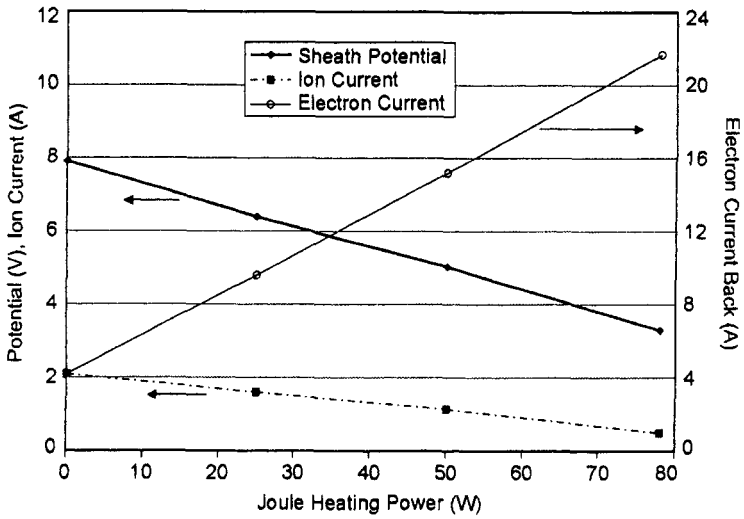

Fig. 6-12. Sheath potential and currents to the insert as a function of the resistive joule heating in the insert plasma.

It is also possible to estimate the axial extent of the plasma in the insert region for Type A and some Type B cathodes with small orifices that again produce diffusion-dominated plasmas. This is useful in understanding the plasma "attachment" or "contact length" with the insert, which impacts where the electron emission can take place. As was shown in Chapter 3, the solution to the 2-D diffusion equation in cylindrical geometry is the product of a zero-order Bessel function radially times an exponential term in the axial direction:

$$n(r,z) = n(0) J_o\left(\sqrt{C^2+\alpha^2}\, r\right) e^{-\alpha z}, \tag{6.4-23}$$

where α is one over the e-folding distance of the plasma density from the reference location on axis at (0,0). This length can be found by considering the ion generation inside the insert. The ion current to the insert surface is the ion generation rate integrated over the volume inside the insert:

$$I_i = 2\pi \int_0^R \int_0^L n_o n e \sigma_i v_e r dr dz\,. \tag{6.4-24}$$

Taking the axial integral in Eq. (6.4-24) to be approximately the e-folding distance ($L = 1/\alpha$), Eq. (6.4-24) is simply

$$I_i = \frac{\pi R^2}{\alpha} n_o \bar{n} e \langle \sigma_i v_e \rangle. \tag{6.4-25}$$

The average plasma density is found from Eq. (6.4-5):

$$\bar{n} = n(0,0)\left[\frac{2J_1(\lambda_{01})}{\lambda_{01}}\right] = n(0,0)\left[\frac{(2)(0.5191)}{2.4048}\right] = 0.43n(0,0). \qquad (6.4\text{-}26)$$

Using Eq. (6.4-26) in Eq. (6.4-25) and solving for the value of α gives

$$\alpha = \frac{0.43\pi R^2}{I_i} n_o n(0,0) e\langle \sigma_i v_e \rangle. \qquad (6.4\text{-}27)$$

For example, the axial plasma density profile from the scanning probe inside the NSTAR hollow cathode [31] operating at 15 A and 3.7 sccm is shown in Fig. 6-13. Taking the peak plasma density from the figure of $n(0,0) = 1.6 \times 10^{21}$ m^{-3} as the reference density at position (0,0) and using the neutral density, calculated inside the insert from Eq. (2.7-2), of 2.5×10^{22} m^{-3}, Eq. (6.4-27) gives a value of $\alpha = 6.0$ if the ion current to the insert is 0.5 A. The fit to the exponential decrease in the plasma density upstream of the orifice shown in Fig. 6-13 gives $\alpha = 6.1$. The assumed value of 0.5 A for the ion current actually results from a two-dimensional model of the insert plasma [5], which will be discussed below. This simple diffusion model shows an exponential behavior in the axial plasma density profile, predicted from Eq. (6.4-23), which is consistent with the near-exponential profiles measured in the NSTAR cathode sufficiently far away from the orifice region.

A closer examination of Eq. (6.4-27) shows that the terms on the right-hand side represent the ionization rate per unit volume. If the geometry of the

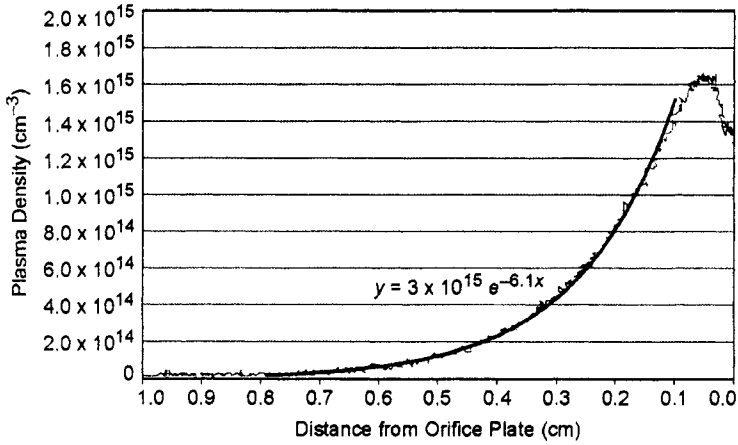

Fig. 6-13. Plasma density measured on axis in the insert region for an NSTAR cathode operating at TH15.

cathode is fixed, then the number of ions flowing to the insert (I_i in the denominator) is proportional to this ionization rate per unit volume. Therefore, the value of alpha will be constant for varying operating conditions of a given size of cathode. This behavior is illustrated in Fig. 6-14, where the density profile for an NSTAR-sized cathode with two different orifice sizes operating at the same discharge current and gas flow is shown. For the larger orifice cathode, the internal pressure at the constant gas flow is lower, and the penetration of the 2-D effects associated with the downstream boundary condition and the electron current funneling into the orifice extends deeper into the insert region. However, once the collisionality establishes a diffusion-limited plasma flow to the insert upstream of the orifice, then Eq. (6.4-23) is again valid and the value of alpha in the cathode is seen to be essentially constant.

It should be noted that the *e*-folding distance for the plasma density measured inside the NSTAR cathode in Fig. 6-13 is $1/\alpha = 1.7$ mm. Therefore, the plasma in the small orifice case is only in significant contact with the insert for a few *e*-foldings, which is less than 1 cm. This rapid plasma density decrease away from the orifice is the result of the very high pressure in the NSTAR cathode [5,6,] and also occurs in most neutralizer cathodes. For high-pressure cathodes like this, utilizing inserts significantly longer than 1 to 1.5 cm in length is not very useful because there is little plasma left beyond this distance to accept the thermionic emission from the insert.

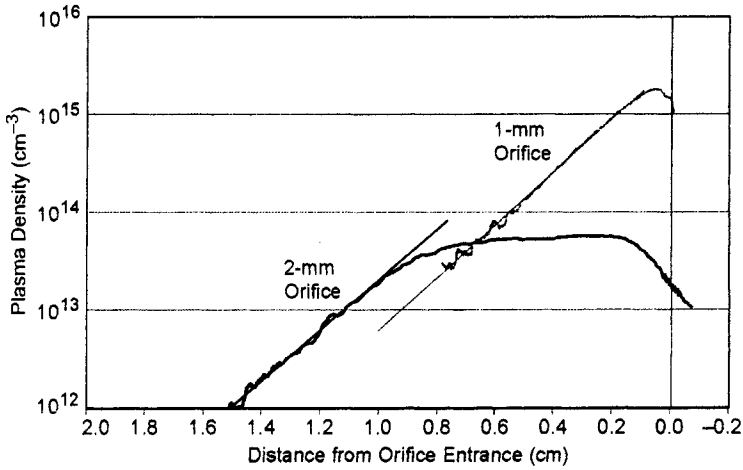

Fig. 6-14. Plasma density measured on axis in the insert region for an NSTAR-sized cathode operating at TH15 with two different orifice sizes.

While the 0-D and one-dimensional (1-D) models described above can provide insight into the operation of hollow cathodes, to self-consistently calculate the plasma density in the insert region, including the effects near the cathode orifice, requires a two-dimensional model [32]. The insert plasma energy balance in this model can be found from the electron and ion energy equations. The conservation of energy equations was described in Section 3.5.3 of Chapter 3. The steady-state electron energy equation can be written

$$0 = -\nabla \cdot \left(-\frac{5}{2}\mathbf{J}_e \frac{kT_e}{e} - \kappa \frac{\nabla kT_e}{e} \right) + \eta J_e^2 - \mathbf{J}_e \cdot \frac{\nabla nkT_e}{ne} - \dot{n}eU^+, \qquad (6.4\text{-}28)$$

where $\mathbf{J}_e$ is the electron current density in the plasma, κ is the electron thermal conductivity given by Eq. (3.5-29), η is the plasma resistivity given by Eq. (3.6-21), and U^+ is the ionization potential of the neutral gas. The steady-state ion energy equation is

$$0 = -\nabla \cdot \left(-\frac{5}{2}\mathbf{J}_i \frac{kT_i}{e} - \kappa_n \frac{\nabla kT_i}{e} \right) + \mathbf{v}_i \cdot \nabla\left(nkT_i\right) + nM\nu_{in}v_i^2 + Q_T\,, \qquad (6.4\text{-}29)$$

where $\mathbf{J}_i$ is the ion current density, κ_n is the thermal conductivity for neutrals, and it is assumed that the ions and neutrals are in thermal equilibrium ($T_n = T_i$) in the collisional insert plasma.

The energy balance equations are used to close the system of equations describing the plasma in the insert region. These equations also are used to describe the self-heating mechanism characteristic of hollow cathodes due to the particle flux and energy hitting the cathode walls. This effect will be discussed in Sections 6.5 and 6.6 with respect to the cathode thermal models.

Writing the steady-state momentum equations from Eq. (3.5-5) for the ions and electrons,

$$0 = en\mathbf{E} - \nabla \cdot \mathbf{p}_i - Mn\left[\nu_{ie}\left(\mathbf{v}_i - \mathbf{v}_e\right) + \nu_{in}\left(\mathbf{v}_i - \mathbf{v}_n\right)\right], \qquad (6.4\text{-}30)$$

$$0 = -en\mathbf{E} - \nabla \cdot \mathbf{p}_e - mn\left[\nu_{ei}\left(\mathbf{v}_e - \mathbf{v}_i\right) + \nu_{en}\left(\mathbf{v}_e - \mathbf{v}_n\right)\right]. \qquad (6.4\text{-}31)$$

Adding these two equations, assuming that the neutrals move slowly compared to the charged particles, and writing the result in terms of the ion and electron fluxes gives

$$\mathbf{J}_i = \frac{m}{M}\frac{\nu_{en}}{\nu_{in}\left(1+\nu\right)}\mathbf{J}_e - \frac{\nabla\left(nkT_i + nkT_e\right)}{M\nu_{in}\left(1+\nu\right)}, \qquad (6.4\text{-}32)$$

where $\nu = \nu_{ie} / \nu_{in}$.

Combining Eq. (6.4-32), which is known as the generalized Ohm's law, with the sum of the ion and electron continuity equations,

$$\nabla \cdot \left(\mathbf{J}_e + \mathbf{J}_i \right) = 0 , \tag{6.4-33}$$

gives the particle balance equation,

$$\nabla \cdot \left(\frac{\nabla \phi}{\eta} \right) = \nabla \cdot \left[\frac{\nabla \left(nkT_e \right)}{\eta ne} + \mathbf{J}_i \left(1 - \frac{\nu_{ei}}{\nu_{en} + \nu_{ei}} \right) \right], \tag{6.4-34}$$

where the electric field is $\mathbf{E} = -\nabla \phi$. The total resistivity in the plasma in Eq. (6.4-34) is given by combining Eqs. (6.4-9) and (6.4-10):

$$\eta = \frac{m \left(\nu_{en} + \nu_{ei} \right)}{ne^2} . \tag{6.4-35}$$

These equations have been used in a full 2-D code [5] to find the plasma density, temperature, and potential in the insert region for the NSTAR discharge operating conditions of 12 A and 4.25 sccm. Utilizing thermionic emission from the insert surface, described by Eq. (6.3-4), with temperatures measured by Polk [33], and applying the proper boundary conditions, the plasma density profile along the axis of symmetry is compared with the laboratory measurement in Fig. 6-15. The 12-A net cathode current was found to result from almost 32-A electron emission by the insert countered by 20 A of plasma (thermal) electron current back to the insert and the orifice plate. The particle balance in the insert is shown in Table 6-2, where only about one-half ampere of the net cathode current is due to ionization of the xenon gas. This is consistent with the previous analysis used to obtain the exponential density scale lengths.

The 2-D code adequately describes what is happening in the cathode insert region. For example, the numerical results in Table 6-2 capture the 2-D effects upstream of the cathode orifice, predicting a density profile that is consistent with the data [2] shown in Fig. 6-16. The code's predictions of the electron temperature and plasma potential are also close to the measured values in the emission zone, which extends less than about 0.5 cm upstream of the orifice entrance in the NSTAR cathode. Figure 6-16(a) shows that the plasma density falls radially, as expected, toward the insert wall. The 2-D plasma potential contours for this case are also shown in Fig. 6-16(b). Good agreement with the measurements has been achieved with this model for larger cathodes as well, such as with the 1.5-cm-diameter NEXIS cathode [5].

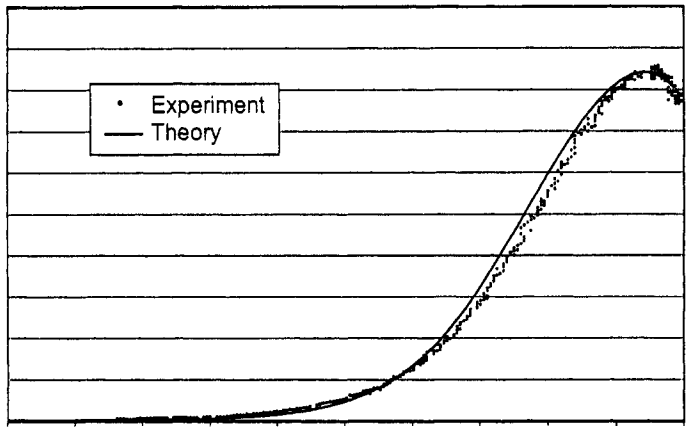

Fig. 6-15. Comparison of the plasma density measured on axis in the NSTAR-sized cathode operating at 12 A and a 4.25-sccm xenon flow with the 2-D code predictions.

Table 6-2. Currents from the 2-D cathode code for the insert plasma of the NSTAR cathode.

Source	Current (A)
Emitted Electrons	31.7
Absorbed Electrons	20.2
Absorbed Ions	0.5
Net Current	12.0

6.5 Orifice Region Plasma

Electrons are extracted from the insert plasma through the orifice into the discharge chamber or ion beam. For cathodes with no orifice, a transition region exists at the end of the insert and cathode tube where the neutral gas density is sufficiently low and the flow becomes collisionless. Orificed cathodes also have a transition region to collisionless neutral flow, which can occur inside the orifice or slightly downstream depending on the orifice size and the gas flow rate. Inside the orifice, the electron current density is the highest in the entire system. In this region, classical electron scattering with the ions and neutral gas produces resistive heating. The hot electrons then ionize a large fraction of the xenon gas, most of which strikes the orifice wall as ions and heats it. The amount of orifice-plasma resistance and orifice-plate heating depends on the geometry, flow rate, and discharge current. Type A cathodes have long, narrow orifices and high pressures, which lead to high resistivity,

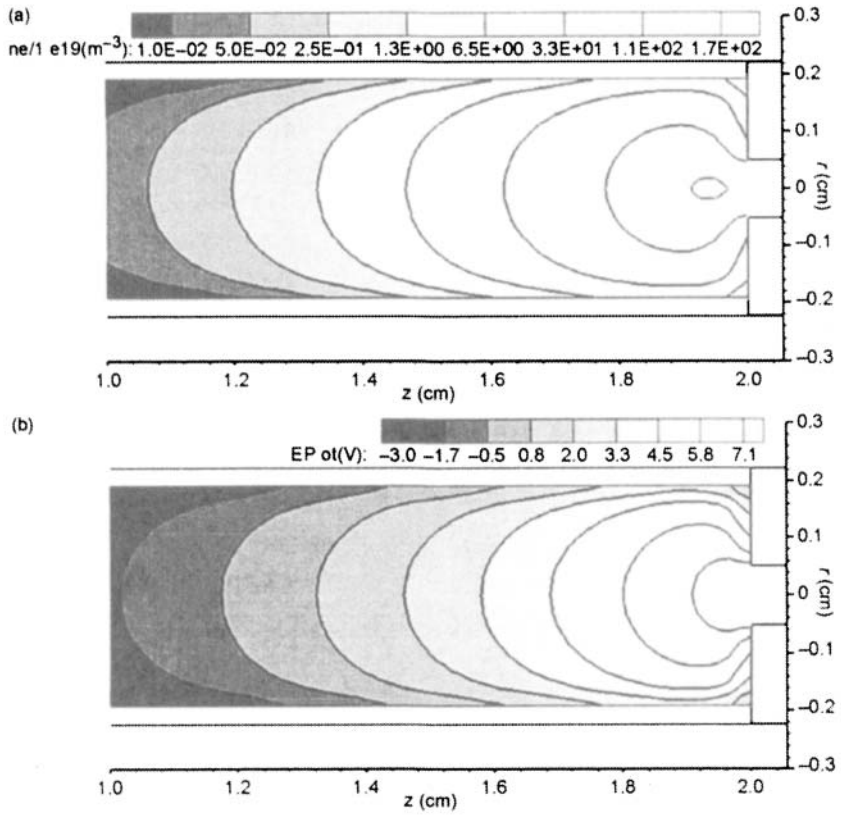

Fig. 6-16. Density (a) and potential (b) contours plotted for the NSTAR cathode from the OrCa2-D code [5].

strong ion bombardment of the orifice wall, and significant local heating. Type B cathodes tend to have smaller orifice heating unless the orifice is relatively small and the gas flow high, both because the resistance is usually lower than in Type A cathodes and because a larger fraction of the power deposited in the plasma in this region convects out into the cathode plume. For example, the 1-mm-diameter orifice NSTAR cathode has significant orifice heating, but the 2.5-mm-diameter orifice NEXIS cathode has lower orifice heating even at higher currents.

In Type A and B cathodes, the ion flow in the cylindrical region of the orifice is diffusion limited because of the short collision mean free path for charge exchange with the neutrals. For example, the NSTAR discharge cathode operates at an internal pressure of about 8 torr ($n_0 \approx 5 \times 10^{22}$ m^{-3}) in the TH15

mode. The mean ion mean free path for resonant CEX collisions for a cross section of $\approx 10^{-18}\,\mathrm{m}^2$ is smaller than even the orifice dimensions:

$$\lambda = \frac{1}{\sigma_{\mathrm{CEX}}\, n_o} \approx 2\times 10^{-5}\,[\mathrm{m}]. \tag{6.5-1}$$

Thus, diffusion is a good approximation for the ion motion in these hollow cathode orifices.

It is instructive to develop a 0-D model of the cathode orifice plasma to show the dependence of the plasma density, electron temperature, and voltage drop in the orifice region. However, such a model provides only a rough estimate of these parameters because there is a large neutral pressure gradient generated along the orifice, whereas the model uses average parameters. It is assumed for now that the orifice is long compared to its length so that the radial ion diffusion equation applies. The solution to this equation for collisional plasmas in the orifice, described above for the insert region, results in the usual eigenvalue equation dependent on the electron temperature:

$$\left(\frac{r}{\lambda_{01}}\right)^2 n_o\, \sigma_i(T_e)\sqrt{\frac{8kT_e}{\pi m}} - D = 0\,, \tag{6.5-2}$$

where r is now the internal radius of the orifice, λ_{01} is the first zero of the zero-order Bessel function, n_o is the neutral density, σ_i is the ionization cross section averaged over a Maxwellian electron temperature, and D is the diffusion coefficient. The electron temperature is again constrained to produce sufficient ions to offset the diffusion losses, as in the insert region analysis. Equation (6.5-2) can be solved for the local electron temperature in the orifice using the terms evaluated in Eqs. (6.4-4) through (6.4-7).

The steady-state electron energy equation [Eq. (6.4-28)] is integrated over the cylindrical orifice, ignoring thermal conduction and radiation losses, to yield an equation for the average plasma density in the orifice. In this case, ohmic heating in the orifice plasma is balanced by convection of the energy deposited in the orifice plasma electrons and ionization losses:

$$I_e^2 R = \frac{5}{2} I_e \left(\frac{kT_e}{e} - \frac{kT_e^{\mathrm{in}}}{e}\right) + n_o \bar{n}_e e \langle \sigma_i v_e \rangle U^+ \left(\pi r^2 \ell\right), \tag{6.5-3}$$

where ℓ is the length of the orifice. Equation (6.5-3) can be solved for the average plasma density in the orifice:

$$\bar{n}_e = \frac{I_e^2 R - \frac{5}{2} I_e \frac{k}{e}\left(T_e - T_e^{\text{in}}\right)}{n_o e \langle \sigma v_e \rangle U^+ \pi r^2 \ell}. \qquad (6.5\text{-}4)$$

An evaluation of the terms in Eq. (6.5-4) for the orifice region uses the same techniques previously described in Section 6.4 for the insert plasma region. The resistance R is given by Eq. (6.4-9), where the conduction length is now simply the orifice plasma length. The input electron temperature, T_e^{in}, is the electron temperature in the insert plasma that comes from the diffusion model used in Section 6.4 or from experimental measurements.

The detailed measurements of the plasma density and temperature in the orifice of the NSTAR discharge cathode [31] will be used as a first example to compare with the model predictions. The NSTAR discharge cathode has an orifice diameter of 0.1 cm, and the case of the full-power TH15 operating point with 13 A of discharge current at a xenon gas flow rate of 3.7 sccm will be used. The pressure measured inside the insert region for this case is about 7.8 torr [31]. Assuming simple Poiseuille flow (see Appendix B), the pressure in the orifice is estimated to fall to less than 3 torr by the end of the 0.75-mm-long cylindrical section of the orifice. Assuming a gas temperature of about 2000 K in the orifice, the solution for the electron temperature in the diffusion equation [Eq. (6.5-2)] versus pressure in the orifice is shown in Fig. 6-17. The electron temperature predicted by this model varies by less than 1 eV along the orifice length, and the average in the channel is about 2.3 eV. This value is close to the experimentally measured values of 2.2 to 2.3 eV found in this region [28].

Using this electron temperature, the density in the orifice is calculated from Eq. (6.5-2) and plotted in Fig. 6-18 versus the discharge current for the NSTAR cathode. The agreement with the experimental data [31] taken for two discharge currents at the nominal 3.7-sccm cathode flow rate is also very good. The resistance calculated from Eq. (6.4-9) for the cylindrical orifice length is 0.31 ohms, which, at 13 A, produces a voltage drop in the orifice of about 4 V. This is the same magnitude as the voltage change observed in the experimental data, which illustrates that the potential drop in the hollow cathode orifice is resistive due to the very collisional plasma that exists there in these xenon hollow cathodes. Detailed 2-D calculations, described below, indicate that roughly half of the power deposited in this region (P = 4 V * 13 A) goes to the orifice wall, and the remainder is convected into the discharge chamber by the plasma.

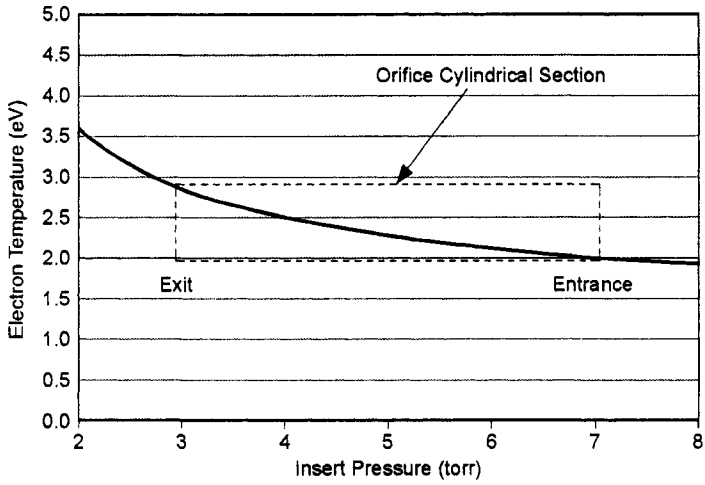

Fig. 6-17. Orifice electron temperature calculated from the 0-D model through the orifice for the NSTAR discharge cathode at TH15.

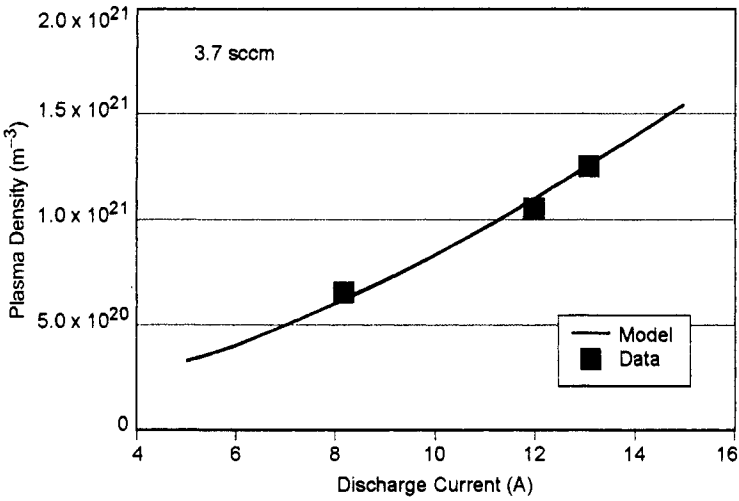

Fig. 6-18. Orifice plasma density calculated from the 0-D model and measured points for the NSTAR discharge cathode at a 3.7-sccm xenon gas flow.

Since the 0-D orifice model with just the average parameters has been shown to provide rough estimates of the orifice parameters, it is reasonable to use it to examine Type A cathode orifice heating. Consider the orifice of the NSTAR neutralizer cathode [34], which has an inside diameter of 0.028 cm. The pressure measured inside the neutralizer during operation at 3.2 A, associated

with the full power TH15 case, is 145 torr. Assuming again simple Poiseuille flow (see Appendix B) through the 3:1 aspect ratio orifice channel in this cathode, the pressure is found to fall to less than 20 torr by the end of the 0.75-mm-long cylindrical section of the orifice. Assuming the same gas temperature of about 2000 K in the orifice again, the solution to the radial diffusion, Eq. (6.5-2), predicts the electron temperature to vary by only 0.5 eV along the orifice, with an average value of about 1.4 eV. It is also assumed that a minimal 1-eV electron temperature exists in the insert region for the T_e^{in} in Eq. (6.5-3).

The plasma density in the orifice is plotted in Fig. 6-19 versus the discharge current. At 3.2 A, corresponding to the neutralizer cathode producing the beam current of 1.76 A plus the keeper current of 1.5 A, the predicted plasma density is about $6 \times 10^{22}\ m^{-3}$. The resistance calculated from Eq. (6.4-9) for the cylindrical orifice section is 3.5 ohms, which, at 3.2 A, produces a resistive voltage drop in the orifice of about 11 V. The power deposited in the plasma ($P = 11\ V * 3.2\ A = 35\ W$) in this case goes primarily to the orifice wall because the convection power loss is low due to the large geometrical aspect ratio of Type A orifices and the low electron temperature. This demonstrates the resistive orifice heating power characteristically found in Type A cathodes.

While 0-D models are useful to illustrate the strong resistive effects in the orifices of all Type A and some Type B cathodes, the use of average pressures and temperatures reduces the accuracy of these models. However, it is possible to construct a 1-D model for the cathode orifice [35] to address this issue. The

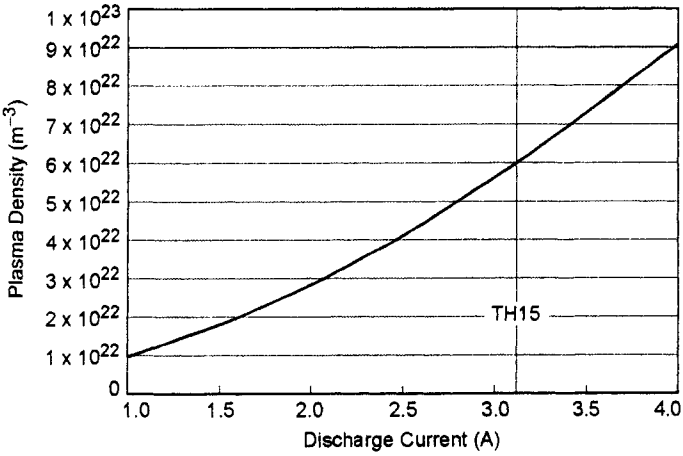

Fig. 6-19. Orifice plasma density calculated from the 0-D model for the NSTAR neutralizer cathode at TH15.

orifice plate is usually chamfered on the downstream side, which must be included in the analysis because the rapidly expanding gas plume in this region often transitions to the collisionlesss regime in which the flow is not dominated by diffusion.

In the orifice, continuity dictates that the ions that hit the orifice wall are re-emitted as neutrals and re-enter the plasma. The continuity equations for the three species (neutrals, ions, and electrons) in the cylindrically symmetric orifice region are

$$\pi r^2\left(-\frac{\partial n}{\partial t}+\frac{\partial v_o n_o}{\partial z}\right)+2\pi r v_{\text{wall}} n = 0 \tag{6.5-5}$$

$$\pi r^2\left(\frac{\partial n}{\partial t}+\frac{\partial v_i n_o}{\partial z}\right)-2\pi r v_{\text{wall}} n = 0 \tag{6.5-6}$$

$$\pi r^2\left(e\frac{\partial n}{\partial t}+\frac{\partial J_e}{\partial z}\right)=0, \tag{6.5-7}$$

where v is the ion or neutral velocity and v_{wall} is the particle velocity at the radial boundary.

The average neutral velocity is found from Poiseuille flow:

$$v_o = -\frac{r^2}{8\zeta}\frac{dP}{dz}, \tag{6.5-8}$$

where ζ is the temperature-dependent neutral gas viscosity. For xenon, the viscosity is [26]

$$\begin{aligned}\zeta &= 2.3\times10^{-5}T_r^{0.965} && \text{for } T_r<1\\ &= 2.3\times10^{-5}T_r^{(0.71+0.29/T_r)} && \text{for } T_r>1,\end{aligned} \tag{6.5-9}$$

with units of Ns/m^2 or Pa-s and a relative temperature given by $T_r = T/289.7$ K. Since a large fraction of the ions undergoes charge exchange within the orifice, the neutral gas is heated and the viscosity is increased. This is incorporated into the model [35] by assuming that the gas temperature varies as

$$T = T_{\text{wall}} + \frac{M}{k}\left[(fv_r)^2 + v_o^2\right], \tag{6.5-10}$$

where the fraction of the neutrals that receives the ion radial velocity via charge exchange is given by

$$f = 1 - \exp\left[-\frac{n}{n_o} \frac{\tau_{\text{wall}}}{\tau_{\text{CEX}}} \right], \tag{6.5-11}$$

and τ_{wall} is the average time between collisions with the wall for a neutral particle. This effective heating mechanism by charge exchange has been observed in experiments where the neutral temperatures are higher than the orifice wall temperatures.

Combining the electron and ion momentum equations [Eqs. (6.4-30) and (6.4-31)] to eliminate the electric field term gives an expression for the particle motion in terms of the ambipolar diffusion coefficient and the ion and electron mobilities:

$$n(v_i - v_o) = -D_a \frac{\partial n}{\partial z} + \frac{\mu_i}{\mu_e} \frac{J_e}{e}. \tag{6.5-12}$$

The ambipolar diffusion coefficient for this case is given by Eq. (6.4-4). In the orifice, the radial drift velocity will often exceed the ion thermal speed due to the radial potential gradient, so the ion scattering velocity must be approximated by

$$v_{\text{scat}} = \sqrt{v_{th}^2 + (v_i - v_o)^2 + v_r}, \tag{6.5-13}$$

where v_r is the radial ion velocity found from Eq. (6.4-7).

The continuity equations in the orifice [Eqs. (6.5-5) through (6.5-7)] are solved using the electron energy equation, Eq. (6.4-28), in the cylindrical orifice, which produces ion density and plasma potential profiles in the orifice region. The first result from this work is that a double sheath postulated in the orifice region [36] is not observed for xenon ion thruster cathodes. There is a potential change through the orifice, but this results from resistive effects in the orifice channel due to electron-ion and electron-neutral collisions.

As an example, Fig. 6-20 shows a plot of the neutral and plasma densities along the axis of an NSTAR neutralizer cathode orifice operating at the TH15 power point, producing 3.76 A of current with a xenon gas flow rate of 3.5 sccm [37]. The peak plasma density occurs in the cylindrical section of the orifice, and the density falls though the chamfered region due to the neutral gas density decrease. It should be noted that the peak plasma density predicted by the 1-D model in the orifice is in reasonable agreement with the 0-D model results shown above that used the average neutral density and temperature along the length of the orifice. Reasonably accurate results can be obtained using simple 0-D models to illustrate the driving physics in this region.

An interesting result of this analysis is that significant ionization occurs in the orifice, which provides electrons to the discharge. Figure 6-21 shows the electron current calculated as a function of the distance along the orifice axis. The electron current is about 50% higher exiting the orifice as compared with the amount extracted from the insert plasma. This is because the very high neutral gas density in the neutralizer cathode orifice region causes significant ionization. Discharge cathodes have much lower electron multiplication factors in the orifice because the neutral and plasma densities are typically an order of magnitude lower.

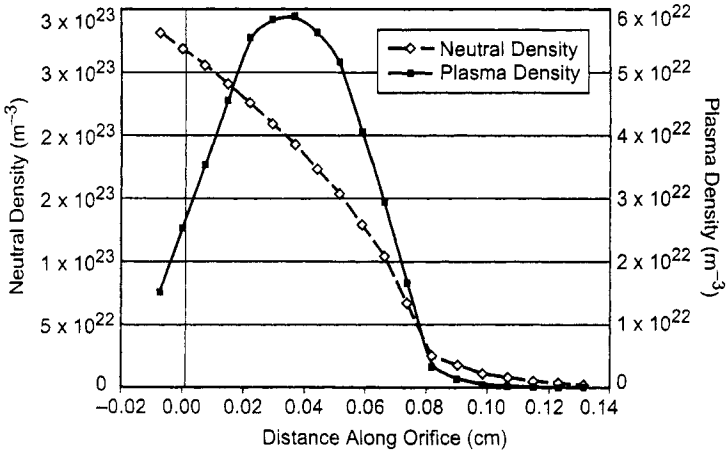

Fig. 6-20. Neutral and plasma densities calculated in the NSTAR neutralizer cathode orifice at the TH15 operation point.

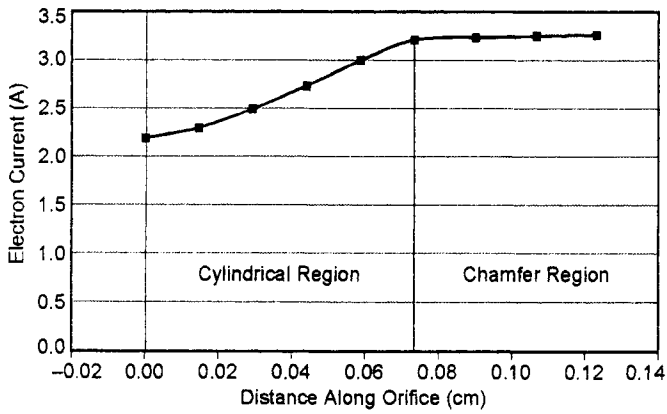

Fig. 6-21. Electron current as a function of distance along the axis in the NSTAR neutralizer cathode orifice at TH15.

The ion current density to the orifice wall, which naturally follows the plasma density profile in Fig. 6-20, is shown in Fig. 6-22. The ion bombardment of the orifice walls is seen to peak well before the chamfer region starts. Since the plasma potential is increasing along the axis from the insert plasma to the exit due to the plasma resistive drop, the ions in this region can have sufficient energy to sputter the wall. This effect was observed in the cross section of the NSTAR neutralizer after the 8200 life demonstration test (LDT) [34] and is shown in Fig. 6-23. The orifice was observed to open up in the center

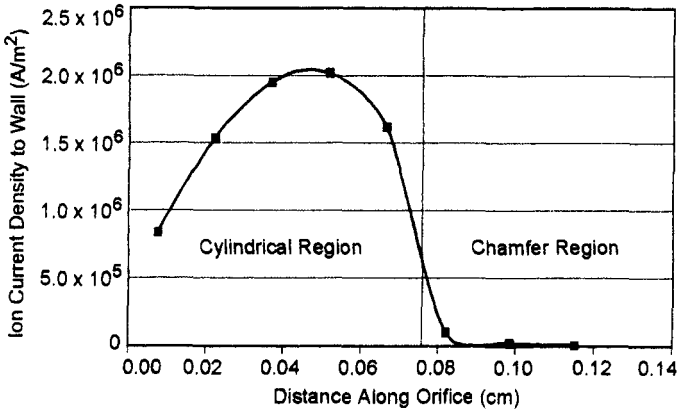

Fig. 6-22. Radial ion current to the orifice wall as a function of distance along the axis in the NSTAR neutralizer cathode at TH15.

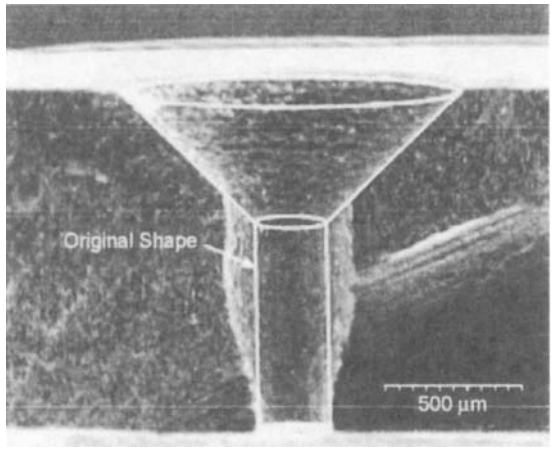

Fig. 6-23. Neutralizer cathode orifice cross section showing the erosion pattern after the NSTAR 8200-hour test [34].

cylindrical region before the chamfer, consistent with the predicted ion bombardment location in Fig. 6-22.

The time required to produce this erosion pattern is not known since Fig. 6-23 shows a destructive analysis after the end of the test. In fact, the erosion pattern shown in the destructive analysis of the neutralizer cathode orifice after the 30,000-hour extended life test (ELT) [38] shown in Fig. 6-24 is nearly identical to the shorter-duration LDT result. The ELT cathode experienced nearly double the operation time of the LDT cathode at the full-power level, which did not further erode the orifice. The 1-D orifice model described above finds that the larger-diameter orifice reduced the neutral pressure and plasma density in the orifice by about a factor of four, which reduced the plasma potential increase along the orifice by a factor of two. The combination of a significantly lower ion bombardment flux, the lower ion energy, and the increase in inner surface area as the cylinder radius increases caused the erosion rate to fall to negligible levels once the orifice opened sufficiently.

One might expect similar erosion behavior from discharge cathode orifices. Figure 6-25 shows the destructive analysis of the LDT discharge cathode orifice plate after 8200 hours at full power. There is no discernable erosion in the cross section. In this case, the 1-D model shows that the much larger initial orifice diameter reduced the neutral pressure, plasma density, and potential in the orifice to the point that the ion bombardment erosion became negligible (similar to the eroded neutralizer cathode orifice case). In addition, the model shows that electron multiplication is reduced due to the lower ionization rate, and so the insert plasma must produce more of the discharge current than in neutralizer cathodes. It is clear that a simple orifice-plasma model can illustrate

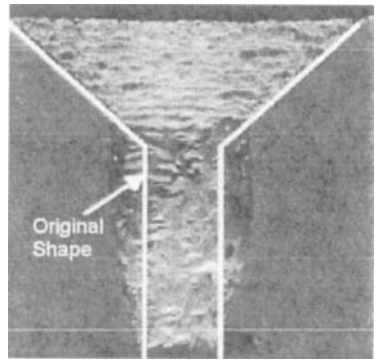

Fig. 6-24. Neutralizer cathode orifice cross section showing the erosion pattern after the NSTAR 30,152-hour extended life test [38].

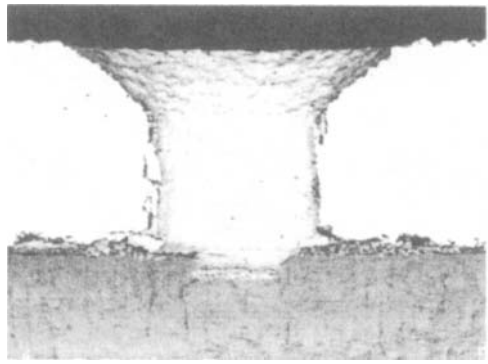

Fig. 6-25. Discharge cathode orifice showing the erosion pattern after the NSTAR 8200-hour long duration test [34].

the extraction and generation of the electrons in the discharge through the orifice and provide insight into the erosion mechanisms.

6.6 Hollow Cathode Thermal Models

While the 0-D insert model described above is illustrative, more accurate models have been constructed that use radiation and thermal conduction models coupled to 2-D insert plasma models [2] that provide the local heat fluxes. Figure 6-26 shows a sample input geometry for a 2-D cathode thermal code [30] in r–z coordinates that uses the ion and electron fluxes from the 2-D plasma codes as input to predict the temperature distribution in the cathode. In this figure, the positive numbers identify different materials, and negative numbers are used to identify radiative boundary conditions. The code includes thermal conduction, radiative heat losses, and, within the insert region, radiative heat transfer. The thermal model uses heat flux inputs calculated from the 2-D IROrCa2D plasma code [5] and includes the heating of the cathode tube and insert due to power deposition in the orifice region. Results from this code are close to the 0-D model results just described for the NSTAR cathode, but with much more accuracy and spatial resolution of the electron emission and plasma bombardment locations. Table 6-3 shows the input fluxes used in the 2-D thermal model. The plasma heating calculated by the detailed 2-D code is about 50% greater than the simple 0-D model above predicts, and most of the heat is deposited on the orifice plate.

As an example of the results from a coupled thermal and cathode plasma model, Fig. 6-27 shows the code predictions [30] and measured temperatures [33] of the insert for the NSTAR cathode running at 12 A of discharge current. The 2-D code predicts an insert temperature of about 1210°C in the first few

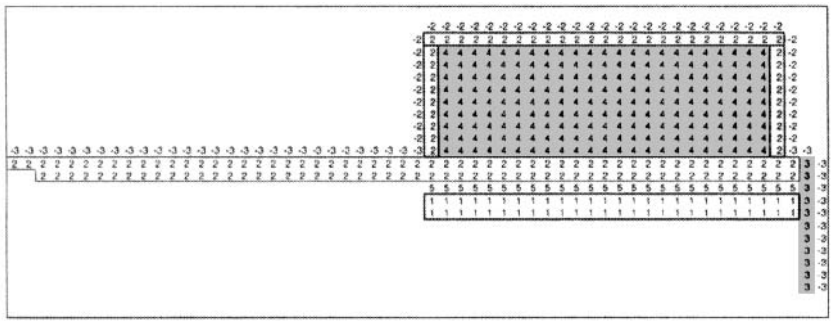

Fig. 6-26. Hollow cathode thermal model input geometry with the different types of cells numbered and the boundary conditions indicated by numbers. Negative numbers indicate radiative boundaries [30].

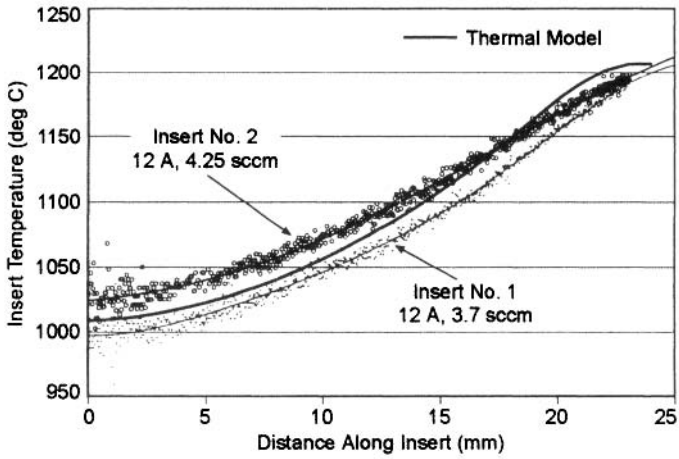

Fig. 6-27. Comparison of the insert temperatures measured [33] and calculated for the NSTAR cathode by the 2-D coupled thermal/plasma model of Katz [30].

Table 6-3. Insert surface and orifice plate heating calculated using the IROrCa2D code for the NSTAR discharge cathode at 12 A and 3.5 sccm.

Element Heated	Power (W)
Insert Surface	12
Orifice Plate	29

millimeters from the orifice plate where the plasma is in good contact with the insert. The thermal model predicts a peak temperature of about 1190°C for the heat loads from a predicted plasma contact area of 5 mm by the plasma code. The 2-D codes also show the sensitivity of the hollow cathode temperature to the emissivity of the orifice plate, the thermal contact between the emitter and

the tube, and orifice heating effects (especially in neutralizer cathodes), which impact the performance and life of the cathode. These effects cannot be obtained from the simple 0-D models used above.

6.7 Cathode Plume-Region Plasma

The cathode insert and orifice regions were examined above with simplified models, and this information was used to provide an understanding of the plasma parameter dependence and self-heating mechanism of the cathode. The final region of the hollow cathode to cover is exterior to the cathode orifice where the cathode plume interacts with the keeper electrode and couples the cathode emission current to the thruster discharge plasma and anode. In this region, the neutral gas expands rapidly away from the cathode and is either collisionless or makes the transition to collisionless. The electrons from the cathode are accelerated by the potential difference between the cathode orifice plasma and the plasma in the discharge chamber that is at a potential usually near the anode voltage. There is usually an applied axial magnetic field on the order of 100 G in this region to provide a transition to the ring-cusp fields in ion thrusters, which produces some confinement of the cathode plume electrons. These electrons generate the cathode plume plasma, which is also rapidly expanding away from the cathode.

The plasma stream exiting the hollow cathode is often reported as having various structures consisting of dark spaces, plasma balls, and brightly divergent plume shapes. Two of these cases are shown in Fig. 6-28, where the cathode is on the right and the anode on the left. The plasma stream consists of the electrons from the hollow cathode, neutral gas expanding from the keeper aperture in addition to more uniform background neutral gas from the thruster, and the plasma ball and stream generated by ionization of this gas by the electrons. The on-axis potential and temperature profiles measured by scanning probes for these two cases [1] are shown in Fig. 6-29. While the discharge current is the same in these two cases, the high gas flow reduced the discharge voltage from about 26 V at 5.5 sccm to 20 V at 10 sccm. The structure of the potential and temperature profiles is significantly different in the plume region as the gas flow and discharge voltage change. The higher gas flow case reduces the potentials and temperatures throughout the system and pushes the plasma ball observed at the cathode exit farther downstream.

To provide some insight into the plasma density, temperature, and potential profiles generated in this plume, a simple 1-D model [39] will be used to examine the plume physics. A full 2-D cathode plume code for the neutral gas and plasma is discussed later in this section to more accurately predict the cathode discharge behavior. The 1-D plasma model follows the same general

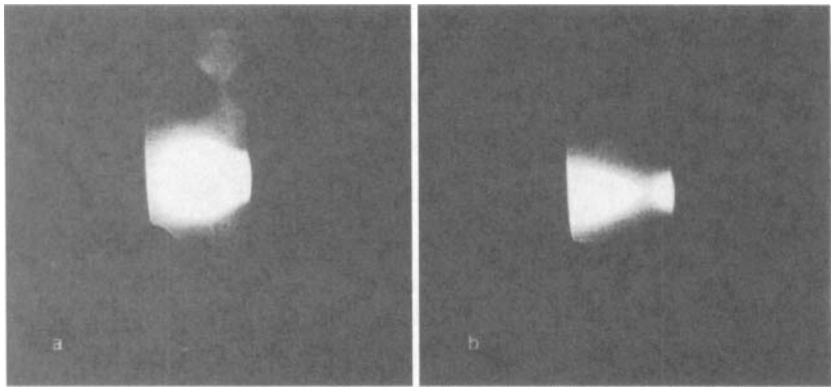

Fig. 6-28. NEXIS cathode plume at 25 A with the plasma ball in (a) at 5.5 sccm and a dark space in (b) at high flow (10 sccm) [1].

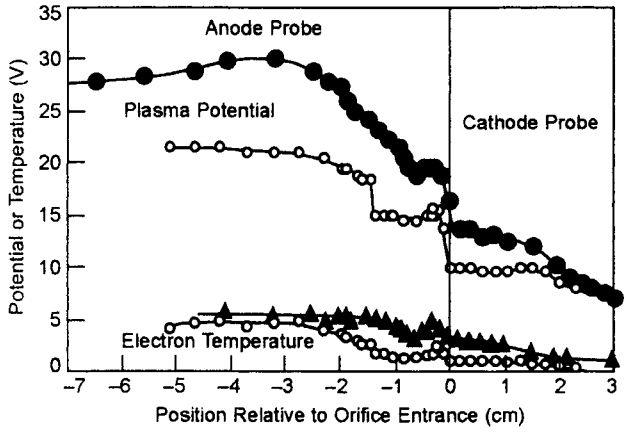

Fig. 6-29. Plasma potential and electron temperature profiles for the two cases in Fig. 6-27, where the closed symbols are the 5.5-sccm, 26.5-V case and the open symbols are the 10-sccm, 19-V case [1].

structure as that used for the orifice region in Section 6.5, but in this case the neutral gas is expanding and the gas and plasma flows are largely collisionless. The steady-state continuity equation is

$$0 = \nabla \cdot (D_a \nabla n) + \frac{\partial n}{\partial t}, \tag{6.7-1}$$

where the diffusion is ambipolar with a diffusion coefficient given by Eq. (6.4-4). Using the electron momentum equation, Eq. (6.4-31), the electron current density on axis in the plume is given by

$$J_e = \frac{1}{\eta}\left(E + \frac{\nabla n T_e}{n} \right), \tag{6.7-2}$$

where the resistivity η for the case of electron-neutral and electron-ion collisions in the partially ionized gas is given by Eq. (6.4-35).

The electron energy equation is given by Eq. (6.4-28) and includes convection, conduction, joule heating, pressure work, and ionization losses. Axial depletion of the neutral gas by ionization can be taken into account using a simple exponential attenuation model. The ionization rate of the neutral gas density is

$$\frac{d n_o}{dt} = -n_o n_e \langle \sigma_i v_e \rangle, \tag{6.7-3}$$

where n_o is the total neutral density in the plume. The neutral density is composed of the flowing component, n_f, from the cathode and the background neutral density in the chamber, n_c:

$$n_o = n_f(z) + n_c. \tag{6.7-4}$$

The density of the flow gas decreases with distance away from the cathode orifice:

$$\frac{d n_f(z)}{dz} = \frac{1}{v_o}\frac{d n_f}{dt} = \frac{1}{vo}\left(\frac{d n_o}{dt} - \frac{d n_c}{dt} \right), \tag{6.7-5}$$

where v_o is the neutral gas velocity. Using Eq. (6.7-3), Eq. (6.7-5) can be written as

$$\frac{1}{n_f(z)}\frac{d n_f(z)}{dz} = -\frac{1}{v_o} n_e \langle \sigma_i v_e \rangle, \tag{6.7-6}$$

which has a solution of the flow density decreasing exponentially away from the cathode. This is the same as the case analyzed in Section 3.6, in which the ionization mean free path is found to be one over the right-hand side of Eq. (6.7-6).

The above equations [Eqs. (6.7-1) through (6.7-6)] are solved in a simple computational mesh shown in Fig. 6-30. The neutral gas is assumed to expand with a full angle of 45 deg. The code has been used to solve for the NEXIS

cathode density and potential profiles at the standard operating condition of 25-A and 5.5-sccm xenon gas flow. The density profile is shown in Fig. 6-31, where the agreement between the 1-D model and the data is reasonably close. The plasma potential and electron temperature profiles are shown in Fig. 6-32, where the agreement is reasonably good. Of interest is the fact that the electron Mach number (electron drift velocity divided by the thermal velocity) is well below 1, indicating that double layers and streaming instabilities are not expected for this case. The visual observation of the cathode plume with a

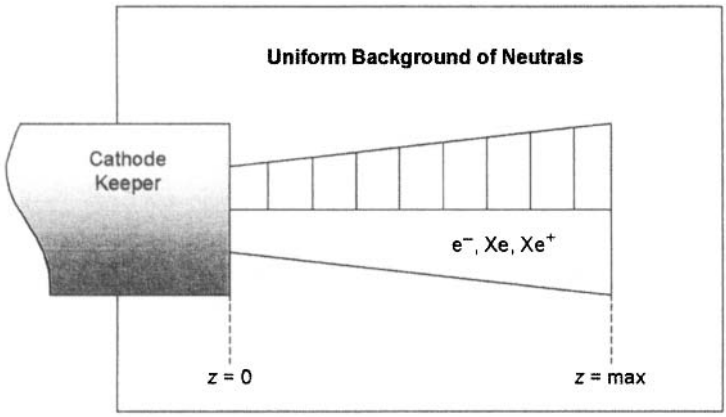

Fig. 6-30. Computational region for the 1-D cathode plume model [39].

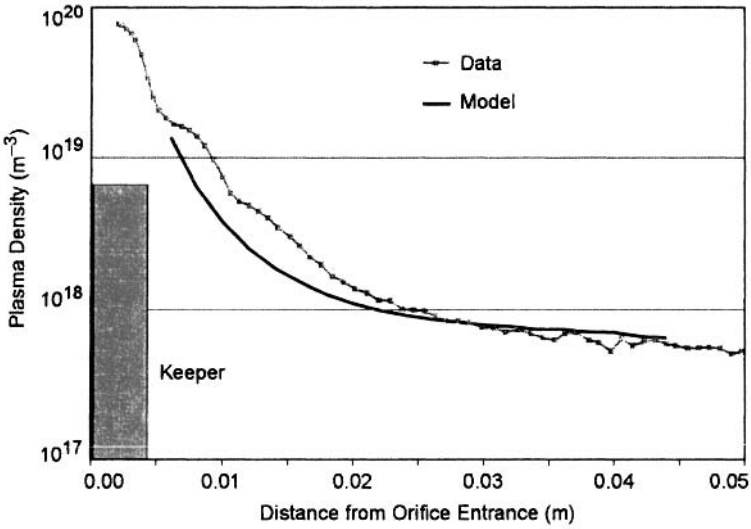

Fig. 6-31. Density profile from the 1-D model and the axial probe data for the NEXIS cathode plume plasma density at 25 A and 5.5 sccm [39].

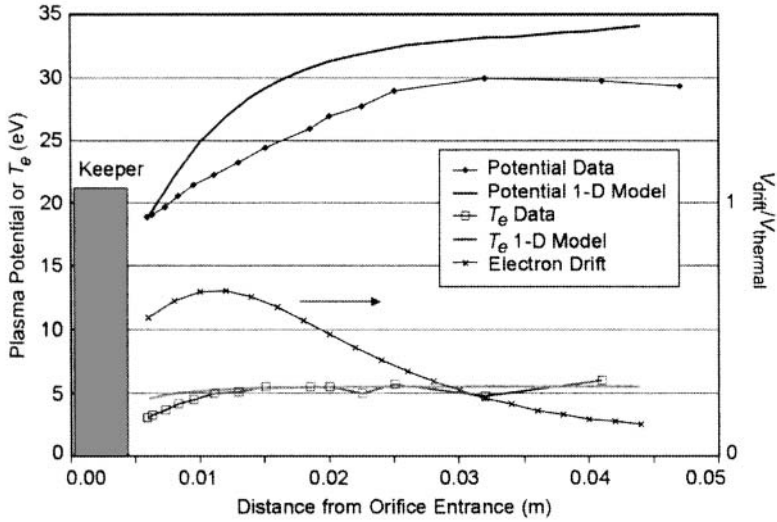

Fig. 6-32. Potential and temperature profiles from the 1-D model and the axial probe data from the NEXIS cathode at 25 A and 5.5 sccm [39].

bright, well defined "plasma ball" shown in Fig. 6-28 might suggest potential or density discontinuities, but this is not the case. The fact that the plasma density is falling exponentially away from the keeper, and that the neutral gas density falls as the inverse distance from the cathode squared as well, suggests that the boundaries of the ball are just the manifestation of a rapidly decreasing excitation rate and the visual integration of transverse chords through this 3-D region by the eye.

The plasma potential and electron temperature profiles for the case of the NEXIS cathode at 25 A with a higher gas flow (10 sccm) are shown in Fig. 6-33. In this case, close to the keeper, the potential and temperature predicted by the model do not agree well with the data, and the photograph in Fig. 6-28(b) suggests a dark space in this region of very low electron temperature that is not captured by the 1-D model. However, the potential discontinuity or jump observed in the experimental data for this case at about 1 cm from the keeper exit corresponds to an electron temperature increase and higher plasma potentials. In the lower temperature region upstream of this potential jump, the model indicates that the electron Mach number is approaching 1, which suggests the generation of a double layer or plasma instabilities that accelerate the electrons and heat the plasma.

Double layers can be formed in regions where the plasma potential changes rapidly between two relative low-field regions. Double layer formation was originally analyzed by Langmuir [40] and was described in Chapter 3. Across

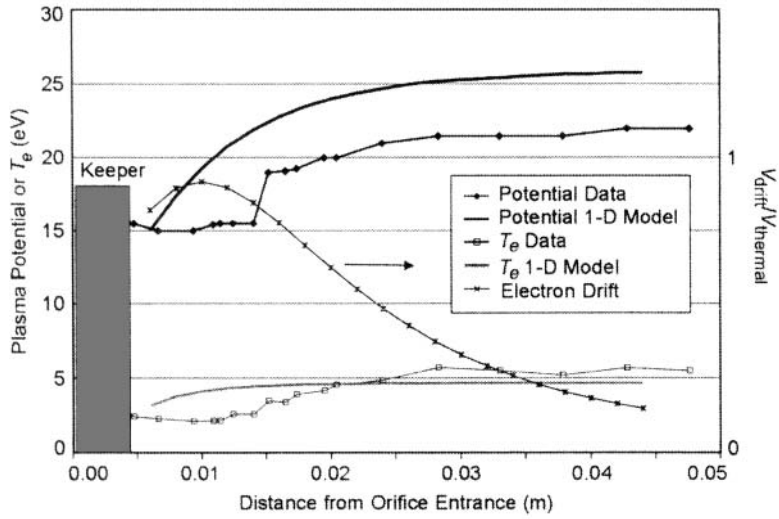

Fig. 6-33. Potential and temperature profiles from the 1-D cathode plume model and the axial probe data for the NEXIS cathode at 25 A and 10 sccm [39].

the double layer, the ion and electron charge densities integrate to zero. The relationship between the ion and electron currents flowing across the layer is given by

$$J_e = k\sqrt{\frac{M}{m}}\,J_i, \tag{6.7-7}$$

where k is a constant that is about 0.5 for $T_e / T_i \approx 10$. The double layer forms if the electron drift speed exceeds the electron thermal speed. This can occur if the ionization rate in the plume along the current path drops and there is insufficient plasma generated to support the discharge current. In this case, the double layer accelerates the electrons to higher energies, which increases the ionization rate.

The axial location of a double layer can be found by finding the location along the cathode plume where Eq. (6.7-7) is satisfied. Assuming that the neutral gas expands at a fixed cone angle, the tangent of which is the half angle α, the neutral density along the plume is

$$n_o(z) = \frac{Q_{\text{gas}}}{v_o \pi (r + \alpha z)^2}. \tag{6.7-8}$$

If the ions are generated by the accelerated electrons within about one local radius downstream of the double-layer flow back through the double layer, the ion current is

$$I_i \approx I_e \int_z^{z+r_o+\alpha z} \sigma_i n_o(z) dz \,. \tag{6.7-9}$$

Substituting Eq. (6.7-8) into Eq. (6.7-9) and integrating, the ion current through the sheath is

$$I_i = I_e \frac{Q_{\text{gas}} \sigma_i}{v_o \pi} \frac{1}{(r_o + \alpha z)} \frac{1}{(1+\alpha)} \,. \tag{6.7-10}$$

Defining the "Langmuir ratio" from Eq. (6.7-7) as

$$R_L \equiv \frac{J_i}{2J_e} \sqrt{\frac{M}{m}} \,, \tag{6.7-11}$$

a stable double layer will form in the location where R_L equals one. Using Eq. (6.7-10), the Langmuir ratio is

$$R_L = \frac{2Q_{\text{gas}} \sigma_i}{v_o \pi} \sqrt{\frac{M}{m}} \frac{1}{(r_o + \alpha z)} \frac{1}{(1+\alpha)} \,. \tag{6.7-12}$$

In the cathode plume, Eq. (6.7-12) indicates that the Langmuir ratio decreases monotonically with distance from the cathode. Alternatively, the axial location where the Langmuir condition equals 1 can be found to identify the location of the double layer. This is shown in Fig. 6-34 where the flow rate at which $R_L = 1$ is plotted versus distance from the cathode orifice. At flow rates of 10 sccm, Fig. 6-34 suggests that a double layer will form over 1-cm downstream from the cathode, consistent with the data shown in Fig. 6-33. The general behavior of the double-layer location moving axially downstream with increasing gas flow has been reported [1] by both visual observations and by probe measurements.

The cathode plume is much more complicated than this simple 1-D model suggests, and the condition of increasing electron-Mach numbers predicted under certain situations by the 1-D code may generate double layers or instabilities in the plasma not well described by the fluid codes. The assumed neutral gas expansion behavior and the associated electron current density in the plume were fortuitously picked to give potential and density profiles that came close to matching the experimental data. In reality, the neutral gas likely expands more rapidly than the 45-deg cone assumed in the 1-D model. The low

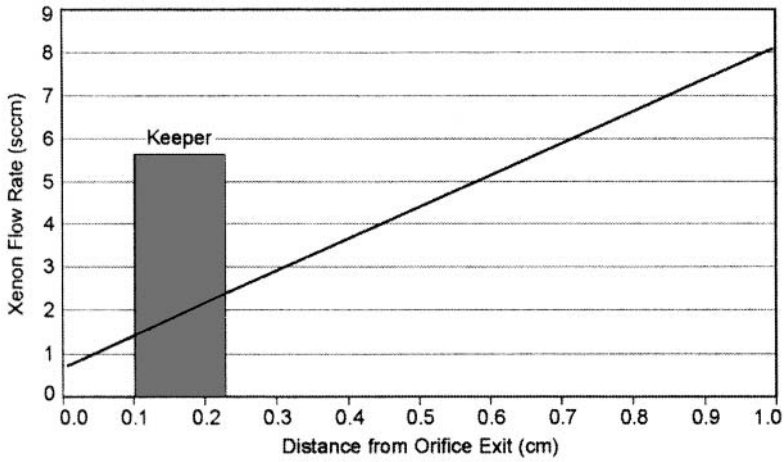

Fig. 6-34. Flow rate at which the Langmuir ratio is equal to one and double layers can be formed as a function of the distance downstream from the NEXIS cathode orifice [39].

electron temperature obtained from classical resistivity, with the low neutral density in the plume, produce insufficient ionization to generate the required plasma density to match the experimental data and carry the current to the anode. This situation leads to the increase in the local electron Mach number and the possible generation of double layers described above or to plasma instabilities that increase the resistivity anomalously and heat the electrons to produce more ionization.

A full 2-D model of the cathode plume is under development at the Jet Propulsion Laboratory (JPL) to investigate these issues [41]. The OrCa2D code uses a 2-D neutral gas fluid code in the insert and cylindrical orifice regions and then transitions to a collisionless neutral gas model from the orifice chamfer region into the plume. This provides the correct neutral gas density profile in the cathode plume region high numerical accuracy. The 2-D plume code then extends the system of equations used in the 2-D orifice model previously described in Section 6.4 [Eqs. (6.4-28) through (6.4-35)] on an adaptive mesh to provide the resolution required near the keeper and minimize the computational time. In solving the above equations, the code also addresses the onset of instabilities as the Mach number approaches one that produces anomalous resistivity and electron heating. For example, Fig. 6-35 shows the plasma density profile calculated by the code for the NEXIS cathode operating at the nominal 25 A and 5.5 sccm for the case of classical and anomalous resistivity in the cathode plume. The use of the classical resistivity given in Eq. (6.4-35) results in a low electron temperature in the plume region and insufficient ionization to match the experimental plasma density profile.

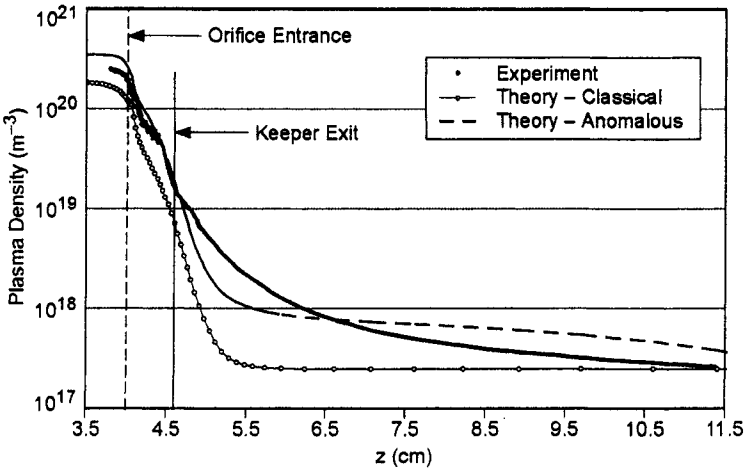

Fig. 6-35. Plasma density profile on axis for the NEXIS cathode showing that an anomalous resistivity is required to provide sufficient ionization to come close to matching the experimental data [41].

Incorporating anomalous resistivity associated with the generation of ion acoustic instabilities in the cathode plume provides higher electron temperatures and more ionization in the plume, which better matches the measured profiles. Additional work is required to complete this model, but as the model development progresses, a clearer picture of the cathode plume physics will result.

The 2-D structure of the cathode plume as it expands from the cathode orifice has been investigated by several authors [28,31,42]. Figure 6-36 shows plasma density contours measured [43] with a fast scanning Langmuir probe. The density is the highest on axis and closest to the cathode orifice, which is consistent with the visual appearance of a bright cathode ball or spot at the cathode exit that expands both radially and axially into the discharge chamber [28]. A reduction in cathode gas flow causes the ball or spot to pull back toward the cathode orifice and the plasma to expand into what is called a plume mode [44,45]. Plume mode operation generally results in high-frequency oscillations in the cathode plume that propagate into the discharge chamber and keeper region, and can couple to the power supply leads if of sufficient amplitude. The plasma potential contours measured in this case by the probe are shown in Fig. 6-37. The potential is actually a minimum on axis near the cathode, and then increases radially and axially away from the cathode exit to a value several volts in excess of the discharge voltage [28,43]. This structure near the cathode is sometimes called the trough because ions generated externally to the cathode tend to funnel into the trough and toward the cathode. Large amplitude plasma

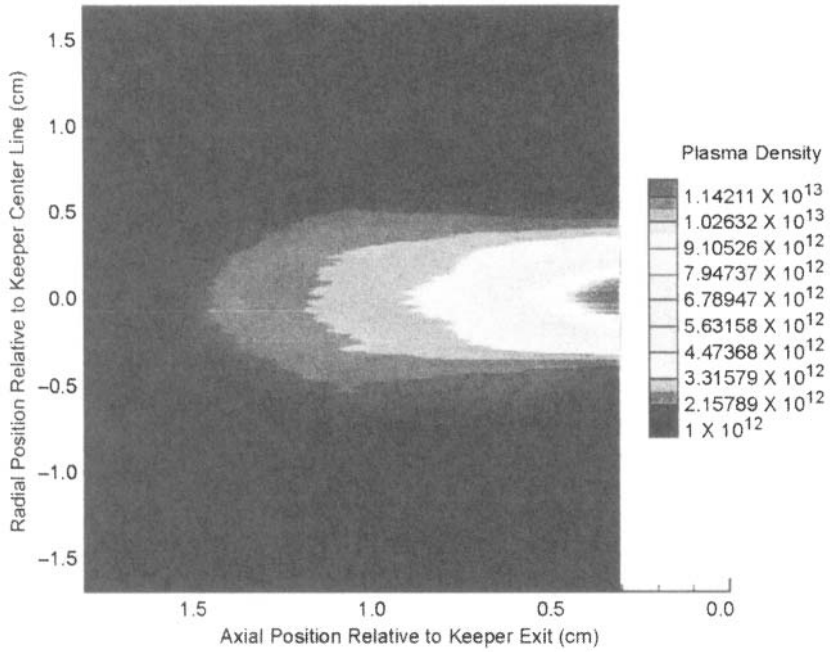

Fig. 6-36. Plasma density contours measured for the NEXIS cathode at the nominal 25-A and 5.5-sccm gas flow discharge condition [43].

potential oscillations in the range of 50–1000 kHz have been observed primarily in and around the edge of the plasma ball and in front of the keeper electrode from high-speed scanning emissive probes [46]. These may be the result of the increased Mach number and instabilities described above under certain conditions.

6.8 Hollow Cathode Life

Cathode insert life is fundamentally determined either by depletion of the BaO emissive mix impregnated into the dispenser cathodes so that the surface work function is degraded or by evaporation of the emissive material in refractory metal cathodes, such as tungsten and tantalum, and in crystalline cathodes, such as LaB_6. The cathode mechanical structure (orifice plate, heater, cathode tube, etc.) also can be worn out or degraded by ion-induced sputtering, which affects the cathode life. The impact on the cathode performance by these two life-limiting fundamental mechanisms is important to understand in designing cathodes for ion and Hall Thrusters. In addition, poisoning of inserts due to impurities in the feed gas or improper exposure to air also can increase the work function and impact cathode life.

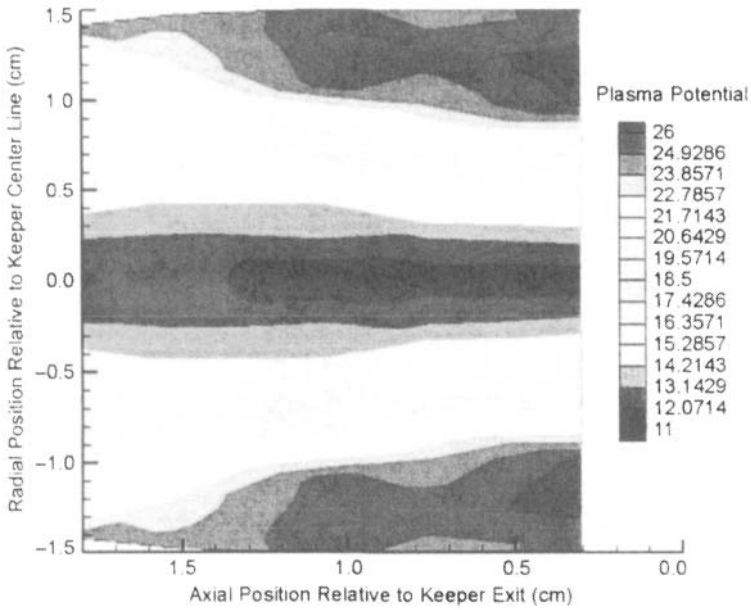

Fig. 6-37. Plasma potential contours measured for the NEXIS cathode at the nominal 25-A, 5.5-sscm discharge condition [43].

6.8.1 Dispenser Cathodes in Insert Plasmas

In dispenser cathodes, evaporation of the barium layer coating the cathode surface is well understood, and depletion life models can be readily constructed if this is the root cause of barium loss [47]. However, the emitter surface is exposed to a plasma, and ion bombardment of the surface by ions from the insert-region plasma can increase the loss of barium from the surface, which will reduce the lifetime of the cathode. While the basic concept of a hollow cathode is to reduce the erosion and modification of the low work-function insert surface with a high-pressure, collisional insert plasma, this benefit had to be validated before the cathode life could be predicted [47].

An experimental and theoretical study of enhanced barium evaporation from dispenser cathode surfaces was undertaken [48] to determine the plasma conditions in the insert region under which an evaporation model could be used. The experimental arrangement measured the barium evaporation from a Type S 4:1:1-impregnated porous tungsten cathode with an embedded heater during xenon plasma bombardment. The cathode could be biased negatively relative to the plasma in order to control the ion bombardment energy. The barium evaporation rate was measured by a fiber optic coupled to a visible wavelength spectrometer tuned to detect the emission intensity of the Ba-I line

at 553.5 nm excited in the plasma. Since the emission intensity depends on the amount of Ba present in the plasma and the electron density and temperature, the plasma parameters were monitored with a probe and the Ba-I signal was normalized to a neutral xenon line to account for any variations in plasma parameters during the measurements.

Figure 6-38 shows the barium loss rate measured at 725°C versus the ion bombardment energy. Increasing the ion bombardment energy from 10 to 30 eV increases the barium loss rate by an order of magnitude. Figure 6-39 shows the barium loss rate as a function of temperature for two cathode bias energies. For the case of the cathode floating relative to the plasma, the ion bombardment energy is only a few eV and the barium loss rate is determined solely by thermal evaporation. For a bias energy of 15 eV, the barium loss rate is found to be the same as for thermal evaporation for cathode temperatures in excess of about 800°C. Since the hollow cathodes in most thrusters operate at insert temperatures in excess of 1000°C, these data show that the barium loss rate is determined by thermal evaporation rates.

A model of the enhancement of barium evaporation for a surface under energetic ion bombardment was developed by Doerner, et al. [49] to explain this behavior. At elevated surface temperatures, two classes of surface particles must be considered at the surface: (a) those particles that are bound to the material lattice structure (denoted here as "lattice atoms") and (b) atoms that have been liberated from the lattice structure, but which are still bound to the

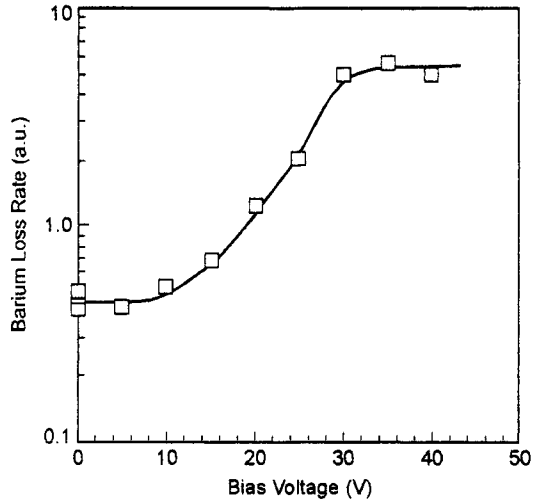

Fig. 6-38. Variation of barium loss rate from the cathode surface at 725°C with cathode bias voltage (redrawn from [48]).

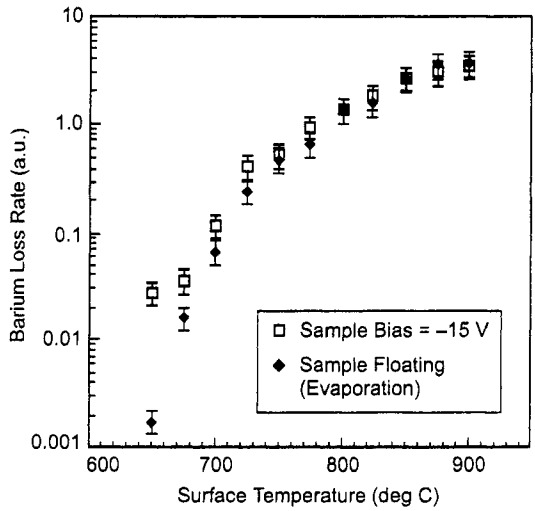

Fig. 6-39. Relative Ba concentration in Xe plasma for two bias conditions (redrawn from [48]).

material surface with a reduced binding energy (denoted here as "adatoms"). Both species can sublimate from the material surface if an atom receives enough kinetic energy from random collisions to break free from the surface; however, because the binding energy for the two species is different, the corresponding loss rate also will be different.

The net flux of material from the surface can be written as

$$J_T = J_i Y_{ps} + K_o n_o \exp^{(-E_o / T)} + \frac{Y_{ad}\, J_i}{\left(1 + A \exp^{(E_{eff}/T)}\right)}, \qquad (6.8\text{-}1)$$

where J_i is the plasma ion flux, Y_{ad} is the adatom production yield from the incident ion flux, Y_{ps} is the sputtered particle yield, and $Y_{ad}\, J_i$ is equal to the adatom loss rate due to both sublimation and recombination. The first term in Eq. (6.8-1) describes physical sputtering of lattice atoms (which is independent of surface temperature); the second term describes the thermal sublimation of lattice atoms, which is independent of ion flux; and the third term describes the losses due to adatom production and subsequent sublimation, which depends upon both the incident ion flux and the surface temperature. For Xe ions incident on BaO at 30 eV, $Y_{ps} = 0.02$, $A = 2 \times 10^{-9}$, and

$$\frac{Y_{ad}}{Y_{ps}} \approx 400. \qquad (6.8\text{-}2)$$

These parameters can be used to model the expected net flux of Ba from a surface under bombardment with 30-eV Xe ions for various surface temperatures. The result of this model is compared with experimental measurements of Ba emissivity under these conditions in Fig. 6-40. The model compares extremely well with the experimental results. The model also qualitatively explains the key experimental observations, including the effect of ion energy on net erosion, the saturation of the adatom loss term at elevated temperatures, and the transition to losses dominated by thermal sublimation of lattice atoms at elevated temperatures. The model has been used to examine the effect of increasing the ion flux to the surface from the values in these experiments to the actual values for the hollow cathodes found from the 2-D plasma model. In this case, the model predicts that thermal evaporation dominates the barium loss rate for ion energies of less than 15 eV and cathode temperatures of over 900°C. The model provides confidence that the barium loss rate effects in the plasma are understood and that the main result of barium loss determined by thermal evaporation rates for the plasma parameters of thruster cathodes examined here is accurate.

6.8.2 Cathode Insert Temperature

Since the barium evaporation rate for the plasma conditions found in the hollow cathodes is determined by the insert surface temperature, a non-contact temperature measurement technique was developed at JPL [50] to directly measure the insert temperature during cathode operation. The technique

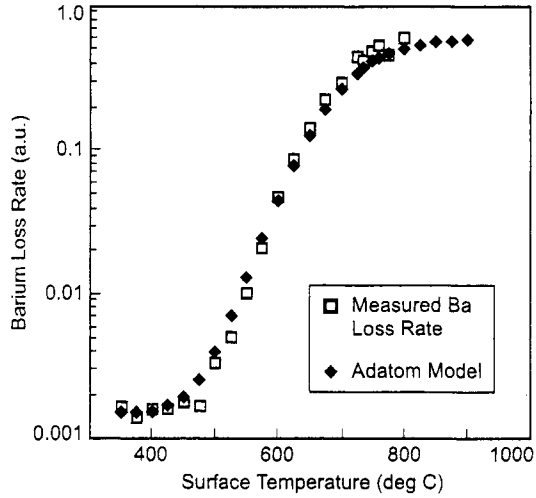

Fig. 6-40. Ba concentration versus cathode surface temperature for –15 V bias. Experimental data are shown by open squares and the model prediction are shown by the diamonds (from [48]).

employs a stepper-motor-driven sapphire fiber-optic probe that is scanned along the insert inside diameter and collects the light radiated by the insert surface. Ratio pyrometry is used to determine the axial temperature profile of the insert from the fiber-optic probe data. Thermocouples attached on the outside of the cathode on the orifice plate provide additional temperature data during operation and are used to calibrate the pyrometer system in situ with a small oven inserted over the cathode to equilibrate the temperature.

Figure 6-41 shows temperature profiles measured for a nominal Space Station Contactor (SSC) cathode [50] operating at four different discharge currents. The peak temperature of the insert at the full 12-A current level is about 1200°C. The insert also has approximately a 10% to 15% temperature gradient along its length. The change in the insert temperature with the xenon flow rate for the cathode producing 12 A of discharge current is shown in Fig. 6-42. High flow rates through the cathode reduce the insert temperature, although the effect is small.

A direct comparison of the insert temperature profile for the NSTAR discharge cathode and the SSC cathode at identical discharge currents of 12 A and xenon flow rates of 6 sccm is shown in Fig. 6-43. The NSTAR insert temperature is higher than the SSC all along the insert. It also appears that the temperatures of the inserts tend to converge near the orifice plate. The high insert temperature for the NSTAR cathode is likely because the plasma contact area is significantly larger at the roughly 50% lower internal pressure as compared with the SSC. In addition, thermocouple measurements on the orifice plate show that the smaller-diameter SSC orifice plate is significantly hotter than the NSTAR orifice plate, consistent with orifice heating effects described in Section 6.5 for smaller orifice diameters.

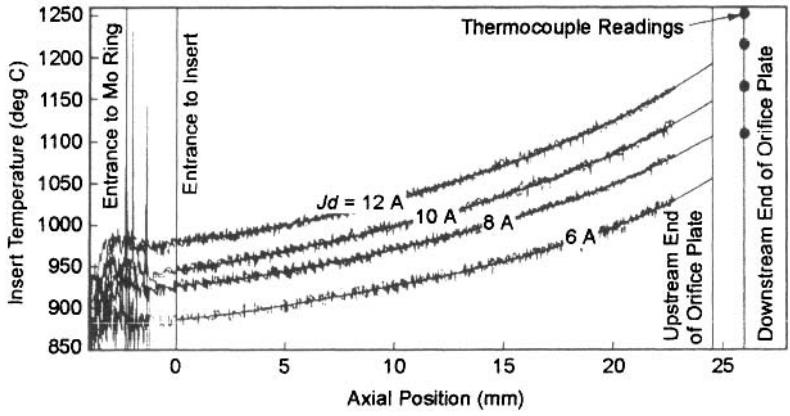

Fig. 6-41. Insert temperature profile measured for a SSC hollow cathode for several different discharge currents (from [50]).

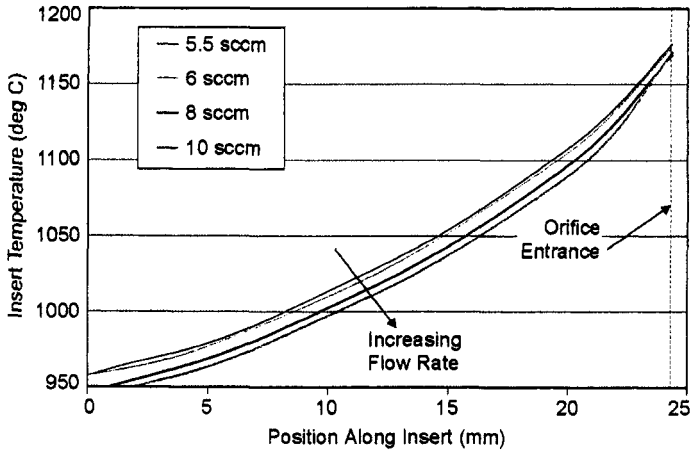

Fig. 6-42. Insert temperature profile for an SSC hollow cathode operating at 12 A of current for several different gas flow rates (redrawn from [50]).

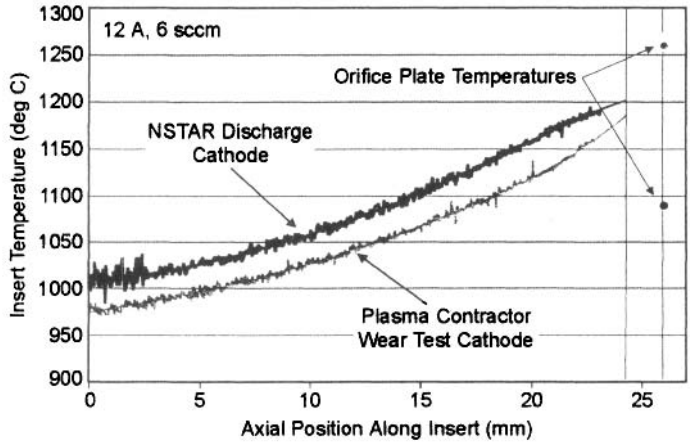

Fig. 6-43. Comparison of the insert temperature profile for the Space Station Contactor cathode and the NSTAR discharge cathode at 12 A (from [33]).

6.8.3 Barium Depletion Model

The previous sections showed that the barium loss rate from hollow cathode dispenser cathode inserts should be essentially the same as dispenser cathode inserts operated in vacuum if the ion bombardment energy is sufficiently low in the hollow cathode. Since plasma potentials on axis in the insert plasma of less than 15 V are routinely measured [1,28] and sheath potentials of less than 10 V

are found from the models discussed above, the insert life will be limited by evaporation in the same manner as in vacuum devices.

Published measurements by Palleul and Shroff [51] of the depth of barium depletion in dispenser cathodes as a function of time and temperature show that barium depletion obeys a simple diffusion law with an Arrhenius dependence on temperature. This is shown in Fig. 6-44 (from [51]), where the impregnate surface layer in the pore recedes with time. The "activation energy" in the diffusion coefficient that determines the slope of the curves in Fig. 6-44 appears to be relatively independent of the cathode type.

From data presented in Fig. 6-44, the operating time to deplete impregnate from the insert material to a depth of 100 μm is

$$\ln \tau_{100\,\mu\mathrm{m}} = \frac{eV_a}{kT} + C_1 = \frac{2.8244e}{kT} - 15.488\,, \tag{6.8-3}$$

where the operating time $\tau_{100\,\mu\mathrm{m}}$ is in hours, e is the elementary charge, V_a is the activation energy, k is Boltzmann's constant, C_1 is a fit coefficient, and T is the insert temperature in kelvins. The activation energy was found from Fig. 6-44. Using this relationship and the fact that the depletion depth is

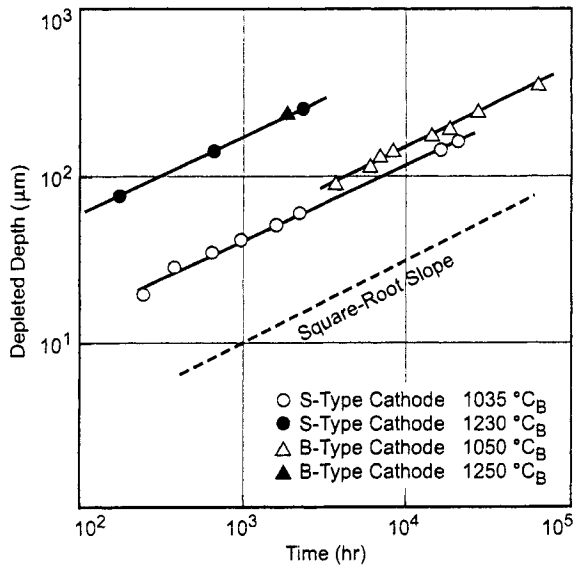

Fig. 6-44. Depletion depth of a porous tungsten insert as a function of time for cathodes at different temperatures (redrawn from [51]).

proportional to the square root of the operating time [51], an equation yielding the insert lifetime due to barium depletion can be derived [47]:

$$\tau_{\text{life}} = \tau_{100\mu\text{m}} \left(\frac{y}{y_{100\mu\text{m}}} \right)^2, \tag{6.8-4}$$

where $\tau_{100\,\mu\text{m}}$ is the time to deplete to 100 μm in depth from Eq. (6.8-3), y is the insert thickness in μm, and $y_{100\mu\text{m}}$ is the 100-μm reference depth. Using Eq. (6.8-3) in Eq. (6.8-4), the life of a Type S dispenser cathode in hours is

$$\tau_{\text{life}} = 10^{-4} y^2 \exp\left(\frac{2.8244e}{kT} - 15.488 \right), \tag{6.8-5}$$

where y is the insert thickness in μm and T is the insert temperature in kelvins. Figure 6-45 shows the insert life for a 1-mm depletion depth versus the insert temperature. Insert life of over 100,000 hours is readily achievable if the insert is thick enough. At around a nominal 1100°C operating temperature, the life increases a factor of 2 if the temperature decreases 40°C.

This model represents a worst-case estimate of the cathode life. In very high-density hollow cathodes, like the NSTAR cathode, the ionization mean free path for the evaporated barium is significantly less than the insert plasma radius. This means that a large fraction of the barium is ionized close to the insert surface. The electric field in this region is primarily radial, which means that some large fraction of the barium is recycled back to the surface. The barium surface coverage is then partially re-supplied by recycling, which can extend the life considerably.

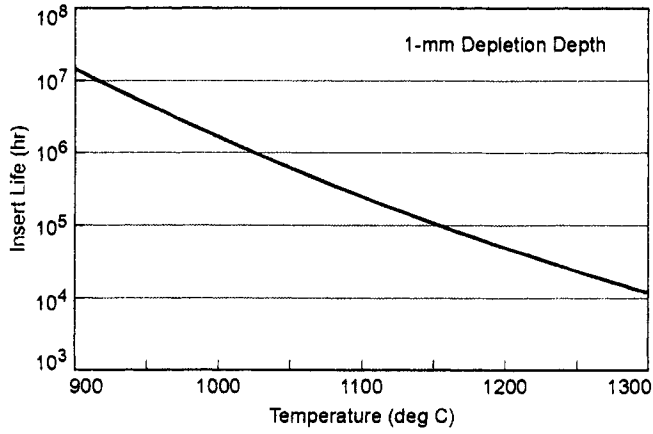

Fig. 6-45. Insert life from barium evaporation calculated for a 1-mm depletion depth versus temperature.

To predict cathode life in a thruster application from an insert depletion mechanism, a relationship between the insert temperature and the discharge current at a given gas flow must be obtained. The SSC insert temperature was measured versus discharge current by Polk [50]. These data are well fit in the plasma contact region (the 3 mm closest to the orifice plate) by

$$T = 1010.6\, I_d^{0.146} [\mathrm{K}]. \tag{6.8-6}$$

At 12 A of discharge current, this gives an insert temperature of 1453 K. Since the insert in this cathode is about 760-μm thick and we assume that the insert is depleted when the depth reaches about two-thirds of the thickness (due to some barium diffusion out the outside diameter of the insert), Eq. (6.8-5) predicts a life of 30,000 hours. This is in good agreement with the SSC life test data where the cathode failed to start after about 28,000 hours at 12 A of discharge current [52]. In this case, barium recycling may not affect the insert life significantly because the plasma is in contact with the insert for only a couple of millimeters, from the orifice plate, and the barium will tend to migrate to regions that are not involved in the emission process.

For the NSTAR cathode, the insert temperature data as a function of discharge current measured by Polk [33] are well fit in the plasma contact region by

$$T = 1191.6\, I_d^{0.0988} [\mathrm{K}]. \tag{6.8-7}$$

At the full-power discharge current of 13 A, and using the insert thickness of 760 μm, Eq. (6.4-5) predicts an insert life of 20,000 hours. The ELT ran at full power for about 14,000 hours and accumulated an additional 16,352 hours at much lower discharge currents [53]. The barium depletion model indicates that the insert should have been depleted in the emission zone in less than 24,000 hours. Measurements indicate partial depletion in the emission region near the orifice, but that as much as 30% of the original barium was still present [53]. Clearly barium recycling in the plasma reduced the effective evaporation rate and extended the life of the cathode significantly.

For the NEXIS hollow cathodes, the operating insert temperature profile has not yet been measured. Estimates of the insert temperature were made using an early version of the combined plasma and thermal model [47]. Since the discharge loss and efficiency performance of the NEXIS thruster are known, the relationships in Chapter 2 can be used to plot thruster life versus engine performance. The NEXIS thruster operates at 75% to 81% efficiency over an Isp of 6000 to 8000 s [54]. Figure 6-46 shows the model-predicted depletion-limited life of this insert versus specific impulse for several thruster power levels. At the nominal operating point of 7000 s Isp and 20 kW, the cathode is

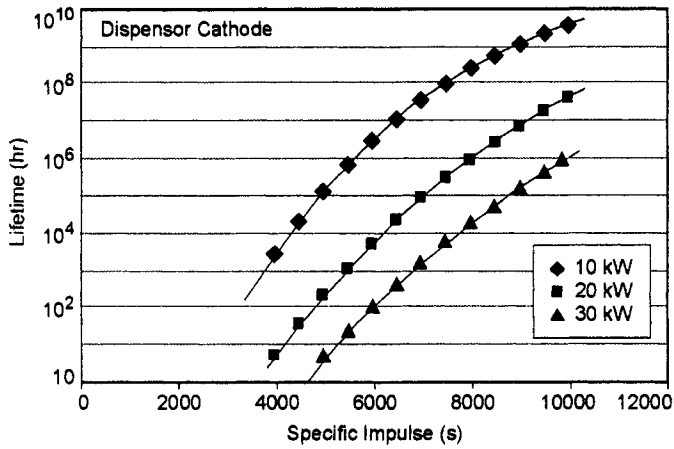

Fig. 6-46. Model prediction of NEXIS dispenser cathode life versus Isp for several thruster powers [47].

projected to operate for about 100,000 hours. Increasing the Isp requires operation at higher beam voltages, which for a given power requires less beam current and, thereby, less discharge current. A lower discharge current reduces the insert temperature for a given cathode size, which reduces the barium evaporation rate and extends the cathode life. Likewise, lower Isp and higher power require higher discharge currents, which translate to a reduction in the cathode life. It should be noted that the cathode life in Eq. (6.8-5) scales as the insert thickness squared, so the life at any operating point in Fig. 6-46 can be extended simply by increasing the thickness of the insert. This may require increases in other dimensions, but proper selection of the cathode diameter and orifice size can be made to maintain the insert temperature at the desired level to provide the desired life.

6.8.4 Bulk-Material Insert Life

Cathodes that are based on bulk insert material instead of dispenser chemistry, such as LaB_6, have a lifetime that is determined by the evaporation of the insert material inside the hollow cathode [18]. In plasma discharges, sputtering of the LaB_6 surface can also impact the life [22]. However, as in dispenser hollow cathodes, the plasma potential is very low in the insert region and the bombardment energy of xenon ions hitting the surface is typically less than 20 V, which virtually eliminates sputtering of the cathode surface. It is assumed that the evaporated material leaves the cathode and does not recycle to renew the insert surface, which will provide a lower estimate of the insert life than might actually exist. Interestingly, as the insert evaporates, the inner diameter increases and the surface area enlarges. This causes the required current density

and temperature to decrease at a given discharge current, which reduces the evaporation rate of the insert with time.

The life of the LaB_6 insert for three different cathode diameters versus discharge current was calculated based on the evaporation rate at the temperature required to produce the discharge current in the thermally limited regime [18]. Assuming that 90% of the insert can be evaporated, the cathode life is shown in Fig. 6-47 as a function of the discharge current. Lifetimes of tens of thousands of hours are possible, and the larger cathodes naturally tend to have longer lives. While other mechanisms, such as temperature variations along the insert, LaB_6 surface removal, or material build-up due to impurities in the gas, can potentially reduce the life, redeposition of the evaporated LaB_6 material will tend to extend the cathode life. Therefore, these life estimates for the different cathode sizes are mostly valid relative to each other, and the actual lifetime of the cathode can be considered to be on the order of the values shown in Fig. 6-47.

To obtain an idea of the lifetime of a LaB_6 cathode relative to a conventional dispenser cathode, the predictions from a dispenser cathode life model [47] applied to the NSTAR cathode are compared with the 0.8-cm LaB_6 cathode life predictions in Fig. 6-48. These two cathodes have similar insert diameters and lengths, and so a direct comparison is possible. The dispenser cathode calculation assumes that barium evaporation from the insert surface causes depletion of nearly all of the barium impregnate at the end of life in the NSTAR dispenser cathode at the measured [33] insert temperature and temperature gradient. This provides an upper limit to the dispenser cathode life if other

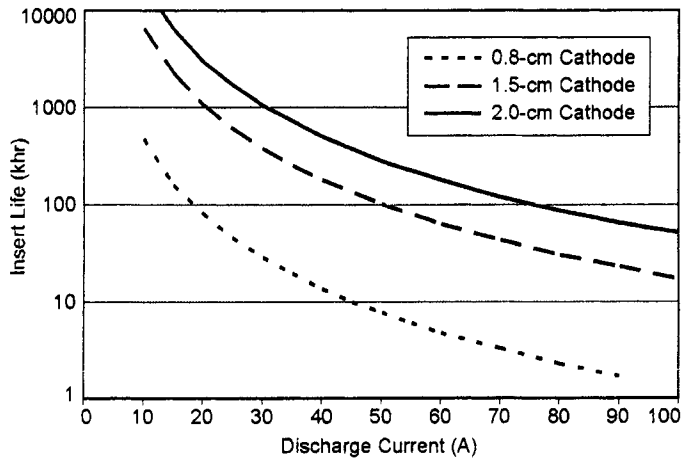

Fig. 6-47. Calculated lifetime in thousands of hours versus the discharge current for three different LaB_6 cathode diameters.

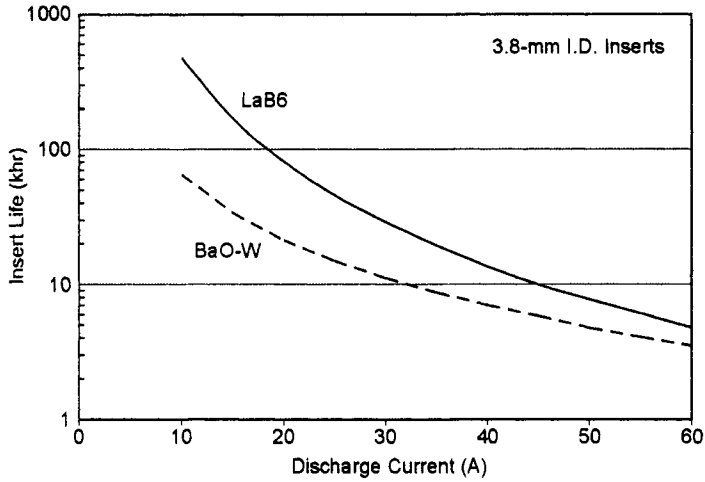

Fig. 6-48. Comparison of the calculated cathode lifetime versus the discharge current for the 0.8-cm outside diameter LaB6 cathode and the NSTAR dispenser cathode.

mechanisms, such as poisoning degrading the work function or impurity build-up plugging the pores, actually cause the cathode life limit. Likewise, recycling of the barium will extend the dispenser cathode life, so uncertainties in the dispenser cathode life estimates by this model have the same uncertainties due to impurities and redeposition that are found for the LaB_6 life model (although LaB_6 is less likely to be affected by impurities). Therefore, a direct comparison of calculated life versus discharge current will be made with the understanding that the curves will likely shift together vertically due to impurity or redeposition issues. The LaB_6 cathode life is projected to exceed the dispenser cathode life by nearly an order of magnitude at the nominal NSTAR full-power currents of less than 15 A. If the NSTAR cathode is capable of producing higher discharge currents than 15 A, the LaB_6 cathode life is still projected to exceed the NSTAR life over the full current range demonstrated by the LaB_6 cathode. As shown in Fig. 6-47, the larger LaB_6 cathodes will have even longer lifetimes, and their life significantly exceeds that projected for the NEXIS 1.5-cm-diameter dispenser cathode [47] that is designed to operate up to about 35 A.

6.8.5 Cathode Poisoning

Comprehensive investigations of the poisoning of dispenser cathodes [17] and LaB_6 cathodes [55] have been published in the literature. The most potent poisons for both cathodes are oxygen and water, with other gases such as CO_2 and air producing poisoning effects at higher partial pressures. Figure 6-49 shows the reduction percentage of the electron emission current density in

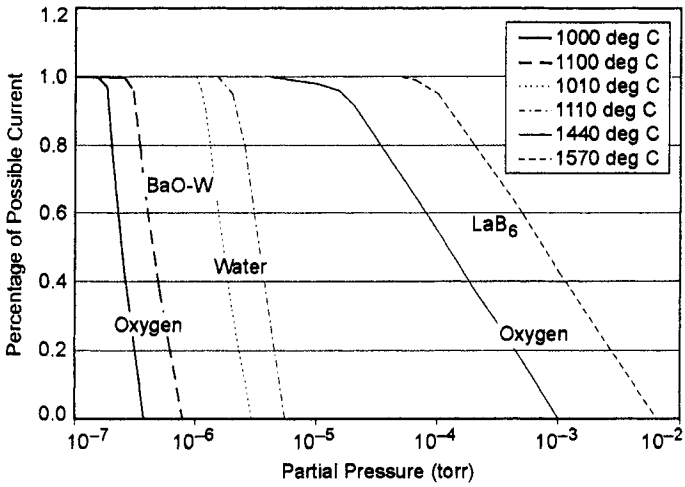

Fig. 6-49. Percentage of possible thermionic emission versus partial pressure of oxygen and water, showing the sensitivity of dispenser cathodes relative to LaB_6 (from [18]).

diode tests of a Type S 4:1:1 dispenser cathode and a LaB_6 cathode as a function of the partial pressures of oxygen and water for two different emitter temperatures. Oxygen partial pressures in the 10^{-7}-torr range can completely poison the dispenser cathode at temperatures of 1100°C. In a similar manner, water vapor at partial pressures in the 10^{-6}-torr range will poison dispenser cathodes at temperatures below 1110°C. For typical pressures inside hollow cathodes in excess of 1 torr, partial pressures in this range represent the best purity level that can be achieved by the gas suppliers, resulting in the high "propulsion-grade" purity mentioned above. This is the reason for the stringent purity requirement levied on conventional dispenser hollow cathodes in the U.S. to date. Recent experiments by Polk [56] showed that oxygen poisoning observed in vacuum devices occurred only in hollow cathodes at low plasma densities (low current) and high oxygen levels (>10 PPM), and that the plasma environment inside hollow cathodes tended to mitigate the poisoning of oxygen in dispenser cathodes. However, the plasma may aid in the formation of volatile tungsten oxides and tungstates from the impurity gases that contribute to tungsten migration and redeposition on the insert surface. This modifies the dispenser cathode surface morphology, which may affect the emission capabilities. It is likely that the life of dispenser cathodes can be degraded to some extent by propellant impurities, which has yet to be fully identified and quantified.

Lanthanum hexaboride is much less sensitive to impurities that can limit the performance and life of the barium dispenser cathodes. Partial pressures of

oxygen in the 10^{-5}-torr range are required to degrade the emission of LaB_6 at temperatures below 1440°C, which is shown in Fig. 6-49. The curves for water and air poisoning of LaB_6 are at much higher partial pressures off the graph to the right. In comparison, LaB_6 at 1570°C, where the electron emission current density is nearly the same as for the dispenser cathode at 1100°C, can withstand oxygen partial pressures up to 10^{-4} torr without degradation in the electron emission. This means that LaB_6 can tolerate impurity levels in the feed gas two orders of magnitude higher as compared with dispenser cathodes operating at the same emission current density. For the case of xenon ion thrusters, LaB_6 cathodes can tolerate the crudest grade of xenon available (≈99.99% purity) without affecting the LaB_6 electron emission or life. LaB_6 cathodes also do not require any significant conditioning or activation procedures that are required by dispenser cathodes. The authors have used LaB_6 cathodes emitting at currents of 5 to 10 A/cm^2 to produce pure oxygen plasmas in background pressures of 10^{-3} torr of oxygen. In this case, the operating temperature of the cathode had to be increased to just over 1600°C to avoid poisoning of the surface by the formation of lanthanum oxide, consistent with the trends in the published poisoning results shown in Fig. 6-49. The authors have also exposed hot, operating LaB_6 cathodes to atmospheric pressures of both air and water vapor. In both cases, the system was then pumped out, the heater turned back on, and the cathodes started up normally. This incredible robustness makes handling and processing electric propulsion devices that use LaB_6 cathodes significantly easier than thrusters that use dispenser cathodes.

6.9 Keeper Wear and Life

The keeper electrode typically encloses the hollow cathode and serves the functions of facilitating the starting of the cathode by bring a high positive voltage close to the orifice and protecting the cathode from ion bombardment from the cathode plume and thruster plasmas. However, the keeper electrode is biased during normal operation at an intermediate potential between cathode and anode to collect a reduced number of electrons, and since it is below the plasma potential, it is subject to ion bombardment and wear. Cathode orifice plate and keeper electrode erosion rates measured or inferred in various experiments [57,58] and in ion thruster life tests [34,53,59] have been found to be much higher than anticipated. For example, Fig. 6-50 shows the NSTAR cathode before and after the 30,352-hour extended life test [38]. The keeper electrode was completely eroded away by the end of the test, exposing the cathode orifice plate to the thruster discharge chamber plasma, which significantly eroded the cathode orifice plate and the sheath-heater surfaces. These results have been attributed to the high-energy ions bombarding and sputtering the cathode and keeper electrodes.

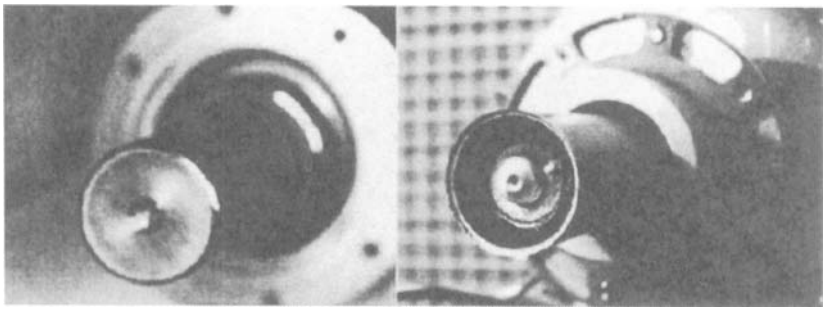

Fig. 6-50. NSTAR discharge cathode before and after the ELT wear test, showing complete sputter erosion of the keeper electrode [38].

A significant effort has been expended trying to understand the mechanism for this rapid erosion. Several organizations have measured the presence of high-energy ions in ion thrusters and in the neighborhood of hollow cathodes using retarding potential analyzers (RPAs) [46,60,61] and laser-induced fluorescence (LIF) [62]. For example, Fig. 6-51 shows the ion energy distribution measured downstream on axis and radially away from the plasma ball for the NSTAR cathode [46]. The high-energy ions are detected in both locations, with varying amounts depending on the position at which they are detected. The energy of some of the ions is greatly in excess of the 26-V discharge voltage, and if these ions were to hit the keeper or cathode orifice, they could cause significant erosion.

The source and characteristics of the high-energy ions have been the subject of much research and debate. Models of a direct current (DC) potential hill [63] located inside or just downstream of the cathode orifice, or ion acoustic instabilities in a double layer postulated in the orifice of the cathode [64], have been proposed to explain the production of these ions. However, in probe studies to date [1,6,28,42], there has been no detectable potential hill or unstable double layer at the cathode orifice or in the cathode plume that might explain the mechanisms responsible for the high-energy ions or the electrode wear rates and erosion patterns. High-frequency plasma potential oscillations in the 50- to 1000-kHz range associated with plasma instabilities have been detected in the cathode plume and across the front of the keeper by scanning emissive probes [46] and have been proposed as a mechanism for accelerating ions to high energy. In this case, ions born at the peak potential gain the full radio frequency (rf) potential energy when striking the keeper or cathode surfaces, which can exceed 40 to 80 eV [46]. The fluctuations then produce sufficient ion energy to explain the keeper-face erosion reported in the literature.

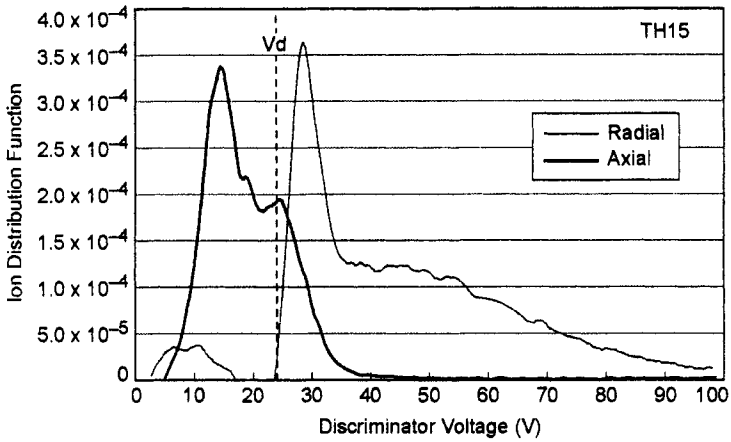

Fig. 6-51. Ion energy distribution measured on axis and radially away from an NSTAR hollow cathode (from [46]).

However, the fluctuations measured to date are not of sufficient amplitude to explain the significant number of ions detected by the radially positioned RPA with energies approaching or even exceeding 100 eV. Katz [65] has shown the importance of charge exchange collisions on radially accelerated ions, and how it leads to ions with higher energies than the measured plasma potentials.

Immediately downstream of the discharge cathode keeper the radial plasma potential profile has a substantial dip on axis. Ions generated on the edges of the potential dip are accelerated towards the centerline. The neutral gas density, which is dominated by un-ionized gas coming out of the hollow cathode, also peaks on axis. Near the cathode, the neutral gas density is high enough that a substantial fraction of ions is neutralized by resonant charge exchange with gas atoms before making it across the potential dip. Since they are now neutral, the xenon atoms do not lose the kinetic energy they gained as ions falling into the dip, passing through to the other side of the potential dip. However, as they continue to drift radially some of the atoms are ionized, either by charge exchange or collisions with electrons, and, again, are influenced by the electric fields. By the time these ions reach the RPA, they have their original thermal energy plus the energy they gained falling down the dip, plus the energy from the plasma potential where they were re-ionized. This process is shown schematically in Fig. 6-52. The measured high energies are attained because, as a neutral particle, the xenon atom is not retarded by the potential rise, but gains the potential energy moving through the trough.

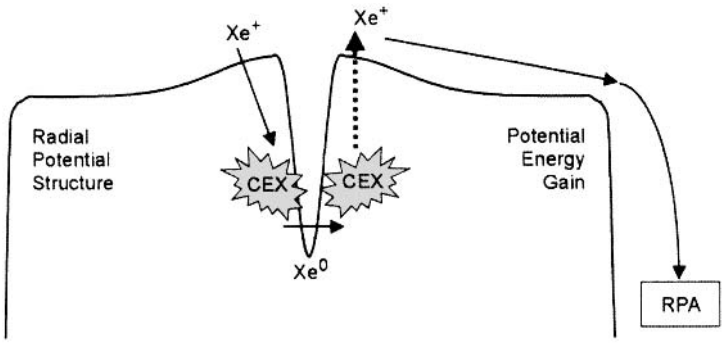

Fig. 6-52. Xenon ions gain energy falling down the potential well, are charge exchanged, travel past the potential rise without losing energy, and regain their charge in a high potential region [65].

For example, a calculated spectrum is shown in Fig. 6-53. The primary, non-charge-exchanged ion spectrum was estimated as a Maxwellian distribution with an energy of 3.5 eV, the measured electron temperature. The high-energy ion portion of the spectrum, while somewhat lower than the measurement, shows the same general features. The calculated spectrum has no ions above 95 V, while the measured spectrum shows a few ions above this energy. Katz [65] suggests that these very high-energy ions may have started out as double ions when they entered the axial potential well and picked up twice the kinetic energy prior to being neutralized by charge exchange. The complete mechanisms for high-energy ion generation, the measured energies of these ions by various techniques, and the enhanced erosion of the cathode and keeper electrodes are still under investigation at this time. Detailed 2-D modeling [66] and additional experimental investigations are under way to understand and mitigate this problem.

6.10 Hollow Cathode Operation

The electron discharge from hollow cathodes can be initiated by several mechanisms. In Type A cathodes and some Type B with small orifices, the electrostatic (vacuum) potential from the keeper or anode electrode does not penetrate significantly through the relatively long, thin orifice into the insert region. In this case, electrons emitted in the insert region cannot be accelerated to cause ionization because there is no anode potential visible inside the cathode. However, if the cathode uses a barium dispenser insert, then barium evaporated from the insert when heated can deposit on the upstream side of the cathode orifice plate and inside the orifice and diffuse onto the downstream surface of the orifice plate [67] facing the keeper electrode. The work function subsequently decreases, and the vacuum thermionic emission from the orifice

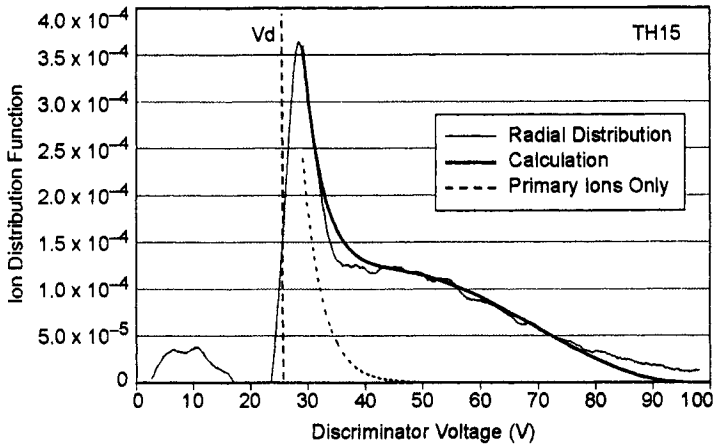

Fig. 6-53. The xenon ions gain most of their kinetic energy in the sheath and the potential well on axis (from [65]).

plate to the keeper can be sufficient to ignite a discharge once gas is introduced. The plasma then penetrates the orifice, extending the anode potential into the insert region and the discharge transitions directly to the insert. The orifice plate is subject to sputter erosion by the ions in the discharge, and the barium layer is removed and has to be reestablished if the cathode is turned off in order to restart [68].

For cathodes with larger orifices (typically 2-mm diameter or larger), a sufficient keeper voltage (typically 100 to 500 V) will cause the applied positive potential to penetrate inside the insert region with levels in excess of the ionization potential of the propellant gas. The electrons from the insert then can be accelerated locally inside the insert and cause ionization, which ignites the discharge through the orifice to the keeper or anode. This is the mechanism used in most of the LaB_6 cathodes developed by the authors to strike the discharge.

For hollow cathodes with smaller orifices or inhibited orifice-plate emission (due to surface impurities, barium depletion, etc.), an arc-initiation technique typically is used. In this case, the applied keeper voltage is pulsed to a high positive value (typically >500 V). The discharge starts due to either field emission of electrons from the orifice plate ionizing the injected cathode gas or Paschen breakdown occurring at the relatively high pressure in the cathode-to-keeper gap generating plasma that penetrates the orifice into the insert region. To ensure reliable thruster ignition over life, it is standard to apply both a DC keeper voltage in the 50- to 150-V range and a pulsed keeper voltage in the

300- to 600-V range. Once the discharge is ignited, the keeper current is limited by the power supply and the voltage falls to a low value below the discharge voltage.

Once ignited, hollow cathodes are well known to operate in distinct discharge "modes." In ion thrusters, the hollow cathode discharge operation has been historically characterized as having a quiescent "spot mode" with a broadly optimum gas flow at a given current, and a noisy "plume mode" with the gas flow below the level at which the spot mode is obtained [44,45]. The spot mode, seen in Fig. 6-28(a), is visually observed as manifesting a ball or "spot" of plasma just downstream of the cathode orifice with little visual glow from the downstream plasma at low currents and a slowly expanding plasma column extending from the spot into the thruster discharge chamber at higher currents. The plume mode is seen visually as a widely diverging plasma cone extending from the cathode, often filling the vacuum chamber with diffuse plasma and little or no spot or ball of plasma in the cathode/keeper orifice. There is a continuous transition between these modes, which is sometime separately identified as a transition mode [3]. A less well-known third mode, sometimes called a "stream mode," occurs at high gas flows well above the optimum for the spot mode. In this stream mode, shown just starting in Fig. 6-28(b), the plasma spot is pushed well down stream of the cathode/keeper orifice, and a dark space between the cathode or keeper electrode and the spot is usually observed. In this case, the plasma expands and disperses faster than in the normal spot mode. Very high cathode flow rates tend to suppress the discharge voltage, which adversely affects the ionization rate and discharge performance in discharge cathodes in ion thrusters. However, higher flow rates tend to reduce the coupling voltage in both Hall and ion thruster neutralizer cathodes, which can improve the performance.

The hollow cathode discharge modes have been examined in detail due to the observed increases in the keeper or coupling voltages in the plume mode [44,45,64,69,70] and increases in keeper wear [53,69]. At flow rates near the optimum for the spot mode, thermionic hollow cathodes can produce quiescent discharges [46,64]. In neutralizer cathodes, transition to plume mode occurs when too low a gas flow rate and/or keeper current is provided for the desired emission current. Plume mode transition is usually detected by increases in the oscillation of the keeper voltage or in the magnitude of the coupling voltage. For example, plume mode onset is defined in the NSTAR neutralizer when the keeper voltage oscillation exceeds 5 V [71]. In discharge cathodes, transition to plume mode also occurs for too low a propellant flow at a given emission current (or too high a discharge current for a given flow), and is usually detected by increases in the discharge voltage oscillations. Transition to plume mode usually occurs at higher emission current densities (related to the size of

the orifice and the discharge current) and can be affected by the anode location and design [46].

As the discharge current is increased for a given cathode orifice size and gas flow rate, the noise in the discharge voltage and in probe signals from the plasma increases [70], and the cathodes produce ions with energies significantly in excess of the discharge voltage and produce significant keeper and cathode orifice erosion. This leads to the keeper and cathode life issues discussed above associated with plume-mode behavior and often determines the cathode geometry and operation conditions selected for any given thruster.

Figure 6-54 shows the discharge voltage versus current for a 1.5-cm-diameter dispenser hollow cathode with a 2.1-mm orifice for several different flow rates [6]. In this case, two different anode geometries were used: one was a 45-deg conical anode and the second was a 5-cm-diameter cylindrical anode. The maximum current in the plot that could be achieved at a given gas flow was due to the onset of strong discharge voltage oscillations of greater than ±5 V. The small cylindrical anode permitted significantly higher discharge currents to be obtained before the oscillation limits and also reduced the discharge voltage at all currents. This is due to the increased gas pressure near the cathode exit increasing the plasma generation in the cathode plume, which could only be achieved with the conical anode by injecting significant amounts of gas directly into the anode region. It is clear that the onset of the oscillations and the transition to plume mode is an anode-plasma effect, which will be discussed further later.

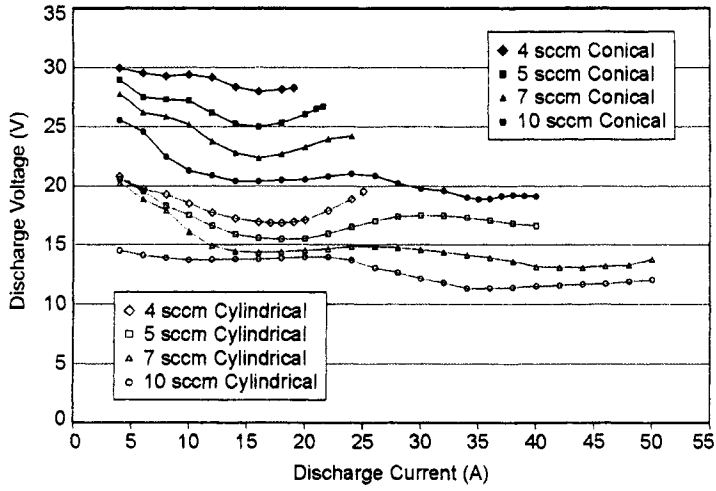

Fig. 6-54. Discharge voltage versus current for several hollow cathode flow rates for two anode configurations.

There are basically three types of oscillations that occur in hollow cathode discharges [46,70]. First, there are plasma discharge oscillations in the frequency range of 50 to over 1000 kHz. These are usually incoherent oscillations in the ion acoustic frequency range with amplitudes that vary continuously from fractions of a volt on the electrodes in the spot mode to tens of volts on the electrodes into the plume mode. If sufficiently large, these ion acoustic oscillations can trigger regulation problems in the power supply, leading to large discharge voltage oscillations on power-supply-regulation times of 100 to 1000 Hz. This behavior is shown in Fig. 6-55.

As the discharge current increases, the ionization percentage in the cathode plume becomes significant and can lead to ionization instabilities or so-called *predator–prey* oscillations. In this case, the plasma discharge burns out a significant fraction of the neutral gas, and the discharge collapses on the time frame of neutral flow into the plume region. The frequency range of these instabilities is in the 50- to 250-kHz range for xenon, depending on the physical scale lengths and size of the discharge components. Ionization instabilities are easily observed in the plasma density, which is shown by the probe's ion saturation current oscillations in Fig. 6-56 and compared to the normally observed oscillations from the incoherent ion acoustic-type modes. Ionization instabilities usually can be inhibited by proper selection of the gas flow and/or magnitude of any applied axial magnetic field in the cathode plume region [46], which modifies the local ion generation rate.

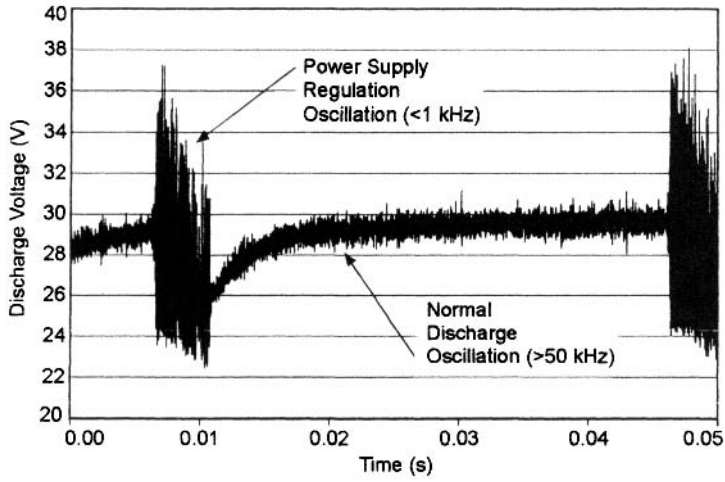

Fig. 6-55. Discharge voltage oscillations showing plasma and power supply oscillations.

It is important to realize that the large discharge oscillations and transition to plume mode is an effect that occurs exterior to the hollow cathode [70]. Figure 6-57 shows the ion saturation current measured inside the insert region and immediately outside the keeper in the above experiments during the ionization instability conditions. The plasma density oscillations inside the cathode insert plasma are small in amplitude and uncorrelated to the ionization and large turbulent instabilities observed outside in the keeper plasma region. The higher gas flows injected to avoid transition to plume mode are required to

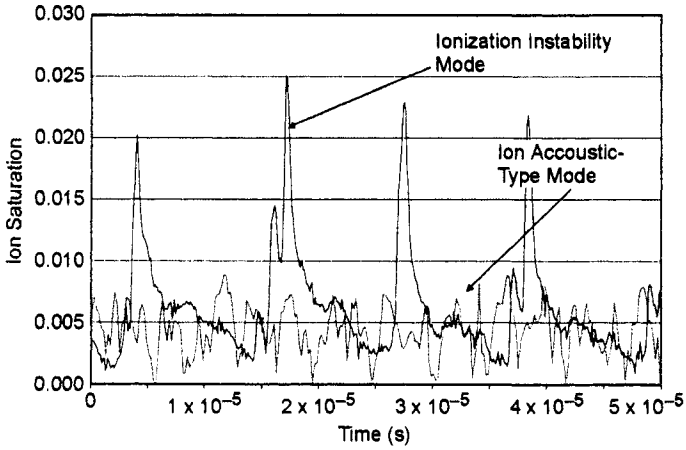

Fig. 6-56. Discharge voltage oscillations showing plasma plume mode oscillations with frequencies in >100-kHz range and ionization-related oscillations in the <100-kHz range.

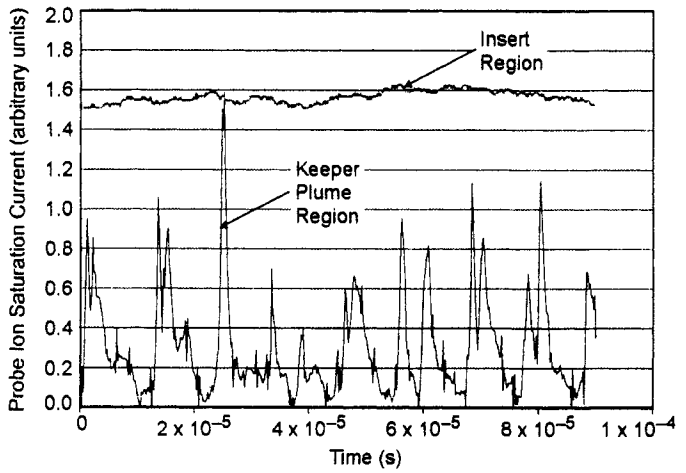

Fig. 6-57. Ion saturation current oscillations inside and outside the cathode, showing oscillation location.

produce sufficient plasma density to carry the discharge current, and the lower electron temperatures and collisional effects in the cathode plume plasma tend to damp or extinguish the oscillations. This oscillatory and damping behavior is suggested by the cathode plume models [39,41,72,73] in the literature and discussed above.

References

[1] D. M. Goebel, K. Jameson, I. Katz, and I. Mikellades, "Hollow Cathode Theory and Modeling: I. Plasma Characterization with Miniature Fast-Scanning Probes," *Journal of Applied Physics*, vol. 98, no. 10, 113302, 2005.

[2] I. Mikellades, I. Katz, D. M. Goebel, and K. K. Jameson, "Plasma Processes Inside Orificed Hollow Cathodes," *Physics of Plasmas*, vol. 13, 063504, 2006.

[3] H. R. Kaufman, "Technology of Electron-Bombardment Ion Thrusters," *Advances in Electronics and Electron Physics*, vol. 36, edited by L. Marton, New York: Academic Press, 1974.

[4] B. A. Arkhopov and K. N. Kozubsky, "The Development of the Cathode Compensators for Stationary Plasma Thrusters in the USSR," 22nd International Electric Propulsion Conference, paper IEPC-91-023, Viareggio, Italy, October 14–17, 1991.

[5] I. Mikellades, I. Katz, D. M. Goebel, and K. K. Jameson, "Hollow Cathode Theory and Modeling: II. A Two-Dimensional Model of the Emitter Region," *Journal of Applied Physics*, vol. 98, no. 10, 113303, 2005.

[6] D. M. Goebel, K. Jameson, R. Watkins, and I. Katz, "Cathode and Keeper Plasma Measurements Using an Ultra-Fast Miniature Scanning Probe," AIAA-2004-3430, 40th Joint Propulsion Conference, Ft. Lauderdale, Florida, July 11–14, 2004.

[7] O. W. Richardson, "Electron Theory of Matter," *Philips Magazine*, vol. 23, pp. 594–627, 1912.

[8] W. H. Kohl, *Handbook of Materials and Techniques for Vacuum Devices*, New York: Reinhold, 1967.

[9] W. Schottky, "Concerning the Discharge of Electrons from Hot Wires with Delayed Potential," *Annalen der Physik*, vol. 44, no. 15, pp, 1011–1032, July 1914.

[10] A. T. Forrester, *Large Ion Beams*, New York: Wiley-Interscience, 1988.

[11] J. W. Gibson, G. A. Haas, and R. E. Thomas, "Investigation of Scandate Cathodes: Emission, Fabrication and Activation Processes," *IEEE Transactions on Electron Devices*, vol. 36, pp. 209–214, 1989.

[12] J. L. Cronin, "Modern Dispenser Cathodes," IEE Proceedings, vol. 128, no. 19, 1981.

[13] J. M. Lafferty, "Boride Cathodes," *Journal of Applied Physics*, vol. 22, p. 299, 1951.

[14] D. Jacobson and E. K. Storms, "Work Function Measurement of Lanthanum-Boron Compounds," *IEEE Transactions on Plasma Science*, vol. 6, pp. 191–199, 1978.

[15] E. Storms and B. Mueller, "A Study of Surface Stoichiometry and Thermionic Emission using LaB6," *Journal of Applied Physics*, vol. 50, pp. 3691–3698, 1979.

[16] R. Levi, "Improved Impregnated Cathode," *Journal of Applied Physics*, vol. 26, p. 639, 1955.

[17] J. L. Cronin, "Practical Aspects of Modern Dispenser Cathodes," *Microwave Journal*, vol. 22, pp. 57–62, September 1979.

[18] D. M. Goebel, R. M. Watkins, and K. K. Jameson, "LaB6 Hollow Cathodes for Ion and Hall Thrusters," *Journal of Propulsion and Power*, vol. 23, no. 3, pp.552–558, 2007.

[19] J. Pelletier and C. Pomot, "Work Function of Sintered Lanthanum Hexaboride," *Applied Physics Letters*, vol. 34, pp. 249–251, 1979.

[20] V. Kim, G. Popov, B. Arkhipov, V. Murashko, O. Gorshkov, A. Koroteyev, V. Garkusha, A. Semenkin, and S. Tverdokhlebov, "Electric Propulsion Activity in Russia," IEPC-2001-005, 27th International Electric Propulsion Conference, Pasadena, California, October 14–19, 2001.

[21] D. M. Goebel, J. T. Crow, and A. T. Forrester, "Lanthanum Hexaboride Hollow Cathode for Dense Plasma Production," *Review of Scientific Instruments*, vol. 49, pp. 469–472, 1978.

[22] D. M. Goebel, Y. Hirooka, and T. Sketchley, "Large Area Lanthanum Hexaboride Electron Emitter," *Review of Scientific Instruments*, vol. 56, pp. 1717–1722, 1985.

[23] E. Storms and B. Mueller, "Phase Relationship, Vaporization and Thermodynamic Properties of the Lanthanum-Boron System," *Journal of Chemical Physics*, vol. 82, p. 51, 1978.

[24] K. N. Leung, P. A. Pincosy, and K. W. Ehlers, "Directly Heated Lanthanum Hexaboride Filaments," *Review of Scientific Instruments*, vol. 55, pp. 1064–1068, 1984.

[25] I. Katz, J. Anderson, J. Polk, and D. M. Goebel, "Model of Hollow Cathode Operation and Life Limiting Mechanisms," IEPC-2003-0243, 28th International Electric Propulsion Conference, Toulouse, France, March 17–21, 2003.

[26] I. Katz, J. Anderson, J. Polk, and J. Brophy, "One Dimensional Hollow Cathode Model," *Journal of Propulsion and Power*, vol. 19, no. 4, pp. 595–600, 2003.

[27] J. S. Miller, S. H. Pullins, D. J. Levandier, Y. Chiu, and R. A. Dressler, "Xenon Charge Exchange Cross Sections for Electrostatic Thruster Models," *Journal of Applied Physics*, vol. 91, no. 3, pp. 984–991, 2002.

[28] K. Jameson, D. M. Goebel, and R. Watkins, "Hollow Cathode and Thruster Discharge Chamber Plasma Measurements Using High-Speed Scanning Probes," IEPC-2005-269, 29th International Electric Propulsion Conference, Princeton University, Princeton, New Jersey, October 31–November 4, 2005.

[29] D. L. Book, *NRL Plasma Formulary*, Naval Research Laboratory, Washington, D.C., 1987.

[30] I. Katz, J. Polk, I. Mikellides, D. M. Goebel, and S. Hornbeck, "Combined Plasma and Thermal Hollow Cathode Insert Model," IEPC-2005-228, 29th International Electric Propulsion Conference, Princeton University, Princeton, New Jersey, October 31–November 4, 2005.

[31] K. Jameson, D. M. Goebel, and R. Watkins, "Hollow Cathode and Keeper Region Plasma Measurements," AIAA-2005-3667, 41st Joint Propulsion Conference, Tucson, Arizona, July 11–14, 2005.

[32] I. Mikelides, I. Katz, D. M. Goebel, and J. Polk, "Theoretical Model of a Hollow Cathode Plasma for the Assessment of Insert and Keeper Lifetimes," AIAA-2005-4234, 41st Joint Propulsion Conference, Tucson, Arizona, July 2005.

[33] J. E. Polk, A. Grubisic, N. Taheri, D. M. Goebel, R. Downey, and S. Hornbeck, "Emitter Temperature Distributions in the NSTAR Discharge Hollow Cathode," AIAA-2005-4398, 41st Joint Propulsion Conference, Tucson, Arizona, July 11–14, 2005.

[34] J. E. Polk, J. R. Anderson, J. R. Brophy, V. K. Rawlin, M. J. Patterson, J. S. Sovey, and J. J. Hamley, "An Overview of the Results from an 8200-Hour Wear Test of the NSTAR Ion Thruster," AIAA Paper 99-2446, 35th Joint Propulsion Conference, Los Angeles, California, June 20–24, 1999.

[35] I. Katz, J. Anderson, J. Polk, and J. Brophy, "A Model of Hollow Cathode Plasma Chemistry," AIAA-2002-4241, 38th Joint Propulsion Conference, Indianapolis, Indiana, July 7–10, 2002.

[36] J. G. Andrews and J. E. Allen, "Theory of a Double Sheath Between Two Plasmas," *Proceedings of the Royal Society of London*, Series A, vol. 320, p. 459–472, 1971.

[37] V. Rawlins, J. S. Sovey, J. R. Anderson, and J. E. Polk, "NSTAR Flight Thruster Qualification Testing," AIAA-98-3936, 34th Joint Propulsion Conference, Cleveland, Ohio, July 13–15, 1998.

[38] A. Sengupta, J. R. Brophy, and K. D. Goodfellow. "Status of The Extended Life Test of The Deep Space 1 Flight Spare Ion Engine After 30,352 Hours of Operation," AIAA Paper 2003-4558, 39th Joint Propulsion Conference, Huntsville, Alabama, July 20–23, 2003.

[39] I. Katz, I. G. Mikellides, and D. M. Goebel, "Model of the Plasma Potential Distribution in the Plume of a Hollow Cathode," AIAA Paper 2004-4108, 40th Joint Propulsion Conference, Ft. Lauderdale, Florida, July 11–14, 2004.

[40] I. Langmuir, "The Interaction of Electron and Positive Ion Space Charges in Cathode Sheaths," *Physical Review*, vol. 33, no. 6, pp. 954–989, 1929.

[41] I. G. Mikellides, I. Katz, D. M. Goebel, and K. K. Jameson, "Towards the Identification of the Keeper Erosion Mechanisms: 2-D Theoretical Model of the Hollow Cathode," AIAA-2006-5151, 42nd Joint Propulsion Conference, Sacramento, California, July 10–13, 2006.

[42] D. A. Herman and A. D. Gallimore, "Near Discharge Cathode Assembly Plasma Potential Measurements in a 30-cm NSTAR Type Ion Engine Amidst Beam Extraction," AIAA-2004-3958, 40th Joint Propulsion Conference, Ft. Lauderdale, Florida, July 11–14, 2004.

[43] K. K. Jameson, D. M. Goebel, I. G. Mikellides, and R. M. Watkins, "Local Neutral Density and Plasma Parameter Measurements in a Hollow Cathode Plume," AIAA-2006-4490, 42nd Joint Propulsion Conference, Sacramento, California, July 10–13, 2006.

[44] G. A. Csiky, "Investigation of a Hollow Cathode Discharge Plasma," AIAA-69-258, 7th Electric Propulsion Conference, Williamsburg, Virginia, March 3–5, 1969.

[45] V. K. Rawlin and E. V. Pawlik, "A Mercury Plasma-Bridge Neutralizer," AIAA-67-670, AIAA Electric Propulsion and Plasmadynamics Conference, Colorado Springs, Colorado, September 11–13, 1967.

[46] D. M. Goebel, K. Jameson, I. Katz, I. Mikellides, and J. Polk, "Energetic Ion Production and Keeper Erosion in Hollow Cathode Discharges," IEPC-2005-266, 29th International Electric Propulsion Conference, Princeton University, Princeton, New Jersey, October 31–November 4, 2005.

[47] D. M. Goebel, I. Katz, Y. Mikellides, and J. Polk, "Extending Hollow Cathode Life for Deep Space Missions," AIAA-2004-5911, AIAA Space 2004 Conference, San Diego, California, September 2004.

[48] R. Doerner, G. Tynan, D. M. Goebel, and I. Katz, "Plasma Surface Interaction Studies for Next-Generation Ion Thrusters," AIAA-2004-4104, 40th Joint Propulsion Conference, Ft. Lauderdale, Florida, July 2004.

[49] R. P. Doerner, S. I. Krasheninnikov, and K. Schmidt, "Particle-Induced Erosion of Materials at Elevated Temperature," *Journal of Applied Physics*, vol. 95, no. 8, pp. 4471–4475, 2004.

[50] J. E. Polk, C. Marrese, B. Thornber, L. Dang, and L. Johnson, "Temperature Distributions in Hollow Cathode Emitters," AIAA-2004-4116, 40th Joint Propulsion Conference, Ft. Lauderdale, Florida, July 11–14, 2004.

[51] P. Palluel and A. M. Shroff, "Experimental Study of Impregnated-Cathode Behavior, Emission, and Life," *Journal of Applied Physics*, vol. 51, no. 5, pp. 2894–2902, 1980.

[52] T. R. Sarver-Verhey, "28,000 Hour Xenon Hollow Cathode Life Test Results," IEPC-97-168, 25th International Electric Propulsion Conference, Cleveland, Ohio, August 24–28, 1997.

[53] A. Sengupta, J. R. Brophy, J. R. Anderson, and C. Garner. "An Overview of the Results from the 30,000 Hour Life Test of The Deep Space 1 Flight Spare Ion Engine," AIAA Paper 2004-3608, 40th Joint Propulsion Conference, Ft. Lauderdale, Florida, July 11–14, 2004.

[54] J. E. Polk, D. M. Goebel, J. S. Snyder, and A. C. Schneider, "Performance and Wear Test Results for a 20-kW Class Ion Engine with Carbon-Carbon Grids," AIAA_2005-4393, 41st Joint Propulsion Conference, Tucson, Arizona, July 11–14, 2005.

[55] H. E. Gallagher, "Poisoning of LaB6 cathodes," *Journal of Applied Physics*, vol. 40, pp. 44–51, 1969.

[56] J. E. Polk, "The Effect of Reactive Gases on Hollow Cathode Operation," AIAA-2006-5153, 42nd Joint Propulsion Conference, Sacramento, California, July 9–12, 2006.

[57] R. D. Kolasinski and J. E. Polk, "Characterization of Cathode Keeper Wear By Surface Layer Activation," AIAA Paper 2003-5144, 39th Joint Propulsion Conference, Huntsville, Alabama, July 20–23, 2003.

[58] M. Domonkos, J. Foster, and G. Soulas, "Wear Testing and Analysis of Ion Engine Discharge Cathode Keeper," *Journal of Propulsion and Power*, vol. 21, pp. 102–110, 2005.

[59] M. J. Patterson, V. K. Rawlin, J. S. Sovey, M. J. Kussmaul, and J. Parkes, "2.3 kW Ion Thruster Wear Test," AIAA-95-2516, 31st Joint Propulsion Conference, San Diego, California, July 10–12, 1995.

[60] I. Kameyama and P. J. Wilbur, "Measurement of Ions from High Current Hollow Cathodes Using Electrostatic Energy Analyzer," *Journal of Propulsion and Power*, vol. 16, p. 529, 2000.

[61] C. Farnell and J. Williams, "Characteristics of Energetic Ions from Hollow Cathodes," IEPC Paper 03-072, 28th International Electric Propulsion Conference, Toulouse, France, March 17–21, 2003.

[62] G. Williams, Jr., T. B. Smith, M. T. Domonkos, A. D. Gallimore, and R. P. Drake, "Laser Induced Fluorescence Characterization of Ions Emitted from Hollow Cathodes," *IEEE Transactions on Plasma Science*, vol. 28, issue 5, pp. 1664–1675, 2000.

[63] I. Kameyama and P. J. Wilbur, "Potential-Hill Model of High-Energy Ion Production near High Current Hollow Cathodes," ISTS 98-a-2-17, 21st International Symposium on Space Technology and Science, Sonic City, Omiya, Japan, May 1998.

[64] V. J. Friedly and P. J. Wilbur, "High Current Hollow Cathode Phenomena," *Journal of Propulsion and Power*, vol. 8, no. 3, pp. 635–643, 1992.

[65] I. Katz, I. G. Mikellides, D. M. Goebel, K. K. Jameson, and J. E. Polk, "Production of High Energy Ions Near an Ion Thruster Discharge Hollow Cathode," AIAA-2006-4485, 42nd Joint Propulsion Conference, Sacramento, California, July 10–13, 2006.

[66] I. G. Mikellides, I. Katz, and D. Goebel, "Partially-Ionized Gas and Associated Wear in Electron Sources for Ion Propulsion, II: Discharge Hollow Cathode," AIAA-2007-5192, 43rd Joint Propulsion Conference, Cincinnati, Ohio, July 8–11, 2007.

[67] W. G. Tighe, K. Chien, D. M. Goebel, and R. T. Longo, "Hollow Cathode Ignition and Life Model," AIAA-2005-3666, 41st Joint Propulsion Conference, Tucson, Arizona, July 11–14, 2005.

[68] W. Tighe, K. Chien, D. M. Goebel, and R. Longo, "Hollow Cathode Ignition Studies and Model Development," IEPC-2005-314, 29th International Electric Propulsion Conference, Princeton University, Princeton, New Jersey, October 31–November 4, 2005.

[69] J. R. Brophy and C. E. Garner, "Tests of High Current Hollow Cathodes for Ion Engines," AIAA-88-2913, 24th Joint Propulsion Conference, Boston, Massachusetts, July 11–13, 1988.

[70] D. M. Goebel, K. Jameson, I. Katz, and I. Mikellides, "Plasma Potential Behavior and Plume Mode Transitions in Hollow Cathode Discharge," IEPC-2007-027, 30th International Electric Propulsion Conference, Florence, Italy, September 17–20, 2007.

[71] J. R. Brophy, D. E. Brinza, J. E. Polk, M. D. Henry, and A. Sengupta, "The DSI Hyper-Extended Mission," AIAA-2002-3673, 38th Joint Propulsion Conference, Indianapolis, Indiana, July 7–10, 2002.

[72] I. D. Boyd and M. W. Crofton, "Modeling the Plasma Plume of a Hollow Cathode," *Journal of Applied Physics*, vol. 95, pp. 3285–3296, 2004.

[73] I. Mikellides, I. Katz, and D. M. Goebel, "Numerical Simulation of the Hollow Cathode Discharge Plasma Dynamics," IEPC-2005-200, 29th International Electric Propulsion Conference, Princeton University, Princeton, New Jersey, October 31–November 4, 2005.

Problems

1. The power radiated from a surface is given by $P = \sigma\varepsilon T^4 A$, where σ is the Stephan–Boltzmann constant, ε is the emissivity of the surface, T is the surface temperature in K, and A is the radiating area.
   a. Design a 0.5-mm-diameter tungsten filament electron emitter that emits 10 A and radiates only 200 W of power. Specifically, what is the filament length and emission current density? You can neglect axial conduction of power to the electrical connections and assume that the emissivity of tungsten is 0.3 at emission temperatures.
   b. You decide to use a 0.25-mm-diameter and 4-cm-long filament to limit the radiated power. What is the temperature of the emitter, and how much power is actually radiated?
2. The insert in a BaO hollow cathode has a 3-mm inside diameter, is 2.5-cm long, and is at a temperature of 1100°C.
   a. Using Cronin's expression for the work function, how much current is emitted by the insert?
   b. If the insert has a uniform plasma with $n_e = 10^{20}\ \mathrm{m}^{-3}$ density and $T_e = 2$ eV inside of it, how much is the electron emission enhanced by the Schottky effect if the sheath is 10 V and 3 Debye lengths thick? What is the total emission current?
   c. Is the emission current space charge limited?

d. Assume that the plasma density falls exponentially from the orifice entrance to $10^{18}\ m^{-3}$ in 1 cm. What is the total electron current that can be emitted into the plasma?

3. A 2.5-cm-long BaO-impregnated insert with a 2-cm inside diameter has xenon gas injected to create an internal pressure of 2 torr at 1500 K in the hollow cathode. Assuming the insert plasma is infinitely long, what is the electron temperature in the insert plasma and the radial ion drift velocity at the wall?

4. For the cathode geometry in Chapter 6, Problem 2, what is the internal plasma density for an emission current of 30 A and a heating power of 100 W, assuming a uniform plasma density with an electron temperature of 1.2 eV? (Hint: estimate the resistivity for the sheath voltage, find the plasma density, then iterate.)

5. A lanthanum hexaboride hollow cathode with a 2-cm inside diameter and 2.5-cm long emits 20 A of electrons into a uniform $2\times10^{19}\ m^{-3}$ plasma with an electron temperature of 1.5 eV. For a heating power of 40 W and an internal xenon pressure of 1.2 torr at 1500 K, find the ion and electron heating powers to the insert. Why is one larger than the other?

6. If a cylindrical discharge cathode orifice is 2 mm in diameter and has an internal pressure of 3 torr at a temperature of 2000 K, what is the electron temperature? (Neglect end losses.)

7. A neutralizer cathode produces 3 A of electron current through a 0.6-mm-diameter orifice that is 1.5-mm long. Assuming that the electron temperature in the orifice is 1.5 eV, the electron temperature in the insert region is 1.2 eV, the pressure is 50 torr at 2000 K, and the sheath voltage at the wall is 12 V, what is the plasma density, the ion heating of the orifice plate, and the axial voltage drop in the orifice plasma?

8. A hollow cathode has an orifice diameter of 2.5 mm and a xenon gas flow of 4 sccm with an effective temperature of 2000 K. Assume that the neutral gas density falls exponentially from the orifice exit with a characteristic length of 0.5 mm (i.e., one *e*-folding for every 0.5 mm of distance from the cathode). Assuming 15-V primary electrons in the cathode plume and that all of the ions generated fall back through the sheath, find the location downstream of the orifice exit where a double layer might occur.

9. A Hall thruster hollow cathode has a cathode orifice diameter of 3 mm and produces 20 A of 15 eV primary electrons with a xenon gas flow of 10 sccm. Assume that the gas is at 2000 K and the neutral plume diverges at 45 deg from the orifice.
   a. Neglecting depletion of the electron current due to ionization, how much of the cathode gas flow is ionized within 10 cm of the cathode?
   b. Assume that every electron that makes an ionization collision is lost (loses most of its energy and is rapidly thermalized) and that the neutral atom is also lost. How much of the cathode gas flow is then ionized within 10 cm of the cathode?
   c. If the primary electron energy is 20 V, how much of the cathode gas flow is ionized within 10 cm of the orifice accounting for both primary electron and neutral gas depletion due to ionization?
10. An ion thruster is operated at 2 A of beam current at 1500 V. The thruster has 5% double ion content, a 10-deg beam divergent half angle, a discharge loss of 160 eV/ion at a discharge voltage of 25 V, and uses 32 sccm of xenon gas and 20 W of power in addition to the discharge power.
   a. What insert thickness is required in an NSTAR-type cathode to achieve 5 years of cathode life if barium loss is the life-limiting effect?
   b. What is the thruster efficiency, Isp, and thrust?

Fundamentals of Electric Propulsion: Ion and Hall Thrusters
by Dan M. Goebel and Ira Katz
Copyright © 2008 John Wiley & Sons, Inc.

Chapter 7
Hall Thrusters

7.1 Introduction

Hall thrusters are relatively simple devices consisting of a cylindrical channel with an interior anode, a magnetic circuit that generates a primarily radial magnetic field across the channel, and a cathode external to the channel. However, Hall thrusters rely on much more complicated physics than ion thrusters to produce thrust. The details of the channel structure and magnetic field shape determine the performance, efficiency, and life [1–5]. The efficiency and specific impulse of flight-model Hall thrusters are typically lower than that achievable in ion thrusters [6,7], but the thrust-to-power ratio is higher and the device requires fewer power supplies to operate. The life of Hall thrusters in terms of hours of operation is usually shorter than ion thrusters (on the order of 10,000 hours), but the throughput is usually higher than in ion thrusters, and the total impulse capability can be comparable. Hall thrusters were originally envisioned in the U.S. and Russia about 50 years ago, with the first working devices reported in America in the early 1960s. Ultimately, Hall thruster technology was developed to flight status in Russia and has only recently been developed and flown outside of that country. Information about flight Hall thrusters is given in Chapter 9.

There are two generic types of Hall thrusters described in the literature. Hall thrusters, Hall-effect thrusters (HETs), stationary plasma thrusters (SPTs), and magnetic-layer thrusters are all names for essentially the same device that is characterized by the use of a dielectric insulating wall in the plasma channel, as illustrated in Fig. 7-1. The wall is typically manufactured from dielectric materials such as boron nitride (BN) or borosil ($BN\text{-}SiO_2$) in flight thrusters, and also sometimes alumina (AL_2O_3) in laboratory thrusters. These dielectric materials have a low sputtering yield and relatively low secondary

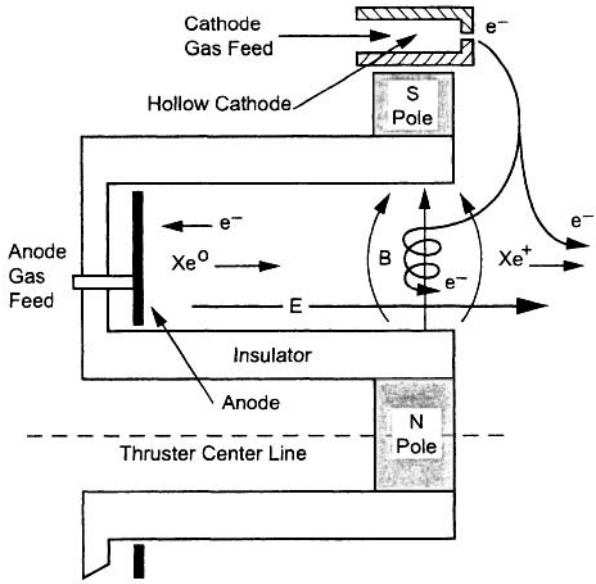

Fig. 7-1. Hall thruster cross-section schematic showing the crossed electric and magnetic fields, and the ion and electron paths.

electron emission coefficients under xenon ion bombardment. In this thruster geometry, the electrically biased metallic anode is positioned at the base of the channel where the majority of the propellant gas is injected into the thruster. The remainder of the propellant gas used by the thruster is injected through the exterior hollow cathode. In the second version of this type of thruster, called a thruster with anode layer (TAL), the dielectric channel wall is replaced by a metallic conducting wall, as illustrated in Fig. 7-2. This geometry considerably shortens the electric field region in the channel where the ion acceleration occurs—hence the name "thruster with anode layer" from the Russian literature [1], associated with the narrow electric field region near the anode. However, this configuration does not change the basic ion generation or acceleration method. The channel wall, which is usually also part of the magnetic circuit, is biased negatively (usually cathode potential) to repel electrons in the ionization region and reduce electron-power losses. The defining differences between these two types of Hall thrusters have been described in the literature [3].

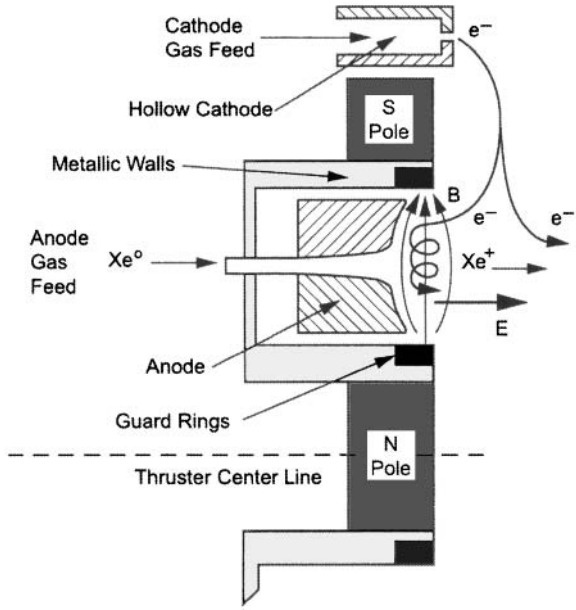

Fig. 7-2. TAL thruster cross-section schematic showing the crossed electric and magnetic fields, and the ion and electron paths.

In the Hall thruster with dielectric walls illustrated in Fig. 7-1, an axial electric field is established between the anode at the base of an annular channel and the hollow-cathode plasma produced outside of the thruster channel. A transverse (radial) magnetic field prevents electrons from this cathode plasma from streaming directly to the anode. Instead, the electrons spiral along the magnetic field lines (as illustrated) and in the $\mathbf{E} \times \mathbf{B}$ azimuthal direction (into the page) around the channel, and they diffuse by collisional processes and electrostatic fluctuations to the anode and channel walls. The plasma discharge generated by the electrons in the crossed electric and magnetic fields efficiently ionizes the propellant injected into the channel from the anode region. Ions from this plasma bombard and, near the channel exit, sputter erode the dielectric walls, which ultimately determines the life of the thruster. Electrons from this plasma also bombard the dielectric wall, depositing a significant amount of power in this region. The reduced axial electron mobility produced by the transverse magnetic field permits the applied discharge voltage to be distributed along the channel axis in the quasi-neutral plasma, resulting in an axial electric field in the channel that accelerates the ions to form the thrust beam. Therefore, Hall thrusters are described as electrostatic devices [1] because the ions are accelerated by the applied electric field, even though a magnetic field is critical to the process. However, since the acceleration occurs in the plasma region near

the channel exit, space charge is not an issue and the ion current density and the thrust density can be considerably higher than that achievable in gridded ion thrusters. The external hollow cathode plasma is not only the source of the electrons for the discharge, but it also provides the electrons to neutralize the ion beam. The single hollow cathode in Hall thrusters serves the same function as the two cathodes in direct current (DC)-electron discharge ion thrusters that produce the plasma and neutralize the beam.

The TAL thruster with metallic walls, illustrated in Fig. 7-2, has the same functional features of the dielectric-wall Hall thruster—namely, an axial electric field is established between the anode in the annular channel and the plasma potential outside of the thruster channel. This field accelerates ions from the ionization region near the anode out of the channel. The transverse (radial) magnetic field again prevents electrons from streaming directly to the anode, and the electron motion is the same as in the dielectric-wall Hall thruster. However, the channel walls at the exit plane have metallic guard rings biased at cathode potential to reduce the electron loss along the field lines. These rings represent the major erosion source in the thruster because of ion bombardment from the plasma, and guard ring material and design often determine the thruster life. The anode typically extends close to the thruster exit and is often funnel-shaped and curved to constrain the neutral gas and plasma to the center of the channel (away from the guard rings) and to not intercept the magnetic field lines, which would cause large electron losses. However, the anode is in close proximity to the high electron-temperature region of the plasma, and electrons collected by the anode can deposit a significant amount of power. The channel width in TAL thrusters is typically twice the channel depth (including the anode shaping). The external hollow cathode plasma provides the electrons for the discharge and for neutralization of the ion beam, the same as for dielectric-wall Hall thrusters.

The azimuthal drift of the electrons around the channel in the crossed electric and magnetic fields in the cylindrical thruster geometry is reminiscent of the *Hall current* in magnetron type devices, which has caused many authors to call this generically a "closed-drift" thruster [1–3]. However, King [8] correctly points out that the orientation of the fields in magnetrons (axial magnetic and radial electric) provides a restoring force to the centrifugal force felt by the electrons as they rotate about the axis, which produces the closed-drift electron motion in magnetrons. There is no corresponding restoring force associated with the different orientation of the crossed fields (radial magnetic and axial electric required to produce axial thrust) in Hall thrusters. The closed-drift behavior of the electron motion in Hall thrusters occurs only because of wall sheath electric fields and the force associated with the magnetic gradient in the radial direction in the channel. In this case, the electrons in the channel

encounter an increasing magnetic field strength as they move toward the wall, which acts as a magnetic mirror to counteract the radial centrifugal force.

The radial magnetic field gradient in the channel also forms an "ion lens," which tends to deflect the ions away from the channel walls and focus the ions out of the channel into the beam. Figure 7-3 shows an example of the magnetic field lines in the NASA-173Mv Hall thruster [9] developed at the National Aeronautics and Space Administration Glenn Research Center (NASA-GRC). The curvature of the field lines in the channel approaching the exit is found to significantly improve the efficiency, especially for higher voltage, high specific impulse (Isp), Hall thrusters [9,10]. The strength of the radial magnetic field in the center along the channel [11] is shown in Fig. 7-4. The radial field peaks near the channel exit and is designed to be essentially zero at or near the anode surface.

7.2 Thruster Operating Principles and Scaling

The operating principles of both types of Hall thrusters and some scaling rules for the geometries can be obtained from a simplified picture of the thruster discharge. Consider a generic Hall thruster channel, shown schematically in cross section in Fig. 7-5. The propellant gas is injected from the left through the anode region and is incident on the plasma generated in the channel. An axial scale length, L, is defined, over which the crossed-field discharge is magnetized, and produces a significant plasma density of width w, which is essentially the channel width. Ions exiting this plasma over the cylindrically

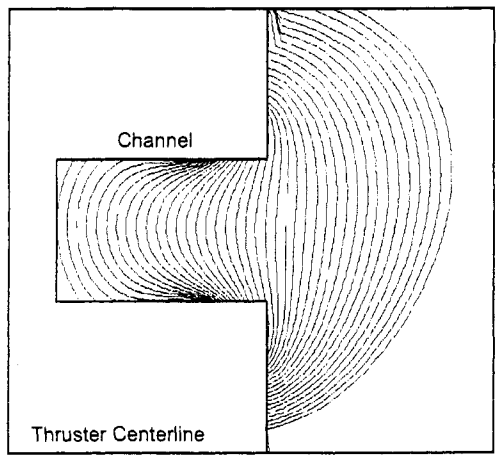

Fig. 7-3. Magnetic field lines in the channel region of the NASA-173Mv Hall thruster (from [9]).

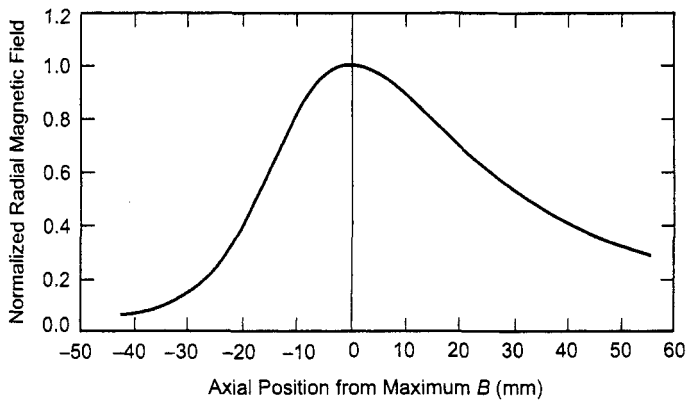

Fig. 7-4. Axial variation centerline radial magnetic field normalized to the peak radial field in the NASA-173Mv Hall thruster (from [11]).

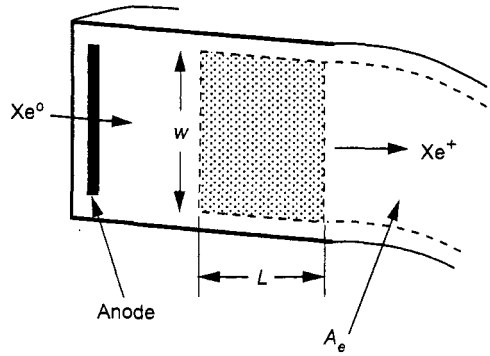

Fig. 7-5. Schematic cross section of the plasma in the Hall thruster channel.

symmetric area A_e form the beam. The applied magnetic field is primarily vertical in the plasma region in this depiction.

7.2.1 Crossed-Field Structure and the Hall Current

The electrons entering the Hall thruster channel from the exterior cathode spiral around the radial magnetic field lines with a Larmor radius derived in Chapter 3 and defined by Eq. (3.3-13). The electron Larmor radius must be less than the characteristic scale length L so that the electrons are magnetized and their mobility to the anode is reduced. If the electron velocity is characterized by their thermal velocity, then the electron Larmor radius is

$$r_e = \frac{v_{th}}{\omega_c} = \frac{m}{eB}\sqrt{\frac{8kT_e}{\pi m}} = \frac{1}{B}\sqrt{\frac{8}{\pi}\frac{m}{e}T_{\mathrm{eV}}} << L, \tag{7.2-1}$$

where T_{eV} is the electron temperature in eV and L is the magnetized plasma depth in the channel. For example, the electron Larmor radius at a temperature of 25 eV and a typical radial magnetic field strength of 150 G is 0.13 cm, which is much smaller than typical channel width and plasma length in Hall thrusters. The electrons must also be considered *magnetized*, meaning that they make many orbits around a field line before a collision with a neutral or ion occurs that results in cross-field diffusion. This is normally described by stating that the square of electron Hall parameter must be large compared to unity:

$$\Omega_e^2 = \frac{\omega_c^2}{\nu^2} >> 1, \tag{7.2-2}$$

where ν is the total collision frequency. The effect of this criterion is clear in the expression for the transverse electron mobility in Eq. (3.6-66), where a large value for the Hall parameter significantly reduces the cross-field electron mobility.

In a similar manner, the ion Larmor radius must be much greater than the characteristic channel length so that the ions can be accelerated out of the channel by the applied electric field:

$$r_i = \frac{v_i}{\omega_c} = \frac{M}{eB}\sqrt{\frac{2eV_b}{M}} = \frac{1}{B}\sqrt{\frac{2M}{e}V_b} >> L, \tag{7.2-3}$$

where the ion energy is approximated as the beam energy. The ion Larmor radius, for example, in the 150-G radial field and at 300 eV of energy is about 180 cm, which is much larger than the channel or plasma dimensions. These equations provide a general range for the transverse magnetic field in the thruster channel. Even if the radial magnetic field strength doubles or ion energy is half of the example given, the criteria in Eqs. (7.2-1) and (7.2-3) are still easily satisfied.

As mentioned above, the magnetic and electric field profiles are important in the thruster performance and life. The radial magnetic field typically is a maximum near the thruster exit plane, as shown in Fig. 7-4, and it is designed to fall near zero at the anode in dielectric-wall Hall thrusters [12]. Electrons from the cathode experience joule heating in the region of maximum transverse magnetic field, providing a higher localized electron temperature and ionization rate. The reduced electron mobility and high electron temperature in the strong

magnetic field region causes the axial electric field also to be maximized near the exit plane, as illustrated in Fig. 7-6. Since the neutral gas is injected from the anode region and the mass utilization is very high (nearly every neutral is ionized before reaching the channel exit), it is common to describe an "ionization region" that is located upstream of the electric field peak. Of course, the ions are accelerated directly by the electric field that peaks near the exit plane, which is sometimes called the "acceleration region." The characteristic scaling length L then spans these regions and is a significant fraction of the total channel depth. The ionization and acceleration regions overlap, which leads to dispersion in the ion velocity and some angular divergence in the resultant beam. This is in contrast to ion thrusters, which have a distinct ionization region in the plasma chamber and a finite acceleration region in the grids that produces nearly monoenergetic beams with low angular divergence determined by the optics and curvature of the grids.

In the crossed electric and magnetic field region of the channel, the electrons move in the azimuthal direction due to the $\mathbf{E} \times \mathbf{B}$ force with a velocity given by Eq. (3.3-16). The magnitude of the azimuthal electron velocity was found in Chapter 3 to be

$$v_E = \frac{\mathbf{E} \times \mathbf{B}}{B^2} \approx \frac{E_r}{B_z} \quad [\mathrm{m/s}]. \tag{7.2-4}$$

The current in the azimuthal direction, called the Hall current, is then the integral of the electron plasma density and this velocity over the characteristic thickness L [3,4]:

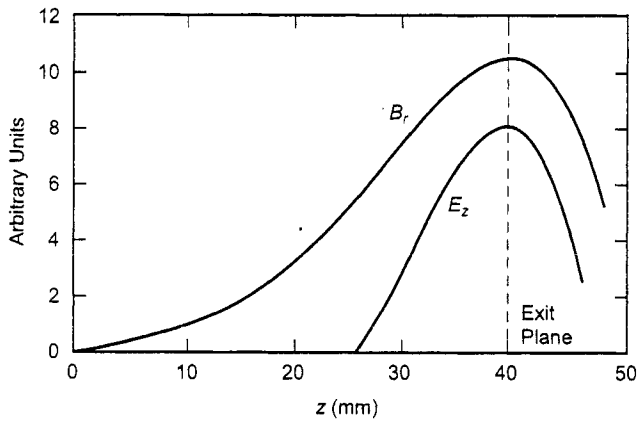

Fig. 7-6. Typical Hall thruster radial magnetic field and axial electric field along the channel length.

$$I_H = n_e e\left(\int_0^L v_E\, dz\right)w = n_e e\left(\int_0^L \frac{E}{B} dz\right)w, \tag{7.2-5}$$

where w is the plasma width (shown in Fig. 7-5) that essentially fills the channel. The axial electric field in the plasma channel is, approximately, the discharge voltage divided by the plasma thickness, so the Hall current is

$$I_H \approx n_e e w \frac{V_d}{B}. \tag{7.2-6}$$

Equation (7.2-6) shows that the Hall current increases with the applied discharge voltage and with the channel width provided that the magnetic field is unchanged. Hofer [10] showed that in Hall thrusters optimized for high efficiency, the optimal magnetic field was proportional to the discharge voltage. This implies that the Hall current is approximately constant for a given plasma density or beam current in high-efficiency Hall thrusters.

The ion current leaving the plasma to form the beam through the area A_e is approximately

$$I_i = n_i e v_i A_e \approx n_i e \sqrt{\frac{2eV_d}{M}} 2\pi R w, \tag{7.2-7}$$

where R is the average radius of the plasma channel. Since the plasma is quasi-neutral ($n_i \approx n_e$), even in the magnetized region, the Hall current can be expressed using Eq. (7.2-7) as

$$I_H \approx \frac{I_i}{2\pi RB}\sqrt{\frac{MV_d}{2e}}. \tag{7.2-8}$$

Increasing the beam current in a fixed thruster design will increase the circulating Hall current for a given magnetic field and discharge voltage. From Chapter 2, the total thrust produced by a Hall thruster is

$$T = \int (\mathbf{J}_H \times \mathbf{B})\, dA = I_H B \approx I_i \sqrt{\frac{MV_d}{2e}}. \tag{7.2-9}$$

This expression for the thrust has the same form as Eq. (2.3-8) derived in Chapter 2, where the force is coupled magnetically to the Hall thruster body instead of electrostatically to the ion thruster grids.

7.2.2 Ionization Length and Scaling

It is clear from the description of the Hall thruster operation above that the electrons must be magnetized to reduce their axial mobility to the anode, but the ions cannot be significantly magnetized so that the axial electric field can efficiently accelerate them to form the thrust beam. In addition, a large majority of the ions must be generated in the channel to permit acceleration by the field in that region and to produce high mass utilization efficiency [13]. This provides some simple scaling rules to be established.

The neutral gas injected from the anode region will be ionized by entering the plasma discharge in the crossed-field "ionization" region. Consider a neutral gas atom at a velocity v_n incident on plasma of a density n_e, electron temperature T_e, and thickness L. The density of the neutral gas will decrease with time due to ionization:

$$\frac{dn_n}{dt} = -n_n n_e \langle \sigma_i v_e \rangle, \tag{7.2-10}$$

where $\langle \sigma_i v_e \rangle$ is the ionization reaction rate coefficient for Maxwellian electrons, described in Appendix E. The flux of neutrals incident on the plasma is

$$\Gamma_n = n_n v_n, \tag{7.2-11}$$

and the neutral velocity is $v_n = dz/dt$, where z is the axial length. Equation (7.2-10) then becomes

$$\frac{d\Gamma_n}{\Gamma_n} = -\frac{n_e \langle \sigma_i v_e \rangle}{v_n} dz. \tag{7.2-12}$$

This equation has a solution of

$$\Gamma_n(z) = \Gamma(0) e^{-z/\lambda_i}, \tag{7.2-13}$$

where $\Gamma(0)$ is the incident flux on the ionization region and the ionization mean free path λ_i is given by

$$\lambda_i = \frac{v_n}{n_e \langle \sigma_i v_e \rangle}. \tag{7.2-14}$$

This expression for the ionization mean free path is different from the usual one, given in Eq. (3.6-6), that applies for the case of fast particles incident on essentially stationary particles. This is because the neutral gas atoms are moving slowly as they traverse the plasma thickness, and the fast electrons can move laterally to produce an ionization collision before the neutral leaves the region. Therefore, the ionization mean-free path depends on the neutral velocity, which determines the time the atom spends in the plasma thickness prior to a collision. The mean-free path also varies inversely with the electron density because a higher number of electrons in the slab will increase the probability of one of them encountering the neutral atom.

The percentage of the neutrals exiting the plasma of length L that are ionized is

$$\frac{\Gamma_{\text{exit}}}{\Gamma_{\text{incident}}} = 1 - e^{-L/\lambda_i} . \tag{7.2-15}$$

For example, in order to have 95% of the incident neutral flux on the plasma ionized before it leaves the plasma, Eq. (7.2-15) gives

$$L = -\lambda_i \ln(1-.95) = 2.996\lambda_i = \frac{3v_n}{n_e\langle\sigma_i v_e\rangle}, \tag{7.2-16}$$

or the plasma thickness must be at least three times the ionization mean-free path. Since some of the ions generated in the plasma hit the channel side walls and re-enter the plasma as neutrals instead of exiting as beam ions, the plasma thickness should significantly exceed the ionization mean-free path to obtain high mass utilization efficiency. This leads to one of the Hall thruster scaling rules:

$$\frac{\lambda_i}{L} = \text{constant} << 1. \tag{7.2-17}$$

In this example, this ratio should be less than 0.33.

The actual channel's physical depth in dielectric-wall Hall thrusters is given by the sum of the magnetized plasma thickness (L) and the geometric length required to demagnetize the plasma at the anode. This is illustrated schematically in Fig. 7-6, where the channel depth is nearly twice the magnetized plasma length. The axial magnetic field gradient has been found to be critical for the thruster performance [12]. A decreasing radial magnetic field strength going toward the anode, as shown in Fig. 7-6, results in higher thruster efficiency [4,12]. At the anode, the plasma is largely unmagnetized, and an anode sheath forms to maintain particle balance, similar to the DC plasma

generator case discussed in Chapter 4. The anode sheath polarity and magnitude depend on the local magnetic field strength and direction, which affects the axial electron mobility, and on the presence of any insulating layers on the anode that affects the particle balance [14–16]. Maintaining the local plasma near the anode close to the anode potential is important in applying the maximum amount of the discharge voltage across the plasma for the acceleration of ions. In addition, the magnetic field profile near the thruster exit strongly affects both the ability to achieve closed electron drifts in the azimuthal direction [8] and the focusing of the ions in the axial direction as they are accelerated by the electric field [9]. Optimal magnetic field design in the exit region reduces the ion bombardment of the walls and improves the ion trajectories leaving the thruster [17].

Additional information on the thruster operation can be obtained by examining the ionization criteria. Properly designed Hall thrusters tend to ionize essentially all of the propellant gas incident on the plasma from the anode, so that

$$n_n n_e \langle \sigma_i v_e \rangle A_e L \approx n_n v_n A_e. \tag{7.2-18}$$

Using Eq. (7.2-6) for the Hall current, Eq. (7.2-18) becomes

$$L = \frac{v_n V_d w}{I_H \langle \sigma_i v_e \rangle B}. \tag{7.2-19}$$

The length of the ionization region naturally must increase with neutral velocity and can decrease with the ionization reaction rate coefficient, as seen in Eq. (7.2-16). This is important in order to achieve high mass utilization when propellants with a lower mass than xenon, such as krypton, are used to increase the Isp of the thruster [18,19].

Studies of optimized Hall thrusters of different sizes [20–25] have resulted in some scaling laws. A detailed comparison of the scaling laws in the literature, with experimental results from the family of empirically optimized stationary plasma thrusters (SPTs), was performed by Daren, et al. [20]. Assuming that the thruster channel inner-to-outer diameter ratio and the ionization mean-free path-to-plasma length ratio are constants, they found

$$\begin{aligned} &\text{power} \propto \text{thrust} \propto R^2 \\ &I_d \propto R^2 \\ &\dot{m} \propto R^2 \\ &w = R(1 - \text{constant}) \\ &A_e = \pi\left(R^2 - r^2\right), \end{aligned} \tag{7.2-20}$$

where R is the outside radius of the channel. These scaling rules indicate that the optimum current density is essentially constant as the thruster size changes. The current density in Hall thrusters is typically in the range of 0.1 to 0.15 A/cm^2. Thus, at a given discharge voltage, the power density in a Hall thruster is also constant. Higher power densities are achieved by increasing the voltage, which has implications for the life of the thruster.

7.2.3 Potential and Current Distributions

The electrical schematic for a Hall thruster is shown in Fig. 7-7. The power supplies are normally all connected to the same reference, called the *cathode common*. The hollow cathode requires the same power supplies as an ion thruster, namely, a heater supply to raise the emitter to thermionic emission temperatures and a keeper supply for ignition and to ensure stable cathode operation at very low currents. The discharge supply is connected between the cathode common (typically also connected to the thruster body or magnetic circuit) and the anode located in the bottom of the channel. As in ion thrusters, the cathode heater is turned off once the discharge supply is turned on, and the cathode runs in a self-heating mode. The keeper is also normally used only during start-up and is turned off once the thruster is ignited. Also shown are the inner and outer magnetic field coils and their associated power supplies. Hall thrusters have been built with the cathode positioned on-axis (not shown), but this does not change the electrical schematic.

The potential distribution in a Hall thruster [26] is also illustrated in Fig. 7-7. In the upstream region of the channel where the transverse magnetic field is low, the plasma is weakly magnetized and the electron mobility is high. The plasma potential is then close to the anode potential. The plasma potential decreases toward the cathode potential near the thruster exit plane as the magnetic field increases (shown in Fig. 7-6) and limits the electron mobility. The difference between the cathode potential and the beam potential is the coupling voltage V_c, which is the voltage required to extract current from the hollow cathode. The beam voltage is then

$$V_b = V_d - V_c. \tag{7.2-21}$$

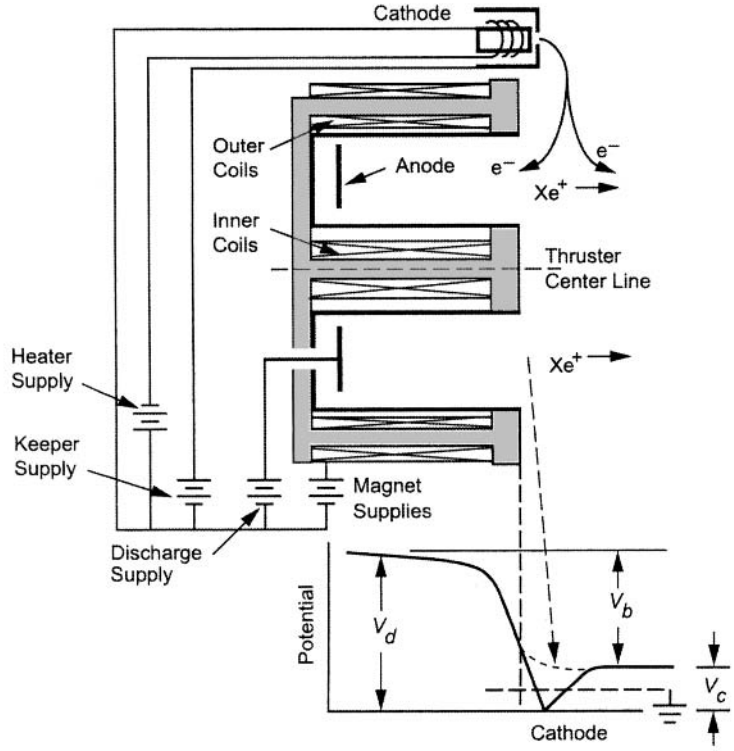

Fig. 7-7. Hall thruster electrical schematic and potential distribution.

It is common in laboratory experiments to sometimes ignore the difference in potential between the beam and ground as small (typically 10 to 20 V) and to write the beam voltage as

$$V_b \approx V_d - V_{cg}, \tag{7.2-22}$$

where V_{cg} is the cathode-to-ground voltage.

The on-axis potential, shown schematically by the dashed line in Fig. 7-7, decreases from the ionization and acceleration regions to the thrust-beam plasma potential. Ions are generated all along this potential gradient, which causes a spread in the ion energy in the beam. Since the majority of the ions are generated upstream of the exit plane (in the "ionization region"), the average velocity of the ion beam can then be expressed as

$$\langle v_b \rangle = \sqrt{\frac{2e\overline{V}_b}{M}}, \tag{7.2-23}$$

where $\overline{V_b}$ represents, in this case, the average potential across which the ions are accelerated. The actual spread in the beam energy can be significant [27,28] and must be measured by plasma diagnostics.

The beam from the Hall thruster is charge neutral (equal ion and electron currents). As in ion thrusters, the thruster floats with respect to either spacecraft common in space or vacuum-chamber common on the ground. The common potential normally floats between the cathode and the beam potentials and can be controlled on a spacecraft by a resistor between the spacecraft common and the cathode common. The actual beam energy cannot be measured directly across the power supplies because the potential difference between the beam and ground or spacecraft common is unknown and must be measured by probes or energy analyzers. The coupling voltage is typically on the order of 20 V in order to operate the cathode discharge properly, which usually ranges from 5% to 10% of the discharge voltage for Hall thrusters with moderate Isp.

In a Hall thruster, the measured discharge current is the net current flowing through the discharge supply. The current flowing in the connection between the anode and the power supply in Fig. 7-7 is the electron and ion current arriving to the anode:

$$I_d = I_{ea} - I_{ia}. \tag{7.2-24}$$

The ion current is typically small due to its higher mass, and so the discharge current is essentially the electron current collected by the anode. Likewise, the current flowing in the cathode leg (neglecting any keeper current) is

$$I_d = I_e + I_{ic}, \tag{7.2-25}$$

where I_e is the emitted current and I_{ic} is the ion current flowing back to the cathode. As with the anode, the ion current to the cathode is typically small, and so the discharge current is essentially just the cathode electron emission current. Therefore, the discharge current is approximately

$$I_d \approx I_e \approx I_{ea}. \tag{7.2-26}$$

Figure 7-8 shows a simplified picture of the currents flowing through the plasma, where the ion currents to the anode and cathode are neglected as small and the ion and electron currents to the dielectric walls are equal and are not shown. Ions are produced in the plasma by ionization events. The secondary electrons from the ionization events, I_{ei}, go to the anode, along with the primary electrons from the cathode, I_{ec}. Primary electrons either ionize neutrals or contribute energy to the plasma electrons so that the energetic

electron distribution can produce the ionization. Since it is assumed that the discharge current is essentially the total electron current collected by the anode (the ion current is small), the discharge current can be written as

$$I_d = I_{ei} + I_{ec}. \tag{7.2-27}$$

The discharge current is also essentially the electron current emitted by the cathode:

$$I_d = I_e = I_{ec} + I_{eb}. \tag{7.2-28}$$

Using the fact that one electron and one ion are made in each ionization event such that $I_{ei} = I_{ib}$, Eq. (7.2-27) becomes

$$I_d = I_{ib} + I_{ec}. \tag{7.2-29}$$

This relationship describes the net current crossing the exit plane, and so it is commonly stated in the literature that the discharge current is the ion beam current plus the backstreaming electron current crossing the exit plane [4,9].

Depending on the plasma conditions, it is possible for some fraction of the secondary electrons produced near the channel exit to diffuse into the beam. Equation (7.2-29) is still valid in this case because for every secondary electron that diffuses into the beam, another electron from the cathode plasma must cross the exit plane in the opposite direction to maintain the net discharge current. The discharge current is still the net ion beam current plus the backstreaming electron current across the exit plane. Finally, the ion beam current is equal to the current of electrons entering the beam:

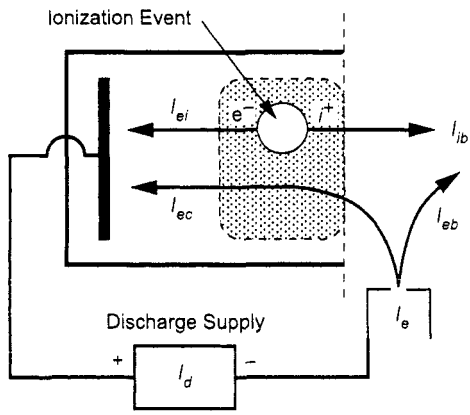

Fig. 7-8. Electrical schematic for the currents flowing through the discharge plasma and power supply.

$$I_{ib} = I_{eb}. \tag{7.2-30}$$

Since there is no current return path for the beam ions and electrons because the thruster floats relative to the spacecraft or the grounded vacuum system, the particles in Eq. (7.2-30) do not directly contribute to the discharge current measured in the discharge power supply.

7.3 Hall Thruster Performance Models

The efficiency of a generic electric thruster was derived in Chapter 2. Since the beam current and ion energy in Hall thrusters are not directly measured as in ion thrusters, it is useful to develop an alternative expression for the efficiency that incorporates characteristics of Hall thruster discharges. Total efficiency is always defined as the jet power, which is the thrust times the exhaust velocity, divided by the total input power:

$$\eta_T = \frac{T\ v}{P_{\text{in}}}. \tag{7.3-1}$$

For any electric thruster, the exhaust velocity is given by Eq. (2.3-6), the Isp is given by Eq. (2.4-1), and the thrust is given by Eq. (2.3-1), which can be combined to give

$$v = \frac{\text{Isp} \cdot g}{2} = \frac{g}{2}\frac{v}{g}\frac{\dot{m}_i}{\dot{m}_p} = \frac{1}{2}\frac{T}{\dot{m}_p}. \tag{7.3-2}$$

The total efficiency is then

$$\eta_T = \frac{T^2}{2\dot{m}_p P_{\text{in}}}. \tag{7.3-3}$$

7.3.1 Hall Thruster Efficiency

In Hall thrusters, the gas flow is split between the anode inside the discharge channel and the hollow cathode:

$$\dot{m}_p = \dot{m}_a + \dot{m}_c, \tag{7.3-4}$$

where $\dot{m}_a$ is the anode flow rate and $\dot{m}_c$ is the cathode flow rate.

Since the cathode gas flow is injected exterior to the discharge channel ionization region and is, thereby, largely lost, the "cathode efficiency" is defined as

$$\eta_c = \frac{\dot{m}_a}{\dot{m}_p} = \frac{\dot{m}_a}{\dot{m}_a + \dot{m}_c}. \tag{7.3-5}$$

The total power into the thruster is

$$P_{\text{in}} = P_d + P_k + P_{\text{mag}}, \tag{7.3-6}$$

where P_d is the discharge power, P_k is the cathode keeper power (normally equal to zero during operation), and P_{mag} is the power used to generate the magnetic field. The electrical utilization efficiency for the other power used in the Hall thruster is defined as

$$\eta_o = \frac{P_d}{P_T} = \frac{P_d}{P_d + P_k + P_{\text{mag}}}. \tag{7.3-7}$$

Using Eqs. (7.3-5) and (7.3-7) in Eq. (7.3-3) gives a useful expression for the total efficiency of a Hall thruster:

$$\eta_T = \frac{1}{2}\frac{T^2}{\dot{m}_a P_d}\eta_c \eta_o. \tag{7.3-8}$$

By placing the Hall thruster on a thrust stand to directly measure the thrust, knowing the flow rates and flow split between anode and cathode, and knowing the total power into the discharge, keeper, and magnet, it is then possible to accurately calculate the total efficiency.

While Eq. (7.3-8) provides a useful expression for evaluating the efficiency, it is worthwhile to further expand this equation to examine other terms that affect the efficiency. Thrust is given from Eq. (2.3-16):

$$T = \gamma \sqrt{\frac{2M}{e}}\, I_b \sqrt{\bar{V}_b}, \tag{7.3-9}$$

where the average or effective beam voltage is used due to the spread in ion energies produced in the Hall thruster acceleration region. The fraction of the discharge current that produces beam current is

$$\eta_b = \frac{I_b}{I_d}. \tag{7.3-10}$$

Likewise, the fraction of the discharge voltage that becomes beam voltage is

$$\eta_v = \frac{V_b}{V_d}. \tag{7.3-11}$$

Inserting Eqs. (7.3-9) through (7.3-11) into Eq. (7.3-8) gives

$$\eta_T = \gamma^2 \frac{M}{e} \frac{I_d}{\dot{m}_a} \eta_b^2 \eta_v \eta_c \eta_o. \tag{7.3-12}$$

Equation (7.3-12) shows that the Hall thruster efficiency is proportional to the ion mass and the discharge current, because these terms dominate the thrust production, and is inversely proportional to the anode mass flow, which dominates the mass utilization efficiency. This equation can be further simplified by realizing that

$$\frac{M}{e} I_d \eta_b = \dot{m}_i, \tag{7.3-13}$$

and that the total mass utilization efficiency can be expressed as

$$\eta_m = \frac{\dot{m}_i}{\dot{m}_p} = \frac{\dot{m}_i}{\dot{m}_a + \dot{m}_c}. \tag{7.3-14}$$

The total efficiency then becomes

$$\eta_T = \gamma^2 \eta_b \eta_v \eta_m \eta_o. \tag{7.3-15}$$

This expression contains the usual gamma-squared term associated with beam divergence and multiply charged ion content and also the mass utilization and electrical utilization efficiencies. However, this expression also includes the efficiencies associated with generating beam ions and imparting the discharge voltage to the beam voltage. This shows directly that Hall thruster designs that maximize beam current production and beam energy and that minimize the cathode flow produce the maximum efficiency, provided that the beam divergence and double-ion content are not adversely affected. Expressions like Eq. (7-3-15) appear in the Hall thruster literature [4,7] because they are useful in illustrating how the efficiency depends on the degree to which the thruster converts power supply inputs (such as discharge current and voltage) into the beam current and beam voltage that impart thrust. Understanding each efficiency term is critical to fully optimizing the Hall thruster performance.

The efficiency of a Hall thruster is sometimes expressed in terms of the anode efficiency:

$$\eta_a = \frac{1}{2}\frac{T^2}{\dot{m}_a P_d} = \frac{\eta_T}{\eta_o \eta_c}, \qquad (7.3\text{-}16)$$

which describes the basic thruster performance without considering the effects of the cathode flow or power used to generate the magnetic field. This is usually done to separate out the cathode and magnet losses so that trends in the plasma production and acceleration mechanisms can be discerned. The anode efficiency should not be confused with the total efficiency of the thruster given by Eq. (7.3-3).

It is useful to show an example of the relative magnitude of the efficiency terms derived above. Figure 7-9 (from [10]) shows the anode efficiency that was defined in Eq. (7.3-16) and the other efficiency terms discussed above for the laboratory-model NASA-173Mv2 Hall thruster operating at 10 mg/s versus the discharge voltage. In this figure, the charge utilization efficiency is the net efficiency decrease due to multiply charged ions [10], the voltage utilization efficiency (η_v) is the conversion of voltage into axially directed ion velocity, the current utilization efficiency (η_b) is the fraction of ion current contained in the discharge current, and mass utilization efficiency (η_m) is the conversion of neutral mass flux into ion mass flux. The anode efficiency increases with discharge voltage, largely because the voltage efficiency and current efficiency increase with voltage. The current utilization is always lower than the other efficiency terms, suggesting that the ultimate efficiency of Hall thrusters is dominated by the electron dynamics involved in producing the plasma and neutralizing the beam. This emphasizes the importance [9,10] of optimizing the magnetic field design to maximize the thruster efficiency.

The value of γ in Eq. (7.3-15) that is typically found for Hall thrusters can be evaluated using Eq. (2.3-15) and the data in the literature. For example, a 10% double-ion content gives a thruster correction factor in Eq. (2.3-14) of $\alpha = 0.973$. The thrust loss due to the beam angular divergence of Hall thrusters is given by Eq. (2.3-10), ($F_T = \cos\theta$). For both SPT-100 Hall thrusters [6] and TAL thrusters [29], a half-angle divergence of θ equal to about 20~deg is observed, producing $F_T = 0.94$. The total correction factor is then $\gamma = \alpha F_T = 0.915$ for typical Hall thruster conditions. Values for γ of about 0.9 have been reported.

The equivalent discharge loss for a Hall thruster can also be calculated [4,6] to provide information on how the thruster design impacts the cost of producing the beam ions. The average energy cost for producing a beam ion is the

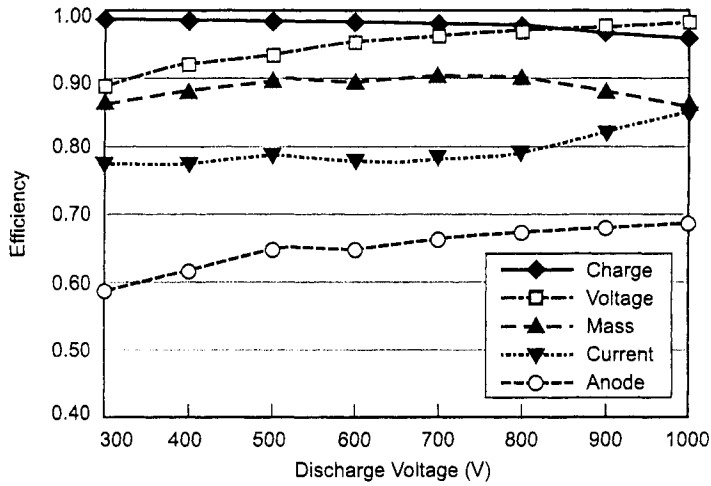

Fig. 7-9. Optimized anode efficiency and the individual efficiency terms versus discharge voltage for the NASA-173Mv2 Hall thruster operating at 10 mg/s (from [10]).

discharge power divided by the number of beam ions minus the beam power per beam ion:

$$\varepsilon_b = \frac{I_d V_d}{I_b} - \frac{I_b V_b}{I_b} = \frac{I_d V_d}{I_b} - V_b = \frac{P_d(1-\eta_b \eta_v)}{I_b}, \qquad (7.3\text{-}17)$$

where Eqs. (7.3-10) and (7.3-11) were used. Equation (7.3-17) has the usual units for discharge loss of watts per beam-amp or electron-volts per ion. As expected, maximizing the current and voltage efficiencies minimizes the discharge loss. As an example of discharge loss in a Hall thruster, consider the SPT-100 thruster operating at the nominal 1.35-kW discharge power and 300 V. The discharge current is then 1350/300 = 4.5 A. The thruster is reported [4–6] to have values of $\eta_b \approx 0.7$ and $\eta_v = 0.95$. The cost of producing beam ions is then

$$\varepsilon_b = \frac{P_d(1-\eta_b \eta_v)}{I_b} = \frac{1350(1-0.7*0.95)}{0.7*4.5} = 144 \text{ [eV/ion]}.$$

This is on the same order as the discharge loss for DC-discharge ion thrusters.

7.3.2 Multiply Charged Ion Correction

In Hall thrusters operating at higher power levels (high mass flow rate and high discharge voltages >300 V), a significant number of multiply charged ions can

be generated, and their effect on the performance may be noticeable. Following the analysis by Hofer [11], the performance model from the previous section can be modified to address the case of partially ionized thruster plasmas with an arbitrary number of ion species.

The total ion beam current is the sum of each ion species i:

$$I_b = \sum_{i=1}^{N} I_i \,. \tag{7.3-18}$$

The current fraction of the ith species is

$$f_i = \frac{I_i}{I_b}. \tag{7.3-19}$$

Likewise, the total plasma density in the beam is the sum of the individual species densities,

$$n_b = \sum_{i=1}^{N} n_i \,, \tag{7.3-20}$$

and the density fraction of the ith species is

$$\zeta_i = \frac{n_i}{n_b}. \tag{7.3-21}$$

The total beam current is then

$$I_b = \sum_i n_i q_i \langle v_i \rangle A_e = \sum_i n_b e \sqrt{\frac{2eV_b}{M}} \zeta_i Z_i^{3/2} \,, \tag{7.3-22}$$

where Z_i is the charge state of each species. The mass flow rate of all the beam ion species is

$$\dot{m}_b = \frac{I_b M}{e} \sum_i \frac{f_i}{Z_i} \,. \tag{7.3-23}$$

Using the current utilization efficiency defined in Eq. (7.3-10), the mass utilization efficiency in Eq. (7.3-14) then becomes

$$\eta_m = \frac{\dot{m}_b}{\dot{m}_p} = \frac{\eta_b I_d M}{\dot{m}_p e} \sum_i \frac{f_i}{Z_i}. \tag{7.3-24}$$

If the current utilization efficiency is the same for each species, then the mass utilization efficiency for arbitrary species can be written as

$$\eta_m = \eta_m^+ \sum_i \frac{f_i}{Z_i}, \tag{7.3-25}$$

where η_m^+ is the usual mass utilization for a singly charged species. This is an easily implemented correction in most models if the species fractions are known. Likewise, the thrust obtained for multiple species can be generalized from Eq. (2.3-16) for Hall thrusters to

$$T_m = \sum_i T_i = \eta_b I_d \sqrt{\frac{2M\eta_b V_d}{e}} \sum_i \frac{f_i}{Z_i} \cos\theta. \tag{7.3-26}$$

7.3.3 Dominant Power Loss Mechanisms

In preparation for examining the terms that drive the efficiency of Hall thrusters, it is useful to examine the dominant power-loss mechanisms in the thruster. Globally, the power into the thruster comes from the discharge power supply. The power out of the thruster, which is equal to the input power, is given to first order by

$$P_d = P_b + P_w + P_a + P_R + P_{\text{ion}}, \tag{7.3-27}$$

where P_b is the beam power given by $I_b V_b$, P_w is the power to the channel walls due to ion and electron loss, P_a is the power to the anode due to electron collection, P_R is the radiative power loss from the plasma, and P_{ion} is the power to produce the ions that hit the walls and become the beam. Additional loss terms, such as the power that electrons take into the beam, the ion power to the anode, etc., are relatively small and can usually be neglected.

In Hall thrusters with dielectric walls, the power loss due to electron and ion currents flowing along the radial magnetic field through the sheath to the channel walls (P_w) represents the most significant power loss. The current deposition and power lost to the walls can be estimated from the sheath potentials and electric fields in the plasma edge. Since the wall is insulating, the net ion and electron currents to the surface must be equal. However, ion and electron bombardment of common insulator materials, such as boron nitride, at

the energies characteristic of Hall thrusters produces a significant number of secondary electrons, which reduces the sheath potential at the wall and increases the power loading.

The requirement of local net current equal to zero and particle balance for the three species gives

$$I_{iw} = I_{ew} - \gamma I_{ew} = I_{ew}(1-\gamma), \tag{7.3-28}$$

where γ is the secondary electron yield from electron bombardment. Using Eq. (3.7-51) for the Bohm current of ions to the wall, Eq. (3.7-52) for the electron current to the wall, and neglecting the secondary electron velocity, Eq. (7.3-28) can be solved for the sheath potential ϕ_s, including the effect of secondary electron emission:

$$\phi_s = \frac{kT_e}{e} \ln\left[(1-\gamma)\sqrt{\frac{2M}{\pi m}}\right]. \tag{7.3-29}$$

This expression is slightly different than that found in the literature [30,31] because we have approximated $e^{-1/2} = 0.61 \approx 0.5$ for the coefficient in the expression for the Bohm current. Nevertheless, as the secondary electron yield increases, the sheath potential decreases from the classic floating potential described in Chapter 3 toward the plasma potential.

Secondary electron yields reported in the literature [30,32,33] for several materials used for the walls of Hall thrusters are shown in Fig. 7-10. In this figure, the measurements were made using a monoenergetic electron gun. Generalizing these data for incident Maxwellian electron temperatures is accomplished by integrating the yield over the Maxwellian electron energy distribution function, which results in multiplying the secondary emission scaling by the gamma function [30]. An expression for the secondary electron yield from electron bombardment of materials is then

$$\gamma = \Gamma(2+b) a T_{eV}^{b}, \tag{7.3-30}$$

where the electron temperature is in electron volts, $\Gamma(x)$ is the gamma function, and the coefficients a and b are found from fits to the data in Fig. 7-10. Values of the coefficients in Eq. (7.3-30) can be found in Table 7-1 for these materials, and the actual secondary electron yield for the Hall thruster walls is plotted versus plasma electron temperature in Fig. 7-11. It should be noted that due to reflection at the wall, the effective secondary electron yield does not go to zero for zero electron energy. This effect is accommodated by linear fits to the data

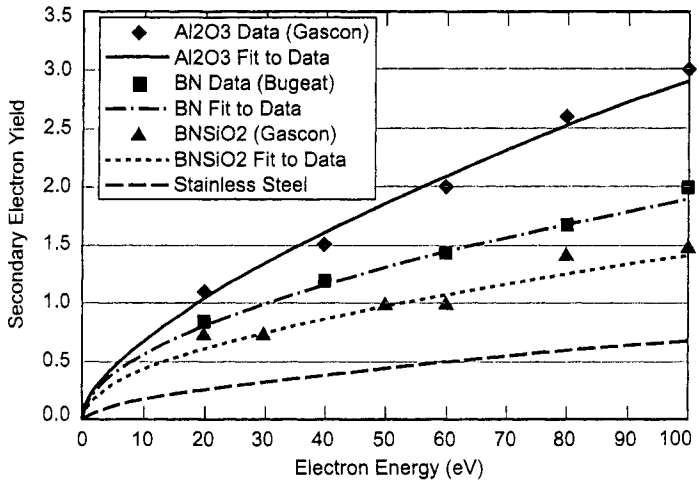

Fig. 7-10. Secondary electron yield for several wall materials used in Hall thrusters, measured with a mono-energetic electron beam.

Table 7-1. Fitting parameters for secondary electron yield data.

	a	b	$\Gamma(2 + b)$
Alumina (Al_2O_3)	0.145	0.650	1.49
Boron Nitride (BN)	0.150	0.549	1.38
$BNSiO_2$	0.123	0.528	1.36
Stainless steel	0.040	0.610	1.44

that result in finite yield at low electron energy. Figure 7-12 shows the data for boron nitride and $BNSiO_2$ with the two different fitting choices. In the evaluation of the sheath potential in the presence of the secondary electron emission below, whether one uses a linear or power fit does not make a significant difference in the ionization and acceleration regions for electron temperatures above about 10 eV.

Measurements of the electron temperature in the channel of Hall thrusters by a number of authors [34–36] show electron temperatures in the channel well in excess of 20 eV. Equation (7.3-29) predicts that the sheath potential will go to zero and reverse from negative going (electron repelling) to positive going (electron attracting) as the secondary electron yield approaches unity for some of the materials. The value at which this occurs for each of the materials shown in Table 7-1 is indicated in Fig. 7-11. For boron nitride and alumina walls this occurs at electron temperatures below 20 eV, and for BN-SiO_2 walls it occurs at

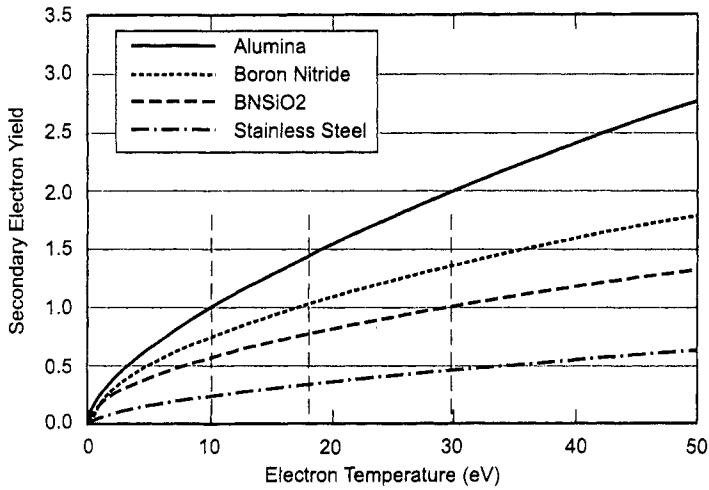

Fig, 7-11. Secondary electron yield from the power-curve fits versus electron temperature, showing the cross-over value at which the yield equals one.

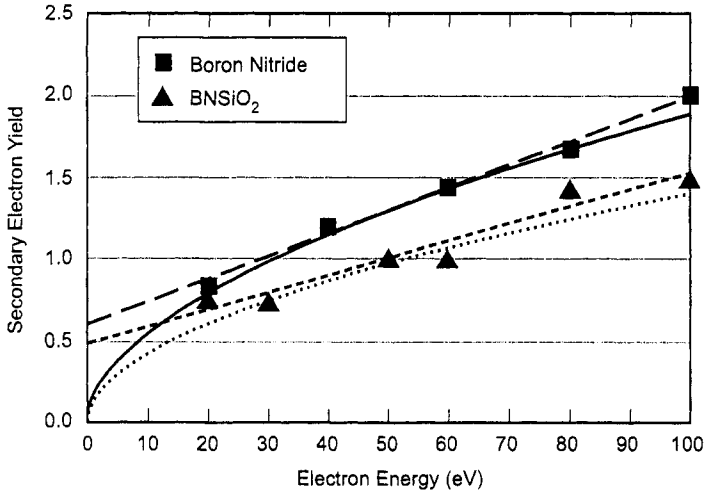

Fig. 7-12. Secondary electron yield versus electron energy, showing linear curve fits to the data producing finite yield at low incident energy.

electron temperatures on the order of 30 eV. In addition, depending on the collision mean-free path, some of the secondary electrons can pass completely through the plasma to strike the opposite wall of the channel. The possibility of the sheath potential reversing to electron attracting was used to predict very high electron power losses to the walls in some early analyses of Hall thrusters

at high electron temperatures [30,31] because the incident electron flux can then equal or exceed the random electron flux along the magnetic field lines in the plasma.

In reality, the sheath potential for a floating boundary can never go significantly more positive than the local plasma potential [37,38] for two reasons. First, the secondary electrons are ejected from the wall with very low energy (typically 1–2 eV). Any positive-going sheath (where the plasma is negative by one or two volts relative to the wall) will repel the secondary electrons and return them to the wall. This clamps the sheath potential to within a few volts positive with respect to the plasma. Second, the secondary electron emission is space charge–limited in the sheath. This effect was analyzed by Hobbs and Wesson [39], who showed that space charge limits the secondary electron current from the wall independently of the secondary electron yield. The local electron space charge in the sheath clamps the sheath voltage to a maximum value that is always negative relative to the plasma.

The effects of space charge on the sheath potential at the wall can be analyzed [39] by solving Poisson's equation for the potential in the sheath:

$$\frac{\partial^2 \phi}{\partial x^2} = \frac{1}{\varepsilon_o}\left(n_e + n_s - n_i\right), \tag{7.3-31}$$

where n_s is the secondary electron density. Using a Maxwellian distribution for the electrons, the plasma density in the channel is

$$n_e = \left(n_o - n_{so}\right) e^{e\phi/kT}, \tag{7.3-32}$$

where n_o is the ion density at the sheath edge, n_{so} is the secondary electron density at the sheath edge, and ϕ is the potential relative to the potential ϕ_o at the wall. The ions are assumed to be cold and to have fallen through the pre-sheath to arrive at the sheath edge with an energy of

$$\mathcal{E} = \frac{1}{2} m v_o^2, \tag{7.3-33}$$

where v_o is the Bohm velocity modified for the presence of the secondary electrons. The ion density through the sheath is then

$$n_i = n_o \left(\frac{\mathcal{E}}{\mathcal{E} - e\phi} \right)^{1/2}. \tag{7.3-34}$$

The secondary electrons are assumed to be emitted with an energy that is small compared to the plasma electron temperature and are accelerated through the sheath. The equation of continuity for current at the sheath edge gives

$$n_s v_s = \frac{\gamma}{1-\gamma} n_o v_o, \tag{7.3-35}$$

where v_s is the secondary electron velocity. The secondary electron density through the sheath is then

$$n_s = n_o \frac{\gamma}{1-\gamma}\left(\frac{m}{M}\frac{\mathcal{E}}{\phi-\phi_o}\right). \tag{7.3-36}$$

Equations (7.3-32), (7.3-34), and (7.3-36) are inserted into Poisson's equation, Eq. (7.3-31), and evaluated by the usual method of multiplying through by $d\phi/dx$ and integrating to produce

$$\begin{aligned}\frac{1}{2\varepsilon_o n_o kT_e}\left(\frac{d\phi}{dx}\right)^2 = {} & \frac{2\mathcal{E}}{kT_e}\left[\left(1-\frac{e\phi}{\mathcal{E}}\right)^{1/2}-1\right] \\ & + \frac{2\gamma}{1-\gamma}\left(-\frac{m}{M}\frac{\mathcal{E}}{kT_e}\frac{e\phi_o}{kT_e}\right)^{1/2}\left[\left(1-\frac{\phi}{\phi_o}\right)^{1/2}-1\right] \\ & + \left[1-\frac{\gamma}{1-\gamma}\left(-\frac{m}{M}\frac{\mathcal{E}}{e\phi_o}\right)^{1/2}\right]\left[\exp\left(\frac{e\phi}{kT_e}\right)-1\right].\end{aligned} \tag{7.3-37}$$

A monotonic sheath potential is found [39] for

$$\mathcal{E} = \frac{kT_e}{2} + \frac{\gamma}{1-\gamma}\left(\frac{m}{M}\right)^{1/2}\left(\frac{-\mathcal{E}}{e\phi_o}\right)^{3/2}\left(\frac{kT_e}{2}-e\phi_o\right). \tag{7.3-38}$$

For the case of no secondary electron emission (γ going to zero), the Bohm criteria solution of $\mathcal{E} \geq kT_e/2e$ is recovered. Due to the large electron-to-ion mass ratio for xenon, the right-hand term is always small and the ion velocity at the sheath edge for the case of finite secondary electron emission will be near the Bohm velocity. Hobbs and Wesson evaluated this minimum ion energy at the sheath edge for the case of space charge–limited emission of electrons at the wall, $d\phi_o/dx = 0$ in Eq. (7.3-37), and they found

$$\mathcal{E}_o = 0.58\frac{kT_e}{e}. \tag{7.3-39}$$

Equation (7.3-39) indicates that the Bohm sheath criterion will still approximately apply (within about 16%) in the presence of secondary electron emission.

The value of the sheath potential for the space charge–limited case can be found by setting the electric field at the wall equal to zero in Eq. (7.3-37) and evaluating the potential using Eq. (7.3-38) and the current continuity equation:

$$\frac{1}{4}\left[1-\frac{\gamma}{1-\gamma}\left(-\frac{m}{M}\frac{\mathcal{E}}{e\phi_o}\right)^{1/2}\right]\exp\left(\frac{e\phi_o}{kT_e}\right)\left(\frac{8kT_e}{\pi m}\right)^{1/2} = \frac{1}{1-\gamma}\left(\frac{2\mathcal{E}}{M}\right)^{1/2}. \tag{7.3-40}$$

The space charge–limited sheath potential for xenon is found to be

$$\phi_o = -1.02\frac{kT_e}{e}. \tag{7.3-41}$$

The secondary electron yield at which the sheath becomes space-charge limited [39] is approximately

$$\gamma_o = 1-8.3\left(\frac{m}{M}\right)^{1/2}, \tag{7.3-42}$$

which for xenon is 0.983.

This analysis shows that the sheath potential for a xenon plasma decreases from $-5.97T_e$ for walls where the secondary electron yield can be neglected to $-1.02T_e$ for the case of space charge–limited secondary electron emission that will occur at high plasma electron temperatures. The value of the sheath potential below the space-charge limit can be found exactly by evaluating the three equations, Eqs. (7.3-37), (7.3-38), and (7.3-40), for the three unknowns (ϕ, γ, and $\mathcal{E}$).

However, the value of the sheath potential relative to the plasma edge in the presence of the secondary electron emission can be estimated by evaluating Eq. (7.3-29) while accounting for each of three species [38]. Quasi-neutrality for the three species in the plasma edge dictates that $n_i = n_e + n_s$, where n_s is the secondary electron density, and the flux of secondary electrons is the

secondary electron yield times the flux of plasma electrons. Equating the ion flux to the net electron flux to the wall gives

$$I_{iw} = n_i e v_i A = I_{ew}(1-\gamma) = \frac{1}{4} n_e (1-\gamma) e \left(\frac{8kT_e}{\pi m} \right)^{1/2} A \exp\left(\frac{e\phi_s}{kT_e} \right), \quad (7.3\text{-}43)$$

where the ion and electron densities are evaluated at the sheath edge. The sheath potential ϕ_s relative to the plasma potential is then

$$\phi_s = -\frac{kT_e}{e} \ln\left[\sqrt{\frac{M}{2\pi m}} \frac{n_e}{n_e + n_s} \frac{v_B}{v_i} (1-\gamma) \right], \quad (7.3\text{-}44)$$

where v_i is the modified ion velocity at the sheath edge due to the presence of the secondary electrons and the ion density is the sum of the plasma and secondary electrons. This equation is useful up to the space charge–limited potential of $\phi_o = -1.02 T_{eV}$ and provides good agreement with the results for xenon described above for $n_e v_B / n_i v_i \approx 0.5$. The sheath potential predicted by Eq. (7.3-44) is plotted in Fig. 7-13 for two wall materials. In the limit of no secondary electron emission ($\gamma = 0$), the classic value for the sheath floating potential is obtained from Eq. (3.7-53). Once the electron temperature is sufficiently high to produce a yield approaching and even exceeding one, then the space charge–limited case of $\phi_o = -1.02 T_{eV}$ is obtained. In between, the sheath potential depends on the electron temperature and material of the wall. Without the space charge–limited sheath regime predicted by Hobbs and Wesson, the potential would have continued along the thin dashed lines for the two cases and incorrectly resulted in very low sheath potentials and high power loadings at the wall.

The total power to the wall of the Hall thruster is

$$P_w = \frac{1}{4} \left(\frac{8kT_e}{\pi m} \right)^{1/2} e n_o A e^{e\phi_s / kT_e} \left(2\frac{kT_e}{e} \right) + n_o e v_o A (\mathcal{E} - \phi_s), \quad (7.3\text{-}45)$$

where the first term is due to electrons overcoming the repelling sheath potential and depositing $2T_e$ on the wall, and the second term is due to ions that have fallen through the pre-sheath potential and then the full sheath potential. Note that n_o in this equation is the plasma density at the sheath edge and is roughly half the average plasma density in the center of the channel due to the radial pre-sheath. The cooling of the wall by the secondary electron

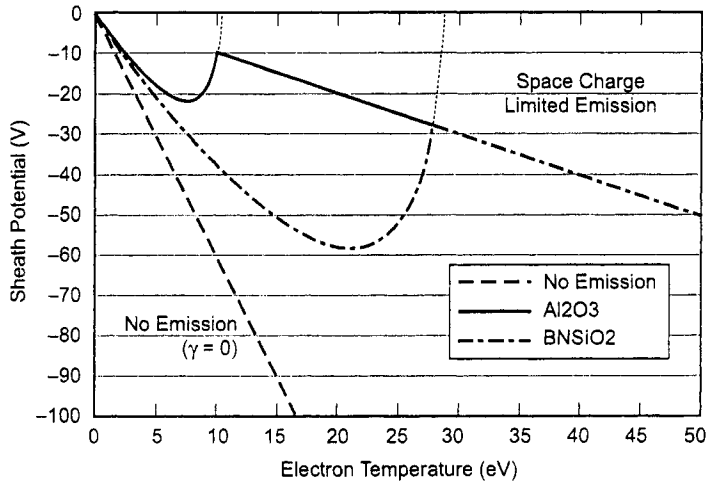

Fig. 7-13. Sheath potential versus electron temperature for two materials. The sheath transitions to space-charge limited where the dashed lines intersect the potential curves.

emission has been neglected. Equation (7.3-45) can be rewritten in terms of the total ion current to the wall as

$$P_w = I_{iw}\left[\left(\frac{M}{2\pi m}\right)^{1/2} e^{e\phi_s/kT_e}\left(2\frac{kT_e}{e}\right)+\left(\mathcal{E}-\phi_s\right)\right]. \qquad (7.3\text{-}46)$$

For the case of space charge–limited secondary electron emission, the sheath potential is $\phi_s = \phi_o = -1.02T_{eV}$, and the ion energy is $\mathcal{E} = 0.58\,T_{eV}$ in order to satisfy the Bohm condition. Equation (7.3-45) predicts the maximum heat loading to the wall in the presence of a Maxwellian electron distribution and secondary electron emission from the wall, which is the dominant power loss mechanism in dielectric-wall Hall thrusters. If the electron distribution function is non-Maxwellian, the heat load to the wall can differ from that predicted by Eq. (7.3-45).

In the case of TAL thrusters, the channel wall is metallic and biased to the cathode potential. This eliminates the zero-net current condition found on the insulating walls of dielectric-channel Hall thrusters and used to determine the local heat flux in Eq. (7.3-45). The electron flux to the cathode-biased TAL channel wall is negligible, and the secondary yield for metals is much lower than for insulators, so the secondary electron emission by the wall in TAL thrusters has little effect on the thruster operation. In addition, the plasma tends to be localized near the channel center by the anode design and gas feed geometry. The plasma then tends to be in poor contact with the guard rings at

the wall that also have a small exposed area to the plasma, resulting in low radial ion currents to the wall. This is evidenced by the erosion pattern typically observed on TAL guard rings [29], which tends to be on the downstream face from particles outside the thruster instead of on the inside diameter from the channel plasma. While the ion and electron currents and power deposition to the inside diameter of the metallic guard ring are likely smaller than in the dielectric-wall thruster case (where the power loss due to the electrons is dominant), the erosion on the face of the guard ring indicates energetic ion bombardment is occurring. This effect is significant in determining the life of the TAL.

However, TAL thrusters are characterized by having the anode in close contact with the magnetized plasma near the channel exit, in contrast to the dielectric-wall Hall thrusters. The magnetized plasma has a high electron temperature, which causes a significant amount of power to be deposited from the discharge current on the anode. It is possible to evaluate this power loss mechanism based on the current and sheath potential at the anode.

As described above, the discharge current is essentially equal to the electron current collected at the anode. In order for the TAL thruster to transfer a large fraction of the discharge voltage to the ions, the potential of the plasma near the anode must be close to the anode potential. Assuming the local plasma potential is then equal to or slightly positive relative to the anode, the electron current to the anode, I_a, deposits $2T_{eV}$ in energy from the plasma (see Appendix C). The power deposited on the anode, P_a, is then given by

$$P_a = 2T_{eV} I_a \approx 2T_{eV} I_d , \tag{7.3-47}$$

where Eq. (7.2-26) has been used. If the plasma potential is negative relative to the anode, the thruster efficiency will suffer due to the loss of discharge voltage available to the ions, and the anode heating will increase due to the positive-going sheath potential accelerating electrons into the anode. Equation (7.3-47) then represents a reasonable, but not worst-case, heat flux to the anode.

This power loss to the anode can be related to the beam current using the fraction of the discharge current that produces beam current, which is defined as

$$\eta_b = \frac{I_b}{I_d} . \tag{7.3-48}$$

Therefore, the power to the anode is

$$P_a = 2T_{\mathrm{eV}} \frac{I_b}{\eta_b}. \tag{7.3-49}$$

In well-designed Hall thrusters, η_b ranges typically from 0.6 to 0.8. Therefore, the power loss to the anode is 3 to 4 times the product of the electron temperature in the near-anode region and the beam current. This is the most significant power loss mechanism in TAL thrusters.

7.3.4 Plasma Electron Temperature

The electron temperature in the channel must be known to evaluate the power loss mechanisms described above. The peak electron temperature in the plasma channel can be found using power balance, described by Eq. (7.3-27). This method provides reasonable estimates because the power loss in the thruster will be shown to be a strong function of the electron temperature. Even though the plasma density and electron temperature peak in different locations along the channel associated with the different ionization and acceleration regions, the strong axial electron temperature profile in Hall thrusters causes the majority of the power loss to occur in the region of the highest electron temperature. This occurs near the channel exit where the magnetic field across the channel is the strongest. Evaluating the plasma parameters and loss terms in this region, which is bounded by the channel width and magnetic axial field extent in the channel, establishes the electron temperature that is required to satisfy the power balance in the plasma for a given thruster current and voltage.

The individual terms in Eq. (7.3-27) will now be evaluated. The input power to the thruster is the discharge current times the discharge voltage ($P_d = I_d V_d$). The power in the beam, using Eq. (7.3-48), is

$$P_b = \eta_b \eta_v I_d V_d = \eta_v I_b V_d, \tag{7.3-50}$$

where the current utilization and voltage utilization efficiencies have to be known or evaluated by some means. The difference between the beam power and the discharge power is the power remaining in the plasma channel to produce the plasma and offset the losses:

$$P_p = (1-\eta_b) I_d V_d = I_{ec} V_d, \tag{7.3-51}$$

where P_p is the power into the plasma. The plasma is produced and heated essentially by the collisional transport of the electrons flowing from the cathode plasma in the near-plume region to the anode inside the thruster. The power into channel walls, from Eq. (7.3-45), can be written as

$$P_w = n_e e A \left[\frac{kT_e}{e} \left(\frac{kT_e}{2\pi m} \right)^{1/2} e^{e\phi_s / kT_e} + \frac{v_i}{2} \left(\mathcal{E} - \phi_s \right) \right], \qquad (7.3\text{-}52)$$

where A is the total area of the inner and outer channel walls in contact with the high temperature plasma region, v_i is the ion velocity toward the wall, and the sheath potential ϕ_s is given by Eq. (7.3-44). Equation (7.3-52) shows the wall power varies linearly with density but with the electron temperature to the 3/2 power. This is why the dominant wall losses occur in the region of the highest electron temperature.

The power into the anode, from Eq. (7.3-47), can be written as

$$P_a = 2 I_d T_{\mathrm{eV}} (\text{anode}) . \qquad (7.3\text{-}53)$$

where the electron temperature in this case is evaluated near the anode. The power radiated is

$$P_R = n_o n_e \langle \sigma_* v_e \rangle V , \qquad (7.3\text{-}54)$$

where the excitation reaction rate coefficient is given in Appendix E as a function of the electron temperature, and V is the volume of the high-temperature plasma region in the channel, which can be taken to be the channel cross-sectional area times the axial thickness L. Equations (7.3-52) and (7.3-54) require knowledge of the plasma density in the high-temperature region in the channel. This can be found to first order from the beam current

$$n_e = \frac{I_b}{e v_b A_c} \approx \frac{\eta_b I_d}{e A_c \sqrt{\dfrac{2\eta_b e V_d}{M}}}, \qquad (7.3\text{-}55)$$

where A_c is the area of the channel exit. Finally, the power to produce the ions in the thruster is the sum of the beam current and the ion current to the walls times the ionization potential:

$$P_{\mathrm{ion}} = \left(I_b + I_{iw} \right) U^+ = \left[\eta_b + I_{ew} \left(1 - \gamma \right) \right] I_d U^+ , \qquad (7.3\text{-}56)$$

where I_{iw} is given by Eq. (7.3-28) and I_{ew} is given by the left-hand side of Eq. (7.3-52) divided by $2T_e$ (because the electron energy hitting the wall is already included in this equation).

The peak electron temperature is found by equating the input power to the plasma in Eq. (7.3-51) with the sum of the various loss terms described above, and then iterating to find a solution. For example, the SPT-100 Hall thruster has a channel outside diameter of 10 cm, a channel inside diameter of 7 cm, and runs nominally at a discharge of 300 V at 4.5 A with a current utilization efficiency of 0.7 and a voltage utilization efficiency of 0.95 [6]. From Eq. (7.3-55), the plasma density at the thruster exit is about $1.6 \times 10^{17} \mathrm{m}^{-3}$. The power into the plasma, from Eq. (7.3-51), is about 433 W. Taking the electron temperature at the anode to be 5 eV and the hot-plasma thickness L to be about 1 cm, the power balance equation is satisfied if the electron temperature in the channel plasma is about 25 eV.

It is a common rule-of-thumb in Hall thrusters to find that the electron temperature is about one-tenth the beam voltage [35]. The result in the example above of $T_e \approx 0.08\, V_d$ is consistent with that observation. It is also important to note that nearly 70% of the power deposited into the plasma goes to the dielectric channel walls in the form of electron heating, and that the radiation losses predicted by Eq. (7.3-54) are negligible for this case because the electron temperature is so high. Finally, the ion current to the wall for this example from the solution to Eq. (7.3-28) is 0.52 A, which is about 12% of the discharge current and 8% of the beam current in this thruster. This amount agrees well with the 10% of the ion current going to the wall calculated by Baranov [40] in analyzing Hall thruster channel wear.

7.3.5 Hall Thruster Efficiency (Dielectric Walls)

The efficiency of a Hall thruster with a dielectric wall can be estimated by evaluating the terms in the thruster efficiency given by Eq. (2.5-7), which requires evaluating the total power-loss terms in Eq. (7.3-27) to obtain a value for the effective electrical efficiency. This also illustrates the dominant loss mechanisms in the thruster.

The first term in Eq. (7.3-27), the beam power due to the accelerated ions, P_b, is just $I_b V_b$, where the effective beam voltage will be used. The power loss to the dielectric wall will be estimated for the SPT-100 Hall thruster [4–6] using the analysis of Hobbs and Wesson [39] described in Section 7.3.3. The heat flux to the wall was given by Eq. (7.3-46):

$$P_w = I_{iw}\left[\left(\frac{2M}{\pi m}\right)^{1/2} e^{e\phi_s/kT_e}\left(\frac{kT_e}{e}\right) + \left(\mathcal{E} - \phi_s\right)\right], \qquad (7.3\text{-}57)$$

where I_{iw} is the ion flux to the wall. Following Hobbs and Wesson, the modification to the Bohm criterion is small and $\mathcal{E} \approx T_e/2$ from the Bohm criterion. From Eq. (7.3-44), the sheath potential for xenon and $BNSiO_2$ walls in the SPT-100 thruster, assuming an average electron temperature along the channel wall of 25 eV, is about –54 V. Plugging these values into Eq. (7.3-57) gives

$$P_w = 45.8 I_{iw} T_{\mathrm{eV}} + 2.65 I_{iw} T_{\mathrm{eV}} = 48.5 I_{iw} T_{\mathrm{eV}}. \tag{7.3-58}$$

The first term on the right-hand side is again the electron power loss to the wall (written in terms of the ion current to the dielectric surface), and the second term is the ion power loss. The power loss to the channel wall due to the electron loss term is an order of magnitude larger than the power loss due to ions.

It is convenient in evaluating the efficiency of the thruster to relate the ion current to the wall in Eq. (7.3-58) to the beam current. In the plasma, there is an electric field toward the wall due to the pre-sheath of approximately $T_{\mathrm{eV}}/2r = T_e/w$. There is also the axial electric field of V_b/L producing the beam energy. It is common in Hall thrusters to find that the electron temperature is about one-tenth the beam voltage [35], and the channel width is usually approximately L [4,20]. Therefore, the axial electric field is on the order of 10 times the radial electric field. On average, then, the ion current to the channel walls will be about 10% of the beam current. This very simple argument agrees with the SPT-100 example results given in the previous section and the results of Baranov [40].

Using Eq. (7.3-58) with the above estimates for the ion current and electron temperature, the power loss to the insulator walls is

$$P_w = 48.5 I_{iw} T_{\mathrm{eV}} = 48.5(0.1 I_b)(0.1 V_b) = 0.49 I_b V_b. \tag{7.3-59}$$

The power loss to the anode is due to the plasma electrons overcoming the sheath potential at the anode surface. From Eq. (7.2-24), the anode electron current is

$$I_{ea} = I_d + I_{ia}. \tag{7.3-60}$$

Neglecting the ion current to the anode as small (due to the mass ratio), and realizing that each electron deposits $2kT_e/e$ to the anode for positive plasma potentials (from Appendix C), the power to the anode is

$$P_a = 2T_{\mathrm{eV}} I_d \,. \tag{7.3-61}$$

The electron temperature near the anode is very low, typically less than 5 eV [34–36]. Using the thruster current utilization efficiency and assuming $\eta_b = 0.7$ and $T_{\mathrm{eV}} = 0.01 V_b$ near the anode, this can be written as

$$P_a = 2\eta_b I_b (0.01 V_b) = 0.014 I_b V_b \,. \tag{7.3-62}$$

The power required to produce the ions is given by Eq. (7.3-56). This can be written as

$$P_{\mathrm{ion}} = (I_b + I_{iw}) U^+ = (1 + \eta_b) I_d U^+ \,. \tag{7.3-63}$$

Taking the beam utilization efficiency as 0.7 and estimating that the ionization potential is roughly 5% of the beam voltage, the power required to produce the ions is approximately $P_i = 0.09\, I_d V_b$. The radiation power and other power loss mechanisms are small and will be neglected in this simple example.

The total discharge power into the thruster is then

$$P_d = I_b V_b + 0.49\, I_b V_b + 0.014\, I_b V_b + 0.09\, I_b V_b = 1.59\, I_b V_b \,. \tag{7.3-64}$$

The electrical efficiency of the dielectric-wall thruster is then

$$\eta_e = I_b V_b / (1.59\, I_b V_b) = 0.63 \,. \tag{7.3-65}$$

The total thruster efficiency, assuming the same beam divergence and double-ion content as evaluated above and a mass utilization efficiency of 95% reported for SPT thrusters [4], is

$$\eta_T = (0.915)^2\, (0.63)(0.95) = 50\% \,. \tag{7.3-66}$$

The SPT-100 thruster is reported to run at about 50% efficiency. Since the power loss is dominated by the electron wall losses, this analysis illustrates how critical the wall material selection is to minimizing the secondary electron yield and maintaining a sufficient wall sheath potential for good efficiency. For example, if the wall had been made of alumina and the electron temperature was about 20 V, the sheath potential would be $-1.02 T_{\mathrm{eV}}$ in the space charge–limited regime. The wall power from Eq. (7.3-57) would then be about three times higher than in the $BNSiO_2$ case:

$$P_w = 142 I_{iw} T_{\mathrm{eV}} = 1.4 I_b V_b \,. \tag{7.3-67}$$

The electrical efficiency of the thruster, assuming the same anode loading and energy loss to the beam, would be , $\eta_e \approx 0.40$ and the total efficiency would be

$$\eta_T = (0.915)^2\,(0.40)(0.95) \approx 32\%. \qquad (7.3\text{-}68)$$

Recent parametric experiments in which different wall materials were used in the SPT-100 [33] showed that changing from $BNSiO_2$ to alumina reduced the efficiency to the order of 30%, consistent with the increased secondary electron yield of the different wall material.

The agreement of this simple analysis with the experimentally measured efficiencies is somewhat fortuitous because the predictions are very sensitive to the secondary electron yield of the wall material and the actual sheath potential. Small errors in the yield data, changes in the wall material properties during thruster operation, and inaccuracies in the empirical values for the electron temperature and ion flux with respect to the beam parameters will significantly affect the calculated results. Other effects may also be significant in determining the thruster efficiency. The analysis of the sheath potential assumed a Maxwellian electron distribution function. It was recognized several years ago [37,41,42] that the electron distribution may not be Maxwellian. Detailed kinetic modeling of the Hall thruster channel plasma [43,44] indicates that the electron velocity distribution is depleted of the high-energy tail electrons that rapidly leave the plasma along the magnetic field lines and impact the wall. This is especially true near the space-charge limit where the sheath voltage is small and a large fraction of the electron tail can be lost. The collision frequencies and thermalization rates in the plasma may be insufficient to re-populate the Maxwellian tail. This will effectively result in a lower electron temperature in the direction parallel to the magnetic field toward the walls [45], which can increase the magnitude of the sheath potential and reduce the electron heat loss to the wall. In addition, re-collection of the secondary electrons at the opposite wall [46,47], due to incomplete thermalization of the emitted secondary electrons in the plasma, modifies the space-charge limits and sheath potential, which also can change the electron heat flux to the wall.

These effects are difficult to model accurately due to the presence of several different electron populations, several collision/thermalization processes, the effect of magnetization on the electrons, and the presence of plasma instabilities. Understanding what determines the electron temperature and velocity distribution as a function of the discharge voltage and current, and uncovering the effects that determine the wall power flux and finding techniques to minimize them, are continuing areas of research at this time.

7.3.6 TAL Hall Thruster Efficiency (Metallic Walls)

As with the 1.35-kW SPT-100 Hall thruster example above, an estimate will be made of the power loss terms in Eq. (7.3-27) to obtain an electrical efficiency for the 1.4-kW D-55 TAL thruster [29]. Equation (2.5-7) will then be used to obtain an estimate for the thruster efficiency. The beam power P_b is, again, just $I_b V_b$. As stated in the previous section, the wall losses (P_w) are essentially negligible in TAL thrusters, and the power to the anode is given by Eq. (7.3-49):

$$P_a = 2T_{eV}\frac{I_b}{\eta_b} = 0.29 I_b V_b . \tag{7.3-69}$$

In Eq. (7.3-69), it is again assumed $\eta_b = 0.7$ and $T_{eV} = 0.1 V_b$, although these values may be somewhat different in TAL thrusters. The power to produce the ions is again approximately $0.09 I_b V_b$.

The total discharge power, Eq. (7.3-27), then becomes

$$P_d = I_b V_b + 0.29\, I_b V_b + 0.09\, I_b V_b = 1.4\, I_b V_b . \tag{7.3-70}$$

Neglecting the power in the cathode keeper (if any) and the magnet as small compared to the beam power, the electrical utilization efficiency from Eq. (2.5-1) is then

$$\eta_e = \frac{P_d}{1.4 P_d} = 0.72 . \tag{7.3-71}$$

The total thruster efficiency, assuming a 10% double-ion content, a 20-deg angular divergence [29,48], and a 90% mass utilization efficiency reported for TAL thrusters [29,49], is then, from Eq. (2.4-7),

$$\eta_T = (0.915)^2\,(0.72)(0.9) = 54\% . \tag{7.3-72}$$

This result is on the same order as that reported in the literature [29,49,50] for this power-level TAL and is essentially the same as the SPT-100 efficiency in this simple example if the wall losses had been included. However, the power loss to the anode is seen as the dominant mechanism in the TAL efficiency.

7.3.7 Dielectric-Wall Versus Metallic-Wall Comparison

It is interesting to make a few direct comparisons of dielectric-wall Hall thrusters with metallic-wall TAL thrusters. Similar discussions have appeared in the literature [1,3,31], often with conflicting opinions. The basic plasma physics in the channel described above applies to both the dielectric-wall Hall thruster and the TAL. The maximum electron temperature occurs in both thrusters near the channel exit in the region of strongest magnetic field where the Hall current is a maximum. The different interaction of the thruster walls with this plasma determines many of the characteristics of the thruster, including life. Dielectric-wall thrusters have a significant amount of their input power deposited as loss on the dielectric channel walls due to electron bombardment. In the above example efficiency calculation, approximately 25% of the power going into the thruster was deposited on the channel walls. The metallic walls in TAL thrusters collect a smaller electron current because they are biased to cathode potential, and they also tend to have a small exposed area in poor contact with the plasma, which limits the amount of ion and power lost to these surfaces. However, the anode is positioned very close to the high electron temperature region and receives a significant amount of power deposition in collecting the discharge current. In the above example TAL efficiency calculation, over 20% of the power going into the thruster was deposited on the anode.

The deep channel in dielectric-wall Hall thrusters, with a low magnetic field strength and low electron temperature near the anode, tends to minimize the power deposition on the anode. In the above simple example, only 1% of the thruster input power was deposited on the anode. Nevertheless, the anode is normally electrically isolated from the thruster body (and therefore thermally isolated), and so anode overheating is sometimes an issue, especially at high power density. The anode in TAL thrusters can also have heating issues because the loading is much higher, even though the view factor for the anode to radiate its power out of the thruster is better than the deep channel in the insulting-wall configuration. In addition, with the anode positioned physically close to the thruster exit in TALs, impurity deposition and material buildup problems can occur. This has been an issue in ground testing of some TAL thrusters [29], where carbon deposition on the anode from back sputtering from the beam dump became significant over time. TAL thrusters with deeper channels can be designed and operated [3]. The performance of the thruster is likely different in this configuration, and ion bombardment and sputtering of the metallic channel walls can become significant and affect the thruster life.

Dielectric-wall Hall thrusters are often described in terms of an ionization zone upstream of the exit plane and an acceleration zone in the region of the exit plane. TAL thrusters have a similar ionization region near the magnetic field maximum, which is now closer to the anode because the magnetic field gradient is greater. The TAL acceleration zone is described as being a layer close to the anode [1,3] that can extend outside of the thruster [48]. The higher electron temperatures associated with TAL thrusters support higher electric fields in the quasi-neutral plasma, which compresses these zones relative to dielectric-wall thrusters. In addition, the metallic walls and higher electric fields are conducive to multiple acceleration stages, which can improve thruster performance and produce higher Isp than a conventional single-stage TAL thruster [1,51]. Multiple-stage dielectric-wall Hall thrusters that operate at high Isp have also been investigated (see [17] and the references cited therein).

Finally, the difference between dielectric-wall Hall thrusters and TAL thrusters is sometimes attributed to the secondary electron coefficients of the different wall materials. The above discussion shows that this is not the dominant difference. Instead, the proximity of the TAL anode electrode to the high temperature plasma region and the thruster exit plane is what changes the electric field profile, power deposition, and sputtering characteristics as compared to the dielectric-wall Hall thruster.

7.4 Channel Physics and Numerical Modeling

As discussed in the previous sections, the detailed physics determining Hall thruster performance is not well understood. Specifically, the electron distribution function in the exit region, the mechanisms responsible for electron transport across the magnetic field, and the role of oscillations on the particle transport and plasma conditions need to be determined. A considerable effort has been made to develop fluid, kinetic, hybrid, and particle-in-cell (PIC) models to predict and explain the performance and effects observed in Hall thrusters. Hirakawa and Arakawa developed [52] a two-dimensional (2-D) particle-in-cell model where anomalous electron diffusion was introduced by using oscillating azimuthal electric fields. Boeuf and Garrigues developed a one-dimensional (1-D) hybrid model [53] in which the electrons were treated as a fluid and the ions were described by a collisionless Vlasov (kinetic) equation. Similar fluid and hybrid models have been developed by other authors [54–56] using various techniques to determine the ion transport, such as Monte-Carlo simulation, Boltzman equation solutions, and "ion free-fall" (essentially a Bohm current solution) to the boundaries. The most widely used code, HPHall, is a 2-D, transient hybrid model originated by Fife and Martinez-Sanchez [30] that has been recently extended with an improved sheath model [41,42,57] and a model of channel erosion [58,59].

7.4.1 Hybrid Hall Thruster Models

Hybrid Hall thruster models, such as HPHall [30, 57], utilize a steady-state fluid electron momentum equation and a time-dependent electron energy equation to solve for electron temperature and potentials in the channel and plume. The codes also use time-dependent ion and neutral particle equations to calculate the plasma density and ion velocities on a time scale much larger than the electron time scale. These codes are also used to model Hall thruster transit-time oscillations that are on the order of time scales related to neutral atom and ion motions (≤1 MHz) but cannot capture the effects of electron instabilities that have much higher frequencies.

From the steady-state electron momentum equation, an Ohm's law representation from Eq. (3.6-20) for the electron field is

$$\eta \mathbf{J}_e = \mathbf{E} + \frac{\nabla \mathbf{p} - \mathbf{J}_e \times \mathbf{B}}{en} - \eta_{ei} \mathbf{J}_i, \tag{7.4-1}$$

where the resistive term has the following form in the magnetic frame of reference:

$$\eta \mathbf{J} = \eta_\perp J_\perp + \eta_\parallel J_\parallel + \eta_\wedge J_\wedge, \tag{7.4-2}$$

and the subscripts represent the directions perpendicular, parallel, and transverse (in the $\mathbf{E} \times \mathbf{B}$ direction), respectively, to the local magnetic field.

Equation 7.4-1 must be separated into the two components of the $\mathbf{J}_e \times \mathbf{B}$ motion in a manner similar to that in Section 3.6 and solved for the electric field. From current conservation, the electron current is taken to be the difference between the discharge current and the ion current from the particle calculations. Typically, the circuit current is chosen at each time step to satisfy the applied voltage ($= \int \mathbf{E} \cdot \mathbf{d}\ell$) boundary conditions.

7.4.1.1 Transverse Electron Transport. Writing the perpendicular resistivity in terms of the perpendicular electron mobility, as defined in Eq. (3.6-66), gives

$$\eta_\perp = \frac{1}{en\mu_{e\perp}} = \frac{1 + \omega_c^2 \tau_m^2}{en\mu_e} = \frac{1 + \omega_c^2 / \nu_m^2}{en\mu_e}, \tag{7.4-3}$$

where the collision time τ_m for momentum transfer is equal to one over the collision frequency ($1/\nu_m$). The perpendicular electron flux from Ohm's law, Eq. (7.4-1), can then be written as

$$J_{e\perp} = \mu_{e\perp}\left(enE_{\perp} + \frac{\partial p_e}{\partial x}\right) - \frac{\mu_{e\perp}}{\mu_{ei}} J_{i\perp}, \tag{7.4-4}$$

and the electron mobility due only to electron–ion collisions is given by

$$\mu_{ei} = \frac{e}{m\nu_{ei}}. \tag{7.4-5}$$

Usually, the ion flux term in Eq. (7.4-4) is neglected and an effective electric field is used such that the electron flux is expressed as

$$J_{e\perp} = en\mu_{e\perp}E'_{\perp}, \tag{7.4-6}$$

where the effective electric field is

$$E'_{\perp} = \left(E_{\perp} + \frac{1}{en}\frac{\partial p_e}{\partial x}\right). \tag{7.4-7}$$

The effective perpendicular electron mobility in Eq. (7.4-4) is

$$\mu_{e\perp} = \frac{e}{m\nu_m}\frac{1}{1+\omega_c^2/\nu_m^2} = \frac{\mu_e}{1+\Omega_e^2}, \tag{7.4-8}$$

where Ω_e^2 is the electron Hall parameter, and the momentum-transferring collision frequency ν_m is described, as in Chapter 3, by

$$\nu_m = \nu_{ei} + \nu_{en}. \tag{7.4-9}$$

This expression for the transverse electron mobility then accounts for both electron–ion and electron–neutral collisions in the partially ionized plasma.

Since the electrons are well magnetized in the plasma near the exit of the channel where the magnetic field strength is the highest, the electron Hall parameter is much greater than unity and the transverse electron mobility across the field lines is found to be small. In fact, calculations of the electron collision frequency based on the classical collision terms in Eq. (7.4-9) are unable to provide sufficient cross-field transport to support the discharge current passing through the thruster [54,57,59]. In addition, the neutral density in the plume of the Hall thruster is low due to the high mass utilization efficiency, which reduces the effective collision frequency in Eq. (7.4-9) and again leads to problems in providing sufficient transport of the electrons from the external

cathode across the transverse field lines and into the channel to support the discharge current. Two mechanisms have been proposed in an attempt to describe "enhanced" cross-field electron transport and explain the observed Hall thruster operation.

Morozov [12] postulated that electron-wall interactions in the channel region will scatter electron momentum and introduce secondary electrons, which can increase the effective cross-field transport. This effect is introduced into the effective collision frequency by a wall-scattering frequency ν_w:

$$\nu_m = \nu_{ei} + \nu_{en} + \nu_w . \tag{7.4-10}$$

The wall-scattering frequency is either given by $\alpha * 10^7$ per second [53], with α an adjustable parameter used to match the experimental data, or the wall collision frequency of electrons is calculated directly in the code [59]. While this effect does increase the electron transport in the channel, it is sometimes found to provide insufficient enhancement of the electron transport. In addition, in the plume of the thruster there are no walls and the neutral density is very low, which precludes the use of Eq. (7.4-10) to increase the cross-field transport sufficiently to explain the experimental data.

Additional cross-field transport has been added in the codes by invoking Bohm diffusion both inside and outside the thruster channel. As discussed in Chapter 3, Bohm diffusion likely arises from $\mathbf{E} \times \mathbf{B}$ driven drift instabilities, which can naturally occur in these thrusters due to the Hall current. Using the Bohm diffusion coefficient from Eq. (3.6-72) and the Einstein relationship of Eq. (3.6-28), a Bohm mobility can be defined as

$$\mu_B = \frac{1}{\beta B} = \frac{e}{\beta m \omega_c}, \tag{7-4-11}$$

where β is an adjustable coefficient changed to make the code predictions of the thruster parameters fit the experimental data. If full Bohm diffusion is required by the code to match the data, such as is often the case in the plume, then $\beta = 16$. The effective Bohm collision frequency is then

$$\nu_B = \beta \omega_c . \tag{7-4-12}$$

The total "anomalous" collision frequency used in the codes is

$$\nu_m = \nu_{ei} + \nu_{en} + \nu_w + \nu_B , \tag{7.4-13}$$

where the wall collision frequency ν_w is neglected in the plume.

7.4.1.2 Transport Along the Magnetic Field. In the direction along the magnetic field lines, the $\mathbf{J}\times\mathbf{B}$ cross product in the electron momentum equation is zero and Eq. (7.4-1) becomes

$$\eta J_e = E + \frac{\nabla p}{en} - \eta_{ei} J_i . \tag{7.4-14}$$

The electric field along the field line is then

$$E = \frac{\nabla p}{en} + \eta J_e - \eta_{ei} J_i = -\nabla\phi . \tag{7.4-15}$$

With the standard assumptions used along magnetic fields in many plasmas of zero net current ($j_e \approx j_i$) and uniform electron temperature, Eq. (7.4-15) can be solved for the potential along the field line to give

$$\phi = \phi_o + T_e \ln\left(\frac{n}{n_o}\right). \tag{7.4-16}$$

This equation was derived in Section 3.5-1 and represents the simple Boltzman relationship for plasmas with Maxwellian electron distribution functions. It is often called the *barometric law* in ion thruster literature and the *thermalized potential* in Hall thruster literature. Thus, the transport along the magnetic field lines is usually considered to be classical.

It is commonly assumed that the density gradient along the magnetic field line is relatively small, so the potential change along a magnetic field line from Eq. (7.4-16) is essentially zero. Therefore, within about kT_e/e, the magnetic field lines represent equipotential lines in the plasma. The simplifying assumptions leading to this conclusion (zero net current, Maxwellian electrons, and small density gradient along the magnetic field lines) are often used and may introduce significant errors in some cases. Nevertheless, the thermalized potential has been used for many years [3] in the design of Hall thrusters to relate the magnetic field shape to the electric field in the plasma [11].

7.4.1.3 Continuity and Energy. Continuity for the neutrals in the thruster can be expressed as

$$\frac{\partial n_o}{\partial t} + v_o \nabla n_o = -n_e n_o \langle \sigma_i v_e \rangle , \tag{7.4-17}$$

where the right-hand side represents the local ionization rate. For ions and electrons, continuity in the plasma gives

$$\nabla \cdot \mathbf{J}_e = \nabla \cdot \mathbf{J}_i. \tag{7.4-18}$$

In addition, charge balance at the insulating wall dictates that

$$J_i = J_e - J_{se}, \tag{7.4-19}$$

where J_{se} is the secondary electron current density, which is equal to the secondary electron yield γ times the incident electron flux.

The electric field in the perpendicular direction ($\hat{z}$) in the plasma can be found from Eq. (7.4-4):

$$E = \frac{J_e}{en_e\mu_{e\perp}} - \frac{1}{en_e}\frac{\partial(n_e kT)}{\partial z} + \frac{\mu_{e\perp}}{\mu_{ei}}J_i. \tag{7.4-20}$$

The potential applied across the plasma is then

$$V = -\int_0^L E(z,t)dx, \tag{7.4-21}$$

which can be used to find the electron current or total current flowing in the plasma.

The electron energy equation is

$$\frac{\partial}{\partial t}\left(\frac{3}{2}n_e\frac{kT_e}{e}\right) + \nabla \cdot \frac{5}{2}T_e\mathbf{J}_e = \mathbf{E}\cdot\mathbf{J}_e - R - S - P_w, \tag{7.4-22}$$

where $\mathbf{E}\cdot\mathbf{J}_e$ is the ohmic power input, R is the radiative energy loss, S is the ionization energy loss, and P_w is the electron energy loss to the walls. The radiative energy loss is

$$R = U^* n_e n_o \langle \sigma_* v_e \rangle, \tag{7.4-23}$$

and the ionization energy loss is given by

$$S = U^+ n_e n_o \langle \sigma_i v_e \rangle. \tag{7.4-24}$$

The ionization and excitation reaction rate coefficients in Eqs. (7.4-23) and (7.4-24) are given in Appendix E. Finally, the electron energy density is given by convection in the plasma as

$$\varepsilon = \frac{5}{2} n_e k T_e . \tag{7.4-25}$$

7.4.1.4 Ion Current. Several methods have been used to describe the ion generation and transport in the Hall thruster models. First, the ions have been modeled as a fluid using continuity equations [54,60], where the axial motion is due to the electric field along the channel and the radial motion to the wall is determined by the ion-neutral scattering frequency. The ion current to the wall is then

$$I_w = n_i n_o \langle \sigma_{\text{in}} v_i \rangle A_w L , \tag{7.4-26}$$

where A_w is the wall area, L is the plasma length, σ_{in} is the ion-neutral collision cross section for 90-deg scattering including elastic and charge-exchange collisions, and the velocity of the neutrals is neglected relative to the ion velocity. In PIC numerical codes, this represents the radial flux to the cell boundary where $A_w L$ becomes the cell volume.

Fife [30] modeled the ion motion using a 2-D PIC code that assumed the ions and neutrals acted as discrete macro-particles in each cell. The time step in the ion-PIC code, in this case, was adjusted (to typically three orders of magnitude slower than the electron model time step) to handle the ion-motion time scales without invoking excessive computational time.

Finally, the ion Vlasov equation has been used to solve for the ion generation and motion [52,53]. This has primarily been applied for investigating low-frequency oscillations on the order of the ion-characteristic time scales. In one dimension, this can be written as

$$\frac{\partial f}{\partial t} + v_x \frac{\partial f}{\partial t} + \frac{e}{M} E \frac{\partial f}{\partial v_x} = n_e n_o \langle \sigma_i v_e \rangle \delta(v_x - v_o), \tag{7.4-27}$$

where f is the ion distribution function and $\delta(v_x - v_o)$ is the Dirac delta function evaluated for the ion velocity relative to the neutral velocity. The ion density is then found from

$$n_i = \int f(x, v_x, t) dv_x . \tag{7.4-28}$$

The plasma is always assumed to be quasi-neutral ($n_i \approx n_e$). At the sheath boundary at the wall, the ion current normally is assumed to be the Bohm current and the electron current is the one-sided random electron flux. Total current continuity requires the ion flux and net electron flux (incident electrons and emitted secondary electrons) to the insulating walls to be equal, which establishes the sheath potential to produce quasineutrality and charge conservation as described above. The hybrid-model equations described above for determining the ion currents are normally evaluated numerically in either 1-D or 2-D with greatly different time steps between the electron fluid evolution and the ion and neutral motion evaluations.

7.4.2 Steady-State Modeling Results

The physics of the Hall thruster discharge related to the transverse electron mobility, electron-wall interactions, and the exact nature of the electron distribution function are not completely understood at this time. However, the 1-D and 2-D models described above are reasonably successful in predicting plasma parameters and thruster behavior provided enhanced electron conductivity is incorporated in the channel due to wall collisions and turbulence, and modifications to the wall heat fluxes are made associated with the secondary electron behavior. In addition, enhanced electron transport in the plume region near the thruster exit is required to match the models' predictions with the experimental results [61], which is normally provided by assuming collective oscillations drive Bohm-like diffusion. In this region, other mechanisms may also be responsible for the cross-field electron transport, and research in this area to determine the responsible mechanism(s) is continuing.

The hybrid codes can provide very reasonable predictions of the steady-state plasma parameters in the thrusters. For example, Fig. 7-14 shows the average profiles (along the channel axis) predicted by a 1-D model [53] for the potential, electric field, plasma density, mean electron energy, neutral density, and ionization rate for the SPT-100 Hall thruster, where 4 cm corresponds to the channel exit. The average plasma density peaks upstream of the exit, as is also predicted by the 2-D HPHall code [30] result shown in Fig. 7-15 for the SPT-100 Hall thruster channel. In both cases, there is a characteristic peak in the plasma density upstream of the channel exit in the ionization region, and a decreasing plasma density is seen moving out of the channel as the ions are accelerated in the electric field of the acceleration region. The plasma density prediction by the 1-D code is slightly lower than the 2-D HPHall result because of differences in the heat flux calculation to the wall and the resulting values of

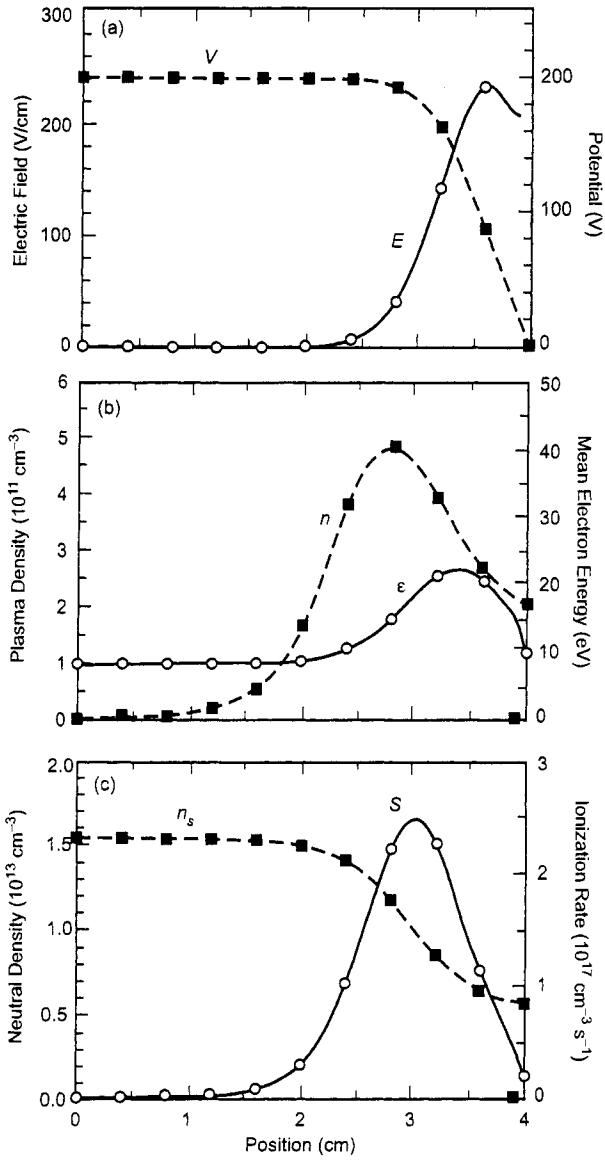

Fig. 7-14. 1-D Hall thruster code [53] for the SPT-100: (a) potential and electric field, (b) plasma density and electron energy, and (c) neutral density and ionization rate (redrawn from [53]).

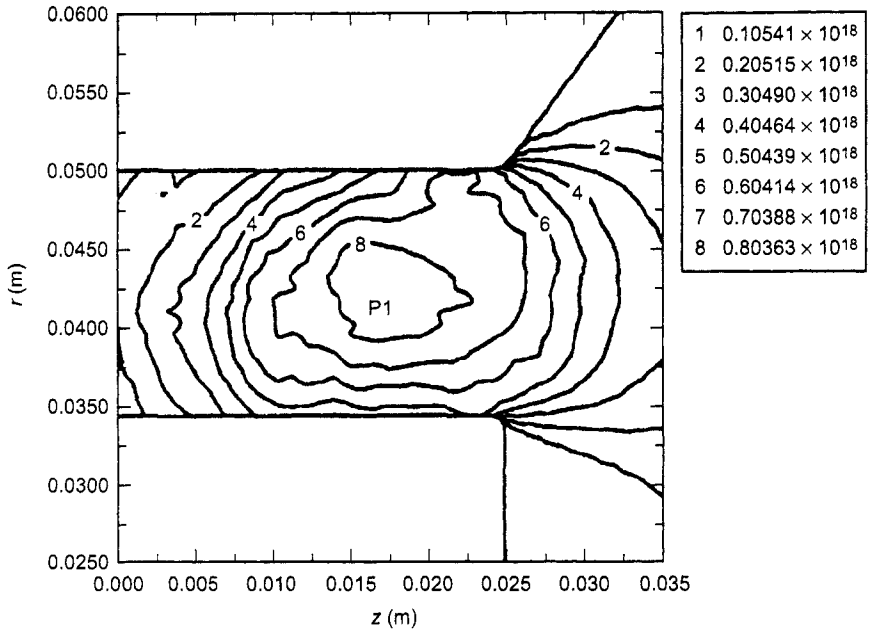

Fig. 7-15. Average plasma density computed by HPHall for the SPT-100, with the peak plasma density at P1 = 8×10^{17} m^{-3} (from [30]).

the electron temperature. Since the distribution function of the electrons can certainly be non-Maxwellian and anisotropic, the actual value of the density in the Hall thruster will differ somewhat from the values calculated by these existing codes.

The profiles shown by the 1-D code results in Fig. 7-14 suggest that three overlapping but distinct regions exist in the plasma channel of a well-designed Hall thruster. Near the anode, the potential drop is small due to the low magnetic field in this region, resulting in good plasma conduction to the anode but small ionization. The ionization zone occurs upstream of the channel exit where the neutral gas density is still high and the electrons are well confined and have significant temperature. The acceleration zone exists near the channel exit where the electric field is a maximum, which occurs at this location because the magnetic field is a maximum and the transverse electron mobility is significantly reduced as described above. Outside the channel, the electric field, plasma density, and electron temperature drop as the magnetic field strength decays and the Hall current decreases.

The current versus voltage predictions from the 1-D code [53] for different values of the transverse magnetic field in the channel for the SPT-100 thruster are shown in Fig. 7-16. As the transverse magnetic field increases, the impedance of the discharge increases significantly and higher voltages are required to obtain the transverse electron mobility required to achieve the desired discharge current. Increases in the mass flow rate increase the collisional effects in the plasma region, and this results in more current at a given voltage and magnetic field. In addition, Fig. 7-16 shows regions where the 1-D code predicts oscillatory behavior, as indicted by the solid points. This is discussed in the next section.

The 1-D hybrid code results shown in Fig. 7-16 suggest that the code captures the trend in the discharge impedance as the magnetic field and applied voltage are changed; i.e., the discharge current decreases as the magnetic field increases at a given discharge voltage due to the lower electron mobility. However, the code does not predict the correct current-versus-voltage behavior for this thruster at low voltages. Figure 7-17 shows the current-versus-voltage data for one condition in the SPT-60 (a 60-mm channel outside-diameter version described in [4]). As the discharge voltage is decreased below about 200 V, the current initially increases until the energy of the electrons at very low voltage is insufficient to produce high ionization fractions, and the plasma density and discharge current then fall. Improvements in the electron transport physics are

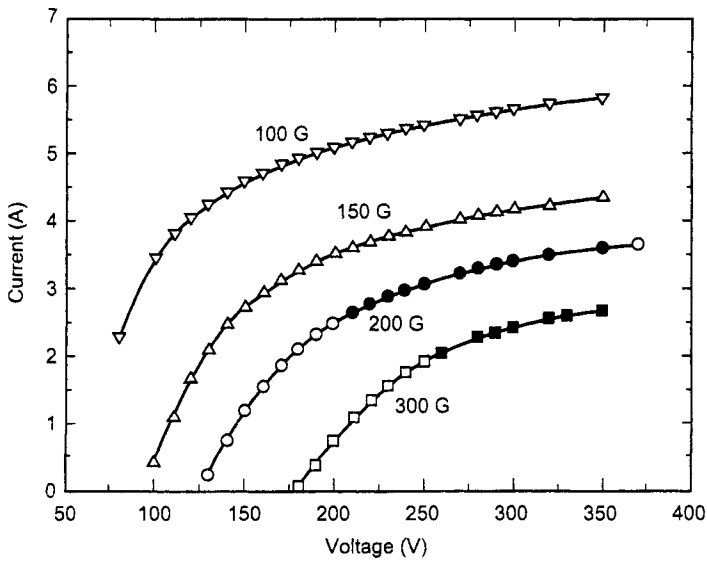

Fig. 7-16. Current-versus-voltage predictions from the 1-D code of Boeuf and Garrigues (from [53]) for the SPT-100, where the solid points indicate regions of predicted oscillations.

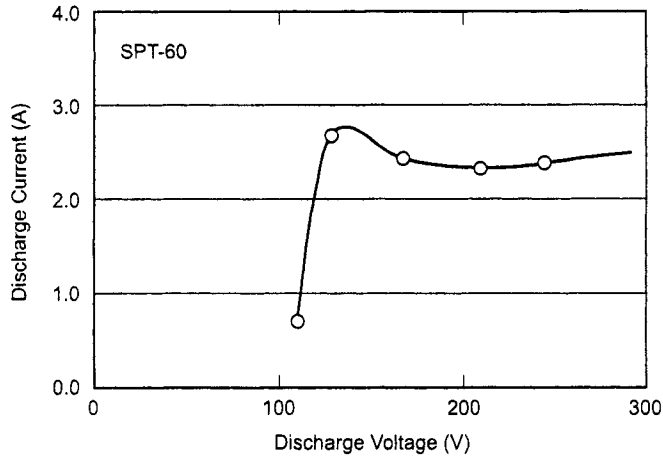

Fig. 7-17. Current versus voltage for one operating condition in the SPT-60 ([redrawn from [4]), showing the non-monotonic current variations usually observed in Hall thrusters at low discharge voltages.

clearly required for the hybrid code to fully predict the Hall thruster behavior. Work continues on developing hybrid codes to better predict the thruster parameters and performance.

7.4.3 Oscillations in Hall Thrusters

Depending on their size and operating characteristics, Hall thrusters have the capability of generating many different waves and instabilities with frequencies from 1 kHz to tens of MHz. A survey of the frequencies of different plasma waves, the characteristic lengths (i.e., of sheaths, etc.) in the thruster, and wave and particle drift velocities expected in typical Hall thrusters was compiled by Choueiri [62]. The most commonly observed oscillations occur in the band of frequencies from 1–30 kHz associated with ionization instabilities and rotational oscillations in the annular discharge channel. Azimuthally propagating waves with frequencies up to 100 kHz that are not associated with ionization instabilities can also occur due to magnetic field gradients [11]. In the range of 100–500 kHz, ion transit time oscillations associated with axial motion of the ions through the ionization and acceleration regions can occur. Above this frequency range, azimuthal drift waves [63] and ion acoustic waves have also been predicted and observed.

The low-frequency time dependence of the ion and neutral behavior can be analyzed with the analytical models [30] by writing the ion conservation equation as

$$\frac{\partial n_i}{\partial t} = n_i n_o \langle \sigma_i v_e \rangle - \frac{n_i v_i}{L}, \tag{7.4-29}$$

and the neutral particle conservation equation as

$$\frac{\partial n_o}{\partial t} = -n_i n_o \langle \sigma_i v_e \rangle + \frac{n_o v_o}{L}, \tag{7.4-30}$$

where v_o is the neutral velocity and L is the axial length of the ionization zone. The perturbed behavior of the ion and neutral densities with time is linearized such that

$$\begin{aligned} n_i &= n_{i,o} + \varepsilon n_i' \\ n_o &= n_{o,o} + \varepsilon n_o', \end{aligned} \tag{7.4-31}$$

where the first term on the right-hand side denotes the unperturbed state. Combining Eqs. (7.4-29), (7.4-30), and (7.4-31) gives

$$\frac{\partial^2 n_i'}{\partial t^2} = n_{i,o} n_{o,o} n_i' \langle \sigma_i v_e \rangle^2 . \tag{7.4-32}$$

This equation represents an undamped harmonic oscillator with a frequency given by

$$f_i = \frac{1}{2\pi} \sqrt{n_{i,o} n_{o,o} \langle \sigma_i v_e \rangle^2} \approx \frac{v_i v_o}{2\pi L}. \tag{7.4-33}$$

The low-frequency oscillatory behavior of Hall thrusters is related to the velocities of the ions and neutrals relative to the scale length of the ionization zone. This indicates that periodic depletion of the neutral gas in the ionization region causes the ion density to oscillate, which impacts the electron conductivity through the transverse magnetic field and thereby the discharge current. The ionization region location can then oscillate axially in the channel on the time scale of neutral replenishment time. The models show [53] that the oscillation depends strongly on the magnetic field strength near the channel exit, and that optimum operation of the thruster generally corresponds to high mass utilization regimes where this instability occurs.

These types of oscillations, which are typically observed in the discharge current when the thrusters are operated in a voltage-regulated mode, have been called "breathing modes" [53] and "predator–prey modes" [30], and an example is shown in Fig. 7-18 for the SPT-100 Hall thruster [55]. The frequency in this experimentally observed example is about 17 kHz. However, the frequency depends on the thruster operating conditions and can range from 10 to 30 kHz for different flow rates, voltages, and magnetic fields. The 1-D numerical code

[53] predictions for the total current, electron current, and ion current at the thruster exit for the SPT-100 are shown in Fig. 7-19. In this case, a frequency of 16 kHz is predicted, in good agreement with the experimental data.

Similar predictions about the low-frequency oscillation behavior of Hall thrusters from the 2-D HPHall code are shown in Fig. 7-20, where the anode current and beam current are plotted versus time. The predicted frequency in this case is 11 kHz, which is less than the value shown in the example of Fig. 7-18. This is likely due to an under-prediction of the electron temperature in the ionization region of the channel [30] by this version of the code.

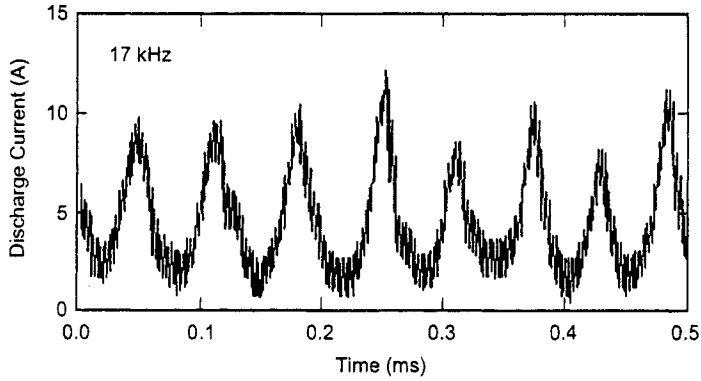

Fig. 7-18. Measured evolution of the discharge current for the SPT-100 (from [55]).

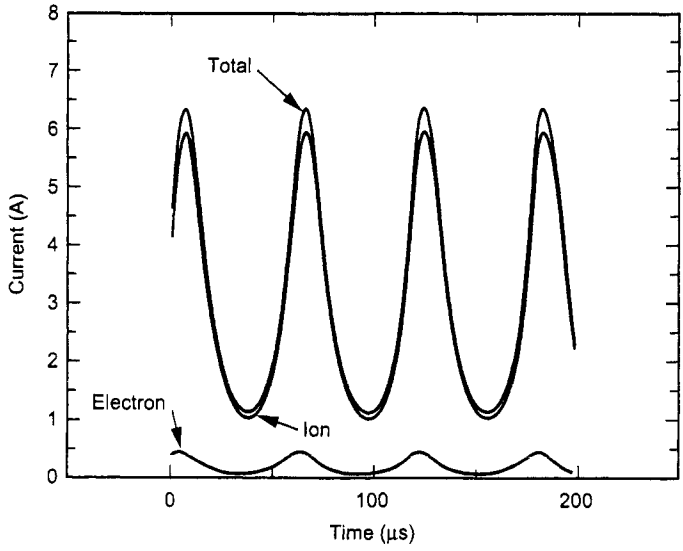

Fig. 7-19. Oscillating current predictions from the 1-D code for the SPT-100 (from [53]).

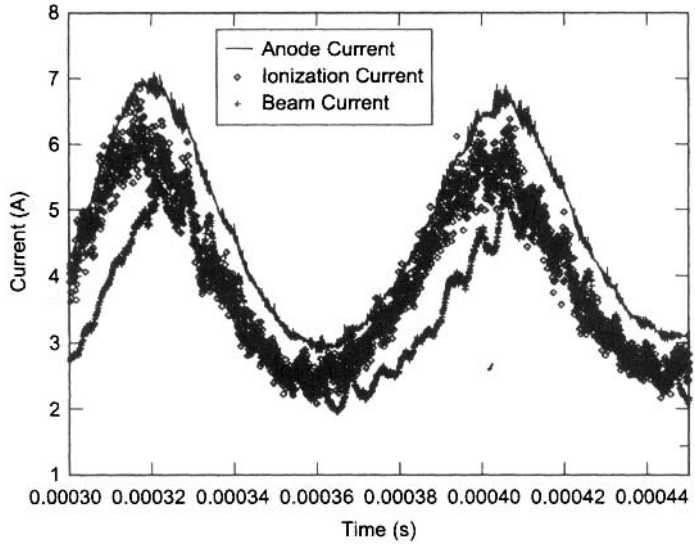

Fig. 7-20. Anode current, ionization, and beam current calculated by HPHall for the SPT-70 Hall thruster (from [30]).

However, the ionization instability driving these oscillations is the same as that analyzed in the 1-D model, and so the behavior of the instability is adequately reproduced by the 2-D model. The low-frequency oscillations can reach 100% of the discharge current depending on the voltage and mass flow (current) for a given thruster design. However, more modern designs, especially those intended for flight, typically have much lower oscillation amplitudes.

7.5 Hall Thruster Life

The operating time and total impulse of a Hall thruster is determined primarily by erosion of the channel wall and the life of the cathode. Hollow cathode wear-out has not represented a life limitation to date because thruster lifetimes of less than 10,000 hours are typical, and robust LaB_6 hollow cathodes have been used in all of the Russian Hall thrusters. Other issues such as deposited material build-up on the electrodes, conductive-flake production, electrical shorting, etc., are also of concern in evaluating the life of a Hall thruster. However, the erosion of the channel wall by ion bombardment sputtering is a very visible process [4] that changes the channel dimensions and ultimately exposes the magnetic circuit, which, when eroded, can degrade the thruster performance. However, life tests of flight thrusters such as the SPT-100 and the PPS-1350 show that they can take hundreds to thousands of hours for magnetic circuit erosion to significantly alter thruster performance. Of greater concern, in this case, is the sputtering of iron from the magnetic circuit, which would have

a significantly higher impact if deposited on most spacecraft components. Therefore, understanding the wall erosion rate and its dependence on thruster materials and operating parameters is of importance in predicting the thruster life and performance over time and its potential impact on the spacecraft.

The erosion rate, given by the rate of change of the wall thickness, w, is

$$\dot{\Re} = \frac{\partial w}{\partial t} = \frac{J_i W}{\rho e A_v} Y(\varepsilon_i), \tag{7.5-1}$$

where J_i is the ion flux, W is the atomic weight, ρ is the material density, e is the ion charge, A_v is Avogadro's number, and Y is the sputtering yield of the material, which is dependent on the ion type and energy ε_i. Since the material properties are known, the issue becomes one of knowing the ion flux, ion energy, and sputtering yield of the wall.

Several analytical models of the Hall thruster have been developed and applied to this problem [37,60,64]. The most accurate predictions have been achieved using a modified 2-D HPHall code [58] to obtain the ion fluxes and energies. The sputtering yield of boron nitride compounds used in dielectric-wall Hall thrusters has been measured by Garnier [65] versus incidence angle and ion energy, and is used in several of these models. However, the Garnier data are at only a few energies and in excess of 300 V. Gamero extrapolated these data to lower energies using the semi-emperical sputtering law scaling of Yamamura and Tawara [66], obtaining the following expression for the sputtering yield in units of mm^3/coulomb:

$$Y = \left(0.0099 + \alpha^2 6.04 \times 10^{-6} - \alpha^3 4.75 \times 10^{-8}\right)\sqrt{\varepsilon_i}\left(1 - \sqrt{\frac{58.6}{\varepsilon_i}}\right)^{2.5}, \tag{7.5-2}$$

where α is the incident angle of the ion. In Eq. (7.5-2), the value 58.6 represents the estimated threshold energy for sputtering required by Yamamura's model. Figure 7-21 shows an example of the yield predicted by Eq. (7.5-2) for two different incidence angles. Equation (7.5-2) was shown [58] to accurately fit the data of Garnier and provides projections of the sputtering yield down to low ion energies predicted by HPHall deeper in the channel.

Figure 7-22 shows the predicted [58] and experimentally measured erosion profiles [67] for the SPT-100 thruster inner and outer channel walls. Good agreement with the observed channel erosion is seen near the thruster exit, and the profiles have the correct functional shape. It is likely that inaccuracies in the extrapolated sputtering yield at low energies caused the disagreement with the

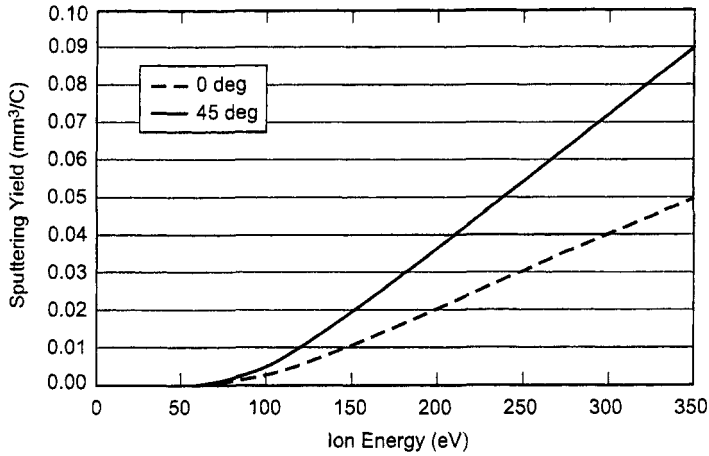

Fig. 7-21. Sputtering yield calculated for singly ionized xenon on $BNSiO_2$ versus ion energy for two incidence angles.

data deep in the channel. This can be remedied by additional sputter-yield measurements at low energy and a refinement of the sputtering yield in Eq. (7.5-2).

It is possible to develop some simple scaling rules for Hall thruster erosion in the magnetized plasma region near the exit plane. It was estimated in Section 7.3.4 that the ion flux to the wall in dielectric-wall Hall thrusters was about 10% of the beam current. It can be assumed that the energy of the ion flux to the wall is related to the beam energy, which is proportional to the discharge voltage. An examination of Fig. 7-21 shows that the sputtering yield is essentially a linear function of the ion energy. The erosion rate in Eq. (7.5-1) then becomes

$$\dot{\Re} \propto K \frac{I_b}{A_w} V_d = K \frac{I_d V_d}{\eta_b A_w}, \tag{7.5-3}$$

where K is a constant, A_w is the wall area, and Eq. (7.3-10) has been used for the beam current efficiency. Equation (7.5-3) shows that the erosion rate of the thruster wall is proportional to the power density in the accelerator channel [4]. This indicates that larger Hall thrusters are required to increase the power for a given operation time as determined by the allowable erosion of the insulator wall thickness. A good rule-of-thumb for the relationship of operation time over a reasonable throttle range of a given Hall thruster design is

$$\text{power} * \text{operation time} \approx \text{constant}.$$

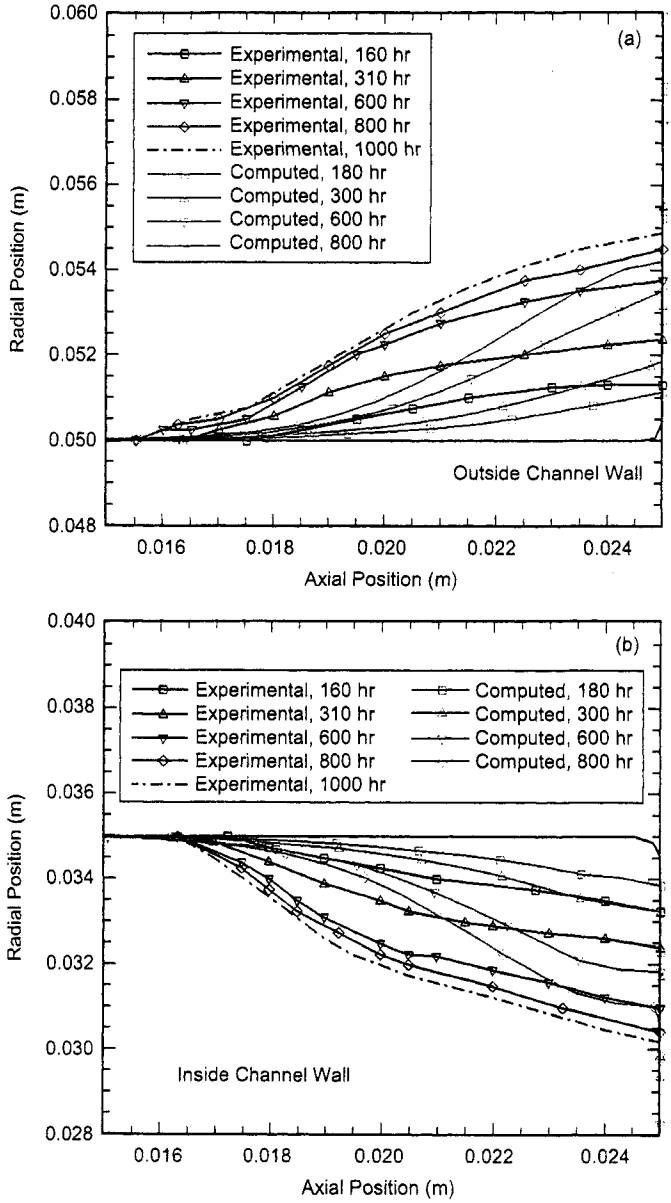

Fig. 7-22. Erosion pattern predicted by the modified HPHall code and measured for the SPT-100 thruster (redrawn from [58]).

Over a limited range, the thrust from a Hall thruster is proportional to the discharge power, and so

$$\text{thrust} * \text{operation time} \approx \text{constant}.$$

This suggests that the total impulse is essentially a constant for a given thruster design. Therefore, operating at lower thrust in throttled mission profiles will result in longer thruster operation time. However, if the throttling is too deep, the thruster performance will degrade (requiring higher input power to produce a given thrust) and the above relationship is no longer valid. Hall thruster throttle ranges of over 10:1 have been demonstrated with good performance, depending on the thruster design.

Finally, the life of TAL thrusters has not been as extensively investigated as the Russian SPT thrusters. The erosion of the channel guard rings has been identified as the primary life-limiting mechanism [29], and alternative materials were suggested to extend the thruster life by reducing the sputtering yield. Since the wall/guard ring is biased at cathode potential, the incident ion energy along the wall depends on the potential profile in the thruster channel and past the exit plane. This certainly influenced the selection of the TAL anode placement and the design of the anode/channel region to minimize the ion energy (and flux) to the walls. The dielectric-wall Hall thrusters limited the ion energy to the floating potential ($\approx 6T_e$ for xenon) for wall materials with very low secondary electron yield, and to lower energies with materials that have secondary electron yields approaching or exceeding one at the electron temperatures of typical operation. The sheath potential at the wall is likely on the order of $3T_e \approx 0.3V_d$ due to space charge and non-Maxwellian electron distribution function effects. However, the lower sheath potential at the wall increases the electron flux, which results in increased power loading at the wall.

The wall material selection, therefore, is a trade off between efficiency and life. Dielectric walls reduce the bombarding ion energy of the wall at the expense of higher electron fluxes and higher power loading. Metallic-wall Hall thrusters have higher ion energies to the wall and therefore sputter-erosion life issues, and so they have to compensate with geometry changes to obtain the desired life. This results in higher heat fluxes to the anode, which dominates the TAL efficiency. An increase in the power of both types of thrusters also requires increases in the thruster size to obtain the same or longer lifetimes. Therefore, Hall thruster design, like ion thruster design, is a trade off between performance and life.

References

[1] S. D. Grishin and L. V. Leskov, *Electrical Rocket Engines of Space Vehicles*, Moscow, Russia: Mashinostroyeniye Publishing House (published in Russian) , 1989.

[2] H. R. Kaufman, "Technology of Closed-Drift Thrusters," *AIAA Journal*, vol. 23, no. 1, pp. 78–87, 1985.

[3] V. V. Zhurin, H. R. Kaufman, and R. S. Robinson, "Physics of Closed Drift Thrusters," *Plasma Sources Science and Technology*, vol. 8, no. 1, pp. R1–R20, 1999.

[4] V. Kim, "Main Physical Features and Processes Determining the Performance of Stationary Plasma Thrusters," *Journal of Propulsion and Power*, vol. 14, no. 5, pp. 736–743, 1998.

[5] A. I. Morosov and V. V. Savelyev, "Fundamentals of Stationary Plasma Thruster Theory," in *Reviews of Plasma Physics*, edited by B. B. Kadomtsev and V. D. Shafranov, vol. 21, New York: Kluwer Academic/Plenum Publishers, 2000.

[6] J. R. Brophy, J. W. Barnett, J. M. Sankovic, and D. A. Barnhart, "Performance of the Stationary Plasma Thruster: SPT-100," AIAA-92-3155, 28th Joint Propulsion Conference, Nashville, Tennessee, July 6–8, 1992.

[7] B. A. Arhipov, L. Z. Krochak, S. S. Kudriavcev, V. M. Murashko, and T. Randolph, "Investigation of the Stationary Plasma Thruster (SPT-100) Characteristics and Thermal Maps at the Raised Discharge Power," AIAA-98-3791, 34th Joint Propulsion Conference, Cleveland, Ohio, July 13–15, 1998.

[8] L. B. King, "A Re-examination of Electron Motion in Hall Thruster Fields," IEPC-2005-258, 29th International Electric Propulsion Conference, Princeton University, New Jersey, October 31–November 4, 2005.

[9] R. R. Hofer, R. S. Jankovsky, and A. D. Gallimore, "High-Specific Impulse Hall Thrusters, Part 1: Influence of Current Density and Magnetic Field," *Journal of Propulsion and Power*, vol. 22, no. 4, pp. 721–731, 2006.

[10] R. R. Hofer and A. D. Gallimore, "High-Specific Impulse Hall Thrusters, Part 2: Efficiency Analysis," *Journal of Propulsion and Power*, vol. 22, no. 4, pp. 732–740, 2006.

[11] R. R. Hofer, "Development and Characterization of High-Efficiency, High-Specific Impulse Xenon Hall Thrusters," Ph.D. Dissertation, Aerospace Engineering, University of Michigan, Ann Arbor, Michigan, 2004.

[12] A. I. Morozov, Y. V. Esipchuk, A. M. Kapulkin, V. A. Nevrovskii, and V. A. Smirnov, "Effect of the Magnetic Field on a Closed-Electron-Drift Accelerator," *Soviet Physics Technical Physics*, vol. 17, no. 3, 1972.

[13] Y. Raitses, J. Ashkenazy, and M. Guelman, "Propellant Utilization in Hall Thrusters," *Journal of Propulsion and Power*, vol. 14, no. 2, pp. 247–253, 1998.

[14] L. A. Dorf, Y. F. Raitses, A. N. Smirnov, and N. J. Fisch, "Anode Fall Formation in a Hall Thruster," AIAA-2004-3779, 40th Joint Propulsion Conference, Ft. Lauderdale, Florida, July 11–14, 2004.

[15] L. Dorf, Y. Raitses, and N. J. Fisch, "Experimental Studies of Anode Sheath Phenomena in a Hall Thruster Discharge," *Journal of Applied Physics*, article 103309, part 1, vol. 97, no. 10, 2005.

[16] L. Dorf, Y. Raitses, and N. J. Fisch, "Effect of Magnetic Field Profile on the Anode Fall in a Hall-Effect Thruster Discharge," *Physics of Plasmas*, article 057104, vol. 13, no. 5, 2006.

[17] R. R. Hofer, P. Y. Peterson, A. D. Gallimore, and R. S. Jankovsky, "A High Specific Impulse Two-Stage Hall Thruster with Plasma Lens Focusing," IEPC-2001-036, 27th International Electric Propulsion Conference, Pasadena, California, October 14–19, 2001.

[18] J. A. Linnell and A. D. Galimore, "Krypton Performance Optimization in High-Voltage Hall Thrusters," *Journal of Propulsion and Power*, vol. 22, no. 4, pp. 921–925, 2006.

[19] J. A. Linnell and A. D. Galimore, "Efficiency Analysis of a Hall Thruster Operating with Krypton and Xenon Thrusters," *Journal of Propulsion and Power*, vol. 22, no. 6, pp. 1402–1412, 2006.

[20] Y. Daren, D. Yongjie, and Z. Shi, "Improvement on the Scaling Theory of the Stationary Plasma Thruster," *Journal of Propulsion and Power*, vol. 21, no. 1, pp. 139–143,2005.

[21] V. Kim, G. Popov, B. Arkhipov, V. Murashko, O. Gorshkov, A. Koroteyev, V. Garkusha, A. Semenkin, and S. Tverdokhlebov, "Electric Propulsion Activity in Russia," IEPC-2001-005, 27th International Electric Propulsion Conference, Pasadena, California, October 14–19, 2001.

[22] A. I. Bugrova, N. Maslennikov, and A. I. Morozov, "Similarity Laws for the Global Properties of a Hall Accelerator," *Journal of Technical Physics*, vol. 61, no. 6, pp. 45–51, 1991.

[23] V. Khayms and M. Martinez-Sanchez, "Design of a Miniaturized Hall Thruster for Microsatellites," AIAA-1996-3291, 32nd Joint Propulsion Conference, Lake Buena Vista, Florida, July 1–3, 1996.

[24] O. Gorshkov, "Russian Electric Propulsion Thruster Today," *Russian Space News*, vol. 61, no. 7, pp. 5–11, 1999.

[25] A. Smirnov, Y. Raitses, and N.J. Fisch, "Parametric Investigations of Miniaturized Cylindrical and Annular Hall Thrusters," *Journal of Applied Physics*, vol. 92, no. 10, pp. 5673–5679, 2002.

[26] M. Keidar, A. D. Gallimore, Y. Raitses, and I. D. Boyd, "On the Potential Distribution in Hall Thrusters," *Applied Physics Letters*, vol. 85, no.13, pp. 2481–2483, 2004.

[27] L. B. King and A. D. Gallimore, "Ion Energy Diagnostics in the Plasma Exhaust Plume of a Hall Thruster," *Journal of Propulsion and Power*, vol. 16, no. 5, pp. 916–922, 2000.

[28] J. E. Pollard, K. D. Diamant, V. Khayms, L. Werthman, D. Q. King, and K. H. Degrees, "Ion Flux, Energy and Charge State Measurements for the BPT-4000 Hall Thruster," AIAA-2001-3351, 37th Joint Propulsion Conference, Salt Lake City, Utah, July 8–11, 2001.

[29] C. E. Garner, J. R. Brophy, J. E. Polk, S. Semenkin, V. Garkusha, S. Tverdokhlebov, and C. Marrese, "Experimental Evaluation of Russian Anode Layer Thrusters," AIAA-1994-3010, 30th Joint Propulsion Conference, Indianapolis, Indiana, June 27–29, 1994.

[30] J. M. Fife, M. Martinez-Sanchez, and J. Szabo "A Numerical Study of Low-Frequency Discharge Oscillations in Hall Thrusters," AIAA-97-3052, 33rd Joint Propulsion Conference, Seattle, Washington, July 6–9, 1997.

[31] E. Y. Choueiri, "Fundamental Difference Between Two Variants of Hall Thrusters: SPT and TAL," *Physics of Plasmas*, vol. 8, no. 11, pp. 5025–5033, 2001.

[32] J. P. Bugeat and C. Koppel, "Development of a Second Generation of SPT," IEPC-95-035, 24th International Electric Propulsion Conference, Moscow, Russia, 1995.

[33] N. Gascon, M. Dudeck, and S. Barral, "Wall Material Effects in Stationary Plasma Thrusters: 1. Parametric Studies of an SPT-100," *Physics of Plasmas*, vol. 10, pp. 4123–4136, 2003.

[34] J. M. Fife and M. Martinez-Sanchez, "Comparison of Results from a Two-dimensional Numerical SPT Model with Experiment," AIAA-96-3197, 32nd Joint Propulsion Conference, Lake Buena Vista, Florida, July 1–3, 1996.

[35] J. M. Haas, "Low-Perturbation Interrogation of the Internal and Near-Field Plasma Structure of a Hall Thruster Using a High-speed Probe Positioning System," Ph.D. Dissertation, University of Michigan, Ann Arbor, Michigan, 2001.

[36] J. A. Linnell and A. D. Gallimore, "Internal Langmuir Probe Mapping of a Hall Thruster with Xenon and Krypton Propellant," AIAA-2006-4470, 42nd Joint Propulsion Conference, Sacramento, California, July 9–12, 2006.

[37] E. Ahedo, P. Martinez-Cerezo, and M. Martinez-Sanchez, "One-Dimensional Model of the Plasma Flow in a Hall Thruster," *Physics of Plasmas*, vol. 8, no. 6, pp. 3058–3068, 2001.

[38] E. Ahedo, "Presheath/Sheath Model with Secondary Electron Emission from Two Parallel Walls," *Physics of Plasmas*, vol. 9, pp. 4340–4347, 2002.

[39] G. D. Hobbs and J. A. Wesson, "Heat Flow Through a Langmuir Sheath in the Presence of Electron Emission," *Plasma Physics*, vol. 9, pp. 85–87, 1967.

[40] V. Baranov, Y. Nazarenko, and V. Petrosov, "The Wear of the Channel Walls in Hall Thrusters", IEPC-2001-005, 27th International Electric Propulsion Conference, Pasadena, California, October 14–19, 2001.

[41] E. Ahedo, J. M. Gallardo, and M. Martinez-Sanchez, "Effects of the Radial Plasma-Wall Interaction on the Hall Thruster Discharge," *Physics of Plasmas*, vol. 10, no. 8, pp. 3397–3409, 2003.

[42] J. M. Fife and S. Locke, "Influence of Channel Insulator Material on Hall Thruster Discharges: A Numerical Study," AIAA-2001-1137, 39th Aerospace Sciences Meeting, Reno, Nevada, January 8–11, 2001.

[43] Y. Raitses, D. Staack, M. Keidar, and N. J. Fisch, "Electron-Wall Interaction in Hall Thrusters," 057104, *Physics of Plasmas*, vol. 12, 2005.

[44] I. D. Kaganovich, Y. Raitses, D. Sydorenko, and A. Smolyakov, "Kinetic Effects in Hall Thruster Discharge," AIAA-2006-3323, 42th Joint Propulsion Conference, Sacramento, California, July 9–12, 2006.

[45] N. B. Meezan and M. A. Capelli, "Kinetic Study of Wall Collisions in a Coaxial Hall Discharge," *Physical Review E*, 036401, vol. 66, 2002.

[46] E. Ahedo and F. I. Parra, "Partial Trapping of Secondary Electron Emission in a Hall Thruster Plasma," *Physics of Plasmas*, 073503, vol. 12, no. 7, 2005.

[47] E. Ahedo and V. DePablo, "Effects of Electron Secondary Emission and Partial Thermalization on a Hall Thruster," AIAA-2006-4328, 42nd Joint Propulsion Conference, Sacramento, California, July 9–12, 2006.

[48] M. T. Domonkos, A. D. Gallimore, C. M. Marrese, and J. M. Haas, "Very-Near-Field Plume Investigation of the Anode Layer Thruster," *Journal of Propulsion and Power*, vol. 16, pp. 91–98, 2000.

[49] A. V. Semenkin, S. O. Tverdokhlebov, V. I. Garkusha, A. V. Kochergin, G. O. Chislov, B. V. Shumkin, A. V. Solodukhin, and L. E. Zakharenkov, "Operating Envelopes of Thrusters with Anode Layer," IEPC-2001-013, 27th International Electric Propulsion Conference, Pasadena, California, October 14–19, 2001.

[50] D. T. Jacobson, R. S. Jankovsky, and R. K. Rawlin, "High Voltage TAL Performance," AIAA-2001-3777, 37th Joint Propulsion Conference, Salt Lake City, Utah, July 8–11, 2001.

[51] A. E. Solodukhin, A. V. Semenkin, S. O. Tverdohlebov, and A. V. Kochergin, "Parameters of D-80 Anode Layer Thruster in One and Two-Stage Operation Modes," IEPC-2001-032, 27th International Electric Propulsion Conference, Pasadena, California, October 14–19, 2001.

[52] M. Hirakawa and Y. Arakawa, "Numerical Simulation of Plasma Particle Behavior in a Hall Thruster," AIAA-96-3195, 32nd Joint Propulsion Conference, Lake Buena Vista, California, July 1–3, 1996.

[53] J. P. Boeuf and L. Garrigues, "Low Frequency Oscillations in a Stationary Plasma Thruster," *Journal of Applied Physics*, vol. 84, pp. 3541–3554, 1998.

[54] E. Ahedo, "One-Dimensional Plasma Structure in Hall Thrusters," AIAA-98-8788, 34th Joint Propulsion Conference, Cleveland, Ohio, July 13–15, 1998.

[55] I. Mikellides, I. Katz, and M. Mandell, "A 1-D Model of the Hall-Effect Thruster with an Exhaust Region," AIAA-2001-3505, 37th Joint Propulsion Conference, Salt Lake City, Utah, July 8–11, 2001.

[56] S. Barral, K. Makowski, Z. Peradzynski, N. Gascon, and M. Dudeck, "Wall Material Effects in Stationary Plasma Thrusters. II. Near-Wall and In-Wall Conductivity," *Phys. Plasmas*, vol. 10, no. 10, pp. 4137–4152, 2003.

[57] F. I. Parra, E. Ahedo, J. M. Fife, and M. Martinez-Sanchez, "A Two-Dimensional Hybrid Model of the Hall Thruster Discharge," *Journal of Applied Physics*, 023304, vol. 100, 2006.

[58] M. Gamero-Castano and I. Katz, "Estimation of Hall Thruster Erosion Using HPHall," IEPC-2005-303, 29th International Electric Propulsion Conference, Princeton University, New Jersey, October 31–November 4, 2005.

[59] R. R. Hofer, I. Katz, I. G. Mikellides, and M. Gamero-Castano, "Heavy Particle Velocity and Electron Mobility Modeling in Hybrid-PIC Hall Thruster Simulations," AIAA-2006-4658, 42nd Joint Propulsion Conference, Sacramento, California, July 9–12, 2006.

[60] D. Manzella, J. Yim, and I. Boyd, "Predicting Hall Thruster Operational Lifetime," AIAA-2004-3953, 40th Joint Propulsion Conference, Ft. Lauderdale, Florida, July 11–14, 2004.

[61] C. Boniface, L. Garrigues, G. J. M. Hagelaar, and J. P. Boeuf, "Anomalous Cross Field Electron Transport in a Hall Effect Thruster," *Applied Physics Letters*, 161503, vol. 89, 2006.

[62] E. Y. Choueiri, "Plasma Oscillations in Hall Thrusters," *Phys. of Plasmas*, vol. 8, no. 4, pp. 1411–1426, 2001.

[63] A. Ducrocq, J. C. Adam, A. Heron, and G. Laval, "High-Frequency Electron Drift Instability in the Cross-field Configuration of Hall Thrusters," *Physics of Plasmas*, 102111, vol. 13, 2006.

[64] V. Abgaryan, H. Kaufman, V. Kim, D. Ovsyanko, I. Shkarban, A. Semenov, A. Sorokin, and V. Zhurin, "Calculation Analysis of the Erosion of the Discharge Chamber Walls and Their Contamination During Prolonged SPT Operation," AIAA-94-2859, 30th Joint Propulsion Conference, Indianapolis, Indiana, June 27–29, 1994.

[65] Y. Garnier, V. Viel, J. F. Roussel, and J. Bernard, "Low Energy Xenon Ion Sputtering of Ceramics Investigated for Stationary plasma Thrusters," *Journal of Vacuum Science Technology A*, vol. 17, pp. 3246–3254, 1999.

[66] Y. Yamamura and H. Tawara, "Energy Dependence of Ion-Induced Sputtering from Monatomic Solids at Normal Incidence," *Atomic Data and Nuclear Data Tables*, vol. 62, pp. 149–253, 1996.

[67] S. K. Absalamov, V. Andrew, T. Colberi, M. Day, V. V. Egorov, R. U. Gnizdor, H. Kaufman, V. Kim, A. I. Korakin, K. N. Kozubsky, S. S. Kudravzev, U. V. Lebedev, G. A. Popov, and V. V. Zhurin, "Measurement of Plasma Parameters in the Stationary Plasma Thruster (SPT-100) Plume and its Effect on Spacecraft Components," AIAA-1992-3156, 28th Joint Propulsion Conference, Nashville, Tennessee, July 6–8, 1992.

Problems

1. You want to design an experimental Hall thruster to operate from 100 to 800 V and from 100 to 300 gauss. Assuming that the electron temperature is always about 10% of the discharge voltage, what are the minimum and maximum lengths of the magnetized region in the channel to have a factor of 5 margin against electron and ion orbit limits? Neglect collisions.

2. Derive Eq. (7.3-42).

3. A Hall thruster has a plasma channel with a 15-cm outer diameter and a 10-cm inner diameter. Measurements made on the thruster indicate that the xenon plasma density in the channel is 5×10^{17} ions per m^3, the electron temperature T_e is 20 eV, and the radial magnetic field B_r is 200 gauss (0.02 tesla). If the thruster is operated at a discharge voltage of 300 V,
   a. What is the beam power?
   b. What is the electron Larmour radius r_L?
   c. What is the electron Hall parameter Ω_e?
   d. If the thrust correction factor $\gamma = 0.9$ and the mass utilization efficiency $\eta_m = 0.8$, what is the thrust and Isp?
   e. What is the Hall current?
4. A xenon Hall thruster has boron nitride walls with a linearly varying secondary electron yield with a value of 0.5 at zero electron energy and 2 for an electron energy of 100 eV.
   a. What is the equation for the secondary electron yield in terms of the electron energy?
   b. Find the equation for the secondary electron yield for a Maxwellian distribution of electron energies [hint: use Eq. (C-5)] in terms of the electron temperature T_e.
   c. What is the electron temperature at which the electron flow to the wall is space-charge limited?
   d. Assuming $n_e v_B / n_i v_i = 0.5$, what is the maximum sheath potential for non-space-charge-limited flow (T_e less than the value found in part b)?
5. Assume that all the ions in a Hall thruster are produced by the Hall current ionizing the neutral gas in the channel.
   a. Neglecting the ion current to the wall as small so that all the ions produced become beam ions, what is the ratio of the Hall current to the beam current if the average electron temperature is 25 eV? (Hint: write the ion production rate in terms of the Hall current and use Appendix E for ionization and excitation collision cross sections.)
   b. For a xenon ion thruster with a mean radius of 9 cm, a radial magnetic field of 150 G, and a discharge voltage of 300 V, what is the ratio of the Hall current to the beam current?

6. A xenon Hall thruster has a channel outside diameter of 10 cm and a channel width of 3.5 cm with $BNSiO_2$ walls. Assume a plasma density of 2×10^{17} m^{-3} and an electron temperature of 20 eV in the channel with the majority of the plasma in contact with 1 cm of the wall axially.
   a. What is the electron current to the wall?
   b. What is the net electron current to the wall?
   c. What is the power deposited on the wall associated with this electron current?
   d. What is the power deposited on the wall associated with ion current?

7. Assume that the thruster in Problem 6 has alumina walls and produces 3.5 A of beam current at 400 V with an electron temperature in the channel of 15 eV. The thruster also has a beam current utilization efficiency $\eta_b = 0.5$.
   a. What is the power into the discharge?
   b. What is the total power into the alumina walls for a contact length L = 2 cm?
   c. Assuming that the electron temperature at the anode is 5 eV, the mass utilization efficiency is 90%, and the thrust correction factor $\gamma = 0.9$, and neglecting all other power loss channels, what is the thruster efficiency?
   d. For a beam voltage utilization efficiency of 0.9, how much thrust and Isp is produced?

8. The electron current to the anode in a Hall thruster can be estimated from the perpendicular electron flux diffusing through the plasma channel.
   a. Neglecting the pressure gradient terms, derive an expression for the current toward the anode in terms of the collision frequency in the channel plasma.
   b. For the thruster in Problem 7 with a transverse magnetic field of 150 G and an axial electric field of 3×10^4 V/m, what is the anode current if only classic electron–ion collisions are considered?
   c. The effective wall collision frequency can be estimated as the electron current to the wall times the secondary electron yield and divided by the total number of particles in the plasma ($\nu_w = \gamma I_{ew} / N$, where N is approximately the plasma density times the channel cross-sectional area times the plasma length L). Derive an expression for the transverse electron current due to the electron-wall collisions in terms of the electron current to the wall.

d. What is the total transverse electron current for this thruster example, using $L = 1$ cm for the bulk of the plasma density?

e. If the walls are made of $BNSiO_2$, what is the anode current? Why does it depend so strongly on the wall material?

9. Calculate the power lost to the wall in a xenon TAL thruster with stainless steel walls that has a plasma density at the sheath edge of 2×10^{17} m^{-3} and an electron temperature of 20 eV. The channel has a 12-cm outside diameter, an 8-cm inside diameter, and is 0.5-cm long. Which power loss channel (ions or electrons) is larger?

10. The life of a TAL thruster is limited primarily by the ion sputtering of the metallic guard rings next to the thruster exit. Assume a TAL has a plasma density near the wall of 10^{17} m^{-3} and an electron temperature of 25 eV.

a. For stainless steel walls, what is the ion current density to the walls (the guard rings) and the sheath potential?

b. Assuming that the stainless-steel sputtering yield is about 0.1 atoms per incident ion at the sheath voltage found in (a), what is the life in hours of the TAL if 2-mm thickness of the stainless-steel guard ring material can be eroded away?

c. Assume that the wall material has been changed to graphite with a secondary electron yield of about 0.5. What is the sheath potential at the wall?

d. Assuming that the graphite sputtering yield is about 5×10^{-3} atoms per incident ion at the sheath voltage found in (c), what is the life in hours of the TAL if 1-mm thickness of the graphite guard ring material can be eroded away?

Fundamentals of Electric Propulsion: Ion and Hall Thrusters
by Dan M. Goebel and Ira Katz
Copyright © 2008 John Wiley & Sons, Inc.

Chapter 8
Ion and Hall Thruster Plumes

8.1 Introduction

Electric propulsion offers advantages for many missions and applications, but like many spacecraft systems, integration of electric thrusters on spacecraft can present significant systems engineering challenges. Assessing thruster plume interactions with the spacecraft is key in determining thruster location and other spacecraft configuration issues, often requiring trades between thrust efficiency and the life of other subsystems, such as the solar arrays.

Electric thruster plumes consist of energetic ions, un-ionized propellant neutral gas, low energy ions and electrons, and sputtered thruster material. Spacecraft systems engineers must account for the interaction between each of the plume components and other spacecraft systems. For north–south station keeping on geosynchronous communications satellites, by far the largest application of electric propulsion, the potential for plume impingement on solar arrays is a significant issue.

As shown in Fig. 8-1, geosynchronous satellites are in a circular orbit coplanar with the Earth's equator, with an orbital period of exactly one day. The satellite appears stationary to an observer on the Earth; however, the Earth's equator is tilted by 28 deg with respect to the Earth's orbit around the Sun. The plane of the Earth's orbit is called the ecliptic plane. The Sun's gravity pulls on a geosynchronous satellite to change the satellite's plane toward the ecliptic. If the orbital plane were allowed to change, the satellite would appear from the ground to move north and south in the sky. Optimal communication would then require the ground-based antennas to constantly scan north and south in order to track the satellite, defeating the big advantage of geosynchronous satellites. Electric thrusters are used on satellites to counter the Sun's pull and prevent the orbital plane from changing. This application is referred to as "north–south

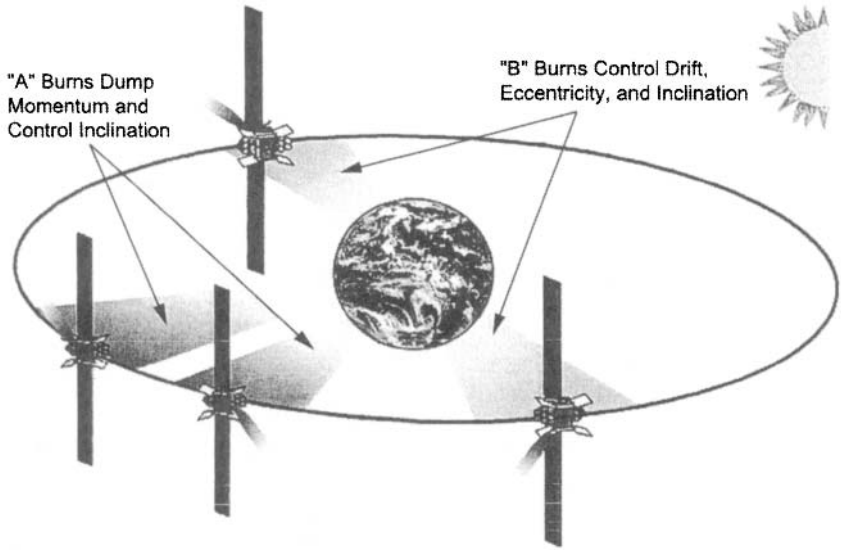

Fig. 8-1. Illustration of the burn arcs of the ion thrusters used for electric propulsion station keeping on Boeing satellites [1,2].

station keeping," and Fig. 8-1 shows the Hughes/Boeing patented [1] strategy for this function.

Most modern satellites are three-axis stabilized with solar arrays that rotate to keep the cells pointed toward the Sun. From a thrust perspective, north–south station keeping is accomplished most efficiently if the thrusters point in the north and south directions. In geosynchronous orbit, the solar array axis of rotation points north and south, directly in the path of plumes from north–south station-keeping thrusters. The thruster energetic ion beam would impinge on the solar arrays and quickly damage them, dramatically shortening satellite life.

The usual solution is to mount thrusters such that the resultant force is in the north–south direction, but each plume is at an angle with respect to the solar array axis. The larger the angle, the greater the thrust loss for station keeping, which leads to requirements for larger thrusters and more propellant mass; the smaller the angle, the greater the array damage, which reduces satellite life. This trade between north–south thrust efficiency and solar array life requires detailed knowledge of thruster plumes and their interactions.

Electric thrusters used for primary propulsion, such as those on the National Aeronautics and Space Administration (NASA) Dawn mission to the asteroid belt, can also create issues associated with plume impact on the spacecraft solar

arrays, exposed components, and scientific instruments. Thruster plumes and their interactions with the spacecraft must be understood and accommodated in order for the spacecraft to perform to specification for the required mission life.

8.2 Plume Physics

The thruster plume is composed of ions and electrons of various energies and some neutral gas. The energetic beam ions accelerated by the thruster fields are the dominant ion species and the major source of thrust. The velocity and angular distributions of these ions can be measured in the laboratory and calculated by the thruster computer models discussed in previous chapters. For ion thrusters, where the accelerating voltages are a thousand volts or more, the weak plume electric fields have little influence on energetic ion trajectories. In this case, the challenge is usually determining the ion trajectories from the shaped-grid accelerator structure. However, for Hall thrusters, where the accelerating voltages are a few hundred volts, the plume electric fields can significantly broaden the energetic ion plume.

The second source of ions is due to charge-exchange reactions between beam ions and neutral xenon gas. The neutral gas is due to un-ionized particles leaving both the thruster and the neutralizer (hollow cathode), and, in the case of laboratory measurements, background neutrals present in the vacuum chamber. Charge-exchange reactions have usually been associated with inelastic collisions processes yielding low-energy ions at large angles with respect to the main-beam direction. However, as thruster voltages increase to provide higher specific impulse (Isp), the energy of these scattered ions can become significant. The total plume plasma density, including all three ion components, is shown schematically in Fig. 8-2 for a 4-kW Hall thruster.

8.2.1 Plume Measurements

Thruster plume characteristics have been measured extensively in the laboratory and in space on a few spacecraft. In the laboratory, most measurements have been of the ion velocities and densities, and some thruster erosion products, but not of the un-ionized neutral gas, which is in most cases dominated by background gas in the test chambers. The balance of the thruster gas flow and the speed of the test facility's vacuum pumps determine the background gas pressure. The maximum facility pressure during high power testing is usually limited to less than 10^{-4} torr. Therefore, the density of un-ionized propellant from Hall and ion thrusters is greater than the background only within a few centimeters of the thruster.

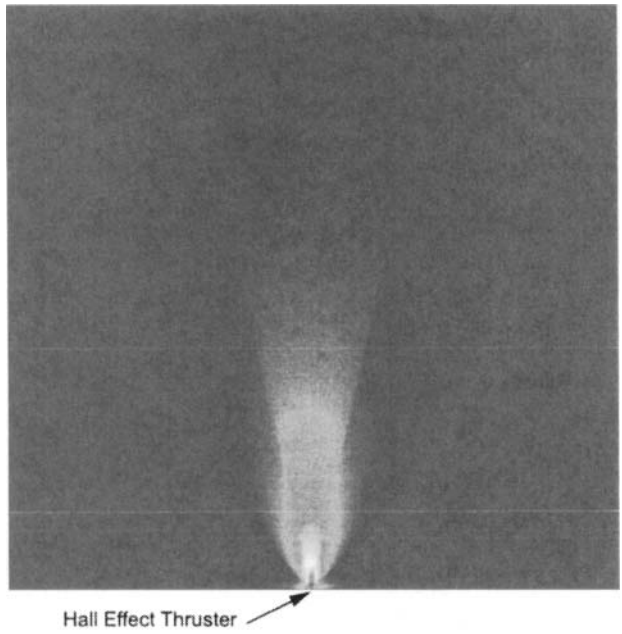

Fig. 8-2. Total ion density in the plume of a 4-kW Hall thruster.

The dominance of test-facility background neutral gases makes it difficult to directly measure in a laboratory the secondary plasma environment, which consists of the ions generated by charge exchange and/or elastic scattering with neutrals, that would be seen on a spacecraft. Spacecraft system engineers, therefore, use detailed models of the plume and secondary ion-generation to predict the in-flight plasma environment. These models [3–6] have been validated with flight data from a few electric propulsion spacecraft.

8.2.2 Flight Data

The first in-flight measurements of the plasma environment generated by an ion thruster were made on NASA's Deep Space 1 (DS1) spacecraft [7]. The NASA Solar Electric Propulsion Technology Applications Readiness (NSTAR) diagnostics package that flew on DS1 included contamination monitors, plasma sensors, magnetometers, and a plasma-wave antenna. The plasma sensors and contamination monitors were mounted on the remote sensor unit (RSU) [7] as shown in Fig. 8-3. The measured plasma density was an order of magnitude lower than that measured during ground tests, but it was in good agreement with model predictions. Figure 8-4 shows a comparison of the ion fluxes

measured during the DS1 mission by the remote sensing unit and the computed values [8]. The ion fluxes at the sensor location are primarily the result of charge exchange between beam ions and un-ionized propellant in the beam.

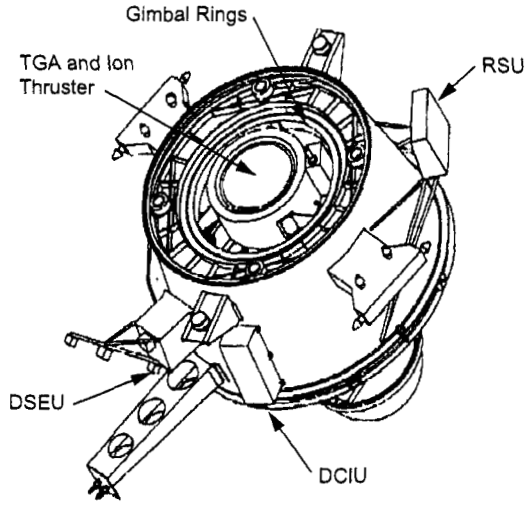

Fig. 8-3. Location of the remote sensor unit on DS1 with respect to the ion thruster.

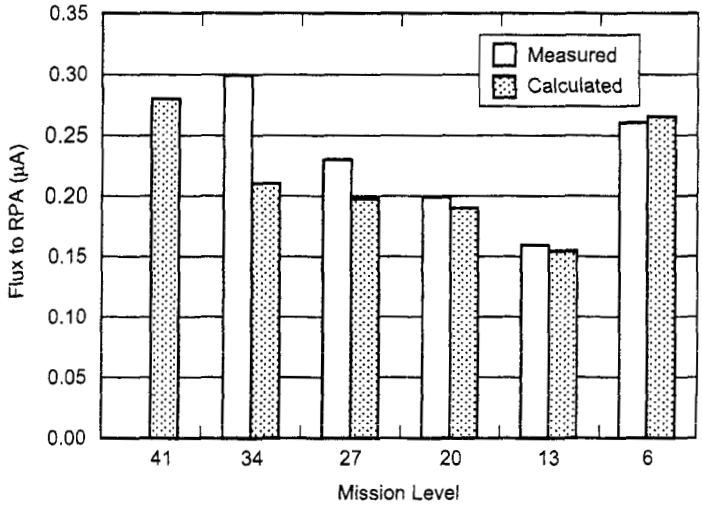

Fig. 8-4. Calculated and measured charge-exchange ion fluxes in the plume of NSTAR at various operating points (from [8]).

Measurements of the plume and secondary ions from Hall thrusters were carried out on a Russian communications satellite, Express-A3 [5]. The satellite had instruments to measure ion fluxes both on the spacecraft body, 90 deg from the thrust direction, and on the solar arrays. These diagnostics monitored effects from the central beam over a cone with a half-angle of about 40 deg. The Stationary Plasma Thruster (SPT)-100 Hall thruster plume calculated using the Electric Propulsion Interactions Code (EPIC) [6,8] is shown in Fig. 8-5. As was the case for ion thrusters, the measured secondary ion fluxes were an order of magnitude less than fluxes measured in ground-based chambers, but, again, in good agreement with plume models. The accuracy of the models is illustrated in Fig. 8-6, where the current density measurements on the Express-A spacecraft are compared with the computed values.

8.2.3 Laboratory Plume Measurements

While the flight measurements show the ability of the models to predict thruster-generated plasma environments, tests in ground-based chambers provide much more detailed measurements than those made in space.

Experiments conducted by The Aerospace Corporation for the Lockheed Martin Space Systems Company on the Busek–Primex Hall Thruster (BPT-4000) provided plume data [9] for comparison with computer models. Measurements were taken using fully exposed flux probes ("uncollimated") for

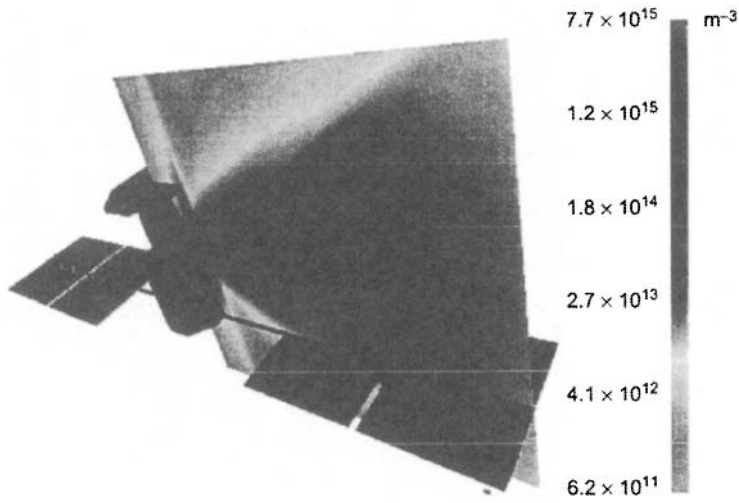

Fig. 8-5. EPIC model of the Express-A spacecraft showing the plume ion density profile during operation of the RT4 SPT-100 thruster (from [5]).

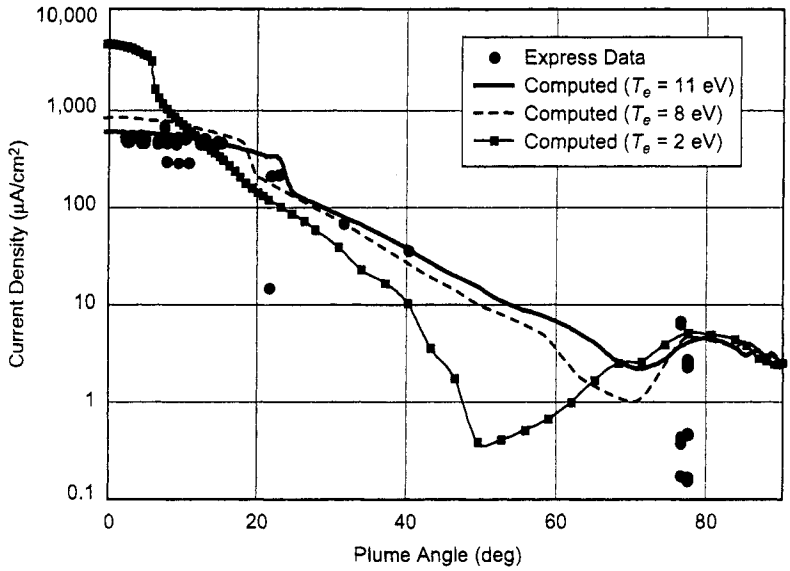

Fig. 8-6. Comparison of current density measurements onboard the Express-A spacecraft and computed values (from [5]).

assessing the non-directional ion flux and probes inside graphite collimators ("collimated").

Figure 8-7 shows experimental data [9] from the BPT-4000 Hall thruster at a discharge power of 3 kW and voltage of 300 V using a collimator for energy spectra at different angles with respect to the thruster axis. The angle-independent, high-energy peak at $E/q \sim 280$ V associated with the main beam is clearly evident. Also apparent is a small-amplitude peak at the lowest energy values of the collimated spectra from the background chamber plasma. This peak was dominant in the uncollimated spectra. Figure 8-7 reveals the existence of secondary current density peaks with relatively high energies compared to the primary resonant charge exchange peak. For example, at an angle of 40 deg, the energy associated with the second maximum is approximately 150 eV. These observed ion-flux crests show a marked energy dependence on angle. In an ideal elastic collision between a moving sphere and an identical stationary sphere, the magnitude of the final velocity for each sphere is proportional to the cosine of the angle between its final velocity and the initial velocity of the moving sphere, and the sphere's kinetic energy varies with the square of the cosine. Because the retarding potential analyzer (RPA) data in Fig. 8-7 show a peak with energy dependence given roughly by $E_b \cos 2\theta_{\text{lab}}$, where E_b is the main ion beam energy and θ_{lab} is the angle with respect to the thruster axis, these peaks have been attributed to simple elastic scattering (momentum

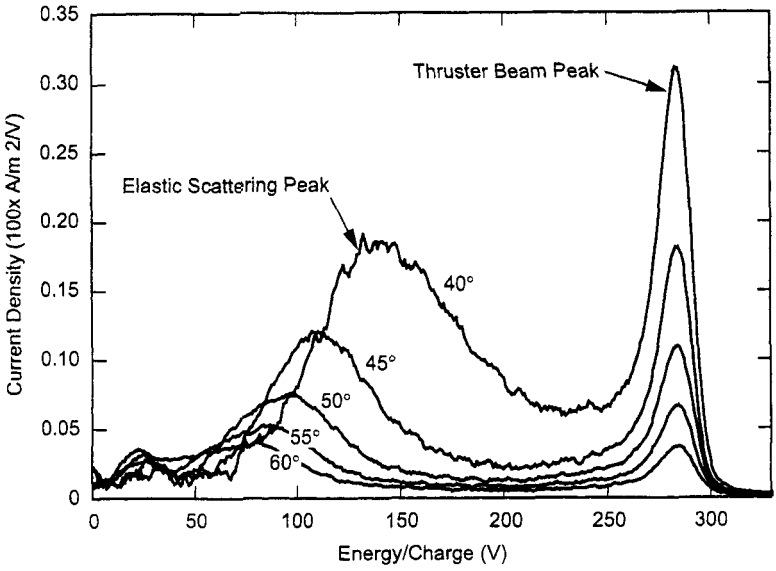

Fig. 8-7. Collimated RPA data for the BPT-4000 showing the angle-independent, high-energy main beam peaks and the angle-dependent, elastic scattering peaks (from [9]).

transfer) between beam ions and neutral atoms. Numerical simulations using calculated differential scattering cross sections confirm that elastic scattering is the cause of the observed mid-energy peak [10].

8.3 Plume Models

8.3.1 Primary Beam Expansion

Before the advent of multi-dimensional computer models of thruster plumes, empirical models of the primary beam expansion were used. These models reproduce the general features of the ion beam angular distribution. Because they are very simple, they are invaluable for initial trades when planning electric propulsion system accommodation on spacecraft.

Parks and Katz [11] derived an analytical model of the expansion of an ion beam with a Gaussian profile in its self-consistent, quasi-neutral electric field with or without an initial distribution of radial velocities. This model is very useful for analytically calculating thruster ion-beam plume characteristics. The steady-state ion continuity and momentum equations in the absence of ionization are

$$\nabla \cdot (\rho_m \mathbf{v}) = 0 \tag{8.3-1}$$

$$\nabla \cdot (\rho_m \mathbf{vv}) = -\nabla p, \tag{8.3-2}$$

where the mass density, ρ_m, is the product of the ion number density and the ion mass.

Assuming the beam has cylindrical symmetry, the axial beam velocity remains constant everywhere and the axial derivative of the pressure can be neglected compared with its radial derivative. The ion continuity and momentum equations can then be rewritten as

$$\frac{1}{r}\frac{\partial}{\partial r}(r \rho_m v_r) + \frac{\partial(\rho_m v_z)}{\partial z} + = 0 \tag{8.3-3}$$

$$v_r \frac{\partial v_r}{\partial r} + v_z \frac{\partial v_r}{\partial z} = -\frac{1}{\rho_m}\frac{\partial p}{\partial r}. \tag{8.3-4}$$

The second equation was obtained from the momentum equation by using the continuity equation to eliminate derivatives of the density. The pressure term is assumed to be the constant temperature electron pressure

$$p = n k T_e. \tag{8.3-5}$$

Using the assumption of constant axial velocity, the axial distance, z, can be replaced by the product of the beam velocity, v_z, and t, the time since the beam left the thruster:

$$z = v_z t. \tag{8.3-6}$$

The axial derivative can be replaced with a time derivative:

$$\frac{\partial}{\partial z} = \frac{1}{v_z}\frac{\partial}{\partial t}. \tag{8.3-7}$$

Equations (8.3-3) and (8.3-4) can then be rewritten as

$$\frac{1}{r}\frac{\partial}{\partial r}(r \rho_m v_r) + \frac{\partial \rho_m}{\partial t} = 0 \tag{8.3-8}$$

$$v_r \frac{\partial v_r}{\partial r} + \frac{\partial v_r}{\partial t} = -\frac{1}{\rho_m}\frac{\partial p}{\partial r}. \tag{8.3-9}$$

These approximations are quite good if the axial velocity is much greater than both the initial radial velocities and the ion sound speed.

With the assumption that the ion beam profile starts out and remains a Gaussian profile, the set of equations can be solved analytically. The beam profile is written as

$$\rho_m(r)=\frac{\rho_o}{h(t)^2}\exp\left(-\frac{r^2}{2R^2h(t)^2}\right), \tag{8.3-10}$$

where the initial ion beam mass density, ρ_o, is

$$\rho_o=\frac{M I_b}{2\pi v_b R^2}, \tag{8.3-11}$$

and the function $h(t)$ describes how the beam expands radially. The parameter R is chosen to best represent initial beam width, and the initial value of the expansion parameter $h(0)$ is unity. The density spreads out as the beam moves axially, but the beam profile remains Gaussian, as shown in Fig. 8-8.

An ion that starts out at a radial position r_o will move radially outward proportionally to $h(t)$:

$$r(r_o,t)=r_o\,h(t). \tag{8.3-12}$$

This implies that the radial velocity, v_r, is proportional to the time derivative of $h(t)$:

$$v_r(r,t)=r_o\,\dot{h}(t). \tag{8.3-13}$$

Equations (8.3-12) and (8.3-13) can be combined to obtain an expression for the local velocity that doesn't use the initial radial position:

$$v_r(r,t)=r\frac{\dot{h}(t)}{h(t)}. \tag{8.3-14}$$

The solution obtained below is valid for a beam with no initial radial velocity, or for an initial radial velocity distribution that is proportional to the radius:

$$v_r(r,0)=v_r^0\,r. \tag{8.3-15}$$

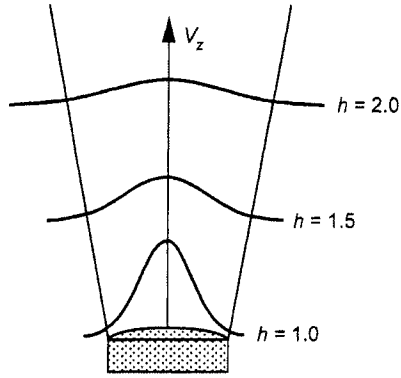

Fig. 8-8. The Gaussian beam density profile broadens as ions move downstream from the thruster exit plane.

The density, defined by Eq. (8.3-10), and the radial velocity, defined in Eq. (8.3-15), both satisfy the ion continuity equation, Eq. (8.3-8), for any function $h(t)$. The first term in Eq. (8.3-8) then becomes

$$\frac{1}{r}\frac{\partial(r\rho_m v_r)}{\partial r} = \frac{1}{r}\frac{\partial}{\partial r}\left(r^2\frac{\dot{h}}{h}\rho_m\right) = \left(2\frac{\dot{h}}{h} - \frac{r^2\dot{h}}{R^2h^2}\right)\rho_m, \qquad (8.3\text{-}16)$$

and the second term in Eq. (8.3-8) becomes

$$\frac{\partial\rho_m}{\partial t} = \left(-2\frac{\dot{h}}{h} + \frac{r^2\dot{h}}{R^2h^2}\right)\rho_m. \qquad (8.3\text{-}17)$$

Making the same substitutions into the momentum equation, Eq. (8.3-9), an equation for $h(t)$ is obtained that is independent of the radius:

$$v_r\frac{\partial v_r}{\partial r} + \frac{\partial v_r}{\partial t} = -\frac{1}{\rho_m}\frac{\partial p}{\partial r}$$

$$r\frac{\dot{h}}{h}\frac{\partial}{\partial r}r\frac{\dot{h}}{h} + \frac{\partial}{\partial t}r\frac{\dot{h}}{h} = -\frac{eT_e}{M\rho_m}\frac{\partial\rho_m}{\partial r}$$

$$-r\frac{\dot{h}^2}{h^2} + r\frac{\dot{h}^2}{h^2} + r\frac{\ddot{h}}{h} = \frac{eT_e}{M\rho_m}\frac{r}{R^2h}\rho_m$$

$$h\ddot{h} = \frac{kT_e}{MR^2} = \frac{v_B^2}{R^2}, \qquad (8.3\text{-}18)$$

where v_B is the Bohm velocity. In Eq. (8.3-18), the right-hand side is a constant. This equation can be integrated by the usual substitution of a new function $w = dh/dt$ for the time derivative of h:

$$\ddot{h} = \frac{d}{dt}\dot{h} = \frac{dw}{dt} = \frac{dw}{dh}\frac{dh}{dt} = w\frac{dw}{dh}. \tag{8.3-19}$$

Using this, Eq. (8.3-18) can be rewritten as

$$w\frac{dw}{dh} = \frac{v_B^2}{R^2 h}. \tag{8.3-20}$$

Integrating once yields

$$\int_{\dot{h}(0)}^{\dot{h}(t)} w\,dw = \int_1^{h(t)} \frac{v_B^2}{R^2 h}\,dh. \tag{8.3-21}$$

Writing this expression in terms of h and its time derivative gives

$$\frac{1}{2}\dot{h}^2 = \frac{v_B^2}{R^2}\ln h + \frac{1}{2}\dot{h}^2(0). \tag{8.3-22}$$

Taking the square root and integrating again, an equation relating h to time is obtained. For the case of no initial radial velocity, $\dot{h}(0) = 0$, the time derivative of h is

$$\dot{h} = \frac{v_B}{R}\sqrt{2\ln h}. \tag{8.3-23}$$

Equation (8.3-23) can be rewritten and integrated to give

$$\frac{dh}{\sqrt{\ln h}} = \frac{v_B}{R}\sqrt{2l}\;dt \tag{8.3-24}$$

$$\int_1^h \frac{dx}{\sqrt{\ln x}} = \int_0^t \sqrt{2}\,\frac{v_B}{R}\,dt = \sqrt{2}\,\frac{v_B}{R}t. \tag{8.3-25}$$

An approximate numerical solution of Eq. (8.3-25) for the expansion parameter, h, is given by

$$h \approx 1.0 + 0.6524\tau + 0.0552\tau^2 - 0.0008\tau^3, \tag{8.3-26}$$

where τ is given by

$$\tau \equiv \sqrt{2}\frac{v_B}{R}t. \tag{8.3-27}$$

These expressions describe the beam expansion for the case of no initial radial velocity or for an initial radial velocity distribution that is proportional to the radius. Examples of schematic beam profiles as a function of distance from the thruster were given in Fig. 8-8. For the case of an initial radial velocity profile, the integral in Eq. (8.3-25) is

$$\dot{h}_0 t = \int_1^h \left(1 + 2\frac{v_B^2}{R^2 \dot{h}_0^2}\ln x\right)^{-1/2} dx, \tag{8.3-28}$$

where the integral has to be calculated numerically. Park's model has been extended by Ashkenazy and Fruchtman [12] to include thermal gradient and two-dimensional effects.

The Park's formula is very similar to an empirical formula developed earlier by Randolph for Hall thrusters [13]. Randolph's formula has two Gaussians but does not have the curved trajectories of the Park's formula. The four parameters, k_0 through k_3, in Randolph's formula are chosen to fit plume measurements:

$$j = \frac{R^2}{r^2}\left\{k_0 \exp\left(-\frac{(\sin\theta)^2}{k_1^2}\right) + k_2 \exp\left(-\frac{\theta^2}{k_3^2}\right)\right\}. \tag{8.3-29}$$

While the analytical expressions above are invaluable for estimating plume interactions, multi-dimensional computer models are normally used for detailed calculations. There is general agreement on the physics that control the expansion of the main ion beam from ion and Hall thrusters, but there are differences in the numerical algorithms used to calculate the expansion. Several researchers [3,4] employ particle-in-cell (PIC) algorithms, where the beam is modeled as a collection of macro-particles with each particle representing a large number of ions. The velocity and acceleration of each particle are followed in the self-consistently calculated electric field.

Another approach, which is much less computationally intensive, is to model the thruster beam as a drifting fluid of cold ions and warm electrons. In this method, the expansion of the fluid-like ion beam is calculated using a Lagrangian algorithm [5,6]. The ion beam profile for the Nuclear Electric

Xenon Ion System (NEXIS) ion thruster [14] calculated using this algorithm is shown in Fig. 8-9. The primary beam is assumed to be composed of a collisionless, singly ionized, quasi-neutral plasma expanding in a density-gradient electric field. The electron drift velocity is small compared to the electron thermal speeds, so momentum balance for the electrons can be written as

$$m_e \frac{d\,\mathbf{v}_e}{d\,t} = e\nabla\phi - \nabla p_e = 0, \tag{8.3-30}$$

where $\mathbf{v}_e$, ϕ, and p_e are the electron velocity, electric potential, and electron pressure, respectively. Assuming an ideal gas electron pressure, the potential follows the *barometric law*,

$$\phi = \frac{kT_e}{e} \ln\left(\frac{n_e}{n_\infty}\right), \tag{8.3-31}$$

where T_e is the electron temperature, n_e is the plasma density ($n_e = n_i$), and n_∞ is a reference plasma density. The plume is also assumed to be isothermal. This is a better approximation for space conditions than for the laboratory, where inelastic collisions with background neutrals will tend to cool the electrons.

In this model, ions are assumed to be very cold compared with the electrons ($p_i \approx 0$), and their acceleration to be dominated by the electric field:

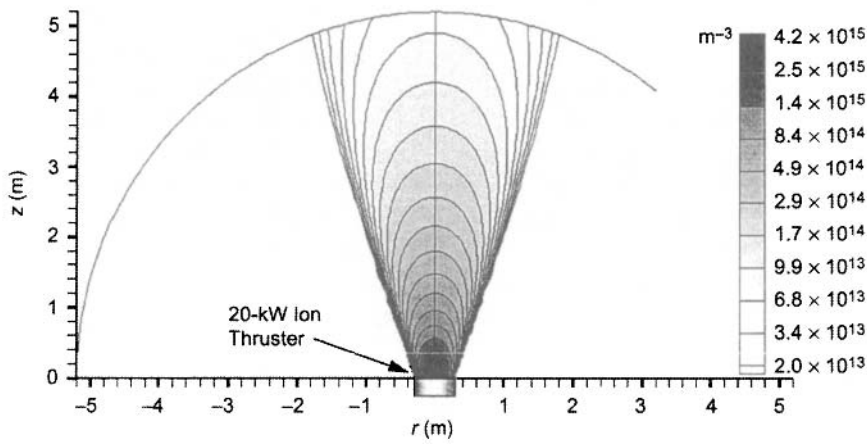

Fig. 8-9. Calculated primary ion beam density profile for the 20-kW NEXIS ion thruster [14].

$$M\frac{D\mathbf{v}_i}{Dt} = -e\nabla\phi. \tag{8.3-32}$$

Since the drift velocity of the ions is much greater than their thermal velocity, the high-velocity ions are modeled as a fluid, with a velocity of $\mathbf{v}_i$. The governing equations, solved in two-dimensional (2-D) (R–Z) geometry, are conservation of mass and momentum:

$$\begin{aligned} \nabla \cdot n\mathbf{v}_\mathbf{i} &= 0 \\ M\mathbf{v}_i \cdot \nabla n\mathbf{v}_\mathbf{i} &= -en\nabla\phi. \end{aligned} \tag{8.3-33}$$

The accuracy of the algorithm has been confirmed by comparisons of analytical solutions with model problems in one and two dimensions [8]. The Lagrangian modeling approach leads to reduced numerical noise as compared with PIC algorithms. However, unlike PIC algorithms, the fluid technique ignores spreading of the beam due to ion temperature and, in the case of ion thrusters, the angular distribution coming out of each grid aperture.

8.3.2 Neutral Gas Plumes

The neutral gas density in a laboratory vacuum chamber has three components: gas from the thruster, gas from the neutralizer hollow cathode, and the background chamber density. To model the neutral gas density, the gas from ion thrusters can be approximated by isotropic emission from a disk with the diameter of the grid:

$$n_a \sim \frac{\cos\theta}{r^2}. \tag{8.3-34}$$

For Hall thrusters, the neutral gas density can be approximated using an annular anode gas flow model with isotropic emission from the channel. This is done by calculating emissions from two disks, one large and one smaller, and subtracting the smaller from the larger. The neutral density drop-off with r and z from a disk emitting a Maxwellian distribution is calculated using an approximate view factor. Energetic charge-exchange (CEX) neutrals are negligible compared to the total neutral density and therefore are not included when modeling the neutral gas density.

For plume models, the neutral gas from the neutralizer hollow cathode is usually assumed to be from isotropic emission at a constant temperature equal to the neutralizer cathode orifice temperature. While the neutralizer is offset from the thruster axis of symmetry, in cylindrical 2-D codes there are an equal number of points from the thruster axis closer to and farther from the

neutralizer. The cylindrically averaged neutral density for any point at a distance z downstream is estimated as if the point were along the thruster centerline. The vacuum chamber background neutral density is usually assumed to be constant. Based on values of the ambient temperature and pressure, the background density can be determined assuming an ideal gas law. No background density is assumed for calculations in space conditions. Figure 8-10 shows each of the three components and the total calculated neutral density [10] for the BPT-4000 Hall thruster.

8.3.3 Secondary-Ion Generation

Low energy ions are created near a thruster exit plane by charge exchange collisions between the main ion beam and the neutral gas. The mechanism is the same for both gridded ion and Hall thrusters. Charge-exchange ion density can be computed using a two-dimensional, R,Z-geometry PIC code, while using the main-beam ion densities computed by the Lagrangian calculations and the neutral gas profile as inputs. The charge-exchange ion production rate, $\dot{n}_{CEX}$, is calculated assuming that the beam ions have a velocity, v_b, much greater than the neutral gas velocity:

$$\dot{n}_{CEX} = n_i n_0 v_b \sigma_{CEX} . \tag{8.3-35}$$

Resonant charge-exchange cross sections between singly charged xenon ions and neutral xenon atoms range from 30 Å^2 to 100 Å^2 for typical ion and Hall thruster energies [15].

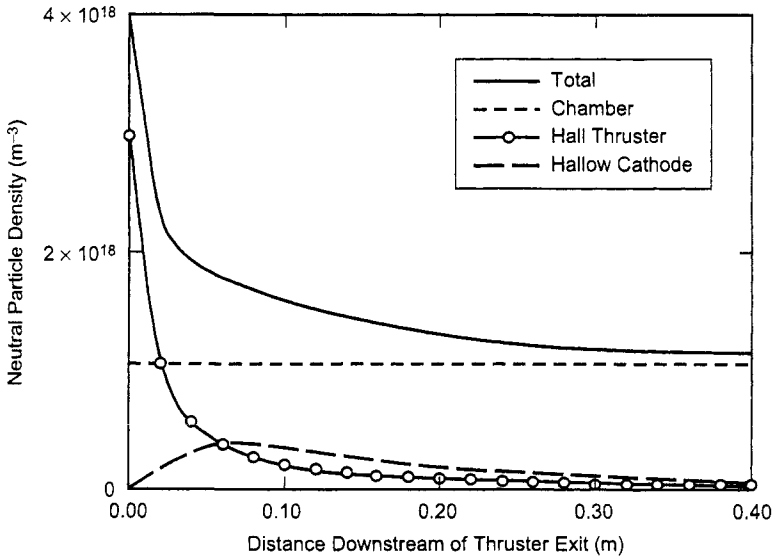

Fig. 8-10. Neutral gas density downstream of the BPT 4000 exit plane (from [10]).

The charge-exchange ion density is calculated by tracking particle trajectories in density-gradient electric fields using a finite-current barometric law for the electron density (electron current equals ion current). Poisson's equation is solved on a finite element grid and iterated until steady-state CEX densities and density-gradient potentials are self-consistent. Comparisons of the CEX plume model with flight data from the NSTAR's ion engine exhibited good agreement [8].

Figure 8-11 shows plume maps at one meter, calculated using this method for the BPT-4000 under both laboratory and space conditions. The CEX density in the laboratory is found to be more than one order of magnitude greater than it is in space due to the dominance of the background neutral gas in the chamber. With the exception of the neutral gas density, all the terms in the expression for charge-exchange ion generation [Eq. (8.3-6) above] are identical for the laboratory and space. Figure 8-10 showed that at distances greater than about a tenth of a meter downstream of the thruster exit plane, the chamber gas density is much greater than the gas coming directly from the thruster, resulting in greater charge-exchange ion generation. The computed total ion current in the laboratory case (5.3 A) is in approximate agreement with measurements of the integrated ion current (5–6 A for collector potential of 20 V) [9]. The calculations assumed a charge-exchange cross section for 300-V ions of 55 $Å^2$ based on the calculations and measurements by Miller [15].

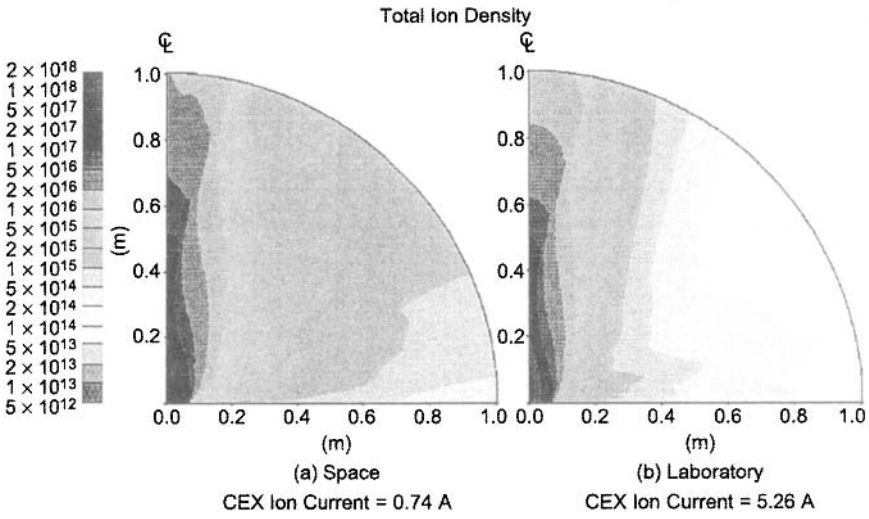

Fig. 8-11. Hall thruster plume maps for (a) space and (b) laboratory and conditions showing dominance of background density in the charge-exchange plume production (from [10]).

The distinctive second peak in the energy spectra captured by the collimated retarding potential analyzer (RPA) data shown in Fig. 8-7 is from elastic scattering of xenon ions by neutral xenon atoms. Mikellides et al. [10] have calculated differential cross-section data for elastic $Xe^{+} - Xe$ scattering in a center-of-mass frame of reference. The calculations involve averaging over the pertinent Xe_2^{+} potentials, without inclusion of charge exchange. The results are then subsequently corrected for charge exchange.

The derived, center-of-mass differential cross sections were converted to values in a fixed frame of reference relative to the laboratory and implemented in the plume model. For comparisons with RPA measurements, the flux of scattered ions Γ_{is},

$$\begin{aligned} \Gamma_{is} &= \int_0^x \frac{I_b n_o}{d^2} \frac{d\sigma}{d\Omega} d\xi \\ &\approx \frac{I_b n_o x_c}{d^2} \frac{d\sigma}{d\Omega}, \end{aligned} \tag{8.3-36}$$

was computed at a radius of 1 m (the RPA location). In Eq. (8.3-36), I_b and n_o are the main-beam ion current and neutral density, respectively. The dimension x_c is the characteristic length of the beam column and d is the radial distance between the thruster and the RPA. The differential contribution due to the column element along the beam is denoted by $d\xi$, and $d\sigma / d\Omega$ is the differential cross section.

The results from the complete calculation, compared with data, are shown in Fig. 8-12. Plotted in the figure are the results of the calculations of the expanding beam ions, and the beam and scattered ions combined. Also plotted are the ion current probe data for four bias levels of 50 V and 100 V. The probe bias potential prevents lower energy ions from being collected. As expected, the beam-only values compare best with the ion probe biased to 100 V, since, at this value, most of the scattered and charge-exchanged ions are excluded. The calculation combining beam and elastic scattering compares well with 50 V-biased probe data since these data include most of the elastically scattered ions.

8.4 Spacecraft Interactions

In order to design a spacecraft to accommodate electric thrusters, it is necessary to understand how the thruster plumes interact with the spacecraft and its

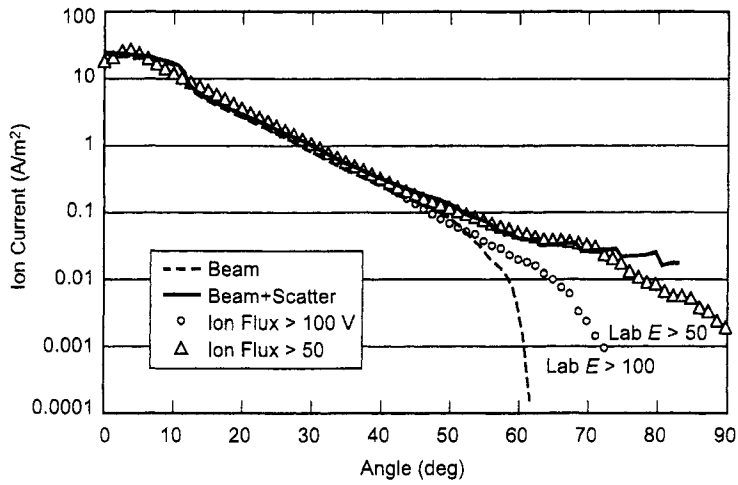

Fig. 8-12. Comparison of high-energy ion current between the calculations and measurements for the BPT-4000 (from [10]).

payloads. Thruster plumes affect the spacecraft immediately during their operation, for example, by momentum transfer from plume impingement or optical emissions and by slow, cumulative processes, such as ion erosion of spacecraft surfaces or contamination of surfaces by materials generated by thruster wear. The immediate interactions may affect spacecraft operations; the longer-term interactions may affect spacecraft life.

Unique to electric propulsion is the interaction between the thruster plumes and the spacecraft electrical system, in particular the solar arrays. Electric thruster plumes are composed of charged particles and can carry currents between the thruster electrical power system and exposed electrical conductors such as solar array cell edges and interconnects. While the currents that flow through the thruster plumes are in general quite small, they may cause changes in subsystem potentials. These potential changes, if not anticipated, may be mistaken for system anomalies by spacecraft operators.

As described in previous sections, while most of the plume is in the thrust direction, a small fraction of the thruster exhaust is emitted at large angles. The large-angle component is mostly composed of low-velocity particles. Some high-energy ions in Hall thruster plumes can be found at angles greater than 45 deg, but at such a low flux density that they will have little impact on spacecraft life. Techniques for quantitatively calculating the effects of thruster plumes on spacecraft are presented in the following sections.

8.4.1 Momentum of the Plume Particles

Just as with chemical thrusters, when electric thruster plumes impact spacecraft surfaces, they exert a force, which causes a torque on the spacecraft. The force is easily calculated as the difference in momentum between the plume particles that impact the surface and the momentum of particles that leave the surface. The momentum of the plume particles is the sum of the ion and neutral atom fluxes. Since the plume consists primarily of ions, and the velocity of the ionized particles is much greater than the neutral atoms, the neutral component can usually be neglected. The ion momentum is

$$\mathbf{p}_i = n_i M_{Xe} \mathbf{v}_i , \tag{8.4-1}$$

and the neutral momentum is

$$\mathbf{p}_o = n_o M_{Xe} \mathbf{v}_o , \tag{8.4-2}$$

so that the total plume momentum is

$$\mathbf{p}_{\text{plume}} = \mathbf{p}_i + \mathbf{p}_o \approx \mathbf{p}_i . \tag{8.4-3}$$

In one extreme, an ion that impacts a surface may scatter elastically and leave the surface with its kinetic energy unchained, but its velocity component normal to the surface is reversed:

$$\mathbf{p}_{\text{surface}}^{\text{elastic}} \cdot \mathbf{n} = -2\, \mathbf{p}_{\text{plume}} \cdot \mathbf{n} . \tag{8.4-4}$$

In the other extreme, the incident xenon ion resides on the surface long enough to transfer its momentum and energy to the surface, and the particle leaves the surface with a velocity distribution corresponding to the surface temperature. This process is called *accommodation*, and the fraction of particles that undergo this process is called the *accommodation coefficient*.

Since spacecraft surfaces are typically less than a few hundred degrees kelvin, the velocities of accommodated atoms are orders of magnitude less than energetic thruster ions. For example, the speed of a xenon atom leaving a 300-K surface is

$$v_i(300\ \text{K}) = \sqrt{\frac{kT}{M}} = 137\left[\text{m/s}\right], \tag{8.4-5}$$

while the speed of a beam ion from a 300-V Hall thruster is

$$v_b(300\text{ eV}) = \sqrt{\frac{2\text{eV}}{M}} = 22{,}000\,[\text{m/s}]. \tag{8.4-6}$$

Because the thermal speeds are so small compared with the beam speeds, the momentum of re-emitted *surface-accommodated* ions can be ignored when calculating surface torques. The momentum transfer per unit area is approximated by

$$\mathbf{F} = (2 - A_c)\mathbf{p}_{\text{plume}}, \tag{8.4-7}$$

where A_c is the surface accommodation coefficient, which has a range of values from 0 to 1. Flight data from the Express-A satellite show that accommodation coefficients for Hall thruster ions on the solar arrays were close to unity [5].

8.4.2 Sputtering and Contamination

A major concern for implementing ion thrusters on Earth-orbiting satellites is that energetic ions from the thruster beam will erode spacecraft surfaces. As discussed above, north–south station keeping with body-mounted thrusters invariably leads to high-energy ions bombarding some part of the solar arrays. When these high-energy ions impact the solar arrays or other spacecraft surfaces, they can cause erosion by sputtering atoms. However, with proper placement and orientation of the thrusters, and the use of stay-out "zones" during which the thrusters are not operated because the plume would impinge on the array, the ion flux can be small enough to keep electric thrusters from limiting satellite life. Whether a given surface erodes or accumulates material depends on the relative rates of sputtering and the deposition of sputter deposits. The deposits result from erosion products from the thruster itself, as well as material sputtered from other spacecraft surfaces.

Sputtering affects spacecraft in two ways. First, spacecraft surfaces can erode by sputtering or be contaminated by the buildup of sputtering products. Primary thruster beam ions are the principal source of sputtering, and spacecraft surfaces within a narrow cone angle of the thrust direction will erode significantly due to ion sputtering. The cone angle where sputtering is important depends on the specific thruster and is usually narrower for ion thrusters than for Hall-effect thrusters. For example, the NEXIS ion thruster primary-beam plume, shown in Fig. 8-9, has a half-angle for all particles of only about 20 deg and 95% of the particles are within a 10-deg half angle.

Second, while ion and Hall thrusters typically use an inert gas propellant, both types of thrusters can contaminate spacecraft surfaces. The sources of

contamination are thruster material sputtered by energetic ions, as well as spacecraft material sputtered by the main thruster beam. In ion thrusters, sputter erosion of grid material not only limits thruster life, but the sputtered grid material may be a significant source of contamination to spacecraft surfaces. This was recognized early in the development of commercial ion thrusters [16], and as a result, a third grid was added to reduce the amount of sputtered grid material coming from the thruster and to shield the spacecraft from grid sputter products. The third grid has the added benefit of dramatically reducing the grid sputter rate by preventing charge-exchange ions made downstream of the third grid from hitting the accelerator grid [17]. For ion thrusters with metal grids, the problem of contamination in the absence of a third grid can be quite important. Only a few monolayers of a metallic contaminant can make large changes to the optical, thermal, and electrical properties of spacecraft surfaces.

For Hall thrusters, the situation can be quite different. The plume from Hall thrusters normally has about twice the angular divergence of an ion thruster, and so sputtered thruster material comes out at large angles. However, early in life most of the contamination comes from sputter erosion of the ceramic channel wall. Although this can produce a substantial flux of sputter products, the products are mainly insulating molecules. Deposition of sputtered insulators, such as Hall-thruster channel ceramic or solar-cell cover glass materials, has little effect on the spacecraft surface optical and thermal properties. More problematic is the sputtered metallic material from the late life erosion of Hall-thruster magnetic pole pieces. In the same manner as with ion thrusters, very thin layers of the deposited metal can radically change the properties of spacecraft surfaces.

One effect discovered with Hall thrusters, but common to both ion and Hall thrusters, is that surfaces can experience net deposition of sputter products or can be eroded away by energetic beam ions, depending on their location with respect to the thruster ion beam [13]. As shown in Fig. 8-13, the plume of sputtered products coming from the thruster is normally much narrower than the main ion beam. For surfaces at small angles with respect to the thrust vector, sputtering from the beam ions is greater than the deposition of thruster erosion molecules. These surfaces will erode over time. However, surfaces located at large angles to the thruster vector are contaminated by thruster erosion products faster than they can be sputter away by energetic beam ions. Over time, sputtered thruster material will accumulate on these surfaces. For the SPT-100 Hall thruster, the dividing line between erosion and deposition is about 65 deg [13].

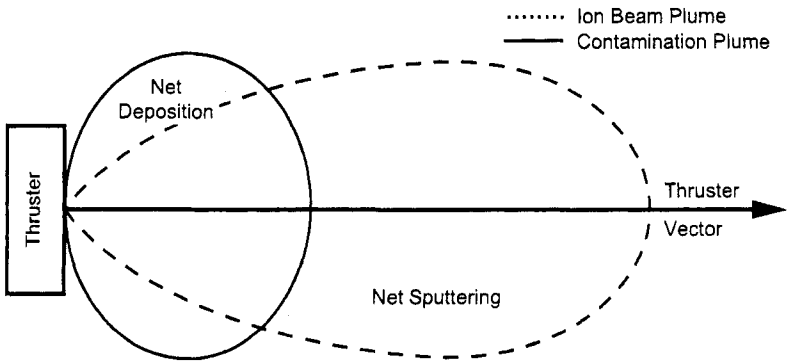

Fig. 8-13. Sputtering by main beam ions dominates at angles close to the thrust vector direction; deposition of thruster erosion products occurs at angles far from the thrust direction.

Besides thruster erosion products, the other source of contamination is spacecraft surface material sputtered by thruster beam ions. Computer codes, such as the Electric Propulsion Interactions Code (EPIC) [6], are used to calculate the erosion and redeposition over the entire spacecraft. EPIC is an integrated package that models the interactions between a spacecraft and its electric propulsion system. The user provides EPIC with spacecraft geometry, surface materials, thruster locations, and plume parameters, along case study parameters such as orbit and hours of thruster operation. EPIC outputs thruster plume maps, surface interactions on the three-dimensional (3-D) spacecraft, one-dimensional (1-D) plots along surfaces (e.g., erosion depth on a solar array as a function of distance from the thruster), and integrated results over the duration of the mission (e.g., total induced torque in a given direction, total deposition of eroded material at a specific location on the spacecraft). Figure 8-14 shows results of a sample EPIC calculation for the Express-A spacecraft during firing of one its four stationary plasma thrusters. The calculation shows both sputter erosion and deposition depths. The thruster erodes the solar array surface that is along the thruster direction. Some of the eroded material deposits on other spacecraft surfaces.

8.4.3 Plasma Interactions with Solar Arrays

Ion and Hall thruster plasma plumes connect thrusters electrically to the exposed spacecraft conducting surfaces. It is important to account for current paths through the plasma to prevent current loops or unintended propulsion system floating potentials.

In order to understand the plasma currents and floating potentials between the electric propulsion system and the rest of the spacecraft, first consider the thruster external cathode as the source of the plasma. As discussed in

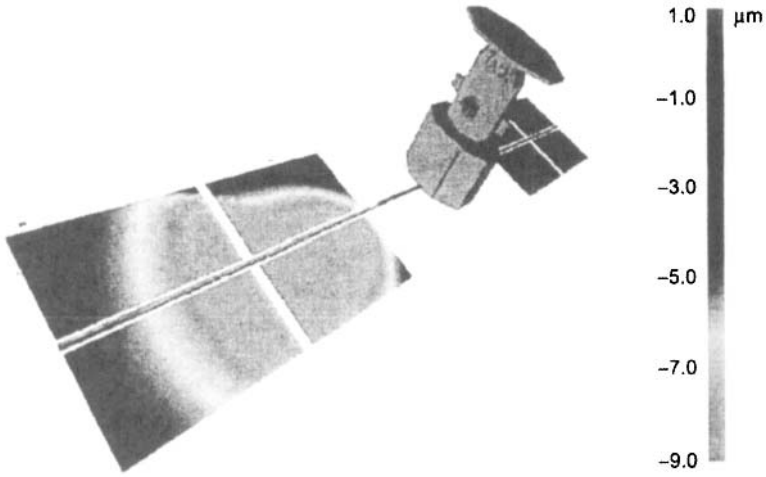

Fig. 8-14. Contours of the erosion (negative numbers) and deposition depths (positive numbers) due to sputtering during operation of the SPT-100 Hall thruster onboard the Express-A spacecraft. The calculation was performed with EPIC [6].

Chapter 6, the sheath drop internal to a hollow cathode and orifice resistive heating produce energetic electrons that ionize the propellant gas and generate plasma. The combined insert and orifice potential drops are typically between 10 and 15 V, causing the external plasma to be about the same value above cathode common, as illustrated in Fig. 8-15. The hollow cathode–generated plasma has an electron temperature of about 2 eV, typical of many laboratory plasmas.

The spacecraft acts as a Langmuir probe in the thruster plume plasma and will float to a potential where the ion and electron currents from the plasma cancel. As discussed in Chapter 3, plasma electron velocities are much higher than ion velocities, so current balance is achieved by repelling most of the plasma electrons. This balance occurs when the surface is a few times the electron temperature negative of the local plasma potential. If the electric propulsion system were isolated from spacecraft ground by a very high impedance, cathode common would float around 10 V negative with respect to spacecraft ground, as illustrated in Fig. 8-16.

When the spacecraft has exposed surfaces at different voltages, predicting the cathode common floating potential is more difficult. An extreme case would be if the spacecraft solar arrays had a large area at high positive voltage immersed in the thruster plume. Then, to achieve current balance, the high-voltage area would be close in potential to the thruster plume plasma. For example, assume that the spacecraft had 100-V solar arrays. Since the cathode common is only

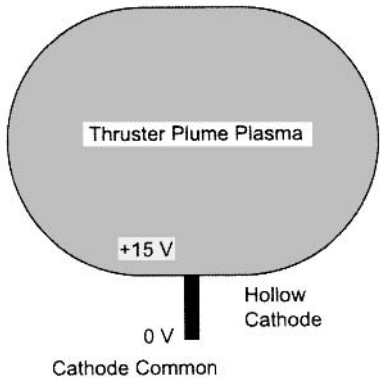

Fig. 8-15. The thruster neutralizer hollow cathode generates a plasma typically 10 to 20 V above the cathode common.

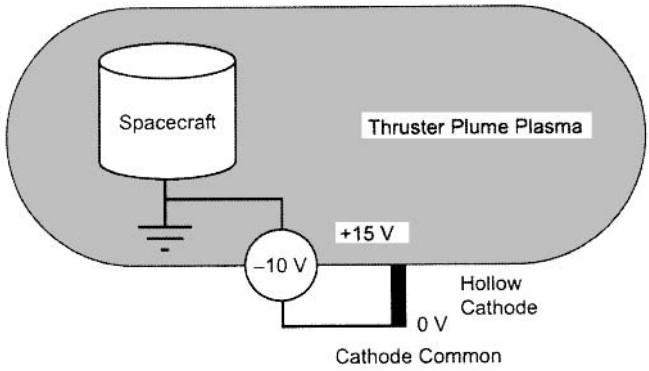

Fig. 8-16. The cathode common would float on the order of 10 V negative on a spacecraft with a conducting surface.

about 10 V negative with respect to the thruster plume plasma, cathode common would be 90-V positive compared to spacecraft ground, as illustrated in Fig. 8-17.

On operational spacecraft, cathode common will float somewhere between the two extremes, –15 V to 90 V, depending on the array construction, and may vary with orientation and season. Cathode common potential can be held at a fixed potential with respect to spacecraft chassis ground by tying the electric propulsion system circuit ground to spacecraft ground with a resistor. Plasma currents collected by exposed spacecraft surfaces will flow through the resistor. These currents can be limited by reducing the exposed conducting area in the thruster plumes. The plasma currents are usually quite small. For example, if the charge-exchange plasma plume density 1 meter from the thruster axis is

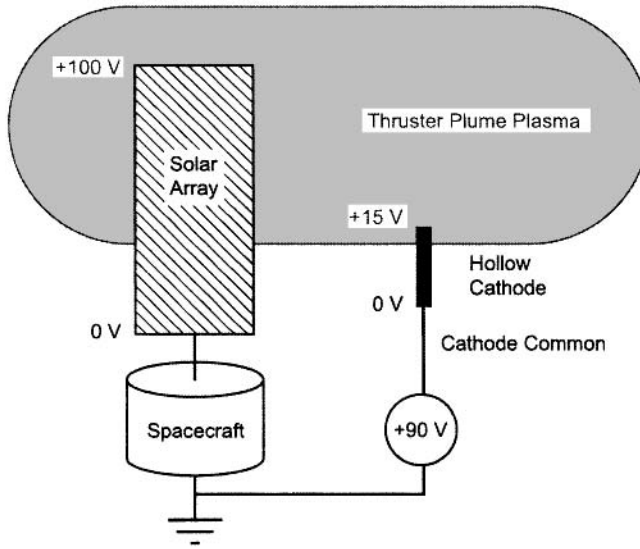

Fig. 8-17. A large area of high voltage solar array exposed to the thruster plume causes the cathode common to float the order of the array voltage positive of spacecraft chassis ground.

~10^{14} m^{-3}, a square meter of exposed conducting area would collect only a few milliamperes of electron current. A kilo-ohm resistor could clamp cathode common within a few volts of spacecraft ground.

8.5 Interactions with Payloads

8.5.1 Microwave Phase Shift

Electromagnetic waves interact with plasmas, particularly if the wave frequency is on the order of or lower than the plasma frequency along its path of propagation. In most spacecraft applications, the communications and payload frequencies are so high (>1 GHz) that there is little effect. For a typical thruster, the plume density drops below 10^{15} m^{-3} less than a meter from the thruster, and then it drops even more rapidly at greater distances. The plasma frequency at this density about 1 meter from the thruster, from Eq. (3.5-24), is 285 MHz.

As a result, microwave signals with frequencies below a few hundred megahertz could be affected by the thruster plasma plume. However, even at higher frequencies, highly directional antenna patterns should be analyzed for possible distortion by small phase shifts caused by the plasma. A plane wave

with frequency f passing through a plasma with density n_e will undergo a phase shift according to the following formula:

$$\Delta\phi \approx \frac{\pi f}{c}\int_0^L \frac{n_e}{n_c} d\ell\,, \tag{8.5-1}$$

where c is the speed of light and n_c is the critical density at which the plasma density has a plasma frequency equal to the microwave frequency. Since the plasma density drops rapidly with distance from the thruster, the scale length over which the plasma frequency is comparable to the wave frequency is usually small.

8.5.2 Plume Plasma Optical Emission

The optical emissions from ion and Hall thrusters are very weak but can be measured by sensitive instruments. The only in-space measurement of the optical emissions from a xenon plasma plume generated by an electric propulsion device is from a shuttle flight that had a "plasma contactor" as part of the Space Experiments with Particle Accelerators (SEPAC) [18] flown on the NASA Space Shuttle Mission STS-45. The "plasma contactor" was actually a Xenon Ion Propulsion System (XIPS) 25-cm thruster without accelerator grids or a neutralizer hollow cathode. Plasma and electron current from the discharge chamber were allowed to escape into space, unimpeded by an ion accelerator grid set.

The absolute-intensity optical emission spectrum measured in space of the xenon plasma plume from the operating plasma source is shown in Fig. 8-18. The spectrum was measured by the Atmospheric Emissions Photometric Imaging (AEPI) spectrographic cameras. The source was the SEPAC plasma contactor [18,19] that generated about 2 A of singly-charged xenon ions in a ring-cusp discharge chamber. The plasma density was about 10^{17} m^{-3}, and its temperature was about 5 eV. Upon leaving the discharge chamber, the quasi-neutral plasma expanded into the much less dense surrounding ionosphere. The spectrum was taken about 15 meters from the contactor plume, focusing on the plume about 1.5 m downstream of the contactor exit plane. The apparent broadness of the lines is due to the spectrograph's relatively wide slit [20].

Optical emissions from the SEPAC plasma contactor are higher than the emissions expected from a similarly sized ion thruster for two reasons. First, the plasma contactor ion density is higher since the contactor ions are traveling about a quarter as fast as thruster beam ions. Second, the electrons in the SEPAC plasma contactor plume originate in the discharge chamber and are much hotter than the neutralizer cathode electrons in an ion thruster plume,

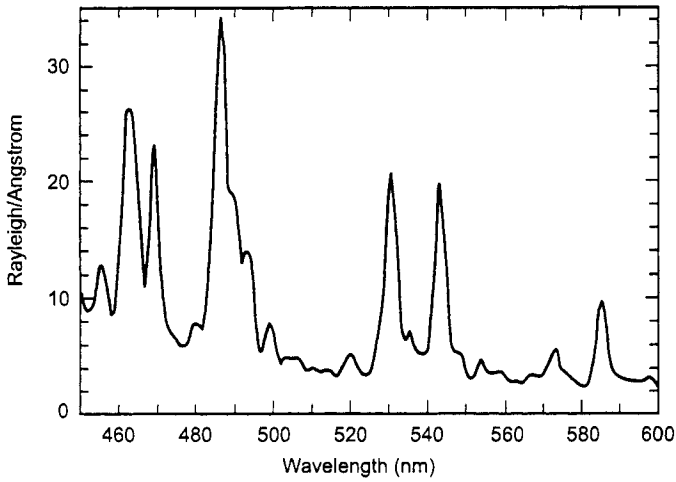

Fig. 8-18. Visible xenon spectra from the SEPAC plasma contactor observed by the AEPI hand-held camera during Shuttle Mission STS-45 (from [20]).

5 eV versus 2 eV. As a result, the absolute magnitude of the spectrum in Fig. 8-18 is about 2 orders of magnitude more intense than one would expect from an operating ion thruster.

The source of the strong visible lines in the xenon spectrum is interesting. Visible emissions from states with allowed transitions to ground contribute very little to the total observed visible spectra. Most of the visible emissions originate from states that do not have allowed transitions to ground. The reason for this is that an optically allowed transition to ground is typically a thousand times more probable than a transition to another excited state. Thus, if allowed, almost every excitation will lead to an ultraviolet (UV) photon. Indeed, most of the radiation from xenon plasmas is in the UV, with only a small part in the visible. Line emissions in the visible are dominated by radiative decay from states where the radiative transitions to ground are forbidden. When an electron collision excites one of these states, it decays though a multi-step process to ground, since the direct radiative decay to ground is forbidden and the collisional decay rate is orders of magnitude slower than the allowed radiative transitions. Although the excitation cross sections from ground to these states are smaller than those to states with optically allowed transitions, the absence of a competing single-step decay path to ground allows these states to dominate the visible emissions.

The total power radiated by a thruster plume, in both the visible and the UV, can be estimated by assuming that both the ion beam and the neutral gas expand

with the same effective cone angle θ. The radius of the beam and neutral plumes as a function of the distance z from the thruster is then

$$R = R_O + z\tan\theta, \tag{8.5-2}$$

where R_O is the initial radius. Assuming a quasi-neutral beam, the ion and electron densities are

$$n_e = n_i = \frac{I_b}{e v_i \pi R^2}. \tag{8.5-3}$$

The neutral density is given by

$$n_O = \frac{I_b}{e v_n \pi R^2}\left(\frac{1-\eta_m}{\eta_m}\right). \tag{8.5-4}$$

Emission from the neutral gas is proportional to the product of the electron density, the neutral gas density, the electron velocity, and the Maxwellian-averaged excitation cross section:

$$\begin{aligned} P_{\text{emission}} &= \int n_e n_o v_e \langle\sigma_{\text{excite}}\rangle e E_{\text{emission}}\, dV \\ &= \int_0^\infty n_e n_o v_e \langle\sigma_{\text{excite}}\rangle e E_{\text{emission}}\, 2\pi R^2\, dz \\ &= \int_{R_o}^\infty n_e n_o v_e \langle\sigma_{\text{excite}}\rangle e E_{\text{emission}} \frac{2\pi R^2}{\tan\theta} dR, \end{aligned} \tag{8.5-5}$$

where the temperature-averaged excitation cross section, $\langle\sigma_{\text{excite}}\rangle$, is from [20]:

$$\sigma_{\text{excite}}(T_{\text{eV}}) = \frac{19.3\exp(-11.6/T_{\text{eV}})}{\sqrt{T_{\text{eV}}}} \times 10^{-20}\ [\text{m}^2]. \tag{8.5-6}$$

For example, at 2 eV, the value of $\langle\sigma_{\text{excite}}\rangle$ is about 0.8×10^{-20} m^2. Integrating over the plume volume, assuming that E_{emission} is 10 eV (approximately the energy of the lowest-lying excited state of xenon), and that the neutral temperature is 500 deg C, the total radiated power in the NSTAR thruster plume at the full power point (I_{beam} 1.76 A, V_{beam} = 1100 V) is

$$P_{\text{emission}} = \frac{2I_b^2}{e v_i v_n \pi R \tan\theta}\left(\frac{1-\eta_m}{\eta_m}\right) v_e \langle \sigma_{\text{excite}} \rangle E_{\text{emission}} \qquad (8.5\text{-}7)$$
$$\approx 0.04\,[\text{W}],$$

which is much less than a tenth of a watt. Emissions in the visible range are usually only about one percent of the total radiated power.

References

[1] B. M. Anzel, U.S. Patent no. 5,443,231, August 22, 1995.

[2] D. M. Goebel, M. Martinez-Lavin, T. A. Bond, and A. M. King, "Performance of XIPS Electric Propulsion in Station Keeping of the Boeing 702 Spacecraft," AIAA-2002-4348, 38th Joint Propulsion Conference, Indianapolis, Indiana, July 7–10, 2002.

[3] I. D. Boyd and A. Ketsdever, "Interactions Between Spacecraft and Thruster Plumes," *Journal of Spacecraft and Rockets*, vol. 38, no. 3, pp. 380–380, 2001.

[4] J. Wang, D. Brinza, and M. Young, "Three-Dimensional Particle Simulations of Ion Propulsion Plasma Environment for Deep Space 1," *Journal of Spacecraft and Rockets*, vol. 38, no. 3, pp. 433–440, 2001.

[5] I. G. Mikellides, G. A. Jongeward, I. Katz, and D. H. Manzella, "Plume Modeling of Stationary Plasma Thrusters and Interactions with the Express-A Spacecraft," *Journal of Spacecraft and Rockets*, vol. 39 no. 6, pp. 894–903, 2002.

[6] I. G. Mikellides, M. J. Mandell, R. A. Kuharski, D. A. Davis, B. M. Gardner, and J. Minor, "The Electric Propulsion Interactions Code (EPIC)," AIAA 2003-4871, 39th Joint Propulsion Conference, Huntsville, Alabama, July 20–23, 2003.

[7] D. E. Brinza, M. D. Henry, A. T. Mactutis, K. P. McCarty, J. D. Rademacher, T. R. van Zandt, P. Narvaez, J. J. Wang, B. T. Tsurutani, I. Katz, V. A. Davis, S. Moses, G. Musmann, F. Kuhnke, I. Richter, C. Othmer, and K.H. Glassmeier, "An Overview of Results from the Ion Diagnostics Sensors Flown on DS1," AIAA-2001-0966, presented at the 39th AIAA Aerospace Sciences Meeting & Exhibit, Reno, Nevada, January 8–11, 2001.

[8] V. A. Davis, I. Katz, M. J. Mandell, D. E. Brinza, M. D. Henry, J. J. Wang, and D. T. Young, "Ion Engine Generated Charge Exchange Environment—Comparison Between NSTAR Flight Data and Numerical Simulations," AIAA-2000-3529, 36th Joint Propulsion Conference, Huntsville, Alabama, July 16–19, 2000.

[9] J. Pollard, K. D. Diamant, V. Khayms, L. Werthman, D. Q. King, and K. H. DeGrys, "Ion Flux, Energy, Charge-State Measurements for the BPT-4000 Hall Thruster," AIAA-2001-3351, 37th Joint Propulsion Conference, Salt Lake City, Utah, July 8–11, 2001.

[10] I. G. Mikellides, I. Katz, R. A. Kuharski, and M. J. Mandell, "Elastic Scattering of Ions in Electrostatic Thruster Plumes," *Journal of Propulsion and Power*, vol. 21, no. 1, pp. 111–118, 2005.

[11] D. E. Parks and I. Katz, "A Preliminary Model of Ion Beam Neutralization," Electric Propulsion and Its Applications to Space Missions," edited by R. C. Finke, *Progress in Astronautics and Aeronautics*, vol. 79, 1981.

[12] J. Ashkenazy and A. Fruchtman, "A Far-field Analysis of Hall Thruster Plume," Division of Plasma Physics (DPP) and International Congress on Plasma Physics Meeting (ICPP), Paper BMI-004, Quebec City, Canada, October 2000.

[13] E. J. Pencil, T. Randolph, and D. H. Manzella, "End-of-life Stationary Plasma Thruster Far-field Plume Characterization," AIAA-1996-2709, 32nd Joint Propulsion Conference, Lake Buena Vista, Florida, July 1–3, 1996.

[14] J. E. Polk, D. M. Goebel, J. S. Snyder, and A. C. Schneider, "Performance and Wear Test Results for a 20-kW Class Ion Engine with Carbon-Carbon Grids," AIAA-2005-4393, 41st Joint Propulsion Conference, Tucson, Arizona, July 11–14, 2005.

[15] J. S. Miller, S. H. Pullins, D. J. Levandier, Y. Chiu, and R. A. Dressler, "Xenon Charge Exchange Cross Sections for Electrostatic Thruster Models," *Journal of Applied Physics*, vol. 91, no. 3, pp. 984–991, 2002.

[16] J. R. Beattie and S. Kami, "Advanced Technology 30-cm Diameter Mercury Ion Thruster," AIAA-82-1910, 16th International Electric Propulsion Conference, New Orleans, Louisiana, November 17–19, 1982.

[17] R. Wirz and I. Katz, "XIPS Ion Thruster Grid Erosion Predictions for Deep Space Missions," 30th International Electric Propulsion Conference, Florence, Italy, September 17–20, 2007.

[18] J. R. Beattie, J. A. Marshall, J. L. Burch, and W. C. Gibson, "Design, Qualification, and On-Orbit Performance of the ATLAS Plasma Contactor," IEPC-93-010, International Electric Propulsion Conference, Seattle, Washington, September 1993.

[19] J. R. Beattie, W. S. Williamson, J. N. Matossian, E. J. Vourgourakis, and J. L. Burch, AIAA-1989-1603, "High-Current Plasma Contactor Neutralizer System," 3rd International Conference on Tethers in Space—Toward Flight, San Francisco, California, May 17–19, 1989.

[20] I. Katz, D. E. Parks, B. M. Gardner, S. B. Mende, H. I. Collin, D. H. Manzella, and R. M. Myers, "Spectral Line Emission by the SEPAC Plasma Contactor: Comparison Between Measurement & Theory," AIAA-95-0369, 33rd Aerospace Sciences Meeting and Exhibit, Reno, Nevada, January 9–12, 1995.

Problems

1. An ion thruster 20 cm in diameter produces a Xe^+ ion beam at 2000 V.
   a. If there is no electron neutralization of the beam, what is the maximum current in the beam if the beam diameter doubles in a distance of 1 m?
   b. What is the effective angular divergence of this beam?
   c. At what current density is electron neutralization required to keep the angular divergence less than 10 deg? (Hint: find the radial acceleration using Gauss's law for the radial electric field in the beam.)
2. You have just been hired as a propulsion engineer by a spacecraft manufacturer who plans to launch a commercial satellite that uses a 30-cm xenon ion engine operated for station keeping. The manufacturer plans to perform a costly test to assess whether a 1-mil-thick Kapton coating over a critical spacecraft surface located near the engine will survive 1500 hours of thruster operation. You immediately recall that your course work may allow you to determine the sputtering erosion of the Kapton layer by analysis, and thus possibly save your employer the high cost of performing the test. The spacecraft surface in question is a flat panel located perpendicularly to the thruster's r–z plane, as shown in Fig. 8-19. The panel length exceeds 6 m. Assuming that the ion beam consists of singly charged ions only,

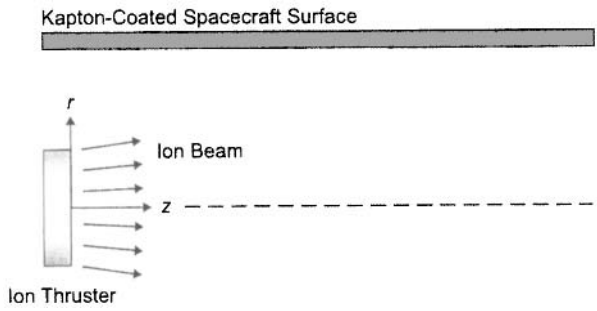

Fig. 8-19. Flat panel positioned over an ion thruster plume.

a. Use the equations in your textbook to express the ion beam density, n, as a function of spatial coordinates (r,z). Produce contour plots of the beam density within a radius of $r = 0.5$ m from the center of the thruster exit ($r = 0$, $z = 0$). Assume that the ion density n_0 at ($r = 0$, $z = 0$) is 4×10^{15} m^{-3} and that the ion beam velocity V_0 is 40 km/s. Also, assume that $u_{\text{Bohm}} / V_0 = 0.03$.

b. Derive an expression for the radial component of the ion beam flux, $\Gamma_r = v_r$, as a function of spatial coordinates (r,z). Plot the radial ion beam flux as a function of z for $r = 0.3$, 0.4, and 0.5 m.

c. Perform a literature search to find the sputtering yield Y of Kapton as a function of ion energy/ion charge, E, and incidence angle, β, and then plot Y for 300-V and 1000-V ions between 0 and 90 deg of incidence angle. (Hint: The sputtering yield for many materials is usually expressed as $Y(E,\beta) = (a + bE)f(\beta)$, where $f(\beta)$ is a polynomial function and a,b are constants.)

d. Compute the erosion rate in (Å/s) caused by the main ion beam along the Kapton plate (in the r-z plane), as a function of z, for $r = 0.3$, 0.4, and 0.5 m. Assume that the molecular weight of Kapton is 382 g/mol and that its mass density is 1.42 g/cm^3 (1Å = 10^{-10} m).

e. If the panel was placed at $r = 0.5$ m from the thruster, how long would it take for the main ion beam to erode completely the Kapton layer?

f. For partial credit, choose one answer to the following question: how would you advise your boss based on your results?

   i. The Kapton coating will be just fine. There's no need to perform a test. Build the spacecraft as is (panel radial location = 0.5 m).

   ii. The Kapton coating will not survive. We must consider changing the location of the panel relative to the thruster.

iii. The Kapton coating will not survive. Why don't we just use chemical propulsion?

iv. I must perform more calculations.

v. ii and iv

vi. The Kapton coating will not survive. The mission cannot be launched.

3. In Section 8.3.3, the differential scattering cross section was introduced.
   a. What is its physical meaning and what are its units?
   b. Figure 8-20 represents the basic picture of a classical scattering trajectory, viewed from the frame of reference of the target particle. In the figure, R is the distance of closest approach, b is the impact parameter, and θ is the defection angle.

      For elastic scattering, the conservation equations of angular momentum and energy allow us to predict the deflection angle as follows:

$$\theta = \pi - 2b\int_R^\infty \frac{dr}{r^2\left[1-(b/r)^2-\Phi(r)/E\right]}$$

      where $\Phi(r)$ is the interaction potential, which is related to the force field between the colliding particles. E is the (relative) energy of the incident particles. The differential ($d\sigma/d\Omega$) and total σ cross sections are given by

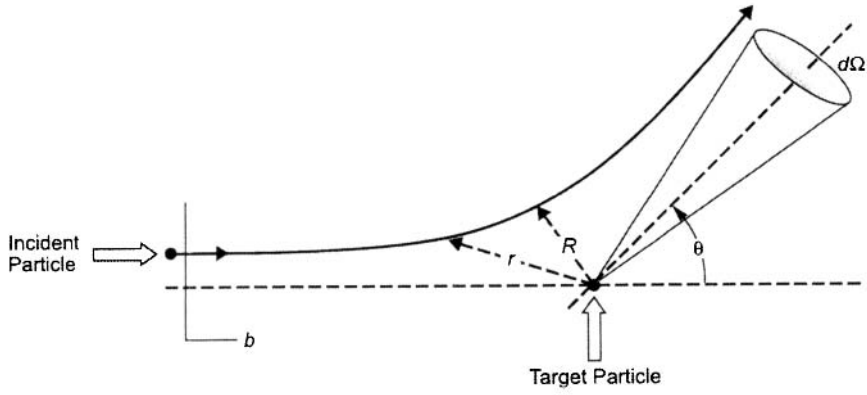

Fig. 8-20. Classic scattering diagram for an incident particle on a target particle.

$$\frac{d\sigma}{d\Omega} = \frac{b}{\sin\theta}\left|\frac{db}{d\theta}\right|$$

$$\sigma = \int \frac{d\sigma}{d\Omega} d\Omega.$$

Compute the differential and total cross sections for (i) collisions between hard spheres of diameter d and (ii) a repulsive force field between particles that varies as k/r^2 (k is a constant).

4. The most general elastic collision process between two particles of unequal masses, m_1 and m_2, velocity vectors before the collision, $\mathbf{u}_1$ and $\mathbf{u}_2$, and after the collision, $\mathbf{u}_1'$ and $\mathbf{u}_2'$, can be represented by the geometrical construction in Fig. 8-21 using the following definitions:

   Relative velocities: $\mathbf{U} = \mathbf{u}_1 - \mathbf{u}_2$, $\mathbf{U}' = \mathbf{u}_1' - \mathbf{u}_2'$

   Center-of-mass (CM) velocity: $\mathbf{u}_c = (m_1\mathbf{u}_1 + m_2\mathbf{u}_2)/(m_1 + m_2)$

   Reduced mass: $M = m_1 m_2/(m_1 + m_2)$

   a. In the case of equal masses, $m_1 = m_2 = m$, and one stationary particle, $\mathbf{u}_2 = 0$, draw the new geometrical construction. What is the relationship between the scattering angle in the CM frame, θ, and the scattering angle in the laboratory frame, β?

   b. Convert the CM differential cross section, $d\sigma/d\Omega_{CM}$, into the laboratory frame of reference, $d\sigma/d\Omega_L$.

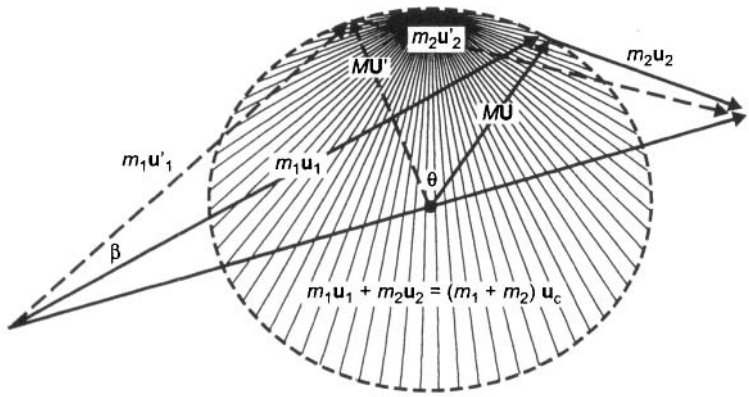

Fig. 8-21. Center of mass depiction of an elastic scattering event.

5. Derive Eq. (8.5-1) for the phase shift of electromagnetic radiation passing through a plasma (hint: assume the phase shift is small).

6. A spacecraft has a 32-GHz communications system that passes into the diverging plume of an ion propulsion system 1 m from the thruster. If the NSTAR thruster beam has an initial radius of 15 cm and produces 1.76 A of xenon ions at 1100 V with a 10-deg half-angle divergence from the initial area, what is the total phase shift in degrees produced when the thruster is turned on or off?

Fundamentals of Electric Propulsion: Ion and Hall Thrusters
by Dan M. Goebel and Ira Katz
Copyright © 2008 John Wiley & Sons, Inc.

Chapter 9
Flight Ion and Hall Thrusters

9.1 Introduction

Ion and Hall thruster technology development programs continue to improve the performance of these engines. However, it is worthwhile to survey the state-of-the-art thrusters that have been flown to date. In this brief look, we are covering modern thrusters that have flown in the last ten to fifteen years in satellite station-keeping and spacecraft prime-propulsion applications. These thrusters are ion thruster and Hall thruster systems that use xenon as the propellant. The parameters given for the thrusters include the neutralizer or external cathode flow rates, since that is required for flight operation on satellites and spacecraft.

9.2 Ion Thrusters

The first of the modern ion thrusters flown were intended for station-keeping applications on geosynchronous satellites and developed by Mitsubishi Electric Corporation (MELCO) for use on the Japanese "Engineering Test Satellite (ETS-6)" in 1994 [1,2]. These 13-cm Kaufman thrusters produced nominally 20 mN of thrust at an Isp of about 2400 s. Despite launch vehicle problems that caused the satellite to fail to reach its planned orbit, the thrusters were successfully operated in orbit. The same electric propulsion subsystem was launched on the COMETS satellite in 1996, which also failed to reach its planned orbit. Development of Kaufman ion thrusters for communications satellite station-keeping applications is continuing at MELCO.

The first successful use of ion thrusters in commercial station keeping applications was the Hughes 13-cm Xenon Ion Propulsion System (XIPS) [3,4], which was launched into orbit in 1997 on the Hughes PAS-5 satellite. The XIPS system utilizes two fully redundant subsystems, each consisting of two thrusters, a power supply, and a xenon gas supply. The performance parameters

for the 13-cm XIPS thruster are shown in Table 9-1. The thrusters produce nominally 18 mN of thrust at an Isp of 2500 s and a total efficiency of about 50%. A schematic of the 13-cm XIPS thruster is shown in Fig. 9-1, and a photograph of the thruster, which is manufactured by L-3 Communications, Electron Technologies, Inc., is shown in Fig. 9-2. Over 60 of these thrusters were launched into orbit and successfully used for North-South station keeping on Hughes and Boeing satellites.

The next ion thruster to fly was NASA's NSTAR ion engine [5,6], which is a ring-cusp, DC electron-bombardment discharge thruster with an active grid

Table 9-1. 13-cm XIPS performance.

Parameter	Station Keeping
Active grid diameter (cm)	13
Thruster input power (W)	421
Average Isp (s)	2507
Thrust (mN)	17.2
Total efficiency (%)	50.0
Mass utilization efficiency (%)	77.7
Electrical efficiency (%)	71.3
Beam voltage (V)	750
Beam current (A)	0.4

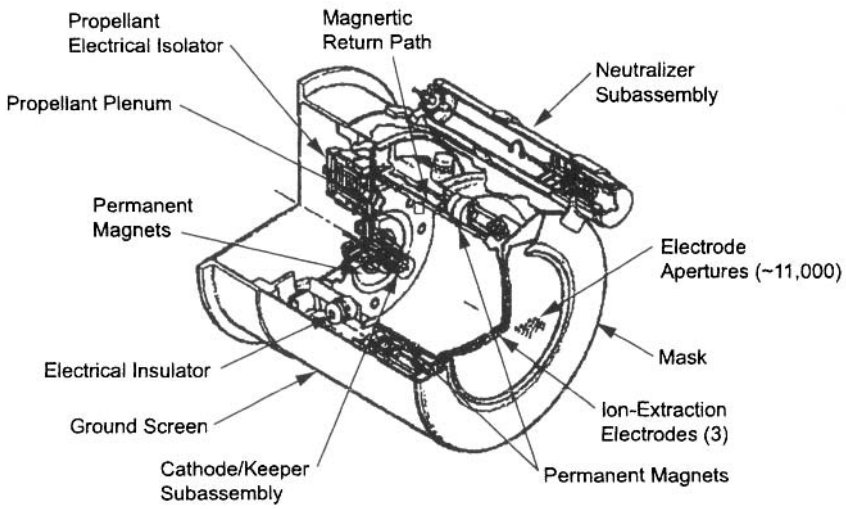

Fig. 9-1. Schematic of the 13-cm XIPS thruster (from [4,10]).

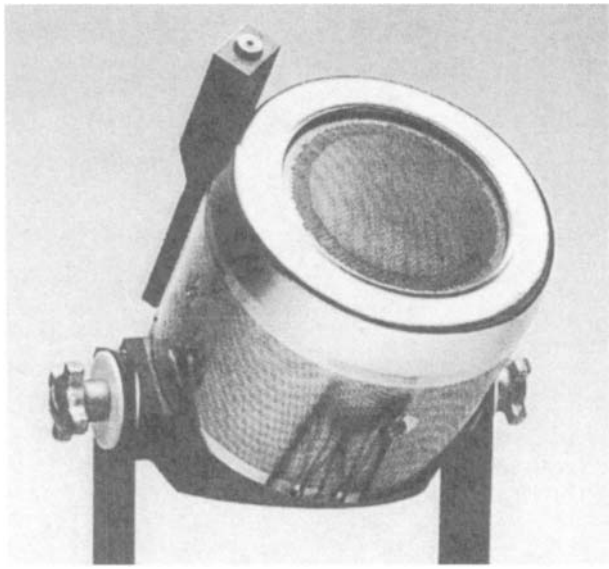

Fig. 9-2. Photograph of the 13-cm XIPS ion thruster (photo courtesy of L-3 Communications, Electron Technologies, Inc.).

diameter of 28.6 cm. NSTAR was developed and manufactured by a team of NASA GRC, JPL and Hughes/Boeing and launched in 1998 on the Deep Space 1 spacecraft. This ion engine has arguably been the most analyzed and tested ion thruster in history, with over 16,000 hours of operation in space, over 40,000 hours of life testing, and hundreds of papers published on its design and performance. NSTAR was operated over a wide throttle range in the DS1 application from a minimum input power to the power processing unit (PPU) of 580 W to a maximum power of over 2550 W. The Extended Life Test of this thruster at JPL demonstrated 30,252 hours of operation distributed across several of the throttle levels and was terminated with the engine still running in order to provide life status and data for the subsequent DAWN mission [7]. The throttle table used on DS1 with parameters for the NSTAR thruster from a review by Brophy [6] is shown in Table 9-2. A photograph of the NSTAR engine manufactured by L-3 Communications, Electron Technologies, Inc. is shown in Fig. 9-3.

The next ion thruster technology launched was designed for both orbit raising and station keeping applications on a commercial communications satellite. The 25-cm XIPS thruster was first launched in 1999 on a Hughes/Boeing 702 satellite. Although the 25-cm XIPS ion thruster was developed [9] at Hughes Research Laboratories in the same time frame as the NSTAR engine and has a similar basic design as the 13-cm XIPS shown in Fig. 9-1, the 25-cm thruster entered production after the 13-cm version and incorporated sufficient

Table 9-2. NSTAR throttle table.

NSTAR Throttle Level	PPU Input Power (W)	Engine Input Power (W)	Calculated Thrust (mN)	Specific Impulse (s)	Total Efficiency (%)
15	2567	2325	92.7	3127	61.8
14	2416	2200	87.9	3164	62.4
13	2272	2077	83.1	3192	63.0
12	2137	1960	78.4	3181	62.8
11	2006	1845	73.6	3196	63.1
10	1842	1717	68.4	3184	62.6
9	1712	1579	63.2	3142	61.8
8	1579	1456	57.9	3115	61.1
7	1458	1344	52.7	3074	59.6
6	1345	1238	47.9	3065	59.0
5	1222	1123	42.6	3009	57.4
4	1111	1018	37.4	2942	55.4
3	994	908	32.1	2843	52.7
2	825	749	27.5	2678	48.7
1	729	659	24.6	2382	47.2
0	577	518	20.7	1979	42.0

improvements to be considered a second-generation device. A photograph of the 25-cm XIPS thruster, which is also manufactured by L-3 Communications, Electron Technologies, Inc., is shown in Fig. 9-4. To date, fourteen of the Boeing 702 communications satellites with a total of 56 XIPS thrusters have been successfully launched and are in operation.

The initial operation of the 25-cm thrusters in space on the 702 satellites was described in 2002 [10]. After launch, these thrusters are first used for orbit raising and then provide all of the propulsion requirements for orbit control including north-south and east-west station keeping, attitude control, and momentum dumping. The ion thrusters are also used for any optional station change strategies and will ultimately be used for de-orbit at the end of the satellite's lifetime. The "high power" orbit insertion mode requires nearly continuous operation by two of the thrusters for times of 500 to 1000 hours, depending on the launch vehicle and satellite weight. This mode utilizes about 4.5 kW of bus power to generate a 1.2-kV, 3-A ion beam, which produces 165-mN thrust at a specific impulse of about 3500 seconds. Once orbit insertion

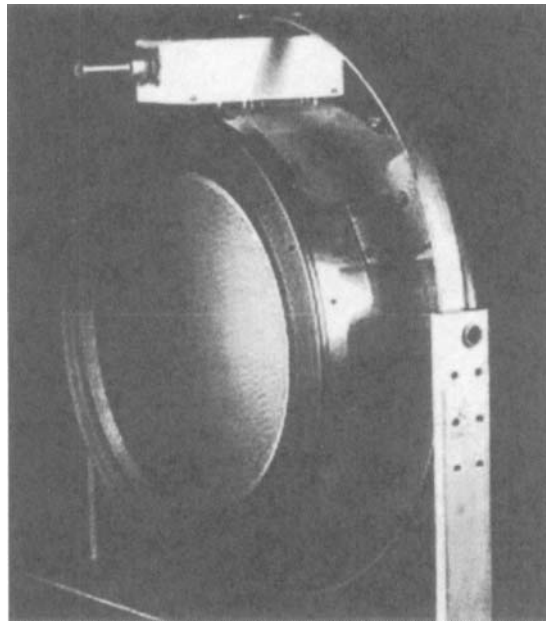

Fig. 9-3. Photograph of the NASA NSTAR ion thruster (photo courtesy of L-3 Communications, Electron Technologies, Inc.).

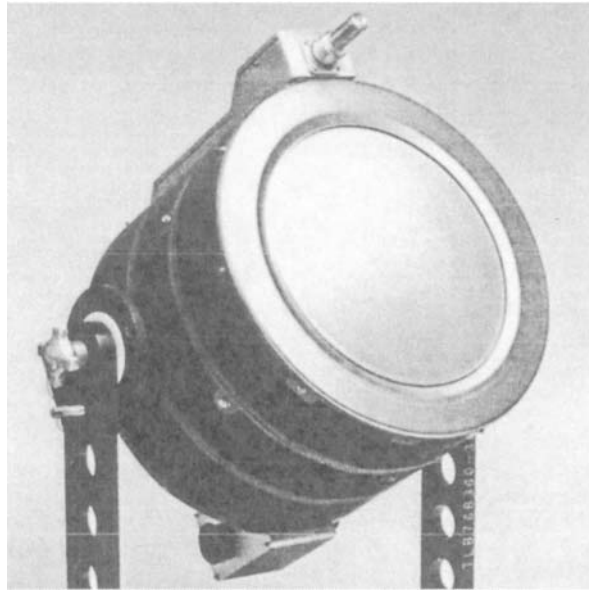

Fig. 9-4. Photograph of the 25-cm XIPS ion thruster (photo courtesy of L-3 Communications, Electron Technologies, Inc.).

is completed, each of the four thrusters is fired once daily for an average of about 45 minutes in a "low power," 2.3-kW mode for station keeping. In this mode, the beam voltage is kept the same, and the discharge current and gas flow are reduced to generate a 1.2-kV, 1.5-A beam that produces nominally 79 mN of thrust at an Isp of 3400 s. The thruster performance parameters are shown in Table 9-3. Recently, tests by the manufacturer L-3 Communications Electron Technologies Inc. have demonstrated that the XIPS engine and PPU can be throttled from a PPU input power level of 400 W to over 5 kW. Over this range, the performance significantly exceeds the NSTAR thruster performance [11].

The next flight of ion thrusters was on the European Space Agency Artemis spacecraft launched in 2001. Artemis carried four ion thruster assemblies, two EITA (Electron-bombardment Ion Thruster Assembly) systems manufactured by Astrium UK, and two RITA (Radio-frequency Ion Thruster Assembly) systems developed by Astrium Germany. The EITA system, also called the UK-10 system, used copies of the T5 thruster [12,13], and the RITA system used RIT-10 ion thrusters [14,15]. Artemis was intended to be launched into a geosynchronous orbit, but a malfunction of the launcher's upper stage placed the satellite into a lower orbit. The ion thrusters were used in an unplanned orbit-raising role to rescue the spacecraft from the lower 31,000-km parking orbit and raise the spacecraft to the proper geosynchronous orbit. The thrusters then successfully performed standard EP station keeping activities.

The EITA/UK-10/T5 thruster is a 10-cm Kaufman thruster [13] presently manufactured by Qinetiq in England. The performance of the T5 Kaufman

Table 9-3. 25-cm XIPS performance parameters.

Parameter	Low-Power Station Keeping	High-Power Orbit Raising
Active grid diameter (cm)	25	25
Thruster input power (kW)	2	4.3
Average Isp (s)	3420	3550
Thrust (mN)	80	166
Total efficiency (%)	67	68.8
Mass utilization efficiency (%)	80	82.5
Electrical efficiency (%)	87	87.5
Beam voltage (V)	1215	1215
Beam current (A)	1.45	3.05

thruster in station keeping applications [13] is shown in Table 9-4. A schematic of a generic Kaufman thruster was shown in Chapter 4, and a photograph of the T5 thruster is shown in Fig. 9-5. The T5 thruster generates an 1100-V, 0.329-A xenon ion beam that produces about 18 mN of thrust at a nominal Isp of 3200 s with a total efficiency of about 55%.

The RITA system uses a RIT-10 rf ion thruster originally developed [14] at the University of Giessen in Germany and manufactured [15] for Artemis by Astrium in Germany. The performance of the RIT-10 thruster in the station keeping application [15] is shown in Table 9-5. A schematic of a generic rf thruster was shown in Chapter 4, and a photograph of the RIT-10 rf ion thruster from [16] is shown in Fig. 9-6. The RIT-10 thruster generates a 1500-V, 0.234-A xenon ion beam that produces 15 mN of thrust at an Isp of 3400 s and a total efficiency in excess of 51%.

The Institute of Space and Astronautical Science of the Japan Aerospace Exploration Agency (JAXA) launched four of the μ10 ECR ion thrusters on the Hayabusa (formerly Muses-C) spacecraft [17] in 2003. These 10-cm grid-diameter thrusters are successfully providing primary propulsion for an asteroid sample return mission that will return to Earth in 2010. The thruster [18,19] uses 4.2-GHz microwaves to produce the main plasma in the thruster and drive the electron neutralizer. A schematic drawing of the thruster was shown in Chapter 4. The performance of the 10-cm ECR thruster is shown in Table 9-6, and a photograph of the thruster from Ref. 20 is shown in Fig. 9-7. The 10-cm ECR ion thruster generates a 1500-V, 0.136-A xenon ion beam that produces 8.1 mN of thrust at an Isp of 3090 s and a total efficiency of 36%.

The most recent launch of a new ion thruster was by the Japan Aerospace Exploration Agency (JAXA), who launched four 20mN-class Kaufman ion thrusters developed by Mitsubishi Electric Corporation on the Engineering Test Satellite VIII (ETS-VIII) [21] in 2006. The 12-cm grid-diameter Kaufman thrusters provide north-south station keeping for this large geosynchronous communications satellite. The performance of the 12-cm Kaufman thruster [22] is shown in Table 9-7, and a photograph of the thruster from [23] is shown in Figure 9-8. At its nominal operating condition, the thruster generates a 996-V, 0.432 to 0.480-A xenon ion beam that produces 20.9 to 23.2 mN of thrust at an Isp of 2402 to 2665 sec and a total efficiency of about 46 to 50%.

There are a significant number of new ion thrusters in development world-wide for prime propulsion and satellite station keeping applications. Since these thrusters have not flown as of this date, they will not be covered in detail and only mentioned here. NASA Glenn Research Center (GRC) is leading the

Table 9-4. T5 Kaufman thruster performance parameters.

Parameter	Station Keeping
Active grid diameter (cm)	10
Thruster input power (W)	476
Nominal Isp (s)	3200
Thrust (mN)	18
Total efficiency (%)	55
Mass utilization efficiency (%)	76.5
Electrical efficiency (%)	76.6
Beam voltage (V)	1100
Beam current (A)	0.329

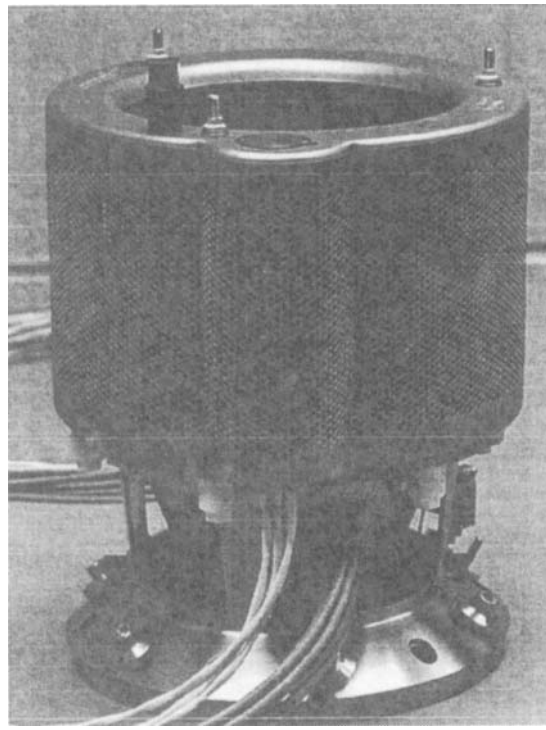

Fig. 9-5. Photograph of the T5 Kaufman ion thruster (photo courtesy of Qinetiq, Limited).

Table 9-5. RIT-10 rf thruster performance parameters.

Parameter	Station Keeping
Active grid diameter (cm)	10
Thruster input power (W)	459
Nominal Isp (s)	3400
Thrust (mN)	15
Total efficiency (%)	52
Mass utilization efficiency (%)	69.3
Electrical efficiency (%)	76.5
Beam voltage (V)	1500
Beam current (A)	0.234

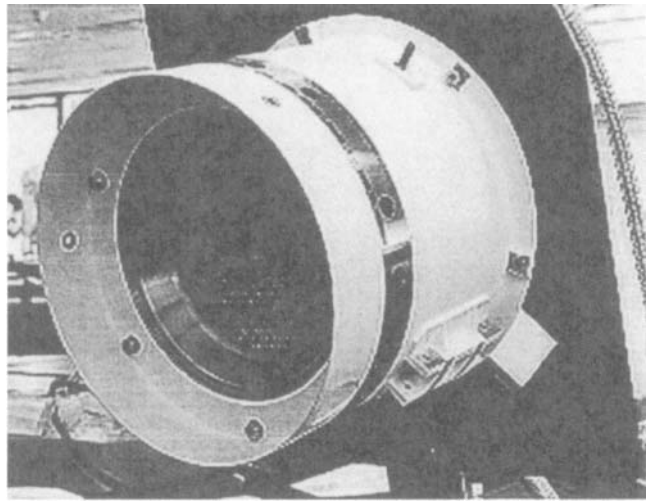

Fig. 9-6. Photograph of the RIT-10 rf ion thruster (from [16]).

development of the 7-kW NASA Evolutionary Xenon Thruster (NEXT) [24]. NASA's Jet Propulsion Laboratory (JPL) led the development of the 25-kW Nuclear Electric Xenon Ion thruster System (NEXIS) [25], which produced the highest efficiency (>81%) xenon ion thruster developed to date. NASA's GRC also led the development of the 30-kW High Power Electric Propulsion (HiPEP) thruster [26], which featured a rectangular geometry with both rf and DC hollow cathode plasma production versions. In England, Qineteq is developing the T-6 20-cm Kaufman thruster [27], which is capable of

Table 9-6. μ10 ECR microwave ion thruster performance.

Parameter	Primary Propulsion
Active grid diameter (cm)	10
Thruster input power (W)	340
Average Isp (s)	3090
Thrust (mN)	8.1
Total efficiency (%)	36
Mass utilization efficiency (%)	70
Electrical efficiency (%)	60
Beam voltage (V)	1500
Beam current (A)	0.136

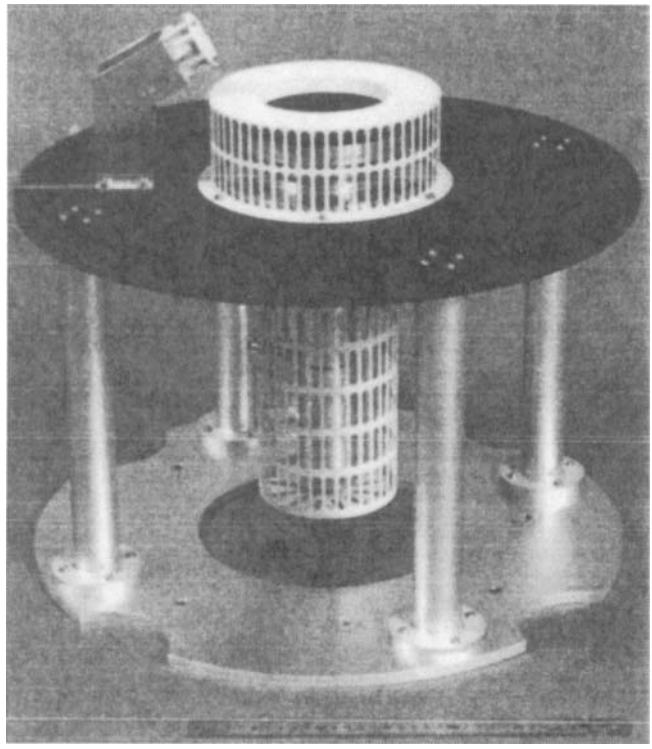

Fig. 9-7. Photograph of the μ10-ECR microwave discharge ion thruster (10-cm grid diameter) and microwave neutralizer [20].

Table 9-7. ETS-8 Kaufman thruster performance parameters.

Parameter	NS-Station Keeping
Active grid diameter (cm)	12
Thruster input power (W)	541–611
Nominal Isp (s)	2402–2665
Thrust (mN)	20.9–23.2
Total efficiency (%)	45.6–49.7
Mass utilization efficiency (%)	66.2–73.5
Electrical efficiency (%)	78.2–79.5
Beam voltage (V)	996
Beam current (A)	0.43–0.48

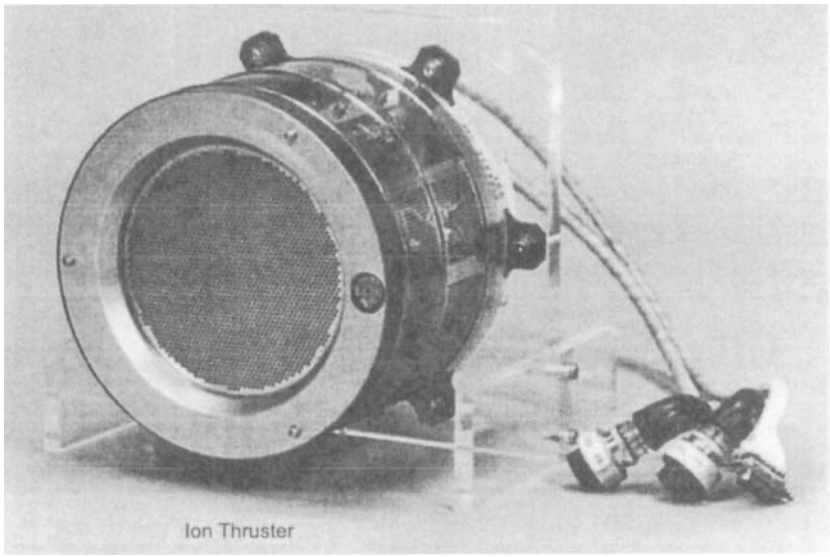

Figure 9-8. Photograph of the ETS-8 Kaufman ion thruster (from [23]).

producing up to 200-mN thrust for European communications satellite station keeping applications. In Japan, the Institute of Space and Astronautical Science is developing a 20-cm-diameter, 30-mN-class microwave ion thruster [28]. In Germany, Astrium is developing a 200-mN-class rf ion thruster (RIT-22) for station keeping applications [29]. Finally, ring-cusp and rf ion thrusters are being miniaturized for applications that require thrust levels of the order of 1 mN or less. The 3-cm Miniature Xenon Ion thruster (MiXI) [30] uses a DC discharge, ring-cusp geometry with closely spaced ion optics to produce up to

3 mN of thrust at beam voltages of up to 1200 V. The micro-Newton Rf Ion Thruster (μN-RIT) [31] use a low frequency (≈1 MHz) rf discharge scaled down to 2 to 4 cm in diameter to produce precision thrust levels as low as 20 μN at beam voltages in excess of 1 kV. There are many additional small research and development programs at universities and in small businesses, but these are too numerous to be covered here.

9.3 Hall Thrusters

The most successful and extensive electric propulsion development and application has been by the Russians flying Hall thrusters for station keeping on satellites [32]. Over 140 Hall thrusters have been operated in space since 1971 when the Soviets first flew a pair of Hall thrusters called Stationary Plasma Thrusters (SPT) on the Meteor satellite [32]. This name is translated from the Russian literature, but refers to the continuous operation ("stationary") of the Hall thruster in comparison to the Pulsed-Plasma Thrusters (PPT) that the Russians had previously tested and flown in the 1960s [32]. SPT thrusters for satellite applications have been developed with different sizes characterized by the outside diameter of the plasma discharge slot of 50 to over 140 mm [32].

The performance of four sizes of the SPT thruster manufactured by Fakel in Russia is shown in Table 9-8. The SPT-100 operates nominally at a discharge voltage of 300 V and current of 4.5 A to produce 82 mN of thrust at an Isp of 1600 s and a total efficiency of 50% averaged over the life of the thruster. The different SPT thrusters shown have been tested at discharge voltages of 200 to 500 V and power levels of a few hundred watts up to 5 kW. These Hall thrusters have also been tested on a variety of gases such as argon and krypton, but xenon is the present standard for space applications. A schematic of the Hall thruster was shown in Chapter 7, and a photograph of a Fakel SPT-100 thruster from [33] is shown in Fig. 9-9.

The first flight of a Hall thruster on a U.S. spacecraft was the 1998 launch of a D-55 TAL (Thruster with Anode Layer) Hall thruster [34,35] manufactured by TsNIIMASH in Russia on the National Reconnaissance Office's Space Technology Experiment Satellite (STEX). The STEX mission was intended to develop and demonstrate advanced spacecraft technologies in space, including Hall thrusters. The xenon D-55 TAL thruster nominally operates at 1.4 kW with an Isp of about 1500 s, but due to power limitations on the spacecraft was required to run at a discharge of 300 V and 2.2 A (660 W).

The European Space Agency (ESA) has demonstrated the use of commercial Hall thruster technology on the SMART-1 (Small Mission for Advanced Research in Technology) spacecraft in a lunar orbiting mission [36]. A

Table 9-8. STP Hall thruster performance.

Parameter	SPT-50	SPT-70	SPT-100	SPT-140
Slot diameter (cm)	5	7	10	14
Thruster input power (W)	350	700	1350	5000
Average Isp (s)	1100	1500	1600	1750
Thrust (mN)	20	40	80	300
Total efficiency (%)	35	45	50	>55
Status	Flight	Flight	Flight	Qualified

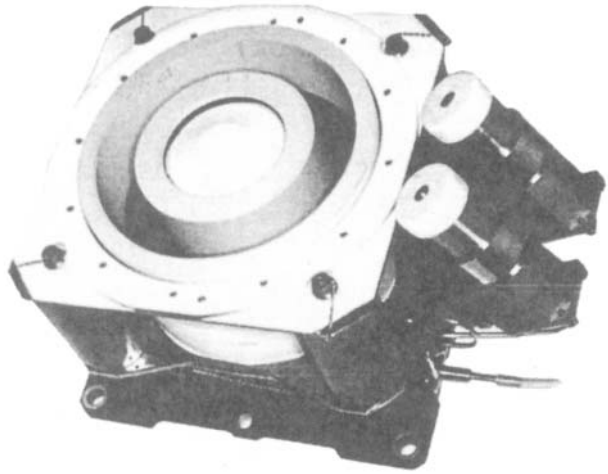

Fig. 9-9. Photograph of an SPT-100 Hall thruster (from [33]).

PPS-1350-G Hall thruster [37,38] manufactured by SNECMA Moteurs in France [39] was launched on SMART-1 in 2003 and provided primary propulsion for this mission. This thruster is based on the SPT-100 and is similar in size and power level. The thruster was operated over a throttleable power range of 462 to 1190 W for this lunar mission, producing a maximum thrust of 70 mN at an Isp of 1600 s. The finite efficiency of the power processing system required that the spacecraft supply 650 to 1420 W to the electric propulsion system. The PPS-1350 Hall thruster accumulated about 5000 hours of operation in space, and processed 82 kg of xenon in a very successful mission that featured several extensions of the mission life due to the thruster capabilities. The nominal performance of this thruster at 1.35 kW is shown in Table 9-9. The thruster schematic was shown in Chapter 7, and a photograph of the PPS-1350 Hall thruster is shown in Fig. 9-10.

The first commercial use of Hall thrusters by a U.S. spacecraft manufacturer was in 2004 by Space Systems Loral on the MBSAT satellite [33], which used Fakel SPT-100s provided by International Space Technologies Incorporated (ISTI). Loral has launched three communications satellites to date that use two pairs of SPT-100 Hall thrusters on each satellite, and plans to continue launching these systems in the future. Busek, Inc. was the first U.S. company to provide flight Hall thruster technology for a spacecraft when the 200-W BHT-200 flew on board the Air Force TacSat-2 spacecraft that was launched in late 2006 [40,41]. Beginning in 2008, Lockheed Martin Space Systems plans to begin flying BPT-4000 Hall thrusters (also developed in the U.S. by Aerojet) on the Air Force Advanced-EHF defense communications satellite [42]. Aerojet

Table 9-9. PPS-1350 Hall thruster performance.

Parameter	Primary Propulsion
Slot diameter (cm)	10
Thruster input power (W)	1500
Average Isp (s)	1650
Thrust (mN)	88
Total efficiency (%)	55
Discharge voltage (V)	350
Discharge current (A)	4.28

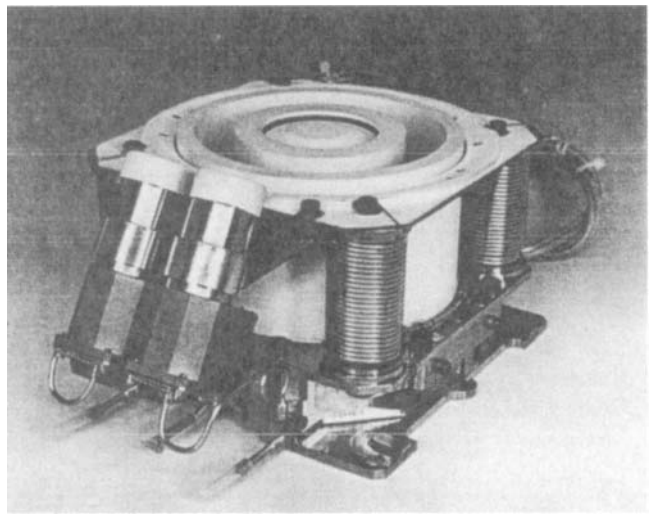

Fig. 9-10. Photograph of the PPS-1350 Hall thruster (photo courtesy of Snecma-Eric Drouin).

and JPL have jointly investigated the applicability of the BPT-4000 to NASA deep-space missions [43] where throttle range and efficiency are important. The throttleability of the BPT-4000 engine [44] from power levels 1 kW to 4.5 kW was demonstrated with very high efficiency observed at low power levels for this size thruster. Hall thruster technology will continue to be developed and used in commercial and scientific missions due to their high performance and relatively simple construction and operation.

References

[1] S. Shimada, K. Satho, Y. Gotoh, E. Nistida, I. Terukina, T. Noro, H. Takegahara, K. Nakamaru, and H. Nagano, "Development of an Ion Engine System for ETS-6," IEPC-93-009, 23rd International Electric Propulsion Conference, Seattle, Washington, September 1993.

[2] T. Ozaki, E. Nishida, and Y. Gotoh, "Development Status of 20mN Xenon Ion Thruster," AIAA-2000-3277, 36th Joint Propulsion Conference, Huntsville, Alabama, July 16–19, 2000.

[3] J. R. Beattie, "XIPS Keeps Satellites on Track," *The Industrial Physicist*, June 1998.

[4] J. R. Beattie, J. D. Williams, and R. R. Robson, "Flight Qualification of an 18-mN Xenon Ion Thruster," IEPC 93-1015, 23rd International Electric Propulsion Conference, Seattle, Washington, September 1993.

[5] M. J. Patterson, T. W. Haag, V. K. Rawlin, and M. T. Kussmaul, "NASA 30-cm Ion Thruster Development Status," AIAA-1994-2849, 30th Joint Propulsion Conference, Indianapolis, Indiana, June 27–29, 1994.

[6] J. R. Brophy, "NASA's Deep Space 1 Ion Engine," *Review of Scientific Instruments*, vol. 73, pp. 1071–1078, 2002.

[7] J. R. Brophy, M. Marcucci, G. Ganapathi, C. Garner, M. Henry, B. Nakazono, and D. Noon, "The Ion Propulsion System for Dawn," AIAA 2003-4542, 39th Joint Propulsion Conference, Huntsville, Alabama, July 20–23, 2003.

[8] http://www.l-3com.com/eti/product_lines_electric_propulsion.htm

[9] J. R. Beattie, J. N. Matossian, and R. R. Robson, "Status of Xenon Ion Propulsion Technology," *Journal of Propulsion and Power*, vol. 6, pp. 145–150, 1990.

[10] D. M. Goebel, M. Martinez-Lavin, T. A. Bond, and A. M. King, "Performance of XIPS Electric Propulsion in Station Keeping of the Boeing 702 Spacecraft," AIAA-2002-5117, 38th Joint Propulsion Conference, Indianapolis, Indiana, July 7–10, 2002.

[11] W. Tighe, K. Chien, E. Solis, P. Robello, D. M. Goebel, and J. S. Snyder, "Performance Evaluation of the XIPS 25-cm Thruster for Application to NASA Missions," AIAA-2006-4999, 42nd Joint Propulsion Conference, Sacramento, California, July 9–12, 2006.

[12] H. Gray, P. Smith, and D. G. Fern, "Design and development of the UK-10 Ion Propulsion System," AIAA-96-3084, 32nd Joint Propulsion Conference, Lake Buena Vista, Florida, July 1–3, 1996.

[13] http://www.qinetiq.com/home/commercial/space/space_technology/ep/t5_ion_thruster.html.

[14] K. H. Groh, O. Blum, H. Rado, and H. W. Loeb, "Inert Gas Radio-Frequency Thruster RIT 10," IEPC-79-2100, 14th International Electric Propulsion Conference, October 30–November 1, 1979.

[15] R. Killinger, H. Bassner, H. Leiter, and R. Kukies, "RITA Ion Propulsion for Artemis," AIAA-2001-3490, 37th Joint Propulsion Conference, Salt Lake City, Utah, July 8–11, 2001.

[16] http://cs.space.eads.net/sp/SpacecraftPropulsion/Rita/RIT-10.html

[17] H. Kuninaka, K. Nishiyama, I. Funakai, Tetsuya, and Y. Shimizu, "Asteroid Rendezvous of Hayabusa Explorer Using Microwave Discharge Ion Engines," IEPC Paper 2005-010, 29th International Electric Propulsion Conference, Princeton, New Jersey, October 31–November 4, 2005.

[18] S. Tamaya, I. Funaki, and M. Murakami, "Plasma Production Process in an ECR Ion Thruster," AIAA-2002-2196, 33rd AIAA Plasma Dynamics and Lasers Conference, Maui, Hawaii, May 20–23, 2002.

[19] H. Kuninaka, I. Funaki, K. Nishiyama, Y. Shimizu, and K. Toki, "Results of 18,000 hour Endurance Test of Microwave Discharge Ion Thruster Engineering Model," AIAA-2000-3276, 36th Joint Propulsion Conference, Huntsville, Alabama, July 16–19, 2000.

[20] Courtesy of Prof Kuninaka, Institute of Space and Astronautical Science, Japan Aerospace Exploration Agency.

[21] T. Ozaki, Y. Kasai, T. Nakagawa, T. Itoh, K. Kajiwara, and M. Ikeda, "In-Orbit Operation of 20 mN Class Xenon Ion Engine for ETS-VIII," 28th International Electric Propulsion Conference, IEPC-2007-084, Florence, Italy, September 17–20, 2007.

[22] T. Ozaki, E. Nishida, Y. Kasai, Y. Gotoh, T. Itoh, and K. Kajiwara, "Development Status of Xenon Ion Engine Subsystem for ETS-VIII," AIAA-2003-2215, 21st International Communications Satellite Systems Conference, Yokohama, Japan, April 15–19, 2003.

[23] T. Ozaki, Y. Kasai, and E. Nishida, "Improvement of 20mN Xenon Ion thruster," 26th International Electric Propulsion Conference, IEPC-99-153, Kitakyusyu, Japan, October 17–21, 1999.

[24] M. Patterson, J. Foster, T. Haag, V. Rawlin, and G. Soulas, "NEXT: NASA's Evolutionary Xenon Thruster," AIAA-2002-3832, 38th Joint Propulsion Conference, Indianapolis, Indiana, July 7–10, 2002.

[25] J. E. Polk, D. M. Goebel, I. Katz, J. Snyder, A. Schneider, L. Johnson, and A. Sengupta, "Performance and Wear Test Results for a 20-kW Class Ion Engine with Carbon-Carbon Grids," AIAA-2005-4393, 41st Joint Propulsion Conference, Tucson, Arizona, July 2005.

[26] J. Foster, T. Haag, H. Kamhawi, M. Patterson, S. Malone, and F. Elliot, "The High Power Electric Propulsion (HiPEP) Ion Thruster," AIAA-2004-3812, 40th Joint Propulsion Conference, Fort Lauderdale, Florida, July 11–14, 2004.

[27] N. Wallace, D. Mundy, D. Fearn, and C. Edwards, "Evaluation of the Performance of the T6 Ion Thruster," AIAA-1999-2442, 35th Joint Propulsion Conference, Los Angeles, California, June 20–24, 1999.

[28] K. Nishiyama, H. Kuninaka, Y. Shimizu, and K. Toki, "30-mN Class Microwave Discharge Ion Thruster," IEPC-2003-62, 28th International Electric Propulsion Conference, Bordeau, France, October 2003.

[29] H. Leiter, R. Kukies, R. Killinger, E. Bonelli, S. Scaranzin, and F. Scortecci, "RIT-22 Ion Engine Development - Endurance Test and Life Prediction," AIAA-2006-4667, 42nd Joint Propulsion Conference, Sacramento, California, July 9–12, 2006.

[30] R. Wirz, J. E. Polk, C. Marrese, and J. Mueller, "Experimental and Computational Investigation of the Performance of a Micro-Ion Thruster," AIAA-2002-3835, 38th Joint Propulsion Conference, Indianapolis, Indiana, July 7–10, 2002.

[31] D. Feili, H. W. Loeb, K. H. Schartner, St. Weis, D. Kirmse, B. K. Meyer, R. Kilinger, and H. Mueller, "Testing of new μN-RITs at Giessen University," AIAA 2005-4263, 41st Joint Propulsion Conference, Tucson, Arizona, July 10–13, 2005.

[32] V. Kim, "Electric propulsion activity in Russia," IEPC-2001-005, 27th International Electric Propulsion Conference, Pasadena, California, October 14–19, 2001.

[33] D. L. Pidgeon, R. L. Corey, B. Sauer, and M. L. Day, "Two Years On-Orbit Performance of SPT-100 Electric Propulsion," AIAA 2006-5353, 42nd Joint Propulsion Conference, Sacramento, California, July 9–12, 2006.

[34] M. T. Domonkos, C. M. Marrese, J. M. Haas, and A. D. Gallimore, "Very Near-Field Plume Investigation of the D55," AIAA-1997-3062, 33rd Joint Propulsion Conference, Seattle, Washington, July 6–9, 1997.

[35] S. O. Tverdokhlebov, A. V. Semenkin, and A. E. Solodukhin, "Current status of multi-mode TAL development and areas of potential application," AIAA-2001-3779, 37th Joint Propulsion Conference, Salt Lake City, Utah, July 8–11, 2001

[36] C. R. Koppel and D. Estublier, "The SMART-1 Hall Effect Thruster around the Moon: In Flight Experience," IEPC-2005-119, 29th International Electric Propulsion Conference, Princeton, New Jersey, October 31–November 4, 2005.

[37] M. Lyszyk, E. Klinger, J. Bugeat, and D. Valentian, "Development Status of the PPS-1350 Plasma Thruster," AIAA-1998-3333, 34th Joint Propulsion Conference, Cleveland, Ohio, July 13–15, 1998

[38] C. R. Koppel and D. Estublier, "The SMART-1 Electric Propulsion Subsystem," AIAA-2003-4545, 39th Joint Propulsion Conference, Huntsville, Alabama, July 20–23, 2003.

[39] http://www.snecma.com

[40] T. Yee, "Roadrunner, a High-Performance Responsive Space Mission," Proceedings of the 18th AIAA/USU Conference on Small Satellites, SSC04-I-5, Logan, Utah, August 2004.

[41] D. R. Bromaghim, J. T. Singleton, R. Gorecki, F. Dong Tan, and H. Choy, "200 W Hall Thruster Propulsion Subsystem Development for Microsatellite Missions," Proceedings of the 53rd JANNAF Propulsion Meeting, Monterey, California, December 5–8, 2005.

[42] K. H. de Grys, B. Welander, J. Dimicco, S. Wenzel, B. Kay, V. Khayms, and J. Paisley, "4.5 kW Hall Thruster System Qualification Status," AIAA 2005-3682, 41st Joint Propulsion Conference, Tucson, Arizona, July 10–13, 2005.

[43] R. R. Hofer, T. M. Randolph, D. Y. Oh, J. S. Snyder, "Evaluation of a 4.5 kW Commercial Hall Thrusters System for NASA Science Missions," AIAA-2006-4469, 42nd Joint Propulsion Conference, Sacramento, California, July 9–12, 2006.

[44] B. Welander, C. Carpenter, K. H. de Grys, R. R. Hofer, T. M. Randolph, and D. H. Manzella, "Life and Operating Range Extension of the BPT-4000 Qualification Model Hall Thruster," AIAA-2006-5263, 42nd Joint Propulsion Conference, Sacramento, California, July 9–12, 2006.

Fundamentals of Electric Propulsion: Ion and Hall Thrusters
by Dan M. Goebel and Ira Katz
Copyright © 2008 John Wiley & Sons, Inc.

Appendix A
Nomenclature

A.1 Constants

A_v	Avogadro's number (atoms/mole)	$6.02214179 \times 10^{23}$
AMU	atomic mass unit	$1.6602176487 \times 10^{-27}$ kg
c	velocity of light	2.9979×10^{8} m/s^2
e	electron charge	$1.602176487 \times 10^{-19}$ C
g	gravitational acceleration	9.80665 m/s^2
k	Boltzmann's constant	1.3807×10^{-23} J/K
m	electron mass	$9.1093822 \times 10^{-31}$ kg
M	proton mass	$1.67262164 \times 10^{-27}$ kg
e/m	electron charge-to-mass ratio	1.75882×10^{11} C/kg
M/m	protron-to-electron mass ratio	1836.153
M_{xe}	mass of a xenon atom	131.293 AMU 2.17975×10^{-25} kg
ε_o	permittivity of free space	8.8542×10^{-12} F/m
μ_o	permeability of free space	$4\pi \times 10^{-7}$ H/m
πa_0^2	atomic cross section	8.7974×10^{-21} m^2
e/k	temperature associated with 1 electron volt	11604.5 K
eV	energy associated with 1 electron volt	$1.602176487 \times 10^{-19}$ J

T_0	standard temperature (0 deg C)	273.15 K
p_o	standard pressure (760 torr = 1 atm)	1.0133×10^5 Pa
n_o	Loschmidt's number (gas density at STP)	2.6868×10^{25} m^{-3}

A.2 Acronyms and Abbreviations

0-D	0-dimensional
1-D	one-dimensional
2-D	two-dimensional
3-D	three-dimensional
AC	alternating current
accel grid	accelerator grid
AEPI	Atmospheric Emissions Photometric Imaging
AMU	atomic mass unit
BaO	barium oxide
BN	boron nitride
BOL	beginning of life
CC	carbon–carbon
CEX	charge exchange
CL	Child–Langmuir
CM	center of mass
CVD	chemical-vapor-deposition
DC	direct current (steady-state)
decel grid	decelerator grid
DS1	Deep Space 1 (mission)
ECR	electron cyclotron resonance (microwave)
EITA	Electron-bombardment Ion Thruster Assembly
ELT	extended life test (NSTAR thruster life test)
EP	electric propulsion

EPIC	Electric Propulsion Interactions Code
ESA	European Space Agency
ETS	Engineering Test Satellite
ETS-6	Engineering Test Satellite (Japanese ETS-6)
eV	electron volt
eV/ion	electron volts per ion
FEEP	field emission electric propulsion
GRC	Glen Research Center
HET	Hall effect thruster
HiPEP	High Power Electric Propulsion
I.D.	inside diameter
ISTI	International Space Technologies Incorporated
JAXA	Japanese Aerospace Exploration Agency
JPL	Jet Propulsion Laboratory
LaB_6	lanthanum hexaboride
LDT	life demonstration test (8200-hour NSTAR thruster wear test)
LIF	laser-induced fluorescence
MELCO	Mitsubishi Electric Corporation
MiXI	Miniature Xenon Ion
MPD	magnetoplasmadynamic thruster
NASA	National Aeronautics and Space Administration
NEXIS	Nuclear Electric Xenon Ion Thruster System
NEXT	NASA's Evolutionary Xenon Thruster
NSTAR	NASA Solar Electric Propulsion Technology Applications Readiness
PG	pyrolytic graphite
PIC	particle in cell
PPT	pulsed-plasma thruster
PPU	power processing unit

rf	radio frequency
RIT	radio-frequency ion thruster
RITA	Radio-Frequency Ion Thruster Assembly
RPA	retarding potential analyzer
RSU	remote sensor unit
sccm	standard cubic centimeters per minute
SEM	scanning electron microscope
SEPAC	Space Experiments with Particle Accelerators
SI	International System
SMART	Small Mission for Advanced Research in Technology
SmCo	samarium cobalt
SPT	stationary plasma thruster (a type of Hall thruster)
SSC	Space Station contactor
STEX	Space Technology for Advanced Research in Technology
STP	standard temperature and pressure
TAL	thruster with anode layer
torr-l/s	torr-liter per second
TWT	traveling-wave tube
UV	ultraviolet
W/A	watts per ampere
XIPS	Xenon Ion Propulsion System (manufactured by L-3 Communications, Electron Technology, Inc.)

A.3 Defined Terms

Isp	specific impulse
F_t	correction to thrust force due to beam divergence
T_e	electron temperature in K
T_{eV}	electron temperature in electron volts
$\ln \Lambda$	Coulomb logarithm

Q_{injested} gas flow recycled into thruster from vacuum system

A.4 Variables

A cross-sectional area

A_a electron loss area at anode

A_{as} total surface area of anode exposed to plasma

A_c surface accommodation coefficient

A_g area of grid

A_p primary electron loss area at anode

A_s area of screen grid

A_w discharge chamber wall area

B magnetic field

B_r radial magnetic field

$\bar{c}$ neutral gas thermal velocity

C constant, conductance of grids

C_1 experimental fitting coefficient in barium depletion model

d gap distance (between electrodes), distance

d_a accel grid aperture diameter

d_b beamlet diameter

d_s screen grid aperture diameter

D diffusion coefficient, Richardson–Dushman coefficient, beamlet diameter

D_a ambipolar diffusion coefficient

D_B Bohm diffusion coefficient

D_i ion diffusion coefficient

$D_\perp$ perpendicular diffusion coefficient

E electric field

E_{accel} electric field at the accel grid

E_{screen} electric field at the screen grid

$\mathcal{E}$	energy
E_{eff}	effective atom activation energy
f	fraction of ions with a radial velocity
f_a	open area fraction of accel grid
f_b	beam flatness parameter
f_c	ion confinement factor for fraction of Bohm current lost
f_i	current fraction of the *i*th species, frequency of ion oscillations
f_n	edge to average plasma density ratio in cathode plasma
f_p	electron plasma frequency
F	force
F_{accel}	force on the accel grid
F_e	force on the electrons
F_i	force on the ions
F_{is}	flux of scattered ions
F_c	force due to collisions causing momentum transfer
F_L	Lorentz force
F_p	pressure gradient force
F_{screen}	force the screen grid
F_t	thrust vector correction factor
h	plume expansion parameter
$H(T)$	total heat lost by hollow cathode (a function of the temperature)
I_a	electron current leaving plasma to anode
I_A	accel grid current
I	current
I_b	beam current
I_B	Bohm current
I_{ck}	current to the discharge cathode keeper
I_d	discharge current
I_{DE}	decel grid current

I_e	electron current, emission current from hollow cathodes
I_{ea}	electron current to anode
I_{eb}	electron backstreaming current
I_{ec}	electron current flowing backwards in a Hall thruster
I_{ew}	electron current to the wall
I_H	Hall current
I_i	ion current
I_{ia}	ion current lost to anode
I_{ib}	ion current in the beam
I_{ic}	ion current lost to cathode
I_{iw}	ion current to the wall
I_k	ion current back to the hollow cathode
I_L	primary electron current lost directly to anode
I_{nk}	current to the neutralizer cathode keeper
I_p	ion production rate in the plasma
I_r	random electron flux
I_s	ion current to the screen grid
I_t	thermionic emission current
I_w	current to the walls
I^-	singly charged ion current
I^{++}	doubly charged ion current
I^*	excited neutral production rate in the plasma
J	current density
j_o	equilibrium current density
j_1	perturbed current density
J_e	electron current density
J_i	ion current density
J_{Hall}	Hall current density
J_{max}	maximum Child–Langmuir current density

$J_{0,1}$	zero and first-order Bessel functions
k	wave number = $2\pi/\lambda$
$k_{0,1,2,3}$	fit parameters for Randolph's plume divergence formula
K	proportionality constant
l	length
ℓ	length for radial ion diffusion between cusps
l_d	distance to merged beamlets in plume
l_e	sheath thickness length
l_g	grid gap length
L	primary electron path length, plasma length, microwave interaction length, length of the plasma in Hall thrusters
L_c	total length of magnetic cusps
L_g	path length for electron gyration
L_T	total path length for helical electron motion
m	mass, electron mass
m_a	mass flow injected into the anode region
m_c	mass flow injected through the cathode
m_d	delivered spacecraft mass
m_i	propellant mass due to ions
m_p	propellant mass
m_s	mass of species "s"
m_t	total mass flow
$\dot{m}_a$	Hall thruster anode mass flow rate
$\dot{m}_c$	Hall thruster cathode mass flow rate
$\dot{m}_i$	ion mass flow rate
$\dot{m}_p$	total propellant mass flow rate
M	ion mass, total spacecraft mass, dipole strength per unit length
M_a	ion mass in AMU
M_p	propellant mass

N	total number of particles, number of magnet coil turns
n	particle density
n_a	neutral atom density
n_b	beam plasma density
n_e	electron density
n_f	neutral density flowing from cathode
n_i	ion density
n_o	neutral density, plasma density at center of symmetry
n_p	primary electron density
n_s	source or sink density term, secondary electron density, density of species "s"
n^+	singly ionized particle density
n^{-+}	doubly ionized particle density
p	plasma pressure
p_e	electron pressure
p_i	thruster plume ion pressure
p_o	thruster plume neutral pressure
P	neutral pressure, probability of a collision, power, perveance
P_a	power into the anode
P_{abs}	absorbed rf power
P_b	beam electrical power
P_d	discharge electrical power
P_f	final neutral pressure
P_{in}	power into the plasma discharge
P_{jet}	jet power (kinetic power in the thrust beam)
P_k	keeper discharge electrical power
P_{max}	maximum perveance
P_o	initial neutral pressure, other electrical power in the thruster
P_{out}	power out of the plasma

P_T	total electrical power into thruster, pressure in Torr
P_w	power into the wall
q	charge, number of magnetic dipoles
q_s	charge of species "s"
Q	total charge = qn, propellant flow rate or throughput
r	radius
r_a	aperture radius
r_e	electron Larmor radius
r_h	hybrid Larmor radius
r_i	ion Larmor radius
r_L	Larmor radius
r_p	primary electron Larmor radius
R	major radius, ratio of beam voltage to total voltage in ion thrusters
R	resistance
R_m	mirror ratio
R_s	mean change in the momentum of particles "s" due to collisions
R^{++}	rate of double ion production
$\dot{\Re}$	erosion rate of the walls
S	ionization energy loss, pumping speed
t	time
t_a	accel grid thickness
t_s	screen grid thickness
T	thrust, temperature [K]
T_a	optical transparency of the grid
T_e	electron temperature [K]
T_{eV}	electron temperature [eV]
T_g	grid transparency
T_i	ion temperature [K]
T_{iV}	ion temperature [eV]

T_m	sum of thrust from multiple species
T_n	temperature of nth species
T_o	temperature of the neutral gas
T_s	effective transparency of the screen grid, temperature of secondary electrons from wall, temperature of species "s"
T_w	wall temperature
U^+	ionization potential
U^*	average excitation potential
v	velocity
v_a	ion acoustic velocity
v_b	beam velocity
v_B	Bohm velocity
v_D	diamagnetic drift velocity
v_e	electron velocity
v_E	$E \times B$ drift velocity
v_{ex}	exhaust velocity
v_f	final velocity
v_i	ion velocity, initial velocity
v_n	velocity of the neutral species, velocity of the nth species
v_o	neutral velocity, initial ion velocity
v_p	primary electron velocity
v_{th}	thermal electron drift velocity
$v_\perp$	perpendicular velocity
$v_\parallel$	parallel velocity
V	volume, voltage
V_a	accel grid voltage
V_b	net beam voltage (screen voltage minus beam plasma potential)
V_{bp}	potential of beam plasma
V_{ck}	potential of discharge cathode keeper

V_c voltage drop in hollow cathode, coupling voltage from neutralizer common potential to beam potential

V_{cg} cathode to ground potential

V_d discharge voltage

V_f floating potential

V_G coupling voltage relative to ground in ion thrusters

V_k voltage of electrons (primaries) from the cathode

V_m magnet volume, minimum potential in grids

V_{nk} potential of neutralizer cathode keeper

V_p voltage drop in plasma, plasma generator potential

V_s screen power supply voltage

V_T total voltage across accelerator gap = $V_s + V_a$

w width

x distance, characteristic length of beam column

y insert thickness

Y sputtering yield

Y_{ad} adatom production yield on cathode surface

Y_{ps} sputtered particle yield from cathode surface

Z atomic number

A.5 Symbols

α thrust correction factor for doubly charged ions, work function correction constant, e-folding distance for plasma density decrease, constant in Bessel's function argument

α_m mass utilization correction factor due to the multiply charge ions

β adjustable coefficient to Bohm collision frequency

γ total thrust correction factor = αF_t, secondary electron yield

γ_o secondary electron yield at the space-charge limit

Γ flux of particles

Γ_o	initial flux of particles
$\Gamma(x)$	Gamma function
Δv	change in velocity
ΔV	potential modification in grids due to space charge
δ	magnet half-height
ε	electron energy density
ε_b	electrical cost of a beam ion
ε_e	energy than an electron removes from the plasma
ε_i	energy than an ion removes from the plasma
ζ	viscosity
η	total plasma resistivity
η_a	anode efficiency of a Hall thruster
η_b	beam current fraction of discharge current
η_c	Clausing factor (conductance reduction)
η_d	discharge loss
η_e	electrical efficiency
η_{ei}	plasma resistivity due to electron–ion collisions
η_{en}	plasma resistivity due to electron–neutral collisions
η_m	mass utilization efficiency
η_{m+}	mass utilization efficiency for only singly ionized particles
η_{md}	mass utilization efficiency of the discharge chamber
η_o	electrical efficiency for other power in a Hall thruster
η_T	total thruster efficiency
η_v	beam voltage fraction of discharge voltage
κ	parameter in double sheath equation $\approx 1/2$, thermal conductivity
λ	mean free path, wavelength

λ_D	Debye length
λ_{01}	first zero of the Bessel function
μ	mobility
μ_B	Bohm mobility
μ_e	electron mobility
μ_{ei}	electron mobility due only to electron–ion collisions
μ_i	ion mobility
ν	collision frequency
ν_{ee}	electron–electron collision frequency
ν_{ei}	electron–ion collision frequency
ν_{en}	electron–neutral collision frequency
ν_{ii}	ion–ion collision frequency
ν_{in}	ion–neutral collision frequency
ν_m	total momentum transferring collision frequency
ν_{sn}	collision frequency between species "s" and the nth species
ν_{scat}	scattering frequency
ξ	normalized dimension = x/λ_D
ρ	charge density = qn
ρ_m	ion mass density = Mq
ρ_o	initial ion mass density
σ	cross section, surface charge density
τ	collision time, mean electron or ion confinement time
τ_c	time for electron–neutral collision
τ_m	total collision time for momentum transferring collisions
τ_p	primary electron confinement time
τ_s	Spitzer electron thermalization time with plasma electrons

τ_t	total thermalization time
ϕ	potential, work function
ϕ_o	potential at sheath edge
ϕ_s	sheath potential
ϕ_{wf}	work function of a material or surface
χ	normalized potential = $e\phi/kT$
ω	cyclic frequency ($=2\pi f$)
ω_c	electron cyclotron frequency
ω_p	electron plasma frequency
Ω_e	electron Hall parameter

Fundamentals of Electric Propulsion: Ion and Hall Thrusters
by Dan M. Goebel and Ira Katz
Copyright © 2008 John Wiley & Sons, Inc.

Appendix B
Gas Flow Unit Conversions and Cathode Pressure Estimates

Conversion between the different systems of flow units is necessary to calculate various parameters used in evaluating thruster performance. Due to the precision required in calculating the thruster performance, it is necessary to carry several significant digits in the constants used to calculate the conversion coefficients, which are obtained from the National Institute of Standards and Technology (NIST) database that can be found on the NIST Web site.

Converting flow in standard cubic centimeters per minute (SCCM) to other flow units for an ideal gas is achieved as follows. A mole of gas at standard pressure and temperature is Avogadro's number ($6.02214179 \times 10^{23}$) of particles at one atmosphere and 0 deg C (273.15 K), which occupies 22.413996 liters. The conversions are

$$1 \text{ sccm} = \frac{6.02214179 \times 10^{23} [\text{atoms/ mole}]}{22.413996 \text{ [liters/ mole at STP]} * 10^{3} [\text{cc/ liter}] * 60 \text{ [s/ min]}} = 4.477962 \times 10^{17} \left[\frac{\text{atoms}}{\text{s}}\right] \tag{B-1}$$

$$1 \text{ sccm} = 4.477962 \times 10^{17} \left[\frac{\text{atoms}}{\text{s}}\right] * 1.6021765 \times 10^{-19} [\text{coulombs/ charge}] = 7.174486 \times 10^{-2} \text{ [equilvalent amperes]} \tag{B-2}$$

$$1 \text{ sccm} = \frac{10^{-3}[\text{liters}] * 760[\text{torr}]}{60[\text{s/ min}]} = 0.01267 \left[\frac{\text{torr}-1}{\text{s}}\right] \tag{B-3}$$

$$\begin{aligned} 1 \text{ sccm} &= 4.47796 \times 10^{17} \left[\frac{\text{atoms}}{\text{s}}\right] * 1.660539 \times 10^{-27} * M_a * 10^6 \\ &= 7.43583 \times 10^{-4} M_a \left[\frac{\text{mg}}{\text{s}}\right], \end{aligned} \tag{B-4}$$

where M_a is the propellant mass in atomic mass units (AMU).

For xenon, $M_a = 131.293$, and a correction must be made for its compressibility at standard temperature and pressure (STP), which changes the mass flow rate by 0.9931468. Therefore, for xenon,

$$\begin{aligned} 1 \text{ sccm (Xe)} &= \frac{7.17448 \times 10^{-2}}{0.9931468} \\ &= 0.0722399 \text{ [equilvalent amperes]} \\ &= 0.0983009 \left[\text{mg/s}\right]. \end{aligned} \tag{B-5}$$

It is possible to make an estimate of the neutral gas pressure inside of a hollow cathode insert region and in the orifice as a function of the propellant flow rate and cathode temperature, using analytic gas flow equations. While these equations may not be strictly valid in some locations, especially the relatively short orifices found in discharge cathodes, they can still provide an estimate that is usually within 10% to 20% of the actual measured pressures.

In the viscous flow regime, where the transport is due to gas atoms or molecules primarily making collisions with each other rather than walls, the pressure through a cylindrical tube is governed by the Poiseuille law [1,2] modified for compressible gas [3]. The rate at which compressible gas flows through a tube of length l and radius a (in moles per second) is given [2] from this law by

$$N_m = \frac{\pi}{8\zeta} \frac{a^4}{l} \frac{P_a \left(P_1 - P_2\right)}{R_o T} = \frac{\pi}{16\zeta} \frac{a^4}{l} \frac{P_1^2 - P_2^2}{R_o T}, \tag{B-6}$$

where a is the tube radius, l is the tube length, P_a is the average pressure in the tube given by $(P_1 + P_2)/2$, ζ is the viscosity, P_2 is the downstream pressure at the end of the tube, P_1 is the upstream pressure of the tube, R_o is the universal

gas constant, and T is the temperature of the gas. The measured gas flow rate, or the gas throughput, is given by the ideal gas law:

$$Q = P_m V_m = N_m R_o T_m , \tag{B-7}$$

where P_m is the pressure and V_m is the volume where the flow is measured for gas at a temperature T_m, and N_m is the mole flow rate. The mole flow rate is then $N_m = P_m V_m / R_o T_m$. Defining $T_r = T / T_m$ and substituting the mole flow rate into Eq. B-1 gives the measured flow as

$$Q = \frac{\pi}{16\zeta} \frac{a^4}{l} \frac{P_1^2 - P_2^2}{T} T_m = \frac{\pi}{16\zeta} \frac{a^4}{l} \frac{P_1^2 - P_2^2}{T_r} . \tag{B-8}$$

Putting this in useful units and writing it in terms of a conductance of the tube, which is defined as the gas flow divided by the pressure drop, gives

$$Q = \frac{1.28\, d^4}{\zeta\, T_r\, l} \left(P_1^2 - P_2^2 \right), \tag{B-9}$$

where Q is the flow in sccm, η is the viscosity in poises, d is the orifice diameter and l the orifice length in centimeters, and the pressures are in torr. The pressure upstream of the cathode orifice is then

$$P_1 = \left(P_2^2 + \frac{0.78 Q \zeta\, T_r\, l}{d^4} \right)^{1/2} . \tag{B-10}$$

While Eq. (B-10) requires knowledge of the downstream pressure, for this rough estimate it is acceptable to assume $P_2 << P_1$ and neglect this term. For xenon, the viscosity in poises is

$$\zeta = 2.3 \times 10^{-4} T_r^{(0.71 + 0.29/T_r)} \text{ for } T_r > 1 , \tag{B-11}$$

where $T_r = T$ (°K)/289.7. The viscosity in Eq. (B-11) is different than Eq. (6.5-9) because 1 Ns/m^2 = 10 poise. It should be noted that the temperature of the gas in the hollow cathode can exceed the temperature of the cathode by factors of 2 to 4 due to charge-exchange heating with the ions, which then affects the viscosity.

As an example, take the NASA Solar Electric Propulsion Technology Applications Readiness (NSTAR) discharge cathode operating at a nominal

flow of 3.7 sccm, with an orifice diameter of 1 mm and the length of the cylindrical section of the orifice 0.75 mm. Assuming the gas in the orifice is 4000 K due to charge-exchange heating and $P_2 = 0$, the upstream pressure is found from Eq. (B-10) to be 6.7 torr. The pressure measured upstream of the cathode tube for this TH15 case is about 8 torr [5]. Correcting for the pressure drop in the insert region (also due to Poiseuille flow), the actual pressure upstream of the orifice plate is about 7.2 torr. The pressure calculated from Eq. (B-10) is low because the downstream pressure is finite (about 2 torr where the barrel section ends) and the bevel region at the output of the orifice has a finite molecular conductance in the collisionless flow regime. In general, it can be assumed that the results of Eq. (B-10) are about 10% low due to these effects. Similar agreement has been found for neutralizer cathodes with straight bore orifices, suggesting that this technique provides reasonable estimates of the pressure in the cathodes.

Finally, once the pressure inside the cathode or in the orifice region entrance is estimated, it is straightforward to calculate the local neutral density from Eq. (2.7-2):

$$n_o = 9.65 \times 10^{24} * \frac{P}{T} \left[\frac{\text{particles}}{\text{m}^3} \right], \tag{B-12}$$

where P is the pressure in torr and T is the gas temperature in kelvins.

References

[1] S. Dushman and J. Lafferty, *Scientific Foundations of Vacuum Techniques*, New York: Wiley and Sons, 1962.

[2] K. F. Herzfeld and H. M. Smallwood, *Taylor's Treatise on Physical Chemistry*, 2nd edition, vol. 1, New York: D. Van Nostrand Co., p. 175, 1931.

[3] A. Roth, *Vacuum Technology*, New York: North-Holland, 1990.

[4] R. C. Reid, *The Properties of Gases and Liquids*, New York: McGraw-Hill, p. 403, 1977.

[5] K. K. Jameson, D. M. Goebel, and R. M. Watkins, "Hollow Cathode and Keeper-Region Plasma Measurements," AIAA-2005-3667, 41st Joint Propulsion Conference, Tucson, Arizona, July 11–13, 2005.

Fundamentals of Electric Propulsion: Ion and Hall Thrusters
by Dan M. Goebel and Ira Katz
Copyright © 2008 John Wiley & Sons, Inc.

Appendix C
Energy Loss by Electrons

The energy lost from the plasma due to electrons being lost to an anode that is more negative than the plasma is derived. Figure C-1 shows the plasma potential distribution in the negative-going sheath towards the anode wall. The Maxwellian electrons are decelerated and repelled by the sheath potential. To determine the average energy removed from the plasma by each electron, moments of the Maxwellian distribution are taken. The electron current density reaching the wall is given by

$$J_e = en\int_{-\infty}^{\infty} dv_x \int_{-\infty}^{\infty} dv_y \int_{\sqrt{2e\phi/m}}^{\infty} v_z \left(\frac{m}{2\pi kT_e}\right)^{3/2} \exp\left(\frac{-m\left(v_x^2+v_y^2+v_z^2\right)}{2kT_e}\right) dv_z$$
$$= \frac{1}{4} en\sqrt{\frac{8kT_e}{\pi m}} \exp\left(-\frac{e\phi}{kT_e}\right). \tag{C-1}$$

The electrons must overcome the sheath potential to reach the wall so the minimum electron speed toward the wall (assumed to be in the z-direction) is $\sqrt{2e\phi/m}$. The plasma electrons lose kinetic energy as they traverse the sheath, so the power flux from plasma is

$$P_e = n\int_{-\infty}^{\infty} dv_x \int_{-\infty}^{\infty} dv_y \int_{\sqrt{2e\phi/m}}^{\infty} v_z \left(\frac{m_e\left(v_x^2+v_y^2+v_z^2\right)}{2}\right)\left(\frac{m}{2\pi kT_e}\right)^{3/2}$$
$$\times \exp\left(\frac{-m\left(v_x^2+v_y^2+v_z^2\right)}{2kT_e}\right) dv_z \tag{C-2}$$
$$= \frac{1}{4} ne\sqrt{\frac{8kT_e}{\pi m}}\left(2\frac{kT_e}{e}+\phi\right)\exp\left(-\frac{e\phi}{kT_e}\right),$$

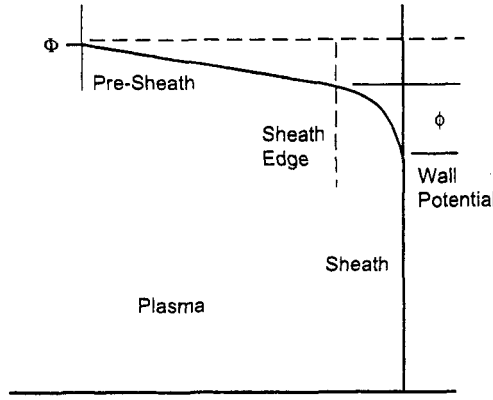

Fig. C-1. Schematic of plasma in contact with the anode wall.

where ϕ is expressed in electron volts (eV). The average energy that an electron removes from the plasma (in eV) is then the ratio of the power per electron to the flux of electrons:

$$E_{\text{ave}} = \frac{P_e}{J_e} = 2\frac{kT_e}{e} + \phi = 2T_{\text{eV}} + \phi\,, \tag{C-3}$$

where T_{eV} is in electron volts (eV). This is the energy removed from the plasma per electron striking the wall through a negative-going sheath.

It should be noted that this energy loss from the plasma per electron is different than the average energy that each electron has when it hits the wall. The flux of electrons hitting the anode wall is the same as analyzed above. The plasma electrons lose kinetic energy as they traverse the sheath; hence, a $-e\phi$ term must be included in the particle energy expression for each electron. The power flux to the insert from plasma electrons is then

$$\begin{aligned} P_e &= n\int_{-\infty}^{\infty} dv_x \int_{-\infty}^{\infty} dv_y \int_{\sqrt{2e\phi/m}}^{\infty} v_z \left(\frac{m_e\left(v_x^2 + v_y^2 + v_z^2\right)}{2} - e\phi \right) \left(\frac{m}{2\pi kT_e} \right)^{3/2} \\ &\quad \times \exp\left(\frac{-m\left(v_x^2 + v_y^2 + v_z^2\right)}{2kT_e} \right) dv_z \\ &= \frac{1}{4} ne \sqrt{\frac{8kT_e}{\pi m}} \left(2\frac{kT_e}{e} \right) \exp\left(-\frac{e\phi}{kT_e} \right). \end{aligned} \tag{C-4}$$

The average energy of each electron is then the ratio of the power to the flux:

$$E_{\text{ave}} = \frac{P_e}{J_e} = 2\frac{kT_e}{e} = 2T_{eV} \quad \text{[energy per electron that strikes the wall]} \qquad \text{(C-5)}$$

Fundamentals of Electric Propulsion: Ion and Hall Thrusters
by Dan M. Goebel and Ira Katz
Copyright © 2008 John Wiley & Sons, Inc.

Appendix D
Ionization and Excitation Cross Sections for Xenon

Ionization and excitation cross sections for xenon are available from the following references:

[1] D. Rapp and P. Englander, "Total Cross Sections for Ionization and Attachment in Gases by Electron Impact. I. Positive Ionization," *The Journal of Chemical Physics*, vol. 43, no. 5, pp. 1464–1479, 1965.

[2] M. Hayashi, "Determination of Electron-Xenon Total Excitation Cross-Sections, from Threshold to 100-eV, from Experimental Values of Townsend's α," *Journal of Physics D: Applied Physics*, vol. 16, pp. 581–589, 1983.

[3] K. Stephen and T.D. Mark, "Absolute Partial Electron Impact Ionization Cross Sections of Xe from Threshold up to 180 eV," *Journal of Chemical Physics*, vol. 81, pp.3116–3117, 1984.

[4] J. A. Syage, "Electron Impact Cross Sections for Multiple Ionization of Kr and Xe," *Physical Review A*, vol. 46, pp. 5666–5680, 1992.

The ionization and excitation cross sections for xenon from threshold to 100 eV from the above references are plotted in Fig. D-1 and tabulated in Table D-1.

Ionization and excitation cross sections for other gases such as argon and krypton are available from the following references:

[5] M. Hayashi, *Bibliography of Electron and Photon Cross Sections with Atoms and Molecules Published in the 20th Century: Argon*, NIFS-DATA-72, National Institute for Fusion Science (Japan), ISSN 0915-6364, 2003.

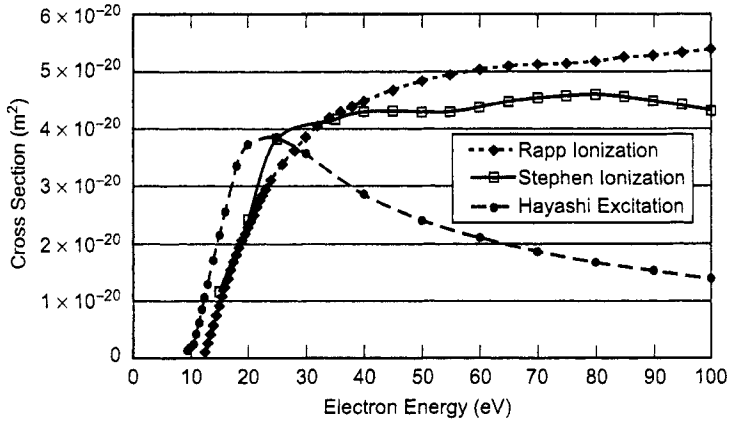

Fig. D-1. Ionization and excitation cross sections for xenon.

[6] R. Rejoub, B. G. Lindsay, and R. F. Stebbings, "Determination of the Absolute Partial and Total Cross Sections for Electron-Impact Ionization of Rare Gases," *Physical Review A*, 042713, vol. 65, 2002.

[7] A. Yanguas-Gil, J. Cotrino, and L. L. Alves, "An Update of Argon Inelastic Cross Sections for Plasma Discharges," *Journal of Physics D*, vol. 38, pp. 1588–1598, 2005.

[8] G. G. Raju, "Electron-Atom Collision Cross Sections in Argon: An Analysis and Comments," *IEEE Transactions on Dielectrics and Electrical Insulation*, vol. 11, pp. 649–673, 2004.

[9] A. A. Sorokin, L. A. Shmaenok, S. V. Bobashey, B. Mobus, H. Richter, and G. Ulm, "Measurements of Electron-Impact Ionization Cross Sections of Argon, Krypton, and Xenon by Comparison with Photoionization," *Physical Review A*, 022723, vol. 61, 2000.

Table D-1. Ionization and excitation cross sections for xenon.

Electron Energy (eV)	Rapp and Englander [1] Ionization (m^2)	Stephen and Mark [3] Ionization (m^2)	Hayashi [2] Total Excitation (m^2)
			2.6×10^{-22}
9.0			1.26×10^{-21}
9.5			1.31×10^{-21}
10.0			1.8×10^{-21}
10.5			2.4×10^{-21}
11			$4. \times 10^{-21}$
11.5			6.2×10^{-21}
12			8.4×10^{-21}
12.5	1.099×10^{-21}		1.05×10^{-20}
13.0	2.558×10^{-21}		1.28×10^{-20}
13.5	4.123×10^{-21}		
14.0	5.714×10^{-21}		1.7×10^{-20}
14.5	7.420×10^{-21}		
15.0	9.055×10^{-21}	1.15×10^{-20}	2.14×10^{-20}
15.5	1.073×10^{-20}		
16.0	1.231×10^{-20}		2.55×10^{-20}
16.5	1.380×10^{-20}		
17.0	1.529×10^{-20}		
17.5	1.670×10^{-20}		
18.0	1.802×10^{-20}		3.35×10^{-20}
18.5	1.925×10^{-20}		
19.0	2.048×10^{-20}		
19.5	2.163×10^{-20}		
20.0	2.277×10^{-20}	2.42×10^{-20}	3.73×10^{-20}
20.5	2.382×10^{-20}		
21.0	2.488×10^{-20}		
21.5	2.619×10^{-20}		
22.0	2.734×10^{-20}		
22.5	2.831×10^{-20}		
23.0	2.928×10^{-20}		
24.0	3.095×10^{-20}		
25.0		3.81×10^{-20}	3.85×10^{-20}
26.0	3.367×10^{-20}		
28.0	3.613×10^{-20}		
30.0	3.851×10^{-20}		3.57×10^{-20}
32.0	4.044×10^{-20}		

Table D-1. (continued).

Electron Energy (eV)	Rapp and Englander [1] Ionization (m^2)	Stephen and Mark [3] Ionization (m^2)	Hayashi [2] Total Excitation (m^2)
34.0	4.185×10^{-20}		
35.0		4.17×10^{-20}	
36.0	4.290×10^{-20}		
38.0	4.387×10^{-20}		
40.0	4.475×10^{-20}	4.30×10^{-20}	2.85×10^{-20}
45.0	4.677×10^{-20}	4.31×10^{-20}	
50.0	4.835×10^{-20}	4.29×10^{-20}	2.4×10^{-20}
55.0	4.941×10^{-20}	4.27×10^{-20}	
60.0	5.029×10^{-20}	4.37×10^{-20}	2.1×10^{-20}
65.0	5.081×10^{-20}	4.47×10^{-20}	
70.0	5.117×10^{-20}	4.54×10^{-20}	1.85×10^{-20}
75.0	5.134×10^{-20}	4.57×10^{-20}	
80.0	5.178×10^{-20}	4.59×10^{-20}	1.66×10^{-20}
85.0	5.249×10^{-20}	4.55×10^{-20}	
90.0	5.266×10^{-20}	4.48×10^{-20}	1.52×10^{-20}
95.0	5.328×10^{-20}	4.42×10^{-20}	
100.0	5.380×10^{-20}	4.31×10^{-20}	1.38×10^{-20}

Fundamentals of Electric Propulsion: Ion and Hall Thrusters
by Dan M. Goebel and Ira Katz
Copyright © 2008 John Wiley & Sons, Inc.

Appendix E
Ionization and Excitation Reaction Rates for Xenon in Maxwellian Plasmas

Ionization and excitation reaction rate coefficients $<\sigma v>$ for xenon calculated from the data in Appendix D averaged over a Maxwellian electron distribution are given in Table E-1. Over the ranges indicated, the data can be well fit to the cross section averaged over a Maxwellian distribution times the electron thermal velocity [1], where T_{eV} is in eV. The fits to the calculated values are

Ionization ($T_{\mathrm{eV}} < 5$ eV):

$$\langle \sigma_i v_e \rangle \approx$$

$$\langle \sigma_i \rangle \bar{v}_e = 10^{-20}\left[\left(3.97 + 0.643T_{\mathrm{eV}} - 0.0368T_{\mathrm{eV}}^2\right)e^{-12.127/T_{\mathrm{eV}}}\right]\left(\frac{8eT_{\mathrm{eV}}}{\pi m}\right)^{1/2}$$

Ionization ($T_{\mathrm{eV}} > 5$ eV):

$$\langle \sigma_i v_e \rangle \approx \langle \sigma_i \rangle \bar{v}_e = 10^{-20}\left[-\left(1.031\times 10^{-4}\right)T_{\mathrm{eV}}^2 + 6.386e^{-12.127/T_{\mathrm{eV}}}\right]\left(\frac{8eT_{\mathrm{eV}}}{\pi m}\right)^{1/2}$$

Excitation:

$$\langle \sigma^* v_e \rangle \approx \langle \sigma^* \rangle \bar{v}_e = 1.9310^{-19}\frac{e^{-11.6/T_e}}{\sqrt{T_{\mathrm{eV}}}}\left(\frac{8eT_{\mathrm{eV}}}{\pi m}\right)^{1/2}$$

Table E-1. Ionization and excitation reaction rates for xenon.

Electron Energy (eV)	Ionization (m^3/s)	Excitation (m^3/s)
0.5	4.51×10^{-25}	1.99×10^{-22}
0.6	3.02×10^{-23}	4.01×10^{-21}
0.7	6.20×10^{-22}	3.61×10^{-20}
0.8	6.04×10^{-21}	1.95×10^{-19}
0.9	3.58×10^{-20}	7.44×10^{-19}
1.0	1.50×10^{-19}	2.21×10^{-18}
1.5	1.16×10^{-17}	6.64×10^{-17}
2.0	1.08×10^{-16}	4.02×10^{-16}
2.5	4.24×10^{-16}	1.23×10^{-15}
3.0	1.08×10^{-15}	2.66×10^{-15}
3.5	2.13×10^{-15}	4.66×10^{-15}
4.0	3.59×10^{-15}	7.12×10^{-15}
4.5	5.43×10^{-15}	9.93×10^{-15}
5.0	7.61×10^{-15}	1.30×10^{-14}
5.5	1.01×10^{-14}	1.61×10^{-14}
6.0	1.28×10^{-14}	1.94×10^{-14}
6.5	1.57×10^{-14}	2.26×10^{-14}
7.0	1.88×10^{-14}	2.57×10^{-14}
7.5	2.20×10^{-14}	2.87×10^{-14}
8.0	2.53×10^{-14}	3.14×10^{-14}
8.5	2.86×10^{-14}	3.34×10^{-14}
9.0	3.20×10^{-14}	3.41×10^{-14}
9.5	3.55×10^{-14}	3.21×10^{-14}
10.0	3.90×10^{-14}	2.48×10^{-14}

A comparison of the ionization and excitation reaction rate coefficients with the curve fits is given in Fig. E-1. The fits provide excellent agreement with the exact calculations over this temperature range. The fitted ionization reaction rate for >5 eV also fits well up to about 30 eV, which is useful for Hall thruster calculations.

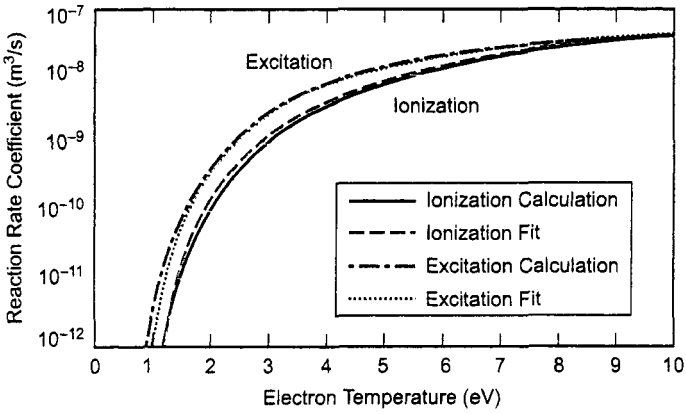

Fig. E-1. Ionization and excitation reaction rate coefficients from the calculation results (black) and fitting equations (gray), showing good agreement.

Reference

[1] I. G. Mikellides, I. Katz, and M. Mandell, "A 1-D Model of the Hall-Effect Thruster with an Exhaust Region," AIAA-2001-3505, 37th Joint Propulsion Conference, Salt Lake City, Nevada, July 8–11, 2001.

Fundamentals of Electric Propulsion: Ion and Hall Thrusters
by Dan M. Goebel and Ira Katz
Copyright © 2008 John Wiley & Sons, Inc.

Appendix F
Electron Relaxation and Thermalization Times

Spitzer [1] derived an expression for the slowing-down time of test particles (primary electrons in our case) with a velocity $v = \sqrt{2V_p/m}$, where eV_p is the test particle energy, in a population of Maxwellian electrons at a temperature T_e. Spitzer defined the inverse mean velocity of the Maxwellian electron "field particles" in one-dimension as $l_f = \sqrt{m/2kT_e}$. The slowing-down time is then given by

$$\tau_s = \frac{v}{\left(1 + m/m_f\right) A_D l_f^2 G(l_f v)}, \tag{F-1}$$

where m is the mass of the test particles, m_f is the mass of the field particles, and A_D is a diffusion constant given by

$$A_D = \frac{8\pi e^4 n_f Z^2 Z_f^2 \ln\Lambda}{m^2}, \tag{F-2}$$

where Z is the charge and $\ln\Lambda$ is the collisionality parameter [2] equal to $23 - \ln\left(n_f^{1/2} / T_e^{3/2}\right)$. The function $G(l_f v)$ is defined as

$$G(x) = \frac{\Phi(x) - x\Phi'(x)}{2x^2}, \tag{F-3}$$

and $\Phi(x)$ is the erf function:

$$\Phi(x) = \frac{2}{\pi^{1/2}} \int_0^x e^{-y^2} dy . \qquad \text{(F-4)}$$

Spitzer gave the values of $G(x)$ in a table, which is plotted in Fig. F-1 and fitted. For $x = l^2 \nu$ greater than 1.8, a power function fits best with the relation $G(x) = 0.463x^{-1.957}$.

In our case, the field particles and the test particles have the same mass, which is the electron mass, and charge $Z = e$. The slowing-down time is plotted in Fig. F-2 as a function of the primary particle energy for three representative plasma densities found near the baffle, in the discharge chamber, and near the grids.

For 15-eV primaries in the discharge chamber plasma with an average temperature of 4 eV and a density approaching 10^{12} cm^{-3}, the slowing-down time is about 10^{-6} s. The slowing-down time is also plotted in Fig. F-3 as a function of the plasma density for several values of the primary electron energy, again assuming the plasma has an electron temperature of about 4 eV. As the plasma density increases, the slowing-down time becomes very small ($<10^{-6}$ s). This will lead to rapid thermalization of the primary electrons.

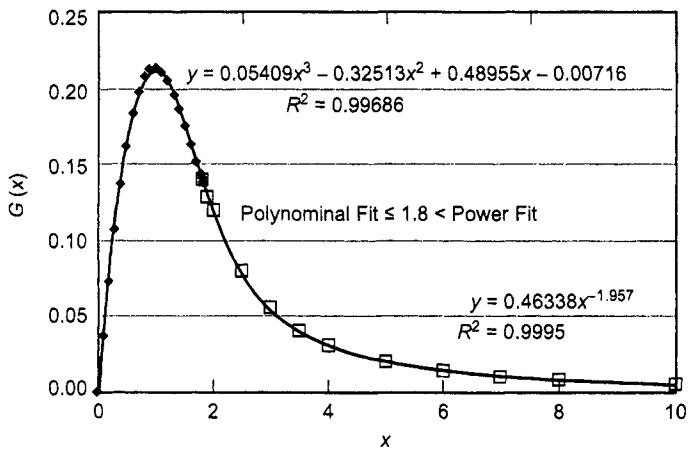

Fig. F-1. Spitzer's $G(x)$ with fits.

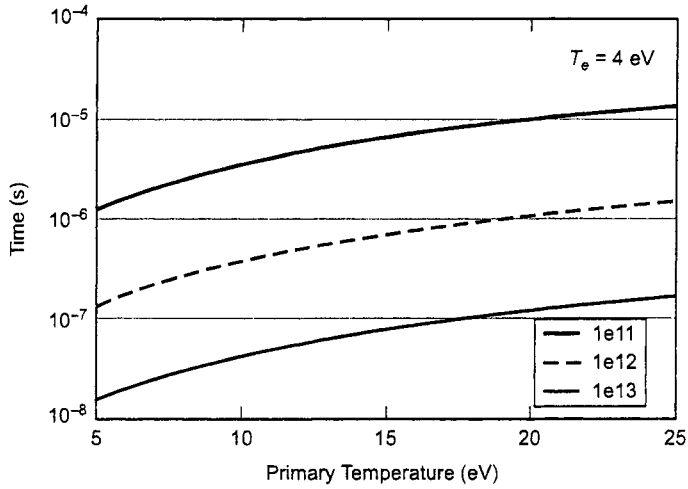

Fig. F-2. Spitzer's slowing-down time as a function of the primary electron energy for three densities of electrons at 4 eV.

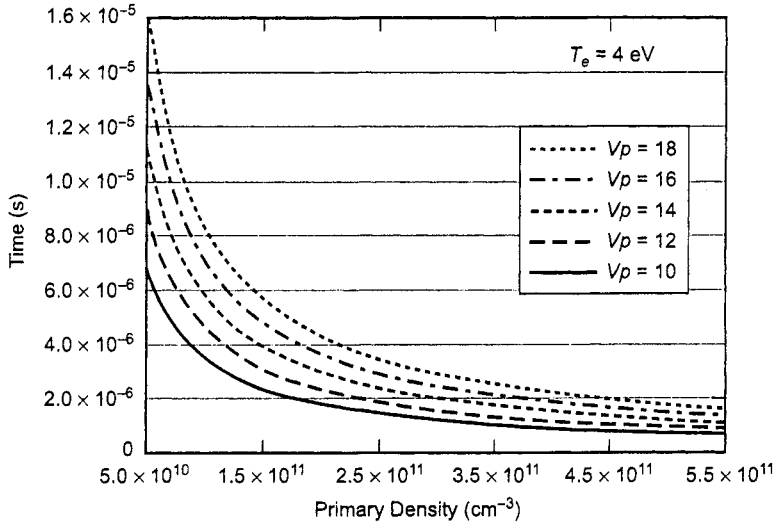

Fig. F-3. Spitzer's slowing-down time as a function of the plasma density with an electron temperature of 4 eV for several primary energies.

For the case of primary electrons with some spread in energy, we can examine the time for the equilibration between that population and the plasma electrons. Assuming that the primaries have a temperature T_1 and the plasma electrons have a temperature T_2, the time for the two populations to equilibrate is

$$\tau_{eq} = \frac{3m^{1/2}\left(kT_1 + kT_2\right)^{3/2}}{8(2\pi)^{1/2} ne^4 \ln\Lambda}. \tag{F-5}$$

As an example, the slowing time for monoenergetic primaries and primaries with a Maxwellian distribution of energies injected into a 4-eV plasma is shown in Fig. F-4. The slowing time is significantly faster than the equilibration time.

References

[1] L. Spitzer, Jr., *Physics of Fully Ionized Gases*, New York, Interscience, pp. 127–135, 1962.

[2] D. L. Book, *NRL Plasma Formulary*, Naval Research Laboratory, Washington D.C., pp. 33–34, 38, 1987.

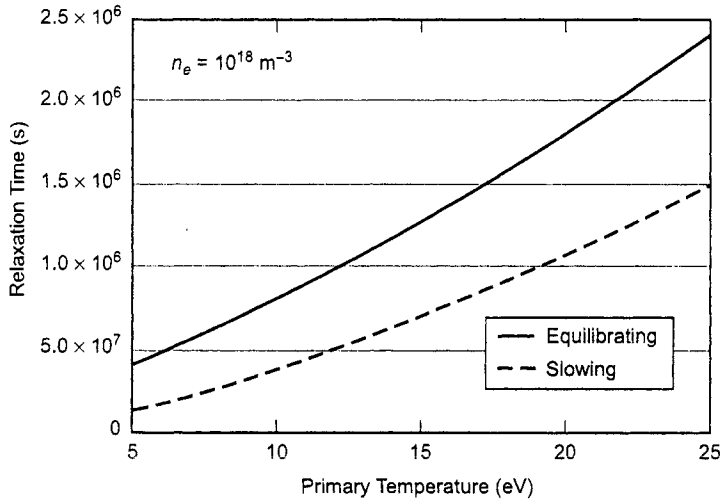

Fig. F-4. Relaxation times of monoenergetic primaries and a Maxwellian primary population in a 4 eV, 10^{18}m^{-3} plasma.

Fundamentals of Electric Propulsion: Ion and Hall Thrusters
by Dan M. Goebel and Ira Katz
Copyright © 2008 John Wiley & Sons, Inc.

Appendix G
Clausing Factor Monte Carlo Calculation

Visual Basic Monte-Carlo calculation of Clausing Factor for thruster grids.

Inputs:

Clausing Factor Calculator

Inputs	Radius (mm)	Diameter
thickScreen	0.381	
thickAccel	0.5	
rScreen	0.9525	1.905
rAccel	0.5715	1.143
gridSpace	0.5	
npart	10^6	

Code:

```
Sub Clausing()
    thickScreen = Range("C4")
    thickAccel = Range("C5")
    rScreen = Range("C6")
    rAccel = Range("C7")
    gridSpace = Range("C8")
    npart = Range("C9")
'  Monte Carlo Routine that calculates Clausing factor for
CEX
'    returns Clausing Factor and Downstream Correction
factor
   Dim gone As Boolean
        Pi = 3.14159265358979
'assumes rTop = 1
```

```
    rBottom = rScreen / rAccel
    lenBottom = (thickScreen + gridSpace) / rAccel
    lenTop = thickAccel / rAccel
    Length = lenTop + lenBottom
        iescape = 0
        maxcount = 0
        icount = 0
        nlost = 0
            vztot = 0#
            vz0tot = 0#
  For ipart = 1 To npart
    ' launch from bottom
            notgone = True
            r0 = rBottom * Sqr(Rnd)
            z0 = 0#
            costheta = Sqr(1# - Rnd)
            If (costheta > 0.99999) Then costheta =
0.99999
            phi = 2 * Pi * Rnd
            sintheta = Sqr(1# - costheta ^ 2)
            vx = Cos(phi) * sintheta
                vy = Sin(phi) * sintheta
                vz = costheta
                rf = rBottom
                t = (vx * r0 + Sqr((vx ^ 2 + vy ^ 2) * rf
^ 2 - (vy * r0) ^ 2)) / (vx ^ 2 + vy ^ 2)
                z = z0 + vz * t
                vz0tot = vz0tot + vz
                    icount = 0
            Do While notgone
                    icount = icount + 1
                If (z < lenBottom) Then
                ' hit wall of bottom cylinder and is re-
emitted
                        r0 = rBottom
                        z0 = z
                        costheta = Sqr(1# - Rnd)
                        If (costheta > 0.99999) Then
costheta = 0.99999
                        phi = 2 * Pi * Rnd
                        sintheta = Sqr(1# - costheta ^ 2)
                        vz = Cos(phi) * sintheta
                        vy = Sin(phi) * sintheta
                        vx = costheta
                        rf = rBottom
                        t = (vx * r0 + Sqr((vx ^ 2 + vy ^
2) * rf ^ 2 - (vy * r0) ^ 2)) / (vx ^ 2 + vy ^ 2)
                        z = z0 + t * vz
                End If ' bottom cylinder re-emission
```

```
                If ((z >= lenBottom) And (z0 < lenBottom))
Then
                ' emitted below but going up
                    ' find radius at lenBottom
                        t = (lenBottom - z0) / vz
                        r = Sqr((r0 - vx * t) ^ 2 + (vy *
t) ^ 2)
                    If (r <= 1) Then
                    '  continuing upward
                        rf = 1#
                        t = (vx * r0 + Sqr((vx ^ 2 + vy ^
2) * rf ^ 2 - (vy * r0) ^ 2)) / (vx ^ 2 + vy ^ 2)
                        z = z0 + vz * t
                    Else
                    '   hit the upstream side of the accel
grid and is re-emitted downward
                        r0 = r
                        z0 = lenBottom
                        costheta = Sqr(1# - Rnd)
                        If   (costheta   >   0.99999)   Then
costheta = 0.99999
                        phi = 2 * Pi * Rnd
                        sintheta = Sqr(1# - costheta ^ 2)
                            vx = Cos(phi) * sintheta
                            vy = Sin(phi) * sintheta
                            vz = -costheta
                        rf = rBottom
                        t = (vx * r0 + Sqr((vx ^ 2 + vy ^
2) * rf ^ 2 - (vy * r0) ^ 2)) / (vx ^ 2 + vy ^ 2)
                        z = z0 + vz * t
                    End If
                End If ' end upward
                If  ((z  >=  lenBottom)  And  (z  <=  Length))
Then
                    '   hit the upper cylinder wall and is
re-emitted
                        r0 = 1#
                        z0 = z
                        costheta = Sqr(1# - Rnd)
                        If   (costheta   >   0.99999)   Then
costheta = 0.99999
                        phi = 2 * Pi * Rnd
                        sintheta = Sqr(1# - costheta ^ 2)
                        vz = Cos(phi) * sintheta
                        vy = Sin(phi) * sintheta
                        vx = costheta
                        rf = 1#
                        t = (vx * r0 + Sqr((vx ^ 2 + vy ^
2) * rf ^ 2 - (vy * r0) ^ 2)) / (vx ^ 2 + vy ^ 2)
```

```
                        z = z0 + t * vz
                        If (z < lenBottom) Then
                        ' find z when particle hits the
bottom cylinder
                            rf = rBottom
                            If ((vx ^ 2 + vy ^ 2) * rf ^ 2
- (vy * r0) ^ 2 < 0#) Then
                               t = (vx * r0) / (vx ^ 2 +
vy ^ 2) 'if sqr arguement is less than 0 then set sqr term
to 0 12 May 2004
                            Else
                                t = (vx * r0 + Sqr((vx ^ 2
+ vy ^ 2) * rf ^ 2 - (vy * r0) ^ 2)) / (vx ^ 2 + vy ^ 2)
                            End If
                            z = z0 + vz * t
                        End If
                End If ' end upper cylinder emission
                If (z < 0#) Then
                    notgone = False
                End If
                If (z > Length) Then
                    iescape = iescape + 1
                    vztot = vztot + vz
                    notgone = False
                End If
                If (icount > 1000) Then
                    notgone = False
                    icount = 0
                    nlost = nlost + 1
                End If
            Loop  ' while
            If (maxcount < icount) Then maxcount = icount
        Next ipart ' particles
         Range("C11") = (rBottom ^ 2) * iescape / npart
         Range("C12") = maxcount
         Range("C13") = nlost
            vz0av = vz0tot / npart
            vzav = vztot / iescape
        DenCor = vz0av / vzav ' Downstream correction
factor
    End Sub ' Clausing
```

Fundamentals of Electric Propulsion: Ion and Hall Thrusters
by Dan M. Goebel and Ira Katz
Copyright © 2008 John Wiley & Sons, Inc.

Index

Absolute-intensity optical emission spectrum, plume plasma optical emission, 419–422
Acceleration region, Hall thruster operation, 332–333
Accelerator grid, ion thrusters:
  basic properties, 189–190
  configurations, 190–196
  design principles, 196–200
  electron backstreaming, 208–216
  high-voltage considerations, 216–224
    carbon-carbon composite materials, 221–223
    electrode breakdown, 217–218
    hold-off and conditioning, 224
    molybdenum electrodes, 218–221
    pyrolytic graphite, 223
  lifespan analysis, 225–235
    barrel erosion, 230–232
    grid models, 227–229
    pits-and-grooves erosion, 232–235
  optics, 200–208
    grid expansion and alignment, 206–208
    ion trajectories, 200–204
    perveance limits, 204–206
  recycling behavior, 137–141
Accommodation and accommodation coefficient, plume emissions, spacecraft interactions, 412–413
Acronyms and abbreviations table, 448–450
Adatom production, hollow cathodes, barium loss rates, 295–296
Alternating current (AC), radiofrequency (rf) ion thrusters, 155–158
Alumina walls, Hall thrusters, dominant power-loss mechanisms, 349–357
Ambipolar diffusion coefficient:
  hollow cathode:
    insert region plasma, 257–270
    orifice region plasma, 277–280
    plume-region plasma, 284–292
  with magnetic fields, 69–71
  without magnetic fields, 65–66
  primary electron motion and ionization, 178–182
  radiofrequency (rf) ion thrusters, 153–158
  ring-cusp ion thruster models, ion confinement, 111–116
Anode wall:
  discharge stability, 134–137
  performance efficiency, 343–345
  ring-cusp ion thruster, ion confinement, 110–116
Antenna design, radiofrequency (rf) ion thrusters, 151–158
Aperture design, ion thruster accelerator grid:
  alignment and expansion, 207–208
  diameter calculations, 190–194
Arakawa/Yamada model, primary electron motion and ionization, 176–182
Arc initiation:
  hollow cathode operation, 310–315
  ion thruster accelerator grid:
    electrodes, hold-off and conditioning, 224
    high-voltage parameters, 217–218
Arcjet, basic properties, 4

Arrhenius temperature dependence, hollow cathodes, barium depletion model, 299–302
Atmospheric Emissions Photometric Imaging (AEPI), plume plasma optical emission, 419–422
Atomic mass units (AMU), ion mass, 447
Atom sputtering rate:
  hollow cathodes, barium loss rates, 295–296
  ion thruster accelerator grid, barrel erosion, 231–232
Avogadro's number, 447
Axial electric field, Hall thrusters, 326–329
Axial magnetic field, radiofrequency (rf) ion thrusters, 149–158
Axial plasma density, hollow cathode:
  insert region plasma, 264–270
  plume-region plasma, 286–292
Axial scale length, Hall thruster operation, 329–330
Azimuthal drift:
  Hall thrusters, 327–328
    operating principles, 332–333
    oscillations, 376–379

Background density, plume emissions, neutral gas plumes, 407–408
Backstreaming limit, ion thruster accelerator grid, 213–216
Barium depletion model, hollow cathodes:
  lifetime analysis, 298–302
  operation, 309–315
Barium-oxide cathodes:
  insert plasmas, evaporation analysis, 293–296
  thermionic electron emission, 252–255
Barometric law:
  fluid plasma, momentum conservation, 48
  hybrid Hall thruster models, magnetic field transport, 369
  primary beam expansion plume models, 406–407
Barrel erosion, ion thruster accelerator grid, lifetime analysis, 225–235
Beam current:
  discharge loss, 126–133
  ion thruster plasma generator design, 96–100
  ring-cusp ion thruster models, density calculations, 119–120
Beam divergence:
  Hall thruster efficiency, 343–345
  ion thruster efficiency, 29
  thrust properties, 23–24
Beam plasma potential, ion thruster accelerator grid, electron backstreaming, 209–216
Beam/plume characteristics, electrical thrusters, 9–10
Beam power, thruster efficiency, 30
Beam steering, ion thruster accelerator grid expansion and alignment, 207–208
Beam utilization efficiency, dielectric-wall Hall thruster efficiency, 343, 361–362
Bessel functions, Fick's law, 64–65
Bias voltage, accelerator grid, 208–216
Bohm current:
  discharge chamber, power and energy balance, 125–126
  Hall thrusters:
    dielectric-wall Hall thruster efficiency, 360–362
    dominant power-loss mechanisms, 348–357
  hollow cathodes, insert region plasma, 260–270
  ion thruster plasma generator design, 93–100
  radiofrequency (rf) ion thrusters, 153–158
  ring-cusp ion thruster models, ion confinement, 111–116
Bohm diffusion:
  hybrid Hall thruster models, transverse electron transport, 368–369
  Kaufman ion thrusters, 142–147
  with magnetic fields, 69–71
  pre-sheath potential, 78–79
Bohm sheath criterion:
  plasma boundary sheaths, 82–84
  pre-sheath potential, 79
  summary of, 86–88
Bohm velocity:

Hall thrusters, dominant power-loss mechanisms, 351–357
ion thruster plasma generator design, 95–100
primary beam expansion plume models, 404–407
Boltzmann's constant:
Debye plasma boundary sheaths, 74–75
electrical thruster density and ingestion, 32–34
hollow cathodes, barium depletion model, 299–302
hybrid Hall thruster models, magnetic field transport, 369
plasma boundary sheaths, 87–88
plasma physics, particle energies and velocities, 44–46
pre-sheath potential, 77–79, 78–79
Boris-type particle-pushing algorithm, primary electron motion and ionization, 176–182
Boron nitride, Hall thrusters, dominant power-loss mechanisms, 349–357
Boundary sheaths, plasma physics, 71–88
Child-Langmuir sheaths, 79–81
Debye sheaths, 73–75
double sheaths, 84–86
generalized sheath solution, 81–84
pre-sheaths, 76–79
summary of effects, 86–88
Breathing mode oscillations, Hall thrusters, 377–379
Bulk-material insert life, hollow cathodes, 302–304

Carbon-carbon composite materials, ion thruster accelerator grid electrodes, 221–223
hold-off and conditioning, 224
Cathode common potential:
Hall thruster potential and current distributions, 337–341
plume emissions, solar array interactions, 416–418
Cathode efficiency, Hall thruster performance, 341–345
Cathode pressure estimates, 463–466
Centripetal force, plasma physics, single particle motions, 40–43
CEX-2D optics code, ion thruster accelerator grid trajectories, 200–204
Channel physics, hall thruster, 365–379
hybrid models, 366–372
continuity and energy, 369–371
ion current, 371–372
magnetic field transport, 369
transverse electron transport, 366–369
lifetime analysis, 379–383
oscillations, 376–379
steady-state models, 372–376
Channel plasma, dielectric-walll Hall thruster efficiency, 362–365
Charge density, fluid plasma particle conservation, 49–51
Charged particle collisions, partially ionized gas diffusion, 55–60
Charge-exchange (CEX) reactions:
hollow cathodes:
insert region plasma, 257–270
orifice region plasma, 271–280
ion thruster accelerator grid:
barrel erosion, 230–232
erosion models, 227–229
lifetime analysis, 225–235
pits-and-grooves erosion, 232–235
particle collisions, 57–60
plume emissions, 395
neutral gas plumes, 407–408
secondary-ion generation, 408–410
Chemical-vapor-deposition (CVD), ion thruster accelerator grid electrodes, carbon-carbon composite materials, 221–223
Child-Langmuir law:
ion thruster accelerator grid, perveance limit, 205–206
plasma boundary sheaths, 79–84, 88
Classical diffusion, with magnetic fields, 66–71
Clausing factor:
discharge chamber neutral and primary densities, 120–124
electrical thruster density and ingestion, 34
ion thruster accelerator grid, 230–232
Monte Carlo, 483–486

Clausing factor *(cont.)*
radiofrequency (rf) ion thrusters, 157–158
Closed-drift thruster, 328–329
Cold gap, ion thruster accelerator grid expansion and alignment, 206–208
Collisionality parameter:
discharge chamber neutral and primary densities, 122–124
electron relaxation and thermalization times, 479–482
hollow cathodes, insert region plasma, 256–270
microwave ion thrusters, 163–171
radiofrequency (rf) ion thrusters, 150–158
Collision frequency, hybrid Hall thruster models, transverse electron transport, 368–369
Collisions, partially ionized gas diffusion, 55–60
Collision transfer momentum, fluid plasma, conservation of, 47–48
COMETS satellite, ion thrusters, 429–440
Communications satellites, flight ion thrusters, 431–440
Conductance correction factor, electrical thruster density and ingestion, 33–34
Confinement factor, discharge loss, 128–133
Contamination, plume emissions, spacecraft interactions, 413–415
Continuity equations:
fluid plasma:
energy conservation, 52–54
particle conservation, 48–51
hybrid Hall thruster models, 369–371
Convective derivative, fluid plasma, momentum conservation, 47–48
Cosine distribution, plasma physics, particle energies and velocities, 45–46
Coulomb collision, particle collisions, 58–60
Coulomb-transfer rating, ion thruster accelerator grid, 217–218
molybdenum electrodes, 219–221
Coupling voltages, hollow cathode operation, 311–315
Cross-field diffusion coefficient:
Kaufman ion thrusters, 142–147
magnetic field diffusion, 69–71
primary electron motion, 178–182
Cross-field electron transport:
Hall thruster operation, 330–333
hybrid Hall thruster models, 368–369
Cross-over values, Hall thrusters, dominant power-loss mechanisms, 350–357
Current cutback, recycling behavior, 139–141
Current density:
Child-Langmuir sheaths, 79–81
hollow cathode geometry, 249–251
plume measurements, 398–400
Current distribution, Hall thruster operation, 337–341
Current fractions:
discharge loss, 127–133
microwave ion thrusters, 166–171
radiofrequency (rf) ion thrusters, 152–158
Current utilization efficiency, Hall thruster, multiply charged ion corrections, 346–347
Current-versus-voltage predictions, hybrid ion thrusters, steady-state equations, 372–376
Cutoff frequencies, microwave ion thrusters, 161–171
Cyclotron frequency, plasma physics, single particle motions, 39–43

Debye sheaths:
floating potential, 87–88
plasma boundary sheaths, 73–75
thickness properties, 83–84
Deep Space missions, 3
flight ion thrusters, 431–440
Density gradient:
hybrid Hall thruster models, magnetic field transport, 369
Kaufman ion thrusters, 145–147
Depletion life models, dispenser cathods in insert plasmas, 293–296
Diagmagnetic drift, magnetic field diffusion, 68–71
Dielectric discharge, radiofrequency (rf) ion thrusters, 157–158

Dielectric materials, Hall thrusters, 325–329
Dielectric-wall Hall thrusters:
  dominant power-loss mechanisms, 347–357
  efficiency of, 359–362
  ionization length and scaling, 335–337
  lifetime analysis, 380–383
  metallic-wall comparisons with, 364–365
  operation, 331–333
Diffusion coefficient:
  ambipolar diffusion, 65–66
  hollow cathodes, orifice region plasma, 271–280
Diffusion-driven particle motion:
  with magnetic fields, 66–71
  without magnetic fields, 60–66
  partially ionized gases, 55–71
Diffusion equation, Fick's law, 61–65
Diffusion thickness, ring-cusp ion thruster models, 114–116
Direct-current-discharge plasma generators:
  basic principles, 91–93
  ion thruster, 100–107
    anode wall ion confinement, 110–117
    discharge chamber:
      neutral and primary densities, 120–124
      power and energy balance, 124–126
    discharge loss, 126–133
    discharge stability, 133–136
    electron confinement, 108–110
    excited neutral production, 117–120
    generalized 0-D ring-cusp model, 102–105
    magnetic multipole boundaries, 105–107
    recycling behavior, 137–142
Discharge chamber:
  neutral and primary densities, 120–124
  power and energy balance, 124–126
  recycling behavior, 137–141
  two-dimensional models, 171–182
  neutral atom model, 172–175
  performance valuation, 179–182
  primary electron motion and ionization, 176–179
Discharge current:
  Hall thruster:
    performance efficiency, 342–345
    potential and current distributions, 339–341
  hollow cathode geometry, 246–248
    barium depletion model, 301–302
    bulk material insert life, 302–304
    orifice region plasma, 275–280
Discharge loss:
  direct-current-discharge plasma generators, 126–133
  Hall thruster performance, dominant power-loss mechanisms, 347–357
  ion thruster plasma generator design, 96–100
  Kaufman ion thrusters, 144–147
  microwave ion thrusters, 167–171
  radiofrequency (rf) ion thrusters, 154–158
Discharge stability, 133–137
Discharge voltage:
  Hall thruster, efficiency, 342–345
  hollow cathode operation, 312–315
  Kaufman ion thrusters, 147
Dispenser cathodes:
  barium depletion model, 298–302
  insert plasmas, lifetime analysis, 293–296
  poisoning of, 304–306
Dispersion relation, microwave ion thrusters, 161–162
Dissipated power, basic principles, 30–32
Distribution function, plasma physics, particle energies and velocities, 44–46
Divergent magnetic field thruster, direct-current-discharge plasma generators, 101–107
Dominant power-loss mechanisms, Hall thruster performance, 347–357
  dielectric-wall Hall thruster efficiency, 359–362
Double ion generation:
  Hall thruster efficiency, 343–345
  ring-cusp ion thruster models, neutral ionization/excitation, 119–120
  two-dimensional discharge chamber models, 180–182
Double sheaths:
  hollow cathodes:
    insert region plasma, 256–270
    plume-region plasma, 287–292

Double sheaths *(cont.)*
plasma boundaries, 84–86
Double-to-single ion content, computation of, 26–27
Downstream reference electron density, ion thruster accelerator grid trajectories, 201–204
Drift velocity, hollow cathode geometry, 246–248

Efficiency, Hall thruster performance models, 341–345
dielectric walls, 359–362
Electrical efficiency, thruster design, 27–30
Electrical propulsion (EP):
defined, 1–2
early applications of, 2–3
electrical thruster types, 3–5
historical background, 2–3
Electrical thrusters:
beam/plume characteristics, 9–10
efficiency, 27–30
force transfer, 18–21
neutral densities and ingestion, 32–34
power dissipation, 30–32
rocket equation, 15–18
specific impulse, 25–27
thrust force, 21–24
types of, 3–4
Electric Propulsion Interactions Code (EPIC), plume emissions:
measurement, 398
sputtering and contamination, 415
Electric thrusters, plume emissions, 394–395
Electrode breakdown, ion thruster accelerator grid high-voltage parameters, 217–218
Electromagnetic thrusters, basic properties, 21
Electron backstreaming, ion thruster accelerator grid, 208–216
Electron bombardment:
direct-current-discharge plasma generators, 91–93
Hall thrusters, dominant power-loss mechanisms, 347–357
Electron-bombardment Ion Thruster Assembly (EITA), flight ion thrusters, 434–440
Electron confinement:
ion thruster plasma generator design, 98–100
0-D ring-cusp model, 108–110
Electron cyclotron resonance heating, microwave ion thrusters, 162–171
Electron distribution, ion thruster plasma generator design, 94–100
Electron-electron collision frequency, particle collisions, 58–60
Electron energy equation:
hollow cathode, plume-region plasma, 285–292
hybrid Hall thruster models, 370–371
Electron energy loss, 467–469
Electron flux, plasma physics, particle energies and velocities, 45–46
Electron heating, hollow cathodes, 247–248
Electron-ion collision frequency, particle collisions, 58–60
Electron-neutral collisions, 60
microwave ion thrusters, 164–171
Electron relaxation times, 479–482
Electron temperature:
discharge chamber neutral and primary densities, 121–124
Hall thrusters:
dominant power-loss mechanisms, 348–357
plasma electron temperature, 357–359
hollow cathode, plume-region plasma, 286–292
hollow cathodes:
insert region plasma, 257–270
orifice region plasma, 273–280
ion thruster plasma generator design, 96–100
microwave ion thrusters, 167–171
primary beam expansion plume models, 406–407
radiofrequency (rf) ion thrusters, 154–158
Electrospray/field emission electric propulsion thruster, basic properties, 4–5
Electrostatic force, ion and Hall thrusters, 20–21

Emitted current, discharge chamber neutral and primary densities, 121–124
Energy balance model:
  discharge chamber, 124–126
  hollow cathodes, insert region plasma, 259–270
  hybrid Hall thruster models, 369–371
Energy conservation, fluid plasma, 51–54
Energy-loss mechanisms, ion thruster plasma generator design, 98–100
Engineering Test Satellite (ETS), 3
  flight ion thrusters, 429–440
Erosion:
  Hall thrusters, lifetime analysis, 380–383
  hollow cathodes, keeper electrode wear and life, 306–309
  ion thruster accelerator grid, 225–235
  plume emissions, solar array interactions, 415–418
Euler-Lagrange equations, primary electron motion and ionization, 176–182
European Space Agency Artemis space craft, flight ion thrusters, 434–440
European Space Agency (Small Mission for Advanced Research in Technology), flight ion thrusters, 440–443
Excitation cross section:
  particle collisions, 57–60
  radiofrequency (rf) ion thrusters, 152–158
  ring-cusp ion thruster models, 117–120
  xenon, 471–474
Excitation reaction rate coefficient:
  Hall thrusters, plasma electron temperature, 358–359
  ion thruster plasma generator design, 97–100
  xenon Maxwellian plasmas, 475–477
Excited neutral ion production, ring-cusp ion thruster models, 117–120
Extended life test (ELT):
  hollow cathodes:
    barium depletion model, 301–302
    orifice region plasma, 280–281
  ion thruster accelerator grid:
    backstreaming limit calculations, 215–216
  keeper erosion, 306–307
  pits-and-grooves erosion, 233–235

Fick's law:
  diffusion equation and, 61–65
  magnetic field diffusion, 68–71
Field emission electric propulsion (FEEP) thrusters, basic properties, 4–5
Flatness parameter:
  discharge chamber power and energy balance, 126
  ion thruster accelerator grid:
    barrel erosion, 231–232
    electron backstreaming, 216
Flight data, plume emissions, 396–398
Flight thrusters:
  Hall thrusters, 440–443
  ion thrusters, 429–440
Floating potential, plasma boundary sheaths, 87–88
Fluid plasma, 46–54
  energy conservation, 51–54
  momentum conservation, 46–48
  particle conservation, 48–51
Force transfer, ion and Hall thrusters, 18–21
Fourier transform, ring-cusp ion thruster models, magnetic multipole boundaries, 106–107
Fowler-Nordheim plot, ion thruster accelerator grid electrodes, hold-off and conditioning, 224
Frictional contributions, fluid plasma energy conservation, 53–54

Gap dimensions, ion thruster accelerator grid expansion and alignment, 206–208
Gas flow rate:
  Hall thruster efficiency, 341–345
  hollow cathodes:
    insert region plasma, 256–270
    orifice region plasma, 276–280
  unit conversions, 463–466
Gaussian beam density, primary beam expansion plume models, 402–407
Gauss's law, ion thruster accelerator grid, electron backstreaming, 211–216
Geometric configuration, hollow cathodes, 248–251
  insert region plasma, 256–270
Geosynchronous satellites, plume emissions, 393–394

Grid models, ion thruster accelerator erosion, 227–229

Hall current, Hall thrusters:
  basic properties, 328–329
  operation, 330–333
Hall-effect thrusters (HETs), classification, 325
Hall thruster:
  basic properties, 4, 325–329
  channel physics and numerical modeling, 365–379
    hybrid models, 366–372
      continuity and energy, 369–371
      ion current, 371–372
      magnetic field transport, 369
      transverse electron transport, 366–369
    lifetime analysis, 379–383
    oscillations, 376–379
    steady-state models, 372–376
  efficiency measurements, 28–30
  flight thrusters, 440–443
  force transfer, 18–21
  geometry, 6–9
  lanthanum hexaboride cathodes, 254–255
  lifetime analysis, 379–383
  operating principles and scaling, 329–341
    crossed-field structure and current, 330–333
    ionization length, 334–337
    potential and current distributions, 337–341
  performance models, 341–365
    dielectric wall efficiency, 359–362
    dielectric wall vs. metallic wall comparison, 364–365
    dominant power loss mechanisms, 347–357
    efficiency, 341–345
    metallic wall TAL efficiency, 363
    multiply charged ion correction, 345–347
    plasma electron temperature, 357–359
  plumes:
    basic properties, 393–395
    flight data, 396–398
    laboratory measurements, 398–400
    measurements, 395–396
    natural gas plumes, 407–408
    payload interactions, 418–422
      microwave phase shift, 418–419
    physical properties, 395–400
    plasma optical emission, 419–422
    primary beam expansion, 400–407
    secondary-ion generation, 408–410
    spacecraft interactions, 410–418
      particle momentum, 412–413
      solar arrays, 415–418
      sputtering and contamination, 413–415
  power dissipation, 32
  thrust properties, 22–24
Heat-exchange terms, fluid plasma energy conservation, 52–54
Helical electron motion, microwave ion thrusters, 163–171
High-frequency oscillations:
  hollow cathode, plume-region plasma, 291–292
  hollow cathodes, keeper electrode wear and life, 307–309
"High power" orbit insertion mode, flight ion thrusters, 432–440
High-temperature regions, Hall thrusters, plasma electron temperature, 358–359
High-voltage parameters, ion thruster accelerator grid, 216–224
  carbon-carbon composites, 221–223
  electrode breakdown, 217–218
  hold-off and conditioning, 224
  molybdenum electrodes, 218–221
  pyrolytic graphite, 223
Hold-off behavior, ion thruster accelerator grid electrodes, 224
Hollow cathodes:
  configurations, 248–251
  geometric properties, 244–245
  historical overview, 243–248
  insert region plasma, 256–270
  keeper electrode wear and life, 306–309
  lifespan testing, 292–306
    barium depletion model, 298–302
    bulk-material inserts, 302–304
    inert plasma, dispenser cathodes, 293–296
    poisoning, 304–306

temperature characteristics, 296–298
operating principles, 309–315
orifice region plasma, 270–281
plume-region plasma, 283–292
thermal models, 281–283
thermionic electron emitter, 251–255
Hot gap, ion thruster accelerator grid expansion and alignment, 206–208
Hybrid two-dimensional ion thruster models, flow diagram, 172–173

Idealized design, ion thruster plasma generator, 93–100
Incident flux, Hall thruster ionization length and scaling, 334–337
Inductive plasma discharge, radiofrequency (rf) ion thrusters, 151–158
Inert gas propellants, ring-cusp ion thruster models, neutral ionization/excitation, 118–120
In-flight measurements, plume emissions, 396–398
Ingestion, electrical thrusters, 32–34
Input power calculations, Hall thrusters, plasma electron temperature, 357–359
Insert region plasma, hollow cathodes, 256–270
Insert temperatures, hollow cathode lifetimes, 296–298
Ion acoustic velocity:
discharge chamber power and energy balance, 126
fluid plasma particle conservation, 51
Hall thrusters, plasma electron temperature, 357–359
hollow cathodes, insert region plasma, 258–270
radiofrequency (rf) ion thrusters, 156–158
Ion beam current:
ion thruster plasma generator design, 94
plume plasma optical emission, 420–422
Ion bombardment:
Hall thrusters:
dominant power-loss mechanisms, 347–357
lifetime analysis, 379–383
hollow cathodes:
barium depletion model, 298–302
keeper electrode wear and life, 306–309
orifice region plasma, 279–280
Ion charge number:
ion thruster accelerator grid, electron backstreaming, 212–216
particle collisions, 58–60
Ion confinement:
microwave ion thrusters, 168–171
radiofrequency (rf) ion thrusters, 156–158
ring-cusp ion thruster models, 110–116
Ion conservation equation, Hall thruster oscillations, 376–379
Ion continuity equations, primary beam expansion plume models, 401–407
Ion current:
hollow cathodes, insert region plasma, 261–270
hybrid Hall thruster models, 371–372
Ion density:
Hall thrusters, dominant power-loss mechanisms, 351–357
hollow cathodes, insert region plasma, 258–270
ion thruster accelerator grid trajectories, 201–204
Ion distribution function, hybrid Hall thruster, ion current, 371–372
Ion energy distribution, hollow cathodes, keeper electrode wear and life, 307–309
Ion exhaust velocity, thrust properties, 22–24
Ion flux:
Hall thrusters:
dominant power-loss mechanisms, 354–357
lifetime analysis, 380–383
hybrid Hall thruster models, transverse electron transport, 367–369
plume emissions, 396–398
Ion generation rate, ion thruster accelerator erosion, 228–229
Ion heating, hollow cathodes, 247–248
Ion-ion collision frequency, particle collisions, 58–60

Ionization cross sections, 471–474
Ionization energy loss, hybrid Hall thruster models, 370–371
Ionization potential, discharge chamber power and energy balance, 125–126
Ionization reaction rates, xenon Maxwellian plasmas, 475–477
Ionization region:
  discharge chamber model, 172–182
    two-dimensional models, 176–182
  Hall thruster operation, 334–337
  hollow cathodes:
    orifice region plasma, 272–280
    plume-region plasma, 285–292
  ion thruster plasma generator design, 93–100
  Kaufman ion thrusters, 146–147
  radiofrequency (rf) ion thrusters, 152–158
Ion Larmor radius, Hall thruster operation, 331–333
Ion plasma density, two-dimensional discharge chamber models, 180–182
Ion production cost, ion thruster accelerator grid, backstreaming limit calculations, 213–216
Ion source term, primary electron motion and ionization, 177–182
Ion thrusters:
  accelerator grid:
    accelerator basics, 196–200
    basic properties, 189–190
    configurations, 190–196
    electron backstreaming, 208–216
    high-voltage considerations, 216–224
      carbon-carbon composite materials, 221–223
      electrode breakdown, 217–218
      hold-off and conditioning, 224
      molybdenum electrodes, 218–221
      pyrolytic graphite, 223
    lifespan, 225–235
      barrel erosion, 230–232
      grid models, 227–229
      pits-and-grooves erosion, 232–235
    optics, 200–208
      grid expansion and alignment, 206–208
      ion trajectories, 200–204
      perveance limits, 204–206
  flight thrusters, 429–440
  plasma generators:
    basic properties, 4, 91–93
    DC electron-discharge system, 100–102
    discharge chamber:
      neutral and primary densities, 120–124
      power and energy balance, 124–126
      two-dimensional computer models, 171–182
    discharge loss, 126–133
    discharge stability, 133–137
    electron confinement, 108–110
    excited neutral production, 117–120
    force transfer, 18–21
    geometry, 6–7
    idealized design, 93–100
    ion confinement, 110–116
    Kaufman ion thrusters, 142–147
    magnetic multipole boundaries, 105–107
    microwave ion thrusters, 158–171
    particle collisions, 56–60
    performance efficiency, 27–30
    power dissipation, 30–32
    radiofrequency ion thursters, 148–158
    recycling behavior, 137–142
    0-D ring-cusp model, 102–105
      limitations, 141–142
  plumes:
    basic properties, 393–395
    flight data, 396–398
    laboratory measurements, 398–400
    measurements, 395–396
    neutral gas plumes, 407–408
    payload interactions, 418–422
      microwave phase shift, 418–419
    physical properties, 395–400
    plasma optical emission, 419–422
    primary beam expansion, 400–407
    secondary-ion generation, 408–410
    spacecraft interactions, 410–418
      particle momentum, 412–413
      solar arrays, 415–418
      sputtering and contamination, 413–415

Japan Aerospace Exploration Agency (JAXA), flight ion thrusters, 435–440
Jet power, thrust properties, 21–24

Kaufman ion thruster:
  basic properties, 142–147
  direct-current-discharge plasma generators, 102
  flight ion thrusters, 434–440
Keeper electrodes:
  bias voltage, discharge loss, 127–133
  Hall thruster performance efficiency, 342–345
  hollow cathodes:
    geometry, 246–248
    operating principles, 309–315
  lifetime analysis, 306–309
Knudsen-flow models, discharge chambers, 173–175

Laboratory plume measurements, 398–400
Lagrangian algorithm, primary beam expansion plume models, 405–407
Landau damping, fluid plasma energy conservation, 54
Langmuir condition:
  hollow cathode, plume-region plasma, 287–292
  plasma double sheaths, 85–86
Langmuir probe, plume emissions, solar array interactions, 416–418
Lanthanum hexaboride:
  Hall thrusters, lifetime analysis, 379–383
  hollow cathodes:
    bulk material insert life, 302–304
    poisoning of, 305–306
    thermionic electron emission, 254–255
Larmor radius:
  Hall thruster operation, crossed-field structure and the Hall current, 330–333
  Kaufman ion thrusters, 143–147
  microwave ion thrusters, 163–171
  plasma physics, single particle motions, 40–43
  0-D ring-cusp model, electron confinement, 108–110
Lattice atoms, hollow cathodes, barium loss rates, 294–296
Life demonstration test (LDT), hollow cathodes:
  barium depletion model, 298–302
  bulk-material inserts, 302–304
  inert plasma, dispenser cathodes, 293–296
  insert life analysis, 292–306
  orifice region plasma, 279–281
  poisoning, 304–306
  temperature characteristics, 296–298
Lifetime analysis:
  extended life test:
    hollow cathodes:
      barium depletion model, 301–302
      orifice region plasma, 280–281
    ion thruster accelerator grid:
      backstreaming limit calculations, 215–216
      pits-and-grooves erosion, 233–235
  Hall thrusters, 379–383
  hollow cathodes:
    barium depletion model, 298–302
    bulk material inserts, 304–306
    keeper electrodes, 306–309
    thermionic electron emission, 255
  inert plasmas, dispenser cathodes, 293–296
  ion thruster accelerator grid, 225–235
    barrel erosion, 230–232
    grid models, 227–229
    pits-and-grooves erosion, 232–235
Linearization, fluid plasma particle conservation, 49–51
Lorentz equation, two-dimensional discharge chamber model, primary electron motion and ionization, 176–182
Lorentz force:
  fluid plasma, momentum conservation, 46–48
  ion and Hall thrusters, 20–21
  plasma physics, single particle motions, 39–43
Loss rates, barium cathodes, lifetime analysis, 293–296
Low-frequency oscillation, Hall thruster, 377–379

Mach number, hollow cathode, plume-region plasma, 286–292
Magnetic field electron transport, hybrid Hall thruster models, 369
Magnetic-layer thrusters, classification, 325
Magnetic mirror, plasma physics, single particle motions, 43
Magnetic multipole boundaries, ion thruster plasma generators, 0-D ring-cusp model, 105–107
Magnetized electrons, Hall thruster operation, 331–333
Magnetoplasmadynamic (MPD) thruster, basic properties, 5
Mass-conservation equations, fluid plasma particle conservation, 48–51
Mass ratio, plasma boundary sheaths, 72–73
Mass utilization efficiencies:
  dielectric-wall Hall thrusters, 361–362
  discharge chamber neutral and primary densities, 120–124
  discharge loss, 131–134
  Hall thruster:
    ionization length and scaling, 336–337
    performance models, 343–345
  Hall thruster operation, 334–337
  ion thruster plasma generator design, 98–100
  microwave ion thrusters, 167–171
  radiofrequency (rf) ion thrusters, 156–158
  recycling behavior, 139–141
Maximum magnetic field strength, ring-cusp ion thruster models, ion confinement, 114–116
Maxwellian distribution:
  discharge loss, 127–133
  discharge stability, 134–137
  Hall thrusters, dominant power-loss mechanisms, 348–357
  hollow cathodes:
    insert region plasma, 256–270
    keeper electrode wear and life, 309
  ionization/excitation reactions, 475–477
  ion thruster accelerator grid trajectories, 201–204
    electron backstreaming, 209–216
  microwave ion thrusters and, 166–171
  radiofrequency (rf) ion thrusters, 151–158
  ring-cusp ion thruster models, 117–120
Maxwellian electron "field particles," 479–482
Maxwell's equations:
  Debye plasma boundary sheaths, 73–75
  fluid plasma particle conservation, 48–51
  ion thruster plasma generator design, electron velocity distribution function, 94–100
  microwave ion thrusters, 159–160
  plasma physics, 38–39
    particle energies and velocities, 44–46
Maxwell three-dimensional magnetic field solver, ring-cusp ion thruster models, 107
Mean collision time, discharge chamber neutral and primary densities, 122–124
Mean confinement time:
  electron confinement, 108–110
  ion thruster plasma generator design, 95–100
Mean free path calculations:
  Hall thrusters, ionization length and scaling, 335–337
  hollow cathode:
    barium depletion model, 300–302
    plume-region plasma, 285–292
  particle collisions, 56–60
Mean ion free path, hollow cathodes, orifice region plasma, 272–280
Metallic-wall Hall thrusters:
  dielectric-wall Hall thruster comparison with, 364–365
  lifetime analysis, 383
  thruster with anode layer (TAL), 363
Microwave ion thrusters, 158–171
Microwave phase shift, plume-payload interactions, 418–419
Miniature Xenon Ion Thruster (MiXI), 439–440
Mirror ratio, microwave ion thrusters, 168–171
Mobility, non-magnetic field diffusion, 60–66
Molybdenum electrodes, ion thruster accelerator grid, 218–221

barrel erosion, 231–232
hold-off and conditioning, 224
Momentum conservation, fluid plasma, 46–48
Momentum equation:
plume emissions:
primary beam expansion models, 400–407
spacecraft interactions, 412–413
primary electron motion and ionization, 177–182
Momentum-transferring collision frequency, hybrid Hall thruster models, transverse electron transport, 367–369
Mono-energetic primary electrons, ion thruster plasma generators, 0-D ring-cusp model, 104–105
Monte-Carlo calculations:
Clausing factor, 483–486
discharge chamber models, 174–182
radiofrequency (rf) ion thrusters, 157–158
two-dimensional discharge chamber model, primary electron motion and ionization, 176–182
Multi-dimensional modeling, discharge chamber, 171–182
Multiply charged ion correction, Hall thruster performance, 345–347
MUSES-C ECR thruster, 170–171

NASA Evolutionary Xenon Thruster (NEXT), flight ion thrusters, 437–440
NASA Glenn Research Center (GRC), flight ion thrusters, 435–440
NASA-173Mv Hall thruster:
basic properties, 329
performance efficiency, 344–345
NASA Solar Electric Propulsion Technology Applications Readiness (NSTAR):
direct-current-discharge plasma generators, 102
discharge chamber models, 174–182
discharge loss, 131–133
electron backstreaming, 210–216
flight ion thruster, 430–440
hollow cathodes:
barium depletion model, 301–302
insert region plasma, 256–270
keeper electrode wear and life, 307–309
orifice region plasma, 271–280
thermal models, 281–283
lifetime analysis, 226–235
barrel erosion, 230–232
insert temperatures, 297–298
perveance limit, 205–206
plume emissions flight data, 396–398
primary electron motion and ionization, 176–182
ring-cusp ion thruster models, ion confinement, 116
throttle table, 432
two-dimensional discharge chamber model, 179–182
Net flux calculations:
Hall thrusters, dominant power-loss mechanisms, 354–357
hollow cathodes, barium loss rates, 295–296
Neutral atom model, discharge chamber, 172–175
Neutral gas density:
discharge chambers, 120–124
two-dimensional models, 174–182
electrical thrusters, 32–34
Hall thruster operation, 334–337
hollow cathode, 249–251
insert region plasma, 263–270
orifice region plasma, 276–280
plume-region plasma, 283–292, 285–292
ion thruster accelerator grid, erosion models, 227–229
ion thruster plasma generator design, 94
microwave ion thrusters, 167–171
plume emissions, 407–408
plume plasma optical emission, 420–422
radiofrequency (rf) ion thrusters, 149–158
recycling behavior, 137–141
view-factor model, 172–182
Neutral gas excitation, ion thruster plasma generator design, 93–100

Neutral gas temperatures, discharge stability, 133–137
Neutral ion production:
hybrid Hall thruster models, continuity and energy, 369–371
ring-cusp ion thruster models, 117–120
Neutral particle conservation equation, Hall thruster oscillations, 376–379
Neutral particle velocity:
Hall thruster:
ionization length and scaling, 334–337
oscillations, 377–379
hollow cathode, orifice region plasma, 276–280
Newton's second law, ion and Hall current force, 20–21
Nomenclature table, 447–448
Non-contact temperature measurement, hollow cathode lifetimes, 296–298
Non-magnetic diffusion and mobility, partially ionized gases, 60–66
ambipolar diffusion, 65–66
Fick's law, 61–65
Non-Maxwellian distribution function:
discharge loss, 132–133
hybrid ion thrusters, steady-state equations, 374–376
ion thruster plasma generator design, 100
Non-uniform plasmas, 0-D ring-cusp model, 141–142
North-south station keeping, plume emissions, 393–394
Nuclear Electric Xenon Ion Thruster System (NEXIS):
discharge loss, 130–134
flight ion thrusters, 437–440
hollow cathode geometry, 245–248
barium depletion model, 301–302
plume-region plasma, 283–292
hollow cathodes, insert region plasma, 262–270
ion thruster accelerator grid, electron backstreaming, 216
plume emissions, sputtering and contamination, 413–415
primary beam expansion plume models, 405–407
recycling behavior, 139–141
ring-cusp ion thruster models, 107
electron confinement, 109–110
Numerical modeling, Hall thruster, 365–379
hybrid models, 366–372
continuity and energy, 369–371
ion current, 371–372
magnetic field transport, 369
transverse electron transport, 366–369
lifetime analysis, 379–383
oscillations, 376–379
steady-state models, 372–376

Ohmic heating, particle collisions, 59–60
Ohm's law:
hollow cathode, insert region plasma, 269–270
hybrid Hall thruster models, 366–372
transverse electron transport, 366–369
particle collisions, 59–60
On-axis potentials:
electron backstreaming, ion thruster accelerator grid, 208–216
Hall thruster potential and current distributions, 338–341
One-dimensional models:
Hall thrusters, 365–366
hollow cathodes, plume-region plasma, 283–292
hybrid Hall thrusters, steady-state equations, 372–376
Optics codes, ion thruster accelerator grid, 200–208
barrel erosion, 230–232
grid expansion and alignment, 206–208
ion trajectories, 200–204
perveance limits, 204–206
pits-and-grooves erosion, 232–235
Orifice dimensions, hollow cathode geometry, 248–251
orifice region plasma, 271–280
Orifice heating, hollow cathodes, 247–248
Oscillations:
fluid plasma particle conservation, 50–51
Hall thrusters, 376–379
hollow cathode operation, 313–315
Over-perveance, ion thruster accelerator grid trajectories, 202–204
O-waves, microwave ion thrusters, 160–161

Oxide cathodes, thermionic electron emission, 252–255

Parallel electron velocity, microwave ion thrusters, 163–171
Park's formula, primary beam expansion plume models, 405–407
Partially ionized gas diffusion, plasma physics, 54–71
  collisions, 55–60
  diffusion and mobility, 60–66
    ambipolar diffusion, 65–66
    Fick's law, 61–65
  with magnetic field diffusion, 66–71
    ambipolar B particle diffusion, 69–71
Particle conservation, fluid plasma, 48–51
Particle energies and velocities:
  ion thruster plasma generators, 0-D ring-cusp model, 103–105
  Kaufman ion thrusters, 142–147
  plasma physics, 43–46
Particle gyration, plasma physics, 41–43
Particle-in-cell (PIC) model:
  Hall thruster, 365–366
  ion current, 371–372
  ion thruster accelerator grid trajectories, 202–204
  plume emissions:
    primary beam expansion models, 405–407
    secondary-ion generation, 408–410
Particle-pushing algorithm, primary electron motion and ionization, 176–182
Particle simulation, two-dimensional discharge chamber model, 176–182
Paschen breakdown mechanism, molybdenum electrodes, ion thruster accelerator grid, 219–221
Path length calculations:
  hollow cathodes:
    insert region plasma, 256–270
    orifice region plasma, 272–280
  ion thruster accelerator grid, erosion models, 229
Payload interactions, plume emissions, 418–422
  microwave phase shift, 418–419
  plasma optical emissions, 419–422
Peak electron temperature, Hall thrusters, 358–359
Penetration distance, particle collisions, 56–60
Performance models:
  discharge loss, 130–133
  Hall thruster, 341–365
    dielectric wall efficiency, 359–362
    dielectric wall vs. metallic wall comparison, 364–365
    dominant power loss mechanisms, 347–357
    efficiency, 341–345
    metallic wall TAL efficiency, 363
    multiply charged ion correction, 345–347
    plasma electron temperature, 357–359
  ion thruster discharge chamber, two-dimensional models, 179–182
  ion thruster plasma generator efficiency, 27–30
Perpendicular electron mobility:
  hybrid Hall thruster models:
    continuity and energy, 369–371
    transverse electron transport, 367–369
  magnetic field diffusion, 67–71
Perturbed electron current density, microwave ion thrusters, 160–161
Perveance limit, ion thruster accelerator grid, 204–206
Phillips type S thruster, hollow cathodes, thermionic electron emission, 252–255
Pits and grooves erosion, ion thruster accelerator grid, lifetime analysis, 225–235
Plasma ball definition, hollow cathode, plume-region plasma, 287–292
Plasma contactors, plume emissions, 419–422
Plasma currents, plume emissions, solar array interactions, 415–418
Plasma density:
  discharge chamber power and energy balance, 126
  Fick's law, 62–65
  Hall thruster operation, 333
  hollow cathodes:
    geometry, 245–251

Plasma density *(cont.)*
insert region plasma, 262–270
orifice region plasma, 273–280
oscillation patterns, 313–315
hybrid ion thrusters, steady-state equations, 374–376
ion thruster plasma generator design, 94–100
Kaufman ion thrusters, 144–147
microwave ion thrusters, 162–171, 165–171
plume emissions, 396–398
Plasma electron temperature, Hall thrusters, 357–359
Plasma frequency, fluid plasma particle conservation, 48–51
Plasma generators, thruster efficiency, 27–30
Plasma ion flux, hollow cathodes, barium loss rates, 295–296
Plasma optical emission, plume-payload interactions, 419–422
Plasma physics:
boundary sheaths, 71–88
Child-Langmuir sheaths, 79–81
Debye sheaths, 73–75
double sheaths, 84–86
generalized sheath solution, 81–84
pre-sheaths, 76–79
summary of effects, 86–88
fluid plasma, 46–54
energy conservation, 51–54
momentum conservation, 46–48
particle conservation, 48–51
hollow cathodes:
insert region plasma, 256–270
orifice region plasma, 270–281
overview, 37–38
partially ionized gas diffusion, 54–71
collisions, 55–60
diffusion and mobility, 60–66
ambipolar diffusion, 65–66
Fick's law, 61–65
with magnetic field diffusion, 66–71
ambipolar B particle diffusion, 69–71
particle energies and velocities, 43–46
single particle motions, 39–43
Plasma potential:
discharge stability, 134–137
Hall thrusters, dominant power-loss mechanisms, 354–357
hollow cathodes:
barium depletion model, 298–302
bulk-material insert life, 302–304
geometry, 245–248
keeper electrode wear and life, 307–309
ion thruster accelerator grid, electron backstreaming, 209–216
Kaufman ion thrusters, 144–147
microwave ion thrusters, 165–171
radiofrequency (rf) ion thrusters, 153–158
recycling behavior, 139–141
Plasma regions, hollow cathode geometry, 243–248
Plate-and-ball testing, molybdenum electrodes, ion thruster accelerator grid, 219–221
Plume emissions:
hollow cathode operation, 311–315
ion and Hall thrusters:
basic properties, 393–395
flight data, 396–398
laboratory measurements, 398–400
measurements, 395–396
natural gas plumes, 407–408
payload interactions, 418–422
microwave phase shift, 418–419
physical properties, 395–400
plasma optical emission, 419–422
primary beam expansion, 400–407
secondary-ion generation, 408–410
spacecraft interactions, 410–418
particle momentum, 412–413
solar arrays, 415–418
sputtering and contamination, 413–415
Plume-region plasma, hollow cathodes, 283–292
Poiseuille flow rate, hollow cathodes, orifice region plasma, 273–280
Poisoning, hollow cathodes:
lifetime analysis, 304–306
thermionic electron emission, 254–255
Poisson's equation:

Debye plasma boundary sheaths, 74–75
electron backstreaming, ion thruster accelerator grid, 208–216
force transfer, 18–21
plume emissions, secondary-ion generation, 409–410
Positive-going anode sheath:
discharge stability, 135–137
Hall thrusters, dominant power-loss mechanisms, 351–357
Potential distribution, Hall thruster operation, 337–341
Potential drop, ion thruster plasma generators, 0-D ring-cusp model, 103–105
Power balance model:
Hall thrusters, plasma electron temperature, 357–359
hollow cathode, insert region plasma, 264–270
Power dissipation:
basic principles, 30–32
discharge chamber energy balance, 124–126
Power processing unit (PPU), flight ion thrusters, 431–440
Power supplies:
direct-current-discharge plasma generators, 92–93
Hall thruster potential and current distributions, 340–341
ion thruster plasma generators:
electrode breakdown, 217–218
0-D ring-cusp model, 105
Predator-prey oscillations:
Hall thrusters, 377–379
hollow cathode operation, 313–315
Pre-sheath potential, plasma boundary sheaths, 76–79
Pressure gradient force:
fluid plasma, momentum conservation, 46–48
hollow cathodes, insert region plasma, 257–270
Pressure increase, recycling behavior, 139–141
Primary beam expansion, plume models, 400–407
Primary electron densities:
discharge chambers, 120–124
two-dimensional models, 176–182
discharge loss, 132–133
discharge stability, 133–137
Hall thruster potential and current distributions, 339–341
ion thruster plasma generator design, 100
Kaufman ion thrusters, 145–147
0-D ring-cusp model, 108–110
Propellant flow rate:
ring-cusp ion thruster models, neutral ionization/excitation, 119–120
thruster efficiency, 28–30
Propellant mass:
rocket equation, 17–18
thrust properties, 21–24
Pulsed plasma thruster (PPT), 440–443
basic properties, 5
Purity standards, hollow cathode poisoning and, 254–255
Pyrolytic graphite, ion thruster accelerator grid electrodes, 223

Quasi-neutral plasma:
boundary sheaths, 71–73
discharge chamber power and energy balance, 126
Hall thrusters, dominant power-loss mechanisms, 353–357
ion thruster plasma generator design, 95–100
radiofrequency (rf) ion thrusters, 152–158

Radial confinement, microwave ion thrusters, 168–171
Radial magnetic field thruster:
basic properties, 329
direct-current-discharge plasma generators, 101–107
ionization length and scaling, 335–337
Radial plasma potential profile, hollow cathodes, keeper electrode wear and life, 308–309
Radial velocity, primary beam expansion plume models, 402–407
Radiation emissions, microwave ion thrusters, 165–171

Radio-frequency Ion Thruster Assembly (RITA), flight ion thrusters, 434–440
Radiofrequency (rf) ion thrusters (RIT):
  basic properties, 148–158
  flight ion thrusters, 437–440
Randolph's formula, primary beam expansion plume models, 405–407
Reaction rate coefficient:
  Hall thruster ionization length and scaling, 334–337
  ion thruster plasma generator design, 96–100
  particle collisions, 57–60
  ring-cusp ion thruster models, neutral ionization/excitation, 118–120
Recycling behavior, ion thruster design, 137–141
Refractory metals, hollow cathodes, thermionic electron emission, 251–255
Remote sensor unit (RSU), plume emissions, 396–398
Resistivity, hollow cathode:
  insert region plasma, 259–270
  plume-region plasma, 290–292
Resistojets, basic properties, 4
Retarding potential analyzer (RPA) data, plume emissions, 399–400
  secondary-ion generation, 410
Richardson coefficients, thermionic electron emission, hollow cathodes, 252–255
Richardson-Dushman equation, thermionic electron emission, hollow cathodes, 251–255
Ring-cusp thrusters, discharge chamber stability, 136–137
Rocket equation, electric thrusters, 15–18

Saddle-point magnetic field, ring-cusp ion thruster models, ion confinement, 115–116
Samarium cobalt (SmCo) magnets, microwave ion thrusters, 170–171
Sapphire fiber optic probes, hollow cathode lifetime measurements, 297–298
Scaling parameters, Hall thruster operation, 334–337
Schottky effect, thermionic electron emission, hollow cathodes, 251–255
Screen current-to-beam current ratio, perveance limit, 205–206
Screen supply, ion thruster plasma generators, 0-D ring-cusp model, 105
Secondary electron temperature, two-dimensional discharge chamber model, 179–182
Secondary electron yield:
  dielectric-walll Hall thruster efficiency, 362–365
  Hall thrusters, dominant power-loss mechanisms, 348–357
Secondary ion measurements, plume emissions, 398, 408–410
Self-heating mechanisms, hollow cathodes, 247–248
  plume-region plasma, 283–292
Sheath potentials, Hall thruster performance, dominant power-loss mechanisms, 347–357
Sheath voltage, hollow cathodes:
  barium depletion model, 298–302
  insert region plasma, 260–270
Single particle motions, plasma physics, 39–43
Slab geometry, Fick's law, 63–65
SMART-1 mission, 3
Solar arrays, plume emissions:
  plasma ineractions with, 415–418
  spacecraft interactions, 411–418
Solenoidal thrusters:
  direct-current-discharge plasma generators, 101–107
  radiofrequency (rf) ion thrusters, 155–158
Space-charge-limited current flow, plasma double sheaths, 85–86
Space charge-limited electron emission, Hall thrusters, dominant power-loss mechanisms, 352–357
Spacecraft, rocket equation, 15–18
Spacecraft interactions, plume emissions, 410–418
  particle momentum, 412–413
  solar arrays, 415–418
  sputtering and contamination, 413–415

Space Experiments with Particle Accelerators (SEPAC), plume plasma optical emission, 419–422
Space Station Contactor (SSC) cathode:
barium depletion model, 301–302
lifetime measurements, 297–298
Space Technology Experiment Satellite (STEX), flight thrusters, 440–443
Specific impulse (Isp):
basic principles, 25–27
Spot-knocking, ion thruster accelerator grid, molybdenum electrodes, 219–221
Spot mode, hollow cathode operation, 311–315
Sputtering yield:
Hall thrusters, lifetime analysis, 380–383
plume emissions, spacecraft interactions, 413–415
Standard gas law, electrical thruster density and ingestion, 32–34
Stationary plasma thrusters (SPTs):
classification, 325
dielectric-wall efficiency, 361–362
flight thrusters, 440–443
ionization length and scaling, 336–337
lifetime analysis, 380–383
performance efficiency, 344–345
plume emissions, sputtering and contamination, 414–415
plume emissions measurement, 398
steady-state equations, 372–376
Stay-out zones, plume emissions, sputtering and contamination, 413–415
Steady-state equations:
Fick's law and, 64–65
hollow cathode:
insert region plasma, 268–270
orifice region plasma, 272–280
plume-region plasma, 284–292
hybrid Hall thruster models, 372–376
ion current, 366–372
plume models, primary beam expansion models, 400–407
Surface-accommodated ions, plume emissions, spacecraft interactions, 413
Surface particle analysis, hollow cathodes, barium evaporation, 294–296
Symbols table, 458–461
Taylor series, pre-sheath potential, 77–79
Temperature effects:
barium depletion model, 298–302
hollow cathodes:
bulk material insert life, 302–304
thermionic electron emission, 252–255
Term definitions, 450–451
Thermal conductivity, fluid plasma energy conservation, 52–54
Thermal contributions, fluid plasma energy conservation, 53–54
Thermal expansion, ion thruster accelerator grid, 206–208
Thermalization, discharge chamber neutral and primary densities, 122–124
Thermalization times, 479–482
Thermalized potential, hybrid Hall thruster models, magnetic field transport, 369
Thermal models, hollow cathodes, 281–283
Thermionic electron emission, hollow cathodes, 251–255
poisoning effects, 304–306
Three-dimensional models:
discharge chambers, 174–182
primary electron motion and ionization, 176–182
Threshold voltage vs. gap measurements, ion thruster accelerator grid electrodes:
carbon-carbon electrodes, 222–223
molybdenum electrodes, 219–221
pyrolytic graphite, 223
Thrust, basic properties of, 21–24
Thrust-beam plasma potential, Hall thruster potential and current distributions, 338–341
Thrust correction factor, 24
Thruster mass utilization efficiency:
basic principles, 27–30
specific impulse, 25–27
Thruster with anode layer (TAL):
basic properties, 326–329
dielectric-wall Hall thruster comparison with, 364–365
dominant power-loss mechanisms, 355–357
flight thrusters, 440–443
lifetime analysis, 3833

Thruster with anode layer (TAL) *(cont.)*
metallic-wall efficiency, 363
Time dependent function:
Fick's law, 62–65
recycling behavior, 138–141
Total collision frequency, Hall thruster operation, 331–333
Total discharge power, dielectric-wall Hall thruster efficiency, 361–362
Total energy flux, fluid plasma energy conservation, 51–54
Total ion beam current:
Hall thruster, multiply charged ion corrections, 346–347
ring-cusp ion thruster models, density calculations, 119–120
Total ion density, plume emissions, 395–396
Total plasma density, Hall thruster, multiply charged ion corrections, 346–347
Total voltage effect, molybdenum electrodes, ion thruster accelerator grid, 219–221
Trajectories, ion thruster accelerator grid, optics codes, 200–204
Transverse electron transport, hybrid Hall thruster models, 366–369
Transverse velocity:
plasma physics, single particle motions, 41–43
ring-cusp ion thruster models, ion confinement, 111–116, 113–116
Traveling-wave tubes (TWT), microwave ion thrusters, 170–171
Trough contours, hollow cathode, plume-region plasma, 291–292
Tungsten matrix, hollow cathodes, thermionic electron emission, 252–255
Two-dimensional models:
Hall thrusters, 365–366
hollow cathode:
insert region plasma, 268–270
plume-region plasma, 283–292
thermal models, 281–283
hybrid Hall thrusters, steady-state equations, 372–376
ion thruster accelerator grid, electron backstreaming, 215–216
ion thruster discharge chamber, 171–182
neutral atom model, 172–175
performance evaluation, 179–182
primary electron motion and ionization, 176–179

Ultraviolet photon, plume plasma optical emission, 420–422
Under-perveance, ion thruster accelerator grid trajectories, 202–204
Uniform plasma, ion thruster plasma generators, 0-D ring-cusp model, 104–105
Uniform vertical magnetic field, plasma physics, single particle motions, 41–43
Upstream reference electron density, ion thruster accelerator grid trajectories, 201–204

Vacuum applications, hollow cathodes, thermionic electron emission, 252–255
Vacuum potential, hollow cathode operation, 309–315
Vacuum region, ion thruster accelerator grid, electron backstreaming, 212–216
Variables table, 451–458
Velocity volume element, plasma physics, 45–46
View-factor model, discharge density, 172–182
Vlasov equation, hybrid Hall thruster, ion current, 371–372

Wall-scattering frequency, hybrid Hall thruster models, transverse electron transport, 368–369
Wirz-Katz model, discharge chambers, 180–182
Work function, thermionic electron emission, hollow cathodes, 251–255

Xenon ionization cross-sections, 471–474
Xenon Ion Propulsion System (XIPS), 3
direct-current-discharge plasma generators, 102
ion thrusters, 429–440

plume plasma optical emission, 419–422
Xenon ion thrusters, direct-current-discharge plasma generators, 102
Xenon thrusters, specific impulse, 25–27

0-D ring-cusp model:
discharge loss, 133
discharge stability, 134–137
electron confinement, 108–110
ion thruster plasma generators, 102–105
limitations, 141–142
magnetic multipole boundaries, 105–107
microwave ion thrusters, 165–171
radiofrequency (rf) ion thrusters, 156–158

Fundamentals of Electric Propulsion: Ion and Hall Thrusters
by Dan M. Goebel and Ira Katz
Copyright © 2008 John Wiley & Sons, Inc.

JPL SPACE SCIENCE AND TECHNOLOGY SERIES

Joseph H. Yuen, Editor-in-Chief

Published Titles in this Series

1. *Fundamentals of Electric Propulsion: Ion and Hall Thrusters*
   Dan M. Goebel and Ira Katz